Handbook of Surface Plasmon Resonance
2nd Edition

Published on 24 May 2017 on http://pubs.rsc.org | doi:10.1039/9781788010283-FP001

View Online

Published on 24 May 2017 on http://pubs.rsc.org | doi:10.1039/9781788010283-FP001

View Online

Handbook of Surface Plasmon Resonance

2nd Edition

Published on 24 May 2017 on http://pubs.rsc.org | doi:10.1039/9781788010283-FP001

Edited by

Richard B. M. Schasfoort
University of Twente, Enschede, The Netherlands
Email: r.b.m.schasfoort@utwente.nl





View Online

Published on 24 May 2017 on http://pubs.rsc.org | doi:10.1039/9781788010283-FP001

Print ISBN: 978-1-78262-730-2
PDF eISBN: 978-1-78801-028-3
EPUB eISBN: 978-1-78801-139-6

A catalogue record for this book is available from the British Library

© The Royal Society of Chemistry 2017

All rights reserved

Apart from fair dealing for the purposes of research for non-commercial purposes or for private study, criticism or review, as permitted under the Copyright, Designs and Patents Act 1988 and the Copyright and Related Rights Regulations 2003, this publication may not be reproduced, stored or transmitted, in any form or by any means, without the prior permission in writing of The Royal Society of Chemistry or the copyright owner, or in the case of reproduction in accordance with the terms of licences issued by the Copyright Licensing Agency in the UK, or in accordance with the terms of the licences issued by the appropriate Reproduction Rights Organization outside the UK. Enquiries concerning reproduction outside the terms stated here should be sent to The Royal Society of Chemistry at the address printed on this page.

Whilst this material has been produced with all due care, The Royal Society of Chemistry cannot be held responsible or liable for its accuracy and completeness, nor for any consequences arising from any errors or the use of the information contained in this publication. The publication of advertisements does not constitute any endorsement by The Royal Society of Chemistry or Authors of any products advertised. The views and opinions advanced by contributors do not necessarily reflect those of The Royal Society of Chemistry which shall not be liable for any resulting loss or damage arising as a result of reliance upon this material.

The Royal Society of Chemistry is a charity, registered in England and Wales, Number 207890, and a company incorporated in England by Royal Charter (Registered No. RC000524), registered office: Burlington House, Piccadilly, London W1J 0BA, UK, Telephone: +44 (0) 207 4378 6556.

Visit our website at www.rsc.org/books

Printed in the United Kingdom by CPI Group (UK) Ltd, Croydon, CR0 4YY, UK

Published on 24 May 2017 on http://pubs.rsc.org | doi:10.1039/9781788010283-FP005

Foreword to the 1st Edition

Make no bones about it, I love surface plasmon resonance (SPR)-based biosensor technology. After spending three years trying to measure binding constants using analytical affinity chromatography, I immediately saw the benefits of SPR the first time I sat down in front of a Biacore in 1991. Even today, no comparable technology exists to characterize molecular interactions in real time without labeling in an automated and robust fashion. But as the technology has expanded over the years, I find that there are three general attitudes towards SPR. There are the nay-sayers who hate the technology. There are long-time users who think they are experts. And there are the users who recognize they do not know everything about SPR but are eager to improve their skills.

Ever since the first commercially viable instrument was unleashed in 1990 by the biosensor group at Pharmacia (which was spun out into a separate company called Biacore in 1996, only to be acquired recently by General Electric, which previously bought Amersham who at one time had merged with Pharmacia, so in fact now the biosensor group has come full circle, even though they have always shared the same cafeteria in Uppsala, Sweden), there have been critics of SPR technology. So much so that in 2003 I created a character called ''Dr Evil Pessimist'', who represents a composite of the various detractors of SPR. Dr Pessimist rants and rages about problems he has with the technology, including nonspecific binding, instrument drift, mass transport and avidity effects. He argues that since SPR uses a surface the rate constants we measure will never reflect solution-based binding constants. In fact, much of his resentment of the technology stems from the fact that his experiments fail or his data never fit a simple model.

It has been my experience that there are two primary causes of this SPRaphobia: poor-quality reagents and/or poor experimental design. Perhaps the molecules Dr Pessimist is studying do not in fact interact or the

Handbook of Surface Plasmon Resonance, 2nd Edition
Edited by Richard B. M. Schasfoort
© The Royal Society of Chemistry 2017
Published by the Royal Society of Chemistry, www.rsc.org

View Online

Published on 24 May 2017 on http://pubs.rsc.org | doi:10.1039/9781788010283-FP005

preparations of samples are not active to begin with. Don't shoot the messenger. Dr Pessimist asserts that his proteins are of high quality because they are "a single band on an SDS page gel". He fails to realize that this is not evidence of an active preparation or a conformationally homogeneous sample. I think biosensor experiments are akin to protein crystallography. No structural biologist I know would attempt to crystallize an impure, half-denatured preparation of protein that has precipitated at the bottom of an Eppendorff tube. The sad thing is that garbage into a biosensor will often give complex responses that users misinterpret as some interesting binding event.

I have found that when experiments are designed appropriately with good-quality reagents and data are processed and analyzed properly, binding responses can be routinely fit to a simple interaction model. However, unlike Dr Pessimist, I do not expect to obtain perfect binding responses when I set up experiments on a new interaction. I realize that obtaining high-quality data is an iterative process. In my research group, we usually set up a trial experiment to verify that the binding partners actually interact. Then we will often try different coupling chemistries, surface densities, and/or buffer conditions to optimize surface activity.

And when it comes to the number one complaint about SPR technology (that the surface will automatically change the thermodynamics of the system), what Dr Pessimist fails to realize is that most biosensor experiments do not use a flat surface. Instead, the surface is coated with a dextran layer, which suspends the molecule in solution. We and others have shown with numerous systems that when experiments are performed properly, binding constants (including thermodynamic parameters) measured with SPR do in fact match those obtained from solution-based measurements.

However, I agree with Dr Pessimist in one regard. Since 1991, I have read every paper that reported using a commercial SPR biosensor and Dr Rebecca Rich and I have composed a yearly review of the literature since 1998. This is becoming a fairly daunting task since more than 1000 research papers are published annually. More, unfortunately, is not always better. We find that the data in most biosensor articles are not worth the paper they are printed on. For example, about half the time authors even fail to present figures showing the binding responses and yet they expect us to believe the rate constants they report for their interactions. Without a visual inspection of the data, we have no idea if the experiments were run properly. And oftentimes, even when data are presented, it is clear that the investigators do not know how to utilize the technology properly. Also, while a fundamental dogma of science is to replicate and randomize samples, less than 3% of published biosensor data include replicate injections even within a single experiment. An overlay of replicate injections demonstrates the stability of the reagents and multiple independent experiments yield an average and standard deviation for the reported binding constants, yet this attention to detail in a biosensor experiment is more rare than finding a four-leaf clover in the outfield at Fenway Park. In addition, less than 5% of the authors who

View Online

Published on 24 May 2017 on http://pubs.rsc.org | doi:10.1039/9781788010283-FP005

report kinetic constants include an overlay of the binding response with the fitted model. And finally, even from a brief glance through the literature, it is apparent that the majority of investigators do not understand that the shape of the response profile should be an exponential in both the association and dissociation phases (maybe many users do not even understand what an exponential is). It is no wonder that scientists outside the biosensor use community think SPR technology does not work. I would think the same thing if all I had to rely on was the published data.

You might ask yourself, ''how did it get to this point?'' I often wonder if all scientists are so poorly educated in basic scientific technique (which could actually explain why we haven't found a cure for the common cold). I place the blame on the ''kit mentality'' that was introduced with molecular biology back in the early 1990s, back when we were listening to our Walkmans while typing on our IBM 286 personal computers. Nowadays you can buy a kit to clone, mutate, express and purify a protein. Well, the kit mentality continued when these same investigators got access to commercially available biosensor technology. Since these instruments are so easy to use, anyone can walk up to the machine, chuck in their proteins, collect some response, fit the data and publish the results, believing that the results must be correct because they came out of this very expensive machine. Unfortunately, it actually takes some skill and know-how to set up, execute and analyze a biosensor experiment properly.

This leads me to the next group of biosensor users that give the technology a black eye. These people are the ones who have been using instruments for a long time and think they are experts. I call them ''SPiRts''. SPiRts are even more threatening than Pessimists because their complacency often leads them to perpetuate poor experimental technique. A common SPiRt mistake published in the literature is the use of multivalent analytes in solution (*e.g.* monoclonal antibodies or GST fusion proteins), which can produce avidity effects. All too often, SPiRts present elaborate biological justifications for the shape of their unusual binding profiles when in fact the responses are simply indicative of poor reagent quality and/or inadequate experimental optimization or data processing. Even worse, SPiRts use complex models to describe their poor-quality data. It seems that the latest fad of these model surfers is to apply a conformational change mechanism. ''My data fit a conformational change model, which must mean there is a conformational change, right?'' Wrong!

To set the record straight, in 1994 my colleague and software engineer extraordinaire, Tom Morton (who I refer to as SoftEE), developed the numerical integration approach to data analysis that allows one to apply any interaction model. Before then, we were in the caveman days of linear transformation and, believe me, you don't want to go back there. We were the first to show that a change in conformation that stabilized a bound complex would in fact produce a change in response even though there was no additional change in mass. However, in the intervening 13 years I have never needed to apply this model to describe the responses obtained from

View Online

Published on 24 May 2017 on http://pubs.rsc.org | doi:10.1039/9781788010283-FP005

more than 1000 systems I have examined. The reason I am reluctant to use this model is that typically a data set that fits a conformational change model can be equally well described by other models such as those for ligand and/or analyte heterogeneity. Even more alarmingly, the rates for the supposed conformational changes measured on the biosensor are extremely slow, often with half-lives of 20–60 minutes if you take the time to calculate them. These rates do not make biological sense to me. A quick search of the classical conformational change literature shows that re-organizational events which occur during binding happen on a nanosecond to millisecond time-scale. The hot ''new'' trend with the SPiRts is to fit their biosensor data with a conformational change model and then present crystal structure data of unbound and bound complexes and say ''See, this change in conformation proves it''. But an objective viewer would disagree. The fact that you see a change in conformation in the structure actually may not relate to the complex binding response you are measuring on the biosensor. Don't be fooled by these sleight-of-hand arguments. (What would help confirm the conformational change suggested by SPR would actually be to use a time-resolved structural method such as circular dichroism or fluorescence resonance energy transfer and demonstrate that the time-dependent changes are the same.) The cause of the complex binding response on the biosensor is actually more likely due to surface aggregation, nonspecific binding, molecular crowding, avidity effects or sample heterogeneity.

This brings me to my favorite SPR users, who I refer to as SPiRits. SPiRits are new users or those having some familiarity of biosensor technology who have a deep desire to learn more about its features, applications and potential. They are the ones who are participating in our yearly benchmark studies, which are geared toward calibrating users' experimental technique. They are willing to put in the effort to troubleshoot their systems and want to improve the quality of the data and not just settle for whatever the machine spits out. SPiRits will be the users who develop novel applications and implement new technologies in the future.

We need SPiRits because the number and types of SPR instruments are exploding. An Internet search reveals more than 20 companies developing SPR-based biosensor systems. Lately, biosensor advances have occurred on two fronts. First, many of the recently released instruments (and others currently under development) are dedicated to specific applications ranging from small-molecule drug discovery to the characterization of complex mixtures in the clinical and food sciences. Corning's Epic plate-based system is an example of targeting the technology for screening applications. Second, we have seen a push to increase the throughput of biosensor analyses. In the past few years, the launches of BioRad's ProteOn XPR36 and Biacore's A100 have dramatically impacted the biosensor field since they allow for parallel processing of multiple analytes over multiple targets simultaneously. Array-based platforms represent the next wave in biosensor development. Biacore's Flexchip and instruments being developed by GWC Technologies, Lumera, IBIS Technologies, Genoptics and Maven open up the

View Online

possibility of characterizing hundreds to thousands of interactions at one time. But not surprisingly, these array formats come with their own sets of challenges. The methods used for spotting DNA may not be optimal for producing protein arrays. Clearly, a lot of work remains to be done before protein array systems meet their full potential.

As biosensor applications expand and new instruments are released, the technology's user base also increases. I worry that higher-throughput systems may allow more users simply to generate more bad data faster. So, we clearly need to improve the skill level of both novice and seasoned users.

This book is a great resource to obtain the fundamental knowledge of biosensor technology, and also discover recent developments in both instrumentation and applications. But in order to turn professional, remember that the biosensor is just a tool. Use it wisely. Be skeptical, but keep an open mind. Know when to say when (not all systems are amenable to biosensor analysis). Go forth and become a good ShePaRd of my favorite technology.

David G. Myszka
University of Utah

Published on 24 May 2017 on http://pubs.rsc.org | doi:10.1039/9781788010283-FP005

Published on 24 May 2017 on http://pubs.rsc.org | doi:10.1039/9781788010283-FP010

Foreword to the 2nd Edition

It is a great honor for me to be writing the Foreword to the 2nd edition of the *Handbook of Surface Plasmon Resonance*, not only because of the high caliber of the contributing authors, forming an ''all-star cast'' in the label-free biosensor field, but also because the Foreword to the 1st edition was written by my post-doctoral mentor, Dr David Myszka, to whom I am grateful for giving me the incredible opportunity to work in his laboratory, which launched my career in SPR. In reading his Foreword, I especially relate to his comments regarding the love of SPR due to the truly awesome insight it offers into how molecules interact with one another and how this can be observed in real time and without the need for labeling. Indeed, ''seeing is believing''! Biosensors are devices that use biological molecules such as proteins to detect the presence of other molecules due to their binding interactions. This rather general definition sets ground zero for the myriad of applications that are now made possible on commercial biosensors, which employ SPR or other label-free detection methods, such as biolayer interferometry (BLI), quartz crystal microbalance (QCM), electrical impedance, or microcalorimetry.

I first learned about SPR in 1997 during my PhD studies when I was seeking a quantitative method for assessing the DNA-binding properties of a panel of mutant NFκB constructs, with the project's goal being gene therapy. I had turned to SPR because I was frustrated at the tedium and lack of quantitation associated with other methods, such as gel shift assays. I was instantly hooked by SPR's real-time label-free method and to this day I am passionate about SPR technologies and excited by the versatility of experiments that can be performed quickly, with relative ease, and with minimal sample consumption to answer basic to more exploratory questions about molecular-level interaction analysis. In the early 1990s, the Biacore 2000 was

Handbook of Surface Plasmon Resonance, 2nd Edition
Edited by Richard B. M. Schasfoort
© The Royal Society of Chemistry 2017
Published by the Royal Society of Chemistry, www.rsc.org

View Online

Published on 24 May 2017 on http://pubs.rsc.org | doi:10.1039/9781788010283-FP010

a state-of-the-art SPR platform and variations on this design are still employed today, with next-generation instruments such as the Biacore T200 employing this classic four-channel module. Over the past 20 years, both hardware and software capabilities have evolved in their sophistication, enabling prolific growth of biosensor platforms in the commercial market that was once monopolized by Biacore. The demand for more automated and higher throughput analysis has led to a variety of multiplexed configurations as offered by platforms such as ProteOn XPR36 and Octet/ForteBio, and a host of array-based SPR imagers such as IBIS, Horiba, Reichert, and others. Traditionally, label-free biosensors have been used for binding kinetics, but the scope of their utility has expanded beyond kinetics to any assay that relies on binding specificity. When the first Biacore instrument emerged, it was considered somewhat of a niche biophysical tool, but now SPR biosensors are a mainstay in laboratories worldwide and used routinely in the pharmaceutical industry, drug and biomarker discovery, the food industry, and academic research.

I have been working with SPR and other label-free technologies in the drug discovery industry for over 12 years, and have extensive hands-on experience with them, and perhaps an addiction to data generation. An exciting application that has streamlined the discovery of therapeutic antibodies is epitope binning. An epitope is the region on an antigen that is recognized by an antibody. Some epitopes are involved in an antigen's interactions with its natural binding partners, and most therapeutic antibodies work by interfering with or blocking them. However, since the epitope targeted by an antibody is an innate property of an antibody that cannot be shifted rationally by engineering, and current *in silico* methods cannot design an antibody with a desired epitope specificity, proper epitope selection is empiric and key to the success of a therapeutic program. In an epitope binning assay, a biosensor is used to detect whether two antibodies can bind their specific antigen at the same time, inferring their non-overlapping epitopes, or whether one antibody blocks another, inferring their overlapping epitopes. When epitope binning assay are performed in high throughout, they scale to large combinatorial experiments, enabling antibodies to be sorted into epitope families or ''bins.'' Bin members often share similar functional characteristics, and only a few bins will target therapeutically interesting epitopes, which can be confirmed in lower throughput and more nuanced biological assays. Epitope binning results essentially reveal the ''epitope landscape'' of an antibody panel, which quickly informs decisions on how to whittle it down to a few leads for further characterization. With antibody production being highly commoditized and library selection methods yielding prolific numbers of genetically diverse and viable clones, there is an ever-growing need for analytical tools to meet this capacity. Array-based SPR biosensor platforms enable researchers to perform higher throughput and higher resolution experiments that can differentiate antibodies from one another both functionally and mechanistically, which is necessary in generating superior drugs.

View Online

The chapters contained herein survey a breadth of topics from the fundamentals of understanding the meaning of the SPR curves themselves to a deep-dive exploration into various applications. I hope you will enjoy this book and feel inspired to learn more about the wonderful world of SPR and its endless possibilities, limited only by our imagination.

Yasmina Noubia Abdiche
Rinat, a part of Pfizer's Oncology Research and Development

Published on 24 May 2017 on http://pubs.rsc.org | doi:10.1039/9781788010283-FP010

Published on 24 May 2017 on http://pubs.rsc.org | doi:10.1039/9781788010283-FP013

Preface to the 1st Edition

Editors, authors often claim that completion of their book was a giant, lonesome and tedious task. Often they add, their mission was ''once in a lifetime''. As they say in Germany with a sense of humor, ''Einstein macht noch kein Haus[†]'' meaning that the cooperation of people is in the heart of big achievements. So it has been with our book: all the authors had to find time in their busy life among other important engagements for timely writing activities, for which we cannot say often enough how grateful we are.

This *Handbook of Surface Plasmon Resonance* is the product of an intensive interaction process and is intended for a wide audience: scientists and students intending to use the technology, the wider public interested in SPR as a phenomenon and its application, but also providers of (parts of) the technology. Although the book as a whole covers many aspects of the technology at present spanning a bridge between theory, instrumentation and applications, the chapters are written so as to be comprehensible individually as well. It is hoped that the readers of this book will share our enthusiasm for biomolecular interaction analysis based on SPR technology. We also hope that we have succeeded in revealing the potential of SPR by showing highly exciting and unique opportunities for unraveling the functional relationships of complex biological processes.

Special thanks are also due to the members of the Biochip Group of the MESA+ Institute for Nanotechnology of the University of Twente who have contributed to the book: Stefan Schlautmann and Hans de Boer for technical support and some of the drawings. In addition, we thank Geert Besselink Bianca Beusink, Angelique Lokate, Dietrich Kohlheyer, Ganesh Krishna-moorthy, Dawid Zalewski, Remco Verdoold, Mayke van der Ploeg and Bjorn Harink for their input. This devoted team provided the warm and

[†]Literally: even Einstein could not build a house and the German meaning of ein stein is one stone.

Handbook of Surface Plasmon Resonance, 2nd Edition
Edited by Richard B. M. Schasfoort
© The Royal Society of Chemistry 2017
Published by the Royal Society of Chemistry, www.rsc.org

View Online

inspiring atmosphere of the Biochip Group during the two-year period from the birth of the idea to completion of the manuscript.

The editors would also like to thank Annie Jacob of the Royal Society of Chemistry for her clear guidance and enduring patience throughout the editorial process. Wout van Bennekom is acknowledged for final reading of several chapters.

Richard Schasfoort and Anna Tudos
Enschede and Amsterdam

Published on 24 May 2017 on http://pubs.rsc.org | doi:10.1039/9781788010283-FP013

Published on 24 May 2017 on http://pubs.rsc.org | doi:10.1039/9781788010283-FP015

Preface to the 2nd Edition

After finishing the first edition of the *Handbook of Surface Plasmon Resonance* in 2008, I thought that the book was a ''once in a lifetime'' effort. With objective comments, the book was promoted as follows: ''This excellent handbook provides comprehensive information with easy to use, stand-alone chapters and will be of great use to anyone working with or affiliated to the technology.'' However, after the initial success and many citations in scientific publications, I felt more and more uncomfortable about the timely content of many of the chapters. Additionally, I received signals from scientists that after almost 10 years this now outdated book should be renewed, restyled, and re-edited. I decided to go for it after my keynote lecture entitled ''Overview of 25 years commercial biomolecular interaction analysis'' at the label-free technologies conference in Boston presented coincidentally exactly at π-time (March 14, 2015, at 9 p.m.: 3.14.15.9). At that conference, I collected information from the active label-free technology companies and consulted some leading scientists to write a chapter for the second edition.

During my life I have done many things twice: always the second time was better. For example, in 1995, I founded the company IBIS Technologies, but by 1999 it was almost bankrupt. Since 2012, it gained a second life and it is growing in SPR imaging applications. And now I am Editor of the second edition of the *Handbook of Surface Plasmon Resonance* and it should be better than the first!

This second edition of the *Handbook of Surface Plasmon Resonance* is new to a great extent (~90%) compared with the first edition and there is definitely a better balance between improved optics, fluidics, surface chemistries and applications. It is intended for a wide audience to provide tutorial information for scientists, laboratory technicians, and students using the technology but also for the wider public interested in SPR as a phenomenon and its applications. Although the book as a whole covers many relevant

Handbook of Surface Plasmon Resonance, 2nd Edition
Edited by Richard B. M. Schasfoort
© The Royal Society of Chemistry 2017
Published by the Royal Society of Chemistry, www.rsc.org

View Online

aspects of biomolecular interaction sensing, it is hoped that readers will share my enthusiasm for SPR technology. My co-authors and I also hope that we have succeeded in revealing the potential of label-free technologies for screening new therapeutic lead candidates and providing highly exciting and unique opportunities for unraveling the functional behavior of complex biological processes.

Richard B. M. Schasfoort
Enschede, The Netherlands

Published on 24 May 2017 on http://pubs.rsc.org | doi:10.1039/9781788010283-FP015

Published on 24 May 2017 on http://pubs.rsc.org | doi:10.1039/9781788010283-FP017

To Femke and Nick; Margot, Niels and Lars

View Online

Published on 24 May 2017 on http://pubs.rsc.org | doi:10.1039/9781788010283-FP017

Published on 24 May 2017 on http://pubs.rsc.org | doi:10.1039/9781788010283-FP019

Contents

Chapter 1 Introduction to Surface Plasmon Resonance **1**
Richard B. M. Schasfoort

1.1 Introduction to Surface Plasmon Resonance 1
1.2 What is a Biosensor? 2
1.2.1 A Simple Experiment 3
1.2.2 From Dip to Real-time Measurement 4
1.3 How to Construct an SPR Assay 5
1.3.1 The Steps of an Assay 5
1.3.2 Concentration Determination 9
1.3.3 Determination of Kinetic Parameters 11
1.3.4 Basics of Instrumentation 12
1.4 Kinetics of Biomolecular Interactions 13
1.4.1 Mass Transport-controlled Kinetics 14
1.4.2 Calibration-Free Concentration Analysis (CFCA) 16
1.4.3 Interaction-controlled Kinetics 17
1.4.4 Equilibrium Analysis 19
1.5 Buffer Solutions for Measuring the Analysis Cycle 20
1.5.1 Baseline or System Buffer 20
1.5.2 Regeneration Buffer 21
1.6 SPR-based Immunoassays 22
1.6.1 Direct Assay 22
1.6.2 Competition Assay 22
1.6.3 Inhibition Assay 24
1.6.4 Sandwich Assay with Secondary Antibody and Signal Enhancers 24

Handbook of Surface Plasmon Resonance, 2nd Edition
Edited by Richard B. M. Schasfoort
© The Royal Society of Chemistry 2017
Published by the Royal Society of Chemistry, www.rsc.org

View Online

1.7 How to Read This Book 25
1.8 Questions 25
References 26

Chapter 2 History and Physics of Surface Plasmon Resonance 27
Richard B. M. Schasfoort

2.1 Introduction 27
2.2 History 29
2.2.1 Early History of SPR Biosensors 29
2.2.2 History of SPR Biosensors After 1990 30
2.3 Surface Plasmon Theory 31
2.3.1 The Evanescent Wave 31
2.3.2 Surface Plasmon Dispersion Equations; Resonance 33
2.3.3 Excitation of Surface Plasmons 35
2.3.4 Surface Plasmon Properties 37
2.3.5 Choice of Experimental Parameters 39
2.3.6 Optimizing SPR Imaging Performance 42
2.4 SPR Instrument Optics 46
2.4.1 Fixed Angle 47
2.4.2 Fan-shaped Beam 48
2.4.3 Scanning Angle 50
2.4.4 Grating Coupler 51
2.4.5 Fiber-based SPR Sensors 51
2.4.6 Other Optical Systems 54
2.4.7 SPR Imaging Instruments 55
2.5 Concluding Remarks 56
2.6 Questions 57
References 58

Chapter 3 Surface Plasmon Resonance Instruments 60
Richard B. M. Schasfoort

3.1 Introduction 60
3.2 The Cornerstones of SPR Technology 62
3.3 General Optical Requirements for SPR Instruments 63
3.4 SPR Liquid Handling Systems 65
3.4.1 Cuvette Systems 66
3.4.2 Flow Systems 68
3.5 SPR Instruments: State of the Art 71
3.5.1 Examples of Fan-shaped Beam SPR Instruments 71

Published on 24 May 2017 on http://pubs.rsc.org | doi:10.1039/9781788010283-FP019

View Online

3.5.2 Examples of Fixed- and Scanning-angle SPR Instruments 78
3.5.3 Examples of Other Label-free Biosensing Instruments 84
3.5.4 Examples of SPR Imaging Instruments 89
3.6 Biacore SPR Systems of GE Healthcare 97
3.6.1 Biacore T100, T200, and S200 98
3.6.2 Biacore A100/4000 100
3.6.3 Biacore 8K 101
3.7 Conclusions 102
3.8 Questions 103
References 103

Chapter 4 SPRpages – Getting a Feeling for the Curves 106
J. Arnoud Marquart

4.1 Introduction 106
4.2 The Exponential 106
4.3 A Curve 108
4.3.1 Baseline 108
4.3.2 Association 109
4.3.3 Steady State 109
4.3.4 Dissociation 109
4.3.5 Response Units 109
4.3.6 Equilibrium and Saturation 110
4.3.7 R_{max} Value 110
4.3.8 Curve Response 112
4.3.9 R_{eq} value 112
4.3.10 Time to Reach Equilibrium 113
4.4 Curve Examples 114
4.4.1 Curve Shape 114
4.4.2 Exponential Curve 114
4.4.3 Mass Transport Limitation (MTL) 116
4.4.4 Biphasic Curves 118
4.4.5 Drift, Jumps and Spikes 119
4.5 Experimental Setup 121
4.5.1 Analyte Concentration Range 121
4.5.2 Blank Injections 122
4.5.3 Multi-cycle Kinetics 122
4.5.4 Single-cycle Kinetics 122
4.5.5 Equilibrium Analysis 123
4.5.6 Fast Kinetics 125
4.5.7 Decaying Surface 125

Published on 24 May 2017 on http://pubs.rsc.org | doi:10.1039/9781788010283-FP019

View Online

Published on 24 May 2017 on http://pubs.rsc.org | doi:10.1039/9781788010283-FP019

4.6 Sensorgram Quality 127
4.7 The Affinity Plot; Getting a Feeling for the Numbers 128
4.8 Curve Fitting 128
4.8.1 Residual Plot 130
4.8.2 Local and Global Fitting 131
4.8.3 Deviations from a 1 : 1 Interaction 131
4.9 Interaction Validation 132
4.10 Publications 132
4.10.1 Evaluating Published Results 133
4.10.2 Minimal Requirements for Describing a Biosensor Experiment 134
4.11 SPR Simulation 135
4.11.1 Different Analyte Concentration (Same Kinetics) 136
4.11.2 Different Association Rate (Different Affinity) 137
4.11.3 Different Dissociation Rate (Different Affinity) 137
4.11.4 Different Kinetics (Same Affinity) 139
4.11.5 Different Injection Times (Same Kinetics) 140
4.11.6 Different Dissociation Times (Same Kinetics) 140
4.12 Questions 141
4.13 Glossary 146
References 147

Chapter 5 Detailed Analysis of Kinetic Binding Traces with Distributions of Surface Sites 149
Huaying Zhao and Peter Schuck

5.1 Introduction 149
5.2 The Physical Picture 151
5.3 Calculating Surface Site Distributions 153
5.3.1 Basic Principle 153
5.3.2 Mass Transport Limitation 155
5.3.3 Higher Order Reaction Schemes 157
5.4 Experimental Design 158
5.4.1 Information Content 158
5.4.2 Effect of Sensor Surface 161
5.4.3 Ligand Immobilization Process 161
5.4.4 Analyte Purity 164
5.5 Conclusions 167

View Online

5.6 Questions 167
Acknowledgements 168
References 168

Chapter 6 Surface Chemistry in SPR Technology 171
Erk T. Gedig

6.1 Introduction 171
6.1.1 Interaction Mechanisms on Biosensor Surfaces 172
6.1.2 The Surface Structure: Between Evanescent Field and Analyte Diffusion 175
6.2 The Metal Layer of SPR Sensor Chips 180
6.3 Adhesion Linking Layers for Noble Metals, Inorganic Dielectrics, and Plastics 183
6.3.1 Adhesion Linking Layers for Noble Metal Surfaces 184
6.3.2 Adhesion Linking Layers for Inorganic Dielectrics 186
6.3.3 Adhesion Linking Layers for Plastics and Carbon Surfaces 186
6.4 Bioinert Matrices 187
6.4.1 Non-specific Adsorption of Biomolecules 187
6.4.2 Functionalization Strategies for Ultralow-fouling Two-dimensional Surfaces 189
6.4.3 Bioinert Hydrogels 192
6.5 Choosing the Optimal Nanoarchitecture 194
6.5.1 Two-dimensional Surfaces 195
6.5.2 Three-dimensional Hydrogels 197
6.6 Coupling Procedures for Ligand Immobilization 202
6.6.1 Adsorptive Immobilization 202
6.6.2 Covalent Immobilization 203
6.6.3 Covalent Activation Chemistries 208
6.6.4 Immobilization *via* Molecular Linkers 225
6.6.5 Immobilization of Membrane Proteins 234
6.6.6 Overview and Selection of Immobilization Chemistries 238
6.7 Considerations for Spatially Resolved Immobilization 242
6.8 Conclusions and Outlook 247
6.9 Questions 248
References 249

Published on 24 May 2017 on http://pubs.rsc.org | doi:10.1039/9781788010283-FP019

View Online

Chapter 7 Fragment and Low Molecular Weight Compound Analysis **255**
Robert Karlsson, O. Karlsson and P. Belcher

7.1 Introduction 255
7.2 Assay Formats for Low Molecular Weight Analysis 256
7.2.1 Direct Binding Assay (DBA) 256
7.2.2 Solution Competition or Inhibition in Solution Assay (ISA) 258
7.2.3 Surface Competition Assay (SCA) 258
7.2.4 Selection of Assay Format 258
7.3 Methodology 261
7.3.1 Immobilization of Proteins 262
7.3.2 Immobilization of Small Molecules 266
7.3.3 Protein Activity 267
7.3.4 Compound Solubility and Concentrations in Screening 268
7.3.5 Compound Refractive Index Increment 268
7.3.6 Buffer Selection 268
7.3.7 Sample Preparation 269
7.3.8 Solvent Correction 270
7.3.9 Z', Positive and Negative Controls 271
7.4 Target Considerations 272
7.4.1 GPCRs 272
7.4.2 Kinases 273
7.5 Fragment Screening Workflow 274
7.5.1 Fragment Libraries 274
7.5.2 Clean Screen 274
7.5.3 Binding Level Screen 276
7.5.4 Data Analysis – Report Points and Curve Shapes 276
7.5.5 Affinity Screen 282
7.5.6 Affinity Analysis 282
7.5.7 Site Specificity – Use of Blocked or Saturated Targets 285
7.6 Hit to Lead Workflow 287
7.6.1 Off-rate Screening 287
7.6.2 Lead Optimization 288
7.7 Tips 290
7.8 Questions 290
References 292

Published on 24 May 2017 on http://pubs.rsc.org | doi:10.1039/9781788010283-FP019

View Online

Chapter 8 Combined Antibody Characterization: High-throughput Ranking, Binning, and Mapping 295
Koen Wagner

8.1 General Introduction 295
8.2 Affinity Ranking 296
8.2.1 Experiment 1: Affinity Ranking of Human IgG Binding Hepatitis C Virus E2 Protein 297
8.2.2 Experiment 2: Affinity Ranking of Rabbit IgG Binding MHC–Peptide Complexes 303
8.2.3 Conclusions on Affinity Ranking and Outlook 307
8.3 Epitope Binning 307
8.3.1 Experiment 3: Epitope Binning of Antibodies Binding the Respiratory Syncytial Virus (RSV) Glycoprotein 309
8.3.2 Conclusions on Epitope Binning and Outlook 312
8.4 Epitope Mapping 313
8.4.1 Experiment 4: Epitope Mapping of Anti-RSV G Antibodies Using a Library of Overlapping Peptides 313
8.4.2 Experiment 5: Mapping the Epitope of Anti-human Parecho Virus Antibody AM18 with Alanine Scanning SPR 320
8.4.3 Conclusions on Epitope Mapping and Outlook 323
8.5 General Conclusions and Outlook 324
8.6 Questions 324
References 325

Chapter 9 Treating Raw Data: Software for SPR Applications 328
Noah T. Ditto and Joshua Eckman

9.1 Introduction 328
9.2 Software Tools for Designing and Executing Experiments 329
9.2.1 General Considerations 329
9.2.2 Pre-assay Studies 331
9.2.3 Software Tools for Pre-assay Planning 331
9.2.4 Takeaways for SPR Study Design and Execution 333

Published on 24 May 2017 on http://pubs.rsc.org | doi:10.1039/9781788010283-FP019

View Online

Published on 24 May 2017 on http://pubs.rsc.org | doi:10.1039/9781788010283-FP019

9.3 Data Analysis 333
9.3.1 Data Output 333
9.3.2 Data Analysis Software Packages 333
9.4 Fundamental Data Processing Techniques 335
9.4.1 Introduction 335
9.4.2 Normalization/Calibration 335
9.4.3 Excluded Volume Correction 335
9.4.4 Referencing 336
9.4.5 Blank Subtraction 337
9.4.6 *x*-Scale Alignment 337
9.4.7 *y*-Scale Zeroing 337
9.5 Example of Competitive Epitope Binning Data Analysis 338
9.5.1 Introduction 338
9.5.2 Epitope Binning Experimental Design 339
9.5.3 Preprocessing of Data Using SPRint 340
9.5.4 Epitope Characterization Using Epitope Binning 2.0 344
9.6 Example of Kinetic Data Analysis 349
9.6.1 Introduction 349
9.6.2 Experimental Design 349
9.6.3 Preprocessing of Data Using SPRint 349
9.6.4 Global Kinetic Analysis in Scrubber 2.0 HT 350
9.7 Conclusions 354
9.8 Questions 354
Acknowledgements 355
References 355

Chapter 10 Biolayer Interferometry (Octet) for Label-free Biomolecular Interaction Sensing 356
David O. Apiyo

10.1 Introduction to Biolayer Interferometry (BLI) 356
10.2 BLI Platforms 358
10.3 BLI Biosensors 359
10.3.1 Biosensor Selection 361
10.3.2 Regeneration of Biosensors 365
10.4 Basics of Binding Kinetics Using BLI 367
10.4.1 Relationship Between R_{eq}, R_{max}, and K_D 370
10.5 Data Acquisition and Analysis on the Octet 370
10.5.1 Data Acquisition on the Octet 370
10.5.2 Data Analysis on the Octet 372

View Online

Published on 24 May 2017 on http://pubs.rsc.org | doi:10.1039/9781788010283-FP019

10.6 Determination of Affinity Constants Using BLI 378
10.6.1 Ligand Surface Immobilization 378
10.6.2 Binding Kinetics 379
10.6.3 Setting Up Kinetics Assays Using BLI 380
10.6.4 Protein Quantitation on the Octet 384
10.7 Emerging Applications 389
10.7.1 Octet Use in Epitope Binning 389
10.7.2 Octet in Virus Titer Studies 391
10.7.3 Analysis of FcRn–Antibody Interactions Using the Octet 393
10.8 Questions 396
References 397

Chapter 11 Strategies for Building Protein–Glycosaminoglycan Interaction Networks Combining SPRi, SPR, and BLI 398
Sylvain D. Vallet, Lisette Deddens, Arnaud Vonarburg, Romain Salza, Clément Faye, Attila Aranyos, Nicolas Thierry-Mieg and Sylvie Ricard-Blum

11.1 Introduction 398
11.2 A Roadmap to Build Protein–Glycosaminoglycan Interaction Networks 400
11.3 Identification of Biomolecular Interactions by Surface Plasmon Resonance Imaging 401
11.4 Building and Functional Analysis of Protein–Glycosaminoglycan Interaction Networks 403
11.5 Contextualization of the Interaction Network with Kinetic Parameters and Affinity 407
11.5.1 Kinetic and Affinity Data Available in Interaction Databases 407
11.5.2 Kinetics and Affinity Calculated by Bio-Layer Interferometry 407
11.6 Conclusion 411
11.7 Abbreviations 411
11.8 Questions 412
Acknowledgements 412
References 412

View Online

Chapter 12 Future Trends in SPR Technology **415**
Richard B. M. Schasfoort

12.1 Introduction 415
12.2 Trends in SPR Instrumentation 417
12.2.1 Nanoparticle-based Localized SPR (LSPR) 417
12.2.2 SPR Imaging 419
12.3 Trends in Fluidics 420
12.3.1 Microarray Spotting on SPR Sensor Chips 421
12.3.2 Gradient Printing for Multiplex Sensing 424
12.4 Trends in Sensor Surfaces 426
12.4.1 SensEye® Sensor: Easy2Spot 427
12.4.2 SensEye Protein A/G, SensEye Anti-IgG, and Fixit Protocol 428
12.5 Hyphenated SPR Technology 430
12.5.1 SPR-MS 430
12.5.2 Other Hyphenated SPR Techniques 431
12.5.3 Implementation of ''Lab-on-a-Chip'' Devices for SPR Systems 432
12.5.4 Electrochemical SPR (E-SPR) Application 434
12.6 Prospects for SPR-based Point-of-care Devices 435
12.6.1 Point-of-care Theranostics 436
12.6.2 Signal Enhancement Cascade for Boosting the Dynamic Range 437
12.7 Trends in Measuring Reliable Kinetic Parameters 439
12.7.1 Affinity Ranking with the Interpolation Method 440
12.7.2 Affinity Ranking with the Interpolated Distribution Analysis Method 444
12.8 SPRi Cytometry 446
12.8.1 Label-free Cell Membrane Antigen Profiling 447
12.8.2 Quantifying the Ratio of Surface Antigens per Cell Population 452
12.8.3 Extracellular Vesicle Monitoring Using SPRi 459
12.8.4 Affinity Ranking of Cell Surface Antigens on Living Cells 463

Published on 24 May 2017 on http://pubs.rsc.org | doi:10.1039/9781788010283-FP019

View Online

12.8.5 Quantifying the Production Rate of Molecules per Individual Cell 465
12.8.6 Microwell Cell Selection Using SPRi: the McSPRinter 467
12.9 Conclusions 474
12.10 Questions 475
References 475

Appendix Questions and Answers 479

Subject Index 508

Published on 24 May 2017 on http://pubs.rsc.org | doi:10.1039/9781788010283-FP019

View Online

Published on 24 May 2017 on http://pubs.rsc.org | doi:10.1039/9781788010283-FP019

Published on 24 May 2017 on http://pubs.rsc.org | doi:10.1039/9781788010283-00001

CHAPTER 1

Introduction to Surface Plasmon Resonance

RICHARD B. M. SCHASFOORT

Medical Cell BioPhysics Group (MCBP), MIRA Institute,
University of Twente, P.O. Box 217, 7500 AE Enschede, The Netherlands
Email: r.b.m.schasfoort@utwente.nl

1.1 Introduction to Surface Plasmon Resonance

During the years following the introduction of the first commercial surface plasmon resonance (SPR) instrument (Biacore) in 1990, the number of publications that include data collected from commercial biosensors increased to more than 20 000 papers by 2016 (PubMed data), as shown in Figure 1.1.

Not only the number of publications but also advances in the technology led to an improvement in detection sensitivity by roughly 100-fold up to 10^{-8} RIU (refractive index unit) or 0.01 RU (resonance or response unit). The range of affinity and kinetic data that can be determined has been extended at least 200-fold as a consequence of the increased sensitivity and due to improvements in data analysis. The number of independent channels or spots grew from four channels in 1990 (Biacore) to at least 192 flow-controlled spots in the new IBIS MX96 imaging instrument and more than 10 000 drop-spotted ligands in SPR imaging instruments from various manufacturers (*e.g.* Plexera). The carboxymethylated dextran surface introduced in 1990,[1] still the first choice for many applications, has been complemented with a range of other surfaces (see Chapter 6). Systems for dedicated applications have been introduced by various manufacturers as complements to all-purpose research instrumentation,[2] and the impact of

Handbook of Surface Plasmon Resonance, 2nd Edition
Edited by Richard B. M. Schasfoort
© The Royal Society of Chemistry 2017
Published by the Royal Society of Chemistry, www.rsc.org

View Online

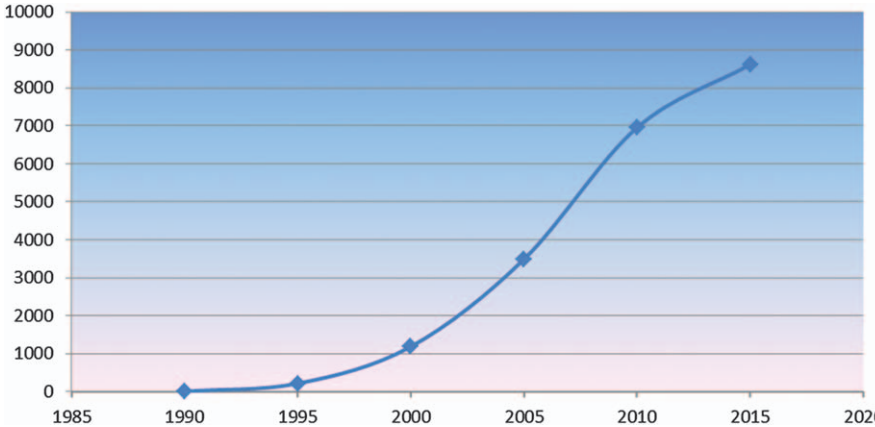


Figure 1.1 SPR papers in PubMed: total >20 000. 1990–1995: 217 articles; 1995–2000: 1190 articles; 2000–2005: 3493 articles; 2005–2010: 6958 articles; 2010–2015: 8617 articles.

Published on 24 May 2017 on http://pubs.rsc.org | doi:10.1039/9781788010283-00001

SPR biosensors on biomolecular interaction studies is growing continuously. With improved experimental design and advanced data analysis methods, high-quality data for the determination of kinetic parameters of biomolecular interaction phenomena can be obtained. These data promise additional insights not only into the affinity of biomolecular pairs but also into the mechanisms of molecular binding events, which will be important for function–regulatory protein interaction studies in order to unravel the exciting processes in living species.

1.2 What is a Biosensor?

The term biosensor was introduced around 1975, relating to the exploitation of transducer principles for the direct detection of biomolecules at surfaces. Currently the most prominent example of a biosensor is the glucose sensor, reporting glucose concentration as an electronic signal, *e.g.* based on a selective enzymatic process. According to the current definition, in biosensors the recognition element (ligand) of the sensor or the analyte should originate from a biological source.

> *Biosensors are analytical devices comprising a biological element (tissue, microorganism, organelle, cell receptor, enzyme, antibody) and a physicochemical transducer. Specific interaction between the target analyte and the biological material produces a physicochemical change detected by the transducer. The transducer then yields an analog electronic signal proportional to the amount (concentration) of a specific analyte or group of analytes.*
>
> Anthony P. F. Turner (Editor, *Biosensors and Bioelectronics*)

View Online

Published on 24 May 2017 on http://pubs.rsc.org | doi:10.1039/9781788010283-00001

Application of SPR-based sensors to biomolecular interaction monitoring was first demonstrated in 1983 by Liedberg *et al.*[3] A historical overview of the use of the phenomenon for biosensor applications is given in Chapter 2. To understand the excitation of surface plasmons, let us start with a simple experiment.

1.2.1 A Simple Experiment

Consider the experimental set-up depicted in Figure 1.2. When polarized light is shone through a prism on a sensor chip with a thin metal film on top, the light will be reflected by the metal film acting as a mirror. On changing the angle of incidence and monitoring the intensity of the reflected light, one observes that the intensity of the reflected light passes through a minimum (Figure 1.2, line A). At this angle of incidence, the light will excite surface plasmons, inducing surface plasmon resonance, causing a dip in the intensity of the reflected light. Photons of p-polarized light can interact with the free electrons of the metal layer; inducing a wave-like oscillation of the free electrons, thereby reducing the reflected light intensity.

The angle at which the maximum loss of the reflected light intensity occurs is called resonance angle or SPR-dip. The SPR-dip angle is dependent on the optical characteristics of the system, *e.g.* on the refractive indices of the media on both sides of the metal, usually gold, and are explained in detail in Chapter 2. Whereas the refractive index at the prism side does not change, the refractive index in the immediate vicinity of the metal surface will change when accumulated mass (*e.g.* proteins) adsorb on the thin gold layer.

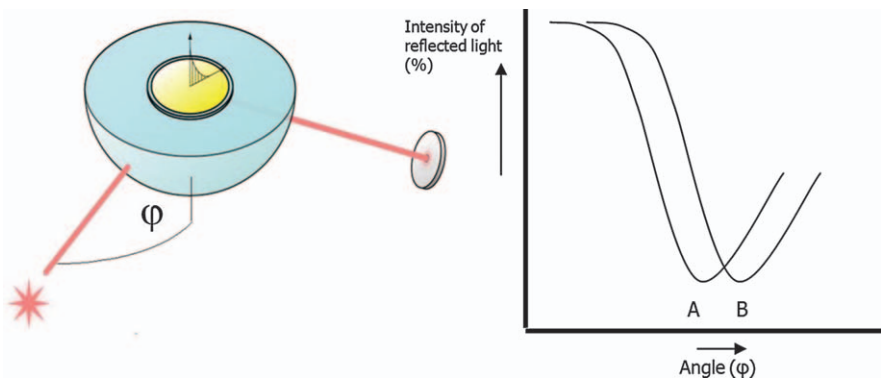


Figure 1.2 Schematic experimental set-up of surface plasmon resonance excitation. A sensor chip with a gold coating is placed on a hemisphere (or prism). Polarized light shines from the light source (star) on the sensor chip. Reflected light intensity is measured in the detector (disk). At a certain angle of incidence (φ), excitation of surface plasmons occurs, resulting in a dip in the intensity of the reflected light (A). A change of refractive index at the surface of the gold film, will cause an angle shift from A to B.

View Online

Hence the SPR conditions are changing and the real-time shift of the SPR angle is suited to provide information on the kinetics of, *e.g.*, protein adsorption on the surface.

Published on 24 May 2017 on http://pubs.rsc.org | doi:10.1039/9781788010283-00001

1.2.2 From Dip to Real-time Measurement

Surface plasmon resonance is an excellent method for monitoring changes in the refractive index in the near vicinity of the metal surface. When the refractive index changes, the angle at which the intensity minimum is observed will shift as indicated in Figure 1.2, where line A depicts the original plot of reflected light intensity *versus* incident angle, and B is the plot after the change in refractive index. SPR is not only suited to measure the difference between these two states, it can also monitor the change in time, if one follows in time the shift of the resonance angle at which the dip is observed. Figure 1.3 depicts the shift of the dip in time, a so-called sensorgram. If this change is due to a biomolecular interaction, the kinetics of the interaction can be studied in real time.

SPR sensors investigate only in a very limited vicinity in a fixed volume at the metal surface. The penetration depth of the electromagnetic field (so-called evanescent field) at which a signal is observed typically does not exceed a few hundred nanometers, decaying exponentially with the distance from the metal layer at the sensor surface. The penetration depth of the evanescent field is a function of the wavelength of the incident light, as explained in Chapter 2.

SPR sensors lack intrinsic selectivity: all refractive index changes in the evanescent field will result in a change of the signal. These changes can be due to a refractive index difference of the medium, *e.g.* a change in the buffer

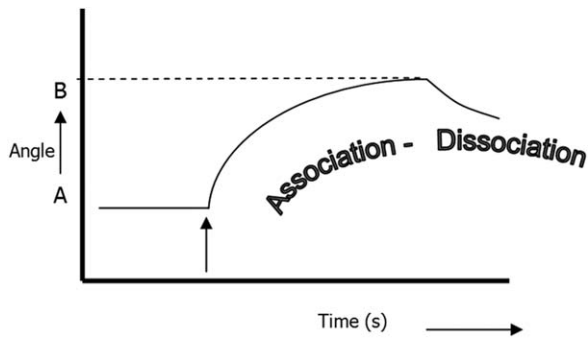


Figure 1.3 A sensorgram: the angle at which the dip is observed *versus* time. First, no change occurs at the sensor and a baseline is measured with the dip at SPR angle (A). After injection of the sample (arrow), biomolecules will adsorb on the surface, resulting in a change in refractive index and a shift of the SPR angle to position B (association). The adsorption–desorption process can be followed in real time and the amount of adsorbed species can be determined. Dissociation of the analyte bound to the ligand occurs when the sample containing the analyte is exchanged again with the system buffer.

View Online

Published on 24 May 2017 on http://pubs.rsc.org | doi:10.1039/9781788010283-00001

composition or concentration, or temperature effects; non-specific and specific adsorption of material on the sensor surface can also cause refractive index changes. The amount of adsorbed species can be determined after injection of the original baseline buffer as shown in Figure 1.3. To allow selective detection at an SPR sensor, its surface needs to be modified with ligands suited for selective capturing of the target compounds (the analyte) but which are not prone to adsorb any other components present in the sample or buffer media.

1.3 How to Construct an SPR Assay

Now we have a basic understanding of the SPR signal and how to measure it in time. We know that the sensor surface needs to be modified to permit selective capturing and thus selective measurement of a target compound or analyte. In the following, we will learn more about an SPR measurement. First, the steps of an SPR assay will be discussed from immobilization through analysis to regeneration in a measurement cycle. Next, we become acquainted with standard 1 : 1 interaction models, including kinetics, followed by examples of assay formats. Finally, a short outlook is provided on the basics of the instrumentation.

1.3.1 The Steps of an Assay

In the simplest case of an SPR measurement, a target component in solution or *analyte* is captured by the capturing element or so-called *ligand.* The ligand is permanently or temporarily immobilized on the sensor surface (Figure 1.4) prior to the measurement of the analyte interaction. Various

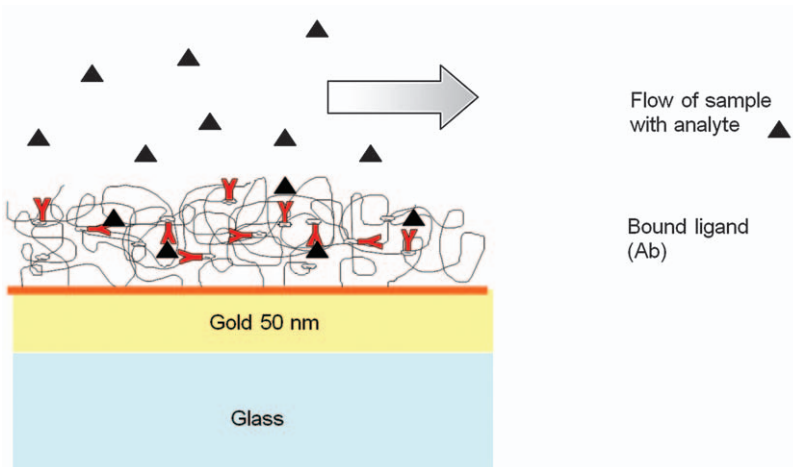


Figure 1.4 Schematic representation of direct detection: the analyte is captured by the ligands (Y) immobilized on the sensor surface. Accumulation of the analyte results in a refractive index change in the evanescent field detected by SPR. Here the ligand is immobilized in a hydrogel.

View Online

Published on 24 May 2017 on http://pubs.rsc.org | doi:10.1039/9781788010283-00001

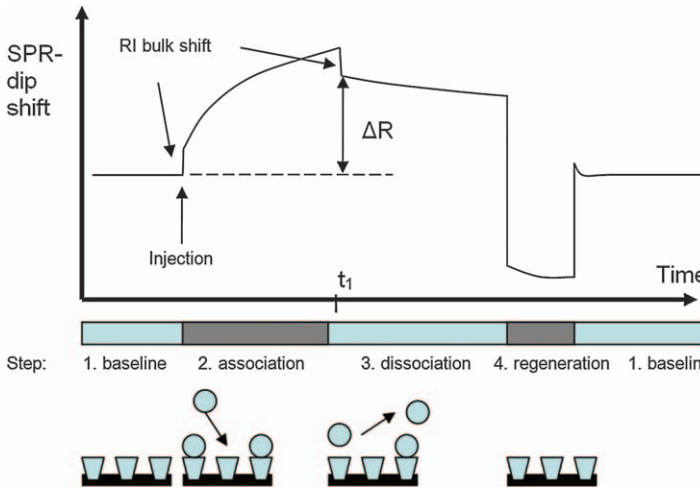


Figure 1.5 Sensorgram showing the phases of an analysis cycle. (1) Buffer is in contact with the sensor (baseline). (2) Continuous injection of sample solution (association phase). A refractive index (RI) bulk shift occurs when the system buffer RI is different from the analyte buffer RI. (3) Injection of buffer (dissociation phase); ΔR indicates the measured response due to the bound target compound. (4) Removal of bound species from the surface during injection of regeneration solution (regeneration step) followed by a new analysis cycle.

sensor surfaces with immobilized ligands are commercially available, and many more can be custom made, as explained in Chapter 6 by Erk Gedig.

In the simplest case, the event of capturing the analyte by the ligand gives rise to a measurable signal; this is called *direct label free detection*. Figure 1.5 shows the sensor signal step-by-step in the measurement cycle with direct detection.

Each measurement starts with conditioning of the sensor surface with a suitable buffer solution (1). It is vital to have a stable baseline before the capturing event starts. Then common mode effects such as temperature or hydrogel swelling no longer fluctuate. At this point, the sensor surface contains the active ligands, ready to capture the target analytes. On injecting the solution containing the analyte (2), these molecules are captured on the surface. Other components of the sample might also adhere to the sensor surface; without the selection of a suitable ligand, this adherence will be non-specific. In this step, the adsorption kinetics of the analyte molecule can be determined in a real-time measurement. Next, buffer is injected onto the sensor and the non-specifically bound components are flushed off during the so-called dissociation phase (3). As indicated in Figure 1.5, the accumulated mass can be obtained from the SPR response (ΔR). The double-headed arrow represents the specific response (ΔR). Also in this step, dissociation of the analyte starts, enabling the kinetics of the dissociation process to be studied. Finally, a regeneration solution is injected, which

View Online

Published on 24 May 2017 on http://pubs.rsc.org | doi:10.1039/9781788010283-00001

breaks the specific binding between analyte and ligand (4). If properly anchored to the sensor surface, the ligands remain on the sensor, whereas the target analytes are quantitatively removed. In order to perform many tests with the same sensor surface, it is vital to use a regeneration solution that leaves the activity of the ligands intact, as the analysis cycle is required to take place repeatedly hundreds, sometimes even thousands, of times. Again, buffer is injected to condition the surface for the next analysis cycle. If the regeneration is incomplete, remaining accumulated mass causes the baseline level to be increased. A typical example of a repeated injection of the same analyte (8×) over eight channels/spots is shown in Figure 1.6. The instrument is generating raw data, which should be zeroed and referenced to obtain a "clean" sensorgram of the biomolecular interaction only [to "scrub" the data that can be performed in Scrubber 2.0 software (see Chapter 9)].

A typical referenced and zeroed sensorgram is shown in Figure 1.7 with the phases of an analysis cycle of Figure 1.5.

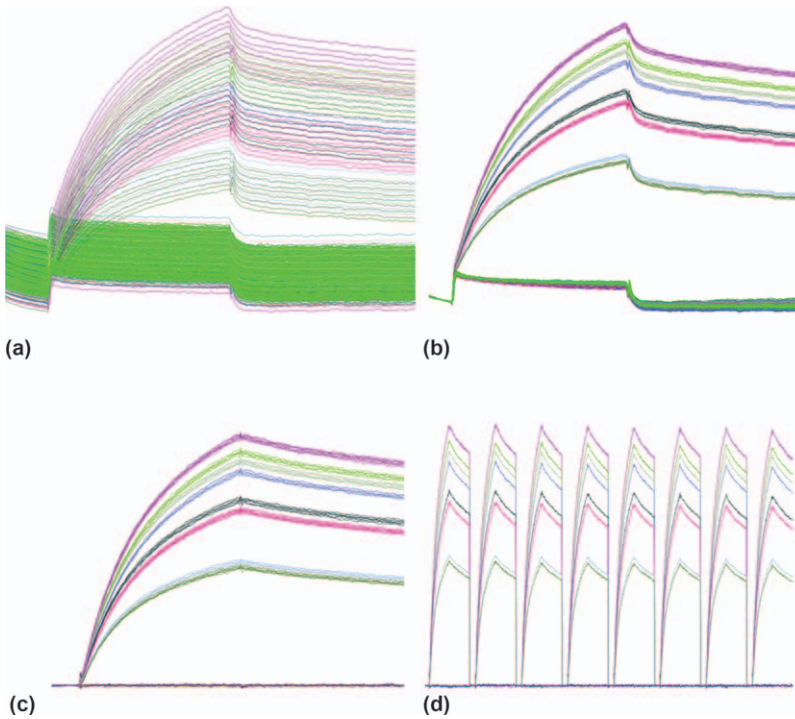


Figure 1.6 Processing (scrubbing) raw data of a real experiment of eight repeated analyte injections exposed to eight channels/spots. (a) Non-zeroed, non-referenced overlay plot; (b) zeroed, non-referenced overlay plot; (c) zeroed, referenced overlay plot; (d) zeroed, referenced serial plot. Observe that the initial slopes of RU shift for all spots are the same. (mass transport-controlled regime, see Section 1.3.1). Only the R_{max} value per spot differs (see Section 1.3.3).
Data generated in the IBIS MX96.

View Online

Published on 24 May 2017 on http://pubs.rsc.org | doi:10.1039/9781788010283-00001

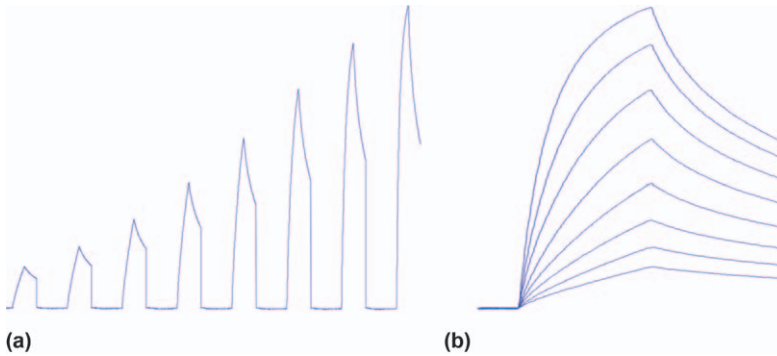


Figure 1.7 For accurate measurement of the kinetic parameters, it is preferred that the analyte is injected at increasing concentrations (a). The serial injections can be aligned to present the data in an overlay plot (b). Software (*e.g.* Scrubber 2) calculates the kinetic parameters from the overlay plot using global fitting (all curves in the overlay plot are fitted simultaneously). Note that the initial slopes are different (see Sections 1.3.1 and 1.3.3). Data generated in the IBIS MX96.

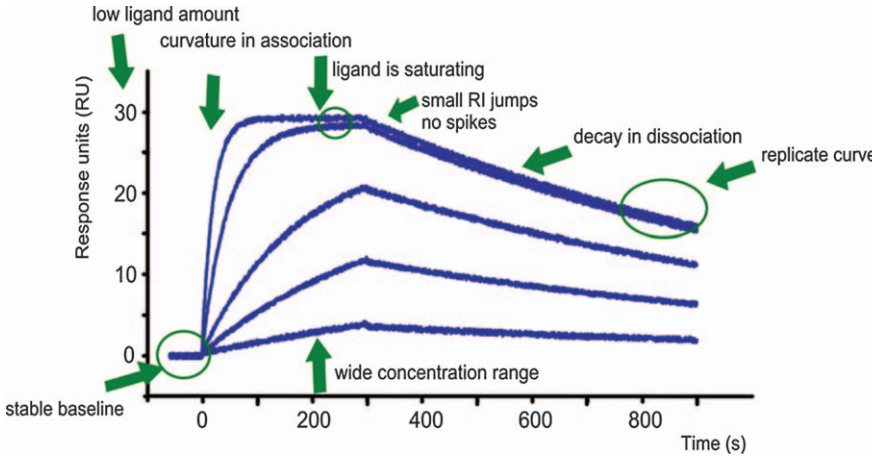


Figure 1.8 Example of a referenced and zeroed overlay plot of various analyte concentrations (same as Figure 4.22, courtesy of Arnoud Marquart).

Referencing means that at least two channels/spots are measured, one with ligand and the other without ligand as a reference channel. The referenced (= subtracted) signal is shown in Figure 1.7 and quality features are given in Figure 1.8.

1. *Baseline phase:* Initially, baseline buffer is in contact with the sensor surface to establish the baseline. For sensor calibration purposes, the injection of a calibration liquid (*e.g.* a tuned glycerol percentage spiked

View Online

Published on 24 May 2017 on http://pubs.rsc.org | doi:10.1039/9781788010283-00001

in baseline buffer) can be incorporated in this phase (not shown) in order to compensate for the RI bulk shift of the analyte buffer.
2. *Association phase*: Sample containing the target compound is injected; the capturing elements on the sensor surface bind the target compound, resulting in complex formation.
3. *Dissociation phase*: Upon injection of baseline = system buffer, target compounds (and also non-specifically bound molecules) dissociate from the surface.
4. *Regeneration phase*: The regeneration solution (*e.g.* low-pH buffer) is injected to remove the remaining bound target compounds (not shown in Figure 1.8).

After this phase, the cycle is completed and a new experiment can start by establishing the baseline again. If remaining accumulated mass is present, the baseline level will increase. Because of the different refractive indices of regeneration liquids and the difficulty of referencing caused by swelling or shrinking of the protein-loaded hydrogel (often by the pH shift–salt step), it is not necessary to show the real-time data of the regeneration process. It is sufficient to measure the baseline shift in the system buffer after the regeneration phase. Regeneration buffer scouting protocols as explained in Section 1.5.2 can be applied to find the optimal regeneration conditions.

Often SPR measurements are carried out to determine the kinetics of a binding process. For realistic results, it is vital to avoid immobilization changing the ligand in such a way that would influence its strength or affinity toward the target (analyte) compound. In addition, kinetic experiments can provide information on the equilibrium dissociation constants and the rate constants (on- and off-rate) and on the thermodynamics, *e.g.* on the binding energy of processes. Examples of kinetic binding curves are provided in Chapter 4 by Arnoud Marquart and the effects of distributed ligand immobilization and kinetic theory can be found in Chapter 5 by Huaying Zhao and Peter Schuck.

1.3.2 Concentration Determination

Apart from kinetic and thermodynamic studies, SPR measurements can also be used for the determination of the concentration of an analyte in a sample (quantitative analysis). In this case, first different concentrations of the analyte are applied in separate analysis cycles. The sensorgrams measured at different concentrations give an overlay plot similar to that depicted in Figure 1.9, with the plateaus of the association step increasing at increasing analyte concentration.[4] However, at a certain high analyte concentration the SPR response saturates.

A calibration curve can be constructed by simply plotting the response (ΔR) after a certain time interval (t_1) *versus* the concentration, but it depends on the affinity of the interaction. For example, if the concentration of the

View Online

Published on 24 May 2017 on http://pubs.rsc.org | doi:10.1039/9781788010283-00001

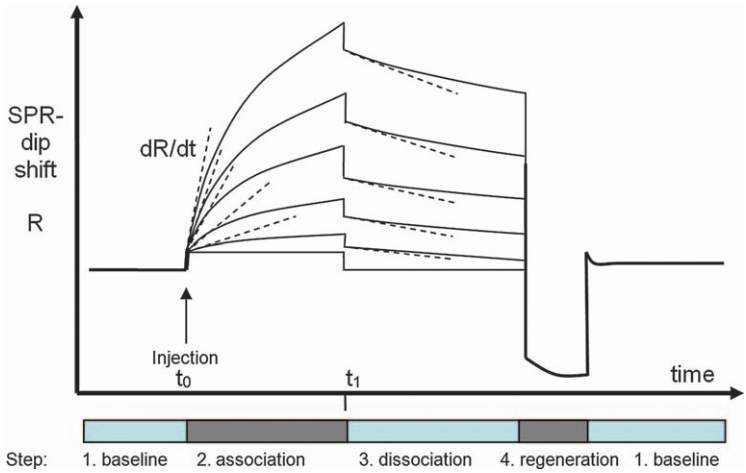


Figure 1.9 Typical overlay plot of sensorgrams from serial diluted analyte concentrations. Just after injection at t_0, a sample specific binding of the analyte occurs and mass transport to the surface is rate limiting and linearly dependent on the concentration. From the slopes for a positive control (dR/dt), the concentration of an unknown sample can be determined. During the association phase, the number of unbound ligand molecules decreases and dissociation takes place, causing bending of the binding curve. The off-rate constant or dissociation constant (k_d) can be determined just after injecting system buffer = baseline buffer at t_1.

analyte in the sample is very high, the undiluted sample will yield results on the upper plateau range of the calibration curve. However, diluted solutions might yield points along the lower, concentration-dependent sections of the calibration curve and the concentration of the target compound can be determined.

A calibration-free concentration analysis (CFCA) can be carried out if the binding of the molecules is partly mass transport limited. This is explained briefly in Section 1.4.2 and in Chapter 7 by Robert Karlsson *et al.* (Section 7.3.3 and Figure 7.12).

As mentioned above, SPR sensing means detection of refractive index changes at the sensor surface, which in practice translates to the amount of mass deposited at the sensor surface. Direct detection is only possible if the capturing event of the analyte brings about measurable refractive index changes. This is easier to achieve if the molecular weight (MW) of the analyte is large (*i.e.* around 1000 Da or higher). However, for small molecules to produce a measurable refractive index change, large numbers would be required, making the analysis intrinsically less sensitive. If the analyte is a small molecule (MW < 1000 Da), the response will be close to the system noise of the instrument (see Chapter 7). Only if high ligand densities are applied in combination with a highly sensitive instrument will the low-MW compound shift the refractive index sufficiently for SPR detection.

View Online

Published on 24 May 2017 on http://pubs.rsc.org | doi:10.1039/9781788010283-00001

Detection of small molecules can also be carried out using a different strategy. Most often, small molecules are detected in a competition or inhibition assay format. In all immune assay formats, not only is the lower detectable concentration limited, but also the physical number of immobilized elements on the sensor surface, which provide a maximum limiting value. Discussions of the different assay formats can be found in Section 1.5 and detection levels in Chapter 7.

1.3.3 Determination of Kinetic Parameters

The most prominent benefit of direct detection using SPR biosensor technology is the determination of the kinetics of (bio)molecular interactions. Reaction rates (k_a and k_d) and equilibrium constants (K_D) of interactions can be determined, *e.g.* the interaction $A + B \rightarrow AB$, where A is the analyte and B is the ligand immobilized on the sensor surface, can be followed in real time with SPR technology (note that in other parts of this book, *e.g.* Chapter 4, the ligand B is denoted L).

Table 1.1 contains the most relevant kinetic parameters, the association constant (k_a) and dissociation constant (k_d) for the simplest case $A + B \rightarrow AB$. The association constant represents the reaction rate of the complex (AB) formation, giving the number of complexes formed per unit time at unit concentrations of A and B. As soon as the complex AB is formed on the sensor surface, its dissociation can commence. The dissociation rate constant (k_d) expresses the number of AB complexes dissociating per unit time. Note that the unit dimensions for the association and dissociation rates are different and can vary with the stoichiometry of the complex. The typical range of the association and dissociation constants shows large variations and is dependent on, *e.g.*, temperature.

When association of A and B starts, no product AB is yet present at the sensing surface. At this point, the rate of the association reaction is highest and that of the dissociation reaction is lowest. As the process progresses, more and more of the AB complex is produced enhancing the rate of dissociation. Equilibrium is reached when the rates of the association and dissociation reactions are equal; definitions are given in Table 1.2. As can be

Table 1.1 Definitions of the most relevant kinetic parameters: the association and dissociation constants.

	Association rate constant, k_a	Dissociation rate constant, k_d
Definition	$A + B \rightarrow AB$	$AB \rightarrow A + B$
Description	Reaction rate of AB formation: number of AB complexes formed per unit time at unit concentrations of A and B	Dissociation rate of AB: number of AB complexes dissociating per unit time
Units	L mol^{-1} s^{-1}	s^{-1}
Typical range	10^3–10^7	10^{-1}–5×10^{-6}

View Online

Table 1.2 Definitions of the equilibrium association and dissociation constants.

	Equilibrium association constant, K_A	Equilibrium dissociation constant, K_D[a]
Definition	$[AB]/[A][B] = k_a/k_d$	$[A][B]/[AB] = k_d/k_a$
Description	Affinity to association: high K_A; high affinity to associate	Stability of AB: high K_D; low stability of AB
Units	L mol^{-1}	mol L^{-1} (M)
Typical range	10^3–10^{12}	10^{-3}–10^{-12}

[a]K_D has the units of concentration in moles per liter (M) and is the preferred term to express affinity. Note the capital D in the subscript.

Published on 24 May 2017 on http://pubs.rsc.org | doi:10.1039/9781788010283-00001

seen, the equilibrium association and dissociation constants, which represent the affinity of an interaction, have a reciprocal relationship with each other. Note that the dissociation equilibrium constant has a capital letter in the subscript (K_D). The effects of parameters such as temperature are described in Chapter 2.

The rate constants (Table 1.1) and equilibrium constants (Table 1.2) of (bio)molecular interactions provide information on the strength of association and the tendency for dissociation. Various aspects of the kinetics, models, and calculation of affinity constants are described in Chapters 4 and 5.

1.3.4 Basics of Instrumentation

To study biomolecular interactions using SPR does not require a detailed understanding of the optical phenomena. It is sufficient to know that SPR-based instruments use an optical method to measure the refractive index near a sensor surface (within ~300 nm from the surface). SPR instruments comprise three essential units integrated in one system: optical unit, liquid handling unit, and the sensor surface. The features of the sensor chip have a vital influence on the quality of the interaction measurement. The sensor chip forms a physical barrier between the optical unit (dry section) and the flow cell (wet section).

SPR instrumentation can be configured in various ways to measure the shift of the SPR-dip. In general, three different optical systems (see Chapter 3) are used to excite surface plasmons: systems with prisms, gratings, and optical waveguides. Most widespread are instruments with a prism coupler, also called instruments in the "Kretschmann configuration".[5] In this configuration, which is shown in Figure 1.2, a prism couples p-polarized light into the sensor coated with a thin metal film. The light is reflected onto a detector that measures its intensity, using a photodiode or a camera. All configurations share the same intrinsic phenomenon: the direct, label-free, and real-time measurement of refractive index changes at the sensor surface. SPR sensors offer the capability of measuring low levels of chemical and biological compounds near the sensor surface. Sensing of a biomolecular binding event occurs when biomolecules accumulate at the sensor surface and change the refractive index by exchanging the background electrolyte or

View Online

Published on 24 May 2017 on http://pubs.rsc.org | doi:10.1039/9781788010283-00001

water molecules. Protein molecules have a higher refractive index than water molecules ($\Delta n \approx 10^{-1}$). The sensitivity of most SPR instruments is in the range of $\Delta n \approx 10^{-5}$–10^{-8} or 10–0.01 pg mm^{-2} of proteinous material at the sensor surface. Often in real-time biosensing, absolute values are not a prerequisite – only the change is monitored as a result of biospecific interactions at the sensor surface. Detailed descriptions of a selection of commercial instruments are given in Chapter 3.

The selectively accumulated mass on the sensor chip surface (which is generally expressed in pg mm^{-2}) correlates linearly with the change in the refractive index near the sensor surface measured by the SPR instrument.[6] A rule of thumb is that for an instrument that uses light of wavelength of 670 nm, *1 ng mm^{-2} protein accumulation gives a signal of about 1000 RU* SPR angle shift. In Biacore instruments, ~8.2 resonance units (RU) correspond to 1 millidegree (m°) SPR angle shift. One resonance unit (RU) corresponds to exactly 10^{-6} RIU by definition. When light of another wavelength is used, then the angle shift should be calibrated. A preferred calibration of instruments is that the output signal of an SPR instrument corresponds ultimately to RU shifts (and not to wavelength or percent reflectivity shifts) calibrated with known RIU glycerol–water mixtures for better comparing ligand densities and kinetics of biomolecular interactions between different instruments.

One resonance unit (RU) corresponds to exactly 10^{-6} RIU

1.4 Kinetics of Biomolecular Interactions

Evanescent wave biosensors offer an easy way to measure the kinetics of the reversible binding of a biomolecule from solution to a ligand (typically another biomolecule) immobilized on the sensor surface. Although theoretical aspects are treated in depth in Chapters 4 and 5, a brief analysis of kinetics is described here. The conventional treatment starts with a simple 1 : 1 interaction model,[7] equivalent to the Langmuir model, which is the simplest physically plausible isotherm based on three assumptions:

- The binding is specific to ligands attached to the surface.
- All sites are equivalent and the ligands are uniformly divided.[†]
- The ability of an analyte to bind to its ligand is independent of the degree of occupation of neighboring sites.

If these conditions are met, the dynamic equilibrium is given by

$$\mathrm{A} + \mathrm{B} \underset{k_\mathrm{d}}{\overset{k_\mathrm{a}}{\rightleftharpoons}} \mathrm{AB} \tag{1.1}$$

[†]This is a theoretical assumption. In Chapter 5, consequences of the ligand heterogeneity are explained.

View Online

Published on 24 May 2017 on http://pubs.rsc.org | doi:10.1039/9781788010283-00001

assuming that A is the molecule binding from solution (analyte) and B is the species immobilized on the sensor surface (ligand) (or L = ligand). The forward and reverse reaction rates are described by the adsorption (association) rate constant (k_a) and the desorption (dissociation) rate constant (k_d), respectively. The association process results in the formation of the complex [AB] on the sensor surface and is described by

$$\frac{d[AB]}{dt} = k_a[A][B] \tag{1.2}$$

while the dissociation rate of the complex [AB] is given by

$$-\frac{d[AB]}{dt} = k_d[AB] \tag{1.3}$$

Once a dynamic equilibrium is established, the rates of the two processes are equal, *i.e.*

$$k_a[A][B] = k_d[AB] \tag{1.4}$$

Hence the equilibrium constants can be expressed by the rate constants according to

$$K_A = \frac{[AB]}{[A][B]} = \frac{k_a}{k_d} \tag{1.5}$$

and

$$K_D = \frac{[A][B]}{[AB]} = \frac{k_d}{k_a} \tag{1.6}$$

where K_A and K_D are the affinity constant and the equilibrium dissociation constant, respectively. This formalism is mathematically identical with that for the treatment of the interaction in a homogeneous phase. However, at the solid/liquid interface the transport (diffusion and convection) of A from the bulk solution to the interface must be taken into account (see Chapter 5). Because K_D has the dimensions of concentration (moles per liter) and relates to the amount that has been bound with respect to the free analyte concentration, it is recommended to apply K_D and not K_A.

1.4.1 Mass Transport-controlled Kinetics

In most SPR systems, the following reaction takes place:

$$A_{bulk} \underset{k_m}{\overset{k_m}{\rightleftharpoons}} A_{surface} + B \underset{k_d}{\overset{k_a}{\rightleftharpoons}} AB \tag{1.7}$$

This reaction describes two events. First, analyte is transported out of the bulk solution to the surface of the sensor. Second, the actual analyte–ligand

View Online

Published on 24 May 2017 on http://pubs.rsc.org | doi:10.1039/9781788010283-00001

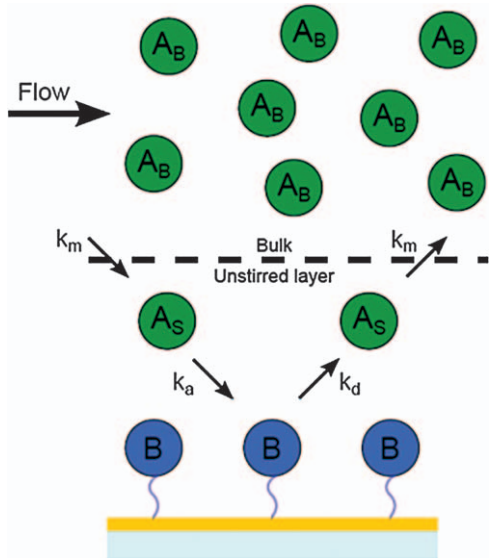


Figure 1.10 Parameters that determine mass transport limitation (MTL).

interaction takes place (see Figure 1.10). Both events have their own rate constants k_m and k_a/k_d. When the diffusion of the analyte from the bulk to the surface is slower than the binding rate of the analyte to the ligand, a shortage of analyte at the surface occurs. In this situation, k_a (and k_d) is limited by the mass transport. The apparent k_a is slower than the real k_a. For kinetic measurements, mass transport limitation (MTL) is obviously unwanted and should be minimized as much as possible. However, for concentration measurements, MTL can be exploited since under full or partial MTL the binding rate is proportional to the analyte concentration as can be observed in Figure 1.9. It is this property of MTL that allows concentration measurements without the need for a calibration curve or calibration standard [see calibration-free concentration analysis (CFCA) as explained briefly in the next section and in Section 7.3.3 and Figure 7.12].

Therefore, in other words, if the surface concentration of B (ligand) is very high, and the mass transport rate k_m is small compared with the association rate constant k_a, *i.e.* $k_m \ll k_a[B]$, in the extreme boundary condition the interaction is controlled by the mass-transport rate only. Then the complex formation rate is dependent solely on the bulk concentration of analyte A, and the binding signal increases linearly with time:

$$\frac{d[AB]}{dt} = k_m[A_{bulk}] \tag{1.8}$$

This can be used for the determination of the concentration of analyte A, since the slope of the initial stage of the binding curve is proportional to the analyte concentration. However, the rate of binding should be totally limited

View Online

Published on 24 May 2017 on http://pubs.rsc.org | doi:10.1039/9781788010283-00001

by mass transport, the degree of which can be determined with the calibration-free concentration analysis (CFCA) method. Theoretically, the linear range of the dose–response curve has no limitation at the lower concentration side. If the reaction rate is fully mass transport limited, the sensor surface acts like an infinite sink and $[A_{surface}] = 0$. In this case, k_m for all practical situations can be described by[8]

$$k_m = 0.98\left(\frac{D}{h}\right)^{\frac{2}{3}}\left(\frac{v}{bx}\right)^{\frac{1}{3}} \tag{1.9}$$

where D is the diffusion coefficient, h and b are the height and the width of the flow cell, respectively, v is the volumetric flow rate, and x is the distance from the flow cell entrance.

1.4.2 Calibration-Free Concentration Analysis (CFCA)

As indicated in the previous section, there is a linear relationship of the slope with respect to the concentration only when the interaction process is 100% mass transport limited. However, a 100% mass transport-limited interaction often cannot be reached and the binding is both mass transport limited and rate (kinetically) limited (note in Figure 1.6c how early the slope of lower density spots deviates from that of higher density spots for the same analyte concentration). By applying two different flow rates, the degree of mass transport limitation can be experimentally determined. This CFCA method was recently introduced by Karlsson and Roos[9] (see also Section 7.3.3 and Figure 7.12).

For CFCA measurements, the initial binding rate of an analyte is measured at two different flow rates, *i.e.* under two different conditions of partial MTL. The two conditions are chosen such that they maximize the difference in degree of MTL while maintaining data quality. In order for CFCA to function correctly, it is preferred that a large amount of ligand is immobilized. Also, the ligand must be stable and a proper regeneration buffer must be used, leaving the ligand intact. From the two initial binding rates obtained, the degree of MTL can be determined by calculating the QC_{ratio}, as explained by Pol *et al.*[10] For a certain analyte (*e.g.* an IgG molecule) the molecular weight is known and a flow cell characteristic parameter can be calculated. An unknown functional concentration of analyte, *e.g.* in supernatants, can then be calculated from

$$[A]_{CFCA} = \frac{[FC_{MW} \times slope_{low}]}{QC_{ratio}} \tag{1.10}$$

where FC_{MW} is a flow cell constant.

Analyte may be present in complex matrices such as culture supernatants or mixtures, where the exact functional concentration determination is difficult. One may establish the activity of the analyte solution by measuring the

View Online

Published on 24 May 2017 on http://pubs.rsc.org | doi:10.1039/9781788010283-00001

concentration by means of A_{280} (absorbance at 280 nm) and comparing this with the CFCA value. In this way, a ''percent activity'' value can be obtained for the analyte solution ($100 \times [A]_{CFCA}/[A]_{A_{280}}$).

In SPR imaging instruments for multiplex analysis of biomolecular interactions (*e.g.* the IBIS MX96), only one ligand spot is necessary to obtain the analyte concentration, which may then be used for the entire array, *e.g.* for early-stage screening experiments such as affinity ranking of monoclonal antibody panels.

To summarize, CFCA allows the functional concentration of an analyte to be determined by SPR without the need for a calibration curve. In practice, this leads to a flow cell constant, FC_{MW}, which can be used to calculate an unknown analyte concentration with the same molecular weight by measuring the initial slope of the association phase under two different mass transport-limited conditions set by the flow rate (see also Section 7.3.3 and Figure 7.12).

1.4.3 Interaction-controlled Kinetics

If the mass transport rate is much larger than the association rate constant, or if the surface concentration of the immobilized species is low, *i.e.* $k_m \gg k_{on}[B]$, then $[A_{surface}] = [A_{bulk}]$ and the binding rate can be expressed as

$$\frac{d[AB]}{dt} = k_a[A][B] - k_d[AB] \tag{1.11}$$

The surface concentration of the free binding site, [B], is the difference between the concentration of the complex at saturation, $[AB_{max}]$, and the current complex concentration, [AB]:

$$[B] = [AB_{max}] - [AB] \tag{1.12}$$

Combining eqn (1.11) and (1.12), and considering that the response R scales linearly with the complex concentration [AB], one obtains

$$\frac{dR}{dt} = k_a c_0 (R_{max} - R) - k_d R \tag{1.13}$$

where c_0 is the concentration of the analyte ($[A]_{bulk}$) and R_{max} is the saturation signal where all functional ligand molecules bound analyte molecules. Theoretically, this means that the R_{max} signal can be reached only at unlimited high analyte concentrations where the degree of dissociation can be fully neglected. Be aware that $[AB]_{max}$ or $[B]_{max}$ corresponds to the maximal *loading* of the ligands with analyte, while R_{max} corresponds to the maximal theoretical SPR signal when analyte molecules occupy all *functional* ligand molecules.[‡] In Figure 1.11, a serial (a) and an overlay plot (b) of binding

[‡]Some software programs sometimes apply $[B]_{max}$ and others apply R_{max}. The latter is the recommended nomenclature to express the functional ligand density based on the analyte response for the specific analyte–ligand interaction.

View Online

Published on 24 May 2017 on http://pubs.rsc.org | doi:10.1039/9781788010283-00001

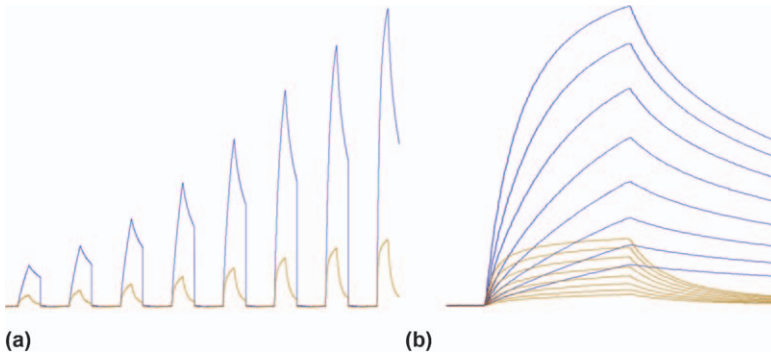


Figure 1.11 (a) Serial plot (referenced and zeroed) of eight analyte injections in two channels (spots). The R_{max} values or analyte capacity (functional ligand density) of the two spots are different. (b) Overlay plot. Data generated with the IBIS MX96.

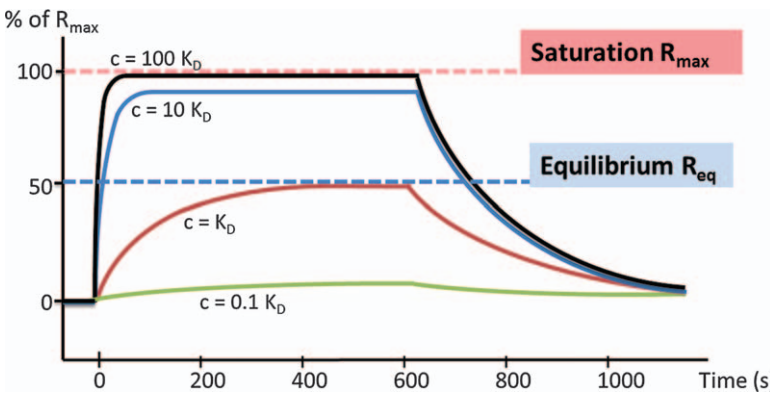


Figure 1.12 Equilibrium analysis based on a 1 : 1 Langmuir model. Only when the sensorgram shows equilibrium [$\%R_{max}$ *versus* time (s)] can equilibrium analysis be applied. Note that if the concentration has the value of K_D the *Y*-value ($\%R_{max}$) is at 50% at equilibrium.

curves from two spots with a high and a low R_{max} value are exposed to the same analyte series of injections (IBIS MX96 data).

Hence the R_{max} value represents the *functional* ligand density on the surface. The solution of eqn (1.12) yields

$$R = \frac{k_a c_0 R_{max}}{k_a c_0 + k_d}\left[1 - e^{-(k_a c_0 + k_d)t}\right] = R_0\left[1 - e^{-(k_a c_0 + k_d)t}\right] \quad (1.14)$$

This is shown schematically in Figure 1.12 in the association phase.

For the dissociation phase, $c_0 = 0$, hence

$$\frac{dR}{dt} = -k_d R \quad (1.15)$$

View Online

Published on 24 May 2017 on http://pubs.rsc.org | doi:10.1039/9781788010283-00001

and the solution becomes [*cf.* Figure 1.12 (dissociation phase)]

$$R = R_0 \, e^{-k_d t} \tag{1.16}$$

Eqn (1.15) and (1.16) can be used to obtain k_a and k_d from a single set of association/dissociation experiments with various analyte injections using global non-linear curve fitting.

1.4.4 Equilibrium Analysis

Once a dynamic equilibrium is reached, the net effect of the association and dissociation process is zero, *i.e.*

$$\frac{dR}{dt} = k_a c_0 (R_{max} - R_{eq}) - k_d R_{eq} = 0 \tag{1.17}$$

where R_{eq} is the equilibrium response at a given analyte concentration c_0. Therefore, the equilibrium signal reflects the affinity constant K_A and dissociation constant K_D of the interaction couple. This can be converted to a format that resembles the 1 : 1 Langmuir isotherm:

$$R_{eq} = \frac{c_0 K_A R_{max}}{c_0 K_A + 1} \tag{1.18}$$

$$= \frac{c_0 R_{max}}{c_0 + K_D} \tag{1.19}$$

The isotherm is an S-shaped curve if using a logarithmic axis for the concentration, as shown in Figure 1.13. Upon application of an analyte concentration of $c_0 = K_D$, R_{eq} is half of the saturation response R_{max}. This is an important observation and the reason why the affinity equilibrium dissociation constant K_D should be used and not K_A. Thus the K_D value expresses the concentration at equilibrium where 50% of the ligands are occupied by an analyte molecule ($= \frac{1}{2} R_{max}$).

Although this pseudo-first-order kinetic model has been used successfully in qualitative studies (such as in the demonstration of interactions between biomolecules), the determination of the kinetic rate constants of binding is often complicated by the fact that most binding curves deviate from the single exponential time course expected for a simple pseudo-first-order reaction. Apart from the experimental causes (*e.g.* sample depletion, noise, drift, impurity), major concerns regarding the deviation are focused on mass transport/rebinding effects, multivalent interactions/avidity effects, heterogeneity in the immobilized ligands/matrix effects, and complex binding mechanisms. It is recommended that with complex kinetics deviating from 1 : 1 binding the experimental conditions should be changed in such a way that it will approach and will be closer to the simple 1 : 1 binding model. On improving the experimental design (*e.g.* by using high flow rates and low

View Online

Published on 24 May 2017 on http://pubs.rsc.org | doi:10.1039/9781788010283-00001

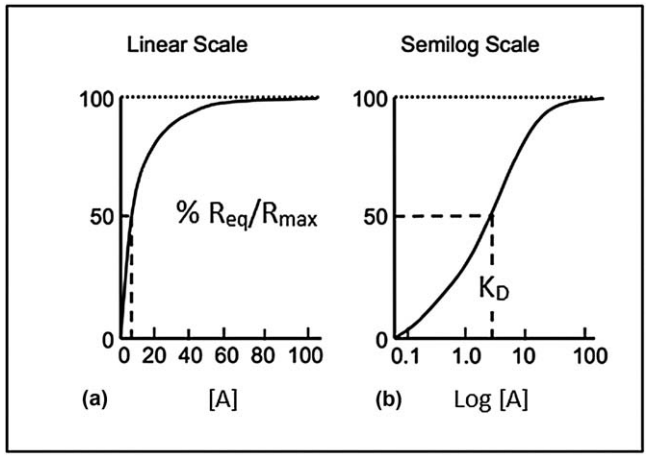


Figure 1.13 The % R_{eq}/R_{max} ratio as a function of the concentration of the analyte [A] can be plotted *e.g.* on a linear scale (a) or semilogarithmic scale (b). Note that the equilibrium dissociation constant depends only on the R_{eq}/R_{max} ratio and not on the actual value of R_{max} (in RU).

surface capacities) and applying advanced analysis algorithms {*e.g.* global analysis[11] and distribution analysis of the constants (Chapter 5), fitting association and dissociation phase data for a series of concentrations simultaneously}, the contribution of most of these effects can be minimized or even corrected.[12]

1.5 Buffer Solutions for Measuring the Analysis Cycle

1.5.1 Baseline or System Buffer

The running, background, baseline, or system buffer should create optimal physiological conditions for the binding of the analyte to the ligand. For biomolecular interactions, the baseline or system buffer is usually a physiological buffer with sufficient salt and (near) neutral pH. Phosphate-buffered saline (PBS) is a standard system buffer. Alternatively, 10 mM HEPES, pH 7.4–0.15 M NaCl (HBS) is often used with small amounts of ions such as potassium added. The addition of a surfactant, *e.g.* Tween-20 (0.03–0.075%) to the buffer is advantageous to minimize non-specific binding. The surfactant not only enhances the ratio between specific and non-specific binding but also helps to prevent adsorption of air bubbles on the surface. However, surfactants should not be added if hydrophobic surfaces are used for non-covalent attachment of membrane-bound components. Sometimes 3 mM EDTA is added to trap remaining bivalent cations (*e.g.* Mg^{2+} or Ca^{2+}), which may interfere with the carboxylate groups in the hydrogel layer. Blocking components may help to reduce non-specific binding, *e.g.* 3% bovine serum albumin (BSA) or human serum albumin

View Online

Published on 24 May 2017 on http://pubs.rsc.org | doi:10.1039/9781788010283-00001

(HSA) if patient serum is used. In order to optimize the system buffer for dedicated biomolecular interaction experiments, the ABA inject protocol (as explained in Section 7.3.6 and Figure 7.13) can be used to find the optimal system buffer. When advanced microfluidic valves are involved in the instrument, the buffer solutions should be prepared with Milli-Q quality water and should preferably be filtered through a 0.22 μm filter and degassed before use. Tuning the refractive index of the background buffer to mimic the sample and using the baseline buffer for dilution of the sample is a way to minimize the bulk refractive index effect. Not measuring a bulk refractive index step is better than correcting the bulk RI effect by advanced referencing.

1.5.2 Regeneration Buffer

For repeated use of the same sensor chip, the surface should be regenerated by removal of analyte and any other non-covalently bound material. However, the ligand should be kept intact and should not be inactivated or denatured during the regeneration phase. Commonly used solutions for regeneration include low-pH buffers, *e.g.* 10 mM glycine · HCl, pH 2.5, or 100 mM phosphoric acid, pH 3, or a high-salt solution, *e.g.* 3 M $MgCl_2$. Optimal sensor regeneration includes a pH shock, and regeneration is preferably performed as two subsequent steps of, for instance, 30 s each, rather than one step of 60 s. Often in the transition the regeneration process takes place. If a negatively charged gel-type sensor is used, not only will the specific bond between ligand and analyte break during low-pH regeneration, but also the hydrogel could collapse, with the analyte being more or less squeezed out of the hydrogel. If the ligand or analyte cannot withstand low pH, sometimes a highly alkaline pH is used, *e.g.* 10 mM NaOH (pH >11). Alternative regeneration solutions have a high salt concentration, and the salts used include chaotropic agents that are chemicals, such as urea and guanidine hydrochloride, that disrupt hydrogen bonding in aqueous solutions. It should be noted that concentrated solutions of these agents may denature proteins, because they also interfere with hydrophobic interactions, and the functional ligand density as determined with the R_{max} value will decrease accordingly. Geuijen *et al.* described the testing of various regeneration buffers.[13]

Furthermore, from the sensorgram without measuring the regeneration phase, the effectiveness of the regeneration procedure can be determined by tracking the baseline levels in a concatenated series of injections. Incomplete regeneration will result in residual analyte and/or non-specifically bound components on the sensor surface, which will increase the baseline, whereas too harsh sensor regeneration will result in a decreased binding capacity of the sensor in subsequent analysis cycles. In multiplex array-based instruments where a single regeneration buffer is injected, a regeneration buffer scouting protocol should be applied to group the ligands for the optimal regeneration buffer (not too mild or too harsh but just right). A general protocol for antibody–analyte interactions is to start with $MgCl_2$ (3 M)

View Online

followed by Gly · HCl (100 mM), pH 3.0, phosphoric acid (100 mM), pH 3.0, Gly · HCl, pH 2.5, and finally Gly · HCl, pH 2.0. Multiple antibodies should be grouped for the optimal regeneration conditions and ranking the affinity and epitope binning experiments should be performed using these conditions (see Chapter 8).

Published on 24 May 2017 on http://pubs.rsc.org | doi:10.1039/9781788010283-00001

1.6 SPR-based Immunoassays

In general, an immunoassay is a laboratory technique based on the binding between an antigen and its homologous antibody in order to identify and quantify a specific antigen or antibody in a sample. In classical immunoassays, the determination of the concentration of an analyte relies on signals generated by various labels (fluorescent dyes, enzymes, or radioisotopes) attached to antigens or antibodies.[14] Labeling may disrupt the binding sites involved in the interaction. Moreover, labeling induces heterogeneity of the biomolecular interaction because in most cases labeling of a specific molecule (*e.g.* an antibody) is not homogeneously distributed. In addition, the label itself might interact with the capturing ligands, leading to false positives. A way to circumvent some of these problems is to use a labeled secondary binding molecule, but this extra step requires an additional, high-affinity binding compound and it will also increase the analysis time required. An SPR-based biosensor measures protein–protein binding directly as a shift in surface-bound masses and therefore it can be applied as an immunoassay.

Figure 1.14 shows different assay formats that are appropriate for SPR, including direct, competitive, inhibition, and sandwich assays.

1.6.1 Direct Assay

The direct assay is described by $A + B \rightarrow AB$. In this simplest type of assay, antibodies directed against the antigen (= target compound) are immobilized on the sensor surface (= ligand). Sample solution containing the antigen (analyte) is then incubated with the sensitized sensor surface. The signal increase resulting from antigen binding correlates with the amount of antigen in the sample. Direct assays can also be designed with the antigen coupled to the surface (= ligand) and detection of the binding of the specific antibody (= analyte).

1.6.2 Competition Assay

This type of assay is typically applied for the detection of low molecular weight antigens that do not generate a sufficient signal, while accumulating at the sensor surface. In this assay format, specific antibodies are immobilized on the sensor surface and sample solution that contains the antigen is mixed with a conjugated antigen. Because of its high molecular weight, the conjugate enhances the SPR angle shift. The antigen–conjugated antigen

View Online

Published on 24 May 2017 on http://pubs.rsc.org | doi:10.1039/9781788010283-00001

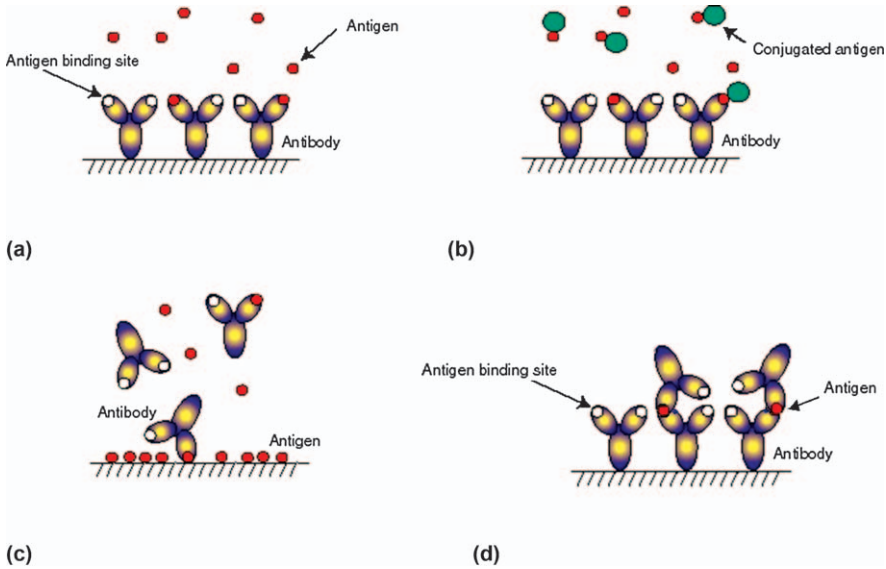


Figure 1.14 Immunoassay formats commonly used in SPR measurements. (a) Direct assay. The ligand (antibody) is immobilized on the sensor surface and interaction with the analyte (here antigen) yields a detectable refractive index shift. (b) Competition assay for measuring small molecules where direct capture of the antigen yields an insufficient refractive index shift, whereas the conjugated antigen is large enough for a measurable refractive index shift. (c) Inhibition assay where the analyte is the same molecule as the immobilized ligand. Antibody is added to the sample in small excess. The analyte forms conjugates with the antibody, inhibiting the binding to the sensor surface. (d) Sandwich assay with secondary antibody.

mixture is incubated with the sensor surface. The difference in signal between a reference sample containing only conjugated antigen and the sample solution indicates the amount of antigen in the sample. In this assay, high antigen concentrations in the sample will result in low signals (less conjugated antigen can be bound). Kinetically, this type of assay shows deviations because the diffusion constants of the analyte and the conjugated analyte will differ significantly. Only equilibrium analysis can be applied.

Competition assays are often used for the detection of toxic compounds. The maximum signal is generated when no free (toxic) analyte is present. When the signal is too low, possibly the analyte is present in the sample or the ligands have been denatured or poisoned by the sample and are no longer active while the analyte is not present. Both outcomes are harmful and will require action. If the competition assay shows a response of the unconjugated antigen as in the direct assay, then detailed calibration procedures have to be performed. Preferably in SPR-based competition immunoassays, the conjugated antigen is a high refractive index label

View Online

(*e.g.* a latex bead or gold nanoparticle) loaded with the antigen. Equilibrium analysis is the preferred approach.

1.6.3 Inhibition Assay

In this assay format, the target antigen is immobilized on the sensor surface. Sample solution containing the antigen is mixed with specific antibodies in excess and incubated with the sensor surface. Antibodies will bind both to antigen in solution and to antigen that is bound to the sensor surface. The difference in signal between a blank sample that does not contain the antigen and the sample solution indicates the amount of antigen in the sample. In this assay, high antigen concentrations in the sample result in low signals (fewer antibodies remain to bind to the surface). Because antibodies have high molecular weight, their binding is directly detected. Both competition and inhibition assays need various injections of ratio dilutions of the antigen with fixed concentrations of the competitor/inhibitor.

1.6.4 Sandwich Assay with Secondary Antibody and Signal Enhancers

In sandwich assays, antibody molecules against the analyte are immobilized on the sensor surface, capturing the analyte molecules when sample solution is incubated with the sensor surface. In the next injection, a secondary antibody binds specifically with either the antigen or the antigen-bound antibody. The antigen is captured by a sandwich of two antibodies. Only very high affinity capture antibodies should be used, in order to avoid a mixture of affinities of each component in the sandwich assay. Several steps can be built in, which complicates the analysis, however, but it may increase the sensitivity and specificity dramatically.

Often, a highly specific goat/rabbit/sheep anti-mouse immunoglobulin G (IgG) is immobilized as the first capturing agent, which traps a monoclonal (mouse) antibody for the antigen. Streptavidin–biotin linkers are often used because of the high affinity constant, which has limited interference with the rate and equilibrium constants of the analyte–ligand pair. The increase in signal (as a result of antigen binding) in a limited time window is proportional to the amount of antigen in the sample. Washing the surface with buffer is followed by the injection of a secondary antibody. The high molecular weight of the secondary antibody is usually sufficient for monitoring the binding process. The calculated R_{max} value of this injection represents the functional antigen density as bound to the sensor surface in the previous step. For further signal enhancement, antibody conjugates with an enzyme generating insoluble precipitates or colloidal gold as refractive index label can be used.[15] An advanced application is described in Section 12.6.2 regarding a signal enhancement cascade for boosting the dynamic range.

Published on 24 May 2017 on http://pubs.rsc.org | doi:10.1039/9781788010283-00001

View Online

Published on 24 May 2017 on http://pubs.rsc.org | doi:10.1039/9781788010283-00001

1.7 How to Read This Book

Although most of the chapters can be read as stand-alone literature on different aspects of SPR technology, this handbook aims to provide the reader with total coverage of the basics of biomolecular interaction sensing and its applications and most relevant developments at the time of reviewing. The next chapter provides the history and a description of the physics of surface plasmons and SPR in its original form.

The description of SPR instrumentation and a survey of currently available commercial products from various companies follow in Chapter 3. An introduction on how to obtain kinetic information from SPR measurements and get a feeling for the curves based on the ''SPR pages'' on the Internet can be found in Chapter 4 by Arnoud Marquart. In Chapter 5, distribution analysis is explained by Huaying Zhao and Peter Schuck. Chapter 6, by Erk Gedig, brings the reader closer to the surface architecture and chemical design strategies for SPR assay protocols.

Specific application areas are highlighted in subsequent chapters. The latest advanced information on Biacore instruments for fragment and low molecular weight compound analysis is discussed in Chapter 7 by Robert Karlsson *et al.* Chapter 8, by Koen Wagner, describes the full characterization of antibodies regarding ranking the affinity, epitope binning, and mapping to the single amino acid level. In Chapter 9, by Noah Ditto and Josh Eckman, modern software tools for processing of raw data and the analysis of biomolecular interactions for affinity determination and epitope binning are treated. Because of the important role of biolayer interferometry (BLI) in label-free interaction analysis, Chapter 10, by David Apiyo, deals the various aspect of BLI technology. Chapter 11, by Sylvie Ricard-Blum *et al.*, is an application chapter about protein interaction networks and is a tutorial for good SPR analysis practice. The final Chapter 12 summarizes SPR technology in general and gives an outlook on future trends including SPR cytometry, which concerns new cell-based applications.

1.8 Questions

1. How can you reduce mass transport-limited interactions?
2. Eqn (1.19) expresses the R_{eq} value for various concentrations of the analyte. Calculate the values of R_{eq} in $\%R_{max}$ for $c_0 = 1/10K_D$, K_D and $10K_D$.
3. Why is it so important for equilibrium analysis that the response of a signal spot shows exactly the same sensitivity to a common refractive index shift (*e.g.* by glycerol) as a reference spot? How do you check that these responses are similar for various glycerol concentrations?
4. The R_{max} value represents the functional ligand density. Explain this and how you can determine the R_{max} value.
5. Explain why the concentration of an analyte in a direct assay should be determined in the MTL regime and in a sandwich assay by determining R_{max} of the sandwicher.

View Online

References

1. B. Johnsson, S. Löfås and G. Lindquist, *Anal. Biochem.*, 1991, **198**, 168–277.
2. J. M. McDonnell, *Curr. Opin. Chem. Biol.*, 2001, **5**, 572–577.
3. B. Liedberg, C. Nylander and I. Lundström, *Sens. Actuators*, 1983, **4**, 299–304.
4. R. Karlsson and A. Fält, *J. Immunol. Methods*, 1997, **200**, 121–133.
5. E. Kretschmann, *Z. Phys.*, 1971, **241**, 313–324.
6. R. Karlsson and A. Fält, *J. Immunol. Methods*, 1997, **200**, 121–133.
7. P. W. Atkins, *Physical Chemistry*, 6th edn, 1998.
8. P. Schuck, *Annu. Rev. Biophys. Biomol. Struct.*, 1997, **26**, 541–566.
9. R. Karlsson and H. Roos, US Patent Application Publication US20140141529, May 22nd, 2014.
10. E. Pol, H. Roos, F. Markey, F. Elwinger, A. Shaw and R. Karlsson, *Anal. Biochem.*, 2016, **510**, 88–97.
11. T. A. Morton, D. G. Myszka and I. M. Chaiken, *Anal. Biochem.*, 1995, **227**, 176–185.
12. D. G. Myszka, T. A. Morton, M. L. Doyle and I. M. Chaiken, *Biophys. Chem.*, 1997, **6**, 127–137.
13. K. P. M. Geuijen *et al.*, *Anal. Biochem.*, 2014, **454**(1), 38–40.
14. *The Immunoassay Book*, ed. D. Wild, Stockton Press, New York, 1994.
15. G. A. J. Besselink *et al.*, *Anal. Biochem.*, 2004, **333**(1), 165–173.

Published on 24 May 2017 on http://pubs.rsc.org | doi:10.1039/9781788010283-00001

Published on 24 May 2017 on http://pubs.rsc.org | doi:10.1039/9781788010283-00027

CHAPTER 2

History and Physics of Surface Plasmon Resonance

RICHARD B. M. SCHASFOORT

Medical Cell BioPhysics Group (MCBP), MIRA Institute,
University of Twente, P.O. Box 217, 7500 AE Enschede, The Netherlands
Email: r.b.m.schasfoort@utwente.nl

2.1 Introduction

In the last three decades, surface plasmon resonance (SPR) has evolved from a fairly esoteric physical phenomenon to an optical tool that is widely used in physical, chemical, and biological investigations where the characterization of (bio)molecular interactions is of interest. This chapter is an adapted version of Chapter 2 in the first edition of this handbook (2008), entitled ''Physics of Surface Plasmon Resonance,'' written by Rob Kooyman, who retired 4 years ago. In the last decade, the field of SPR nano-optics has been expanded such that metallic structures on a nanoscale can be designed so that they can perform certain optical functions. However, this chapter is dedicated only to the more conventional, well-understood planar SPR theory used in applications for biomolecular interaction sensing.

Essential for the generation of surface plasmons (SPs; also called plasmon polaritons) is the presence of free electrons at the interface of two materials; in practice, this almost always implies that one of these materials is a metal (usually gold) where free conduction electrons are abundant. This condition follows naturally from the analysis of a metal/dielectric interface by Maxwell's equations. From this analysis, the picture emerges that surface plasmons can be considered as *propagating electron density waves occurring at the interface between a metal and a dielectric*. Photons excite under certain conditions, which

Handbook of Surface Plasmon Resonance, 2nd Edition
Edited by Richard B. M. Schasfoort
© The Royal Society of Chemistry 2017
Published by the Royal Society of Chemistry, www.rsc.org

View Online

will be explained physically in this chapter, as free electrons in a metal as in a gas plasma. Hence the word ''PLASMON'' is an abbreviation of ''PLASM-a'' and ''electr-ON.'' Actually, it is the single quantum of a plasma oscillation, similar to a photon, which is a single quantum of an electromagnetic oscillation.

Published on 24 May 2017 on http://pubs.rsc.org | doi:10.1039/9781788010283-00027

Basic Principles of SPR

A qualitative description of the principles of ''SPR for dummies'' can be found here.

Surface plasmon resonance is a phenomenon that occurs when light is reflected off thin metal films. A fraction of the light energy that shines at a sharply defined angle can interact with the delocalized electrons in the metal film (plasmon), thus reducing the reflected light intensity.

From a physical point of view, surface plasmons are surface electromagnetic waves that propagate in a direction parallel to the metal–dielectric (glass or water) interface. Since the wave is on the boundary of the metal and the external medium (water, for example), these oscillations are very sensitive to any change of this boundary, such as the adsorption of molecules on the metal surface. In order to excite surface plasmons in a resonant manner, one can use a light beam of a certain wavelength (visible and infrared are typical). The incoming beam has to match its momentum to that of the plasmon as described in this chapter.

In the case of p-polarized light (polarization occurs parallel to the plane of incidence), this is possible by passing the light through a block of glass with an evaporated thin metal layer on top and achieving the resonance condition at a given wavelength and angle. s-Polarized light (polarization occurs perpendicular to the plane of incidence) cannot excite electronic surface plasmons. The precise angle of incidence of p-polarized light at which this occurs is determined by a number of factors that are explained in this chapter.

Typical metals that support surface plasmons are silver and gold, but others such as copper, titanium, and chromium have also been used. In the Kretschmann configuration, the metal film is evaporated onto a prism or any higher refractive index glass block. The light illuminates the prism and an evanescent wave penetrates through the metal film. The plasmons are excited in the thin metal film between the lower RI medium (*e.g.* water) and higher RI medium (glass).

This Kretschmann configuration is used in most commercial SPR instruments and the principal determinant becomes the refractive index close to the metal film, to which ligand molecules are immobilized and addressed by analyte molecules in a mobile phase. If binding to the immobilized ligand occurs, the local effective refractive index changes, which results in a change in SPR angle. This can be monitored in real time, producing a sensorgram. The size of the change in SPR signal is directly proportional to the mass being captured by specific immobilized ligand molecules.

View Online

Published on 24 May 2017 on http://pubs.rsc.org | doi:10.1039/9781788010283-00027

Alternatively, surface plasmons (SPs) can be viewed as electromagnetic waves strongly bound to this metal interface; it is found that the surface plasmon field intensity at the interface can be made very high, which is the main reason why SPR is such a powerful tool for many types of interface studies.

Experimental research on SPs started with electron beam excitation; in 1968, optical excitation was demonstrated by Otto[1] and Kretschmann and Raether.[2] This last approach turned out to be much more versatile.

2.2 History

2.2.1 Early History of SPR Biosensors

Since its first observation by Wood in 1902,[3,4] the physical phenomenon of SPR found its way to practical applications in sensitive detectors, capable of detecting sub-monomolecular coverage of proteins. What is surface plasmon resonance? Wood observed a pattern of ''anomalous'' dark and light bands in the reflected light when he shone polarized light on a mirror with a diffraction grating on its surface. Physical interpretation of the phenomenon was initiated by Lord Rayleigh,[5] further refined by Fano,[6] but a complete explanation of the phenomenon was not possible until 1968, when Otto[1] and in the same year Kretschmann and Raether[2] reported the excitation of surface plasmons.

In Lundström's pursuit of physical methods for the label-free, real-time detection of biomolecules, an application of SPR-based sensors in biomolecular interaction monitoring was first demonstrated in 1983 by Liedberg, Nylander, and Lundström, then of the Linköping Institute of Technology (Sweden).[7] They adsorbed human immunoglobulin G (IgG) on a 60 nm silver film and used the assay to detect anti-human IgG in aqueous solution. Other physical techniques were explored for probing the intrinsic properties of the molecules, *e.g.* mass, refractive index, and/or charge distribution,[8] using ellipsometry, refractometry, and photothermic detection methods, among others. At the National Defense Research Laboratory of Sweden, protein–protein interactions were monitored in real time, label free, using ellipsometry. Most importantly, the refractive index change at a light-reflecting surface was the operating transducer mechanism. Although successful in the detection of refractive index change due to the binding of biomolecules on optical transducer surfaces, a disadvantage of the ellipsometer is that light passes through the bulk of the sample solution, hence light-absorbing or particle-containing samples cannot easily be measured.

Among other research laboratories in the same period, the University of Twente (The Netherlands) was active in the search to find new transduction principles for measuring immunochemical reactions with field-effect transistor devices (immunoFET),[9] and at surfaces with an optical readout [immunochemical optical biosensor (IMOB)]. Optical transducer principles,[10] including ellipsometry, SPR, and interferometric principles

View Online

Published on 24 May 2017 on http://pubs.rsc.org | doi:10.1039/9781788010283-00027

(Mach Zehnder), showed promise for direct transduction of the biomolecular binding event.[11] Successful measurements of immunochemical reactions using SPR were carried out and published as early as in the mid-1980s.[12]

Pharmacia Biosensor chose SPR as their platform technology for the direct sensing of biomolecular interactions and resolved the issues regarding fluidics and surface chemistry in a 6 year development program. The Kretschmann configuration offered advantages in freedom of design of the liquid handling system. Coming from the higher refractive index medium (the prism), light does not pass through the liquid, but is reflected at the sensor surface covered with a thin metal layer. Gold was chosen as the best inert metal film required for SPR, although from a physical point of view silver provides a better SPR effect (see Figure 2.5).

Studies on the surface chemistry led to modification of the gold with a self-assembling layer of long-chain thiols to which a hydrogel could be attached. Carboxylated dextran was immobilized at the surface, which provided a substrate for efficient covalent immobilization of biomolecules, and also a favorable environment for most biomolecular interactions. The thickness of the dextran hydrogel of 100–200 nm is perfectly compatible with the ~400 nm decaying evanescent field. The reliable production of these high-quality sensor chips was unequivocally the basis for the successful launch of SPR instruments by Pharmacia Biosensor in 1990.[13]

Techniques were developed to etch silica to form a casting mold for the manufacture of microfluidic flow channels. Also, development proceeded of optogels for use between the prism in the optical unit of the instrument and the sensor chip. The optogel ensures optical contact with the prism, allowing simple replacement of the sensor chip. These efforts in research and development relied on the combination of three unrelated research fields, optics, microfluidics, and surface chemistry, and resulted in the successful development of the instrumental concept of biomolecular interaction analysis (BIA).

2.2.2 History of SPR Biosensors After 1990

In 1990, Pharmacia Biosensor launched the first commercial SPR product, the Biacore instrument.[14] The instrument was the most advanced, sensitive, accurate, reliable, reproducible, direct, label-free biosensor technique and SPR became (and still is after more than 25 years!) the ''gold standard'' of transducer principles for measuring real-time biomolecular interactions. Since the early 1990s, producers have been struggling to meet the standards set by Biacore. Fisons Instruments[†15] made serious attempts to compete with Biacore's technology; their cuvette-based IAsys instrument used evanescent field-based technology, so-called resonant mirror technology, essentially not SPR, for the study of biomolecular interactions.

[†]Later Affinity Sensors.

View Online

Published on 24 May 2017 on http://pubs.rsc.org | doi:10.1039/9781788010283-00027

In 1995, the cuvette-based single-channel SPR system of IBIS Technologies was launched. The instrument was compatible with the Biacore sensor chip but optically according to the scanning angle principle (see Section 2.4.3). In 1997, the IBIS II, a two-channel cuvette-based SPR instrument with autosampler operation, was introduced.[16] Following the merger with the sensor surface coating company Ssens BV in 1999, IBIS Technologies started the development of an SPR imaging instrument;[17] however, including the development of replacing the cuvette system with a unique back-and-forth flow cell system, it took many years to meet the high standards set by Biacore for the reliable detection of biomolecular interactions.

Although it is impossible to describe accurately the history of the developments of the 25 companies producing SPR and SPR-like instruments (see Chapter 3), it is reasonable to treat the history along the Biacore product line. In Chapter 3, upcoming new and withdrawn old products in the market are updated as of 2016. However, first the optics should be explained further in more detail. The following treatise is by no means intended to provide an in-depth physical theory of SPR – rather, it is an attempt to give a low-threshold introduction to the physics of SPR for those who are actually involved in SPR work and want to understand something more than "*measuring the shift of the SPR-dip*."

2.3 Surface Plasmon Theory

2.3.1 The Evanescent Wave

Before we discuss surface plasmons in more detail, it may be appropriate to provide a mathematical description of the evanescent wave, which is central in the concept of SPR sensing. This can be explained by considering the phenomenon of total internal reflection occurring in the evanescent field of a reflecting surface.

We consider the refraction of an electromagnetic wave at an interface between two media 1 and 2 with refractive indices n_1 and n_2, respectively (see Figure 2.1). Then $\boldsymbol{k}$ is the wavevector;[18] its direction is parallel to that of the wave propagation and its magnitude is given by

$$k = \sqrt{k_x^2 + k_y^2 + k_z^2} = n\frac{2\pi}{\lambda} = n\frac{\omega}{c} \tag{2.1}$$

where λ and c are the wavelength and propagation velocity in vacuum, respectively.[19]

Without loss of generality, we can choose the direction of the light beam such that $k_z = 0$, and our problem becomes essentially two-dimensional. From elementary physics, we know that for this situation Snell's law holds:

$$n_1 \sin\alpha = n_2 \sin\beta \tag{2.2a}$$

View Online

Published on 24 May 2017 on http://pubs.rsc.org | doi:10.1039/9781788010283-00027

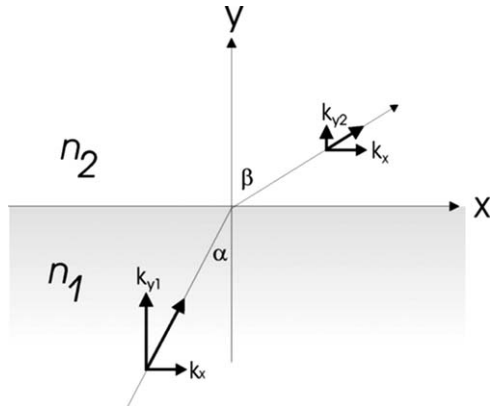


Figure 2.1 Refraction of light at an incident angle α at an interface of two materials with refractive indices n_1 and n_2. This is the applied definition of the axis system and quantities.

or, equivalently,

$$k_{x_1} = k_{x_2} \equiv k_x \tag{2.2b}$$

By using eqn (2.1) and (2.2b), we can find an expression for the component of the wavevector $\boldsymbol{k_y}$ perpendicular to the interface[‡] (so excited by p-polarized[§] light):

$$k_{y_2}^2 = n_1^2 \left(\frac{2\pi}{\lambda}\right)^2 \left(\frac{n_2^2}{n_1^2} - \sin^2\alpha\right) \tag{2.3}$$

Now, let us assume that $n_1 > n_2$, which is the case when the light comes from a medium of higher refractive index (*e.g.* prism) to a medium of lower refractive index (*e.g.* water). From eqn (2.3), it is seen that for $\sin\alpha > n_2/n_1$, so at total internal reflection, the right part is negative and, consequently, k_y is purely imaginary. We conclude that for this case in medium 2 there is only a traveling wave *parallel*, so in the *x*-direction to the interface:

$$E_2 = E_0 \mathrm{e}^{-\kappa_{y_2} y} \exp(j\omega t - jk_x x) \tag{2.4}$$

where E_0 is the amplitude of the electric field, ω is the angular frequency, and $j = \sqrt{-1}$. Here the amplitude of the electric field is exponentially decaying along the *y*-direction with a characteristic distance $1/\kappa_{y_2} \equiv 1/jk_{y_2}$. Note that eqn (2.4) represents a traveling wave only if the exponent is complex.

For obvious reasons, this field in medium 2 is denoted the *evanescent field.* When a single wavelength is applied, the evanescent field can be considered as a fixed refractive index sensitive volume in medium 2 and the field strength is decaying from the surface.

[‡]Note that the direction $\boldsymbol{y}$ in this chapter is always perpendicular to the surface.
[§]p-Polarized light has its electric field vector in the plane of incidence.

View Online

Published on 24 May 2017 on http://pubs.rsc.org | doi:10.1039/9781788010283-00027

Eqn (2.4) can be used to calculate its penetration depth, which is of the order of half a wavelength. This explains the interface sensitivity of the evanescent field: only close to the interface is an electromagnetic field present; thus only a changing dielectric property (*e.g.* a changing refractive index) in the vicinity of the interface will influence this field. Hence total internal reflection from a medium of high to a medium of low refractive index will generate an evanescent or decaying field at a certain wavelength of the incident light. The evanescent wave creates a fixed-volume evanescent field where close to the surface the average refractive index in that volume determines the reflectivity conditions. We shall see that surface plasmons excited in a thin metal layer also generate an evanescent field.

2.3.2 Surface Plasmon Dispersion Equations; Resonance

There are several approaches that all result in the dispersion relation for a surface plasmon, that is, a relation between the angular frequency ω and the wavevector $\boldsymbol{k}$. A particularly elegant approach was suggested by Cardona.[20] For reasons that will be clear in the course of Section 2.3.3, we will discuss only p-polarized light interacting with an interface. For any interface between two media, the complex reflection coefficient r_p for p-polarized incident light electric field is described by Fresnel's equations (see, *e.g.*,[21] for a derivation on the basis of Maxwell's equations):

$$r_p = \frac{E_i}{E_r} = |r_p| e^{j\varphi} = \left|\frac{\tan(\alpha - \beta)}{\tan(\alpha + \beta)}\right| e^{j\varphi} \tag{2.5a}$$

where E_i and E_r are the incident and reflected electric field, respectively, and the angles α and β are defined as shown in Figure 2.1.[¶]

Of course the angles α and β are again related by Snell's law [eqn (2.2)]; in addition, a phase change φ of the reflected field relative to the incident field occurs, depending on the refractive indices of the materials involved. Phase changes are relevant for interferometric phenomena; this is beyond the scope of this chapter. For the reflectance, defined as the ratio of the reflected *intensities*, the following relation holds:

$$R_p = |r_p|^2 \tag{2.5b}$$

Now, following Cardona, two special cases exist: if $\alpha + \beta = \pi/2$, then the denominator of eqn (2.5a) becomes very large and thus R_p becomes zero. This situation describes the Brewster angle, where there is no reflection for p-polarized light. The other special case occurs when $\alpha - \beta = \pi/2$: we see from eqn (2.5a) and (2.5b) that R_p becomes infinite: there is a finite E_r for a very small E_i. This circumstance corresponds to *resonance.* From this relation between α and β we can deduce the dispersion relation if $\alpha - \beta = \pi/2$, then

[¶]Note that in Figure 2.1, the direction y (instead of z) is perpendicular to the surface.

View Online

$\cos\alpha = -\sin\beta$, and $\tan\alpha = k_{1x}/k_{1y} = -n_2/n_1$. For the components of the wavevector $\boldsymbol{k} = (k_x, k_y)$ we can write

$$k_x^2 = k_1^2 - k_{y_1}^2 = k_1^2 - k_x^2 \frac{\varepsilon_1}{\varepsilon_2} \tag{2.6}$$

$$k_x = \frac{\omega}{c}\sqrt{\frac{\varepsilon_1\varepsilon_2}{\varepsilon_1+\varepsilon_2}} \quad \text{and} \quad k_{y_i} = \frac{\omega}{c}\sqrt{\frac{\varepsilon_i^2}{\varepsilon_1+\varepsilon_2}} \tag{2.7}$$

where ε_1 and ε_2 are the dielectric constants[‖] of materials 1 and 2, respectively, and $i = 1$ or 2. Eqn (2.7) is the sought SPR dispersion equation for an interface between two half-infinite media.

Next, we investigate the case where medium 2 is a metal, which implies that the low refractive index medium (*e.g.* water) becomes medium 3. This medium then contains a large number of free electrons, and the consequence is that at an angular frequency $\omega < \omega_p$ its dielectric constant ε_2 will be negative:[21]

$$\varepsilon_2(\omega) = 1 - \frac{\omega_p^2}{\omega^2} \tag{2.8a}$$

$$\omega_p = \sqrt{4\pi n_e e^2/m_e} \tag{2.8b}$$

where ω_p is the so-called plasma frequency, n_e is the free electron density, and e and m_e are the electron charge and mass, respectively.

Generally, this implies that for $\omega < \omega_p$ no electromagnetic field can propagate in a metal [cf. eqn (2.4)]. More specifically, provided that $\varepsilon_2 > -\varepsilon_1$, we find for the interface that k_{y_i} is imaginary, whereas k_x remains real. Thus an electromagnetic wave exists, propagating strictly along the interface, with evanescent tails extending into both sides of the interface. To get a feeling for the quantities involved, it is instructive to calculate penetration depths for a real case, on the basis of eqn (2.4). We take $\lambda = 700$ nm, thus $\omega = 2.69\times10^{15}$ s^{-1}, and a gold/water interface. At this wavelength, $\varepsilon_{gold} \approx -16$ and $\varepsilon_{water} \approx 1.77$. We calculate for the penetration depths $1/k_{y,water} = 238$ nm and $1/k_{y,gold} = 26$ nm.

Now all ingredients are available to appreciate the use of SPR in sensor applications. Let us assume that we have a situation where molecules X are allowed to adsorb at the water/metal interface. We can view this as a process in which water molecules are replaced by molecules X.

Because, generally, $\varepsilon_X \neq \varepsilon_{water}$, the average dielectric constant in the volume close to the interface will change. Eqn (2.7) then describes the concomitant change of the wavevector $\boldsymbol{k_x}$. Because the SP field is evanescent in the direction perpendicular to the interface, a change in the dielectric constant

[‖]Dielectric constant and refractive index are related by $\varepsilon = n^2$.

Published on 24 May 2017 on http://pubs.rsc.org | doi:10.1039/9781788010283-00027

View Online

Published on 24 May 2017 on http://pubs.rsc.org | doi:10.1039/9781788010283-00027

ε_2 is detectable only if this change occurs within the penetration depth of the SP field: an SPR sensor will only be sensitive to molecular processes (binding, adsorption, *etc.*) that occur at a distance from the metal surface that is roughly 1/e times the wavelength of the light used, so in the volumetric portion that fits the evanescent field.

2.3.3 Excitation of Surface Plasmons

By substitution of eqn (2.8a) and (2.8b) into eqn (2.7), we can obtain a graphical representation of the SPR dispersion relation as shown in Figure 2.2. In Figure 2.2, the dispersion relation for ''normal'' light is also depicted [light line (a)]. We immediately see that, apart from the origin, there is no point where the SPR curve and the light line (a) intersect, implying that in this geometry ''normal'' light cannot *simultaneously* provide the correct wavevector and angular frequency to excite a surface plasmon.

One way to circumvent this problem is to introduce a second interface, as depicted in the inset in Figure 2.2. Here a thin metal layer (dielectric constant ε_m) is sandwiched between two dielectric materials 1 and 3 with different dielectric constants ε_1 and ε_3, with $\varepsilon_1 > \varepsilon_3$. By applying Fresnel's

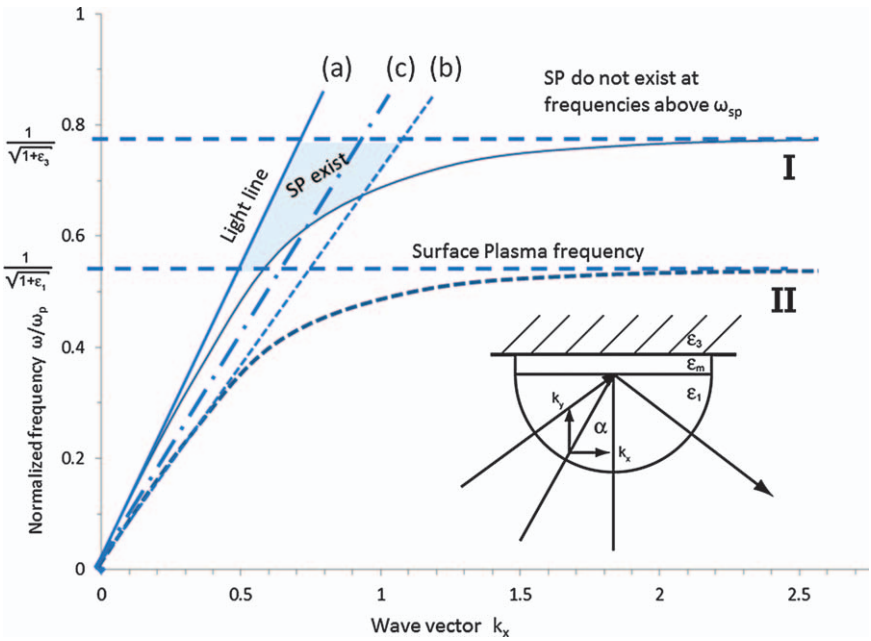


Figure 2.2 Dispersion relation for surface plasmons. Curves I and II represent the SP dispersion for the interfaces $\varepsilon_3/\varepsilon_m$ and $\varepsilon_1/\varepsilon_m$, respectively. The lines (a) and (b) are the dispersion relations for ''normal'' light in media with ε_3 and ε_1, respectively, which are dependent on the angle of incidence α in the experimental setup as indicated in the inset. By varying α, any line (c) between lines (a) and (b) can be realized.

View Online

Published on 24 May 2017 on http://pubs.rsc.org | doi:10.1039/9781788010283-00027

equations to the two interfaces, more complicated dispersion equations than eqn (2.7) are found, which is far beyond the depth of SPR theory as treated in this chapter; however, the essential physics remains unchanged.

We now find *two* dispersion equations for k_x, one for each interface, and we see that the line representing the dispersion relation for ''normal'' light in medium 1 [line (b)] intersects the SP dispersion line for the metal/medium 3 interface. This indicates that light incident from medium 1 can excite SPs: by proper adjustment of the incoming angle α (Figure 2.2, inset), we can tune the incoming wavevector $\boldsymbol{k_x} = kn_1 \sin\alpha$ to match the wavevector necessary for SP excitation. In this way, any k_x between the two lines, labeled (a) and (b) in Figure 2.2, can be set. As an example, one such line, labeled (c), is indicated. This so-called ATR (attenuated total reflection) technique was first demonstrated** by Kretschmann and Raether,[2] and since then has become almost the standard explanation for SP excitation.

In this graphical presentation regarding the SP conditions in Figure 2.2, all tunable parameters result in a change in this graph. For example, if the *ratio* of dielectric constants of medium 1 and medium 3 (glass or water) (refractive index squared) change, then the ''space'' between the horizontal surface plasma frequency lines will also vary. Temperature has a more prominent influence on the refractive index of water than on that of glass and the SP conditions will change accordingly. Further, the wavelength of the incident light influences the light line and the conditions for SP generation will change. For Kretschmann-configured instruments, the SPR condition can be tuned by the angle of incidence (changed wavevector $\boldsymbol{k_x}$) and the other parameters should be fixed tightly in order to obtain a close to linear relation between the refractive index change and the shift of the SPR-dip according to

$$\mathrm{dSPR-dip} <> \sqrt{\frac{\mathrm{d}\varepsilon_3}{\varepsilon_1 + \varepsilon_3 + \mathrm{d}\varepsilon_3}} \sim \mathrm{d}(n_3) \tag{2.9}$$

So far, the required polarization direction of the incoming light has not been mentioned. As already pointed out, SPs are conductivity fluctuations brought about by collective surface charge density oscillations. These charge density waves have to be excited by an external electromagnetic field. Only a field with a component perpendicular to the interface can induce a surface charge density; only p-polarized light has a perpendicular electric field component. Hence s-polarized light will reflect total without plasmon excitation.

Eqn (2.9) describes the linear relation between the shift of the SPR-dip and the shift of the refractive index. However how much it shifts should be calculated from the actual refractive index shift after protein adsorption at the sensor surface at a certain excitation wavelength. A very important ''rule

**In fact, Otto[3] was the first to demonstrate this in a somewhat less versatile form.

View Online

of thumb'' for Biacore-like instruments is the following observation which is generally accepted in the SPR community:

1 ng mm^{-2} protein adsorption results in a shift ca. 1000 RU

Published on 24 May 2017 on http://pubs.rsc.org | doi:10.1039/9781788010283-00027

2.3.4 Surface Plasmon Properties

With SPs, a number of specific properties are associated that are particularly relevant to sensor applications, such as (1) the field enhancement and (2) the SP coherence length.

Field enhancement. Calculation of the electric field transmission coefficient on the basis of Fresnel's equations for the interface reveals that the electric field at the low index side of the metal can be much larger than that at the other side of the metal layer.

In Figure 2.3, the intensity enhancement is depicted as a function of the angle of incidence of incoming light for a number of different thicknesses of a gold layer. It is found that very close to the SPR angle, the intensity can be enhanced by a factor of more than 30. This circumstance accounts for much of the remarkable sensitivity that the SPR condition has to a changing dielectric environment. Noise levels of current (2016) SPR devices are in the order of 0.01 RU, corresponding to changes of 10^{-8} RIU. Hence refractive

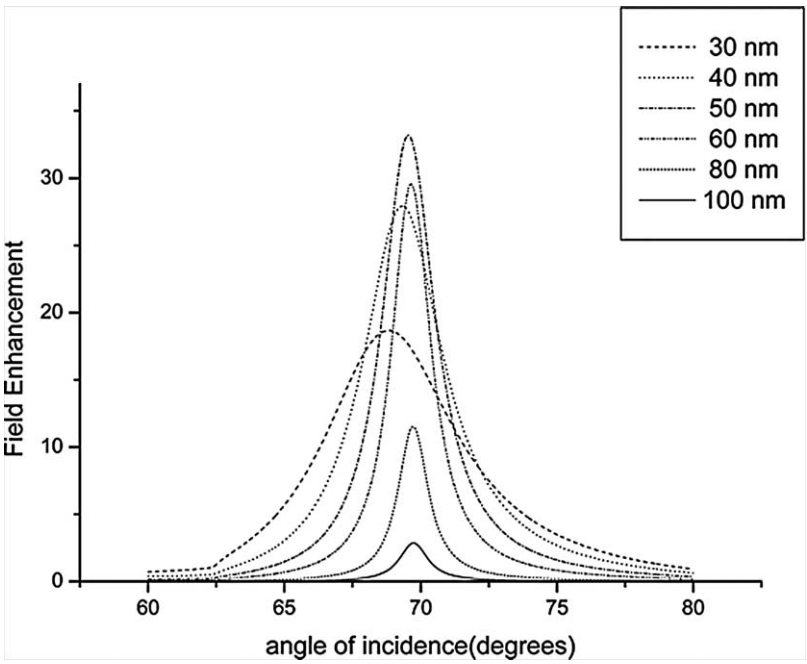


Figure 2.3 Field enhancements for various values of the thickness of the gold layer. Wavelength of the excitation light, 700 nm; the low refractive index side of the metal layer consists of water ($\varepsilon_3 = 1.77$).

View Online

Published on 24 May 2017 on http://pubs.rsc.org | doi:10.1039/9781788010283-00027

index changes of 1.33999999 to 1.34000000 can be detected with the most sensitive instruments on the market!

The shape of the curve (small SPR-dip for better detection of the minimum) is currently less relevant for measuring the reflectivity minimum, because a fitting algorithm (*e.g.* the weighted centroid method or the fixed-boundary centroid algorithm[22]) is applied in modern instruments that apply the whole reflectivity curve and the minima are calculated from these fitting routines (see Figure 2.6). The exact routines generally are not revealed, as they belong to the intellectual property of the instrument manufacturer (see Section 6.2).

SP coherence length. Generally, the metal's dielectric constant ε_2 is complex, which results in a complex propagation constant $k_x = \kappa_x' + j\kappa_x''$ [*cf.* eqn (2.7)], where κ_x' and κ_x'' are the real and imaginary parts, respectively. For a surface plasmon, traveling along the interface with wavevector $\boldsymbol{k_x}$, this implies that the field intensity decays with a characteristic distance $1/2\kappa_x''$. For gold as the standard metal in sensor applications, the imaginary part of the dielectric constant increases with decreasing wavelength, and the SP propagation length decreases accordingly.

This is illustrated in Figure 2.4: here a layer system was prepared in which a 30 nm SiO_2 strip was deposited on a 50 nm silver layer. For two wavelengths, the angle of incidence was chosen such that SPs were excited in the area outside the strip, and for these two wavelengths the whole area was illuminated with a collimated light beam under a constant angle of incidence.

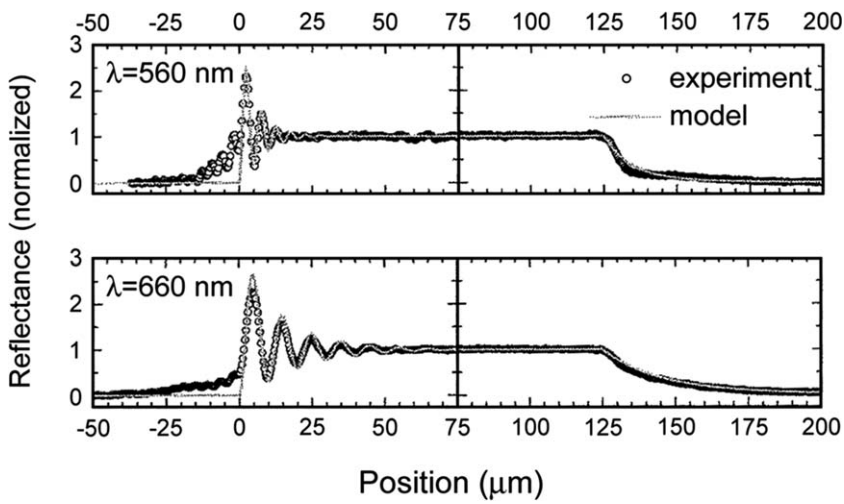


Figure 2.4 SPR response to a dielectric step at 560 and 660 nm. For each wavelength, the light angle of incidence is set such that outside the strip (extending from 0 to 125 μm) the interrogating k_x is resonant with the surface plasmon wavevector. The surroundings of the strip have dielectric constant $\varepsilon_3 = 1$.

View Online

Published on 24 May 2017 on http://pubs.rsc.org | doi:10.1039/9781788010283-00027

Because of the contrast in dielectric constant between the strip and its surroundings (air), the SP resonance condition is not fulfilled in the area below the strip, and we see the decaying SP (increasing reflectance) at the left edge of the strip. Beyond the right edge of the strip, the SPR condition is again fulfilled, and the SP resonance builds up. Figure 2.4 nicely demonstrates that at decreasing wavelength the SP propagation length becomes shorter: the blurring on the left side of the strip becomes less prominent for the 560 nm than the 660 nm wavelength. It turns out that in the wavelength range 500–800 nm the propagation length varies between than ~10 and ~40 μm.

Both this model and the experiments indicate that a plasmon needs roughly four times the propagation length L_x for a full decay or for a full build-up; this propagation length can be loosely defined as[12]

$$L_x = \frac{1}{2\kappa_x''} \tag{2.10}$$

This implies that SPs with mutual distances significantly larger than L_x are independent. This is a very important conclusion because it is the basis of SPR imaging with some applications in SP microscopy.[23] On a sensor surface, we can define areas that in an SPR experiment will behave mutually independently, provided that these areas are significantly larger than L_x.[2]

For SPs on gold, excited at $\lambda = 632$ nm, $L_x \approx 7$ μm, and on a total sensor area of 1 cm^2 more than 10^6 independent sensor "patches" that each have an area of somewhat smaller than 10×10 μm can in principle be defined, of which the optical responses can be simultaneously read out by using an imaging system. As a rule of thumb, for 800 nm wavelength in SPR instruments the propagation length (defined as the distance for the surface plasmon polariton intensity to decay by a factor of 1/e) is ~25 μm[24]

2.3.5 Choice of Experimental Parameters

It is impossible to define a general set of optimum SPR parameters; for instance, optimal spatial resolution in an SPR imaging setup requires values of the experimental parameters other than those to obtain maximum sensitivity for dielectric changes. Therefore, this section provides only some general guidelines, based on consideration of the properties of the metal layer. To obtain maximum sensitivity, it is advantageous to maximize the steepness of the reflectance as a function of the angle of incidence (in reflectivity instruments), because this allows for a more accurate determination of the angle of minimum reflectance (*cf.* Figure 2.5). When centroid fitting is applied, then the reflectance depth (dip) is important, so the quality of the metal layer to generate SPs is also important (see Section 2.3.4).

This implies optimization of the reflectance minimum R_{min} and minimization of the width of the resonance curve. R_{min} can be made very close to

View Online

Published on 24 May 2017 on http://pubs.rsc.org | doi:10.1039/9781788010283-00027

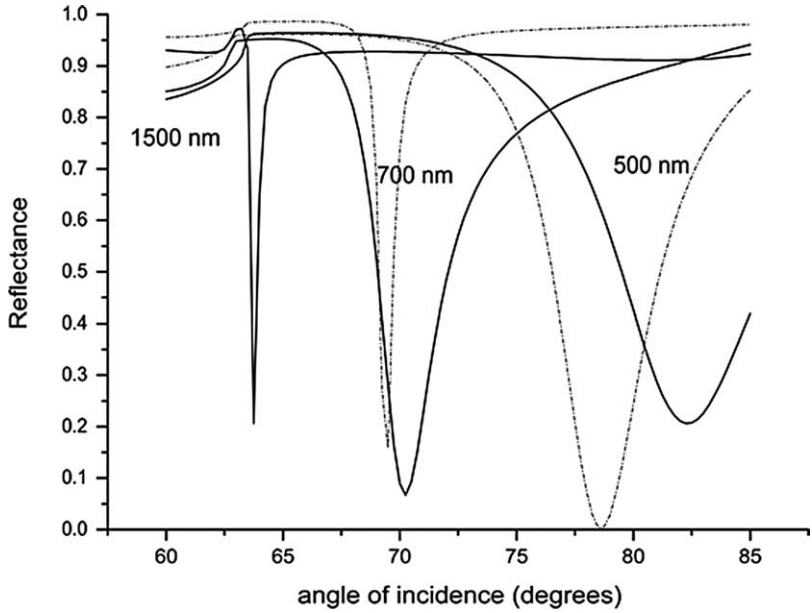


Figure 2.5 The SPR-dip for 46 nm of silver (dashed lines) and gold (solid lines) with water on the low refractive index side, for three excitation wavelengths. Dielectric data for the metal layer were obtained from ref. 3 and 73.

zero by selecting the appropriate thickness of the metal layer; as can be seen in Figure 2.5, optimum thicknesses are dependent on the applied wavelength and are between 40 and 50 nm. The width of the resonance curve is mainly determined by the complex value of the metal's dielectric constant. Generally, a large (negative) real part, together with a small imaginary part, results in narrow resonance curves. In practice, only two options are available for the choice of the metal layer: gold or silver. As seen in Figure 2.5, silver has better SPR characteristics owing to its larger real part of the dielectric constant; however, it is chemically less inert. In Figure 2.5, it is also seen that the use of longer excitation wavelengths has an appreciable effect on the width of the resonance curve. This is one of the reasons why (near-) infrared SPR experiments are gaining attention.[25,26] However, it should be realized that narrowing the reflectance curve necessarily implies increasing the SPR propagation length [eqn (2.10)], which can be a disadvantage in certain SPR imaging applications. For a gold layer, it can be calculated that an increase in wavelength from 450 to 1500 nm results in a change in the propagation length from 100 nm to almost 1 mm. Finally, it should be mentioned that an increase in wavelength results in an increase in the penetration depth $1/k_y$ [*cf.* eqn (2.3) and (2.4)], with the consequence that the reflectance minimum will become more sensitive to dielectric changes relatively far from the metal/dielectric interface; thus, the surface-sensitive

View Online

Published on 24 May 2017 on http://pubs.rsc.org | doi:10.1039/9781788010283-00027

character of SPR becomes less prominent. This implies that for detection of the growth of thin layers, the optimum choice of wavelength will be different from that in a situation where a more bulk-like change of refractive index has to be detected.[27] The IBIS MX96 has been developed with settings of ''best of both worlds'' regarding sensitivity and imaging quality.

In most SPR-based sensor applications, the system of interest consists of a gold layer on which one or more thin layers are deposited in an aqueous environment. For biosensor applications, the approach of an effective dielectric constant ε_{eff} can be applied. Thus, the actual multilayered system is replaced by the effective dielectric constant ε_{eff}, given by the average of all dielectric constants in the layer system, weighted by the penetration depth y_0 of the SPR evanescent field:[28,29]

$$\varepsilon_{\text{eff}} = \frac{2}{y_0}\int_0^{\infty} \varepsilon(y)\mathrm{e}^{-2y/y_0}\mathrm{d}y \tag{2.11}$$

This is the physical explanation for why a sensor surface with coupled ligand molecules is less sensitive than a bare sensor surface and calibration of the channel responses to steps of refractive index is necessary for accurate compensation of the bulk refractive index responses using a reference channel.

These exact calculations always need assumptions for the parameters, *e.g.* what is the effective refractive index of a protein molecule that penetrates the evanescent field and binds to ligand molecules on the sensor surface? Remember the ''rule of thumb'' that *a 1000 RU shift corresponds to adsorption/capture of* $\sim$*1 ng mm*$^{-2}$ of protein molecules with an average amino acid composition. An average amino acid composition is important for the rule of thumb, because the aromatic amino acids contribute more to the refractive index shift than, *e.g.*, the aliphatic amino acid glycine.

SPR phenomena are not restricted to planar multilayers as discussed so far; it turns out that for metal particles with dimensions much smaller than the wavelength of the interacting light, SP effects can be much more prominent. Thus metal nanoparticles can be considered as surface plasmon-assisted field amplifiers (for a review, see ref. 30). However, this intrinsic SP effect applied to Raman and SERS applications is beyond the core of this handbook and the interested reader should consult ref. 31.

Additional to this intrinsic effect, these particles can also be exploited as intrinsic refractive index labels, analogous to familiar planar SPR experiments (for reviews, see ref. 32 and 33). The physical basis of this application is the light extinction (absorption and scattering), which is heavily dependent on the dielectric constant, size, and geometry of the nanoparticles, and also on the dielectric constant ε_1 of the surrounding medium.[34]

The best refractive index labels for use as signal amplifiers in planar SPR devices are gold or silver nanoparticles. More sophisticated models (see, *e.g.*, ref. 35) also account for the size and shape of the nanoparticles, and

View Online

computer programs are available in the public domain that can predict the extinction spectrum of nanoparticles of any shape,[36] by modeling the particle as a series of dipoles placed in an oscillating electromagnetic field.

Published on 24 May 2017 on http://pubs.rsc.org | doi:10.1039/9781788010283-00027

2.3.6 Optimizing SPR Imaging Performance

For any target application, the performance requirements for an SPR imaging instrument can be broken down into two categories: RI resolution and lateral resolution over the field of view. Optimization of these performance parameters in SPR imagers is discussed in this section.

2.3.6.1 Refractive Index Resolution

An SPR imager requires adequate RI resolution for detecting low levels of the target analyte(s). In SPR imaging, the signal-to-noise ratio (SNR), the ratio of the SPR signal (the change in reflectivity that results in the change in the SPR-dip shift) to noise (the uncertainty in the measurement), can be expressed as

$$\mathrm{SNR} = \sqrt{I} \times \frac{\mathrm{d}R}{\mathrm{d}n} \times \frac{\Delta n}{\sqrt{R}} \tag{2.12}$$

where I is the illumination intensity, R is the reflectivity, Δn is the change in RI, and the sensitivity, $\mathrm{d}R/\mathrm{d}n$, is the derivative of reflectivity with respect to RI.[37] Because the SPR-dip shift is the direct result of the change in reflectivity, the resolution for the dip shift is similar to eqn (2.12) improved by the square root of the number of angles measured from the first inflection point to the second inflection point of the SPR-dip. The reflectivity will change only slightly during measurement of a typical binding event, so for measurement of the RI resolution, Δn_{LOD}, eqn (2.12) can be expressed as

$$\Delta n_{\mathrm{LOD}} \propto \frac{1}{\sqrt{I}\dfrac{\mathrm{d}R}{\mathrm{d}n}} \tag{2.13}$$

Optimization of the RI resolution translates into maximizing the quantity $\sqrt{I}(\mathrm{d}R/\mathrm{d}n)$. The main parameters available to the user for maximizing $\mathrm{d}R/\mathrm{d}n$ are the interrogation wavelength and angle. Greater $\mathrm{d}R/\mathrm{d}n$ values occur at longer wavelengths[38,39] because the plasmon propagation length will be longer and the evanescent field deeper. The choice of angle is more involved because the incident angle that maximizes $\mathrm{d}R/\mathrm{d}n$ varies depending on the sample RI, but for a chosen illumination wavelength such an angle can be found. Increasing I should be accompanied by changes in the detector that enable an increased number of photoelectrons to be accumulated without saturating the detector.

One way to increase I is to increase the range of imaging wavelengths and incident angles ($\Delta\lambda$ and $\Delta\theta$) for a given measurement. However, adjustment

View Online

Published on 24 May 2017 on http://pubs.rsc.org | doi:10.1039/9781788010283-00027

of either $\Delta\lambda$ or $\Delta\theta$ will increase I but reduce dR/dn. Determination of the optimal $\Delta\lambda$ and $\Delta\theta$ is effected by balancing these effects. Nelson *et al.* reported a threefold increase in the SNR of their system (leading to an improved RI resolution) through the use of a source filter with a 10 times wider bandpass (10 nm compared with a 1 nm wide bandpass filter).[40]

2.3.6.2 *SPR-dip Detection*

Because the reflectivity intensity can only be detected at discrete angles, the position of the SPR minimum should be calculated from these intensities. A brief introduction is given in Figure 2.6. An algorithm for determining the surface plasmon resonance (SPR) angle, called the fixed-boundary centroid algorithm,[22] performs well with aspects such as operation time, sensitivity to shot noise, signal-to-noise ratio (SNR), resolution, and measurement range. The distance between nodes and the side length of triangles formed by beacon nodes as the weighting factor is taken (see Figure 2.6 and page 64 in ref. 49). The algorithm has improved the SPR-dip positioning accuracy greatly. In the literature, many other protocols have been described for fitting the minimum, but the instrument providers do not reveal how they

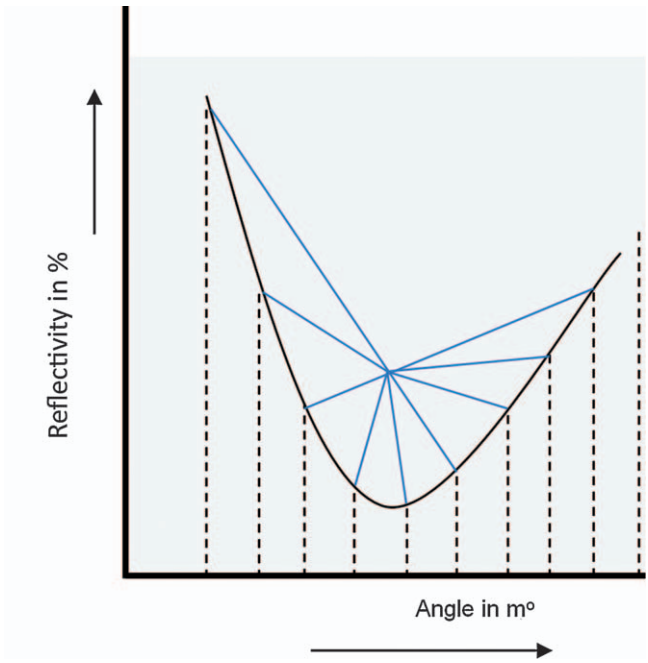


Figure 2.6 The fixed-boundary centroid algorithm[22] performs well with respect to aspects such as operation time, sensitivity to shot noise, signal-to-noise ratio (SNR), resolution, and measurement range. The distance between nodes and the side length of triangles formed by beacon nodes as the weighting factor is taken.

View Online

Published on 24 May 2017 on http://pubs.rsc.org | doi:10.1039/9781788010283-00027

apply these algorithms in their instruments as part of their intellectual property.

Image averaging and normalization can also be used to improve the RI resolution. A signal ''region of interest'' (RoI) and a reference RoI can be applied to normalize the responses. Because the reference sector is not in resonance, any changes in its brightness are expected to be due to light source variations, camera fluctuations, and other systematic effects. Image averaging and normalization successfully reduce the measured noise to a level that is inversely proportional to the square root of the number of pixels averaged.[41,42] In contrast, the noise level of the non-normalized data decreases at a slower rate for high levels of averaging, indicating the presence of noise components that are correlated across pixels and thus cannot be reduced with averaging.

Uniform SPR response is required across the instrument field of view in order to make quantitative comparisons between multiple RoI locations. A comparison of the normalized reflectivity of multiple regions of interest across the image provides a useful measurement of the response uniformity. An example of this is shown in Figure 2.7. During sensing operations, the incident angle is typically adjusted (see Figure 2.7) such that the reflected intensity of the signal spots is approximately one-third up the left side of the curve while the reference spots are in the best resonance condition giving a dark background. (vertical fix line in Figure 2.7). Binding to the sensor surface will cause a local increase in RI, a shift of the SPR curve to higher angles, and an increase in reflected intensity. Changes in intensity will be approximately linear with respect to small RI shifts, provided that the operating point remains on the portion of the SPR curve that is close to linear.[43]

2.3.6.3 *Lateral Resolution Over the Field of View*

The SPR imager should have adequate lateral resolution to distinguish the surface structures of interest for the target application. In the case of an instrument designed to make measurements on multiple analytes simultaneously, the lateral resolution will determine the minimum area of the independent capture regions and also place an upper limit on the number of possible parallel measurements. Specifications for the target application will influence the desired quality of focus over the field of view of the instrument and the choice of operating wavelength.

One factor that affects the lateral resolution of an SPR imager is the quality of focus over the instrument field of view. A notable feature of SPR imager optics is that the object (*i.e.* the SPR sensing surface) is tilted relative to the optical axis of the imaging optics. If standard imaging optics are used, much of the object is either closer or further away than is required for best focus. SPR imagers in the literature often accept this limited depth of field. An alternative approach with potentially better performance is to use a tilted image plane as dictated by the Scheimpflug condition,[44] *i.e.* if the object and

View Online

Published on 24 May 2017 on http://pubs.rsc.org | doi:10.1039/9781788010283-00027

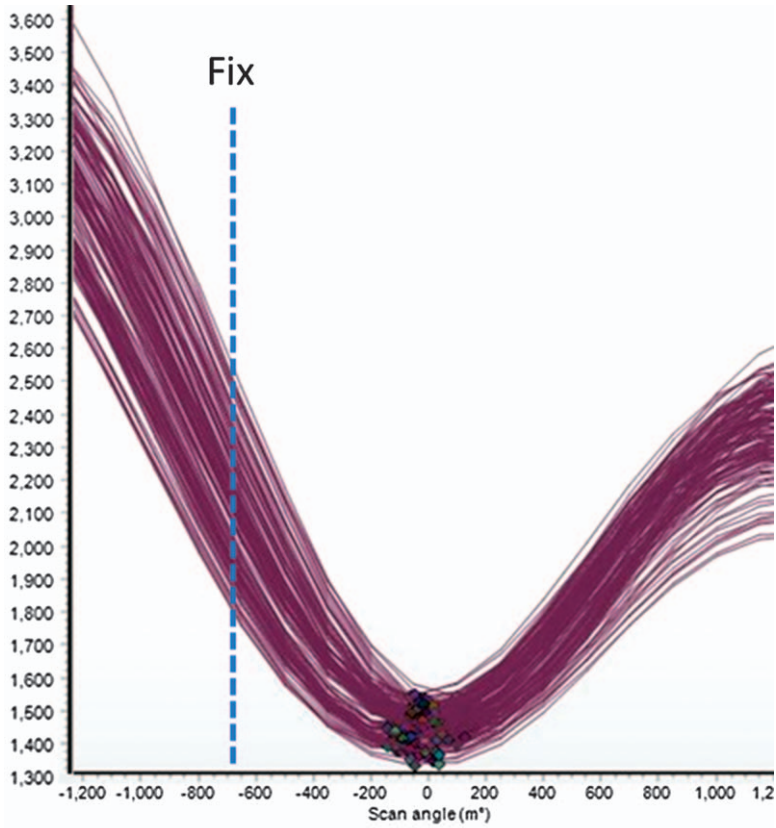


Figure 2.7 Reflectivity as a function of the scan angle for 144 SPR dips simultaneously. (IBIS MX96). The SPR-dip positions are determined for each curve (marks at the minimum). Shifts in reflectivity are most prominent in the inflection point of the SPR curve. An ''average'' inflection point (line fix) should be determined to generate the most contrast in the image.

image are tilted such that the object plane, the image plane, and the lens plane meet in a single line, the entire image will be in focus. The use of a tilted image plane becomes most important when a large depth of field is needed and the collimation of the input light has been relaxed in order to increase light throughput. For an SPR imager, the object tilt is often fairly large, and meeting the Scheimpflug condition may present some difficulties (*e.g.* typical lens mounts for commercially packaged imagers will block light that has a sufficiently oblique angle of incidence, and some image detectors have properties that make them unsuitable for use at oblique angles of incidence). Figure 2.8 demonstrates the quality of focus that can be gained by satisfying the Scheimpflug condition.

As already stated, the change in the SPR reflectivity per unit RI is greater at longer wavelengths. However, use of longer wavelengths also produces

View Online

Published on 24 May 2017 on http://pubs.rsc.org | doi:10.1039/9781788010283-00027

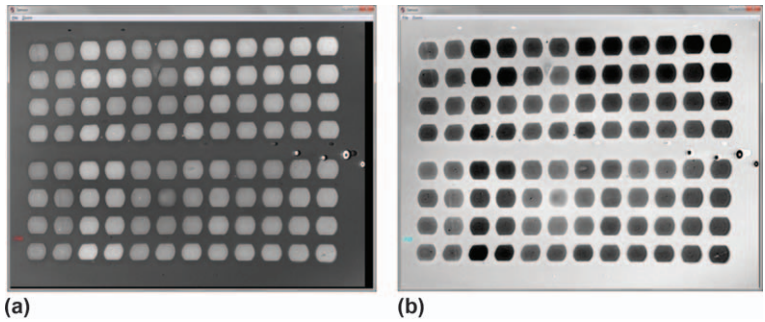


Figure 2.8 SPR reflectivity image of a spotted 8×12 array irradiated at two incident angles in (A) and (B). (A) The reference areas are in full resonance whereas the spots with immobilized ligands are not in resonance. (B) The reference areas show reflectivity whereas the signal spots are in the resonance condition. The images were measured using the IBIS MX96 instrument.

surface plasmons with longer propagation lengths (*e.g.* ~25 μm for a gold layer at 830 nm[45] compared with 0.1 μm for a gold layer at 488 nm[46]). This surface plasmon propagation length presents an inherent limit to the lateral resolution of the imager, but only in the dimension parallel to surface plasmon propagation. de Bruijn *et al.*[47] demonstrated the utility of rotating an object such that the critical dimension is perpendicular to the direction of surface plasmon propagation. The lateral resolution for the critical dimension is then determined only by the optics of the system. A balance between the lateral resolution and the RI resolution should be established given the requirements for the target application.

2.4 SPR Instrument Optics

SPR instrumentation can be configured in various ways to measure the shift of the SPR-dip. In general, three different optical systems are used to excite surface plasmons: systems with prisms, gratings, and optical waveguides, as explained in the previous section and more extensively by Homola.[48] Most widespread are instruments with a prism coupler, also called the "Kretschmann configuration".[49] In this configuration, a prism couples p-polarized light into the SP film and reflects the light onto a light intensity detecting device, *e.g.* a photodiode or even a camera. A sensorgram can be obtained in at least three ways: (1) reflectivity shift *versus* time, (2) angle shift *versus* time, or (3) wavelength shift *versus* time. This configuration can be further divided into three subgroups: fixed angle, fan-shaped beam and angle scanning SPR instruments, as explained in the following sections. In instruments with a grating-coupler,[50] light is reflected at the lower RI substrate. In practice, this means that light travels through the liquid before photons generate surface plasmon waves in a similar manner to ellipsometer instruments.[51] Apart from the grating couplers, some instruments apply optical waveguide couplers[52]

View Online

Published on 24 May 2017 on http://pubs.rsc.org | doi:10.1039/9781788010283-00027

or apply the SPR wavelength shift as a result of the biomolecular interaction process.[53] In the following section, basic features and characteristics of the different optical SPR systems are treated. In the final section, SPR imaging principles are discussed.[54] In Chapter 3, key commercial instruments are described based on the principles described in this chapter.

2.4.1 Fixed Angle

In the left part of Figure 2.9, the reflectivity, *i.e.* the ratio of incoming and reflected light *versus* angle of incidence, passes through a minimum depending on the angle of incidence of the p-polarized light. On adsorption or binding of molecules, the RI at the sensor surface will change in real time, causing a shift of the reflectivity curve. This shift can be observed as shown in the sensorgram on the right in Figure 2.9.

Fixed-angle SPR instruments (Figure 2.10) measure the reflectivity on the left flank of an SPR curve resulting from the shift of the SPR-dip as shown by the vertical line between X_1 and X_{11} in Figure 2.9. The ''fix line'' (Figure 2.7) in an SPR imaging instrument can also be applied to measure the shift in reflectivity. In many instruments of this type, the angle can be adjusted to find the inflection point of the SPR curve in order to achieve the maximum reflectivity change. Sometimes a stepper motor-operated angle positioner

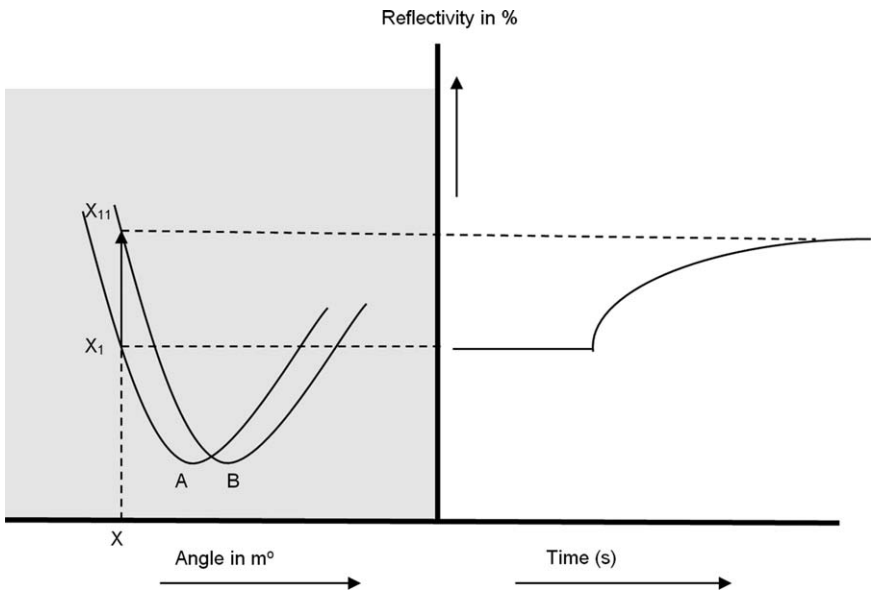


Figure 2.9 Shift of the SPR-dip from A to B. A derivative parameter of the shift of the SPR curve is the reflectivity (*y*-axis) measured at a fixed angle at the left flank of the SPR-dip (see arrow showing reflectivity shift of X1 to X11). In the sensorgram on the right the reflectivity shift as a function of time is shown.

View Online

Published on 24 May 2017 on http://pubs.rsc.org | doi:10.1039/9781788010283-00027

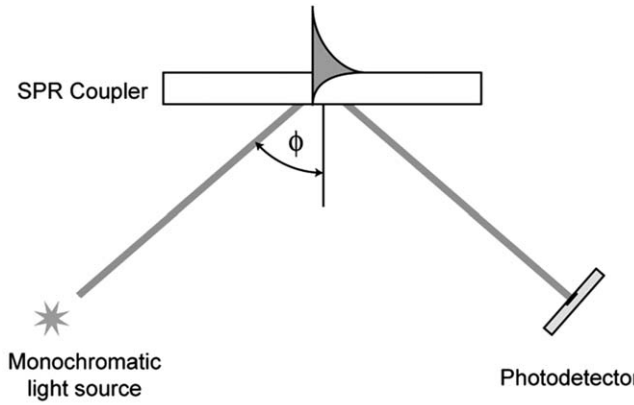


Figure 2.10 In a fixed-angle SPR instrument, the reflectivity is detected at a set angle. The angle position (X-position in Figure 2.9) can be set manually or using an angle stepper motor.

(or mirror) is applied to automate the setting of the (optimal) starting angle. An inflection point can be determined from the second derivative of the SPR curve, which gives the user the most sensitive starting angle or highest slope of the reflectivity shift *versus* angle shift. In the image it results in the best contrast. However, two differently treated channels usually require different optimal starting angles and therefore the reflectivities cannot be quantitatively compared without correction for the shape of the SPR curve. The linearity of SPR-dip shift *versus* reflectivity shift holds for only a very small angular window.

Errors in the position of the starting angle on the initial SPR curve can result in a highly unreliable sensorgram. Importantly, a bulk refractive index shift or background response will be generated if the RI of the medium changes, *e.g.* due to differences in solvent composition. Reflectivity measurements should be checked with the measurement of the angle- (or wavelength-) resolved SPR curve.

2.4.2 Fan-shaped Beam

In Figure 2.11, a sensorgram of analyte binding *versus* time is presented, together with a rotated view of an SPR-dip. While the SPR-dip shift is the most representative and linear parameter of the biomolecular interaction process in time, one should follow the angle of the SPR minimum (dip). As the dip shifts in the left section from A to B, the SPR-dip in the right part of Figure 2.11, the angle shift as a function of time, is shown, called the sensorgram.

Usually, the SPR curve is measured or fitted, and the angle of the SPR-dip is determined, followed by plotting the angle of the SPR minimum in the sensorgram (right part of Figure 2.11).

View Online

Published on 24 May 2017 on http://pubs.rsc.org | doi:10.1039/9781788010283-00027

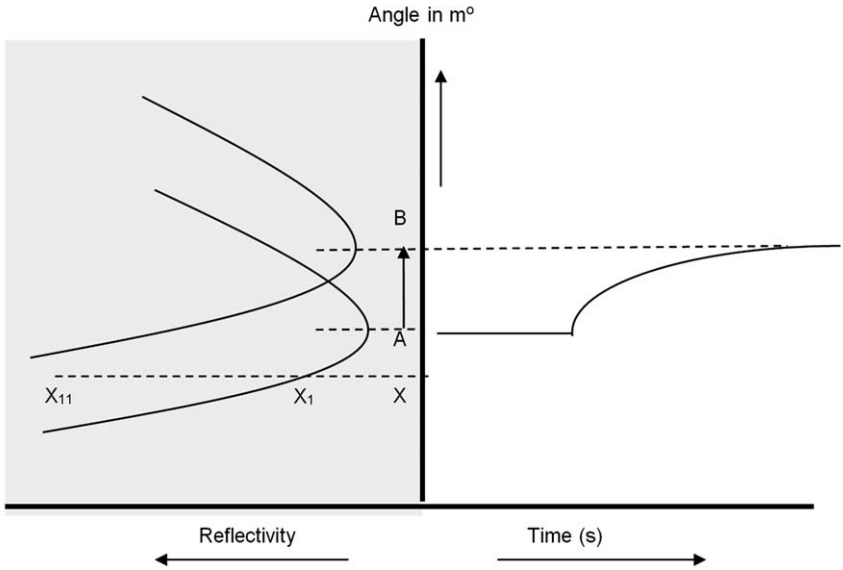


Figure 2.11 Rotated presentation of the SPR-dip (left) that forms directly the pointer of the sensorgram (right). The angle shift of the SPR-dip is determined (left, A to B), followed by plotting the angle of the SPR minimum in the sensorgram *versus* time (right). Here the SPR-dip minimum of the initial curve (A) shifts with time toward a higher angle (B).

In order to measure the shift of the dip position, the construction of the instrument should be different, as with reflectivity instruments.

In a fan-shaped beam instrument, a converging or diverging beam of p-polarized light is coupled in the higher RI medium using a cylindrical or triangular prism. In a *converging* beam fan-shaped instrument (*e.g.* Biacore), the beam is focused onto an infinitely narrow line on the sensor chip. A photodiode array is used to detect the reflected diverging beam with the SPR-dip (see Figure 2.12). A line on the sensor can be imaged on a camera by measuring, *e.g.*, 4–20 sensor spots. This principle has been successfully applied in Biacore instruments since 1990. Other instruments in this category often use a *diverging* fan-shaped beam, resulting in a not spatially defined location of the SPR-dip on the sensor chip: the position of the SPR minimum ''walks'' over the sensor chip while the biomolecular interaction process proceeds.

A sensorgram can be obtained from a monochromatic light source using either the reflectivity change at fixed angle (y-axis in $\%R$) or the SPR-dip shift (y-axis in RU = μRIU or millidegrees), as illustrated in Figures 2.9 and 2.11, respectively.

However, if a sensorgram of a comparable experiment is plotted either as reflectivity (Figure 2.9) or as SPR angle (Figure 2.11) on the y-axis *versus* time, the two sensorgrams are not equal and large deviations of the presented

View Online

Published on 24 May 2017 on http://pubs.rsc.org | doi:10.1039/9781788010283-00027

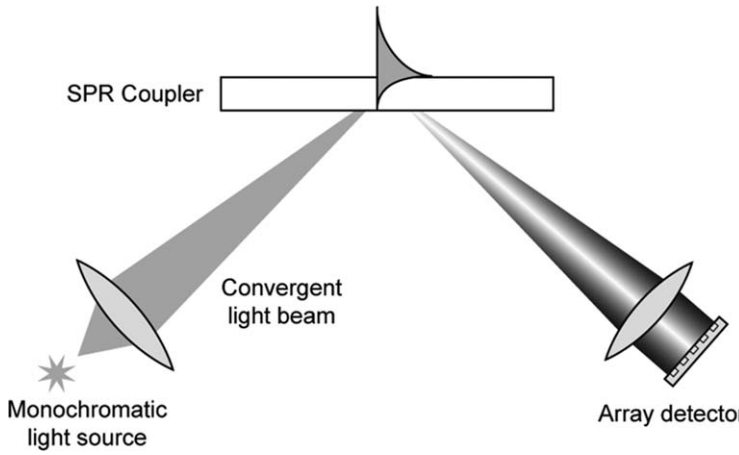


Figure 2.12 In a fan-shaped beam instrument, the SPR-dip can be followed in real time without moving parts.

binding curve may occur! A reflectivity change cannot be exchanged with a shift of the SPR-dip without knowing the exact shape of the SPR curve. From theory as described in the previous sections, the amount of biomolecules accumulated in the evanescent field results in an (almost) linear shift of the SPR-dip [eqn (2.9)]. Therefore, only real-time measurement of the SPR-dip as indicated in Figure 2.11 is the preferred mode of operation.[55] Reflectivity change is only a derivative parameter of this shift. Therefore, optimally the SPR-dip shift should be detected continuously to follow changes at the surface during, *e.g.*, a biomolecular interaction event.[56]

Moreover, the shape of SPR curve can reveal the quality of the sensor surface. For example, if inhomogeneities or agglutinates (particles) are present on the surface, the SPR curve becomes shallower and broader as a result of spatial differences in resonance conditions within a sensing area. Therefore, checking the SPR curve is a prerequisite for good SPR measurement practice.

2.4.3 Scanning Angle

The SPR curve can be scanned rapidly (see double-headed arrow in Figure 2.13) in a so-called scanning angle SPR instrument. An angle-controlled mirror is applied to follow the position of the SPR-dip in real time. The surface of the sensor chip is at a certain angle in full resonance, with the advantages that an image can be taken and that the area of the light beam is averaging the reflectivity and therefore potential defects of homogenously coated sensor chips. To acquire the data of a full scan very rapidly, an angle-controlled mirror (or angle scanner) is preferred. Advanced optics are required to scan the angles while the image is not moving during the angle scan. The SPR imaging instrument of IBIS Technologies applies such a

View Online

Published on 24 May 2017 on http://pubs.rsc.org | doi:10.1039/9781788010283-00027

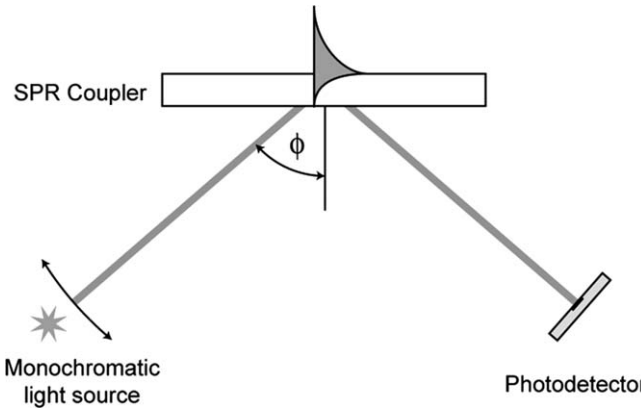


Figure 2.13 In scanning-angle SPR instruments, an angle scanner scans the sensor surface in a small angle window (*e.g.* 5°) very fast. At a certain moment, the total surface, not just a part, is in full resonance, resulting in improved sensitivity.

scanning principle, with additional, controlled-angle scanning features and curve-fitting routines, while measuring the angle shift of multiple regions of interests.

2.4.4 Grating Coupler

Although grating coupler instruments are regarded as SPR instruments, they are quite different and in 2009 a grating coupler-based instrument (Flexchip) was withdrawn from the market by GE Healthcare (data on the Flexchip instrument to reveal protein interaction networks are described in Chapter 11). Whereas in prism-coupled SPR optical cells the light never passes through the sample, in the Flexchip grating coupler instrument the light passes through the sample solution in the flow cell (see Figure 2.14), resulting in decreased stability of the sensor signal in comparison with instruments that apply the Kretschmann configuration. To avoid unwanted internal reflection effects, flow cells of grating coupler SPR devices have a large height. Therefore, the sample volume in grating coupler instruments is normally larger than in instruments using the Kretschmann configuration, where the height of the flow cell always exceeds the evanescent field of the reflected light. The attractive feature of grating coupler SPR devices is the option of using disposable gratings, which can be mass produced by injection molding replication techniques.

2.4.5 Fiber-based SPR Sensors

In the first edition of this Handbook, an additional principle that could be implemented in commercial instruments was not described – the so-called fiber-based SPR optics that apply optical fibers to excite SPs were not

View Online

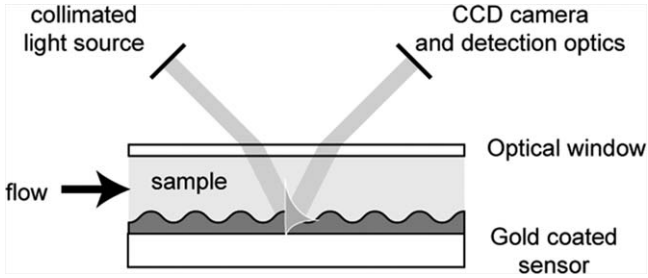


Figure 2.14 In a grating coupler, the SPR phenomenon is exploited differently, as the light beam travels through the flow cell.

commercialized. Why not? What was the reason? In contrast, an alternative SPR-like label-free fiber technology, so-called biolayer interferometry (BLI), marketed by FortéBio since 2006, expanded rapidly because of the ''dip and read'' concept. Because of the importance of this BLI technology, denoted ''Octet,'' this SPR-like approach is explained in detail in Chapter 10 by David Apiyo. However, in order to give a brief insight into trials in the past to develop similar fiber-based SPR biosensors, some fiber-based SPR configurations are described here.

The development of optical fiber biosensing technology started in the early 1990s. Jorgenson and Yee replaced the traditional prism-based systems by an optical fiber design.[57] To generate SPs, they removed a segment of the cladding on a multimode fiber and coated a silver film around the exposed fiber core. In the same period, Maria *et al.* used the fiber tip of the optical fiber to excite SPs, but only as proof of principle and not for biomolecular interaction monitoring.[58]

Later, in 2001, Slavik *et al.* applied a side-polished SPR fiber for detecting IgG proteins using anti-IgG monoclonal antibodies immobilized on the SPR sensor edge surface.[74] The polished sensor surface was functionalized and crosslinked with glutaraldehyde with a double-layer of anti-IgG molecules. Depolarized light and spectral interrogation were used to overcome interfering sensitivity to fiber deformations. The sensor was operated using a flow injection system. The sensor was demonstrated to be able to measure refractive index variations as small as 0.5 RU.

In 2009, Jang *et al.* combined the side-polished SPR fiber biosensor and the sandwich assay method for the detection of prostate-specific antigen.[59] However, they found a reduced sensitivity of 2.5 RU.

The methods mentioned require removal of the fiber cladding to allow core guided light to escape into the cladding, which excites the surface plasmons at the fiber core/metal layer interface (see Figure 2.15). In order to obtain a reproducible device, one must fabricate the SPR biosensors carefully, which results in too costly production of these ''disposable'' fiber-optic sensors with high QC demands, hindering commercialization.

To overcome the disadvantages of the need for careful polishing of the cladding of the fiber, other fiber grating biosensors have been suggested.[60]

Published on 24 May 2017 on http://pubs.rsc.org | doi:10.1039/9781788010283-00027

View Online

Published on 24 May 2017 on http://pubs.rsc.org | doi:10.1039/9781788010283-00027

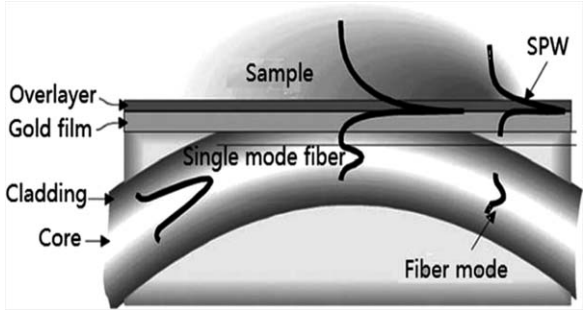


Figure 2.15 Side-polished fiber SPR biosensor.[74]
Reprinted from R. Slavik. J. Homola and E. Brynda, A miniature fiber optic surface plasmon resonance sensor for fast detection of staphylococcal enterotoxin B, *Biosens. Bioelectron.*, **17**, 591–595. Copyright 2002 Elsevier Science BV. All rights reserved.

For example, long-period fiber gratings (LPFGs) couple light from the core mode to a forward-propagating cladding mode.[61] Short-period tilted fiber Bragg gratings (TFBGs) reflect the core field directly onto the cladding/sample interface through a tilted grating surface,[62] which is analogous to the process in prism-based biosensors. By coating a metal layer on the fiber cladding, it was shown that it is possible to excite a particular cladding mode whose effective refractive index is perturbed by the plasmon resonance of the metal coating on the fiber under phase-matching conditions.[63] Again, production of such ''disposables'' has high QC demands.

In 2006, Tang *et al.* presented a long-period fiber grating (LPFG) biosensor on which self-assembled gold colloids were coated.[64] The transmission spectra and optical properties of gold colloids change with the variations in the refractive index of the environment near the surface of the colloids, as is the case with LSPR (see Section 12.2.1 and the instruments described in Sections 3.5.2.2 and 3.5.2.5). The sensor response of gold colloids increases linearly with solvents of increasing refractive index. When the colloidal gold surface was modified with a dinitrophenyl (DNP) compound, the experimental results showed that the signal increases linearly with increasing concentration of the analyte, and the detection limit of the sensor for anti-DNP is 0.95 nM.

In 2011, Shevchenko *et al.* demonstrated that a short-period TFBG SPR sensor manufactured from a single mode fiber (Figure 2.16).[65] A thrombin aptamer immobilized on the surface of the sensor was used as a recognition element for binding of the thrombin protein. There is an advantage associated with the use of TFBG, because a temperature cross-sensitivity is eliminated and production of disposables with high repeatability is less challenging than with other fiber-based SPR concepts.

FOx Diagnostics (Leuven, Belgium) developed a commercial fiber-optic SPR device (FO-SPR). More information can be found in Section 3.5.3.7.

View Online

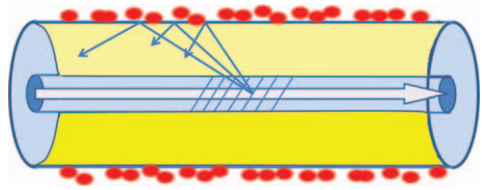


Figure 2.16 TFBG SPR biosensor.[75]
Reprinted from X. Guo, Surface plasmon resonance based biosensor technique: a review. *J. Biophotonics*, 2012, **5**(7), 483–450. Copyright 2012 Wiley-VCH Verlag GmbH & Co. KGaA, Weinheim.

Published on 24 May 2017 on http://pubs.rsc.org | doi:10.1039/9781788010283-00027

2.4.6 Other Optical Systems

Some other instruments measure the refractive index change in the evanescent field of the optical device by modulation of the coupling wavelength, as shown in Figure 2.17. A spectrophotometer is applied as detector to follow the shift of the ''plasmon'' wavelength. Another class of instruments uses modulation of the phase or polarization,[66] and this phenomenon is exploited in ''SPR-like'' resonant mirror instruments.[67] The principle of resonant mirror measurements, as commercialized in the early 1990s by Fisons (later Affinity Sensors), is that two phases of the reflected light are measured and, owing to the relative phase differences of the two modes (TE and TM components), a signal can be obtained as a result of refractive index changes in the evanescent field. Although plasmons are not generated and enhancement of the evanescent field does not occur, multiple reflections in the resonant mirror contribute to a high-sensitivity measurement of refractive index changes in the evanescent field. Because the system utilizes a less inert oxide layer than gold, more uncontrolled drift behavior can be observed than in conventional gold-based SPR systems. Because of this unreliable drift, the sensitivity of this instrument is lower than that of other ''real'' SPR systems.

Interferometric read-outs of optical wave guides also use the refractive index change as a result of biomolecular interaction events at the surface of the device. An evanescent field is formed when reflection occurs at the medium of higher refractive index. Although physically ''SPR-like'' instruments, including interferometers, might be more sensitive than SPR-based instruments, they lack the inertness of the gold surface. The oxides with the required refractive indices often show uncontrolled and unreliable baseline drifts, including memory effects from previous sample/salt additions. Various examples have been described,[68] but only a few have been commercialized.[69] Carmen Estevez *et al.* reviewed various technologies of integrated optical devices for lab-on-a-chip biosensing applications.[70]

An exception to the above shortcomings is the biolayer interferometry concept developed by FortéBio since 2006 as the Octet system. FortéBio (acquired by Pall Life Sciences in 2011) has been very successful in the past decade and they are the fastest growing company, with a range of Octet

View Online

Published on 24 May 2017 on http://pubs.rsc.org | doi:10.1039/9781788010283-00027

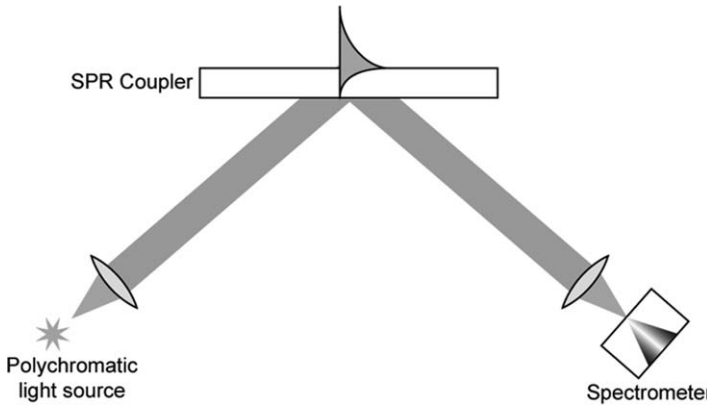


Figure 2.17 A wavelength interrogation-based surface plasmon resonance device applies a polychromatic light source to follow the wavelength-dependent SPR shift, *i.e.* the color of the light shifts as a result of the biomolecular interaction.

instruments from the BlitZ (one tip) to the HTX (96 tips). This technology is described in detail in Chapter 10.

2.4.7 SPR Imaging Instruments

In SPR imaging instruments, the sensor surface is optically imaged by a camera. Although some SPR instrument manufacturers use a camera for measuring the SPR shift, a prerequisite for classification as an SPR imaging instrument is that a microscopic view of the SPR sensor surface is generated. In other words, every pixel of the camera is an SPR sensor. Any non-homogeneities, surface coating defects, errors of spotting, including missing spots, and effects of drying of the surface can be directly observed in the microscopic reflectivity image of the SPR sensor surface. If, for example, air bubbles adsorb on the surface or appear in the flow system, they can be observed directly on the SPR image monitor. Prior to performing the analysis cycle, immobilization of capturing entities or ligands is usually carried out offline by spotting selective ligands in a microarray format.[††] In 1988, Rothenhäusler and Knoll described SPR microscopy,[71] and later Kooyman[‡‡] *et al.* established the principles of SPR imaging in reflectivity mode. Berger *et al.* showed that in total 16 different sensor spots could be imaged[72] in a two-dimensional (4×4) array of antibody–antigen sensor surfaces in real time.

Many SPR imaging instruments measure reflectivity as a parameter derived from the refractive index in the evanescent field. However, for accurate kinetic measurements of biomolecular interactions, only the shift

[††]A microarray contains a number of predefined selective regions or spots ordered in rows and columns.
[‡‡]The author of Chapter 2 in the first edition of this book.

View Online

Published on 24 May 2017 on http://pubs.rsc.org | doi:10.1039/9781788010283-00027

of the SPR-dip, which is linear with respect to the refractive index/mass change [eqn (2.9)] of the microarray spots, is reliable, because an optimal fixed angle position based on the inflection point of the SPR-dip can be found only for one spot and not for hundreds of spots simultaneously. Using the scanning angle principle, the IBIS MX96 microarray imaging instrument can follow the shift of the SPR-dip for all the regions of interests simultaneously even when spots deviate by >20 000 RU in resonance angle.

SPR imaging is the most promising next-generation technology and the editor of this book is certain that this technology in combination with advanced microfluidics will have an enormous impact. The commercial failure of both the Flexchip in 2009 and the Proteon XPR36 in 2015 proves the difficulty of integrating microfluidic parts of the technology with the optical requirements for ''good biosensing practice''. However, the experience and strategies of implementing optics and fluidics are now at a stage where not just a single-injection multiplex instrument using the power of the array is available. The 6×6 criss-cross approach in the Proteon XPR36 turned out to be a too mediocre step in terms of applications and the instrument was too complicated in an engineering sense. The author expects that a highly advanced SPR imaging instrument will be launched in the next decade that operates beyond the Biacore 8K (see Section 3.6.3) for multi-analyte injection and multiplex monitoring simultaneously in a single instrument. But then the applications should be the driver to construct such an instrument, including the development of dedicated software to treat the enormous data stream of tens of thousands of interactions measured in a single run.

2.5 Concluding Remarks

The history of SPR can be divided into two periods; before and after 1990. Since 1990, the launch of the Biacore instrument resulted in a boost of SPR publications (now >20 000). Now for many users of the technology, SPR is synonym for applying the phenomenon to study biomolecular interactions in aqueous solutions label free and in real time. The phenomenon of SPR has led to applications that are highly important to both applied science and society. The success is not due solely to the optics, but also its exploitation in a total concept of the three cornerstones of the technology: optics, fluidics, and (disposable) sensor chips.

In this chapter, the optical aspects of planar SPR technology have been treated, and particularly the combination of field enhancement and relatively short coherence length has contributed to its success in biosensor applications. The general physical picture of planar SPR is well understood and described by mathematical equations. It allows for a unique sensor concept that provides both multiplexing capabilities in combination with very high sensitivity for label-free biomolecular interactions. Further important aspects such as penetration depth of the evanescent field and propagation length of the surface plasmon have been treated for planar SPR devices.

View Online

Published on 24 May 2017 on http://pubs.rsc.org | doi:10.1039/9781788010283-00027

The physical SPR phenomenon is applied in various other commercial instruments and these instruments can be categorized into six sections according to their optical configuration. Typically, SPR-dip shifts are monitored in reflectivity mode or angle shift mode. Gold, because of its inherent inertness, is still the gold standard for generating the surface plasmon resonance phenomenon in all available commercial instruments. These basic principles are applied in commercial and highly advanced SPR instruments that are treated in Chapter 3.

2.6 Questions

1. When a signal channel containing ligand molecules on the sensor surface and a reference channel without ligands is exposed to the same bulk refractive index step, will the RU shift of the reference channel be higher than, equal to or lower than the signal channel? Please explain.
2. A particular SPR application could be the detection of microorganisms in, *e.g.*, waste water, by detecting changes in *bulk* refractive index. Which SPR excitation wavelength region would be more favorable, the blue/UV or the IR region?
3. SPR imaging requires lateral resolution and sensitivity. Describe what the influence is of the wavelength of the SPR excitation. Which wavelength region (blue/UV or IR) is favorable for the best lateral resolution?
4. Calculate for a gold/water interface at $\lambda = 700$ nm ($\varepsilon_{gold} = -16$, $\varepsilon_{water} = 1.770$) the refractive index shift in RU of the SPR dip when ε_{water} increases to 1.775. For the light incoupling we use a semicircular glass piece with refractive index $n_{glass} = 1.5$.
5. Estimate the effective dielectric constant for the system shown in Figure 2.18 when the gold/water interface is probed with a wavelength $\lambda = 700$ nm (for dielectric constants of gold and water, see previous question) ($\varepsilon_{gold} = -16$, $\varepsilon_{water} = 1.770$). The squares in Figure 2.18 represent cubes of protein molecules in an aqueous environment, adsorbed on the gold surface. Each protein molecule has a volume of $5 \times 5 \times 5$ nm^3 and a dielectric constant $\varepsilon_{protein} = 2.30$. The average distance between the edges of the cubes is 7 nm. (Compare the answer with the SPR rule of thumb: 1 ng mm^{-2} protein adsorption results in a shift of ~1000 RU.)
6. What happens with the SPR curve with respect to a reference area when a channel/region of interest contains an inhomogeneous precipitate? Please explain.

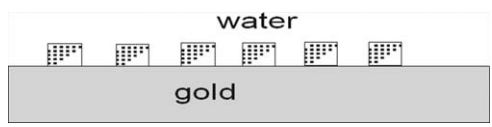


Figure 2.18 Cubes of protein molecules on gold.

View Online

Published on 24 May 2017 on http://pubs.rsc.org | doi:10.1039/9781788010283-00027

References

1. A. Otto, *Z. Phys.*, 1968, **216**, 398.
2. E. Kretschmann and H. Raether, *Z. Naturforsch.*, 1968, **230**, 2135.
3. R. W. Wood, *Philos. Mag.*, 1902, **4**, 396–402.
4. R. W. Wood, *Philos. Mag.*, 1912, **23**, 310–317.
5. L. Rayleigh, *Proc. R. Soc.*, 1907, **A79**, 399.
6. U. Fano, *Opt. Soc. Am.*, 1941, **31**, 213–222.
7. B. Liedberg, C. Nylander and I. Lundström, *Sens. Actuators*, 1983, **4**, 299.
8. Z. Salamon, H. A. Macleod and G. Tollin, *Biochim. Biophys. Acta*, 1997, **1331**, 117–129.
9. R. B. M. Schasfoort *et al.*, *Biosens. Bioelectron.*, 1990, **5**, 103–125.
10. J. Homola, *Surface Plasmon Resonance Based Sensors*, Series ed. O. S. Wolfbeis, Springer Series on Chemical Sensors and Biosensors, 2006, p. 4.
11. M. Nirschl, F. Reuter and J. Vörös, *Biosensors*, 2011, **1**(3), 70–92.
12. R. P. H. Kooyman *et al.*, *Anal. Chim. Acta*, 1988, **213**, 35–45.
13. B. Liedberg, C. Nylander and I. Lundström, *Biosens. Bioelectron.*, 1995, **10**(8), i–ix.
14. U. Jonsson *et al.*, *BioTechniques*, 1991, **11**(5), 620–627.
15. L. A. Chtcheglova *et al.*, *Biopolymers*, 2006, **83**, 69–82.
16. T. Wink *et al.*, *Anal Chem*, 1999, **71**, 801–805.
17. J. B. Beusink *et al.*, *Biosens. Bioelectron.*, 2007, **23**(6), 839–844.
18. J. M. Elson and J. M. Bennett, *Opt. Eng.*, 1979, **18**(2), 182116.
19. H. Raether, *Surface Plasmons on Smooth and Rough Surfaces and on Gratings*, Springer-Verlag, Berlin, 1988.
20. M. Cardona, *Am. J. Phys.*, 1971, **39**, 1277.
21. J. R. Reitz *et al.*, *Foundations of Electromagnetic Theory*, Addison-Wesley, New York, 1993.
22. S. Zhan, X. Wang and Y. Liu, *Meas. Sci. Technol.*, 2011, **22**(2), 025201.
23. M. Zizisperger and W. Knoll, *Prog. Colloid Polym. Sci.*, 1998, **109**, 244–253.
24. Brockman *et al.*, *Annu. Rev. Phys. Chem.*, 2000, **51**, 41–63.
25. B. P. Nelson *et al.*, *Anal. Chem.*, 1999, **71**, 3928.
26. S. Patskovsky *et al.*, *Opt. Soc. Am. A*, 2003, **20**, 1644.
27. K. Locharoenrat, H. Sano and G. Mizutani, *Sci. Technol. Adv. Mater.*, 2007, **8**(4), 277.
28. K. Tiefentahler and W. Lukosz, *J. Opt. Soc. Am. B*, 1989, **6**, 209.
29. R. G. Heideman, Optical waveguide based evanescent field immunosensors, (1993) PhD thesis, University of Twente, Enschede, NL.
30. C. R. Yonzon *et al.*, *Talanta*, 2005, **67**, 438.
31. U. Kreibig and M. Vollmer, *Optical Properties of Metal Clusters*, Springer, Berlin, 1995.
32. S. Zeng, D. Baillargeat, H. P. Ho and K. T. Yong, *Chem. Soc. Rev.*, 2014, **43**(10), 3426–3452.
33. J. B. González-Díaz *et al.*, *Small*, 2008, **4**(2), 202–205.
34. K. Kneipp *et al.*, *J. Phys.: Condens. Matter*, 2002, **14**, R597.
35. G. X. Du, *Appl. Phys. Lett.*, 2010, **96**(8), 81915.
36. S. Zeng *et al.*, *Sens. Actuators, B*, 2013, **176**, 1128.

View Online

Published on 24 May 2017 on http://pubs.rsc.org | doi:10.1039/9781788010283-00027

37. T. Chinowsky, A. Mactutis, E. Fu and P. Yager, Proceedings of SPIE, (2004), No 5261.
38. J. Homola, S. Yee and G. Gauglitz, *Sens. Actuators, B.*, 1999, **54**, 3.
39. K. Johansen, H. Arwin, I. Lundstrom and B. Liedberg, *Rev. Sci. Instrum.*, 2000, **71**, 3530.
40. B. Nelson, A. Frutos, J. Brockman and R. Corn, *Anal. Chem.*, 1999, **71**, 3928.
41. E. Fu *et al.*, *Rev. Sci. Instrum.*, 2004, **75**, 2300.
42. T. Chinowsky *et al.*, *Sens. Actuators, B.*, 2003, **91**, 266.
43. J. Shumaker-Parry and C. Campbell, *Anal. Chem.*, 2004, **76**, 907.
44. W. Smith, *Modern Optical Engineering*, McGraw-Hill, New York (2000).
45. B. Nelson, A. Frutos, J. Brockman and R. Corn, *Anal. Chem.*, 1999, **71**, 3928.
46. C. Berger, R. Kooyman and J. Greve, *Rev. Sci. Instrum.*, 1994, **65**, 2829.
47. H. de Bruijn, R. Kooyman and J. Greve, *Appl. Opt.*, 1993, **32**, 2426.
48. J. Homola, *Surface Plasmon Resonance Based Sensors*, Series ed. O. S. Wolfbeis Berlin, Springer Series on Chemical Sensors and Biosensors, 2006, p. 4.
49. E. Kretschmann, *Z. Phys.*, 1971, **241**, 313–324.
50. D. Wassaf *et al.*, *Anal. Biochem.*, 2006, **351**, 241–253.
51. M. Pérez-Moralesa *et al.*, *Thin Solid Films*, 2005, **488**(1–2), 247–253.
52. J. Ctyrokya, J. Homola and M. Skalskya, *Opt. Quantum Electron.*, 1997, **29**, 301–311.
53. C. R. Yonzon *et al.*, *J. Am. Chem. Soc.*, 2004, **126**, 12669–12676.
54. J. Homola, S. S. Yee and G. Gauglitz, *Sens. Actuators, B*, 1999, **54**, 3–15.
55. E. Stenberg *et al.*, *Colloid Interface Sci.*, 1991, **143**, 513–526.
56. M. Malmqvist, *Nature*, 1993, **361**, 186–187.
57. R. C. Jorgenson and S. S. Yee, *Sens. Actuators, B*, 1993, **12**, 213–220.
58. L. D. Maria, M. Martinelli and G. Vegetti, *Sens. Actuators*, 1993, **B12**, 221–223.
59. H. S. Jang *et al.*, *Opt. Commun.*, 2009, **282**, 2827–2830.
60. X. F. Chen *et al.*, *Opt. Lett.*, 2007, **32**, 2541–2543.
61. S. Maguis, *Opt. Exp.*, 2008, **16**, 19049–19062.
62. J. L. Tang *et al.*, *Sens. Actuators, B*, 2006, **119**, 105–109.
63. Y. Shevchenko and J. Albert, *Opt. Lett.*, 2007, **32**, 211–213.
64. J. L. Tang *et al.*, *Sens. Actuators, B*, 2006, **119**, 105–109.
65. Y. Shevchenko *et al.*, *Anal. Chem.*, 2011, **83**, 7027–7034.
66. J. Ctyrokya, J. Homola and M. Skalskya, *Opt. Quantum Electron.*, 1997, **29**, 301–311.
67. C. R. Yonzon *et al.*, *J. Am. Chem. Soc.*, 2004, **126**, 12669–12676.
68. J. Homola, S. S. Yee and G. Gauglitz, *Sens. Actuators, B*, 1999, **54**, 3–15.
69. P. A. Lowe *et al.*, *J. Mol. Recogn.*, 1998, **11**, 194–199.
70. M. Carmen Estevez *et al.*, *Laser Photonics Rev.*, 2012, **6**(No. 4), 463–487.
71. B. Rothenhäusler and W. Knoll, *Nature*, 1988, **332**, 615–617.
72. C. E. H. Berger *et al.*, *Anal. Chem.*, 1998, **70**, 703–706.
73. K. Locharoenrat, H. Sano and G. Mizutani, *Sci. Technol. Adv. Mater.*, 2007, **8**(4), 277.
74. R. Slavik, J. Homola and E. Brynda, *Biosens. Bioelectron.*, 2002, **17**, 591–595.
75. X. Guo, *J.Biophotonics*, 2012, **5**(7), 483–501.

Published on 24 May 2017 on http://pubs.rsc.org | doi:10.1039/9781788010283-00060

CHAPTER 3

Surface Plasmon Resonance Instruments

RICHARD B. M. SCHASFOORT

Medical Cell BioPhysics Group (MCBP), MIRA Institute, University of Twente, P.O. Box 217, 7500 AE Enschede, The Netherlands
Email: r.b.m.schasfoort@utwente.nl

3.1 Introduction

The general optical configurations of surface plasmon resonance (SPR) instruments were described in Chapter 2. However, not only may instruments differ optically but also the liquid handling system may be different for the various commercially available systems. Additionally, the quality and features of sensor chips determine the quality of measurements of biomolecular interactions (sensor surfaces are treated in detail in Chapter 6).

Instruments also differ in the degree of automation and in the applications portfolio. Easy-to-use software is a key feature for selling instruments to potential customers. The software to run a certain instrument is unique to that instrument, but the software to treat and analyze the data for general kinetic applications can be similar from instrument to instrument. The main software application analysis tools are treated in Chapter 9 by Noah Ditto and Joshua Eckman. In this chapter, general features of the various liquid handling systems and the instrument-specific operational automation of commercial SPR instruments are also treated. The latest instruments of Biacore, the largest company in the SPR market, with a complete SPR product line, are discussed separately in Section 3.6. Chapter 7, by Robert Karlsson *et al.*, treats further Biacore applications regarding fragment and low molecular weight compound screening.

Handbook of Surface Plasmon Resonance, 2nd Edition
Edited by Richard B. M. Schasfoort
© The Royal Society of Chemistry 2017
Published by the Royal Society of Chemistry, www.rsc.org

View Online

Published on 24 May 2017 on http://pubs.rsc.org | doi:10.1039/9781788010283-00060

In the first edition of this Handbook in 2008, most commercial SPR instruments were treated separately. However, because of the now much increased number of instrument providers, it was decided to highlight the active providers as of 2016 and provide brief typical features of the other instrument providers. Some of the instruments that have been withdrawn from the market are mentioned only briefly, with technical or other reasons why these instruments were discontinued where possible. Further, in Table 3.1. an overview of SPR instruments and their manufacturers, updated to summer 2016, including web addresses, is given. Because of the timely character of the information described in this

Table 3.1 Overview of SPR instruments and their manufacturers available up to mid-2016.[23,24]

Manufacturer	Type	Name of SPR system	Internet address
Analytical µ-Systems	Fixed angle	BIOSUPLAR-6	www.biosuplar.de
Biacore	Fan shaped, converging	Biacore product line[a]	www.biacore.com
Bionavis	Angular scan	MP-SPR-Navi™	www.bionavis.com
Bioptix	Differential phase shift	404pi	www.bioptix.com
Bio-Rad Laboratories	Imaging	ProteOn™ XPR36[b]	www.bio-rad.com
Biosensing Instruments	Fan shaped, converging	BI-4500 series	www.biosensingusa.com
GWC Technologies	Imaging	SPRimager®II	www.gwctechnologies.com
Horiba Scientific	Imaging	Xel-Plex™, OpenPlex	www.horiba.com
IBIS Technologies	Imaging/ scanning	IBIS MX96	www.ibis-spr.nl
KE Instruments	Angle scanning	SPRINGLE/ ESPRIT	www.ke-instruments.com
K-MAC (Korea)	Fixed angle + imaging	SPRmicro and SPRi™	www.kmac.com/eng
Nicoya	Fixed angle	Open-SPR	www.nicoyalife.com
Plexera	Imaging	PlexArray® HT System	www.plexera.com
Reichert Technologies	Fan shaped, diverging	SR7500DC – 4SPR	www.reichertai.com
Seattle Sensors	SPREETA fixed angle	SPiRiT™	www.seattlesensors.com
Sensia	Fixed angle	Indicator-G	www.sensia.es
SensiQ Technologies	Fan shaped, diverging	Pioneer FE	www.sensiqtech.com
Sierra Sensors	Imaging	MASS-1	www.sierrasensors.com

[a]Biacore product line including Bialite, Biacore J, X, 1000, 2000, 3000, C, S51, Q, A-100, T-100, X-100. 4000, S200 and 8K.
[b]Bio-Rad has discontinued the production of the Proteon XPR36 (spare parts will be supplied until 2019).

View Online

chapter, the current websites of the various instrument manufacturers will give the latest detailed information regarding new technology and advanced applications.

3.2 The Cornerstones of SPR Technology

Real-time and label-free biomolecular interaction sensing is unthinkable at present without the surface plasmon resonance principle.[1,2] Instruments currently on the market differ in performance based on differences in their optical systems, their degree of development, and their automation. SPR optics, liquid handlings, and the sensor chip are integrated in the SPR instrument as depicted schematically in Figure 3.1. As indicated, the sensor chip is inserted between the optical system and the liquid handling unit, *e.g.* flow cell.

In many instruments, the optics are designed at the top of the instrument whereas the fluidics are positioned at the bottom with respect to the sensor surface. When leakage of the fluidics occurs then it does not affect the optical compartment. The angle shift in Kretschmann-operated SPR instruments can be expressed in different units in the various instruments, for

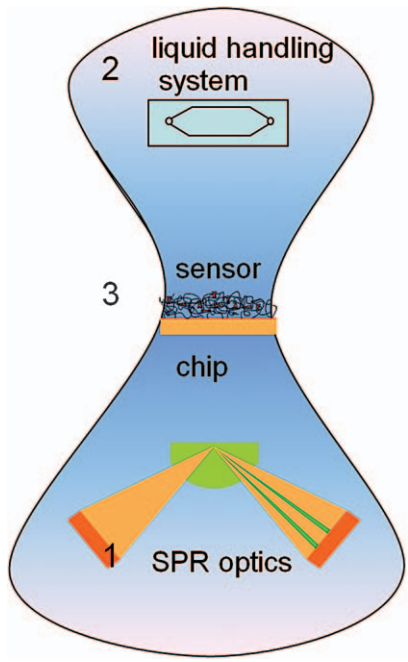


Figure 3.1 Schematic view of the three main units of an SPR system: (1) SPR optics; (2) liquid handling unit; (3) sensor chip. The biomolecular interaction takes place on the wet site of the sensor. The core and bottleneck for a researcher is the sensor chip.

Published on 24 May 2017 on http://pubs.rsc.org | doi:10.1039/9781788010283-00060

View Online

Published on 24 May 2017 on http://pubs.rsc.org | doi:10.1039/9781788010283-00060

example, in response units {RU in Biacore instruments, Bio-Rad's Proteon, and IBIS MX96;[3] μRIU in Reichert instruments (Section 3.8)} or in millidegrees (KEI systems[4]), which directly depict the SPR angle shift, and also in percentage reflectivity (%*R*) (GWC Technologies system, Horiba's EzPlex, Xelplex, and K-MAC[5,6]), or even wavelength shifts (Graffinity Pharmaceuticals[7,8] and the L-SPR devices of Nicoya and Affinité). Because of a near-linear relationship between the amount of surface-bound protein and the SPR signal, the sensorgram of the SPR-dip shift provides quantitative, real-time data. Further, it is a rule of thumb that a 1 RU (by definition equal to 1 μRIU) shift by protein accumulation is close to a surface mass shift of $\sim$1 pg mm^{-2}. In order to compare sensitivity between instruments, the unit on the *y*-axis of the sensorgram should be uniform and should be calibrated using a general bulk refractive index shift. Because a calibratable μRIU is close to a response unit (RU) as introduced by Biacore, all instruments that measure dip shifts should give similar responses calibrated by bulk refractive index shifts due to glycerol injections. Then *1 mRIU is equal to 1000 RU*, which is close to a surface mass shift of $\sim$1 ng mm^{-2} for a fixed wavelength ($\sim$700 nm).

1 000 000 RU = 1 RIU 1 RU = 1 μRIU

3.3 General Optical Requirements for SPR Instruments

The dynamic range of an instrument in the Kretschmann configuration for studying biomolecular interactions is determined by its range of angles. The larger the dynamic range, the smaller the angle resolution of an instrument should be in order to maintain the required sensitivity. Therefore, an instrument is usually built to zoom into a small-angle window (*e.g.* 30 000 RU) to measure tiny angle shifts, *e.g.* in the order of 0.1 RU or less. However, if the angle range is very small, the SPR-dip might be outside the available range of angles. A way to overcome this shortcoming is to apply the wavelength mode (see Figure 2.14), with the disadvantage that the penetration depth of the evanescent field and the propagation length of the plasmon are not constant for different light colors. The penetration depth of the evanescent field, and also the lateral resolution of SPR, are dependent on the wavelength of the incident light (see also Section 2.2). The lateral resolution which is correlated to the propagation length of the plasmon at 680 nm wavelength incident light is about 10 μm.[9] If different wavelengths are used to excite SPR, the volume of the evanescent field is not constant and it will affect the response curve. Hence most instrument manufacturers choose a single wavelength window for SPR excitation. In every instrument, the polarity of the excited light needs to be kept perpendicular to the surface (p-polarized light) in order to generate the surface plasmon resonance effect.

View Online

Published on 24 May 2017 on http://pubs.rsc.org | doi:10.1039/9781788010283-00060

The polarization filter under full resonance conditions should be trimmed to obtain an optimal reflectance minimum.

An additional experimental requirement is to provide refractive index (RI) matching between the coated gold surface of the sensor chip and the optical element (prism, hemicylinder, hemisphere, *etc.*). Biacore solved this problem by applying an optogel[†] to coat the prism to ensure RI matching. The first instrument of Biacore launched in 1990 contained the optogel for use as the medium between the prism in the optical unit of the instrument and the sensor chip, which turned out to be a crucial factor for the initial success of Biacore. The optogel ensures optical contact, simplifying exchange of the sensor chip. Currently, almost every commercial SPR player in the market has solved the RI matching problem and oil for optical RI matching is no longer used.

At present, gold on sensor chip surfaces is the ''gold standard'' in SPR technology. Although from a physical point of view silver is better, gold provides greater chemical inertness. Attempts to protect the thin, non-inert silver layer have so far failed and the performance of these sensors usually decreases rapidly to an unacceptable level. Protection of the silver with, *e.g.*, deposited oxides leads to unwanted ionic effects and drift of the sensor signal. Currently all manufacturers apply the physically second-best metal for SPR: gold.

The RI of aqueous liquids is highly temperature dependent: at least a *minus* 115 RU shift per degree Celsius is observed; the minus means that the higher the temperature, the lower is the RI. Therefore, temperature control of the instrument is essential. Temperature stabilization (better than 0.01 $^{\circ}$C) is a prerequisite for reliable measurements in the single-digit RU range. Moreover, bulk RI subtraction is essential to overcome common mode effects, *e.g.* temperature drift, and also a bulk RI shift caused by variable ionic/compound composition of the sample with respect to the buffer, but cannot compensate for the temperature effect on the affinity constant of biomolecular interactions. However, the latter is less prominent in the sub-degree Celsius range.

In order to determine accurately the kinetics of biomolecular interactions,[10] the shift of the SPR-dip is the parameter that should be measured to determine the amount of accumulated mass at the sensor surface, expressed as pg mm^{-2}. We pointed out previously that the measurement of reflectivity change at a fixed angle position of the SPR curve is an inaccurate parameter to determine accumulated mass. Many cost-effective instruments on the market apply reflectivity (in %R) in the sensorgram without tracking the SPR minimum, including most of the SPR imaging instruments.

A way to test the quality of an SPR instrument is not only to look just at noise levels, but also to inspect whether the ''referencing'' of the signals

[†]Proprietary product of Biacore.

View Online

Published on 24 May 2017 on http://pubs.rsc.org | doi:10.1039/9781788010283-00060

effectively compensates for bulk RI steps. The following protocol should be carried out:

1. Prepare at least three sample solutions that contain different concentrations of glycerol between 1% and 7% dissolved in system buffer (not in water!).
2. Inject the various samples in a series of baseline, association, and dissociation phases and observe how fast the system responds to the bulk RI shifts.
3. Apply the routines that the manufacturer describes to clean up the data, *e.g.* a calibration measurement, if necessary.
4. Apply referencing to the signals by subtracting the RU shift of the reference channel with the ligand channel/spot.
5. Observe if the instrument had measured a referenced ''flat-liner,'' which means that the glycerol step is fully compensated. During this step, a referenced ''spike'' is often measured that can be attributed to small fluidic differences between the channels. However, the level of injection after zeroing the baseline should be (very) close to zero RU for these glycerol injections. If not, equilibria are affected by bulk RI steps.

The quality of the optical components and optical alignment of the beam, including lenses, noise of both light source and photodetector or camera all contribute to the quality of the measurements. Finally, the software, including the algorithms for averaging, subtracting, calibrating, or eliminating raw data points, and also the performance of hardware contribute to the quality of the SPR instrument in terms of sensitivity, repeatability, accuracy, and robustness.

3.4 SPR Liquid Handling Systems

In combination with the optical unit and sensor chips, the liquid handling system forms a vital part of SPR instruments. As shown in Figure 3.1, the bottleneck remains the integration of these parts in one instrument provided that the quality of the weakest part will be the limiting factor for the overall performance of the system. For instance, high-quality optics can never compensate for a low-quality sensor surface. Additionally, the way in which the sample is exposed to the sensor surface determines the kinetic profiles in terms of rate constants, mass transport limitation, stagnant layer, diffusion gradient, and depletion at the surface. Two main liquid handling systems in the past can be identified: cuvettes and flow cells.

Although in the past several commercial instruments were equipped with a cuvette, currently all high-performance instruments are supplied with flow cell-based fluidics. An exception of a label-free cuvette or multi-well based instrument is the Octet (FortéBio, Pall). The dip and read principle is applied in this SPR-like [biolayer interferometry (BLI) is not SPR] instrument and

View Online

Published on 24 May 2017 on http://pubs.rsc.org | doi:10.1039/9781788010283-00060

currently there are a range of instruments on the market, *e.g.* single pin or BlitZ, two pins (Octet K2), eight pins (Octet Red), 16 pins (Octet 384), and 96 pins (Octet HTX). The importance of this BLI technology increased in the last decade from a minor player in 2006 (see the first edition of this Handbook) to the fastest growing player in the label-free technologies field with more than 1200 instruments in 2016. As an (SPR) exception, this technology is described separately in Chapter 10.

3.4.1 Cuvette Systems

Cuvette liquid handling systems consist of an open container filled manually or automatically by a liquid handling robot or liquid handler. The cuvette must be mounted leak-free on the sensor chip and the correct configuration of the optics is required in order to apply the open container or cuvette. The biomolecular interaction takes place on the replaceable SPR sensor chip at the bottom of the cuvette. Cuvette systems should be equipped with a mixing system. If the liquid is not optimally mixed, the sensorgrams are deformed owing to uncontrolled molecular transport to the surface. In contrast to flow cells, cuvette systems are not prone to clogging, hence liquid samples with solid particles can be measured in cuvette systems, provided that the sensor surface is not damaged by impinging particles. Examples of such samples are fermentation media, blood plasma, cell cultures, and food products. Because the sample remains in the cuvette during the association phase of the biomolecular interaction process, the undiluted sample can be recovered almost completely. However, because the geometry of the cuvette is open and not confined, the hydrodynamic conditions are less fixed than with planar flow cell-based systems.

In principle, a sample volume in the region of 25 μL is sufficient to study biomolecular interactions for up to 1 h. A disadvantage of the cuvette system is the open architecture, allowing uncontrolled evaporation of the sample solution and increases in salt concentration and RI. When low-concentration samples are used, depletion of the analyte occurs and kinetic models should compensate for this effect as described in Chapter 5 in the first edition of the Handbook. In the last decade, cuvettes have become less often applied in favor of flow cells. Only a few systems on the market in 2016, *e.g.* from KE Instruments, still apply a cuvette.

Various mixing systems can be used to agitate the sample in the cuvette, including stirrers,[11] vibrating acoustic plates,[12] and aspirate/dispense mixing.[13] In principle, every device can be applied that controllably and effectively induces mixing to homogenize the sample solution in the cuvette. For example, the IAsys resonant mirror instrument was equipped with a high-speed rotating stirrer.[14] A disadvantage was that mass transport to the surface is not effectively controlled even at fast rotation speeds. Later, a vibrating plunger/piston was developed that showed better mass transport characteristics,[15] but the IAsys resonant mirror instrument was discontinued in 2011.

View Online

Published on 24 May 2017 on http://pubs.rsc.org | doi:10.1039/9781788010283-00060

Mixing can also be achieved with a syringe pump[‡] with a controllable automatic aspirate–dispense of liquid using a needle that is immersed in the cuvette, *e.g.* with a tip that is positioned say 1 mm from the surface. In these instruments, a syringe pump is constantly aspirating and dispensing the sample in the cuvette during real-time measurements to obtain more reproducible sensorgrams. Relevant hydrodynamic parameters of non-confined aspirate–dispense mixing system are sample volume, mixing volume, which should be part of the sample volume, speed or frequency of mixing, diameter of the nozzle (inner diameter of the needle), distance and position of the nozzle to the sensor surface, diameter of the cuvette, and viscosity and temperature of the sample solution.

The cuvette needs to be drained after the interaction process, but the surface should not become dry, hence hydrophilic coatings are used to prevent the sensor surface from being exposed to air. If the hydrogel dries out, irreproducible effects will occur.

Physical or biomolecular mass transport determines how fast the sample molecules are transported to the surface. Mass transport limitations arise when the concentration of the analyte at the sensor surface is lower than the sample bulk concentration (for detailed descriptions, see Chapters 1 and 6). The BLI read-and-dip Octet technology as introduced by FortéBio (see Chapter 10) is also cuvette based but, because the biomolecular interaction takes place at the tip and not at the bottom of the cuvette, better controlled hydrodynamic conditions exist. However, the well/cuvette is exposed to air (evaporation) and during the dissociation process a ''cloud'' of dissociating molecules exists around the BLI tip, affecting the determination of the rate constants.

In aspirate–dispense mixing systems, mass transport to the surface is greatly increased and the diffusion-controlled stagnant layer at the surface is strongly reduced. The process can be described by the dynamic free wall-jet principle first described by Glaubert.[16] As various parameters affect the biomolecular interaction process, the reproducibility of the measurement can be maintained best in automated operation with constant hydrodynamic parameters.

Resuming, the cuvette can be described as a multiparameter, (un?)-controllable batch reactor, in which binding events take place at the bottom or sensor surface. Because such cuvettes are exposed to air, undesired evaporation of the sample can take place when long biomolecular interactions are carried out. Further cuvettes are prone to hydrodynamic variations on signal and reference areas. However, the many parameters that influence locally the spatial resolution, especially in the last decade, showed that flow-based systems, as treated in the next section, are superior to cuvette systems, as they can be better controlled and are more accurate and reliable than cuvette-based instruments.

[‡]The systems SPRINGLE and ESPRIT of KE Instruments.

View Online

Published on 24 May 2017 on http://pubs.rsc.org | doi:10.1039/9781788010283-00060

3.4.2 Flow Systems

In most instruments that are currently on the market, flow systems are applied with various degrees of automation ranging from simple to highly automated cartridges. Samples can be transported using syringes or peristaltic pumps, either with or without pneumatic valves and sample loops. In the SPR instrument, liquid is transported into the flow cell to expose it to the sensor surface to study (bio)molecular interactions.[17] Peristaltic or syringe pumps are applied to pump the liquid along the sensor chip surface, not only to inject the sample but also to keep the hydrodynamic conditions under control. Many instruments apply automated injection systems, definitely improving performance.

3.4.2.1 Planar Flow Cells

Because of the small dimensions of flow cells, the Reynolds number ($\rho v d/\eta$) will be far below 1000, with the result that there is never turbulence but always laminar flow.[18] Sometimes the sample is separated from the buffer by an air bubble; however, when air bubbles pass over the sensor surface they may affect the surface properties of the sensor chip. When valves are very close to the sensor surface, then dilution effects are minimized and samples can be injected instantly (*e.g.* Biacore).

Flow cells can be created by pressing a micromachined device with preformed microfluidic channels against the sensor surface. In 1990, Biacore introduced a microfluidic system for its SPR technology based around integrated (micro)fluidics cartridge (IFC) technology (Figure 3.2). The IFC allows analyte to pass over the sensor surface in a continuous, pulse-free and controlled flow, maintaining constant analyte concentrations and hydrodynamic conditions at the sensor surface. The biospecific interaction analysis procedures are automated using a liquid handling system. The IFC in Biacore instruments is connected to the sensor surface for three reasons:

- Dispersion and dead volumes are minimized.
- Thermostating of the sample and sensor chip is optimal.
- The transitions (buffer → sample → buffer) are instantaneous (within 1 s).

Three major flow cell configurations are generally applied in SPR systems (Figure 3.3). Most commonly used are planar flow cells and hydrodynamic addressing flow cells. The wall-jet flow cell is no longer used because the surface area is not addressed uniformly owing to the radial flow velocity profile. In high-end instruments such as the Biacore 4000 and the MASS-1 (Sierra Sensors), hydrodynamic addressing/isolation flow cells are applied in order to measure greater sensor areas, *e.g.* for signal and referencing in the same flow cell.

View Online

Published on 24 May 2017 on http://pubs.rsc.org | doi:10.1039/9781788010283-00060

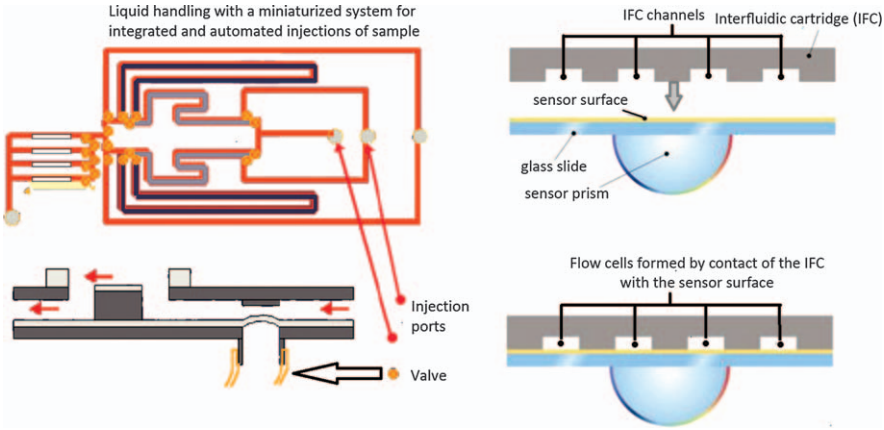


Figure 3.2 The integrated microfluidic cartridge (IFC) of the Biacore 3000 instrument. Flow cells are formed when a microfluidic cartridge is pressed against a sensor surface (top). Pneumatic valves are used to guide the sample in the injection loop followed by flowing the sample over the sensor surface (bottom).

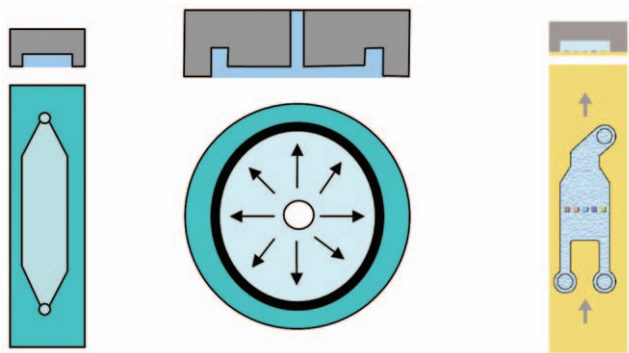


Figure 3.3 Top and side views of three flow cells: left, planar flow cell; middle, wall-jet flow cell; right, hydrodynamic addressing flow cell. The last flow cell is discussed further in Section 3.6.2.

A planar flow cell (FC) contains a simple inlet and outlet and a single channel through which the sample flows and interacts with the sensor surface. Instruments can be applied with several FCs, *e.g.* four in the Biacore T-200 and S-200 and even eight in the Biacore 8K as introduced by GE Healthcare in 2016. Owing to the small chamber[§] and low Reynolds numbers, the flow is laminar.[19] The pneumatic system of a microfluidic cartridge in the Biacore instruments (Figure 3.2) opens and closes valves in user-defined protocols to control the flow in the flow cell. Sample loops can

[§]The smaller the sample volume the better.

View Online

be manufactured at a very close distance to the sensor surface, minimizing dead volumes and dispersion, creating clearly defined injection plugs. Small deviations are related to the dead volumes (<1 μL) and to dispersion between flow cells if, for example, four parallel flow cells are used.

Published on 24 May 2017 on http://pubs.rsc.org | doi:10.1039/9781788010283-00060

3.4.2.2 *Hydrodynamic Addressing/Isolation*

As shown in Figure 3.3 (right) hydrodynamic addressing can be used for the simultaneous measurement of multiple interactions in a single flow cell. Four combined flow cells are shown in Figure 3.31.[20] A basic hydrodynamic focusing principle was first applied in the Biacore S51 and later in the Biacore A100/4000 (see Section 3.6.2). By adjusting the flow at the two inlets (one for the sample and the other for buffer), liquids can be directed to different addressable detection areas. In this way, a four-plex measurement (four signal spots and a reference spot) can be carried out. The hydrodynamic addressing or isolation flow cell allows rapid switching of flow between buffer and sample and exposure to the detection spots. As there is delay, highly accurate reference subtraction allows the measurement of very rapid kinetics. By immobilizing several ligands in a single flow cell, comparative binding properties can be examined under identical experimental conditions. Sierra Sensors also applies an advanced hydrodynamic addressing flow protocol in the MASS-1 and MASS-2 instruments to prevent switching of tiny vulnerable valves, the so-called hydrodynamic isolation (HI) principle (see Section 3.5.4.7).

3.4.2.3 *Air-park Flow Cell Technology with Back-and-forth Flow Mixing*

The IBIS MX96 applies patent-pending air-park technology[21] in order to expose the analyte to an array of spotted ligands. Only 100 μL of sample is aspirated and transported to the thermohead of a standard planar flow cell with an inlet and outlet. An air bubble separates the sample from the buffer (Figure 3.3, bottom). The thermohead contains the planar flow cell and is connected with four lines: the inlet and outlet lines and two air-park lines. The air-park control is both for the inlet and for the off-stream control of the sample in the flow cell. This valveless operation permits a fixed low volume of the sample and air never comes in contact with the sensor surface with the risk of destroying the quality of the hydrogel. During the baseline measurement, the sample is thermostated and just before injection the air bubble is aspirated *via* a T-connection and the sample is injected rapidly.

The sample is exposed to the sensor surface using back-and-forth flow fluidics and the off-stream air bubble protects the mixing of the system buffer with the sample. In this way, optimal hydrodynamic conditions are achieved (low mass transport limitation) while the sample retains its

View Online

Published on 24 May 2017 on http://pubs.rsc.org | doi:10.1039/9781788010283-00060

concentration and is not consumed. Only the molecules that bind to the spots of the microarray could in principle deplete the sample. It can be calculated that also at very low concentrations of the 100 μL sample, the depletion effect is extremely small when the interaction takes place at only a few spots (take the ''rule of thumb'' into account that 1 ng mm^{-2} will result in an SPR shift of 1000 RU). Fast interactions, *e.g.* 30 s, can be measured, or very long interactions (up to equilibrium at lower affinities of the biomolecular interaction) can be followed, *e.g.* hours, without consuming the sample. After the interaction process, the sample can be recovered by pumping it back into a well of the microtiter plate. Another advantage of valveless operation of the fluidics is that raw, unfiltered samples can be applied without the risk of clogging of the IFC. Further, even living cells, extracellular vesicles, blood platelets, *etc.*, can be gently injected and exposed to an array of anti-CD receptor antibodies. The latest developments are described in Section 12.8 concerning SPR cytometry. Remarkably, the IBIS MX96 and the continuous flow microspotter (CFM) of Wasatch Microfluidics apply the back-and-forth mixing/injection principle,[22] although it was developed independently of each other. The CFM is treated further in Sections 3.5.4.8 and 12.3.1.

3.5 SPR Instruments: State of the Art

Numerous SPR instruments are now available from various manufacturers. In Table 3.1 and the following sections, short descriptions are given of some typical commercially available SPR instruments, sorted by their optical configuration, describing their main features and advantages. It is hoped that the coverage of commercially available instruments up to mid-2016 is comprehensive, but note that the importance of the technology in the market for various applications cannot be judged from the relative amounts of text devoted to them here.

In addition, other instruments can be identified that detect biomolecular interactions in real time and label free that are not directly based on the SPR phenomenon or apply a different configuration. For example, FOx Diagnostics (Leuven, Belgium; company founded in 2015) developed a commercial fiber-optic SPR device (FO-SPR). Information on these products and manufacturers is compiled in Table 3.2. It should be noted that this list may not be complete but provides only an illustration of the range of products and manufacturers in the label-free biosensor area.

3.5.1 Examples of Fan-shaped Beam SPR Instruments

3.5.1.1 GE Healthcare

Biacore[¶] (Uppsala, Sweden), acquired by GE Healthcare in 2006, dominates the SPR market with more than 80% of installed products and 87% of the

[¶]Acquired by GE Healthcare in 2006.

Published on 24 May 2017 on http://pubs.rsc.org | doi:10

Table 3.2 Non-SPR instruments for label-free monitoring of biomolecular interactions.[25]

Manufacturer	Product name	Working principle	Internet address
Attana	Attana Cell 200	QCM technology	www.attana.com
Axela Biosensor	dotLab system	Grating-based light diffraction	www.axelabiosensors.com
Berthold	bScreen (RIDe)	Reflectometric interference detection	www.berthold.com
Biolin Scientific	Q-sense	QCM-D	www.biolinscientific.com/q-sense/
Corning	Epic system	Dynamic mass redistribution (DMR)	www.corning.com/lifesciences
Creoptix	Wave system	Grating coupled interferometry	www.creoptix.com
Dynamic Biosensors	Switch sense technology	Electrically switchable nanolevers	www.dynamic-biosensors.com
Farfield Scientific	AnaLight®	Dual polarization interferometry	www.farfield-scientific.com
FortéBio (Pall)	Octet™ lines: Blitz, K, QKe, QK384, Red96, Red384, HTX	Biolayer interferometry (BLI) Optical fiber biosensor (see also Chapter 10)	www.fortebio.com
FOx Diagnostics	FO-SPR	Fiber-optic SPR	www.biw.kuleuven.be/biosyst/mebios
Genalyte	Maverick	Ring resonator	www.genalyte.com
Maven Biotechnologies	Polaron reader	Label-free internal reflection ellipsometry, LFIRE™	www.mavenbiotech.com
Nanotemper	Monolith NT	Microscale thermophoresis	www.nanotemper-technologies.com
Nanotemper	Seismos NT Series	Surface acoustic wave (SAW)	www.nanotemper-technologies.com
Plasmore	Plasmore	Nanoplasmonics	www.plasmore.com
Silicon Kinetics	SKI Pro®	Optical biosensor substrate	www.siliconkinetics.com
Wyatt	CG-MALS	Dynamic light scattering (DLS)	www.wyatt.com

View Online

Published on 24 May 2017 on http://pubs.rsc.org | doi:10.1039/9781788010283-00060

publications that appeared in 2015,[40] and dictates the standards serving as references for all other instrument manufacturers. The principle of fan-shaped SPR instruments has been used by the developers of Biacore since the launch of the first product in 1990. In Biacore instruments, a light-emitting diode ($\lambda = 760$ nm) is used and a convergent light beam reflects at an exact position at the sensor surface. A photodiode array is used to determine accurately the SPR-dip position. Extending the fan of light into a wedge and using a two-dimensional detector allows detection along a line on the sensor surface. The benefit of using a fan of light and a linear array detector is that no moving parts are required to carry out SPR assays. A computer algorithm with proprietary fitting routines calculates the mathematical minimum to a fraction of the size of a single diode. The accuracy of the SPR dip corresponds to about a 0.001 millidegree (m°) (hence the RMSD noise levels of the instruments are better than 0.01 RU).

Biacore applies an optogel to match optically the sensor chip with the cylindrical prism. With different probes immobilized at defined spots along a line, simultaneous measurement of different biomolecular interactions is realized. Biacore applies several types of flow cells connected to a microfluidic cartridge. In Figure 3.4, some older Biacore instruments are shown. At the end of this chapter (see Section 3.6) the latest instruments of Biacore are described, including the recently launched Biacore 8K.



Figure 3.4 Part of the SPR product line of Biacore: Biacore X, 3000, S51 and X100, respectively. The other Biacore systems (A-100/4000, T-100, T200, S200, and 8K) are not shown here but are covered separately in Section 3.6.

View Online

Published on 24 May 2017 on http://pubs.rsc.org | doi:10.1039/9781788010283-00060

3.5.1.2 Reichert Technologies

Reichert Technologies, a company that has manufactured advanced optical and analytical instruments for more than 150 years, continues to develop the highest level of innovative, sensitive, and flexible instruments. Reichert has been providing SPR technology and systems to life science researchers for over 15 years. The optics are based on the Kretschmann configuration – the recognized standard for maximum sensitivity and reproducibility. Ultimate sensitivity and fast sample rates (up to 10 Hz) enable these SPR systems to provide the highest quality data. Reichert SPR instruments can handle difficult sample compositions such as crude samples, cells, phage, and serum.

The Reichert 4SPR system (Figure 3.5, right) is ideal for academic core laboratories, biotech and pharma research groups and contract research organizations (CROs). With its four-channel configuration, it provides the right balance of ease of use, throughput, and flexibility. The instrument can be set up to run with three targets and a reference or, for lower throughput experiments (or method development), two channels at a time can be used. The SPR sensor chip is coupled to the prism and then a flow cell is placed on top that defines the flow path and is tightened down *via* a clamp. Sensor chip docking, sampling, and flow rate capabilities are similar to those with the SR7500DC (Figure 3.5, left). Experiments are typically performed at 20 or 25 °C, but the instrument has the capability to control reaction temperature from 10 °C below ambient up to a maximum of 70 °C. The autosampler accommodates two sample trays that can be any combination of 96- or 384-well plates or 48- or 12-vial trays for a maximum sample capacity of 768, similarly to the SR7500DC.

The sample storage compartment can be cooled to 4 °C to preserve the activity of thermally sensitive samples. The pump module features a built-in degasser with solvent switching possible between two buffers or buffer and water. Experimental flow rates are typically in the 10–100 $\mu L\,min^{-1}$ range, but can be adjusted down to 0.1 $\mu L\,min^{-1}$ or up to 3000 $\mu L\,min^{-1}$ (flow rates higher than 300 $\mu L\,min^{-1}$ require the use of wider diameter tubing) for increased flexibility.



Figure 3.5 The Reichert SR7500DC (left) and 4SPR (right) instruments.

View Online

Published on 24 May 2017 on http://pubs.rsc.org | doi:10.1039/9781788010283-00060

Designed for simplified determinations of real-time interactions and kinetic studies, the Reichert 4SPR system pushes the limits of detection and sensitivity, and does so without requiring major upkeep. The Reichert 4SPR system accelerates and enhances the drug discovery process in the following ways:

- easy set-up and streamlined workflow;
- utmost sensitivity and maximum uptime;
- robust fluid handling system to run demanding assays;
- reliable support from expert application scientists.

The SR7500DC dual-channel system is a two-channel SPR system, with incomparable sensitivity and stability to generate high-quality binding data for interactions of interest. The SR7500DC provides high performance in a package that is financially accessible for academia. This flexible, component-based platform is ideal for carrying out any type of biomolecular interaction and, owing to its remarkable sensitivity, gives researchers confidence when working at very low ligand immobilization levels or when exploring low molecular weight compounds. Paired with user-friendly, integrated software, sample injections are fully automated, allowing efficient experimentation and high-quality data for researchers. The accessible fluidics and availability of a variety of flow cells make the SR7500DC a flexible platform for experimentation. Working with ''difficult'' samples becomes easier when tubing diameters can be varied. Reichert SPR systems accommodate the widest range of sample compositions, including cells, crude samples, phage, and serum. Affinity analysis for interactions with K_D values from 1 pM to 1 mM can be carried out, in addition to concentration analysis.

Reichert's powerful software platform has been designed to make SPR user friendly and GxP-compliant software offers data security and integrity.

Reichert SPR instruments provide the core capability for determining binding kinetics and affinities. The low noise and low drift exhibited by the Reichert 4SPR and SR7500DC make both systems excellent choices for investigating biomolecular interactions, whether the research focus is on small molecules, protein–protein interactions, or even whole cells. In addition, with their unique flexibility, Reichert SPR instruments provide even more opportunities for researchers:

- *Sample composition* – Reichert SPR is uniquely suited to handle crude samples, cells, phage, and serum without increasing maintenance costs or risking downtime.
- *Thermodynamic studies* – Accurate and programmable temperature control allows for the measurement of temperature-dependent binding kinetics and affinity from which all thermodynamic parameters can be calculated using the van't Hoff relationship.

View Online

Published on 24 May 2017 on http://pubs.rsc.org | doi:10.1039/9781788010283-00060

- *Electrochemistry* – Reichert offers an electrochemistry flow cell to perform surface plasmon resonance–electrochemistry experiments (ESPR) using a potentiostat to control the potential applied at the sensor chip (working electrode) surface. Physical, surface, and polymer chemists have found particular utility for this type of flow cell. While the electrochemistry experiment is being run, SPR data are also being generated simultaneously.
- *Fluoro-SPR* – Utilizing another unique Reichert flow cell, the quartz window flow cell, allows the coupling of light from a secondary light source into the SPR flow chamber. The primary purpose of the flow cell is to induce a photochemical change within a given molecule immobilized on the sensor chip that can be monitored by SPR. An additional application of the flow cell is to monitor fluorescence along with SPR to provide additional information about a binding event.
- *SPR–mass spectrometry* – Reichert has combined MALDI-MS pins with a flow cell to identify binders in an SPR experiment. This is particularly interesting when working with mixtures since SPR cannot provide any definitive information about the identity of what bound to the target. Scientists can identify both the interaction partner and the structure of the complex formed using SPR–MS. SPR–MS can even be used to analyze complex biological samples with little or no sample preparation.

3.5.1.3 *Biosensing Instruments*

The BI-SPR of Biosensing Instruments (Tempe, AZ, USA) (BI4500 series) (see Figure 3.6) uses a divergent beam method to detect the SPR angle. A shift of the SPR angle results in a shift in location of the SPR-dip on the detector

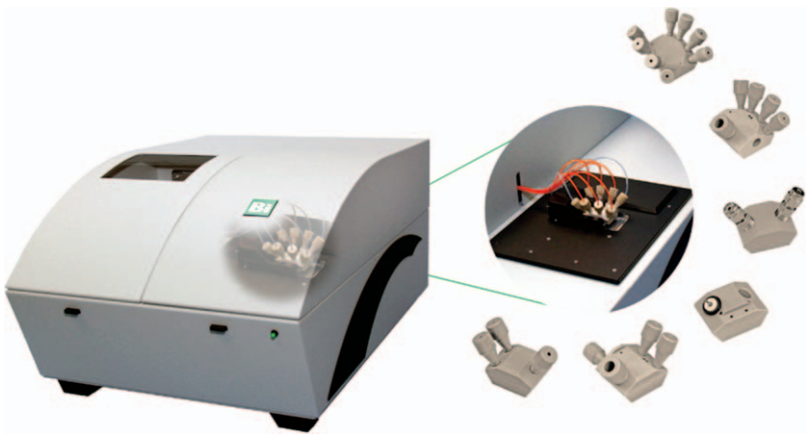


Figure 3.6 The BI-SPR of Biosensing Instruments with flexibility in applying various flow cells.

View Online

Published on 24 May 2017 on http://pubs.rsc.org | doi:10.1039/9781788010283-00060

surface. The two flow channels can be used in conjunction with two valves for the simultaneous measurement of two samples. Alternatively, one channel can be used for background subtraction. The system provides a quick and easy set-up with various cell modules for protein–protein interactions, DNA sequencing, ligand–receptor recognition and drug development applications. The optional EC cell module for electrochemical SPR measurements is not included with the basic system.

3.5.1.4 SensiQ Technologies

SensiQ Technologies (Oklahoma City, OK, USA) has developed the Pioneer line of SPR instruments since 2007. The operations of SensiQ Technologies, formerly a division of ICx Nomadics/FLIR Systems, were acquired by the private equity group TechVen Partners in May 2012. In 2017 Pall Life Sciences acquired SensiQ Technologies to extent the application range of the Fortebio Octet systems.

The technology of SensiQ, OneStep®, is a proprietary injection method featured on many Pioneer models and all models of Pioneer FE (Figure 3.7). Taylor dispersion is exploited to generate an analyte concentration gradient that provides a high-resolution dose response in a single injection. The technique mainly applied for low molecular weight fragment screening dramatically increases throughput. It provides a method for determination of the analyte diffusion coefficient and for assessing whether the analyte is heterogeneous or aggregated. First described in 2012 under the name TDi, the injection method has since been renamed OneStep®. Another dynamic injection SPR (diSPR®) principle is FastStep® which is a proprietary *in situ* dilution method enabling stepped analyte gradient injections according to a predefined profile. The analyte concentration is modulated *en route* to the flow cell. The sample throughput is increased by >10-fold for low molecular weight applications compared with conventional methods.

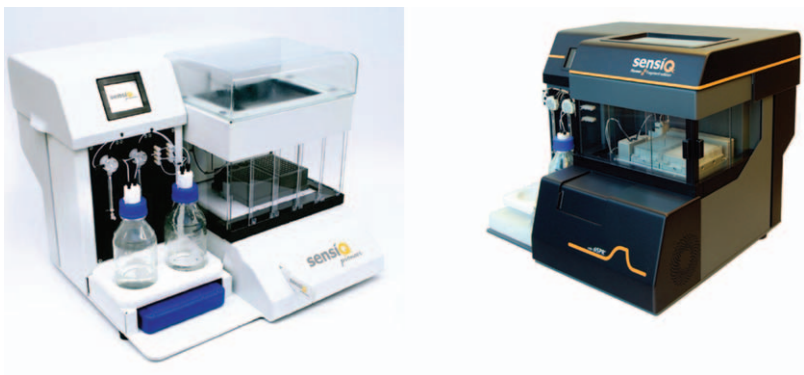


Figure 3.7 Pioneer instruments of SensiQ Technologies.

View Online

Published on 24 May 2017 on http://pubs.rsc.org | doi:10.1039/9781788010283-00060

3.5.2 Examples of Fixed- and Scanning-angle SPR Instruments

3.5.2.1 Analytical μ-Systems

The BIOSUPLAR series of Analytical μ-Systems/Mivitec GmbH (Sinzing, Germany) were introduced to the market at the end of the 1990s. Currently, the third generation is in production (BIOSUPLAR-6) (Figure 3.8). The device has two optical channels that can be used independently or as a combined sensing and reference channel for differential measurements. The basic configuration permits practical training and tutorials for new SPR users. The compact instrument seems to be one of the most cost-effective instruments in the SPR market and can compete with the OpenSPR instrument of Nicoya.

3.5.2.2 Nicoya

The OpenSPR instrument of Nicoya (Kitchener, ON, Canada) (Figure 3.9) allows label-free analysis using the localized SPR (LSPR) principle with gold nanoparticles immobilized on the sensor surface. A sensitive spectrophotometer detects shifts of the resonance wavelength. Sensitivity is in the order of 10 RU. The instrument has a very basic set-up of the sample injection. It is the most inexpensive SPR instrument in the market (the price is between $10 000 and $15 000). Recently, Nicoya launched the OpenSPR XT, which is the automated version of the OpenSPR platform.

3.5.2.3 Sensia

The Indicator-G research platform of Sensia (Madrid, Spain) (Figure 3.10) applies the Kretschmann configuration to achieve total internal reflection resonance conditions. Polarized light from a laser diode reflects at the gold surface of two flow cells, each with a volume of 300 nL, suited for the

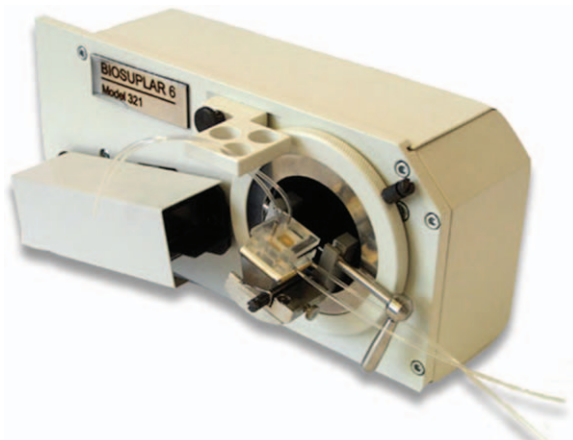


Figure 3.8 The BIOSUPLAR-6 of Analytical μ-Systems.

View Online

Published on 24 May 2017 on http://pubs.rsc.org | doi:10.1039/9781788010283-00060

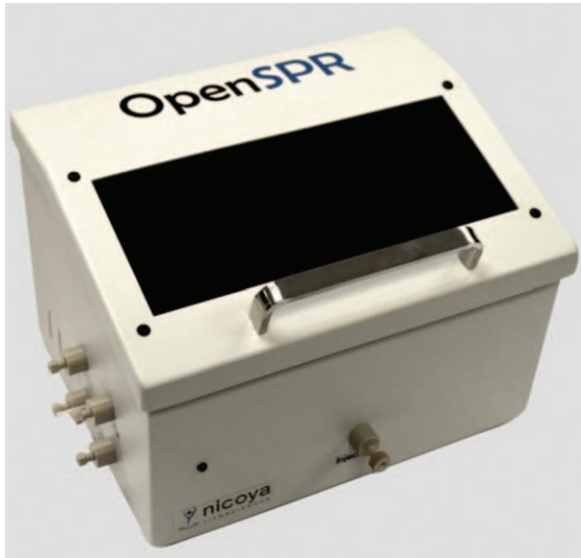


Figure 3.9 Nicoya's OpenSPR instrument.

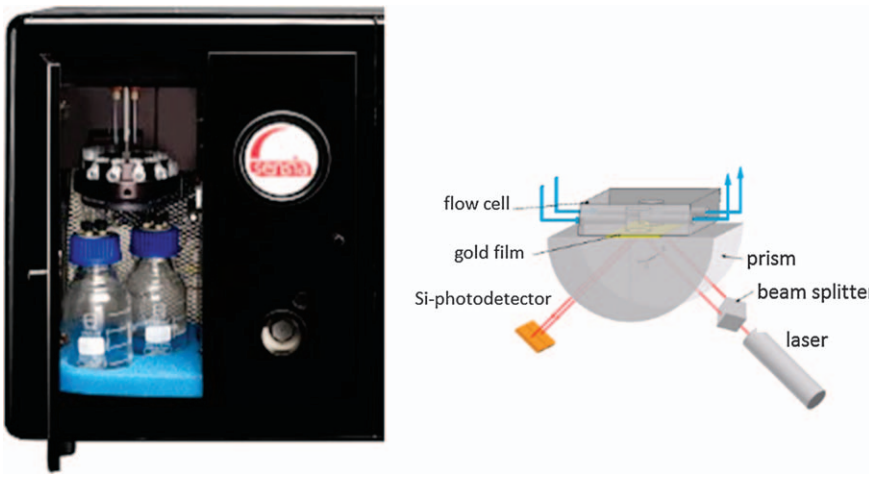


Figure 3.10 The Indicator-G research platform of Sensia.

simultaneous measurement of two biomolecular interactions or a single referenced interaction. The platform operates with a sample and a reference cell. The technology is simple from the user's point of view; however, alignment of the beamsplitter and guiding reflected light from the small flow cell make the system complicated from a technical point of view, but the company has solved these technical challenges. A prism and a multi-photodiode are located on a concentric rotary stage with an angular resolution of 0.001°. The Indicator-G SPR system has a refractive index detection limit of 10^{-6} RIU = 1 RU.

View Online

Published on 24 May 2017 on http://pubs.rsc.org | doi:10.1039/9781788010283-00060

3.5.2.4 *Affinité Instruments*

The portable, four-channel SPR (P4SPR) instrument of Affinité Instruments (Montréal, Canada) (Figure 3.11) delivers high-performance data for specific targets in complex media such as drugs or disease biomarkers (*e.g.* antibodies, antigen, hormones)[36–38] in blood serum or toxic chemicals (*e.g.* microorganism toxins, industrial organic compounds)[39,40] in underground waters. The cost-effective P4SPR is an attractive label-free device for academic research and startup laboratories performing system characterization, assay optimization, or routine monitoring of proteins and chemicals in lysate, milk, blood, or simple buffer. The P4SPR's open architecture makes it easy to combine with other analytical methods such as chromatography and mass spectrometry.

3.5.2.5 *NanoSPR LLC*

The NanoSPR8 481 of NanoSPR LLC (Chicago, IL, USA) (Figure 3.12) is an eight-channel electrochemical SPR spectrometer capable of performing real-time biokinetic, immunosensing, and biosensing measurements. LSPR nanochips apply an array of randomly distributed nanoparticles of gold or silver on a glass substrate that supports localized surface plasmon resonance (LSPR) excitation. Similarly to SPR slides, it can be used for the study of biomolecules and biomolecular interactions. However, measurements with LSPR nanochips are performed by excitation at different wavelengths in the

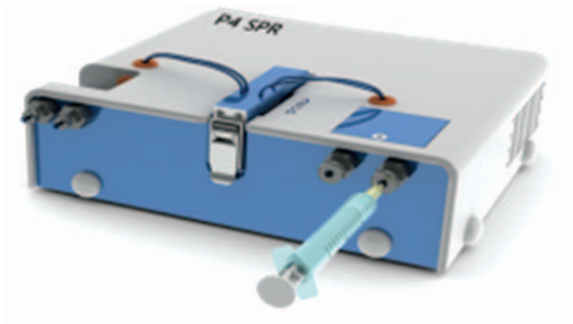


Figure 3.11 The P4SPR of Affinité Instruments.

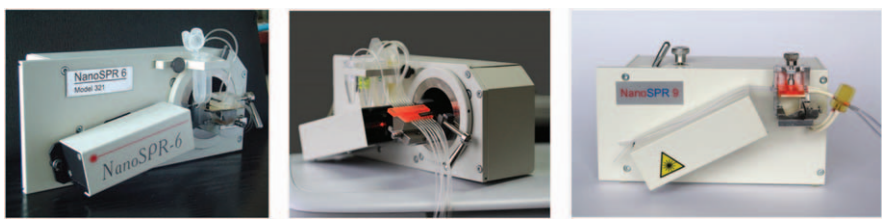


Figure 3.12 The three available instruments of NanoSPR LLC: the NanoSPR-6, -8 and -9.

View Online

visible spectral region. LSPR nanochips can be used similarly to SPR slides for studies of optical parameters of thin films and the kinetics of biomolecular interaction processes in real-time.

- Eight-channel measurements (for elimination of the drift some channels can be used as a reference).
- Open architecture (allows easy access to gold chip, optical set-up customizations).
- Thermo-stabilization available.
- Possibility of electrochemical measurements (external potentiostat is required).
- Four measurement modes: single/multiple curves, tracking, and slope mode.
- Measurements in air and liquid.
- Full SPR curve during measurements (can be used for fitting).
- Inexpensive 20×20 mm gold chips, ability to evaporate one's own chips.
- Software integration and applying a peristaltic pump.

3.5.2.6 K-MAC

K-MAC (Korea Materials and Analysis Corp., Daejeon, Korea) is an analytical instruments venture company of. In 2003, K-MAC started the development of SPR instruments with the SpectraBio2000, subsequently renamed the SPR$^{LAB™}$, a motor-operated, fixed-angle instrument. At present two instruments, the SPRmicro (Figure 3.13A) and SPRi™ (Figure 3.13B), are available and the latter is based on SPR imaging technology for protein analysis in drug discovery and disease diagnosis applications (SPRi™).

SPRmicro is a scanning-angle instrument with gold-covered prisms; its liquid handling system combines a microfluidic flow cell with a precision syringe pump. The instrument is characterized by a combination of a wide dynamic range and high sensitivity to detect mass changes on the gold sensor surface. It is suited for work with strong acids and bases and organic solvents, including dimethyl sulfoxide and carbon tetrachloride. The stepper motor-operated angle position instrument can be tuned to follow the angle shift as a function of time.

The SPRi™ imaging system is a reflectivity-based SPR imaging instrument with manual setting of the angle of incidence, designed for rapid monitoring of the biochip sensor, an array of various biomolecules, such as proteins, cells, or other microorganisms. SPR imaging is used for high-throughput analysis of biomolecular interactions by fabricating DNA/protein arrays on biochip gold surfaces. The company supplies a range of sensor chips, including prism-coated gold slides.

3.5.2.7 BioNavis

BioNavis (Tampere, Finland) developed a research line of instruments, the multi-parametric surface plasmon resonance (MP-SPR) range

Published on 24 May 2017 on http://pubs.rsc.org | doi:10.1039/9781788010283-00060

View Online

Published on 24 May 2017 on http://pubs.rsc.org | doi:10.1039/9781788010283-00060

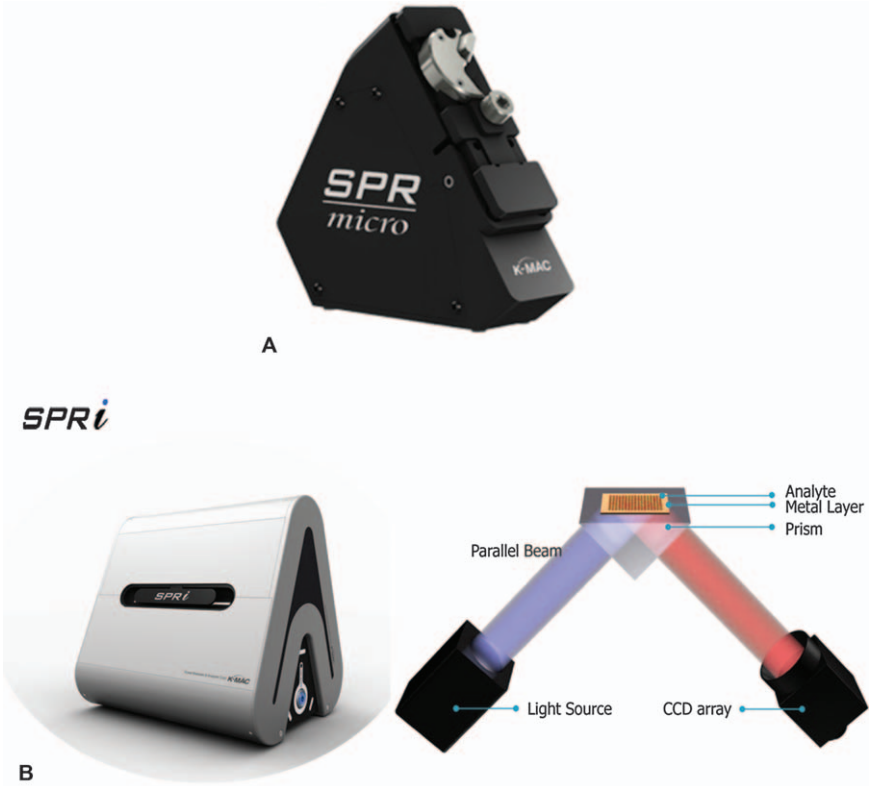


Figure 3.13 The (A) SPR micro and (B) SPR imaging SPRi™ systems of K-MAC.



Figure 3.14 The BioNavis MP-SPR Navi™ family of products. From left to right: MP-SPR Navi™ 200 OTSO, MP-SPR Navi™ 210A VASA, MP-SPR Navi™ 220A NAALI, and MP-SPR Navi™ 420A ILVES.

(Figure 3.14), based on the information that is hidden in the physical SPR phenomenon and not in the SPR-dip shift only. The key to MP-SPR is the measurement of full SPR curves and the change of the SPR curve as a result of biomolecular interactions. When measured as a function of time (with a scanning rate of one curve every few seconds), the results can be

View Online

Published on 24 May 2017 on http://pubs.rsc.org | doi:10.1039/9781788010283-00060

recalculated to give various physical parameters describing the additional properties, *e.g.*

- True thickness: Refractive index (RI) and thickness can be determined by fitting of curves using the Fresnel formalism. With additional excitation lasers, a singular solution can be found without known RI or thickness.
- From Å to μm: Unique wide angle (broad band) range measurement allows the measurement of both thin layers (ångströms) and thicker layers of up to a few micrometers.
- No vacuum required for exposure in air and liquid: The method allows measurements of substrates in air, in a specific gas, under humidity or in a liquid environment.
- Real-time interactions: MP-SPR is a real-time method and allows, for instance, measurements of swelling of materials when exposed to dry and wet environments. It also provides real-time data on material–solvent interactions.

The MP-SPR Navi™ range (Figure 3.14) widens the application range of traditional SPR from small molecules up to nanoparticles and even living cells.

3.5.2.8 KE-Instruments

The SPR system of Kinetic Evaluation Instruments (KE-Instruments) (former EcoChemie, Utrecht, The Netherlands), initially developed by IBIS Technologies in the 1990s, applies angle scanning optics. The minimum of the SPR-dip is detected as fast as ~76 Hz, hence it is fair to say that this instrument detects the true SPR-dip continuously. The robust initial design of the instrument[‖] has proven its reliability and flexibility over about two decades. The SPRINGLE (Figure 3.15, left) is marketed as a single-beam instrument and TWINGLE as a double-beam instrument, while the ESPRIT system (Figure 3.15, right) operates with two channels and has automated sample transfer with an autosampler. The SPR angle resolution and noise levels are better than 0.1 millidegrees, <1 RU. The cuvette-based instrument applies aspirating–dispensing mixing through a syringe, and the interaction process is followed in real time. A unique feature is the integrated Autolab electrochemical measurement workstation (Metrohm Autolab, Utrecht, The Netherlands) to perform electrochemical SPR (E-SPR) measurements. In this application, the gold surface is used as an electrode connected to the potentiostat output of the Autolab workstation. Real-time SPR can be combined with electrochemical measurements in one experiment.

[‖]Previously marketed by IBIS Technologies as IBIS I and IBIS II instruments.

View Online

Published on 24 May 2017 on http://pubs.rsc.org | doi:10.1039/9781788010283-00060

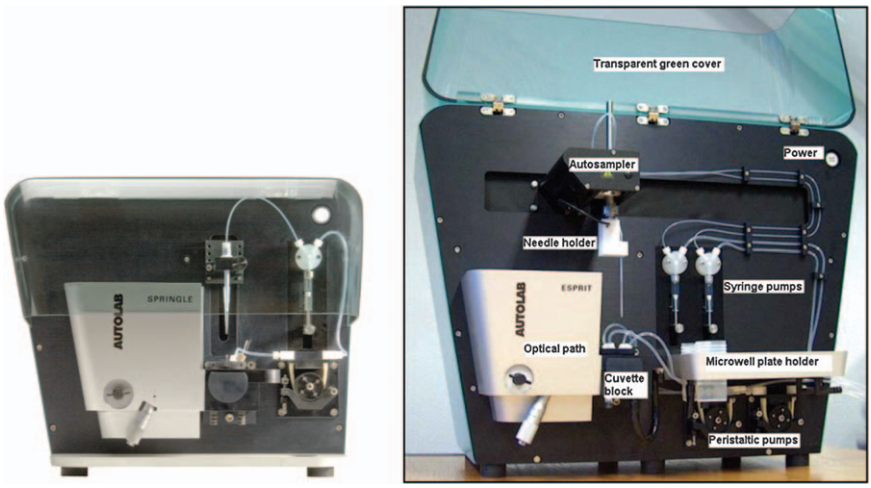


Figure 3.15 The SPRINGLE (left) and ESPRIT (right) systems of KE-Instruments.

3.5.3 Examples of Other Label-free Biosensing Instruments

3.5.3.1 Neosensors

In the mid-1990s, the IAsys system was first commercialized by Affinity Sensors (Cambridge, UK) and later by NeoSensors (Sedgefield, UK) as a cuvette-based alternative to Biacore instruments. This so-called resonant mirror technology is basically not SPR but is an alternative real-time label-free technology. Because of the impact it had in the 1990s, it is mentioned briefly here. Unfortunately, because of sensor drift and issues with the less favorable cuvette system, NeoSensors decided to stop production of this instrument in 2011.

3.5.3.2 Maven Biotechnologies

LFIRE™ from Maven Biotechnologies (Pasadena, CA, USA) is a non-SPR instrument for real-time measurements of specific interactions between biomolecules in a microarray or well-plate format. These biomolecules can be proteins, lipids, nucleic acids, small molecules such as drugs or steroids, or even whole cells. LFIRE™ is based on ellipsometry that measures changes in the polarization of light upon reflection from the interface between materials. The optical set-up is similar to the Kretschmann configuration commonly used in SPR instruments (Figure 3.16). As a ''real-time'' system, it monitors reactions as they happen, providing kinetic information on biomolecular interactions.

3.5.3.3 BiOptiX

The 404pi™ Enhanced SPR system of BiOptiX (Figure 3.17) offers a high-sensitivity, low-noise instrument at a much lower price than systems with equivalent performance. The 404pi concurrently offers high reliability,

View Online

Published on 24 May 2017 on http://pubs.rsc.org | doi:10.1039/9781788010283-00060

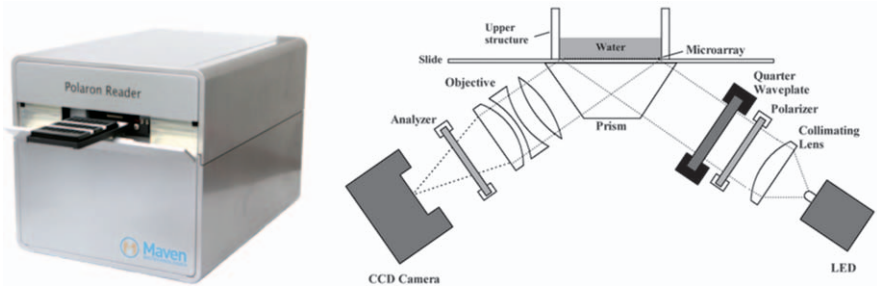


Figure 3.16 The LFIRE™ of Maven Technologies is not an SPR imaging system but an ellipsometry imaging system in attenuated total reflection configuration. Biomolecules in the evanescent field will change the polarization of the reflected light.



Figure 3.17 The 404pi™ Enhanced SPR system of BiOptiX.

easy-to-use software for experimental and great experimental flexibility. The BiOptiX 404pi™ combines the SPR phenomenon with interferometry, creating a unique and accurate detection method called Enhanced SPR. BiOptiX offers an affordable solution for drug discovery applications that require label-free, real-time detection of biomolecular interactions.

3.5.3.4 FortéBio (Pall Life Sciences)

The very successful biolayer interferometry (BLI) technology developed by FortéBio since 2005 (acquired by Pall Life Sciences in 2011) is treated separately in Chapter 10.

3.5.3.5 MicroScale Thermophoresis by Nanotemper Technologies

MicroScale Thermophoresis (MST), introduced in 2008 by Nanotemper Technologies (Munich, Germany), is a method to quantify the equilibrium

View Online

Published on 24 May 2017 on http://pubs.rsc.org | doi:10.1039/9781788010283-00060

dissociation constant of biomolecular interactions in solution. It measures the motion of molecules in microscopic temperature gradients and detects changes in their hydration shell, charge, or size. By combining precise fluorescence detection with the flexibility and sensitivity of thermophoresis, MST provides a flexible and robustway to measure molecular interactions. In the last decade, Nanotemper Technologies was one of the fastest growing companies in the field of biomolecular interaction analysis. Although the detection principle is not SPR, it is justified to treat this relevant technology for measuring equilibrium dissociation constants K_D as they can be measured with SPR also. On and off rate constants (k_d and k_a) cannot be measured with MST technology.

The Monolith instruments apply a capillary format that reduces the cost per sample that are typically associated with standard molecular interaction technologies. It also avoids regular maintenance and time-consuming assay preparation steps since no valves or pumps are needed to transport the analyte and experiments are performed in free solution without surface coupling.

The concentration of a fluorescent molecule is kept constant and the concentration of a binding partner is decreased. Only 4 μL of the respective samples are filled in MST capillaries by capillary forces. An IR laser is applied to create a localized microscopic temperature gradient in the capillary. Simultaneously, local changes in fluorescence intensity due to the motion of labeled molecules in the glass capillaries are measured. For fluorescence readout a label/fluorescent protein (Nano/Pico detector of Monolith NT.115, NT.115Pico, or NT.Automated) (Figure 3.18) or a source for intrinsic fluorescence such as tryptophan is used, making the detection label-free (LabelFree detectors of Monolith NT.LabelFree or NT.Automated).

Molecules or fluorescent particles are initially distributed evenly and diffuse freely in solution. By switching on the IR laser, the molecules are exposed to a thermophoretic force in the temperature gradient and they



Figure 3.18 The Monolith NT.Automated system of Nanotemper Technologies.

View Online

Published on 24 May 2017 on http://pubs.rsc.org | doi:10.1039/9781788010283-00060

typically move out of the heated spot. In the steady state while the laser is still on, this molecular flow is counterbalanced by ordinary mass diffusion. After turning the laser off, the molecules diffuse back to re-establish a homogeneous distribution again. The following stages are monitored for each sample: fluorescence signal before turning the IR laser on, real-time thermophoresis of molecules and back-diffusion after switching the laser off. The signal is recorded in all capillaries with varying concentration of the non-fluorescent ligand. Any change in thermophoretic property is observed as a change in fluorescence intensity.

The applications range from small-molecule binding events to protein–protein interactions and interactions of multi-protein complexes.

3.5.3.6 Sapidyne Instruments (KinExA®)

Sapidyne Instruments (Boise, ID, USA) was founded in 1995 by Steve Lackie and Tom Glass to manufacture instruments based on their patented kinetic exclusion assay (KinExA®) technology. The theory of a kinetic exclusion assay[26] is that when a receptor and ligand are in equilibrium in solution, three species are present, the ligand, the receptor, and the receptor–ligand complex. A kinetic exclusion assay is a competition assay that measures the free concentration of either the receptor or the ligand without perturbing the equilibrium. The detection of the free analyte is accomplished by exposing the sample mixture to a solid phase on which the ligand is immobilized. The exposure time is critical and should be long enough to reach the level of equilibrium.

The principle of KinExA is that the signal from the captured analyte represents only the concentration that is free in the solution. Knowing the initial equilibrium concentration of analyte allows the determination of the binding constants. The instruments for performing KinExA assays [Sapidyne's KinExA 3200 (Figure 3.19) and 3100] apply a small column of particles through which the sample and other reagents are passed. The contact time of a portion of the sample with the solid phase is then the transit time through the column and can be controlled by the applied flow rate (from around 50 ms to about 1 s). Systems with nanomolar-range binders or tighter will be in the kinetic exclusion assay mode (KinExA mode). Weaker binders can still be measured KinExA is particularly well suited for measuring the affinity constant of tight binders.

3.5.3.7 FOx Diagnostics

FOx Diagnostics (Leuven, Belgium) developed in cooperation with Prof. Jeroen Lammertyn (IMEC) a commercial fiber-optic SPR device (FO-SPR) (Figure 3.20). The product was announced for the first time at the World Congress on Biosensors in Gothenburg, Sweden, in May 2016. The FO-SPR applies a white light source, spectrophotometer, bifurcated optical fiber, and sensor probes. This set-up is integrated on a robotic arm for 3D

View Online

Published on 24 May 2017 on http://pubs.rsc.org | doi:10.1039/9781788010283-00060



Figure 3.19 The KinExA 3200 of Sapidyne Instruments.



Figure 3.20 The FO-SPR of FOx Diagnostics.

movement of the sensor tips in *e.g.* a 96-well microplate. The bifurcated fiber guides white light to the sensor tip where it is reflected back to the spectrometer. A 50 nm thick layer of gold is deposited on the sensor tip. As the light interacts with the surface of the optical fiber, a surface plasmon resonance is generated in this gold layer for a typical wavelength of the light.

View Online

Published on 24 May 2017 on http://pubs.rsc.org | doi:10.1039/9781788010283-00060

A binding event on the outside of the gold layer disturbs these surface plasmons, changing the resonance conditions and hence shifting the resonance wavelength. This detection principle allows many biochemical interactions to be monitored in real time.[27]

FOx Diagnostics developed a cost-effective biosensor platform that can allow fast and sensitive detection of infliximab (IFX), a therapeutic monoclonal antibody, which is highly effective for inducing and maintaining remission in patients with inflammatory bowel disease (IBD). The sensitivity was boosted by applying gold nanoparticles functionalized with compatible IFX-specific antibodies. The assay time of the FO-SPR platform (10 min) was significantly reduced compared with ELISA (2 h), while keeping the detection limit at 1.5 ng mL^{-1}. This demonstrates the potential of this platform as a point-of-care diagnostic tool for improving therapeutic outcomes of IBD patients. The features and benefits of the commercial FO-SPR have been published[28] and the company website provides the latest developments.

3.5.4 Examples of SPR Imaging Instruments

3.5.4.1 GWC Technologies

SPRimager®II (Figure 3.21) of GWC Technologies (Madison, WI, USA) was originally developed in the group of Robert M. Corn of the University of California–Irvine, an author of Chapter 8 in the first edition of this Handbook.[29] It captures data on the entire sensor surface simultaneously with a CCD camera. A fixed angle is set manually at the left angle flank of the SPR-dip. As described in Section 2.4, the optimal angle in terms of maximum reflectivity is in the inflection point of the SPR-dip. However, this angle can be set for only

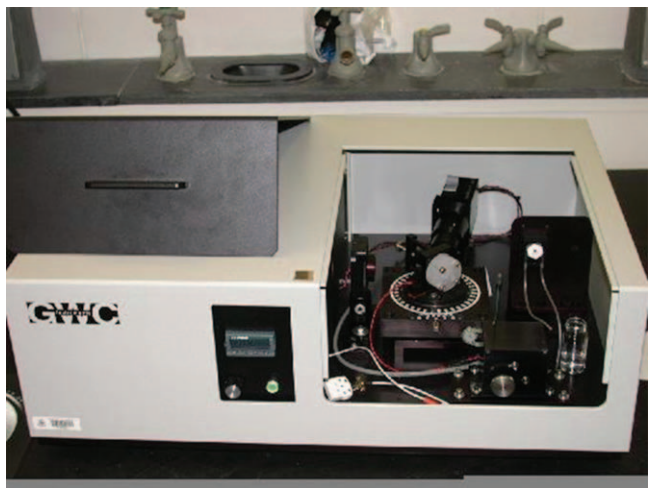


Figure 3.21 The SPRimager®II of GWC Technologies. The SPR angle should be set manually using a spindle.

View Online

Published on 24 May 2017 on http://pubs.rsc.org | doi:10.1039/9781788010283-00060

one spot at a time (*e.g.* a reference spot) and not for all different spots simultaneously. Under appropriate conditions, the SPR response is a linear function of the surface coverage provided $\Delta\%R \leq 10\%$. The instrument can be used to study biomolecular interactions at different spots, for example in a 5×5 microarray. The instrument provides various manually operated control features to check the quality of the interactions. The degree of automation is limited and a single peristaltic pump is used to pump the sample through a vertically positioned, gold-covered sensor mounted in a flow cell. The instrument uses disposable sensors of SF10 glass. These very high refractive index substrates are not compatible with standard optical glass substrates (*e.g.* K5 or BK7), hence the prism is also made of SF10 glass. Refractive index matching oil is used between the disposable sensor and the prism.

3.5.4.2 *Horiba Scientific*

Horiba Scientific (Longjumeau, France) obtained exclusive, worldwide distribution rights for GenOptic's SPRi-Lab+™ detector and GenOptics SPRi-Plex™ model. Subsequently GenOptics (Orsay, France) was acquired by Horiba Scientific, which is a laboratory instrumentation provider of various high-performance research systems not limited to SPR. Horiba's high-end instrument EzPlex (Figure 3.22) and XelPlex systems apply the Kretschmann configuration, and the instrument is equipped with a rotating mirror for setting the angle of incidence at the flank of the SPR reflectivity dip. This scan allows for selection of the best average reflectivity performance of the sensor chip for monitoring protein–protein interactions in real time. Software decides which fixed angle is used for a certain spot and the reflectivity of the spot is followed in real time. A broad monochromatic polarized light illuminates the whole functionalized area of the SPRi-Biochip™, which is combined with a detection chamber. Information can be quickly obtained from the interaction process while monitoring reflectivity variations against time.



Figure 3.22 The EzPlex of Horiba Scientific.

View Online

Published on 24 May 2017 on http://pubs.rsc.org | doi:10.1039/9781788010283-00060

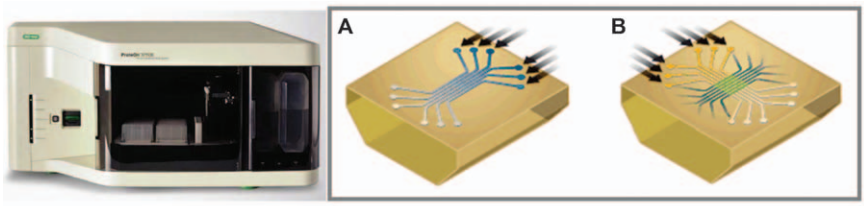


Figure 3.23 The ProteOn™ XPR36 of Bio-Rad with criss-cross microfluidics. (A) Ligands can be immobilized in six lanes. (B) The analyte can be passed perpendicular in six lanes over the surface and detection at the cross-sections takes place.

3.5.4.3 Bio-Rad Laboratories

The ProteOn™ XPR36 (Figure 3.23) protein interaction array system of Bio-Rad Laboratories (Hercules, CA, USA) is a reflectivity SPR imaging biosensor with multi-channel fluidics and interaction array sensor chip for analysis of up to 36 protein interactions in a single injection step. The ProteOn XPR36 system generates rapidly a 6×6 interaction array between six ligands and six analytes. It increases the throughput, flexibility, and versatility of experimental design for a wide range of biomolecular interaction studies. A 90° mechanical switch allows the criss-cross placement of six flow lines on the sensor surface. Six different ligands can be immobilized on the sensor surface. Then perpendicular to the immobilized ligands in lines, the user can inject the analyte over the ligand lines and acquire kinetic data in so-called one-shot kinetics of six biomolecular interactions in six analyte dilutions in a single run. Owing to issues with the criss-cross system, in spring 2015 Bio-Rad decided to discontinue the production of the ProteOn XPR36 and the delivery of spare parts and disposables will cease in 2019.

3.5.4.4 Plexera LLC

Plexera® LLC (Woodinville, WA, US), a spin-off company of Lumera, developed the PlexArray® HT, a high-throughput biomolecular interaction detection system based on surface plasmon resonance imaging (SPRi) technology. The PlexArray® HT (Figure 3.24) is a fully integrated platform for analyzing tens, hundreds, or thousands of biomolecular interactions in a single experiment. K_X Array Technology offers significant advantages over protein array technologies that require additional labeling and generate only qualitative end-point data. K_X Array Technology permits multiplexed quantitative analysis of absolute and relative affinities, specificities, and concentrations without data bias introduced by label-based detection methods. Proteomic researchers can study not only what is binding, but also how well, how much, and for how long.

View Online

Published on 24 May 2017 on http://pubs.rsc.org | doi:10.1039/9781788010283-00060

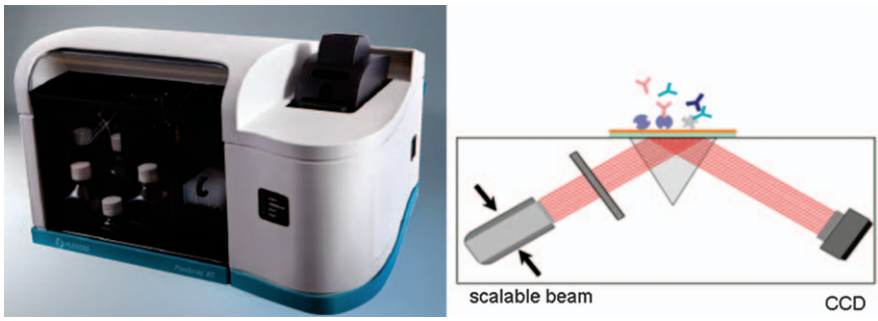


Figure 3.24 The PlexArray® HT of Plexera LLC. A scalable beam is applied and the reflectivity can be monitored for thousands of spots simultaneously.

3.5.4.5 *Graffinity Pharmaceuticals*

Graffinity Pharmaceuticals (Heidelberg, Germany), a member of the NovAliX group of companies, developed the Plasmon Imager® for the discovery of small molecular hit and lead compounds. The in-house build platform is applied to find novel small molecules for drug discovery and chemical genomics approaches. Graffinity developed additionally high-density chemical microarrays for fragment screening consisting of small molecules immobilized on gold chips in combination with high-density spotting.[30]

Using a customized high-throughput and high-precision pin-tool spotting robot, the synthesized fragment libraries are spotted on the sensor fields. In Graffinity's set-up, a wavelength shift is recorded upon biomolecular binding of the target by end-point measurements within 3 h. Graffinity's Plasmon Imager® allows parallel readout for up to 9612 sensor fields per array. The Plasmon Imager® instrument has not been marketed commercially, but is used in projects for partners of Graffinity Pharmaceuticals.

3.5.4.6 *Sierra Sensors*

Sierra Sensors (Hamburg, Germany) developed hydrodynamic isolation (HI), which is a microfluidic sample delivery technology that permits the simultaneous addressing of different solutions to different locations on an open 2D detection array under conditions of continuous flow. Samples are addressed to the sensing surface as highly discrete streams within the buffer flow, and can be addressed over one or more sensor locations at the same time. This, in combination with the ability of SPR imaging technology to analyze a relatively large detection area with extremely high resolution, has the potential to expand dramatically the use of real-time, label-free analysis in drug and protein screening and small-molecule characterization. No mechanical micro-valves flow-based analysis and quick transitions from buffer to sample are critical for accurate real-time kinetic rate determinations, and this is one of the core strengths of HI.

View Online

Published on 24 May 2017 on http://pubs.rsc.org | doi:10.1039/9781788010283-00060

Historically, microfluidic delivery systems used mechanical micro-valves to facilitate discrete sample delivery. These valves are expensive and often unreliable. Additionally, their physical size limits multiplexing options. In HI, transitions between buffer and sample at the sensor location occur in less than 0.5 s. By combining hydrodynamic focusing and location-specific delivery and evacuation, HI forms what are essentially ''liquid valves.'' As HI does not employ mechanical micro-valves, the hardware is robust and easy to build, with multiplexing limited only by the size of the fluid delivery ports. The SPR+ detection technology (developed by Agilent Laboratories) is an SPR imaging method that derives its high sensitivity from combining SPR imaging (SPRi) with a high-intensity laser diode light source. The intensity of the light source permits the use of high-speed cameras, which in turn permits more measurements of the resonance angle per scan. The net result is lower RMS noise and improved sensitivity in accurately measuring small responses.

The eight dual-sensor flow cells of the MASS-1 allow simultaneous active and control analysis for all samples. Proper control analysis is essential for accurate kinetic rate measurements. The dual-sensor design of the MASS-1 flow cells ensures that all samples can be addressed to an active and control sensor. The MASS-2 (Figure 3.25) system is a high-throughput, high-performance real-time, label-free (RT-LF) biomolecular interaction analysis system. It has eight flow cells with four detection spots for a total of 32 individually addressable sensors, robust microfluidic sample delivery, and high sensitivity SPR+ detection.

3.5.4.7 IBIS Technologies and Wasatch Microfluidics

The IBIS I and II systems of IBIS Technologies (Enschede, The Netherlands) were developed in the early 1990s and have been marketed since 1995. In 2007, IBIS Technologies launched an advanced imaging SPR instrument with



Figure 3.25 The MASS-2 of Sierra Sensors.

View Online

Published on 24 May 2017 on http://pubs.rsc.org | doi:10.1039/9781788010283-00060

patent-pending scanning-angle imaging technology (IBIS-*i*SPR). The system can be categorized as a combination of a scanning-angle SPR and an SPR imaging instrument. The development of the IBIS-*i*SPR instrument, with inclusion of the scanning-angle principle, was the first product that resulted in the reliability and accuracy required for microarray imaging of multiple biomolecular interactions. Separately, Wasatch Microfluidics (Salt Lake City, UT, USA) started the development of their Continuous Flow Microspotter™ (CFM)[31] for the Flexchip instrument of Biacore in 2006. This CFM device is described in detail in Section 12.3.1. In 2009, GE Healthcare discontinued the production and sale of the Flexchip. In the meantime, IBIS Technologies was investigating various spotting equipment, including pin spotting and drop spotting (Top spot, Biodot, *etc.*), with which at that time there were difficulties obtaining high-quality data owing to contact-angle variations and evaporation issues. Wasatch Microfluidics was looking for a high-quality SPR imager, and after the setting up of a strategic alliance with Wasatch Microfluidics for combining the SPR imaging technology with continuous flow microspotting, the IBIS MX96 instrument (Figure 3.26) was introduced in 2012.

The IBIS MX96 instrument allows the simultaneous monitoring of multiple binding interactions on microarrays spotted on the sensor surface. The instrument is equipped with a standard planar flow cell applying new patent-pending back-and-forth mixing and air-park technology to maintain the hydrodynamic conditions for kinetic operation of the biomolecular interaction process. In this way, a low volume of only 100 μL can be applied to address a large microarray-containing flow cell, while there is no consumption of the sample. The rapid injection of the thermostated sample occurs within 0.5 s, while the air-plug is parked in the air-park lines of the patent-pending flow cell. Consequently, there is no limitation on the interaction time of the sample with the sensor surface. A liquid handler operates the instrument automatically using various vials or a 96-well microtiter plate, enabling extended stand-alone operation for up to 144 h.

The IBIS MX96 system combines the detection of the SPR-dip with imaging of the entire sensor surface. In a dynamic scan operation, the



Figure 3.26 The IBIS MX96 and CFM of IBIS Technologies and Wasatch Microfluidics, respectively.

View Online

Published on 24 May 2017 on http://pubs.rsc.org | doi:10.1039/9781788010283-00060

reflectivity change that is normally applied in fixed-angle imaging instruments is converted into a SPR-dip angle shift. The shift in RU is used for real-time detection and also calculation of the kinetic parameters of binding events at user-defined spots on a microarray, even when the spots have SPR-dip differences above 30 000 RU. The SPR-dip shifts are still linear (similarly as in Biacore instruments) and are calibrated for perfect local referencing even when high bulk refractive index shifts occur. In the software, the SPR-dip shifts of reference and control spots can be subtracted from each other without remaining bulk shift effects (see Figures 1.6, 1.7, and 3.28). In addition, the user can define hundreds of regions of interest, adding enormous flexibility to the system. Images of the entire microarray can be observed at once from the microscopic view on the monitor (see Figure 2.8). In a technical sense, the IBIS MX96 system combines the best of both worlds: real-time imaging of the entire sensor surface is combined with an SPR-dip scan (instead of reflectivity) of hundreds of biomolecular interactions. The instrument is compatible with sensor chips supplied by two companies (SensEye® sensors from Ssens, Enschede, The Netherlands, and sensor prisms from Xantec, Düsseldorf, Germany).

The MX96 imaging platform facilitates real-time sensing of analyte interactions on a 6×8, 4×12, 8×12, or 16×12 ligand array. In Figure 3.27, the printhead of the CFM with multiple flow cells is shown. A cycle of 96 concatenated sample injections of 100 µL in combination with a 384-spot microarray generates 36 864 referenced sensorgrams during unattended operation in a single run (see Figure 3.28 for six injections over a 96-spot array). MX96 software has been developed to analyze biomolecular

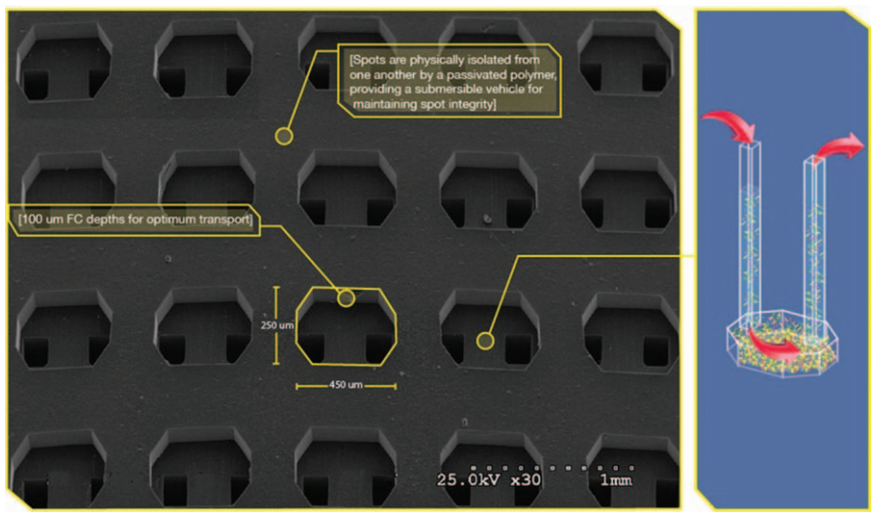


Figure 3.27 Scanning electron micrograph of the CFM printhead with dimensions of the flow cells. The spots in Figure 2.8 were created with such a printhead. More details are given in Section 12.3.1.

Published on 24 May 2017 on http://pubs.rsc.org | doi:10

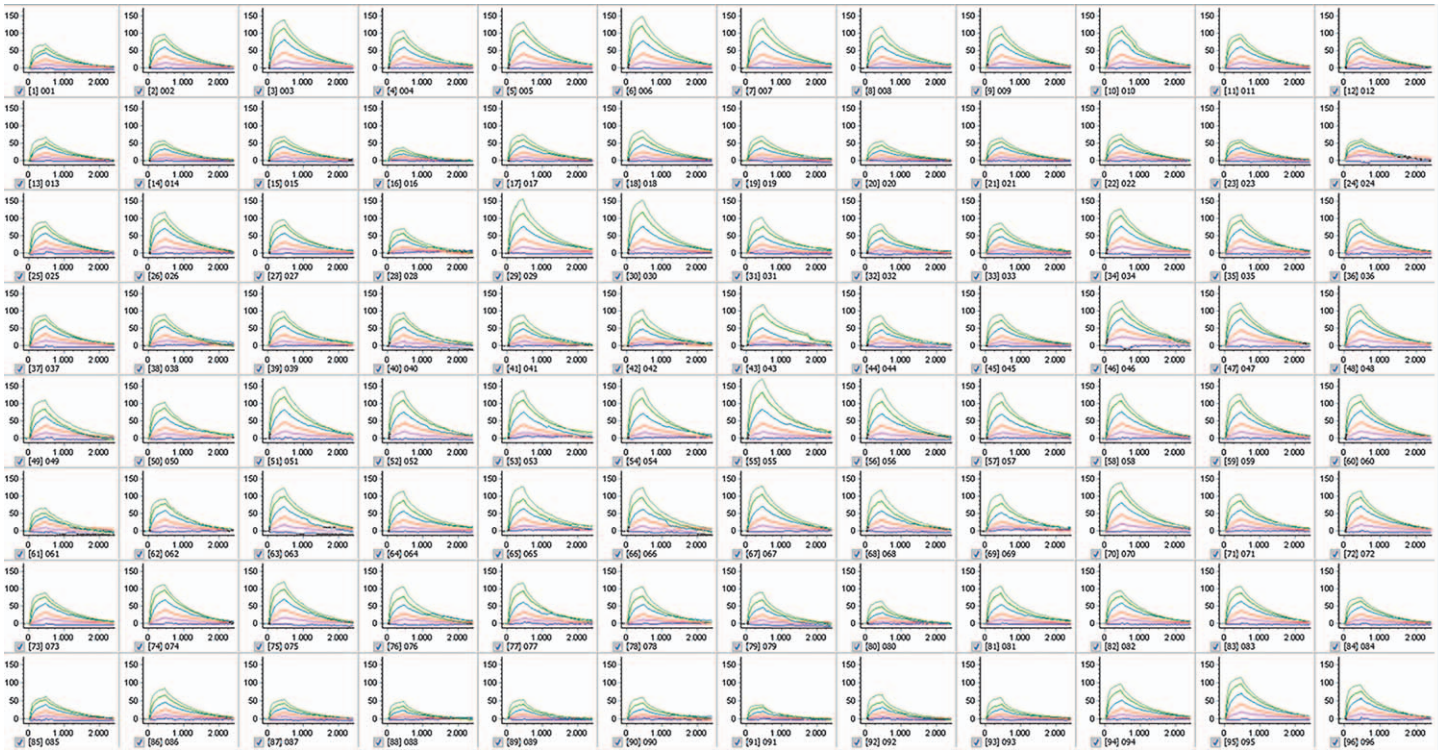


Figure 3.28 Tiled overlay plot of six injections over an array of 96 spots obtained with the CFM and IBIS MX96.

View Online

interactions in an organized straightforward way. It enables the user to analyze high-content screening assays with convenient data processing tools. In Chapter 9, by Noah Ditto and Joshua Eckman, general software tools are treated.

Published on 24 May 2017 on http://pubs.rsc.org | doi:10.1039/9781788010283-00060

3.6 Biacore SPR Systems of GE Healthcare

Biacore, acquired by GE Healthcare in 2006, is the market leader of SPR-based analytical instruments since their introduction to the market in 1990. The data from these systems have provided scientists with an unprecedented wealth of information on protein function, within areas as diverse as learning how specific protein domains contribute to biological function to the ability to make informed judgments on the potential of specific proteins as targets in drug development. The Biacore product line includes the Bialite, Biacore J, X, 1000, 2000, 3000, C, S51, Q, A-100, T-100, X-100, T200, S200, 4000, Flexchip (discontinued), and 8K (see Table 3.3).

The first four-channel Biacore (later renamed Biacore 1000) was followed by the introduction of the Biacore 2000. Biacore X, a two-channel instrument launched in 1996, and the Biacore 3000 in 1998 with four channels were successful instruments in different price ranges. The latter was later extended with recovery tools for mass spectrometry interfacing.[32] In 2000 Biacore Q was introduced to the food analysis market. The introduction of Biacore S51 for small-molecule analysis and drug discovery marked a technology shift in terms of detection, flow cell design, and sample capacity. The

Table 3.3 Overview of Biacore instruments from 1990 to 2016.

1990 Pharmacia Biosensor AB *(Introduction of Biacore)*

- BIAcore (1990) (4 channels)
- BIAlite, Biacore 1000, and Biacore 2000 (1993–1995)

1996 Biacore AB Corporation

- Biacore X (1996)
- Biacore 3000 (1998) → 4 channels
- Biacore Q (2000) → food analysis
- Biacore S51 (2002) → small molecules
- Biacore C (2002)
- Flexchip (2005) → HTS → ABI → Biacore (CFM for Flexchip)
- Biacore A100 (2005) → 4 flow cells times 5 sensor spots
- Biacore T100 (2005)

2006 GE Healthcare

- Biacore X100 → (2007)
- Flexchip (2009) discontinued
- Biacore T200 → (2010) high sensitivity – LMW
- Biacore 4000 → (2010) improved A100
- Biacore S200 → 2015 improved T200
- Biacore 8K → 2016 (8 needles)

View Online

Published on 24 May 2017 on http://pubs.rsc.org | doi:10.1039/9781788010283-00060

area of the detected spot was reduced from 1 to 0.01 mm^2 and the number of spots was increased from four to six. In 2004, a high-end instrument was introduced with four channels, each with five sensor spots (Biacore A100, now with improved software tools renamed the Biacore 4000). This instrument combines the flow cell of the Biacore S51 and the performance of the four-channel Biacore 3000 in a 20 in-line sensor array for high throughput detection. The technology is not suitable to image the surface, however.

In order to get an imaging instrument in the pipeline, in 2005 Biacore acquired the grating coupler SPR system of HTS Biosystems that was co-developed with Applied Biosystems (8500 Affinity Analyzer), which was capable of imaging the sensor surface. At least 400 interactions could be measured simultaneously (400-plex) after injection of a single analyte. After restyling, the grating coupler SPR imaging system (named Flexchip) was launched in 2006.[33] However the instrument was discontinued in 2009 because of several issues, *e.g.* (1) the instrument needed very large sample volumes, (2) the sensitivity was too low with respect to the Biacore line of instruments, and (3) the quality of data was poor, mainly caused by drop-spotting and pin-spotting protocols. Later, the Biacore 4000, which delivers high-quality data on up to 3800 interactions in 24 h, replaced the Flexchip for higher throughput in biomolecular interaction analysis. In 2016 GE Healthcare introduced the Biacore 8K as highest through-put instrument in the Biacore family of instruments (see Section 3.6.3).

3.6.1 Biacore T100, T200, and S200

The Biacore T100, with upgrades in 2010 to the T200 and in 2015 to the S200 (Figure 3.29) is a highly automated system for comprehensive protein



Figure 3.29 The Biacore T200 of GE Healthcare.

View Online

Published on 24 May 2017 on http://pubs.rsc.org | doi:10.1039/9781788010283-00060

interaction analysis from early drug discovery through drug development to QC. In addition to providing detailed information on kinetics and affinity, software support allows interactions to be thermodynamically characterized. Both the sample compartment and flow cell system of the instrument are temperature-controlled.

Although the key features of Biacore's protein interaction analysis systems have remained consistent over the years, developments were not directed only in terms of kinetic resolution, ease of use, automation, and regulatory compliance, but also in the depth of information on individual interactions. For example, in addition to measuring kinetic profiles it is now also simple to characterize the thermodynamic principles that drive interactions. Additionally there is the possibility of integrating the Biacore T200 into an identification workflow together with mass spectrometry, and hence protein identification, which has firmly placed the system in the field of functional proteomics.

The design of the flow cell system in the Biacore S200 creates optimal conditions for accurate reference subtraction. Four flow cells allow single, paired, or serial runs while paired, on-chip flow cell connections mean that the void volume between flow cells is as small as possible. Kinetic rate constants can be measured over a broad range, from the fastest on-rates encountered in biological systems to the slowest off-rates; on-rates from 10^3 to 10^7 L mol^{-1} s^{-1} (and higher for macromolecular analytes) and off-rates from 10^{-5} to 0.5 s^{-1} can be measured. Samples may be stored from 4 to 45 °C in a temperature-controlled compartment, for unattended analysis of temperature-sensitive samples. Assuming an analysis cycle of 7 min, up to 384 samples can be processed during 48 h of unattended operation in a single run. Finally, dedicated software supports kinetic evaluation of low molecular weight compound interactions involving binding partners with molecular weights as low as 100 Da.

In addition to a cooling compartment, the entire flow cell system is temperature controlled and is monitored with an integrated buffer degasser, making possible the analysis of samples at elevated temperatures. Interactions may be studied at 37 °C, enabling the behavior of therapeutics *in vivo* to be more confidently predicted. This is an important advantage of Biacore T200 over typical ''benchtop'' assays in applications such as the characterization of monoclonal antibodies in biotherapeutics, where interaction profiles with target proteins may differ radically at ambient and physiological temperatures.

Several examples of how SPR systems and matrix-assisted laser desorption/ionization time-of-flight MS (MALDI-TOFMS) have been combined to capture (Biacore) and identify (mass spectrometry) proteins from complex matrices may be found in the literature[34,35] and have been refined and optimized for the Biacore T200.

Characteristics of buffers such as salt concentration, ion content, and pH are all variables that can radically affect the profile of an interaction. ''Buffer scouting'' using the ABA protocol (see Section 7.3.6) is a novel feature of the

View Online

Published on 24 May 2017 on http://pubs.rsc.org | doi:10.1039/9781788010283-00060

Biacore T200 and is intended to help the user rapidly find the optimal buffer conditions to suit a specific interaction; up to four different buffers can be tested at one time. In addition, this flexibility allows the user to study micro-environmental effects on binding properties in mechanistic and stability studies, and to define the kinetic properties of protein samples in varied biochemical or biophysical environments. This information may be crucial when selecting candidates intended for use in the complex and variable environment of clinical treatment.

3.6.2 Biacore A100/4000

The Biacore A100, renamed Biacore 4000 (Figure 3.30) by GE Healthcare, is a protein interaction analysis system delivering good-quality concentration, kinetic, affinity, and specificity data. The open, flexible format permits multiplexed assays that create new possibilities for faster data acquisition. The system offers enhanced productivity in key areas such as antibody selection, biotherapeutic and low molecular weight drug development, immunogenicity studies, and proteomics. An optional package is available for work in regulated environments.

Hydrodynamic addressing (HA) (Figure 3.31) can be applied for multiple interactants that are immobilized on detection spots in a single flow cell, for multiplex analysis of interactions. As there is no delay between the sample exposure to signal and reference areas, highly accurate reference subtraction can be applied for the measurement of very rapid kinetics. The HA flow cell is further described in Section 3.4.2.2.

The flow cell configuration of the Biacore 4000 enables up to 3800 interactions to be detected in a 24 h run. The capacity for parallel processing and the high quality of kinetic data make the Biacore 4000 an attractive option for applications such as interaction proteomics, drug discovery or biotherapeutics development, where it is vital to be able to handle many samples and have confidence in the data.



Figure 3.30 The Biacore 4000 of GE Healthcare.

View Online

Published on 24 May 2017 on http://pubs.rsc.org | doi:10.1039/9781788010283-00060

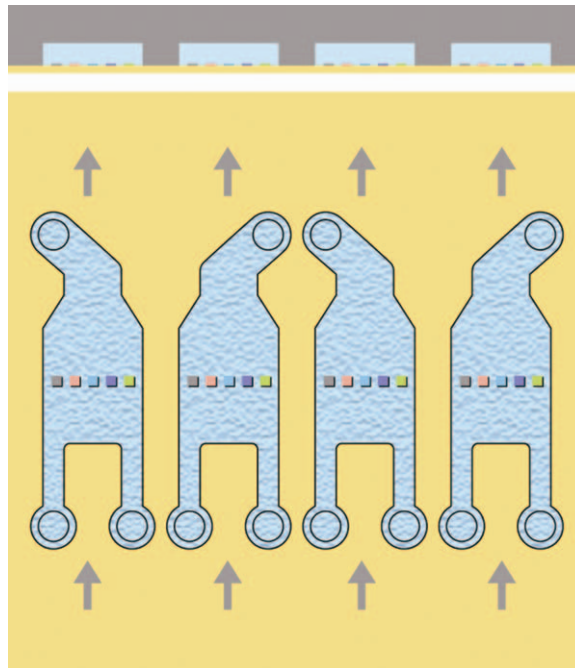


Figure 3.31 Schematic view of the flow system in the Biacore 4000. Planar view: the four injection ports allowing unique interaction conditions and parallel analysis at five measurement spots in each flow cell. Top: side view of flow cell with sensor surface and measurement spots on the bottom and flow cell cartridge (gray) on top.

In drug discovery programs, the Biacore 4000 can provide information-rich data, to allow the identification of lead compounds. Direct binding analysis, offering comprehensive characterization of critical selectivity and kinetic properties, provides data to guide key decisions. The identification of highly selective compounds against complex therapeutic targets may benefit strongly from a comprehensive panel approach in order to eliminate potential target-dependent artifacts that may result in false-positive or false-negative leads.

3.6.3 Biacore 8K

GE Healthcare's Life Sciences business launched the first of next-generation Biacore systems, the Biacore 8K (Figure 3.32), in June 2016. The Biacore 8K marks the start of a new generation of Biacore systems maintaining high data quality at high throughput. The Biacore 8K specifically supports small-molecule and biotherapeutic screening and characterization with high quality of affinity and kinetic data, increasing operational efficiency. The eight-needle high-sensitivity SPR system rapidly provides kinetic and affinity data, shortening the time to results by up to eightfold compared with

View Online

Published on 24 May 2017 on http://pubs.rsc.org | doi:10.1039/9781788010283-00060



Figure 3.32 The Biacore 8K launched by GE Healthcare in June 2016.

single-needle systems. The combination of system flexibility and throughput reduces the experimental cycle time, even for complex targets and new drug formats such as biospecific antibodies.

With its parallel eight-channel set-up with multiple microplate capacity, the Biacore 8K rapidly generates screening data for selection of the most relevant hits based on binding information. Using a binding-level screen approach, more than 2300 small-molecule fragments can be screened and ranked in 24 h based on binding response and desired sensorgram profile. For screening based on kinetic information, an initial single concentration screen of 384 samples is performed in less than 6 h, leaving time for setting up and starting the follow-up experiment on the samples with the best kinetic profile before the end of the day.

3.7 Conclusions

The instruments considered here contain at least three integrated components: (1) SPR instrumental optics, (2) the sensor chip, and (3) a liquid handling system, and the quality of the less developed component reflects the overall performance of the SPR instrument. This chapter has presented brief descriptions of SPR and SPR-like products from 27 companies. Gold is still the ''gold standard'' for generating the SPR phenomenon in almost all commercially available instruments. The commercial availability of sensor surfaces contributes strongly to accurate and reliable results. Although in the past mainly only Biacore dominated the market (>90%), new players can now be identified. However, as explained in this chapter, not all instruments from these manufacturers will generate reliable quantitative kinetic data for kinetic evaluation of rate and affinity constants, but should be regarded as instruments that are able to show qualitatively binding of the analyte with the immobilized ligand. The degree of automation, which also contributes to accurate and reliable kinetic data retrieval, differs from totally manual to

View Online

highly automated and can greatly enhance the performance of the SPR instrument.

Typically, SPR-dip shifts are monitored in angle-shift mode, reflectivity mode or wave length-mode. Instruments are divided into six categories according to their optical configuration. The liquid handling systems mainly comprise flow cells. Special attention has been paid to three Biacore instruments, the S200, 4000, and 8K, and their application to protein and low molecular weight molecule studies. As indicated in this timely chapter, the market is now more open than ever before, and competition between companies is taking place in several aspects of these SPR systems. The customers for these instruments will profit further from this competition, offering greater flexibility, innovation, and cost-effectiveness.

Published on 24 May 2017 on http://pubs.rsc.org | doi:10.1039/9781788010283-00060

3.8 Questions

1. An SPR instrument can be considered as a total analysis system that consists of three main technology cornerstones. Which three cornerstones are essential in an instrument for the detection of biomolecular interactions?
2. A divergent-beam SPR instrument shows ''walking of the SPR-dip over the sensor surface,'' as illustrated. Explain the effect.
3. In SPR imaging instruments, a parallel beam of light will bring a homogeneous surface in full resonance. How can we make an image of the surface and follow the SPR angle of each region of interest during the biomolecular interaction process? Also, how can we calculate the SPR angle position of each spot?
4. Consider a scanning mirror in a Kretschmann operated instrument that vibrates periodically with a constant amplitude and frequency. The SPR curves that are generated in time before and after binding are shown here. Explain how time-resolved dip detection can be applied to monitor the SPR-dip shift in real time.
5. Each commercial instrument applies the exposure of the sample to the sensor surface. What are the major criteria of the fluidics for high-quality biomolecular interaction sensing?

References

1. B. Liedberg, C. Nylander and I. Lundstrom, *Biosens. Bioelectron.*, 1995, **10**, i–ix.
2. R. Karlsson, *J. Mol. Recognit.*, 2004, **17**, 151–161.
3. B. Johnsson, S. Lofas and G. Lindqvist, *Anal. Biochem.*, 1991, **198**, 268–277.
4. T. Wink, S. J. van Zuilen, A. Bult and W. P. van Bennekom, *Anal. Chem.*, 1998, **70**, 827–832.
5. Nelson *et al.*, *Anal. Chem.*, 1999, **71**, 3928–3934.
6. Nelson *et al.*, *Anal. Chem.*, 2001, **73**, 1–7.

View Online

7. L. M. Zhang and D. Uttamchandani, *Electron. Lett.*, 1988, **24**, 1469–1470.
8. S. Dickopf *et al.*, *Anal. Biochem.*, 2004, **335**, 50–57.
9. C. R. Yonzon *et al.*, *J. Am. Chem. Soc.*, 2004, **126**, 12669–12676.
10. P. Schuck, *Annu. Rev. Biophys. Biomol. Struct.*, 1997, **26**, 541–566.
11. R. Cush *et al.*, *Biosens. Bioelectron.*, 1993, **8**, 347–364.
12. L. A. Chtcheglova *et al.*, *Biopolymers*, 2006, **83**, 69–82.
13. T. Wink, S. J. van Zuilen, A. Bult and W. P. van Bennekom, *Anal. Chem.*, 1998, **70**, 827–832.
14. H. J. Watts, D. Yeung and H. Parkes, *Anal. Chem.*, 1995, **67**, 4283–4289.
15. P. Schuck, *Annu. Rev. Biophys. Biomol. Struct.*, 1997, **26**, 541–566.
16. M. B. Glaubert, *J. Fluid Mech.*, 1956, **1**, 625–643.
17. T. A. Morton, D. G. Myszka and I. M. Chaiken, *Anal. Biochem.*, 1995, **227**, 176–185.
18. H. A. Stone, A. D. Stroock and A. Ajdari, *Annu. Rev. Fluid Mech.*, 2004, **36**, 381–411.
19. M. B. Glaubert, *J. Fluid Mech.*, 1956, **1**, 625–643.
20. C. L. Baird and D. G. Myszka, *J. Mol. Recognit.*, 2001, **14**, 261–268.
21. G. H. M. Engbers and R. B. M. Schasfoort, Patent application: WO2012045325A1; SPR measuring system.
22. S. Natarajan *et al.*, *Anal. Biochem.*, 2008, **373**, 141–146.
23. Internet references August 2016. URL addresses: www.biosuplar.de; www.biacore.com; www.bionavis.com; www.bioptix.com; www.bio-rad.com; www.biosensingusa.com; www.gwctechnologies.com; www.horiba.com; www.ibis-spr.nl; www.ke-instruments.com; www.k-mac.co.kr; www.nicoyalife.com; www.plexera.com; www.reichertai.com; www.seattlesensors.com; www.sensia.es; www.sensiqtech.com; www.sierrasensors.com.
24. A. Marquart, Surface Plasmon Resonance. SPR pages. http://www.sprpages.nl/.
25. Internet references of non-SPR instruments August 2016: URL addresses: www.attana.com; www.axelabiosensors.com; www.berthold.com; www.biolinscientific.com/q-sense; www.corning.com/lifesciences; www.creoptix.com; www.dynamic-biosensors.com; www.farfield-scientific.com; www.fortebio.com; www.biw.kuleuven.be/biosyst/mebios; www.genalyte.com; www.mavenbiotech.com; www.nanotemper-technologies.com; www.plasmore.com; www.siliconkinetics.com; www.wyatt.com.
26. T. R. Glass and D. J. Winzor, *Anal. Biochem.*, 2, **456**, 38–42.
27. K. Knez, D. Spasic, F. Delport and J. Lammertyn, *Biosens. Bioelectron.*, 2015, **67**, 394–399.
28. J. Lu *et al.*, *Biosens. Bioelectron.*, 2016, **79**, 173–179.
29. H. Jin Lee, T. T. Goodrich and R. M. Corn, *Anal. Chem.*, 2001, **73**, 5525–5531.
30. J. M. Brockman, B. P. Nelson and R. M. Corn, *Annu. Rev. Phys. Chem.*, 2000, **51**, 41–63.
31. S. Natarajan *et al.*, *Anal. Biochem.*, 2008, **373**, 141–146.

Published on 24 May 2017 on http://pubs.rsc.org | doi:10.1039/9781788010283-00060

View Online

32. D. Nedelkov, A. Rasooly and R. W. Nelson, *Int. J. Food Microbiol.*, 2000, **60**(1), 1–13.
33. D. Wassaf *et al.*, *Anal. Biochem.*, 2006, **351**, 241–253.
34. E. A. Smith and R. M. Corn, *Appl. Spectrosc.*, 2003, **57**, 320A–332A.
35. D. Nedelkov and R. W. Nelson, *Am. J. Kidney Dis.*, 2001, **38**, 481–487.
36. S. S. Zhao *et al.*, Miniature multi-channel SPR instrument for methotrexate monitoring in clinical samples, *Biosens. Bioelectron.*, 2015, **64**, 664–670.
37. H. Yockell-Lelièvre *et al.*, Plasmonic sensors for the competitive detection of testosterone, *Analyst*, 2015, **140**, 5105–5111.
38. J. Homola *et al.*, Surface plasmon resonance sensors for detection of chemical and biological species, *Chem. Rev.*, 2008, **108**, 462–493.
39. D. R. Shankaran, *et al.*, Recent advancements in surface plasmon resonance immunosensors for detection of small molecules of biomedical, food and environmental interest, *Sens. Actuators, B*, 2007, **121**(1), 158–177.
40. S. Herranz *et al.*, An SPR biosensor for the detection of microcystins in drinking water, *Anal. Bioanal. Chem.*, 2010, **298**(6), 2625–2634.

Published on 24 May 2017 on http://pubs.rsc.org | doi:10.1039/9781788010283-00060

Published on 24 May 2017 on http://pubs.rsc.org | doi:10.1039/9781788010283-00106

CHAPTER 4

SPRpages – Getting a Feeling for the Curves

J. ARNOUD MARQUART

Sanquin Blood Supply Foundation, Plesmanlaan 125, 1066 CX Amsterdam, The Netherlands
Email: contact@sprpages.nl

4.1 Introduction

In this chapter, many aspects regarding the analysis of biomolecular interactions are treated. It is fairly simple to generate a ''binding curve,'' but what does it mean? Does it tell us something about the specific biomolecular interaction or are we looking at artifacts? The first result from a surface plasmon resonance (SPR) experiment is the sensorgram. Each sensorgram contains a wealth of information to the trained eye. Therefore, it is essential to recognize good from bad curves.

A bad curve represents a bad experiment, producing bad results from which conclusions cannot be drawn. And be aware, there is a lot of rubbish in the SPR literature! For example, read the articles by David Myszka and Rebecca Rich.[1,2]

4.2 The Exponential

A good understanding of the binding curves is the first step in interpreting the data. Let us start with the binding between two dissimilar molecules (Figure 4.1). One molecule, the analyte (A), binds to one molecule, the

Handbook of Surface Plasmon Resonance, 2nd Edition
Edited by Richard B. M. Schasfoort
© The Royal Society of Chemistry 2017
Published by the Royal Society of Chemistry, www.rsc.org

View Online

Published on 24 May 2017 on http://pubs.rsc.org | doi:10.1039/9781788010283-00106

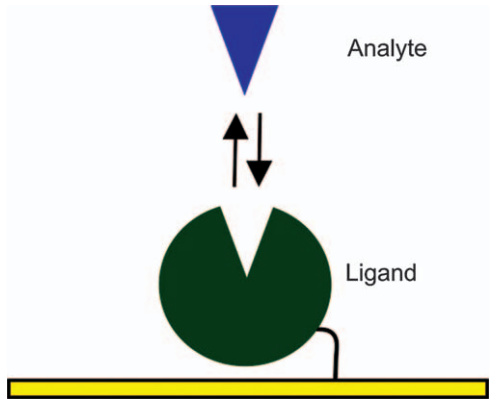


Figure 4.1 Representation of a 1 : 1 biomolecular interaction event.

ligand (L), in a reversible way. The velocity or rate of binding (association) is denoted by the association rate constant k_a in L mol^{-1} s^{-1}. The breaking up of the complex (dissociation) is denoted by the dissociation rate constant k_d in s^{-1}. The ratio k_d/k_a defines the equilibrium dissociation constant K_D in mol L^{-1}, which represents the analyte concentration that will saturate 50% of the ligand. In SPR, generally the nomenclature is that the ligand is the molecule bound to the sensor surface and the analyte is the molecule in the flow buffer.

Eqn (4.1) shows the rate equation for a 1 : 1 interaction between the ligand and analyte. Eqn (4.2) provides the calculation of the equilibrium dissociation constant K_D (see also Section 1.4.4).

$$\mathrm{L} + \mathrm{A} \underset{k_d}{\overset{k_a}{\rightleftharpoons}} \mathrm{LA} \tag{4.1}$$

$$K_D = \frac{k_d}{k_a} (\mathrm{mol\,L^{-1}}) \tag{4.2}$$

At the start of the interaction, all the ligand is unbound and the baseline is measured. By introducing the analyte, ligand–analyte (LA) complexes are formed. The amount (concentration) of complex formed by the interaction can be calculated with the differential eqn (4.3):

$$\frac{\mathrm{d[LA]}}{\mathrm{d}t} = k_a[\mathrm{L}][\mathrm{A}] - k_d[\mathrm{LA}] \tag{4.3}$$

Integrating eqn (4.3) gives an integrated rate equation, which describes the complete interaction curve as opposed to the differential rate equation, which describes the slope of the curve. For the association, in eqn (4.4), R_t is the response at time t and R_{eq} is the response at equilibrium that can be reached with the injected analyte concentration C; $t - t_0$ is the time interval

View Online

since the start of the analyte injection. For the dissociation, in eqn (4.5), R_0 is the response at the start of the dissociation.

$$R_t = R_{eq}\left[1 - e^{-(k_a C + k_d)(t - t_0)}\right] \tag{4.4}$$

$$R_t = R_0 e^{-k_d(t - t_0)} \tag{4.5}$$

Both eqn (4.4) and (4.5) describe a simple exponential binding profile. No other curve shapes such as parabolic, hyperbolic, concave and convex can describe the binding profile. Therefore, train yourself to recognize an exponential binding curve!

4.3 A Curve

Let us consider the single exponential interaction curve in Figure 4.2. The example curve consists of a baseline, an association, steady state and dissociation phase. What is important in the different parts of an interaction curve?

4.3.1 Baseline

Biomolecular interactions are measured from a starting baseline (set to zero) while the sensor is exposed to the system buffer only. It is important that the baseline is stable. At the start of an experiment, the baseline can drift due to chemicals of the immobilization or from a previous regeneration step. In addition, flow rate changes can also give drift. In most cases the drift is resolved after a few minutes of flow.

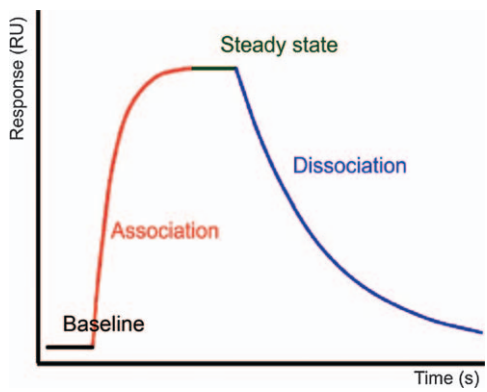


Figure 4.2 A curve representing a 1 : 1 biomolecular interaction binding event.

Published on 24 May 2017 on http://pubs.rsc.org | doi:10.1039/9781788010283-00106

View Online

Published on 24 May 2017 on http://pubs.rsc.org | doi:10.1039/9781788010283-00106

4.3.2 Association

At the start of the analyte injection, the transition between flow buffer and analyte, known as the bulk refractive index shift or bulk shift, should be small and proportional to the analyte concentration. The bulk shift originates from the (refractive index) differences between the flow buffer and the sample buffer. The initial part of the curve should not be linear. Non-linearity indicates a mass transport limitation-free interaction (see below). The association should follow a single exponential and have at least some curvature before the analyte injection ends.[1,3] The rate of complex formation depends on the association rate constant, the analyte concentration and the number of free ligand sites.

4.3.3 Steady State

When the analyte injection time is long enough, the curve should level out, indicating that the number of association events is equal to the number of dissociation events. The curve should be horizontal! Although not strictly correct, this situation is often referred to as equilibrium. The response at steady state (equilibrium) is denoted R_{eq} and is dependent on the number of ligand binding sites, the analyte concentration and the equilibrium dissociation constant. A slow dissociation rate will require a long injection period to reach steady state. When the dissociation is fast ($k_d < 5 \times 10^{-2}$ s^{-1}), steady state is reached quickly upon analyte injection.

4.3.4 Dissociation

During the dissociation phase, the curve should follow a single exponential. The dissociation is dependent only on the dissociation rate constant but in case of a strong interaction, the curve can be almost horizontal. To analyze a slow dissociation, the dissociation period should be long enough to have at least 5% signal decrease compared with the initial response.[4] However, even a slow dissociation curve should level out to the value of the baseline at the beginning of the interaction. When there is a residual response after the dissociation, this can be an indication of a non-specific interaction with the matrix. To force the analyte from the ligand or matrix, an injection with, for instance, a low pH or high salt solution can be performed provided that the ligands will stay intact.

4.3.5 Response Units

The level of response and the units in which this is expressed differ between the various types of instruments but generally the response unit (RU) is applied, which is the calibrated value of 10^{-6} refractive index units (RIU of water is $\sim$1.33) (see Section 1.3.4). Calibration of instruments can be carried out with calibrated glycerol samples. As explained in Chapter 2, the physics behind the measurement may differ and in certain ranges many instruments

View Online

Published on 24 May 2017 on http://pubs.rsc.org | doi:10.1039/9781788010283-00106

measure interactions in a linear way, meaning that there is a linear relation between the amount of analyte bound and the signal displayed. Furthermore, no matter what kind of linear conversion factor is used to transform the measured response level, the shape of the interaction curve is still an exponential. Therefore, a conversion from measured values to actual complex concentrations is possible only when instruments are calibrated to RU levels. For example, as a rule of thumb, a 1000 RU shift corresponds to 1 ng mm^{-2} bound analyte (protein).[5]

4.3.6 Equilibrium and Saturation

There is a distinct difference between the response at equilibrium (steady state) and at ligand saturation. When the interaction time is long enough, the binding response levels out and is said to have reached equilibrium. At this point, the number of newly formed complexes equals the number of complexes breaking up. However, when a higher analyte concentration is injected, a new equilibrium is reached at a higher response. The analyte concentration can be raised even further until all the ligand binding sites are occupied and the maximal response is reached. Nevertheless, at full ligand saturation, the interaction is at equilibrium because complexes are formed and breaking up. Thus, while a response that reaches saturation will be at equilibrium, an equilibrium response may not be at saturation.[1] Hence in principle, the R_{max} value cannot be measured but it is a theoretical value representing the functional ligand density for that analyte.

If the analyte concentration is expressed in equivalents of the K_D, some new insights follow (see Figure 4.3):

- Even at low concentrations, the curve will reach steady state. At low analyte concentrations, the time to reach equilibrium will be longer than at high analyte concentrations.
- When the analyte concentration equals the K_D, the response is half the theoretical maximum response. Therefore, half of the functional ligand molecules are occupied by the analyte.
- At least 10 times the K_D in analyte concentration is needed to reach $\sim$90% of the R_{max}.
- To reach the true R_{max}, a very high analyte concentration is needed. Luckily, it is not necessary to saturate the ligand to obtain meaningful results. Curve fitting programs extrapolate the data to calculate the theoretical R_{max} value. Optimally, the analyte concentration range should be wide enough to result in 10% and 90% ligand saturation (*e.g.* 0.1–10 times the K_D).

4.3.7 R_{max} Value

The maximal response (R_{max}) upon analyte binding is reached when all ligand binding sites are occupied by the analyte. The maximal response

View Online

Published on 24 May 2017 on http://pubs.rsc.org | doi:10.1039/9781788010283-00106

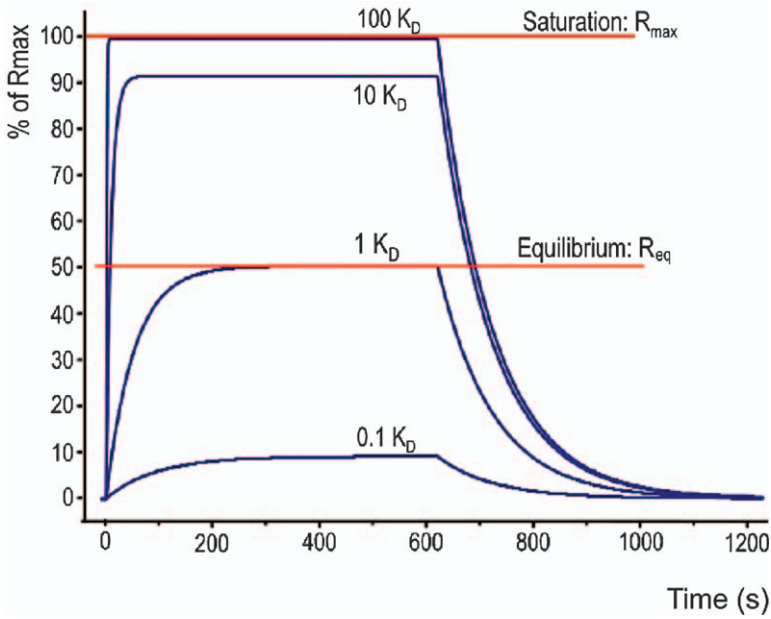


Figure 4.3 Response levels of analyte concentration in relation to K_D.

depends on the number of ligand molecules that were immobilized (R_{ligand}) on the sensor chip and the size (mass) of the ligand and analyte (ligand to analyte molecular size ratio: Mr_{ligand}, $Mr_{analyte}$). Furthermore, the response depends on the number of interaction sites of both ligand and analyte ($Valency_{ligand}$, $Valency_{analyte}$). Eqn (4.6) shows the relationship between the parameters.

$$R_{max} = \frac{R_{ligand} \times Mr_{analyte} \times Valency_{ligand}}{Mr_{ligand} \times Valency_{analyte}} (RU) \qquad (4.6)$$

When comparing different analyte molecules on the same immobilized ligand surface, the relative size ratios between ligand and analyte should be kept in mind when monitoring the analyte response levels. Although the kinetic constants are independent of the ligand density, it is advised to use a low ligand density to avoid mass-transfer limitation and rebinding effects (see below).

In the situation that the analyte has more than one binding site, the maximal response and kinetic rate constants are less straightforward. For instance, an antibody has two binding sites. When the first binding site docks to a ligand, it will generate a response. However, when the second binding site of the antibody binds, there is no extra mass added on the sensor surface, hence the response level does not increase. Although the response level does not change, one antibody can block two ligand sites, which will lower R_{max}. In addition, the overall binding strength of one

View Online

Published on 24 May 2017 on http://pubs.rsc.org | doi:10.1039/9781788010283-00106

antibody molecule increases since both arms contribute to the interaction. If the ligand density is decreased, fewer antibodies form bridges and although the interaction process is considered to be biphasic, the biomolecular interaction goes more in the direction of a 1 : 1 interaction. Therefore, it is better, if possible, to immobilize polyvalent interaction species. In the case of an antibody as ligand, each arm contributes to the total number of binding sites; however, every binding site is treated as an independent one.

4.3.8 Curve Response

The response of the curves should match the amount of immobilized ligand and the concentration of analyte used. Because it is known which ligand and analyte pair is used, the theoretical R_{max} can be calculated with eqn (4.6).

Although a valid equation, in general it is not practical because the fraction of active ligand is unknown. Depending on the immobilization technique used, only a fraction of the ligand molecules are still biologically active. For instance, covalent coupling chemistries can give highly active biological surfaces, but when the reactive group used for the covalent binding is close to the interaction site, the immobilized ligand activity can be severely diminished. The strategy of ligand capturing can be beneficial in these cases because the orientation of the ligand can be predicted. Several capture systems are available, such as 6xHIS,[6–8] FLAG-tag, GST-tag[9] and non-interfering antibodies. The interaction strength between the capture system and ligand should be sufficiently high (K_D in the sub-nanomolar range) to provide a stable ligand surface.

To define the actual R_{max}, it can be determined by saturating the ligand by injecting high analyte concentrations. However, this is not always possible (see Section 4.2.3). Luckily, it is not necessary to measure R_{max} directly to obtain meaningful kinetic results. During the fitting procedure, R_{max} is determined as one of the parameters. Provided that the calculated R_{max} is in agreement with the measured values, full saturation of the ligand is not necessary. However, for a good estimation of R_{max}, it is essential to use a wide range of analyte concentrations (*e.g.* five concentrations covering $0.1–10 \times K_D$).

In addition, high analyte concentrations and the resulting high responses tend to have problematic kinetic behavior. Therefore, it should be kept in mind that curves with a low response level ($R_{max} \approx 100$ RU) are better than curves with a high response.

4.3.9 R_{eq} value

The R_{eq} value is the response of the injected analyte concentration when the injection time is long enough to reach equilibrium. The response at equilibrium (R_{eq}) can be calculated using R_{max}, the kinetic constants (k_a, k_d) and the analyte concentration C. Rearrangement of eqn (4.7) makes the relation

View Online

Published on 24 May 2017 on http://pubs.rsc.org | doi:10.1039/9781788010283-00106

with the equilibrium dissociation constant visible. Eqn (4.8) shows that when the analyte concentration is equal to K_D, then R_{eq} is half R_{max}.

$$R_{eq} = \frac{k_a C}{k_a C + k_d} R_{max} \tag{4.7}$$

$$R_{eq} = \frac{R_{max}}{1 + \frac{K_D}{C}} \tag{4.8}$$

4.3.10 Time to Reach Equilibrium

The time required to reach equilibrium (t_Θ) can be calculated using eqn (4.9), where Θ denotes the fraction of equilibrium. For instance, to reach 95% equilibrium, $\Theta = 0.95$.

$$t_\Theta = \frac{-\ln(1-\Theta)}{k_a C + k_d} (\text{s}) \tag{4.9}$$

To reach steady state faster, it is possible to raise the analyte concentration C, but this will not always work. Analyte concentrations above 100 times K_D often give binding curves that are not an exponential and the bulk shift disturbs the curve significantly. It is better to increase the injection time. However, as shown in Table 4.1, this can take a very long time. The time to reach steady state depends mainly on the dissociation rate constant. Long injection times are not always feasible owing to the limited amount of sample or the maximal injection volume. One option is to recirculate the analyte in the flow buffer. When using recirculation, start with a low concentration of analyte in the flow buffer and wait until equilibrium is reached, then add more analyte or replace the flow buffer with one with a higher analyte concentration and wait until the interaction reaches equilibrium once more. Repeat the process until most of the ligand sites are occupied. Then, lower the analyte concentration to show that the interaction is fully reversible.[10]

In the case of equilibrium analysis (see below) it is imperative that for each analyte concentration at least 95% of the equilibrium response is reached.

Table 4.1 Approximate time required to reach 99.9% steady state at analyte concentrations ranging from 0.01 to 100 times K_D ($k_a = 1\times10^5$ L mol^{-1} s^{-1}).[25]

	k_d (s^{-1})			
Analyte concentration	10^{-1}	10^{-2}	10^{-3}	10^{-4}
$0.01\times K_D$	68 s	11.5 min	115 min	1140 min
$0.1\times K_D$	63 s	10.5 min	105 min	1047 min
$1\times K_D$	34 s	5.8 min	57 min	576 min
$10\times K_D$	6 s	1 min	10.5 min	105 min
$100\times K_D$	1 s	0.1 min	1 min	11 min

View Online

For kinetic measurements, it is not necessary to have curves that are at equilibrium provided that the curves have sufficient curvature.

4.4 Curve Examples

4.4.1 Curve Shape

Although the 1 : 1 interaction curve is a single exponential, the shape can vary considerably depending on the values of the parameters. The overall shape of the curve can be deduced from eqn (4.4) and (4.5) and is determined by the analyte concentration and association rate and dissociation rate constants. The number of ligand binding sites and the relative size differences between the ligand and analyte determine the level of response. In addition, the analyte injection period and the dissociation period determine what portion of the interaction curve is recorded (Figure 4.4).

Although the rate constants k_a and k_d are specific for a particular ligand–analyte pair, they are independent of the concentration of both ligand and analyte. However, the rate constants are dependent on the buffer composition, pH and temperature of the solution.[11] Therefore, it is important to maintain the experimental conditions constant and to describe these in publications.

4.4.2 Exponential Curve

The first example is a simple exponential curve (Figure 4.5). The association is relatively fast, but after some time there is curvature and a short moment of steady state before dissociation occurs. The total response is relatively low and the dissociation is fast enough to wash away the analyte in a short period. In this simulated figure, there is no bulk shift and no mass transfer limitation. From a kinetic point of view this is a textbook curve.

In Figure 4.6, there are four curves with the same association rate of 10^5 L mol^{-1} s^{-1} but with different dissociation rates (10^{-2}–10^{-5} s^{-1}).

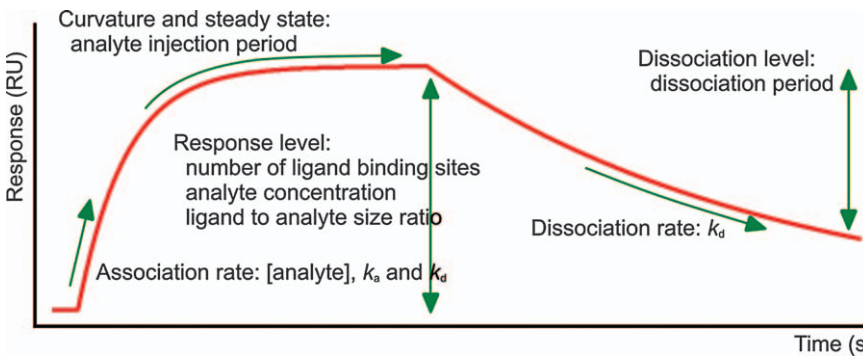


Figure 4.4 Curve dependences.

Published on 24 May 2017 on http://pubs.rsc.org | doi:10.1039/9781788010283-00106

View Online

Published on 24 May 2017 on http://pubs.rsc.org | doi:10.1039/9781788010283-00106

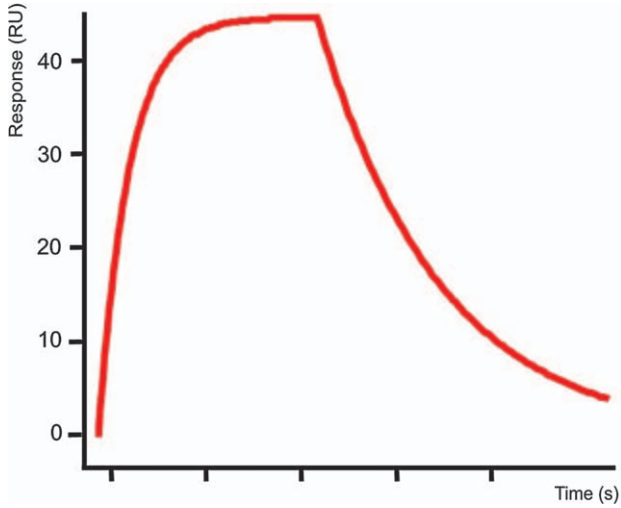


Figure 4.5 Exponential curve.

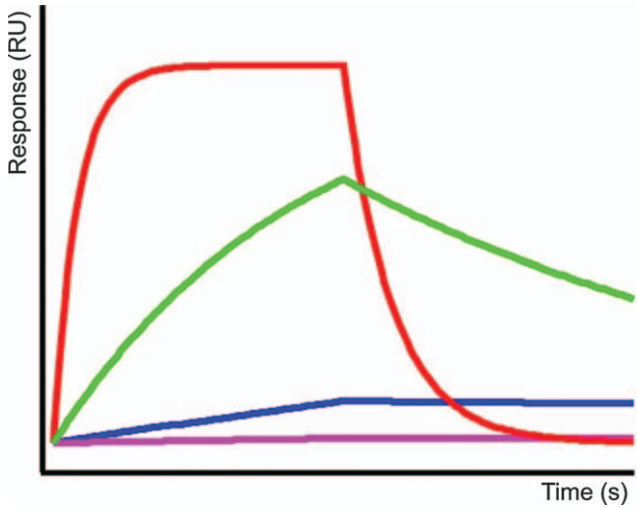


Figure 4.6 Different dissociation rates.

The analyte concentration of each curve is one times K_D. The figure shows that the dissociation rate constant has a huge impact on the shape of the curve. The curve with the fastest dissociation rate will reach steady state much quicker than the others. Can you deduce which curve has the fastest dissociation rate?

Although only one curve reaches equilibrium in this figure (the analyte concentration is equal to K_D, hence the response is half R_{max}), every curve will reach the same equilibrium response if the association period is long enough. Thus, when the dissociation rate constant is very slow, the

View Online

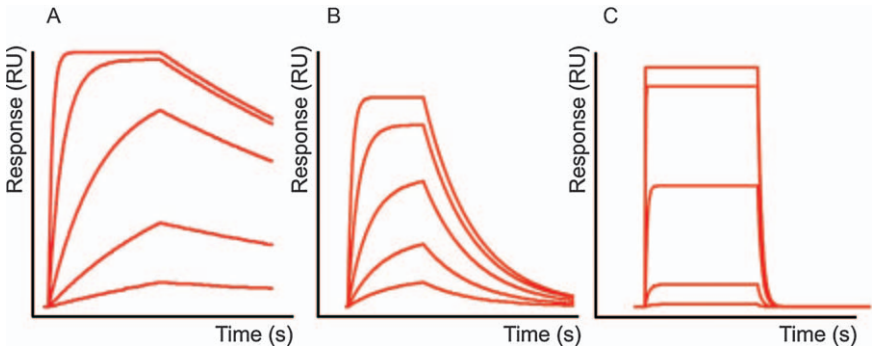


Figure 4.7 Overlay plots of typical 1 : 1 exponential sensorgrams.

interaction curve looks almost linear when only a short association period is observed. In addition to prolonging the analyte injection period, the analyte concentration can be raised to obtain greater curvature. However, keep in mind that the analyte concentration should be within a biologically relevant concentration range.[1]

Figure 4.7 provides an overview of the possible other curve shapes, all of which are exponential, but differ in kinetics. Even though the curves differ in association and dissociation rates, the shape is always an exponential.

4.4.3 Mass Transport Limitation (MTL)

Figure 4.8 shows sensorgrams that have curves with an initial binding profile, which appears to be linear. This is an example of (partial) mass transfer-limited kinetics.

The apparent linearity can be explained by the fact that the binding of an analyte to a ligand is a two-step event (Figure 4.9). First, the analyte is transported from the bulk solution towards the sensor surface by convection and diffusion.[12] Second, the analyte binds to the ligand and generates a response. The first step is also known as mass transport limitation or mass transfer limitation.

Under full or partial mass transfer-limited conditions, the diffusion of the analyte from the bulk solution to the sensor surface is slower than the rate of binding of the analyte to the ligand, creating a shortage of analyte close to the surface. Therefore, under these conditions, the rate of binding reflects the mass transfer rate (k_m) instead of the true binding kinetics (k_a and k_d).

Only when diffusion is faster than the interaction kinetics can true association and dissociation rates be measured. The mass transfer rate is influenced by the diffusion coefficient of the analyte, which in turn depends on the molecular weight and shape of the analyte.

Because the diffusion rate of the analyte is the same at every time point, the interaction curve is linear during mass transfer. When the analyte binding rate falls below the diffusion rate, the interaction curve will bend

Published on 24 May 2017 on http://pubs.rsc.org | doi:10.1039/9781788010283-00106

View Online

Published on 24 May 2017 on http://pubs.rsc.org | doi:10.1039/9781788010283-00106

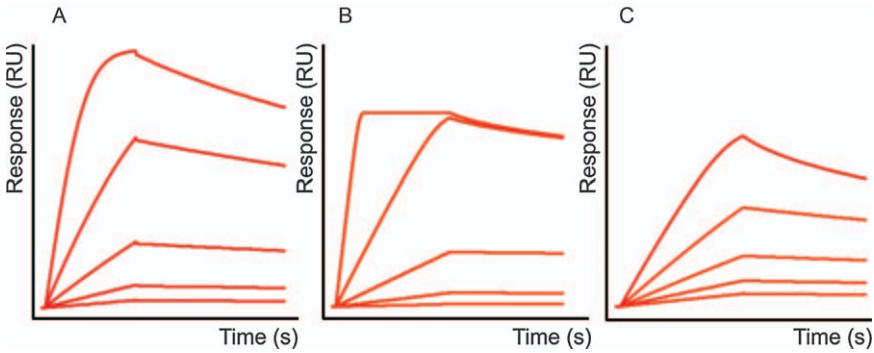


Figure 4.8 Mass transfer-limited curves.

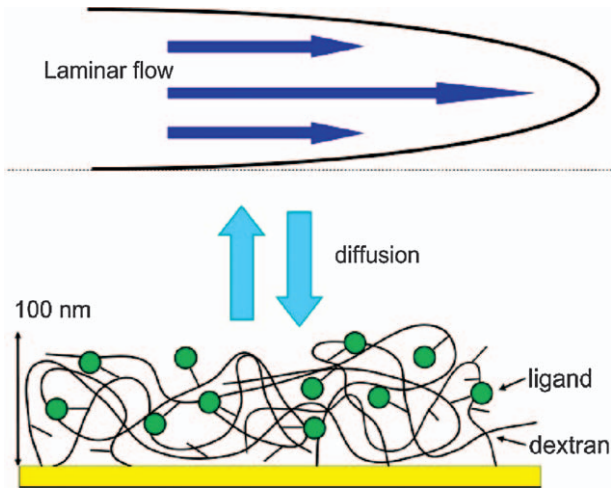


Figure 4.9 Representation of the two-step event of analyte transport and analyte binding.

and eventually level out to the equilibrium response. The interaction changes from ''diffusion limited'' to ''kinetic limited.'' Mass transfer-limited association is often followed by mass transfer-limited dissociation. If, during dissociation, the analyte is not flushed away fast enough, it is possible that the analyte will rebind to the ligand. Owing to the rebinding of the analyte, the apparent dissociation seems to be slower than it really is. Rebinding of the analyte during the dissociation can be reduced by adding free ligand to the dissociation phase.

During the analysis of mass transfer-limited curves, it is easy to incorporate mass transfer limitation in the fitting models, but it is better to avoid mass transfer by proper design of the experiment. The best option is to lower the ligand density and therefore the number of ligand interaction sites. Increasing the flow rate has some effect by making the diffusion layer

View Online

Published on 24 May 2017 on http://pubs.rsc.org | doi:10.1039/9781788010283-00106

thinner and transporting more analyte to the interaction site, but the effect is limited compared with lowering the ligand density.

Testing for mass transfer limitation is performed by injecting the analyte at increasing flow rates (*e.g.* 5, 20, 50, 100 $\mu L\,min^{-1}$). When the association rate constant increases with increase in flow rate, it is an indication that there is mass transport limitation in the system. As pointed out above, the ligand density should be lowered such that the interaction is free of mass transport limitation.

4.4.4 Biphasic Curves

The sensorgrams shown in Figure 4.10 are often referred to as having biphasic binding responses. Although not always immediately visible from the curves, when these curves are fitted with a 1 : 1 model, it becomes immediately apparent that the curves are not following a 1 : 1 interaction.

Biphasic responses are said to consist of a strong and a weak interaction. For example, when the antibody is the analyte then both arms of the antibody will induce a biphasic behavior. At low analyte concentrations and ligand densities the binding is close to a 1 : 1 interaction, but at higher analyte concentrations the analyte starts to bind to the weak interaction sites, giving rise to a biphasic curve. Because a biphasic response can be described equally well by different models,[1] it is virtually impossible to solve the interaction mechanism by modeling alone. Instead of trying to fit biphasic curves, it is recommended to optimize the experimental parameters for the interaction by lowering both the functional ligand density and the analyte concentration. Potential sources of a biphasic interaction are the random immobilization of, for instance, the amine coupling, impure ligand or analyte as shown later in Section 6.6.3. Therefore, the ligand and analyte should be checked if both have a single band on a PAGE gel. In addition, adding extra salt or detergent to the flow and dilution buffer can lower nonspecific binding by blocking low-affinity interactions. If possible, try a different immobilization technique to lower the random immobilization or

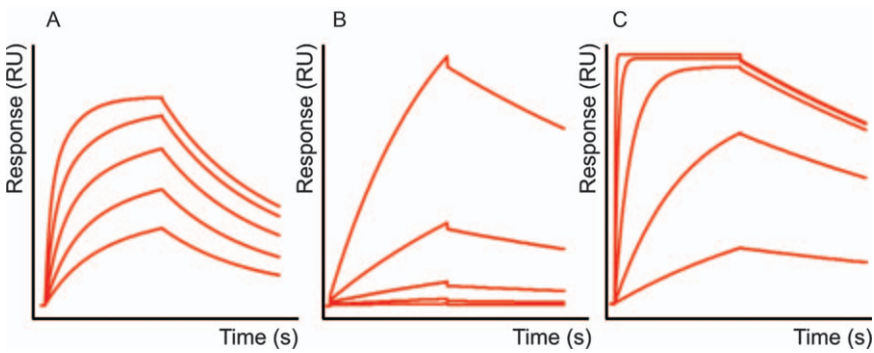


Figure 4.10 Overlay plots of biphasic responses.

View Online

reverse the ligand and analyte on the sensor chip. In addition, use a ligand density that will give an analyte response close or below 100 RU.

4.4.5 Drift, Jumps and Spikes

Recognizing problems in the experimental setup is important. Analyzing suboptimal sensorgrams will give erroneous results and waste experimental time. When changing the flow buffer, it is important to wash the pumps, tubing and flow channel thoroughly to avoid baseline drift (Figure 4.11A). Baseline drift is usually a sign of non-optimal equilibrated sensor surfaces. Especially after immobilization it can be necessary to run the flow buffer overnight to equilibrate the surfaces. In addition, a change in flow rate can cause a drift in the sensorgram that will level out over time (5–30 min) (Figure 4.11B). The duration of this effect depends on the type of sensor chip and the ligand bound to it.

Some SPR systems do not have a continuous flow over the sensor surface and some start-up drift can be possible. Therefore, it is advisable to perform a steady buffer flow for a longer time and some ''warm-up'' regeneration steps before the first analyte injection is carried out. In systems where this is not possible, a short buffer injection and a 5 min dissociation time can stabilize the baseline. In addition, incorporate several dummy injections (flow buffer) including a regeneration step at the start of an experiment to stabilize the system.

It is better to avoid bulk shifts at the beginning and end of the injection by matching flow and analyte buffer. Low shifts (<10 RU) due to buffer differences are easily compensated for by the reference surface, but larger bulk refractive index shifts should be avoided. If the analyte is provided in a solution with a high refractive index compared with the standard flow buffer, it can be beneficial to dialyze the analyte in a compatible buffer. If, for instance, dimethyl sulfoxide (DMSO) is necessary to keep the analyte in solution, dialyze against the buffer with DMSO and use the solution of the last dialysis buffer exchange as running and dilution buffer. This will minimize

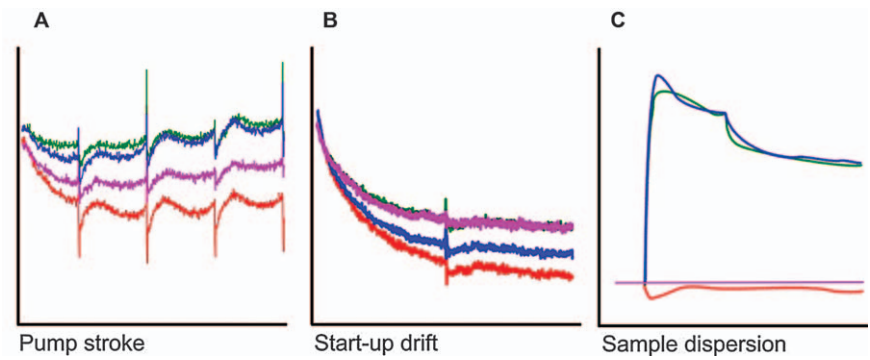


Figure 4.11 Problems of jumps, drift and sample dispersion.

Published on 24 May 2017 on http://pubs.rsc.org | doi:10.1039/9781788010283-00106

View Online

Published on 24 May 2017 on http://pubs.rsc.org | doi:10.1039/9781788010283-00106

buffer jump, since even small differences in DMSO concentration will give large jumps in the sensorgram. Furthermore, the vials should be capped, since evaporation of the analyte solution will also lead to buffer jumps during the analyte injection.

If the response during the analyte injection is dropping, it may indicate that there is sample dispersion (Figure 4.11C) and the sample is mixing with the flow buffer, resulting in an effective lower analyte concentration.[13] Most SPR instruments have special routines to separate the flow buffer from the sample. Use the best injection routine and check if the sample is properly separated from the flow buffer.

Problems with carryover and sample dispersion are easily recognized by injecting a higher concentration of NaCl (0.05 M) and a flow buffer solution (Figure 4.12). The NaCl solution should give a sharp rise and fall when injected and have a flat steady state. The flow buffer injection should give an almost flat line, indicating that the needle was sufficiently washed.

Sudden spikes at the beginning of the analyte injection can point to carryover. If this is observed, add extra wash steps between the injections. Take special care with high salt or viscous solutions.

Figure 4.13 depicts three sets of curves that show examples of buffer jumps, spikes and drift. The spiky and wobbly curves are a warning to clean the instrument. Prepare new degassed reagents and start again. In addition, mix and centrifuge the ligand and analyte for 10 min at 16 000 *g* before use to remove any aggregates.

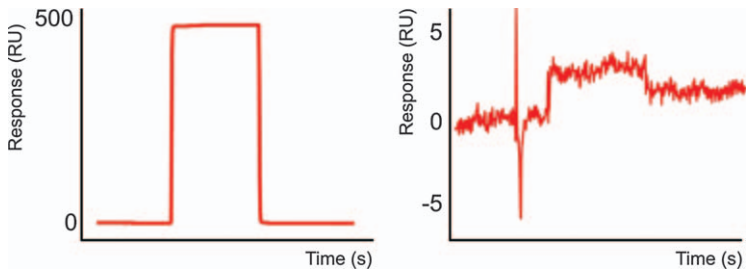


Figure 4.12 Sensorgram of a high-salt and buffer injection.

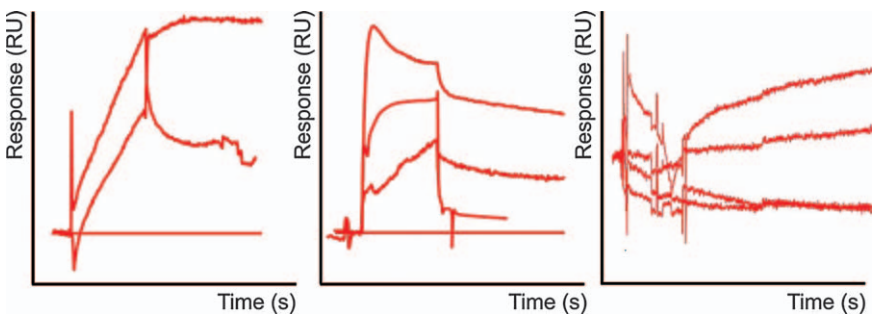


Figure 4.13 Distorted curves.

View Online

Published on 24 May 2017 on http://pubs.rsc.org | doi:10.1039/9781788010283-00106

4.5 Experimental Setup

4.5.1 Analyte Concentration Range

The concentration range of the injected analyte is important. If the analyte concentration is too high, the curves tend to bunch together in the upper part of the sensorgram, and concentrations that are too low will give low responses and little curvature. The best concentration range is between 0.1 and 10 times the K_D of the interaction, which will space the curves evenly over the sensorgram, having high and low responses. This requires knowledge of the kinetics. The best approach is to start with a low analyte concentration, for instance 1 nM, and increase the concentration stepwise until good curves are obtained. For example, a kinetic titration experiment can be performed as described later in Section 12.7.1. When the analyte concentration range is established, design an experiment with a dilution series. It is better to use a dilution series because they are easier to prepare and problems with the injections are more quickly detected. Try to make a dilution series covering the 0.1–10 times K_D. Use a minimum of five analyte concentrations for creating the overlay plots and repeat at least one concentration twice to show that the system is reproducible.

Figure 4.14 shows sensorgrams with an analyte concentrations that are (a) too high, (b) optimal and (c) too low. These sensorgrams clearly indicate the required (optimal) concentration of analyte to be used.

In addition to the analyte concentration, the order of analyte injection can be important when regeneration of the sensor surface is carried out. Simply injecting the analyte from low to high concentration as performed in a kinetic titration experiment can hide problems with regeneration and baseline drift. It is better to inject the analyte concentrations in a randomized manner to remove bias and other sources of extraneous variation that are not controllable (*e.g.* regeneration). This randomization can be delegated to control software of the instrument by using a special command or the user can arrange the vials with the analyte concentrations in random order.

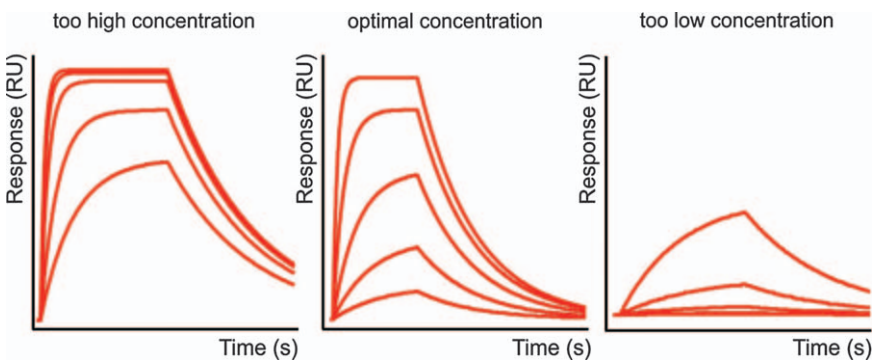


Figure 4.14 Different analyte concentration ranges.

View Online

Published on 24 May 2017 on http://pubs.rsc.org | doi:10.1039/9781788010283-00106

4.5.2 Blank Injections

Blank injections (analyte buffer only) after immobilization of the ligand and preparation of the reference surface will provide information about the stability of the sensor chip surface. In addition, blank injections ensure that the system is fully equilibrated and free of residual chemicals from the immobilization procedure. It is therefore beneficial to add at least three blank injections at the beginning of an experiment. Blank injections within an experiment can be used to identify and correct baseline drift. By first subtracting the reference channel from the active channel and then the blank injections from the analyte injections, most differences between the reference and active channels or spots can be filtered out. This is generally referred to as double referencing.[14]

4.5.3 Multi-cycle Kinetics

With multi-cycle kinetics or ''classic'' kinetics, each analyte injection is in a separate cycle. The procedure generally starts with two or three dummy injections with flow buffer replacing the analyte. Each cycle consists of a stabilization period before the analyte is injected. The association and dissociation times are chosen such that the association curve has some curvature and during the dissociation the response decays at least 5%. If the interaction is stable, a regeneration solution can be injected to force the analyte from the ligand. When all the analyte concentrations have been injected, the cycles are overlaid in one sensorgram. Before analysis, the stabilization period and the regeneration injections are removed.

4.5.4 Single-cycle Kinetics

Single-cycle kinetics, also known as a kinetic titration, consists of a series of analyte injections with increasing concentration. The benefit of single-cycle kinetics is that there is only one regeneration cycle per analyte injection series.[15,16] In addition, between the analyte injections there is only a short dissociation period and only after the last analyte injection a long one. The short in-between dissociations and reduced number of regenerations can shorten the experimental time. In the Biacore T200, so far, only five subsequent injections can be analyzed. In, for example, the IBIS MX96, an operator is free to set any number of subsequent injections in order to rank a wide range of affinities from sub-nanomolar up to high micromolar. Furthermore, single-cycle kinetics still needs blank cycles to compensate for channel differences during reference subtraction and to compensate for drift. In addition, to validate the interaction, each analyte concentration series has to be injected twice. Similarly to the classical kinetic experiments, the aim with single-cycle kinetics is to use an analyte concentration that saturates the ligand between 10 and 90%.

Single-cycle kinetics can be beneficial with labile ligands because of the reduced number of regeneration steps. In combination with ligand

View Online

Published on 24 May 2017 on http://pubs.rsc.org | doi:10.1039/9781788010283-00106

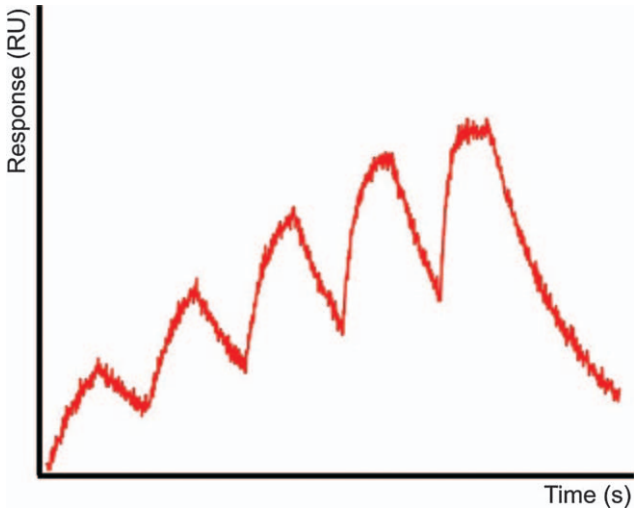


Figure 4.15 Single-cycle kinetic analysis.

capturing, single-cycle kinetics (Figure 4.15) can be a versatile approach to complex interactions.[17] The evaluation software provided with the Biacore T100/T200 series is capable of analyzing the single cycle kinetics and the Scrubber2 software (BioLogic Software, Australia) can analyze multiplex kinetic titration experiments from the IBIS MX96 instrument. For the equations to analyze single-cycle kinetics in the old evaluation software, the reader is referred to papers by Karlsson *et al.*[15] or Palau and Di Primo.[16]

4.5.5 Equilibrium Analysis

One of the most common mistakes is to apply equilibrium analysis on curves that are not in equilibrium.[1] Equilibrium is reached when the number of associations equals the number of dissociations and consequently the response level remains constant!

Figure 4.16 shows three sensorgrams, of which only part (C) can be used for equilibrium analysis because only there do all of the green curves level out before the end of the injection. This is important, because only at equilibrium is the response of the complex directly proportional to the concentration of the analyte, and only with the response at equilibrium can a reliable equilibrium dissociation constant K_D be determined.

For equilibrium analysis, it is not necessary to saturate the ligand fully provided that the equilibrium curve (not the sensorgram – see Figure 4.17) has sufficient curvature to be equilibrium fitted accurately. As an example, in Figure 4.17, the same data are analyzed five times but each time with fewer measured points. The results of the five fittings are given in Table 4.2. The conclusion from the figure is that for a reliable result, at least 40–50% of the ligand must the saturated. This means that at least one analyte concentration equal to the equilibrium dissociation constant has to be injected.

View Online

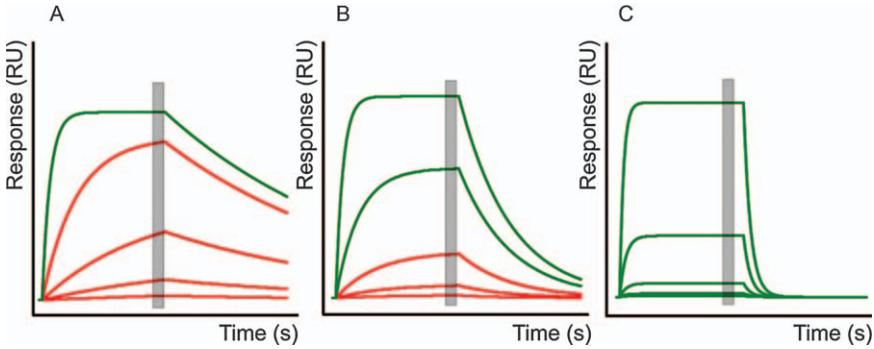


Figure 4.16 Curves at equilibrium.

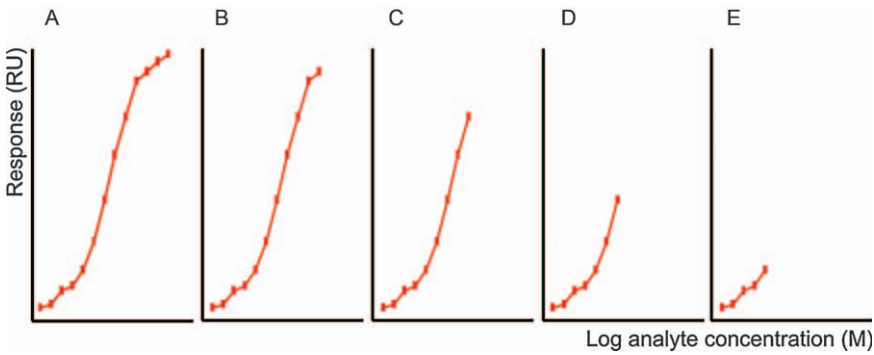


Figure 4.17 Equilibrium fitting according to Langmuir.

Table 4.2 Equilibrium fitting results of Figure 4.15.

	K_D (M)	R_{max} (RU)
A	$9.0 \pm 0.3 \times 10^{-7}$	99.0 ± 0.7
B	$8.9 \pm 0.3 \times 10^{-7}$	98.4 ± 0.7
C	$9.1 \pm 0.3 \times 10^{-7}$	99.3 ± 1.2
D	$9.0 \pm 0.5 \times 10^{-7}$	98.3 ± 2.5
E	$5.9 \pm 2.7 \times 10^{-7}$	71 ± 23

For the best result, it is recommended to use at least five different analyte concentrations covering ligand saturation between 10 and 90%. Using an analyte concentration range that is too low can lead to an underestimation of R_{max} and the equilibrium dissociation constant K_D.

The equilibrium values can be plotted with linear or a logarithmic analyte concentrations on the *x*-axis (Figure 4.18). The linear plot performs better when the analyte concentrations are high enough to approximate R_{max}. The logarithmic plot gives a better overview of how the low analyte concentrations are spaced. It is a matter of taste which plot is preferred.

Published on 24 May 2017 on http://pubs.rsc.org | doi:10.1039/9781788010283-00106

View Online

Published on 24 May 2017 on http://pubs.rsc.org | doi:10.1039/9781788010283-00106

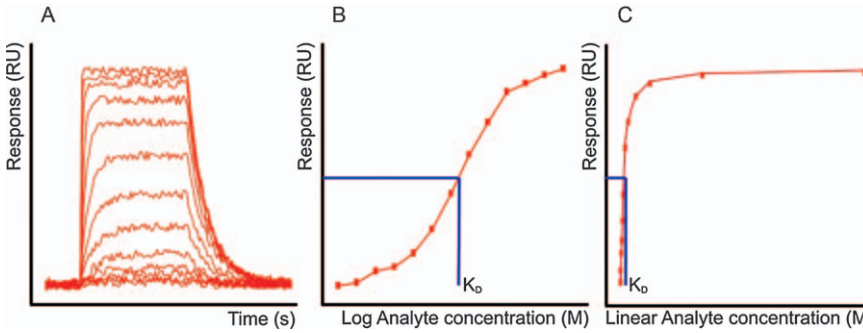


Figure 4.18 Equilibrium analysis: determination of K_D.

4.5.6 Fast Kinetics

What about these fast on- and off-phases? Are they actual kinetics of the biomolecular interaction or is it bulk shift?

When it is actual kinetics of the biomolecular interaction, the shape of the curves is almost totally determined by the dissociation rate. Because of the fast dissociation, the curves reach equilibrium very quickly. The height of the response is directly proportional to the analyte concentration according to Langmuir equilibrium. With increasing analyte concentration, the surface will saturate as opposed to increasingly higher responses induced by high salt, DMSO, glycerol or non-specific binding. Proper referencing is very important in this case.

Because of the fast association and dissociation kinetics, the rate constants of these interactions are difficult to calculate. Sometimes a high sample rate can provide more data points to work with, but in many instances this will not be sufficient. In such situations, the only kinetic parameter that can be calculated is the equilibrium dissociation constant K_D using equilibrium analysis software.

Thus, real kinetic processes can saturate the ligand at high analyte concentrations (usually the micromolar range and higher). If the response continues to increase with increasing analyte concentration, other effects such as non-specific binding or bulk refractive distortion (*e.g.* by high salt, DMSO or glycerol) can cause these high responses. These effects can be clearly observed in the reference channel or at the reference spots.

Figure 4.19 presents two examples with the same fast kinetics but each with a different analyte concentration range. In the left-hand example it is difficult to determine if the analyte will saturate the ligand. Therefore, high analyte concentrations are necessary to show that the ligand is saturating and that the maximum response level reaches a plateau. Examples of fast kinetics were given by Magotti *et al.*[18] and Souphron *et al.*[19]

4.5.7 Decaying Surface

Sometimes, the sensor surface is modified with special groups (*e.g.* nitrilotriacetic acid, antibodies, aptamers) to allow the capture of a ligand. The

View Online

Published on 24 May 2017 on http://pubs.rsc.org | doi:10.1039/9781788010283-00106

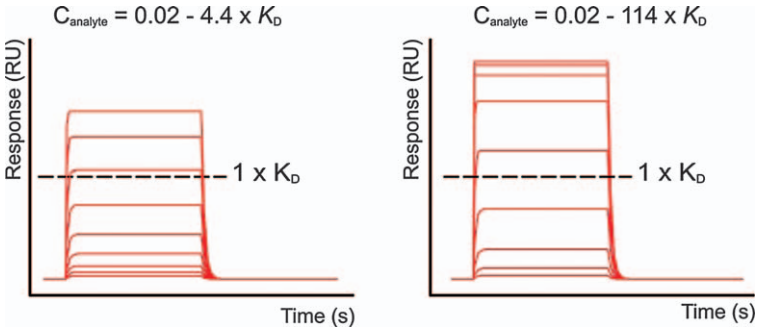


Figure 4.19 Fast on and off curves showing the equilibration dissociation constant.

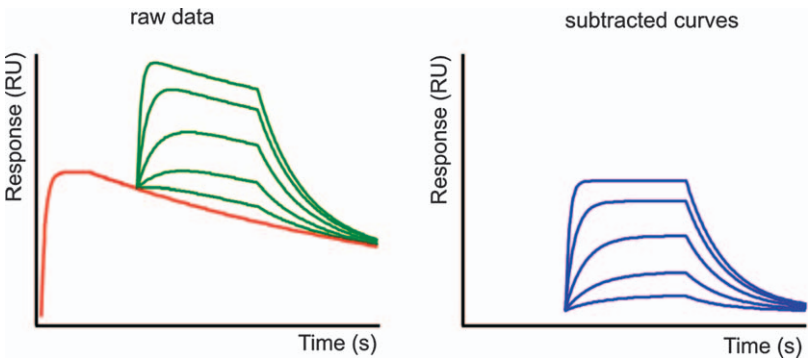


Figure 4.20 Decaying ligand surface.

modifications are covalently bound to the surface and therefore permanent. However, the captured ligand is transiently bound and will immediately start to dissociate after loading.[20,21] When the analyte of interest is flowed over this decaying surface, the resulting response curve is the sum of both the analyte interaction and ligand dissociation.

When using the classical approach of injecting one analyte concentration per cycle, each cycle has to start with the loading of the ligand. The amount of ligand loaded on the surface should be the same in every cycle in order to keep the ligand dissociation rate the same. When buffer-only injections are included in the experiment, the decaying surface response can be subtracted from the analyte interaction, leaving only the analyte response.

Some analysis programs can analyze both the ligand capturing and analyte binding curves at the same time, extracting kinetic parameters for both interactions. In the analysis of the biomolecular interaction, theoretically the dissociation rate constants of the decaying surface ($k_d{}^1$) and the rate constant of both processes together ($k_d{}^{1+2}$) should be subtracted to obtain the dissociation rate of the subtracted curve only ($k_d{}^2 = k_d{}^{1+2} - k_d{}^1$) (Figure 4.20).

View Online

4.6 Sensorgram Quality

In the previous sections, the important parts of the curves and sensorgrams were considered. Here we show a low-quality (Figure 4.21) and a high-quality sensorgram (Figure 4.22).

In conclusion: what is important before fitting a set of curves?

- The baseline is flat. When the running buffer is flowing, the drift of the baseline is close to zero.
- Upon injection of the analyte, the buffer jump is very low; the baseline to association and association to dissociation phase connect after referencing.
- The association is free of mass transport limitation.
- The curves follow a single exponential.

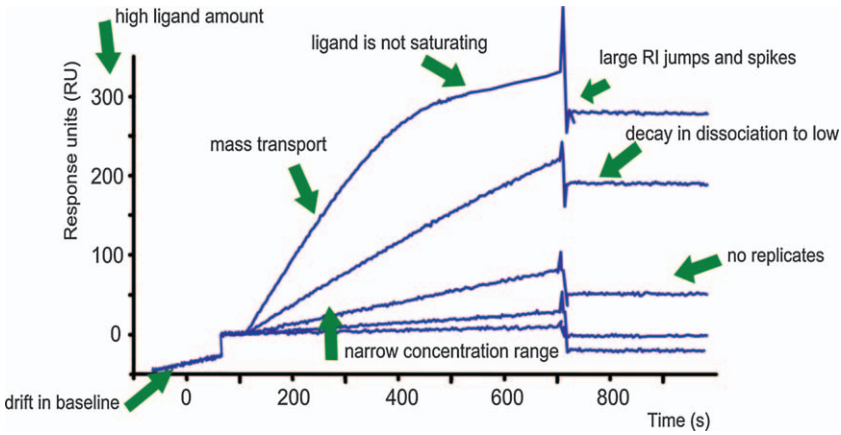


Figure 4.21 Low-quality sensorgram.

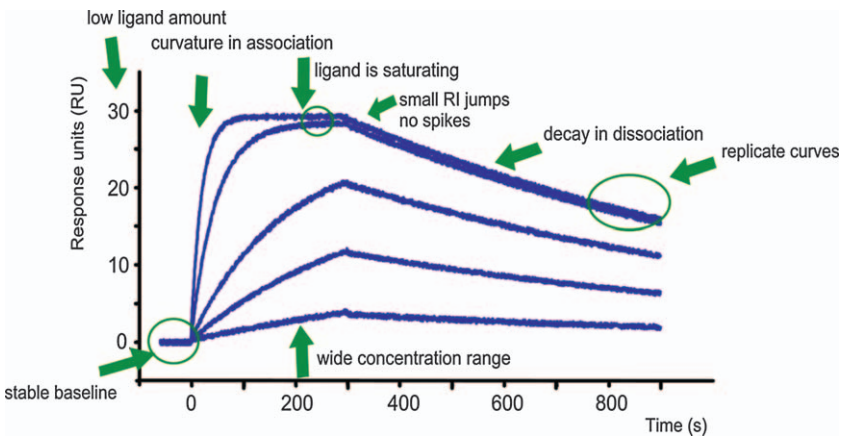


Figure 4.22 High-quality sensorgram.

Published on 24 May 2017 on http://pubs.rsc.org | doi:10.1039/9781788010283-00106

View Online

- The curves have sufficient curvature.
- There is at least one replicate.
- The analyte concentration is between 0.1 and 10 times the expected K_D.
- The curves are well spaced in the sensorgram.
- At least one of the curves is reaching steady state (when possible).
- The overall response is low hence the ligand density (R_{max}) is low.
- The response is proportional to the analyte concentration and kinetics.
- The dissociation is long enough for a sufficient decay in response.
- The injections are randomized to avoid systematic errors.

When the curves are not of high quality, optimize the experimental conditions before attempting any fitting. Fitting bad curves will give bad answers and waste time. Therefore, start optimizing.[1]

The following steps can be taken:

- Check ligand and analyte for purity and uniformity.
- Lower the ligand density on the sensor chip.
- Increase the flow rate to check for mass transport limitation.
- Reverse the ligand and analyte on the sensor chip.
- Change the immobilization chemistry when possible (*e.g.* thiol coupling).
- Use site-directed ligand coupling or capture the ligand.
- Increase or decrease the concentration of salts in the flow buffer.
- Increase or decrease the concentration of detergents in the flow buffer.

4.7 The Affinity Plot; Getting a Feeling for the Numbers

The affinity plot (Figure 4.23) shows the relation between the association (k_a) and dissociation (k_d) rate constants and the equilibrium dissociation constant (K_D).

The association rate constants are on the *y*-axis in red, the dissociation rate constants are on the *x*-axis in blue and the intersections of k_a and k_d are the equilibrium dissociation constant in green. The green lines connect the points with the same K_D. The intermediate yellow box marks the range in which most of the association and dissociation rate constants can be expected. The four red circles show examples of the curves at the intersections (the analyte concentration is 100 nM). When comparing different analytes, the affinity plot can be of great help because both kinetic rate constants and the equilibrium dissociation constant are visualized.

4.8 Curve Fitting

A robust fitting starts with high-quality data from several independent runs or experiments. In addition, the data must be cleaned of unwanted curves, regeneration parts and air spikes. Further, reference subtraction and double referencing can be used to compensate for unmatched refractive indices and

Published on 24 May 2017 on http://pubs.rsc.org | doi:10.1039/9781788010283-00106

View Online

Published on 24 May 2017 on http://pubs.rsc.org | doi:10.1039/9781788010283-00106

baseline drift. The removal of injection and pump spikes will lower the χ^2 value.[4] After the initial data processing, a fitting can be performed. The first and only model to use is the 1 : 1 Langmuir interaction describing the single exponential of the data. With the first fitting attempt, leave the bulk contribution and the drift on zero and do not fit. Start by providing the initial fitting values for the kinetic parameters and press "fit" to see the result. If the sensorgram consists of good curves (Figure 4.24), the fit is ready in seconds; the fitted line follows the curves and will provide well-defined values with small errors (Table 4.3).

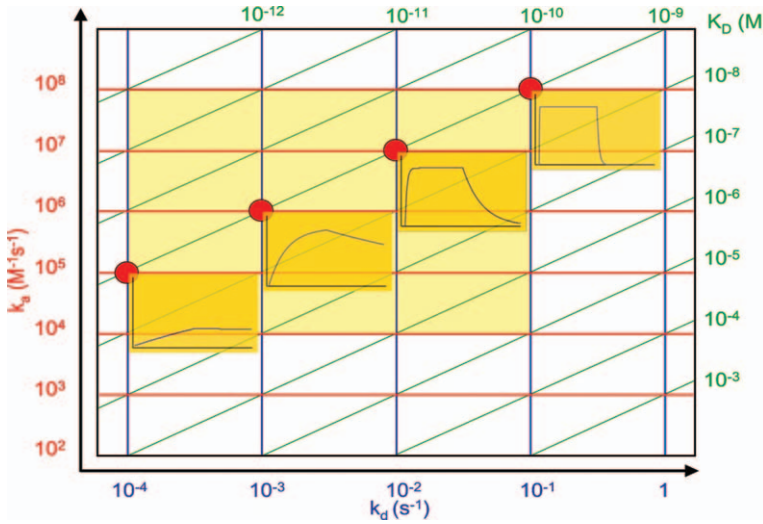


Figure 4.23 Affinity plot k_a *versus* k_d with isoaffinity K_D diagonals.

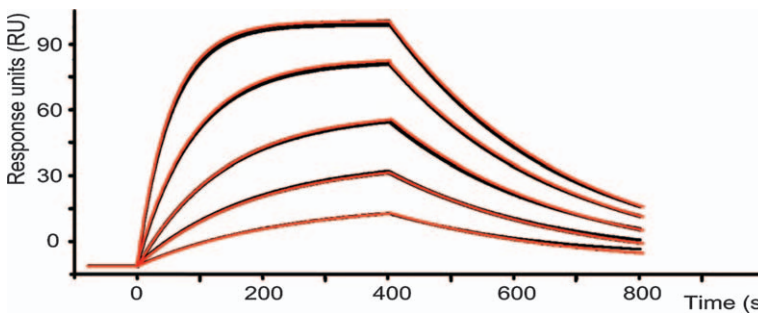


Figure 4.24 A biomolecular 1 : 1 model interaction fitting.

Table 4.3 Fitted values.

k_a (L mol^{-1} s^{-1})	k_d (s^{-1})	R_{max} (RU)	K_D (M)
$1.02 \pm 0.01 \times 10^5$	$4.70 \pm 0.00 \times 10^{-3}$	98.6 ± 0.7	$4.6 \pm 0.3 \times 10^{-8}$

View Online

Published on 24 May 2017 on http://pubs.rsc.org | doi:10.1039/9781788010283-00106

More realistically, optimization of the initial values and adjusting the fitting ranges may be necessary. This is normal and it is a good idea to fit the sensorgram with several initial values that differ by a magnitude in scale. If, after fitting with different initial values, the results converge to the same values, it can be assumed that the values are well defined and robust. After the initial fittings, bulk contribution and/or drift can be fitted when necessary. Both bulk contribution and drift should be small compared with the curve response and proportional to the analyte concentration.

The next step is to compare critically the fitting with the measured curves. Does the fitting follow the curves? Are the calculated buffer jump values in line with the curves? Are the values of the parameters (R_{max}, k_a, k_d) possible? Some instruments provide a quality control on the fitted parameters; however, always inspect the parameter values and the curves.

4.8.1 Residual Plot

The fitting procedure also produces a residual plot. A residual is the vertical distance between a measured value and the closest point on the fitted curve. In other words, the residual is obtained by subtracting the experimental plot from the fitted curve. The residual plot is a graphical representation of the accuracy of the fitting. Looking carefully at the fitting (A) in Figure 4.25, it can be seen that the fitted line follows the data reasonably well. However, the residuals plot (A) shows that the data points are not randomly distributed above and below the fitted curve; there are clusters of points all above or all below. Non-randomly distributed residuals are an indication that the model is not adequately explaining the data. Either the model is incorrectly describing the interaction or the experimental conditions are sub-optimal, giving rise to mass transfer, non-specific binding or rebinding during dissociation. A fitting that closely follows the measured data will give random residuals in a close band around zero (Figure 4.25B).

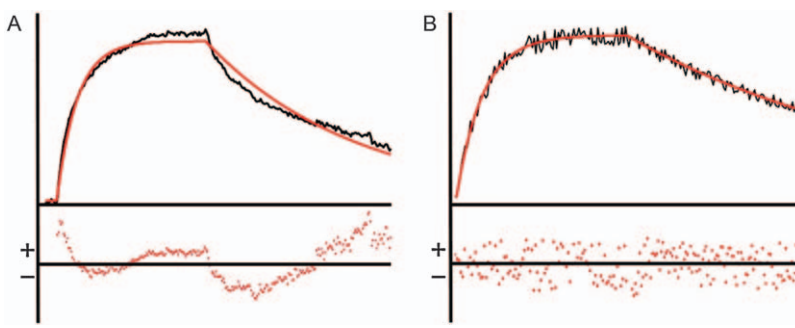


Figure 4.25 Non-random and random residuals.

View Online

Published on 24 May 2017 on http://pubs.rsc.org | doi:10.1039/9781788010283-00106

4.8.2 Local and Global Fitting

Many fitting programs (*e.g.* BiaEvaluation and Scrubber2) allow the calculation of the kinetic values for single curves or of a single value for all the simultaneously fitted curves. The former method is referred to as ''local fitting'' and the latter a ''global analysis.'' In most situations, a global analysis is preferred and will give the most robust answer. When using the global fitting, the k_a, k_d, R_{max} and mass transport constants are fitted simultaneously to all curves, giving one value for each parameter. Parameters such as bulk refractive index shift and drift are fitted locally because they are dependent on analyte concentration.

4.8.3 Deviations from a 1 : 1 Interaction

In Figure 4.26, the fit does not follow the curves during the dissociation phase. By adding a larger buffer jump, the program attempts to make the fit better. Do not use the values calculated by the fitting.

Large calculated refractive index (RI) jumps can originate from badly positioned injection start markers. Especially when the markers are positioned automatically, check if they are at the start of the analyte injection and that there are no spikes or jumps at this point. One other possibility is that the interaction is not following 1 : 1 kinetics.

One other aspect that is apparent is that the overall response is too high. Lowering the amount of immobilized ligand may help to lower the non-1 : 1 interaction. In addition, check the analyte for purity and centrifuge the analyte before use for 5 min at 14 000 *g* to remove aggregates.

Figure 4.27 shows a fitting with multiple problems. For instance, the response of the data is fairly high. In addition, at the highest analyte concentration, some biphasic dissociation can be seen. On a positive note, owing to the slow dissociation rate, a long dissociation time is used to give some decay in signal. Also, because of the slow dissociation, a longer association time is used to give some curvature in the association phase.

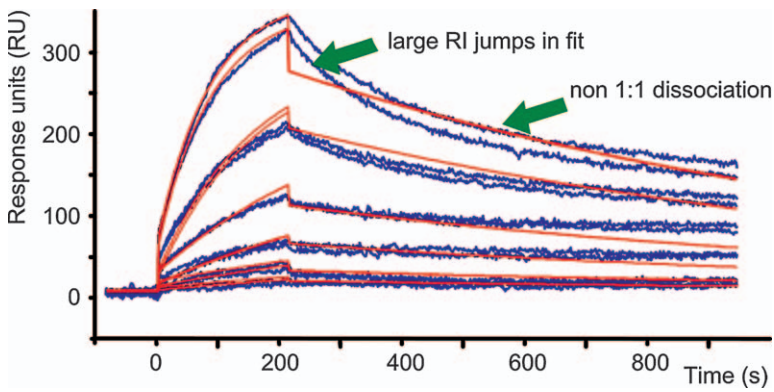


Figure 4.26 A 1 : 1 fit with large bulk RI jumps.

View Online

Published on 24 May 2017 on http://pubs.rsc.org | doi:10.1039/9781788010283-00106

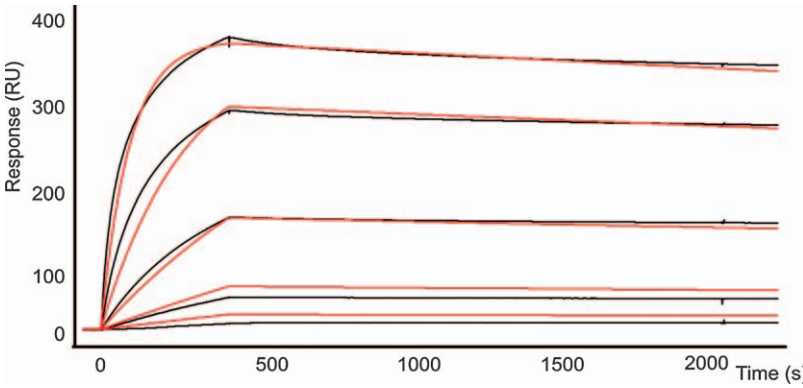


Figure 4.27 Inadequate fitting.

Nevertheless, the fitted curves (in red) do not follow the data, especially in the association phase. In addition, at low analyte concentrations the fitted curves have more response than the measured curves. To optimize this interaction, less ligand should be immobilized. This will most likely solve the non-1 : 1 interaction because, in general, a lower ligand density and analyte concentration will give an interaction that is closer to a 1 : 1 model. In addition, because of the slow dissociation, changing the injection strategy to single-cycle kinetics can save some experimental time.

4.9 Interaction Validation

To validate the interaction further, several more steps are necessary. Repeat the experiment with different batches of the same reagents to identify batch-to-batch variations. Keep in mind that global fitting gives only one value (and standard error) per parameter per data set. By running replicate experiments, more values per parameter are obtained. This is the correct way to obtain statistics, even if local fittings are used. Separate curves in a sensorgram with a concentration series should not be treated as replicates for statistical purposes; they are part of a single data set.[22]

If a kinetic protocol was used, try an equilibrium experiment. In addition, reverse the ligand and analyte and perform the experiments again. In all cases, the same values for the kinetic constants are expected.

4.10 Publications

When reporting results, always show the curves and the overlay of the fitting[1] at least in the supplementary data. A figure is worth 1000 words! Just reporting values is insufficient and leaves the reader in doubt as to whether the fitting followed the curves properly. Only the curves and the overlaid fitting will convince the reader of the quality of the experiment and the fitting.[2] In Figure 4.28, all the important parts of the sensorgram and legend

View Online

Published on 24 May 2017 on http://pubs.rsc.org | doi:10.1039/9781788010283-00106

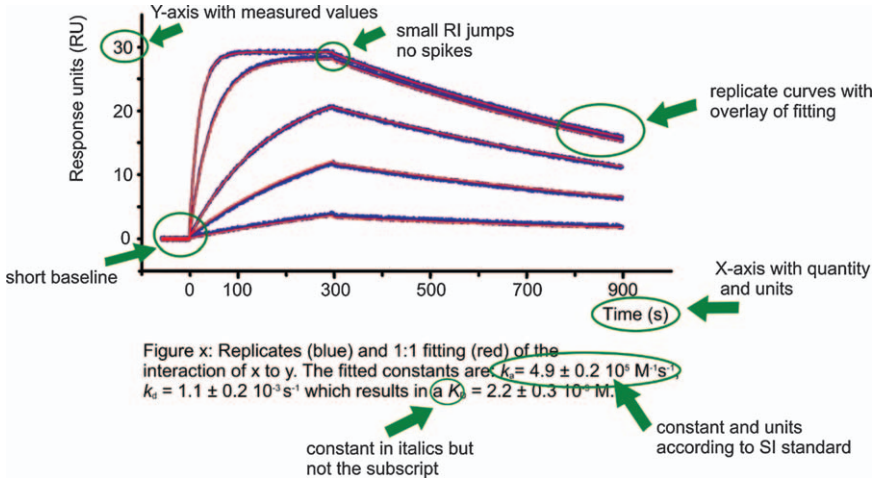


Figure 4.28 A high-quality SPR figure.

Table 4.4 Kinetic constants and units.

Constant	Symbol	Units
Association rate constant	k_a	L mol^{-1} s^{-1}
Dissociation rate constant	k_d	s^{-1}
Dissociation constant	K_D	M

are specified. In addition to the sensorgram, likely the kinetic values will be given in the text or in a table. Remember to use SI units (see Table 4.4).

Report the calculated values with care. Do not overestimate the precision of the analysis. In general, the equipment used has upper and lower limits to the values that can be accurately determined.[23] In addition, analyte concentration errors have a direct influence on k_a and therefore on K_D. Only the functional concentration should be used in the analysis and the calibration-free concentration analysis (CFCA) method described in Section 1.4.2 is ideal for obtaining the best kinetic values. Furthermore, make sure to round the values and associated errors to the first significant digit. Instead of reporting $k_a = 4.32 \pm 0.17 \times 10^5$ L mol^{-1} s^{-1}, report $k_a = 4.3 \pm 0.2 \times 10^5$ L mol^{-1} s^{-1}. For more information on reporting values, see for instance ref. 24.

4.10.1 Evaluating Published Results

When reading a publication with biomolecular interaction data, it has often one or two figures and a table with results. After reading this chapter carefully, you should not be fooled any more by a representative sensorgram and a table with values.[2] The best way to check if the reported values are true is to simulate the curves with the kinetic constants from the table. Start with copying the representative sensorgram to a drawing program. Then simulate the curves

View Online

Published on 24 May 2017 on http://pubs.rsc.org | doi:10.1039/9781788010283-00106

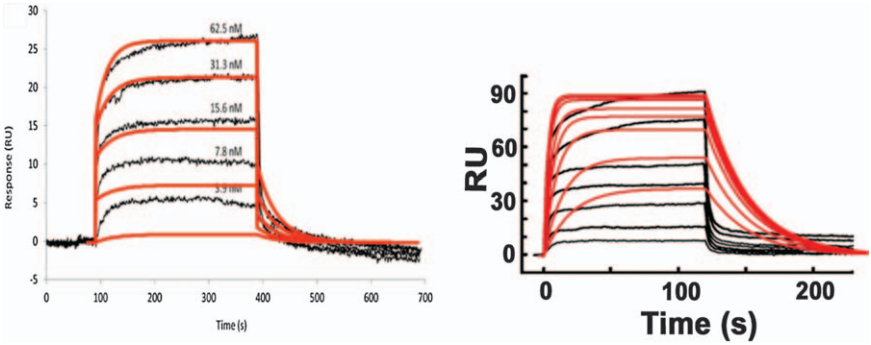


Figure 4.29 Simulated curves from published data.

with a kinetic evaluation program and copy the simulated curves to the drawing program. Try to overlay the curves (resize the curves if necessary). As an alternative, use the SPR-Simulation program from SPRpages (see below).

Figure 4.29 shows simulated curves over measured data from publications. Clearly, the simulations differ from the curves, which means that the reported values do not represent the actual kinetics. Therefore, always show a curve with fittings and present the values in a table. Most journals have the possibility of adding additional information in the online supplementary section, so there is no excuse for not showing both curves with fittings and a table with results.

4.10.2 Minimal Requirements for Describing a Biosensor Experiment

Equally important to the results is the way in which experiments are performed. It is well known that it can be very difficult to repeat a published experiment, mainly because the original author did not describe all the experimental conditions. This shortcoming was recognized by Rich and Myszka, who proposed the TBMRFAADOBE (The Bare Minimum Requirements For An Article Describing Optical Biosensor Experiments).[2] The suggested minimal requirements are as follows:

- instrument used in analysis;
- identity, source and molecular weight of the ligand and the analyte;
- sensor surface type;
- immobilization conditions (buffer, pH, concentrations, contact times);
- ligand density after immobilization;
- experimental buffer;
- experimental temperature;
- analyte concentrations;
- regeneration conditions;
- figure with overlay of replicate analyses;

View Online

- overlay of fitting in the figure;
- model used to fit the data;
- binding constants with standard errors.

As an example, here is a possible text for the Methods part of a publication.

The surface plasmon resonance experiments were performed using an [*instrument*] equipped with a [*sensor chip name*] sensor chip. The ligand (60 kDa, >90% pure based on SDS-PAGE) was immobilized using amine-coupling chemistry. The surfaces of two flow cells were activated for 7 min with a 1 : 1 mixture of 0.1 M NHS (*N*-hydroxysuccinimide) and 0.1 M EDC [3-(*N*,*N*-dimethylamino)propyl-*N*-ethylcarbodiimide] at a flow rate of 5 $\mu L\,min^{-1}$. The ligand at a concentration of 5 $\mu g\,mL^{-1}$ in 10 mM sodium acetate, pH 5.0, was immobilized at a density of 200 RU on flow cell 2; flow cell 1 was left blank to serve as a reference surface. Both surfaces were blocked with a 7 min injection of 1 M ethanolamine, pH 8.0.

To collect kinetic binding data, the analyte (34 kDa, >95% pure based on SDS-PAGE) in 10 mM HEPES, 150 mM NaCl, 0.005% P20, pH 7.4, was injected over the two flow cells at concentrations of 1.1, 3.3, 10, 30 and 90 nM at a flow rate of 60 $\mu L\,min^{-1}$ and a temperature of 20 °C. The complex was allowed to associate and dissociate for 90 and 300 s, respectively. The surfaces were regenerated with a 5 s injection of 10 mM H3PO4. Triplicate injections (in random order) of each sample and a buffer blank were flowed over the two surfaces. Data were collected at a rate of 1 Hz. The data were fitted to a simple 1 : 1 interaction model using the global data analysis option available within [*software name*] software.

As an additional service to the readers, a figure depicting the layout of the interaction can be incorporated (Figure 4.30).

4.11 SPR Simulation

The main problem when starting a new interaction experiment is what analyte concentration should be injected. Ideally, the analyte concentration is such that it saturates 10–90% of the ligand. These ligand saturation levels correspond to an analyte concentration of ~0.1–10 times K_D. When after initial analyte injections the kinetic constants are determined, they can serve as a basis for curve simulation. The simulation of interaction curves based

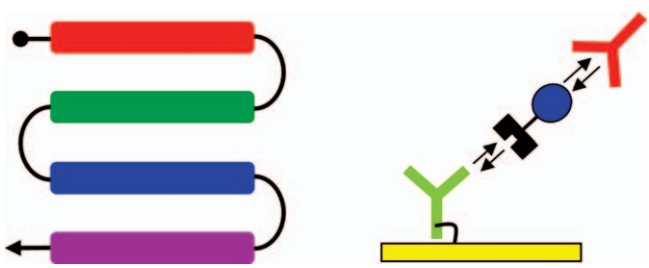


Figure 4.30 Images of the flow cell connection and type of interaction.

Published on 24 May 2017 on http://pubs.rsc.org | doi:10.1039/9781788010283-00106

View Online

Published on 24 May 2017 on http://pubs.rsc.org | doi:10.1039/9781788010283-00106

on the fitting results can give extra information to improve the experimental setup. Therefore, the SPR-Simulation program was developed to aid the simulation and to help researchers to design better experiments.

The SPR-Simulation program is a standalone Windows application to simulate kinetic interaction curves. The program draws the curves after the input of the kinetic rate constants, the analyte concentration and the association and dissociation times. The program can simulate multi- and single-cycle kinetics and also the decaying surface kinetics. Other features are the simulation of equilibrium sensorgrams and plotting an overlay over an imported sensorgram figure. The program can be found on the SPRpages website (www.sprpages.nl/downloads/software).

The following text highlights the effects of changing parameters in 1 : 1 Langmuir kinetics. In the simulations, the injection and dissociation periods are set at 300 s unless stated otherwise. R_{max} is set to 100 RU. The tables give the values of the parameters used in the simulations.

4.11.1 Different Analyte Concentration (Same Kinetics)

Table 4.5 gives the kinetic constants used for the simulation of Figure 4.31. From the figure, it is clear that the response at the end of the injection time correlates with the analyte concentration used. In addition, it is apparent that the higher analyte concentrations reach equilibrium within a shorter

Table 4.5 Different analyte concentration (same kinetics).

	Concentration (nM)	k_a (L mol^{-1} s^{-1})	k_d (s^{-1})	K_D (M)	K_D (×)
	1	10^5	10^{-3}	10^{-8}	0.1
	10	10^5	10^{-3}	10^{-8}	1.0
	100	10^5	10^{-3}	10^{-8}	10.0
	1000	10^5	10^{-3}	10^{-8}	100.0

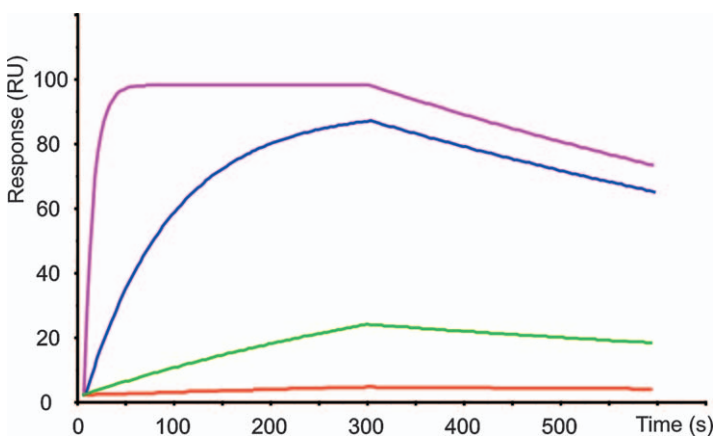


Figure 4.31 Different analyte concentrations (same kinetic parameters).

View Online

Table 4.6 Different association rate (different affinity).

	Concentration (nM)	k_a (L mol^{-1} s^{-1})	k_d (s^{-1})	K_D (M)	K_D (×)
	100	10^3	10^{-3}	10^{-6}	0.1
	100	10^4	10^{-3}	10^{-7}	1.0
	100	10^5	10^{-3}	10^{-8}	10.0
	100	10^6	10^{-3}	10^{-9}	100.0

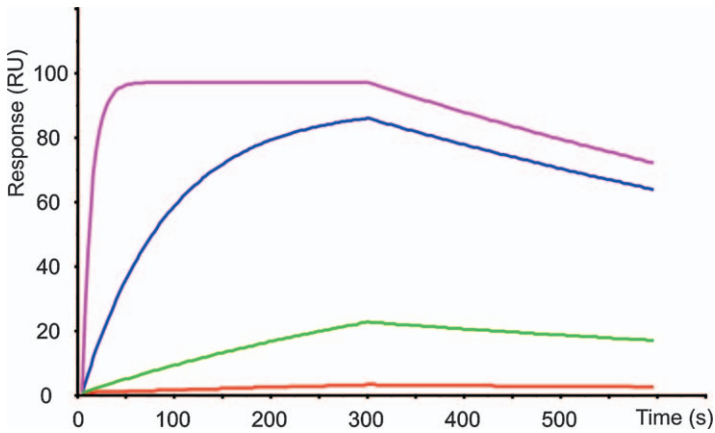


Figure 4.32 Different association rate (different affinity).

injection period. The lowest two concentrations have a slight curvature and therefore contain little kinetic information. Figure 4.31 highlights the fact that there is an optimum between the kinetic constants, analyte concentration and the association and dissociation times to obtain meaningful results.

4.11.2 Different Association Rate (Different Affinity)

Table 4.6 gives the kinetic constants used for the simulation of Figure 4.32. In the figure, the curves show an association rate binding dependency. However, as can be seen from the table, the analyte concentration differs greatly compared with the equilibrium dissociation constant. Compared with the previous figure, it can be seen that the different kinetic conditions lead to the same curve shapes. Therefore, because of the interdependency between the kinetic constants and the analyte concentration, comparisons of association curves between different interactions pairs are not possible without a thorough knowledge of the kinetic constants.

4.11.3 Different Dissociation Rate (Different Affinity)

Tables 4.7 and 4.8 give the kinetic constants used for the simulation of Figures 4.33 and 4.34. Both simulations differ in the analyte concentrations used. In both Figures 4.33 and 4.34 it can be seen that the dissociation rate constant has a strong influence on the shape of the curve. In addition, it is

Published on 24 May 2017 on http://pubs.rsc.org | doi:10.1039/9781788010283-00106

View Online

Table 4.7 Different dissociation rate (different affinity) with constant analyte concentration.

	Concentration (nM)	k_a (L mol^{-1} s^{-1})	k_d (s^{-1})	K_D (M)	K_D (×)
	100	10^4	10^{-2}	10^{-6}	0.1
	100	10^4	10^{-3}	10^{-7}	1.0
	100	10^4	10^{-4}	10^{-8}	10.0
	100	10^4	10^{-5}	10^{-9}	100.0

Table 4.8 Different dissociation rate (different affinity) with analyte concentration of $1\times K_D$.

	Concentration (nM)	k_a (L mol^{-1} s^{-1})	k_d (s^{-1})	K_D (M)	K_D (×)
	1000	10^4	10^{-2}	10^{-6}	1.0
	100	10^4	10^{-3}	10^{-7}	1.0
	10	10^4	10^{-4}	10^{-8}	1.0
	1	10^4	10^{-5}	10^{-9}	1.0

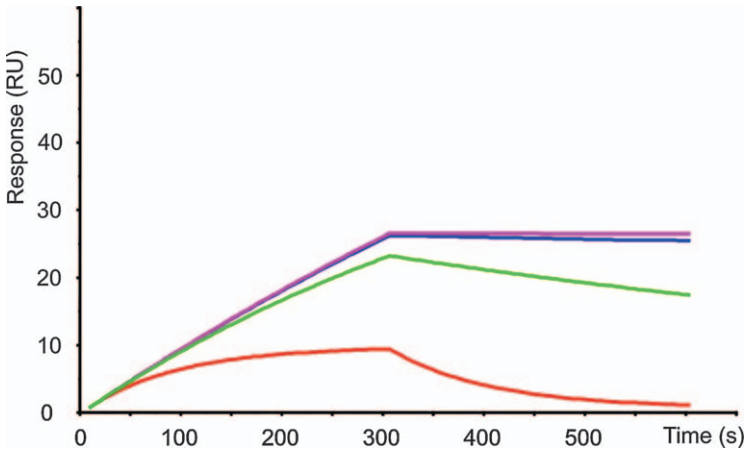


Figure 4.33 Different dissociation rate (100 nM analyte).

clear that k_d also has a strong influence on the binding rate and therefore on the response level at the end of the analyte injection. Furthermore, with a fast dissociation rate, equilibrium is reached earlier than with a slow dissociation rate.

In the simulation with the analyte concentration equal to the equilibrium dissociation constant, R_{eq} for each curve will eventually be half of R_{max}. However, reaching equilibrium with a dissociation rate constant lower than 10^{-3} s^{-1} can take a long time. Likewise, interactions with a low dissociation rate constant will take a long time to reach baseline during dissociation. To calculate the complex half time ($t_{1/2}$), eqn (4.10) can be used.

$$t_{\frac{1}{2}} = \frac{\ln 2}{k_d} \cong \frac{0.69}{k_d}\,(\mathrm{s}) \tag{4.10}$$

Published on 24 May 2017 on http://pubs.rsc.org | doi:10.1039/9781788010283-00106

View Online

Published on 24 May 2017 on http://pubs.rsc.org | doi:10.1039/9781788010283-00106

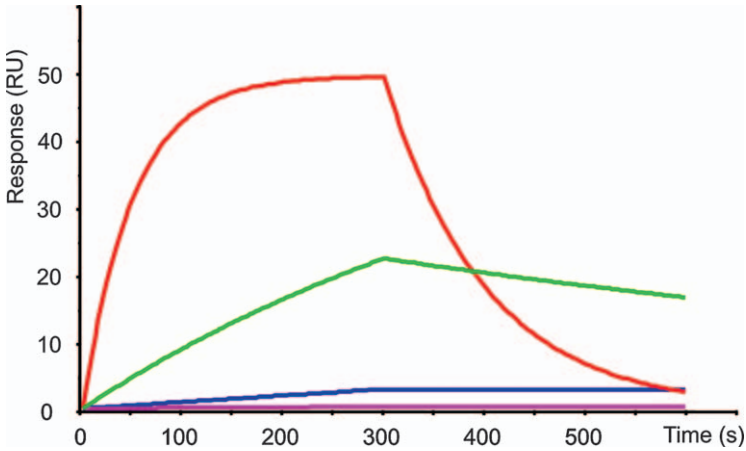


Figure 4.34 Different dissociation rate (analyte $-1 \times K_D$).

Table 4.9 Different kinetics (same affinity).

	Concentration (nM)	k_a (L mol^{-1} s^{-1})	k_d (s^{-1})	K_D (M)	K_D (×)
	100	10^3	10^{-5}	10^{-8}	10
	100	10^4	10^{-4}	10^{-8}	10
	100	10^5	10^{-2}	10^{-8}	10
	100	10^6	10^{-2}	10^{-8}	10

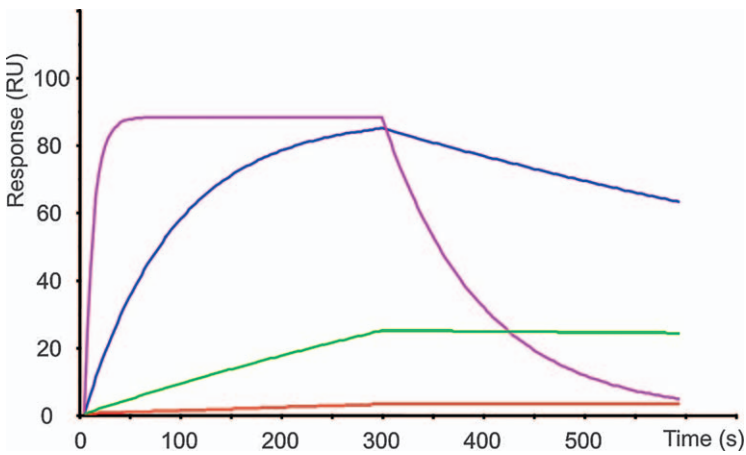


Figure 4.35 Different kinetics (same affinity).

4.11.4 Different Kinetics (Same Affinity)

Table 4.9 gives the kinetic constants used for the simulation of Figure 4.35. In the figure, all four curves have the same equilibrium dissociation constant of 10^{-8} M but the rate constants vary by three orders of magnitude.

View Online

Table 4.10 Different injection times (same kinetics).

	Concentration (nM)	k_a (L mol^{-1} s^{-1})	k_d (s^{-1})	K_D (M)	K_D (×)	Time (s)
	10	10^6	10^{-3}	10^{-9}	10	60
	10	10^6	10^{-3}	10^{-9}	10	120
	10	10^6	10^{-3}	10^{-9}	10	300
	10	10^6	10^{-3}	10^{-9}	10	600

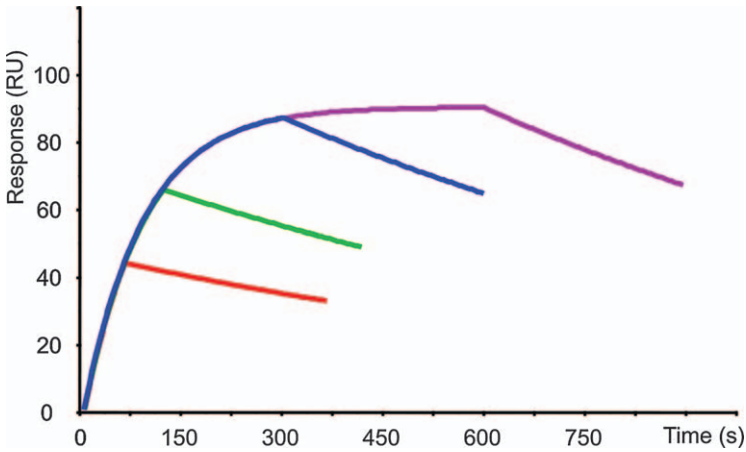


Figure 4.36 Different injection times (same kinetics).

Reactions with a fast k_a and k_d reach equilibrium in a short period of time and display a rapid dissociation. For association rate constants of 10^4 L mol^{-1} s^{-1} and lower, longer injection times are needed achieve sufficient curvature in the curves and to reach equilibrium.

4.11.5 Different Injection Times (Same Kinetics)

Table 4.10 gives the kinetic constants used for the simulation of Figure 4.36. The variation in injection times shows that to reach 90% equilibrium takes at least 600 s in this example. The shape of the binding curves does not change. Although it is not necessary to reach equilibrium during analyte injection, the association curve should have at least some curvature in order to have some kinetic information. The curvature is needed to calculate the R_{max} value. If there is full linearity then the calculated R_{max} value becomes unrealistically high.

4.11.6 Different Dissociation Times (Same Kinetics)

Table 4.11 gives the kinetic constants used for the simulation of Figure 4.37. The curves do not differ when using longer dissociation times. For dissociation rate constants lower than 10^{-3} s^{-1}, longer dissociation times are

Published on 24 May 2017 on http://pubs.rsc.org | doi:10.1039/9781788010283-00106

View Online

Table 4.11 Different dissociation times (same kinetics).

	Concentration (nM)	k_a (L mol^{-1} s^{-1})	k_d (s^{-1})	K_D (M)	K_D (×)	Time (s)
	100	10^6	10^{-2}	10^{-8}	10	60
	100	10^6	10^{-2}	10^{-8}	10	120
	100	10^6	10^{-2}	10^{-8}	10	300
	100	10^6	10^{-2}	10^{-8}	10	600

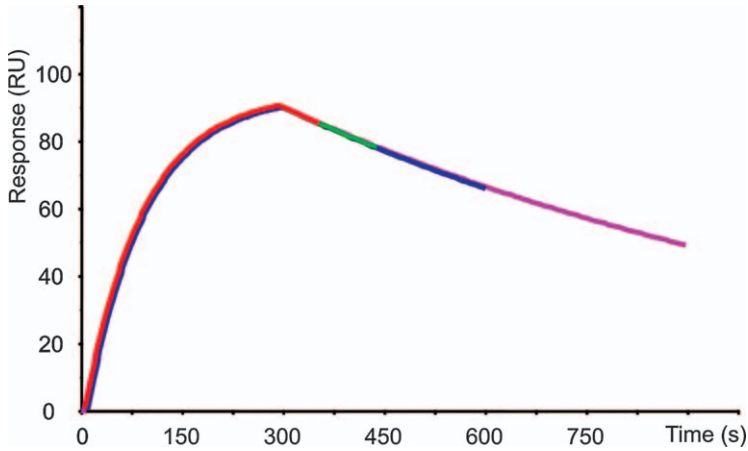


Figure 4.37 Different dissociation times (same kinetics).

needed to obtain sufficient dissociation of the analyte (in response units) to obtain a reliable fitting. As a rule of thumb, at least 5% of the initial response should be dissociated.[4]

4.12 Questions

Test your knowledge with a quiz about typical features of the sensorgram curves. Here there are nine questions, but if you want to do the full quiz, go to www.sprpages.nl and click on Sensorgrams – Quiz. You can find the answers to this quiz at www.sprpages.nl/quiz-answers and in the Appendix.

1. Looking at the sensorgrams in Figure 4.38, which sensorgram does not contain exponential interaction curves?
2. Which of the sensorgrams in Figure 4.39 can be used for equilibrium analysis?
3. Figure 4.40 shows four curves with different kinetic rate constants but with the same affinity. Which curve has the fastest association rate constant?
   A. Curve A.
   B. Curve B.
   C. The analyte concentration should be known.
   D. R_{max} should be known.

Published on 24 May 2017 on http://pubs.rsc.org | doi:10.1039/9781788010283-00106

View Online

Published on 24 May 2017 on http://pubs.rsc.org | doi:10.1039/9781788010283-00106

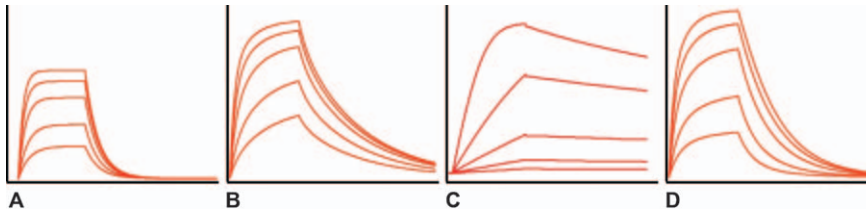


Figure 4.38 Biomolecular interaction curves.

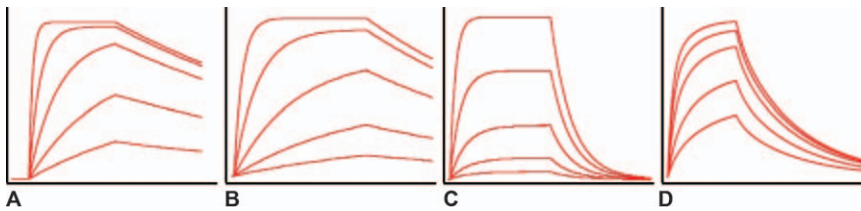


Figure 4.39 Biomolecular interaction curves.

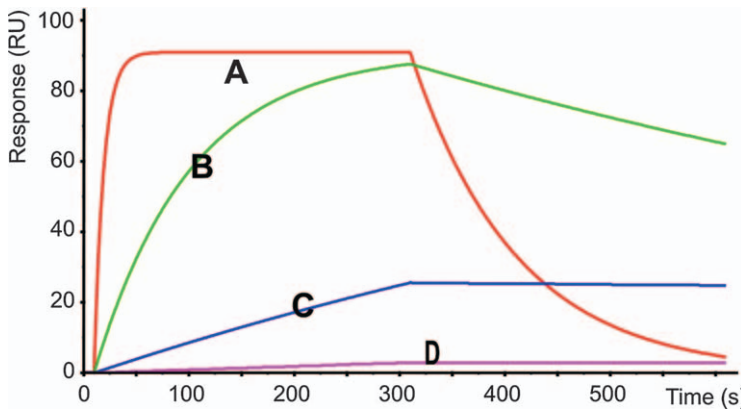


Figure 4.40 Different kinetics (same affinity).

4. Given the affinity plot in Figure 4.41, which curve has the highest equilibrium dissociation constant?
   A. Point A.
   B. They are all the same.
   C. The analyte concentration should be known.
   D. Point D.
5. Which of the fitting results in Figure 4.42 should be reported?

View Online

Published on 24 May 2017 on http://pubs.rsc.org | doi:10.1039/9781788010283-00106

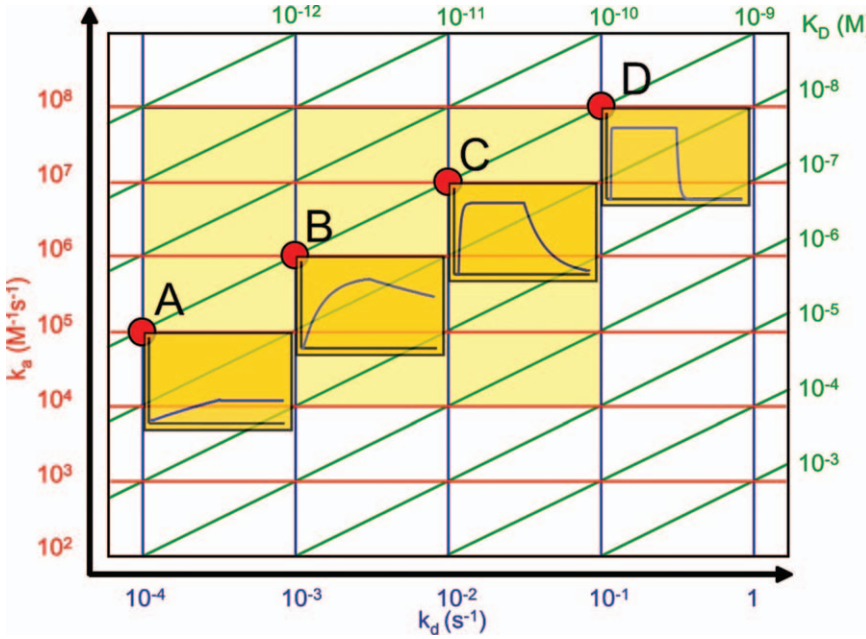


Figure 4.41 Affinity plot.

k_a	k_d	K_D
($M^{-1}s^{-1}$)	(s^{-1})	(M)
1.1±0.1 E5	4.7±0.2 E-3	4.27 E-8

A

k_a	k_d	K_D
(1/Ms)	(1/s)	(M)
1.1± 0.1 10^5	4.7±0.2 10^{-3}	4.3±0.5 10^{-8}

B

k_a	k_d	K_D
($M^{-1}s^{-1}$)	(s^{-1})	(M)
1.1±0.1 10^5	4.7±0.2 10^{-3}	4.27±0.46 10^{-8}

C

k_a	k_d	K_D
($M^{-1}s^{-1}$)	(s^{-1})	(M)
1.1±0.1 10^5	4.7±0.2 10^{-3}	4.3±0.5 10^{-8}

D

Figure 4.42 Fitting results.

6. With the four options below, what is the best combination to optimize the interaction in Figure 4.43?
   Option 1: lower ligand concentration.
   Option 2: match buffers better.
   Option 3: equilibrate better.
   Option 4: use higher flow rate.

View Online

Published on 24 May 2017 on http://pubs.rsc.org | doi:10.1039/9781788010283-00106

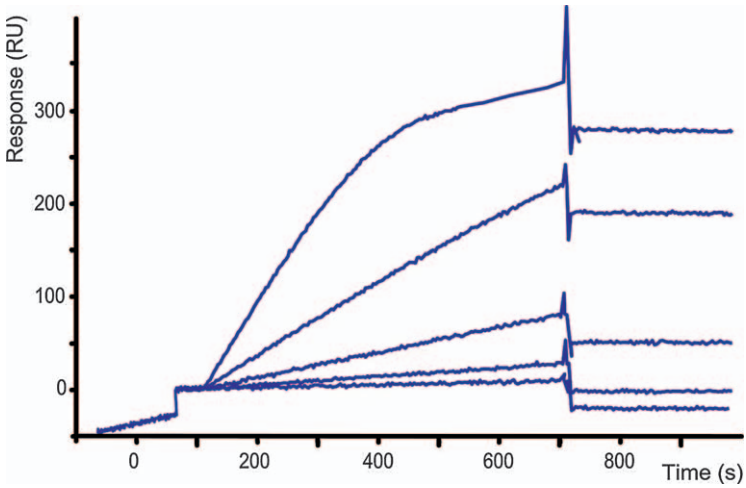


Figure 4.43 Interaction between Abc and Klm.

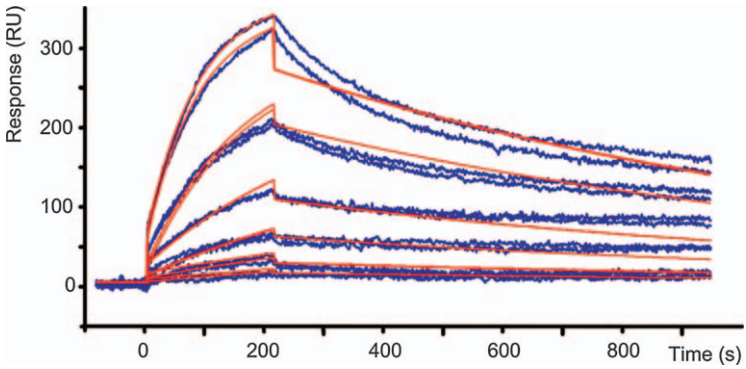


Figure 4.44 1 : 1 fit of the interaction between Gh and Sh.

Multiple choice:

A. Options 1 and 4.
B. Options 1, 2 and 3.
C. Options 1, 2 and 4.
D. Options 2, 3 and 4.

7. When the result of the fitting is as in Figure 4.44, what is the best combination of options to improve it?
   Option 1: lower ligand concentration.
   Option 2: match buffers better.
   Option 3: check the ligand for purity.
   Option 4: use higher flow rate.

View Online

Published on 24 May 2017 on http://pubs.rsc.org | doi:10.1039/9781788010283-00106

Multiple choice:

A. Options 1 and 3.
B. Options 1 and 4.
C. Options 2 and 3.
D. Options 2 and 4.

8. Are the values given in the inset in Figure 4.45 plausible with the sensorgram?
   A. Yes.
   B. No, dissociation looks faster.
   C. No, dissociation looks slower.
   D. No, R_{max} is to high.
9. What can be said about the sensorgram in Figure 4.46?
   A. The analyte concentration range is not wide enough.
   B. The response does not follow exponential kinetics.
   C. There is mass transport limitation.
   D. This looks an excellent sensorgram.

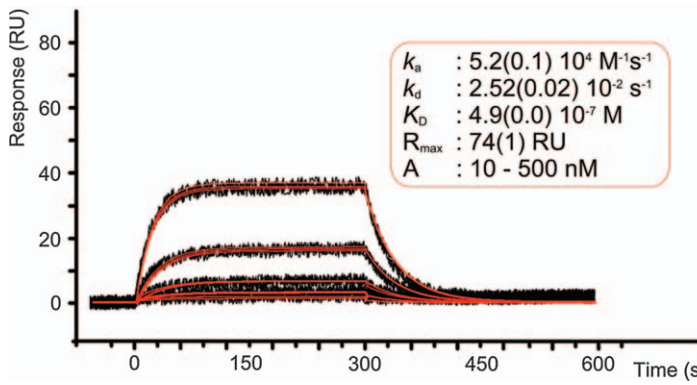


Figure 4.45 1 : 1 fitting of the interaction of A with B.

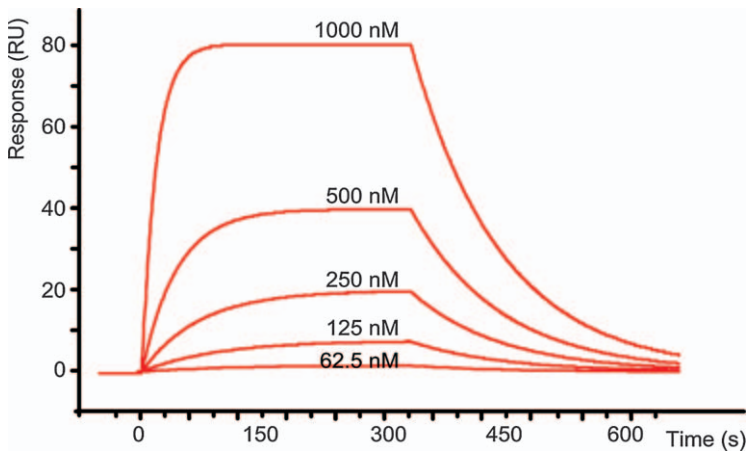


Figure 4.46 Interaction between A and L.

View Online

4.13 Glossary

Activity	The activity of the ligand and analyte depends on the intention of the researcher. More general: the integrity of a protein so that it is fully functional
Affinity	The overall strength of a binding between two molecules
Analyte	In SPR, the molecule that is in the liquid phase
Association rate	The rate at which two molecules bind together
Baseline	Response signal when only buffer is flowing over the sensor chip
BIA	Biomolecular interaction analysis
Binding	The process by which two or more molecules interact to form a complex
Biomolecule	In this context, all molecules that belong to biological processes, such as proteins, nucleic acids and lipids but also small compounds
CFCA	Calibration-free concentration analysis
Cycle	The recording of one sequence of injections
Dissociation rate	The rate at which two molecules separate
Double referencing	The two-step correction of the response between reference channel and active channel using blank injections
Equilibrium	In SPR, the situation where the number of association events equals the number of dissociation, events effectively giving no signal change. Strictly this situation is steady state
Equilibrium dissociation constant	Kinetic constant defining the analyte concentration that will occupy half of the available ligand interaction sites
Flow cell	The part of a flow system where detection occurs
Global analysis	Simultaneous analysis of several interaction curves in one fitting to obtain one value for each of the interaction constants
Immobilization	Binding biomolecules to the sensor surface by means of forming a chemical bond or affinity capturing
Kinetics	The procedure of binding (association rate) and breaking apart (dissociation rate) two or more molecules
Kinetic titration	The injection of analyte in sequentially higher concentrations to generate an interaction curve in one cycle

Published on 24 May 2017 on http://pubs.rsc.org | doi:10.1039/9781788010283-00106

View Online

Ligand	In SPR, the molecule attached to the static phase
Matrix	In SPR, the surface modification of the sensor chip that is used to couple the ligand
Multi-cycle kinetics	The injection of one analyte concentration per interaction cycle. At the end all cycles are combined into one sensorgram
Real-time measurement	Meaning that every event is recorded without a time delay
Regeneration	Removing the analyte from the ligand with a special solution, leaving the ligand intact
Running buffer	The solution transporting the analyte to a sensor chip
Sensor chip	The surface to which the ligand is immobilized and where the interaction study takes place
Sensorgram	The graphical output of the interaction
Single-cycle kinetics	The injection of analyte in sequentially higher concentrations to generate an interaction curve in one cycle
SPR	Surface plasmon resonance
Steady state	In SPR, the situation where the number of association events equals the number of dissociation events, effectively giving no signal change

Published on 24 May 2017 on http://pubs.rsc.org | doi:10.1039/9781788010283-00106

References

1. R. L. Rich and D. G. Myszka, *J. Mol. Recognit.*, 2008, **21**, 355–400.
2. R. L. Rich and D. G. Myszka, *J. Mol. Recognit.*, 2010, **23**, 1–64.
3. R. L. Rich and D. G. Myszka, *J. Mol. Recognit.*, 2003, **16**, 351–382.
4. P. S. Katsamba *et al.*, *Anal. Biochem.*, 2006, **352**, 208–221.
5. E. Stenberg, B. Persson, H. Roos and C. Urbaniczky, *J. Colloid Interface Sci.*, 1991, **143**, 513–526.
6. L. Nieba *et al.*, *Anal. Biochem.*, 1997, **252**, 217–228.
7. K. M. Müller, K. M. Arndt, K. Bauer and A. Plückthun, *Anal. Biochem.*, 1998, **259**, 54–61.
8. S. Lata and J. Piehler, *Anal. Chem.*, 2005, **77**, 1096–1105.
9. J. J. Lichty *et al.*, *Protein Expression Purif.*, 2005, **41**(1), 98–105.
10. D. G. Myszka, M. D. Jonsen and B. J. Graves, *Anal. Biochem.*, 1998, **265**, 326–330.
11. K. Andersson *et al.*, *J. Mol. Recognit.*, 2001, **14**, 62–71.
12. R. W. Glaser, *Anal. Biochem.*, 1993, **213**, 152–161.
13. R. L. Rich and D. G. Myszka, *J. Mol. Recognit.*, 2002, **15**, 352–376.
14. D. G. Myszka, *J. Mol. Recognit.*, 1999, **12**, 279–284.

View Online

15. R. Karlsson, P. S. Katsamba, H. Nordin, E. Pol and D. G. Myszka, *Anal. Biochem.*, 2006, **349**, 136–147.
16. W. Palau and C. Di Primo, *Talanta*, 2013, **114**, 211–216.
17. W. Palau and C. Di Primo, *Biochimie*, 2012, **94**, 1891–1899.
18. P. Magotti *et al.*, *J. Mol. Recognit.*, 2009, **22**, 495–505.
19. J. Souphron *et al.*, *Biochemistry*, 2008, **47**, 8961–8969.
20. L. Joss, T. A. Morton, M. L. Doyle and D. G. Myszka, *Anal. Biochem.*, 1998, **261**, 203–210.
21. C. Di Primo, *J. Mol. Recognit.*, 2008, **21**, 37–45.
22. A. B. Biacore, in *Information about BiaEvaluation* 3.0, 2000.
23. K. Y. Yau *et al.*, *J. Immunol. Methods*, 2003, **281**, 161–175.
24. Wikipedia, International System of Units (https://en.wikipedia.org/wiki/International_System_of_Units), 2011.
25. A. B. Biacore, *BIACORE Technology Handbook*, 1994.

Published on 24 May 2017 on http://pubs.rsc.org | doi:10.1039/9781788010283-00106

Published on 24 May 2017 on http://pubs.rsc.org | doi:10.1039/9781788010283-00149

CHAPTER 5

Detailed Analysis of Kinetic Binding Traces with Distributions of Surface Sites†

HUAYING ZHAO AND PETER SCHUCK*

Dynamics of Macromolecular Assembly Section, Laboratory of Cellular Imaging and Macromolecular Biophysics, National Institute of Biomedical Imaging and Bioengineering, National Institutes of Health, Bethesda, Maryland 20892, USA
*Email: schuckp@mail.nih.gov

5.1 Introduction

Chapter 4 provided an introduction to the nomenclature and phenomenology of kinetic data analysis. A major result is that ideal simple bimolecular reactions with 1:1 binding stoichiometry will exhibit single-exponential sensorgrams.[1] However, as was noted shortly after the introduction of surface plasmon resonance (SPR) biosensors, common characteristics of surface binding experiments in practice are deviations from this behavior,[1–3] which will show in misfits and residuals when fitting a 1:1 model – even when studying ligand–analyte pairs that are pure and conform to the 1:1 binding scheme when interacting in solution. Most commonly, the origin of the discrepancy is the presence of surface sites with non-uniform binding properties, sometimes exacerbated by insufficient mass transport.[4] Factors contributing to heterogeneity are inherent

†The U.S. Government is authorized to reproduce and distribute reprints for Government purposes notwithstanding any copyright notation hereon.

Handbook of Surface Plasmon Resonance, 2nd Edition
Edited by Richard B. M. Schasfoort
© The Royal Society of Chemistry 2017
Published by the Royal Society of Chemistry, www.rsc.org

View Online

Published on 24 May 2017 on http://pubs.rsc.org | doi:10.1039/9781788010283-00149

in surface binding techniques, and include variations in the physical microenvironment of the surface and effects of chemical crosslinking. Therefore, heterogeneity of surface sites is possible and likely even when working with homogeneous macromolecular samples. Multiple sites may exist naturally on the macromolecules under study, but polydispersity of the surface sites is to be expected, also due to unavoidable imperfections and heterogeneity in the surface properties on the microscopic scale. For this reason, a distribution model that can describe this ubiquitous heterogeneity should be the first choice when imperfect fits with ideal single-site models and/or multiphasic binding curves are encountered. Making the same assumption of simple bimolecular reactions as in Chapter 4, this chapter presents a more detailed analysis that accounts for such non-uniformity of the surface sites and, to some extent, mass transport limitation.

It is a tribute to the sensitivity of SPR instruments and the associated information content of SPR sensorgrams to reveal these ''non-ideal'' features. Although they are mostly unwelcome aspects of the process, the approach of using a model for data interpretation that allows accommodation of polydisperse binding properties – without artificial restrictions to a small number of classes of sites – can efficiently address this problem. It permits excellent fits of the experimental data, and leads to conclusive interpretation provided that the data are sufficiently informative. Following the principle of Occam's razor, a safeguard against over-interpretation is provided by the mathematical technique of regularization, which produces the broadest distribution that is consistent with the experimental data.[5] The data can also be probed with Bayesian models that produce distributions most consistent with certain prior knowledge or prior expectation.[6] Although at first glance this may appear to be an almost esoteric statistical detail of data modeling, this aspect of the analysis relates back directly to important questions of experimental design, by highlighting the actual information content of the data for specifying kinetic rate and affinity constants. Similarly, the distribution analysis is an effective tool to study the effect of surface immobilization chemistry, immobilization density, and time-dependent decay of the surface.[7] This provides a practical opportunity to optimize the experimental design, and reveals which assumptions can and cannot be made for any given system of ligand, analyte, and surface.

The analysis strategy of surface site distributions described in this chapter was first introduced more than a decade ago[8] and was subsequently refined and extended,[6,7,9] and has found many applications in diverse fields of biomolecular interactions.[4,10–26] It is implemented in the software EVILFIT (named after the aphorism ''God made the solid state, he left the surface to the devil'' by Enrico Fermi or Wolfgang Pauli[27]), which can be freely downloaded from https://sedfitsedphat.nibib.nih.gov/software/Shared%20Documents/evilfit_standalone_V3.zip. An instructional video on how to use EVILFIT in practice is available on YouTube (https://www.youtube.com/watch?v=QXkXTN0gwck) and can also be downloaded along with

View Online

installation instructions and demo data from https://sedfitsedphat.nibib.nih.gov/tools/EVILFIT%20demo/Forms/AllItems.aspx. Commonly this model arrives at a superior quality of fit to the experimental data and reveals subpopulations of molecules with different binding properties.

Published on 24 May 2017 on http://pubs.rsc.org | doi:10.1039/9781788010283-00149

5.2 The Physical Picture

Throughout, we will assume that the analyte and ligand are monodisperse and will undergo bimolecular reaction with 1 : 1 stoichiometry when free in solution. An essential feature of SPR experiments is the need to attach the ligand to the surface, or a polymeric matrix, so as to allow detection of analyte binding within the evanescent field of the surface electromagnetic field. Thus, the surface is a third component that will provide non-uniform microenvironments with different chemical and physical properties potentially impacting the measured binding. Local heterogeneity on a molecular scale is also intrinsic to extended polymeric matrices, which have density gradients perpendicular to the surface, and may introduce additional gradients of electrostatic and steric forces. The role of different surface modifications in view of the nanoscale structure and physical forces on ligand and analyte has been discussed in detail by Gedig[28] and is also considered in Chapter 6.

Beyond the surface itself, the attachment of the ligand to the surface is an additional potential source of non-uniformity, as it may occur in different orientations relative to the surface. Furthermore, in many cases it relies on chemically heterogeneous crosslinking, which will render the ligands chemically distinct species. The use of capturing techniques will enforce a uniform orientation of the analyte relative to the capturing molecule, but the latter itself is typically subject to the same original polydispersity of microenvironments and orientations (and may have the unintended effect of introducing additional non-specific sites of interaction with the analyte). With regard to the impact of immobilization on the ligand, it is a common observation that a fraction of the immobilized ligand is apparently completely inactive. This naturally raises the question of whether this is not just an on/off choice. It is easily conceivable that some fraction of the immobilized molecules may be in only partially active conformations with more or less reduced binding energies.

Obviously, on a molecular scale the binding sites likely do not adhere to a simple cartoon representation of their conformation and microenvironment, but nevertheless, Figure 5.1 is an attempt to depict various factors that would be expected to contribute to the binding energy of analytic binding sites on the ligand and possible ''non-specific'' sites. Therefore, rather than expecting uniformity in binding properties, it appears to be more realistic to consider the surface-immobilized molecules in various states that leaves them with a range of binding energies and a range complex lifetimes, even if the starting state is perfectly homogeneous in solution.

View Online

Published on 24 May 2017 on http://pubs.rsc.org | doi:10.1039/9781788010283-00149

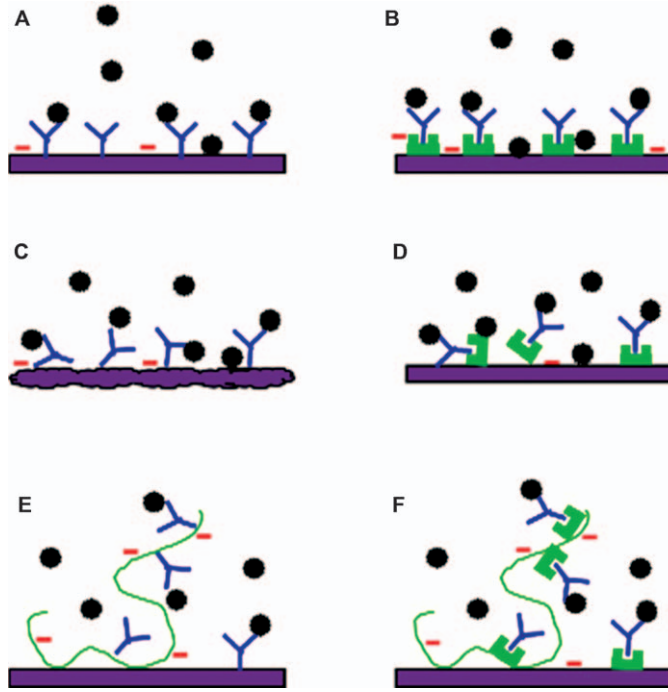


Figure 5.1 Cartoon illustrating different sources of heterogeneity of surface binding sites. Filled circles depict the analyte molecules, and Y depicts the macromolecular binding partner to be immobilized and serve as surface binding site. (A) Surface site heterogeneity may occur fundamentally from non-specific binding to the surface. (B) The same is true in the presence of a capturing protein (*e.g.* an antibody or streptavidin) for the macromolecule of interest. In addition, the capturing molecules may contribute to the available ''non-specific'' surface sites. (C) The surface is heterogeneous on a molecular scale with respect to both surface rugosity and also surface charges and local pH. Surface sites may not be attached uniformly. (D) The same is true for a capturing protein, which itself may not be oriented uniformly and expose the analyte to different microenvironments. (E) If a polymeric immobilization matrix is used, immobilization to different regions can give rise to different extents of steric hindrance and a heterogeneous microenvironment from spatial and chemical non-uniformity of the matrix. (F) The same effects occur when using a capturing protein, possibly exacerbated due to the overall higher degree of functionalization of the immobilization matrix (higher total protein concentration at the surface).[4]
Reproduced from P. Schuck and H. Zhao, *Surface Plasmon Resonance: Methods and Protocols*, The role of mass transport limitation and surface heterogeneity in the biophysical characterization of macromolecular binding processes by SPR biosensing, **627**, 2010, 15–54, Copyright © 2010, Springer Science + Business Media, LLC. With permission from Springer.

View Online

Published on 24 May 2017 on http://pubs.rsc.org | doi:10.1039/9781788010283-00149

5.3 Calculating Surface Site Distributions

5.3.1 Basic Principle

As a consequence, the data analysis aims at determining the functional distribution of binding sites $P(K_D, k_d)$ with given equilibrium dissociation constant K_D and dissociation rate constant k_d. It is a differential distribution such that the integral $P(K_D, k_d)\mathrm{d}K_D\mathrm{d}k_d$ is the surface density of sites with the particular properties K_D and k_d in signal units of RU. If we write as $s_a(K_D, k_d, c, t)$ the theoretical binding signal for 1 RU of this site exposed to analyte at concentration c for the duration of the contact time t_c:

$$s_a(K_D, k_d, c, t) = \frac{1}{1 + K_D c^{-1}} \times \{1 - \exp[-(k_a c + k_d)t]\} \tag{5.1}$$

[equivalent to eqn (4.4) in Chapter 4], and $s_d(K_D, k_d, c, t)$ as the following dissociation phase, starting from the binding level at the end of the association phase:

$$s_d(k_d, c, t) = s_a(K_D, k_d, c, t_c) \times \exp[-k_d(t - t_c)] \tag{5.2}$$

[compare eqn (4.5)], then the complete response $s_1(K_D, k_d, c, t)$ for a surface density that has a total binding capacity of 1 RU of this site (indicated by the subscript 1) during the entire experiment can be combined into

$$s_1(K_D, k_d, c, t) = \begin{cases} s_a(K_D, k_d, c, t) & \text{for } t \le t_c \\ s_d(K_D, k_d, c, t) & \text{for } t > t_c \end{cases} \tag{5.3}$$

With eqn (5.3), we can add up the signal from all sites as the integral

$$s_{tot}(c, t) = \int_{K_{D,min}}^{K_{D,max}} \int_{k_{d,min}}^{k_{d,max}} s_1(K_D, k_d, c, t) P(K_D, k_d) \mathrm{d}K_D \mathrm{d}k_d \tag{5.4}$$

as the theoretical signal from a particular distribution $P(K_D, k_d)$.[8] To calculate the unknown distribution P, eqn (5.4) needs to be discretized over a range of values (best on a logarithmic scale, using at least 3–4 points per decade; see circles in Figure 5.2), and compared with the experimental sensorgram data $s_{exp}(c, t)$ acquired at multiple concentrations:

$$\underset{P_i}{\mathrm{Min}} \sum_{c,t} \left[s_{exp}(c, t) - \sum_i s_1(K_{D,i}, k_{d,i}, c, t) P_i(K_{D,i}, k_{d,i}) \right]^2 \tag{5.5}$$

where i simply enumerates the grid points of a two-dimensional mesh of all (K_D,k_d) combinations. Since the theoretical unit signals s_1 can be easily calculated, the only unknowns in eqn (5.5) are the P_i values, which leads to a linear equation system for the distribution at the grid points. This calculation amounts to a global fit of all experimental binding curves

View Online

Published on 24 May 2017 on http://pubs.rsc.org | doi:10.1039/9781788010283-00149

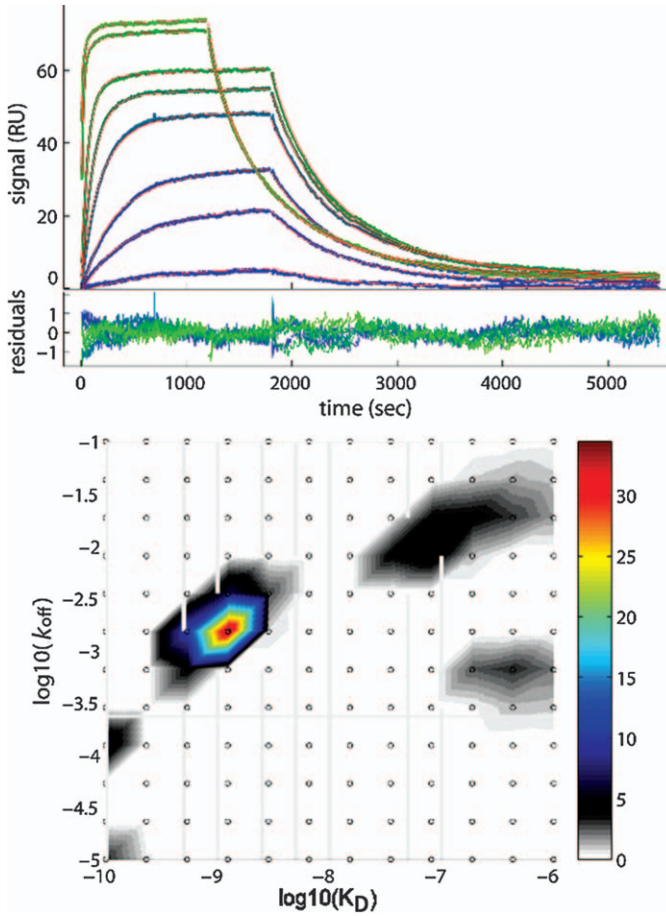


Figure 5.2 The experimental data and fits for binding of soluble β_2-microglobulin (B2MG) to a monoclonal IgG antibody directly immobilized (3200 RU) on a CM3 sensor surface. (Top panel) Binding traces (blue to green lines) and best-fit (red lines, superimposed by the blue/green lines) from surface site distribution model. (bottom panel) The distributions are presented as a contour plot with the color temperature interpolated from the population at the (K_D,k_{off}) grid points (shown as small black circles). The density of the distribution values can be read from the color bar on the right of the panel. The grid spacing is chosen logarithmically in both K_D and k_{off} directions, such that lines of constant k_{on} are diagonal. The experimental analyte concentrations are plotted as vertical grey lines in the contour plot. The horizontal grey line represents the inverse of the longest time constant for which the experimental data would permit observing a (1/e)-fold decay. Excellent fit is achieved with an r.m.s.d. of 0.36 RU. The binding traces and best fits are shown on the top panel, and the distribution of the fit is shown on the bottom. The concentrations of B2MG of all the traces are between 0.1 and 100 nM.[7]
Reproduced from H. Zhao, I. I. Gorshkova, G. L. Fu and P. Schuck, A comparison of binding surfaces for SPR biosensing using an antibody–antigen system and affinity distribution analysis, *Methods*, **59**(3), 328–335. Copyright 2013 with permission from Elsevier.

View Online

Published on 24 May 2017 on http://pubs.rsc.org | doi:10.1039/9781788010283-00149

simultaneously and it should be carried out avoiding any truncation of experimental data except for possible regions of artifacts from buffer changes or injections.

Inverse problems such as the integral eqn (5.4) are well known to be ill-posed, *i.e.* there may be many different distributions P_i that provide a statistically indistinguishable quality of fit within the noise of data acquisition.[5] This problem arises similarly in many different physical science disciplines and several biophysical methods,[29–32] and can be addressed in a powerful way using the principle of Occam's razor: Rather than the strictly best-fit distribution, we instead calculate the *simplest* distribution that is statistically equivalent to the best fit to the experimental data. The *simplest* distribution can be unequivocally defined. Technically, a straightforward strategy to accomplish this is the extension of eqn (5.5) with a regularization constraint, such as Tikhonov regularization:[33]

$$\underset{P_i}{\mathrm{Min}}\left\{\sum_{c,t}\left[s_{\mathrm{exp}}(c,t)-\sum_{i}s_1(K_{\mathrm{D},i},k_{\mathrm{d},i},c,t)P_i(K_{\mathrm{D},i},k_{\mathrm{d},i})\right]^2+\alpha\sum_{i,j}P_iH_{i,j}P_j\right\} \quad (5.6)$$

where $H_{i,j}$ is a second-derivative matrix. This drives the result toward smooth distributions if not constrained by the experimental data. α is a scaling factor for the constraint that is adjusted by *F*-statistics such that the quality of fit to the experimental data obtained is statistically equivalent to the best possible fit without regularization.[8] Using slightly modified regularization matrices, in a Bayesian approach it is possible to probe the extent to which the given data are consistent with a very narrow distribution resembling a single class of sites.[6] All computations are embedded in the public domain software EVILFIT.[6,8,9]

A typical example is shown in Figure 5.2. A main peak can be discerned representing the surface sites of interest in this study. Integration of $P(K_\mathrm{D}, k_\mathrm{d})$ only in the region of the main peak in EVILFIT will report an estimate of the dissociation equilibrium constant and dissociation rate constant of this interaction. The main sites coexist with surface sites exhibiting lower and higher affinity at lower populations. The additional sites are the cause of an unsatisfactory fit with a simple 1 : 1 binding model, but they can be readily excluded from consideration after they have been identified.

5.3.2 Mass Transport Limitation

Obviously, under conditions where mass transport dominates the surface binding, we cannot hope to learn much about binding kinetics, since the measured accumulation of analyte at the binding surface becomes essentially independent of the molecular association constants if the analyte cannot escape once in proximity of the surface. Erroneous assumptions were made in the early SPR literature concerning the nature and impact of

View Online

Published on 24 May 2017 on http://pubs.rsc.org | doi:10.1039/9781788010283-00149

mass transport limitation.[2,34,35] Whether mass transport impacts the measured surface binding and dissociation depends chiefly on the number of surface sites, *i.e.* ligand density, in combination with the probability of capture into the site, *i.e.* the association rate constant. In addition, mass transport also depends on other factors in the vicinity of the sites that can slow analyte diffusion, including transient non-specific electrostatic or steric interactions with the polymer matrix. The details of the binding curve will then depend on the effective analyte diffusion coefficient, the details of the spatial configuration of flow, partitioning into and hindered transport through the hydrogel, surface density profiles both laterally and perpendicular to the surface, and the spatial sensitivity profiles of the sensor response.[1,4,9,34,36,37]

Highly mass transport-limited binding curves often take a more linear shape, as described in Section 4.3.3. However, depending on a variety of factors, such as the spatial profiles of immobilization, this can vary, and convex or even concave association phases and signal increases during the dissociation phase can occasionally be observed.[9,36] Often the observed dissociation will be biphasic, and show a faster dissociation when started from near complete saturation, since occupied sites will be unable to capture and prevent a molecule from dissociation. By contrast, when dissociation is started from lower saturation levels, more sites are able to contribute to rebinding of dissociated analyte molecules.[34]

These features are characteristic of mass transport-limited binding, and will not allow any satisfactory fit with an affinity distribution model.[9] Therefore, a satisfactory fit with the distribution model in EVILFIT is a good (although imperfect) first indicator for the absence of mass transport limitation effects. More reliable are experimental controls. Tests for a possible flow rate dependence are straightforward to carry out but, unfortunately, this dependence is weak since the mass transfer in a laminar flow is dependent only on the cube root of the flow rate. Furthermore, conditions where transport limitation arises mainly from the limited diffusivity inside the hydrogel will not be recognized with the flow rate test.[1,4,36] A more powerful approach is the variation of the number of surface sites, *i.e.* the test whether the observed kinetics are independent of the immobilization level of the ligand. Later, in Section 12.7.2, an example is shown of distribution analysis effects using multiplex detection of analyte injection exposed to an array of various ligand density spots. There may be other reasons for a dependence on the immobilization level (as described below), but the invariance of the kinetics with respect to the immobilization level over a large range of surface densities is, in most circumstances, a good indicator for the absence of mass transport limitation. Finally, another simple test that can often be easily carried out is the injection of a soluble form of the ligand during the analyte dissociation. If surface binding is mass transport limited, rebinding will be suppressed by the soluble ligand molecules competing for the surface sites and allowing the analyte to leave the surface.

View Online

Published on 24 May 2017 on http://pubs.rsc.org | doi:10.1039/9781788010283-00149

Under conditions where the surface binding kinetics are only slightly limited by mass transport, all the different transport processes may be subsumed into a generic two-compartment transport model.[9] In this simplified model, the effective transport rate constant k_m may be obtained by curve fitting from the experimental data, but is difficult to interpret in detail. The precise value of this transport rate constant also cannot be predicted *a priori*; it will depend not only on flow, but also on the exact hydrodynamic shape of the analyte (noting that shape-dependent hydrodynamic friction coefficients may alter the diffusion coefficients of macromolecules of a given mass by a factor of two or more[38]), and also steric and electrostatic interactions with the polymer matrix; for example, even low-level transient interactions may impact diffusivity significantly[2,39]).

An extension of the surface site distribution model is possible to account approximately for mass transport limitation in this partially kinetically controlled regime.[9] This requires a slightly different approach from eqn (5.3) and (5.5), since binding to different sites is not independent: under mass transport-limited conditions, an analyte molecule just dissociated from one class of ligand sites may rebind to a different class of ligands. Therefore, the total signal from a distribution of sites is better described by a systems of rate equations:

$$\frac{\mathrm{d}c_{\mathrm{surf}}}{\mathrm{d}t} = k_{\mathrm{tr}}(c - c_{\mathrm{surf}}) - \sum_i \frac{\mathrm{d}s_i}{\mathrm{d}t}$$
$$\frac{\mathrm{d}s_i}{\mathrm{d}t} = k_{\mathrm{a},i} c_{\mathrm{surf}} \left[P_i(K_{\mathrm{D},i}, k_{\mathrm{off},i}) - s_i\right] - k_{\mathrm{d},i} s_i \tag{5.7}$$

where c_{surf} is an effective analyte concentration at the surface and $s_i(t)$ is the signal contribution from sites with properties $P_i(K_{\mathrm{D},i}, k_{\mathrm{d},i})$, again allowing for an array (with index i) of sites on a mesh of K_{D} and k_{d} values.[9] In this case, the total signal is fitted to the experimental data in a global fit, with non-linear regression for the populations P_i and also k_m. Extending the experimental information, data obtained for the same surface under different flow rates can be fitted in a global fit with this surface site distribution model.[9] However, data obtained for different surfaces with different density of immobilized ligand should not be globally fitted, since in general the affinity distribution of the immobilized sites may change at different immobilization levels (see below).

5.3.3 Higher Order Reaction Schemes

A different approach to interpret binding curves that do not follow the expected single exponentials for 1 : 1 bimolecular reactions is the consideration of more complex chemical reaction schemes between discrete ligand and analyte molecules. Multi-site models with independent ligand sites conceptually correspond to a special case of the distribution model (except

View Online

for a different interpretation of R_{max}). A variation of the distribution model has been developed to account for stepwise addition of analyte,[40] and the possibility of data interpretation with the distribution model applied to multivalent analyte binding has been demonstrated by Vorup-Jensen and colleagues.[16,41,42]

Fundamentally different are binding models that assume only a few discrete classes of sites, not accounting for surface heterogeneity. For example, this includes various chemical reaction schemes for cooperative interactions and conformational change models. A caveat of these models is that owing to the introduction of additional fitting parameters they will invariably improve the quality of fit compared with the single-site model, but this alone does not rationalize the model for the interaction under study. Furthermore, the problem arises that different discrete models may fit the data similarly well.[43] In the light of these difficulties, it is good practice to compare the performance of these models with that of the conceptually simpler surface site distribution model. In this regard, it should be noted that binding curves arising from processes where uniform analyte–ligand complexes can undergo conformational transitions to states with different stability will not be fitted well with the above model of distribution of surface sites each with simple 1 : 1 reactions.[6] This should make these processes distinguishable on the basis of the quality of fit. If more complex binding schemes fit the data best and seem warranted based on the understanding of the physical nature of the interacting system, it is highly recommended to verify binding stoichiometry and affinity independently using different techniques, for example, in a global multi-method analysis (GMMA)[44,45] or in side-by-side experiments.[46]

Published on 24 May 2017 on http://pubs.rsc.org | doi:10.1039/9781788010283-00149

5.4 Experimental Design

5.4.1 Information Content

The surface site distribution model offers a powerful representation of the information content of the experimental binding curves, since the default Tikhonov regularization will result in the broadest distribution statistically consistent with the data within the given signal-to-noise ratio. Thus, we can consider data informative if they force sharp, well-defined features of the distribution that define the binding constants and binding site populations very well. On the other hand, data that lead to distributions with very broad features are inferior in information content. In the extreme case, hypothetical binding curves that consist only of noise will produce a very broad, uniform distribution, reflecting the lack of any information from the experiments.

The features of experimental traces that govern information content are the observed curvature in the association and dissociation traces, and also the concentration range relative to the K_D values of the surface site populations to be characterized. As a general rule, equilibrium constants will be

View Online

Published on 24 May 2017 on http://pubs.rsc.org | doi:10.1039/9781788010283-00149

more precisely determined if they approach the ideal shapes where (1) the binding curves at both association and dissociation show significant curvature or (2) the contact time in the association phase is sufficiently long to allow for an approach of steady-state signals for the entire concentration range spanning concentrations from 0.1 to 10 times K_D (approaching saturation of the surface). On the other hand, configurations that produce short segments of curves with low curvature that always remain far from steady state will have relatively poor information on binding rate constants and affinity constants. The problem is further compounded in configurations that do not start injection cycles from empty surfaces, which would leave the surface site distributions in an ill-defined state prior to each injection,[47,48] and similarly for continuous analyte concentration gradients.[49,50] (If regeneration-less configurations are necessary, we would recommend using sufficient contact times such that starting and end-points of injections are well-defined steady-state signals.[51,52])

An example is shown in Figure 5.3, which compares two experiments carried out with the same immobilized surface: a family of binding curves comprising very short contact times and dissociation phases (Figure 5.3A) and one collected with extended observation time and larger concentration range (Figure 5.3C). The experimental design in Figure 5.3A was taken from the work of Roden and Myszka,[53] intended to demonstrate the existence of a single class of sites. Although the data can be easily reproduced and fitted with a single class of site model, the extension of the contact time for the same surface reveals the true presence of multiple classes of sites, which may be visually discerned from the multi-phasic association.[52] In fact, it is obvious that ''sufficient'' restrictions in both the observation time – and/or similarly in the signal-to-noise ratio level – will always lead to data that can be fitted reasonably well with a single class of site model, irrespective of the true heterogeneity and populations and their affinities and kinetic constants, simply because of their lack of information content. However, the resulting values will be, at best, an ill-defined average. (For an analysis of signal-to-noise ratio on the precision of estimates for single-site systems, see ref. 54) An important virtue of the distribution model is that it can flag the poor experimental design by the resulting broad distribution, as shown for this example in Figure 5.3B. This can prevent one from overstating the results of the experiment. In contrast, the curvatures and wider concentration range allows us to resolve multiple distinct populations of surface sites (Figure 5.3D).

This example highlights an important general aspect of distribution analysis in cases where the surface binding sites do not adhere to the ideal expectations. Rather than truncation of the range of data sets subjected to the analysis (which was advocated in early days of SPR analysis[2,34]), or up-front truncation of the data collected in terms of information content, to an extent that an ideal 1 : 1 binding model seems applicable without obvious deviations [*e.g.* as applied in Scrubber2 analysis (see Chapter 9)], the distribution analysis now allows and encourages the inclusion of all available

View Online

Published on 24 May 2017 on http://pubs.rsc.org | doi:10.1039/9781788010283-00149

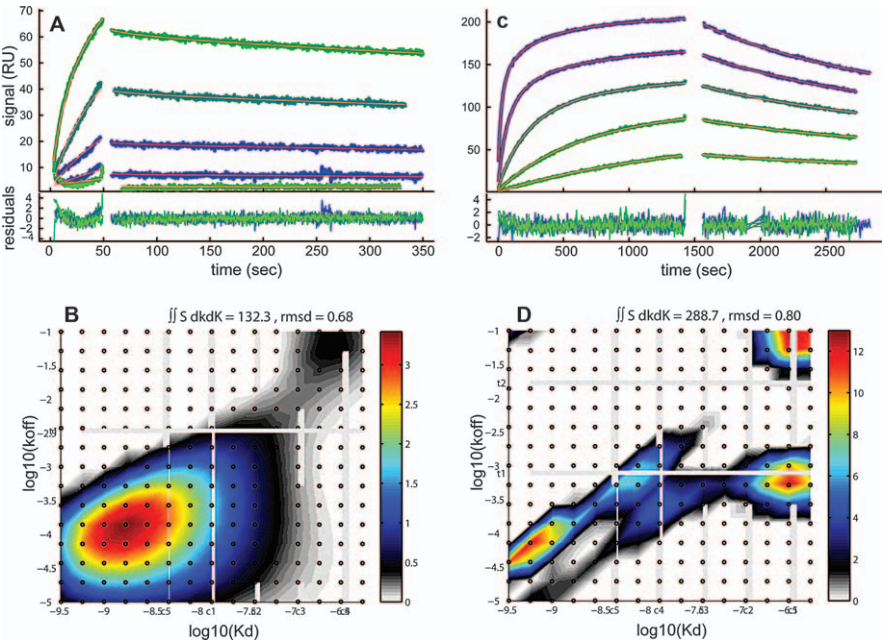


Figure 5.3 Comparison of affinity and kinetic rate constant distribution obtained from the same surface from binding experiments with different design. This is the distribution analysis of the same data sets as shown in Figure 2.3. Excellent fits are achieved for both experimental designs, but the regularization in the distribution analysis exposes different information content. (A, B) Arbitrarily truncated data and analysis with short association and dissociation times and a small analyte concentration range. The resulting distribution exhibits only broad features, suggesting not more than the order of magnitude of both the kinetic and affinity binding constants. (C, D) Experimental binding data and analysis of longer contact times and larger analyte concentration range. The resulting distribution is very detailed, resolving multiple classes of surface sites.[4] For experimental details, see ref. 8.
Reproduced from P. Schuck and H. Zhao, *Surface Plasmon Resonance: Methods and Protocols*, The Role of Mass Transport Limitation and Surface Heterogeneity in the Biophysical Characterization of Macromolecular Binding Processes by SPR Biosensing, **627**, 2010, 15–54, Copyright © 2010, Springer Science + Business Media, LLC. With permission from Springer.

data at the highest possible information content. It will generally achieve an excellent fit to the raw data, and offer a view of experimental ''imperfections'' in the space of populations of sites with different affinity and kinetic rate constants. In some sense, one can understand the distribution analysis in EVILFIT as a ''data transform'' that allows us to make rational decisions on the interpretation of the data in a space of binding constants, which can be more readily interpreted than the original data space. For example, broadly distributed populations of low-affinity sites joining a major high-affinity peak may often be identified as ''non-specific'' binding sites that are not of

View Online

interest and excluded from further interpretation. Similar exclusion is not possible in the original data space without significant deterioration of information on the sites of interest causing arbitrary results.

Published on 24 May 2017 on http://pubs.rsc.org | doi:10.1039/9781788010283-00149

5.4.2 Effect of Sensor Surface

The distribution analysis can offer insights into the effects of different sensor surfaces on the interaction studied. This was demonstrated using β_2-microglobulin and a monoclonal antibody as a model system, immobilized on different surfaces with different linkage strategies.[7] Figure 5.4A and B show distributions obtained with antibody immobilized using standard amine coupling to carboxymethyldextran surfaces (Biacore chips CM3 and CM5) at moderate immobilization levels (achieving binding capacities of $\sim$86 and 176 RU, respectively). The distribution exhibited a main peak with slightly different K_D of 1.2 and 3.2 nM, respectively, in combination with a broad tail of sites with lower affinity. Interestingly, the apparent on-rate constant of the main peak was slightly lower for the CM5 chip (0.72×10^6 L mol^{-1} s^{-1} relative to 1.6×10^6 L mol^{-1} s^{-1}) and was further reduced with immobilizations to CM5 at higher surface density (0.49×10^6 L mol^{-1} s^{-1}) (panel C), in which case the surface binding was observed to be partially mass transport limited. Capture of the biotinylated antibody through immobilized streptavidin (panels D, E and F) did not make the surface much more uniform, but in some cases introduced different kinds of heterogeneity and ''non-specific'' sites. Interestingly, the highest affinity of $K_D = 0.8$ nM was observed with streptavidin capture to a dextran-less chip (Biacore C1 sensor chip, panel D), which is similar to a more homogeneous main population with $K_D = 0.9$ nM on a streptavidin-coated short dextran chip using biotin capture (panel E). The same capture to long dextran CM5 again provided slightly weaker binding ($K_D = 1.4$ nM, panel F).

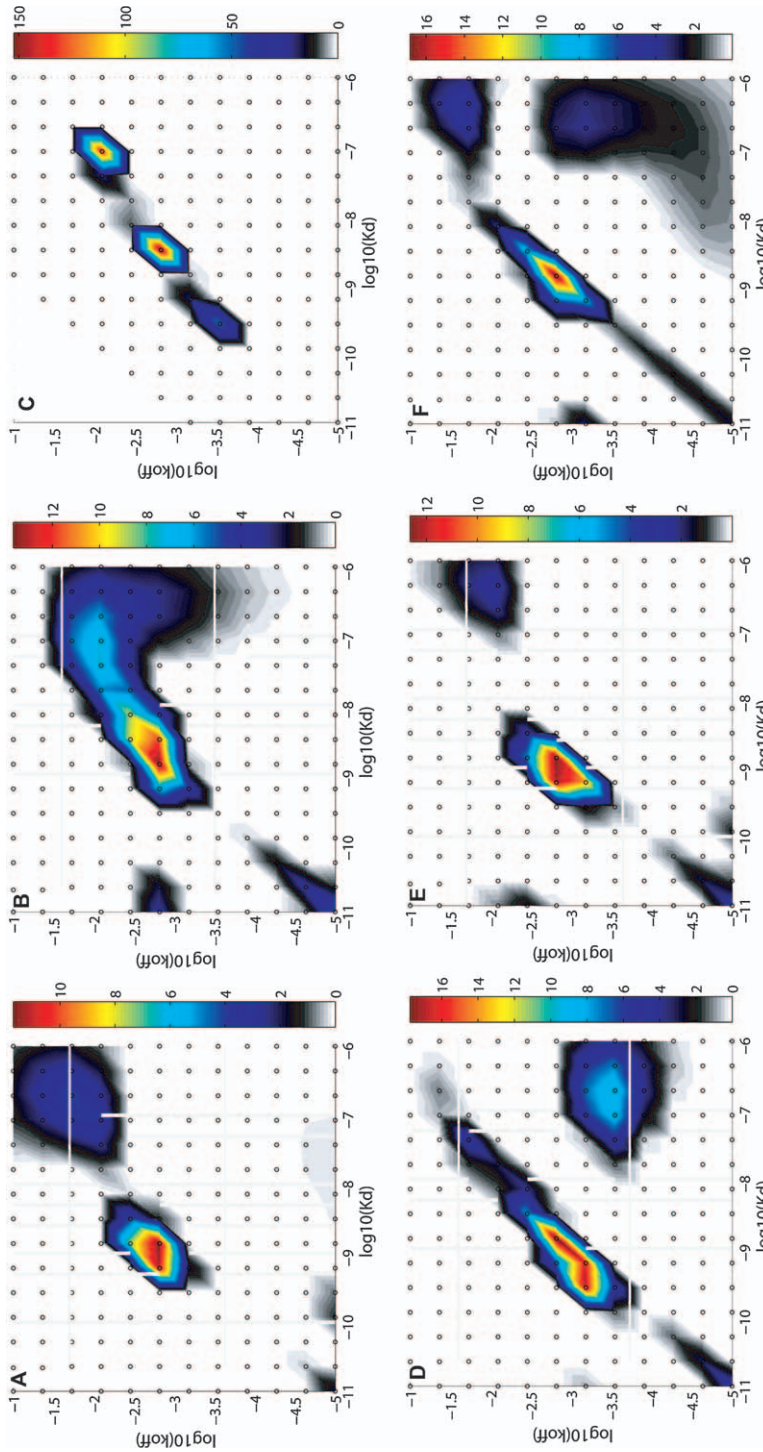
Although similar patterns of distributions – exhibiting a main peak of interest, in combination with broad range of sites with weaker affinity at similar on-rate constant and/or poorly reversible ''non-specific'' sites – have frequently been observed for antibody–antigen interactions, it is not clear to what extent the impact of the different surfaces on the observed binding site distributions will be similar. However, for any given system, a comparison of the distribution obtained with different surfaces will allow one to gain confidence in the assignment of binding site populations of interest, and the distinction of these from surface-induced artificial or impaired binding sites.

5.4.3 Ligand Immobilization Process

A second aspect related to the surface immobilization that can be readily probed with the surface site distribution model is the optimal density of immobilization, and also parameters related to the process of ligand immobilization, such as the ligand concentration, the degree of surface

View Online

Published on 24 May 2017 on http://pubs.rsc.org | doi:10.1039/9781788010283-00149



View Online

Published on 24 May 2017 on http://pubs.rsc.org | doi:10.1039/9781788010283-00149

activation and the length of time allowed for the immobilization reaction. Even though we would like to assume that none of this will impact the measured binding parameters between ligand and analyte, once we accept the idea that the local microenvironment can significantly alter the binding energies and probabilities of complex formation, then the ideal picture that the binding sites are invariant no matter when and where immobilization took place does not necessarily apply. For example, the expectation that an increase in the total surface density of immobilized ligand will simply create proportionally more sites of all classes may not hold true.

This question is easy to probe experimentally by carrying out analyses of binding curves to ligands immobilized under different conditions. Importantly, when applying the same immobilization conditions in replicate experiments, generally highly reproducible distributions of surface sites are achieved (*e.g.* Figure 5 in ref. 6). Figure 5.5A and B show an example where doubling the surface density leads to very similar, although heterogeneous, populations of surface sites, suggesting that the molecules added later in the immobilization process have the same probabilities of turning out with certain binding properties as the molecules added earlier. In contrast, Figure 5.5C and D show a different ligand–analyte pair where the increase in surface immobilization density results in a disproportionally higher increase in the population of a high-affinity site. One could speculate that a spatially inhomogeneous immobilization process, such as observed experimentally in two-color SPR by Zacher and Wischerhoff,[37] may well cause such uneven shifts in surface site distributions.[6] Likewise, undesirable effects from high surface density, such as surface-promoted aggregation processes, would be exacerbated at higher immobilization density.[55]

A general conclusion to be drawn from these data is that the common assumption that surfaces with different coupling densities provide just fewer or more of the same sites may not be true in all systems. Therefore, the

Figure 5.4 Comparison of the experimental data and fits for binding of soluble using β_2-microglobulin and a monoclonal antibody immobilized on different sensor surfaces. β_2-Microglobulin analyte concentrations are between 0.1 and 100 nM, as indicated by vertical grey lines. Antibody was attached to (A) a short carboxymethyldextran surface (CM3) using amine coupling achieving a surface density of 1350 RU; (B) a long carboxymethyldextran surface (CM5) using amine coupling to achieve a surface density of 3000 RU; (C) same as (B) but with a higher surface density of 6000 RU; (D) a C1 surface with previously immobilized streptavidin, achieving a level of 1500 RU using a biotin tag; (E) a streptavidin-modified CM3 surface, achieving a density of 800 RU; (F) a streptavidin-modified CM5 surface, achieving a density of 1000 RU. Surface distributions were calculated in EVILFIT, extended for mass transport analysis for the high-density CM5 configuration in (C).[7]
Reproduced from H. Zhao, I. I. Gorshkova, G. L. Fu and P. Schuck, A comparison of binding surfaces for SPR biosensinng using an antibody–antigen system and affinity distribution analysis, *Methods*, **59**(3), 328–335. Copyright 2013 with permission from Elsevier.

View Online

Published on 24 May 2017 on http://pubs.rsc.org | doi:10.1039/9781788010283-00149

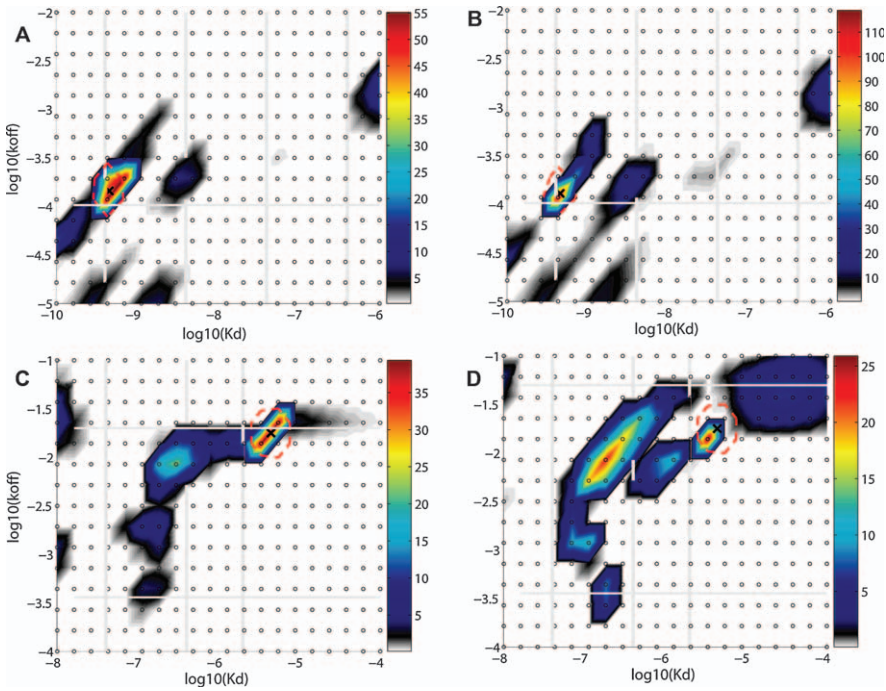


Figure 5.5 Dependence of the affinity and kinetic rate distributions on the total surface sites density. Examples are shown for two different Fab–antigen systems. (A, B) Binding of soluble monoclonal Fab to its immobilized antigen protein at a low surface density of 1400 RU leading to a total binding capacity of ~340 RU (A) and a high surface density of 3800 RU leading to a total binding capacity of ~700 RU (B). (C, D) Binding of a third soluble monoclonal Fab to its antigen protein immobilized at a low surface density of 920 RU leading to a total binding capacity of 381 RU (C) and immobilized at a higher surface density (1500 RU) leading to a total binding capacity of 464 RU (D). The black cross encircled with red dashed line represents the Bayesian prior assumption that there is only a single class of sites with the indicated binding parameters.[6]
Reprinted with permission from I. I. Gorshkova, J. Svitel, F. Razjouyan and P. Schuck, Bayesian analysis of heterogeneity in the distribution of binding properties of immobilized surface sites, *Langmuir*, 2008, **24**(24), 11577. Copyright 2008 American Chemical Society.

global analysis of SPR data incorporating different sensor surfaces – such as proposed for the analysis of mass transport-limited binding – should be avoided without experimental tests.

5.4.4 Analyte Purity

A final aspect that we will examine is heterogeneity of the analyte. Experimentally, it is well known that analyte purity is of the utmost importance in SPR experiments, and that reversibly formed oligomers or irreversible

View Online

Published on 24 May 2017 on http://pubs.rsc.org | doi:10.1039/9781788010283-00149

aggregates can have a profound impact on the binding curves.[55] Unfortunately, detailed measurement of oligomer and aggregate content by sedimentation velocity analytical ultracentrifugation is not always possible, and even size-exclusion chromatographic (SEC) purification may not be practical for all samples. Therefore, it is of interest to ask what the effect of analyte polydispersity is on the measured surface binding distribution.

In principle, an analogous model of affinity and lifetime distributions of analyte–ligand complexes is conceivable for the case where a single class of surface sites is available, which is probed with a heterogeneous analyte sample.[8] Strictly, this problem takes a different mathematical form, since different analyte populations will compete for the same surface sites, and kinetic exchange between analytes with short complex lifetimes and long lifetimes may occur as a function of surface contact time.[8] A rigorous analysis would be further complicated by the need to consider both surface site distributions and analyte distributions, which appears to far exceed typical experimental information content. However, one ray of hope is that at least steady-state binding levels from analyte distributions will obey the same Langmuir isotherm for binding to surface sites, reflecting an (analyte) population average binding affinity to the surface site,[8] and this should hold independently for all classes for surface sites. Furthermore, it may be possible to carry out experiments that avoid conditions close to saturation where competition would dominate. Finally, one can imagine that some analyte impurities may occupy mainly non-specific sites. Irrespective of theoretical complications, therefore, one may apply the ligand distribution model to experimental binding curves of non-homogeneous analyte samples, and consider the observed affinity and dissociation rate constant distribution of analyte–ligand interaction pairs in the standard EVILFIT distribution model in a more empirical approach.

An example of the application of distribution analysis to highlight analyte purity is shown in Figure 5.6. Here, the same Fab fragment was studied twice in binding experiments with binding to the same antigen-coated surface, initially without additional SEC purification (A–C), and after chromatographic purification (D). From the binding traces in Figure 5.6A for the unpurified sample, a steadily increasing signal can be discerned for the high concentrations (400 nM and 2 μM) in the association phase, indicating the presence of weak interactions. Also noteworthy is the incomplete dissociation of these traces, apparently leveling off at signals significantly above the baseline. This suggests that the complexes formed during association at the high concentrations are poorly reversible. Correspondingly, a large peak is found in the resulting distribution (Figure 5.6C) for weak sites with very low off-rate constant. Importantly, these apparent sites are absent in the analysis of chromatographically purified analyte (Figure 5.6D). This indicates that the low-affinity, poorly reversible binding events in the original experiment were likely caused by analyte oligomers or aggregates at low concentrations. Despite the striking effect of analyte purification, the minor peaks in the original analysis (Figure 5.6C) are well resolved and very similar to the

View Online

Published on 24 May 2017 on http://pubs.rsc.org | doi:10.1039/9781788010283-00149

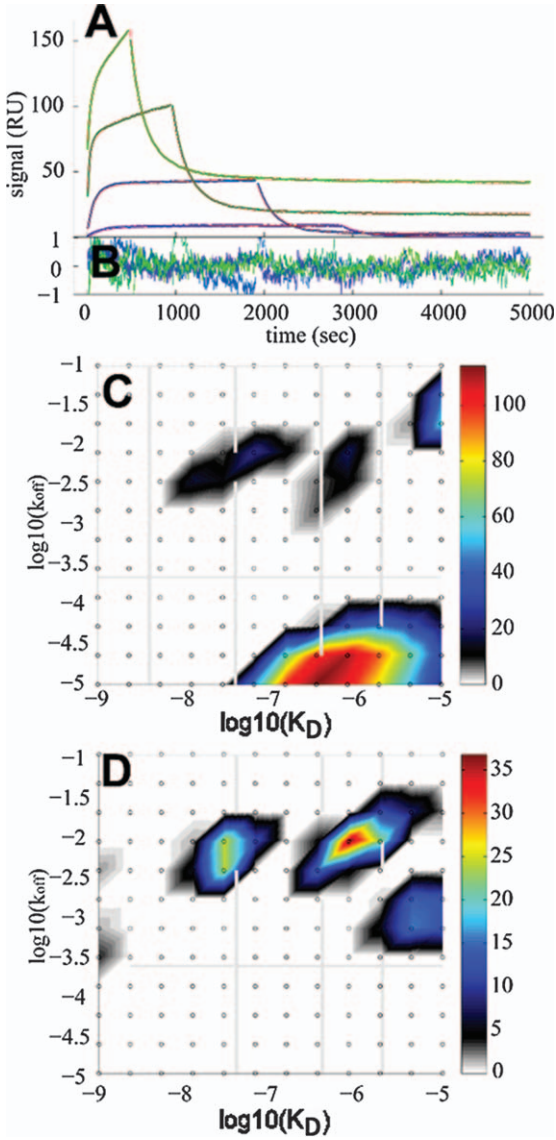


Figure 5.6 SPR kinetic binding analysis of an antibody–antigen interaction with and without analyte size-exclusion purification. The antigen was immobilized directly to a short-chain carboxymethyldextran sensor surface (CM3). (A) Binding curves (blue to green lines) measured for a Fab fragment of a monoclonal IgG antibody prior to SEC purification, applied at concentrations of 4 nM, 40 nM, 400 nM and 2 μM. Best-fit binding curves from surface site distribution model are shown as red lines, essentially superimposing the data. (B) Residuals of this fit. (C) Affinity and rate distribution corresponding to the fit in (A). For comparison, (D) shows the affinity and rate distribution for binding curves obtained under identical conditions with the same surface but using the Fab fragment sample after SEC purification.

View Online

remaining peaks after purification (Figure 5.6D). This shows the power of distribution analysis to extract information from experimental binding traces even when superimposed by unwanted binding events.

5.5 Conclusions

Owing to the exquisite sensitivity and precision of SPR data, in practice deviations from single-site models are often encountered and virtually unavoidable. Drawing reliable conclusions from such analyses is problematic, as is the truncation of data in the analysis or data acquisition, or the *ad hoc* extension to invoke more complicated binding schemes. By contrast, distribution analysis is a natural extension of the discrete-site model that accounts for polydispersity in the surface sites to be reasonably expected in most experiments, and it exhibits little correlation with discrete models describing more complicated multi-site interactions. In our experience, it usually describes the experimental data extremely well, in support of this more realistic view of surface sites. By distinguishing populations of surface sites according to their affinity and kinetic rate constants, it offers the possibility of focusing on the sites of interest for further interpretation. In addition, the observed polydispersity offers opportunities to optimize experimental design, including aspects of information content, immobilization strategy and analyte purity. Exciting new developments include applications of the concept of surface site distributions to multivalent and multi-step interactions,[10,40,41] such as are frequently encountered in the study of nanoparticles and immunological molecules.

5.6 Questions

1. Which factors are potential contributors to heterogeneity of affinity of surface binding sites?
   a. Variations in the physical microenvironment of the surface, such as surface roughness.
   b. If an immobilization matrix is used composed of macromolecules such as dextran, the chain density distribution perpendicular to the surface.
   c. Variation in the amino acid residue involved in chemical crosslinking.
   d. Partial deactivation and limited unfolding of protein ligands.
   e. Mass transport limitation.
2. To detect mass transport-limited binding conditions, order the following experimental tests/observations according to their effectiveness, and explain why.
   a. Change of immobilization density.
   b. Change of analyte flow rate.
   c. Inspection of binding traces for convex shape in the association phase and transiently increasing signal in the dissociation phase.

Published on 24 May 2017 on http://pubs.rsc.org | doi:10.1039/9781788010283-00149

View Online

Published on 24 May 2017 on http://pubs.rsc.org | doi:10.1039/9781788010283-00149

   d. Application of soluble ligand in the flow during dissociation phase as competitor for rebinding.
   e. Increasing analyte concentration to compensate for mass transfer limitation.
   f. Analyze data only from the approach of steady-state signals
3. What are the units of the K_D–k_{off} distribution?
4. Explain why the regularization principle in the distribution analysis is related to the scientific principle of Occam's razor.
5. What is the key feature of surface binding experiments that makes it possible to study high-affinity interactions easily?

Acknowledgements

This research was supported by the Intramural Research Program of the National Institute of Biomedical Imaging and Bioengineering, NIH.

References

1. P. Schuck, *Annu. Rev. Biophys. Biomol. Struct.*, 1997, **26**, 541–566.
2. P. Schuck, *Curr. Opin. Biotechnol.*, 1997, **8**, 498–502.
3. R. Karlsson, H. Roos, L. Fägerstam and B. Persson, *Methods*, 1994, **6**, 99–110.
4. P. Schuck and H. Zhao, *Methods Mol. Biol.*, 2010, **627**, 15–54.
5. S. W. Provencher, *Makromol. Chem.*, 1979, **180**, 201–209.
6. I. Gorshkova, J. Svitel, F. Razjouyan and P. Schuck, *Langmuir*, 2008, **24**, 11577–11586.
7. H. Zhao, I. Gorshkova, G. L. Fu and P. Schuck, *Methods*, 2013, **59**, 328–335.
8. J. Svitel, A. Balbo, R. A. Mariuzza, N. R. Gonzales and P. Schuck, *Biophys. J.*, 2003, **84**, 4062–4077.
9. J. Svitel, H. Boukari, D. Van Ryk, R. C. Willson and P. Schuck, *Biophys. J.*, 2007, **92**, 1742–1758.
10. T. Vorup-Jensen, Integrin and Cell Adhesion Molecules, *Methods Mol. Biol.*, 2012, **757**, 55–71.
11. T. Vorup-Jensen, C. V. Carman, M. Shimaoka, P. Schuck, J. Svitel and T. A. Springer, *Proc. Natl. Acad. Sci. U. S. A.*, 2005, **102**, 1614–1619.
12. J. N. Cash, E. B. Angerman, C. Kattamuri, K. Nolan, H. Zhao, Y. Sidis, H. T. Keutmann and T. B. Thompson, *J. Biol. Chem.*, 2012, **287**, 1043–1053.
13. A. P. Goncalvez *et al.*, *J. Virol.*, 2008, **82**, 7009–7021.
14. Z. Chen, M. Moayeri, D. Crown, S. Emerson, I. Gorshkova, P. Schuck, S. H. Leppla and R. H. Purcell, *Infect. Immun.*, 2009, **77**, 3902–3908.
15. F. S. Groothuizen *et al.*, *Nucleic Acids Res.*, 2013, **41**, 8166–8181.
16. X. Zhang, G. Bajic, G. R. Andersen, S. H. Christiansen and T. Vorup-Jensen, *Biochim. Biophys. Acta, Proteins Proteomics*, 2016, **1864**, 471–478.
17. T. Eichhorn *et al.*, *Biochem. Pharmacol.*, 2013, **85**, 38–45.

View Online

Published on 24 May 2017 on http://pubs.rsc.org | doi:10.1039/9781788010283-00149

18. S. Sabban, H. Ye and B. Helm, *Vet. Immunol. Immunopathol.*, 2013, **153**, 10–16.
19. R. G. Walker, E. B. Angerman, C. Kattamuri, Y.-S. Lee, S.-J. Lee and T. B. Thompson, *J. Biol. Chem.*, 2015, **290**, 7506–7516.
20. N. G. Sgourakis, K. Natarajan, J. Ying, B. Vogeli, L. F. Boyd, D. H. Margulies and A. Bax, Viral Immune Modulator Family, *Structure*, 2014, **22**, 1263–1273.
21. R. Wang, K. Natarajan, M. J. R. Revilleza, L. F. Boyd, L. Zhi, H. Zhao, H. Robinson and D. H. Margulies, *Proc. Natl. Acad. Sci.*, 2012, **109**, E3578–E3587.
22. M. Roos, Hall *et al.*, *Nucleic Acids Res*, 2015, **43**, e9.
23. M. Clerici, M. P. A. Luna-Vargas, A. C. Faesen and T. K. Sixma, *Nat. Commun.*, 2014, **5**, 5399.
24. E. Kläning *et al.*, *Biochim. Biophys. Acta, Proteins Proteomics*, 2015, **1854**, 930–938.
25. R. Stapulionis *et al.*, *J. Immunol.*, 2008, **180**, 3946–3956.
26. M. R. Jensen *et al.*, *J. Biol. Chem.*, 2016, **291**, 16963–16976.
27. R. B. M. Schasfoort and P. Schuck, Future Trends in SPR Technology, in *Handbook of Surface Plasmon Resonance*, ed. R. B. M. Schasfoort and A. J. Tudos, RCS Publishing, Cambridge, U.K., 2008, pp. 354–392.
28. E. T. Gedig, Surface Chemistry in SPR Technology, in *Handbook of Surface Plasmon Resonance*, ed. R. B. M. Schaasfort and A. J. Tudos, RSC Publishing, Cambridge, U.K., 2008, pp. 173–220.
29. P. Schuck, Fredholm Integral Equations in Biophysical Data Analysis, in *26th Southern Biomedical Engineering Conference. SBEC 2010*, ed. K. E. Herold, J. Vossoughi and W. E. Bentley, April 30 - May 2, 2010, Springer, Coll. Park. Maryland, USA, Berlin Heidelberg, 2010, pp. 340–343.
30. P. Schuck, *Biophys. J.*, 2000, **78**, 1606–1619.
31. A. K. Livesey, P. Licinio and M. Delaye, *J. Chem. Phys.*, 1986, **84**, 5102–5107.
32. P. J. Steinbach, *Biophys. J.*, 1996, **70**, 1521–1528.
33. W. H. Press, S. A. Teukolsky, W. T. Vetterling and B. P. Flannery, *Numerical Recipes in C*, University Press, Cambridge, 2nd edn, 1992.
34. P. Schuck and A. P. Minton, *Anal. Biochem.*, 1996, **240**, 262–272.
35. L. G. Fägerstam, A. Frostell-Karlsson, R. Karlsson, B. Persson and I. Rönnberg, *J. Chromatogr. A.*, 1992, **597**, 397–410.
36. P. Schuck, *Biophys. J.*, 1996, **70**, 1230–1249.
37. T. Zacher and E. Wischerhoff, *Langmuir*, 2002, **18**, 1748–1759.
38. C. R. Cantor and P. R. Schimmel, *Biophysical Chemistry. II. Techniques for the study of biological structure and function*, W.H. Freeman, New York, 1980.
39. J. Crank, *The Mathematics of Diffusion*, Oxford University Press, Oxford, 1975.
40. L. E. Kapinos, R. L. Schoch, R. S. Wagner, K. D. Schleicher and R. Y. H. Lim, *Biophys. J.*, 2014, **106**, 1751–1762.

View Online

41. T. Vorup-Jensen, The Nanoscience of Polyvalent Binding by Proteins in the Immune Response, in *Nanomedicine*, ed. K. A. Howard, T. Vorup-Jensen and D. Peer, Springer New York, New York, NY, 2016, pp. 53–76.
42. L. C. Gjelstrup *et al.*, *J. Immunol.*, 2012, **188**, 1292–1306.
43. R. W. Glaser and G. Hausdorf, *J. Immunol. Methods*, 1996, **189**, 1–14.
44. H. Zhao and P. Schuck, *Anal. Chem.*, 2012, **84**, 9513–9519.
45. H. Zhao, G. Piszczek and P. Schuck, *Methods*, 2015, **76**, 137–148.
46. R. J. Fisher *et al.*, *Nucleic Acids Res.*, 2006, **34**, 472–484.
47. Y. Tang, R. Mernaugh and X. Zeng, *Anal. Chem.*, 2006, **78**, 1841–1848.
48. R. Karlsson, P. S. Katsamba, H. Nordin, E. Pol and D. G. Myszka, *Anal. Biochem.*, 2006, **349**, 136–147.
49. M. L. Shank-Retzlaff and S. G. Sligar, *Anal. Chem.*, 2000, **72**, 4212–4220.
50. J. G. Quinn, *Anal. Biochem.*, 2012, **421**, 391–400.
51. M. Abrantes, M. T. Magone, L. F. Boyd and P. Schuck, *Anal. Chem.*, 2001, **173**, 606–1619.
52. P. Schuck, D. B. Millar and A. A. Kortt, *Anal. Biochem.*, 1998, **265**, 79–91.
53. L. D. Roden and D. G. Myszka, *Biochem. Biophys. Res. Commun.*, 1996, **225**, 1073–1077.
54. R. J. Ober and E. S. Ward, *Anal. Biochem.*, 1999, **273**, 49–59.
55. P. Schuck, L. F. Boyd and P. S. Andersen, *Curr. Protoc. Cell Biol.*, 1999, **17**, 17.6.1–17.6.22.

Published on 24 May 2017 on http://pubs.rsc.org | doi:10.1039/9781788010283-00149

Published on 24 May 2017 on http://pubs.rsc.org | doi:10.1039/9781788010283-00171

CHAPTER 6

Surface Chemistry in SPR Technology

ERK T. GEDIG

XanTec bioanalytics GmbH, Merowingerplatz 1A, 40225 Düsseldorf, Germany
Email: gedig@xantec.com

6.1 Introduction

Whereas the preceding chapters focused mainly on the physical basics of surface plasmon resonance (SPR), instrumentation, and assay design, we will now turn to the heart of SPR and related biosensors: the sensor chip and its surface chemistry. It is here where the biomolecular interaction takes place; furthermore, although the sensor chip is extremely small in size (the coating thickness is measured in nanometers), its surface has a great influence on the behavior of the SPR device and the quality of the data retrieved.

As shown in Figure 6.1, the nanocomposite coating of a biosensor chip usually consists of the following elements:

- The substrate, which can be simply a mechanical carrier (*e.g.* glass) covered with the metal (*e.g.* gold), which enables surface plasmons to be excited. The substrate material and geometry should be compatible with the instrument's optics.
- A passivation or adhesion linking layer that links the gold surface with the immobilization matrix.

Handbook of Surface Plasmon Resonance, 2nd Edition
Edited by Richard B. M. Schasfoort
© The Royal Society of Chemistry 2017
Published by the Royal Society of Chemistry, www.rsc.org

View Online

Published on 24 May 2017 on http://pubs.rsc.org | doi:10.1039/9781788010283-00171

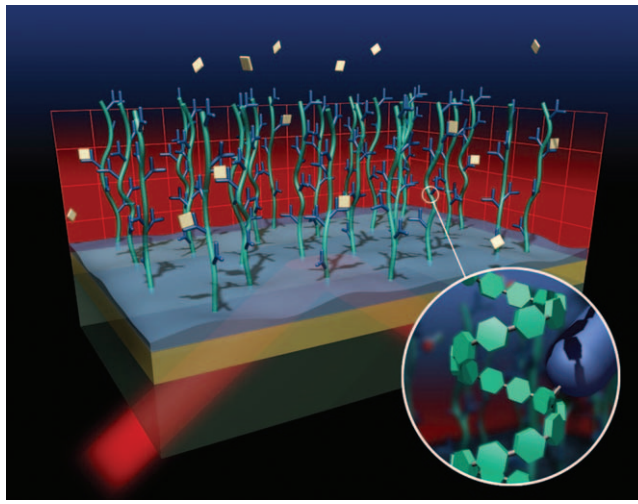


Figure 6.1 Nanoarchitecture of a typical SPR sensor chip. The gold-coated transparent substrate is covered by an adhesion linking layer (gray–blue) to which the immobilization matrix [here, a brush-structured hydrogel (green) is grafted]. Ligands (blue) are covalently coupled to the hydrogel chains and specifically bind analyte molecules (beige cubes).

- The immobilization matrix, which is the most critical element as it is in direct contact with the ligand and the sample and thus determines the specificity and other key characteristics of the biosensor.
- The immobilized ligand – usually a biomolecule – that is linked to the immobilization matrix and should interact selectively with the analyte.

In this chapter, the Introduction is followed by descriptions of the adhesion linking layer and immobilization matrix. A thorough treatment is given of the protocols used to immobilize the ligand to the immobilization matrix (see Figure 6.2), followed by various applications.

6.1.1 Interaction Mechanisms on Biosensor Surfaces

Recognition processes between biomolecules are the key to a thorough understanding of almost all processes in living organisms. To characterize them, direct optical biosensors are excellent tools as they allow for fast and quantitative analyses without the need for labels. Although direct detection is an elegant method, label-free detection bears the inherent disadvantage that not only the desired specific components of a biomolecular interaction contribute to the sensor signal, but also the non-specific binding (NSB) of other matrix components. This is a major difference in comparison with methods employing labels that detect the labeled component only and are insensitive to other, unlabeled species. Although NSB can be referenced by the use of a second channel, the data quality is much better when the ratio of specific to non-specific interactions is high.

View Online

Published on 24 May 2017 on http://pubs.rsc.org | doi:10.1039/9781788010283-00171

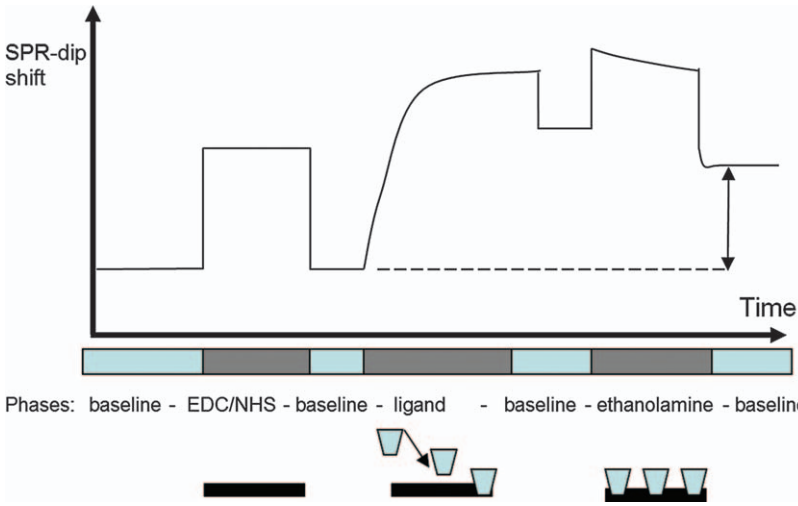


Figure 6.2 A typical sensorgram of a covalent immobilization cycle to capture a ligand to a dextran hydrogel sensor *via* EDC–NHS chemistry (see also Protocol 6.3), which is the most widely used immobilization method. The double-headed arrow reflects the resulting amount of immobilized ligand in the deactivated hydrogel.

The second important distinction from traditional methods such as blotting or other solid-phase techniques is the ability to reuse the chips multiple times. Owing to the significant variations between derivatized chip surfaces and also cost and time considerations, chip surfaces are reused as much as possible and at least for a series of continuous measurements. Complete regeneration requires that the analyte and the immobilized ligand interact with the surface only through specific interactions and the mostly covalent bonding to the immobilization matrix, respectively. Proteins and many other biomolecules tend to adsorb irreversibly on untreated metal, glass, or plastic surfaces, often causing the loss of 90% or more of their activity. This results in a chip surface with a low density of active ligands that can be only partially regenerated and is practically unusable after a few cycles (see Figure 6.3).

Further, the time-resolved nature of direct optical techniques leads to additional requirements for the chip surface. In contrast to common solid-phase assays, which yield one data point per assay, a biosensor delivers the full time course of the interaction. As outlined in Chapters 1 and 4, this information can be used to determine either the analyte concentration or, typically using a surface with a different structure, the association and dissociation kinetics of the interaction.

To understand the underlying processes occurring on the surface of a sensor chip, it is helpful to take a closer look at the basic forces that determine the interactions of biomolecules at the molecular level (Table 6.1). Two of the interactions, electrostatic (ionic) and hydrophobic interactions,

View Online

Published on 24 May 2017 on http://pubs.rsc.org | doi:10.1039/9781788010283-00171

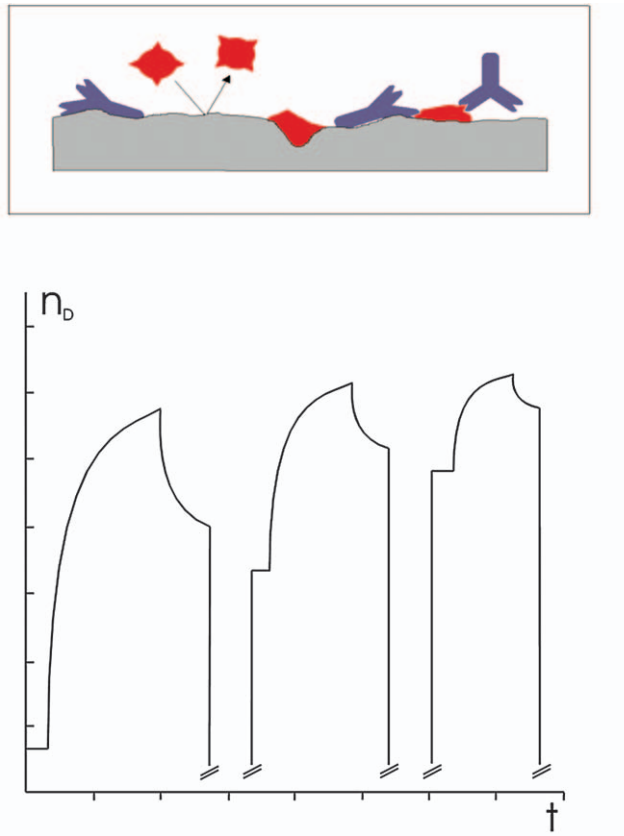


Figure 6.3 Unstable immobilization and partial denaturation of a ligand (red) and analyte (blue) on an incompatible surface, resulting in incomplete regeneration, increasing baseline, and decreasing binding capacity from cycle to cycle.

Table 6.1 Molecular forces contributing to biomolecular interactions.[1,2]

Force	Energy (kJ mol^{-1})	Distance dependence
Hydrophobic interaction	Up to 15	Not applicable
Electrostatic interaction	Up to 12.5	r^{-2}
Hydrogen bonding	Up to 4	r^{-6}
Van der Waals forces	Up to 0.4	r^{-10}

are the most relevant as they account for ~85% of the overall energy. If the chip surface and the interacting species are charged, the extent and sign of the electrostatic interaction can be manipulated within a relatively broad range by modifying the ionic strength and pH of the buffer. An increasing salt concentration screens charged groups and usually has a practically pH-independent repulsion effect on hydrophilic and charged immobilization matrices because ion pairs that can neutralize the charged domains are

View Online

Published on 24 May 2017 on http://pubs.rsc.org | doi:10.1039/9781788010283-00171

formed. At low ionic strengths (*i.e.* below 0.1 M), the pH of the buffer becomes more important as the electrostatic interactions that are dominant in this regime are governed by the ligand's overall charge, which is positive at pH values below the ligand's isoelectric point and negative in the more alkaline pH range. Depending on the charge of the sensor chip surface, strong attractive or repulsive forces between a dissolved species and the surface can result.

The *hydrophobic interaction* cannot be easily controlled, as it is not an attractive force, but is instead caused by the exclusion of hydrophobic domains with low surface energy in highly energetic solvents such as water. Hydrophobic interactions are induced by a change in the degree of organization of water molecules and are therefore an entropy effect. The entropy of the total system (water and interacting molecules) will increase when hydrophobic interactions take place. Generally, substances that strengthen the inner structure of water (*e.g.* most salts) increase the contribution of hydrophobic interactions (the salting-out effect is caused by a change in entropy); chaotropic substances such as guanidine or ethanol lower the contribution. The influence of pH is moderate, although a pH close to the p*I* of the interacting species usually minimizes the extent of electrostatic forces and thus increases the relative influence of hydrophobic interactions. As a consequence, the precipitation of protein molecules often occurs around the p*I* due to the decreased electrostatic repulsion between molecules. As hydrophobic interactions can lead to partial unfolding and thus to significant activity losses of immobilized proteins, the fraction of hydrophobic domains on the sensor chip surface should be kept as low as possible, with the exception of surfaces for the immobilization of membrane proteins.

Keeping the above in mind, it is obvious that the surface charge and surface energy of biosensor chips must be carefully controlled to achieve high immobilization yields, minimize the non-specific interaction of the matrix, retain the biological activity of the immobilized ligand, and achieve high signal-to-noise ratios. Other factors for consideration include the charge distribution and density and surface structure and functionality, which are key for adapting a sensor chip surface for particular applications.

6.1.2 The Surface Structure: Between Evanescent Field and Analyte Diffusion

Surface plasmons at the interface between a metal and a dielectric material have a combined electromagnetic wave and surface charge character, as shown in Chapter 2. This combined character results in the electric field component perpendicular to the surface being enhanced near the surface and decaying exponentially with distance away from it. The field in this perpendicular direction is said to be evanescent, reflecting the bound, non-radiative nature of surface plasmons. In the sample buffer above the metal, the decay length of the field, δ_d, is on the order of half the wavelength of light

View Online

Published on 24 May 2017 on http://pubs.rsc.org | doi:10.1039/9781788010283-00171

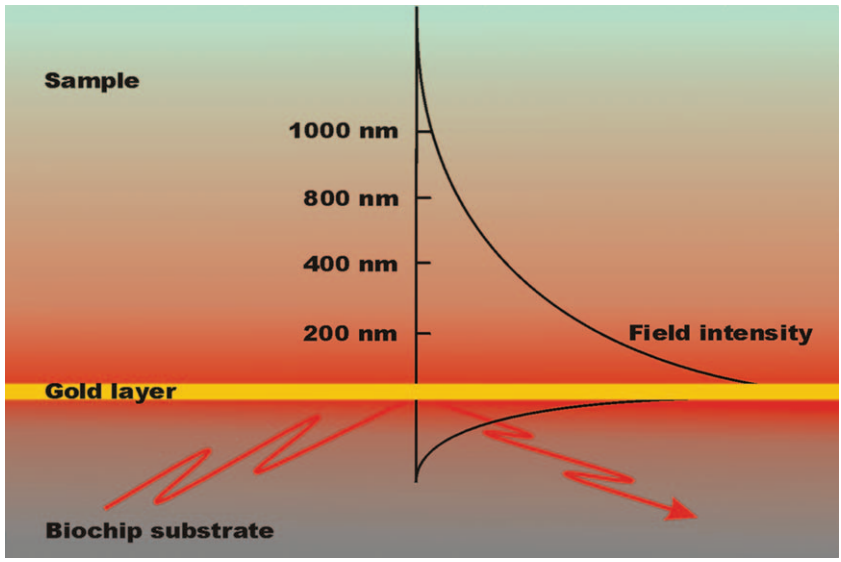


Figure 6.4 The intensity of the evanescent field decays exponentially with increasing distance from the plasmon-carrying metal layer. The shift in SPR angle corresponds to the change in effective refractive index in this volume close to the surface.

involved and is usually defined as the distance over which the intensity of the evanescent field drops to 1/e (*i.e.* to about 37%). In most commercial instruments that use light with a wavelength between 600 and 800 nm, δ_d is in the range 300–400 nm (see Figure 6.4).

One immediate consequence of the exponential decay of the evanescent field intensity is that a typical SPR biosensor is practically blind at distances beyond 600 nm from the sensor chip surface. The high signal-to-noise ratios achievable with evanescent field sensors are partially due to this insensitivity towards changes in the bulk phase. In addition, identical interactions give rise to different signal shifts, depending on how close to the sensor surface the interaction occurs. For example, receptor–ligand binding along with non-specific interactions observed within 10 nm of the metal surface result in a nearly three times greater response than the same processes at a distance of 300 nm from the surface.

In addition to these characteristics of evanescent field optics, the physical laws governing the transport of solutes to the chip surface should be considered. Molecular transport and association to a sensor chip surface can be divided into three phases: convection, diffusion, and binding to the immobilized ligand. The product of these three processes results in the sensorgram, which is consequently influenced by a number of factors contributing to any of the three phases. Analyte transport to the sensor surface is primarily affected by convection. In the linear flow cells that are used in many commercial instruments, convection transport can be controlled simply by

View Online

Published on 24 May 2017 on http://pubs.rsc.org | doi:10.1039/9781788010283-00171

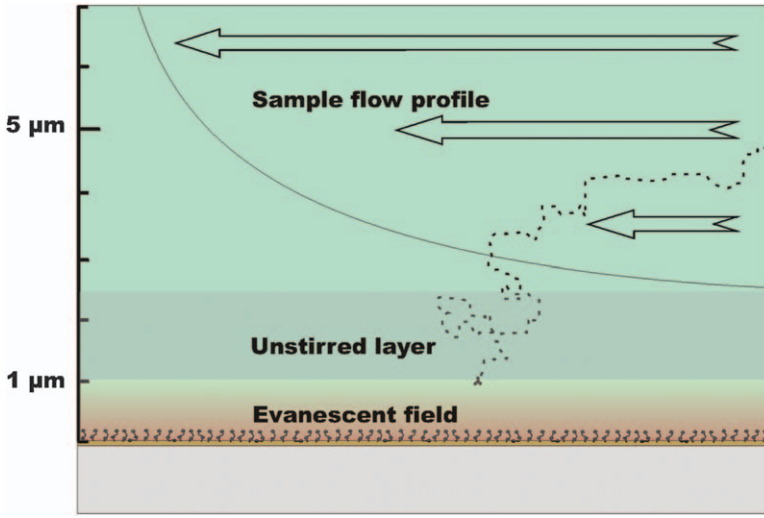


Figure 6.5 Dimensions of the evanescent field and the unstirred diffusion layer. Analyte molecules are first transported primarily by convection and then solely by diffusion.

adjusting the flow rate. A certain flow rate results in the so-called stagnant layer. High flow rates induce small stagnant layers. However, a stagnant layer of less than 2 µm is difficult to achieve. Other cuvette geometries, such as those employing the free wall-jet principle, allow the variation of more parameters, for example, the distance of the injector tip from the sensor surface, as described in Section 3.4.1 in Chapter 3. In all of these cases, the analyte is more or less efficiently transported to a distance of a few micrometers from the sensor chip surface but is still relatively far away from the evanescent field and any three-dimensional surface structures. Here, the unstirred diffusion layer begins, through which transport is solely affected by diffusion (see Figure 6.5).

The diffusion rate through this layer depends largely on the diffusion constant of the analyte molecules, which varies from 3×10^{-6}–6×10^{-6} $cm^2\ s^{-1}$ for low molecular weight substances to below 10^{-7} $cm^2\ s^{-1}$ for macromolecules with molecular weights of several hundred kDa. This corresponds to an average diffusion time through the unstirred layer ranging from less than 1 s for small molecules up to several seconds for high molecular weight compounds. The effective concentration of larger molecules in the evanescent field but not yet bound to the ligands at the sensor surface is thus typically lower than the concentration in the bulk solution. Even at the maximal flow rates, mass transport is often limiting for typical protein molecular weights above 10 kDa. Owing to their higher diffusion constants, the relative binding rates of small molecules are usually not affected by diffusion phenomena, even at high ligand densities. The effects of this mass transport limitation are clearly described in Section 4.3.3 in Chapter 4.

View Online

Published on 24 May 2017 on http://pubs.rsc.org | doi:10.1039/9781788010283-00171

For a given flow cell geometry at moderate flow rates, it is usually not possible to enhance the diffusion rate significantly above a certain upper limit because the limited volume of the sample or injection loops determines the maximum flow rate. In such cases and applications where diffusion limitations should be strictly avoided (*e.g.* kinetic analysis), the only way to circumvent diffusion-related problems is to decrease the density of immobilized ligand and/or increase the analyte concentration. If mass transport-limited binding is desired (*e.g.* for concentration determination), in addition to decreasing the flow and thus the diffusion rate, higher immobilization densities of the ligand should be chosen. For both low and high immobilization densities, a correctly selected surface nanoarchitecture can be extremely useful to control the amount of immobilized ligand. The final step in the process of biomolecular interaction is the (specific) capture of the analyte by the immobilized ligand, which is governed by the kinetics of the interaction and the properties of the nanoenvironment around the ligand–analyte pair.

In kinetic analysis, it is essential that the binding sites are not sterically hindered and that their affinity is not affected by the immobilization process, as both can lead to heterogeneously distributed affinities.[3,4] Chapter 5 describes a method for determining rate and equilibrium constants based on distribution analysis. A detailed characterization of the distribution of binding properties provides a useful tool for the optimization of surface immobilization in order to study immobilization processes and surface properties in more detail, with the goal of efficient functionalization of biosensor surfaces with uniform high-affinity binding sites[5] (see Figure 6.6).

Sufficient spacing between ligands is helpful in decreasing steric problems caused by an overly high ligand density; however, a nanoscale homogeneous immobilization matrix is still required. This can be achieved by controlling the immobilization density or, better – as shown in Figure 6.7 – by structuring the sensor surface so that a diluted ligand density is an intrinsic characteristic of the sensor surface itself. In this way, unwanted steric effects and artifacts caused by a too high density of charged groups are minimized.

Furthermore, directed immobilization through molecule capture may be necessary for ligands that cannot be immobilized by other methods or to maintain the homogeneity of a binding site population that might otherwise be compromised by the random distribution of covalent bonds with the immobilization matrix. Finally, the surface charge can affect the interaction kinetics along with the extent of non-specific interactions, hence this feature should also be controlled.

Qualitative checks and assays with the purpose of analyte quantification are generally less critical as a certain degree of diffusion limitation is allowable, if not desired. In most cases, relatively thick hydrogels with high immobilization densities are advantageous for maximizing the specific signal and deplete the unstirred layer of analyte during the initial phase of interaction. Under these conditions, analyte binding is heavily diffusion controlled, and the linear slope of the binding curve is then directly

View Online

Published on 24 May 2017 on http://pubs.rsc.org | doi:10.1039/9781788010283-00171

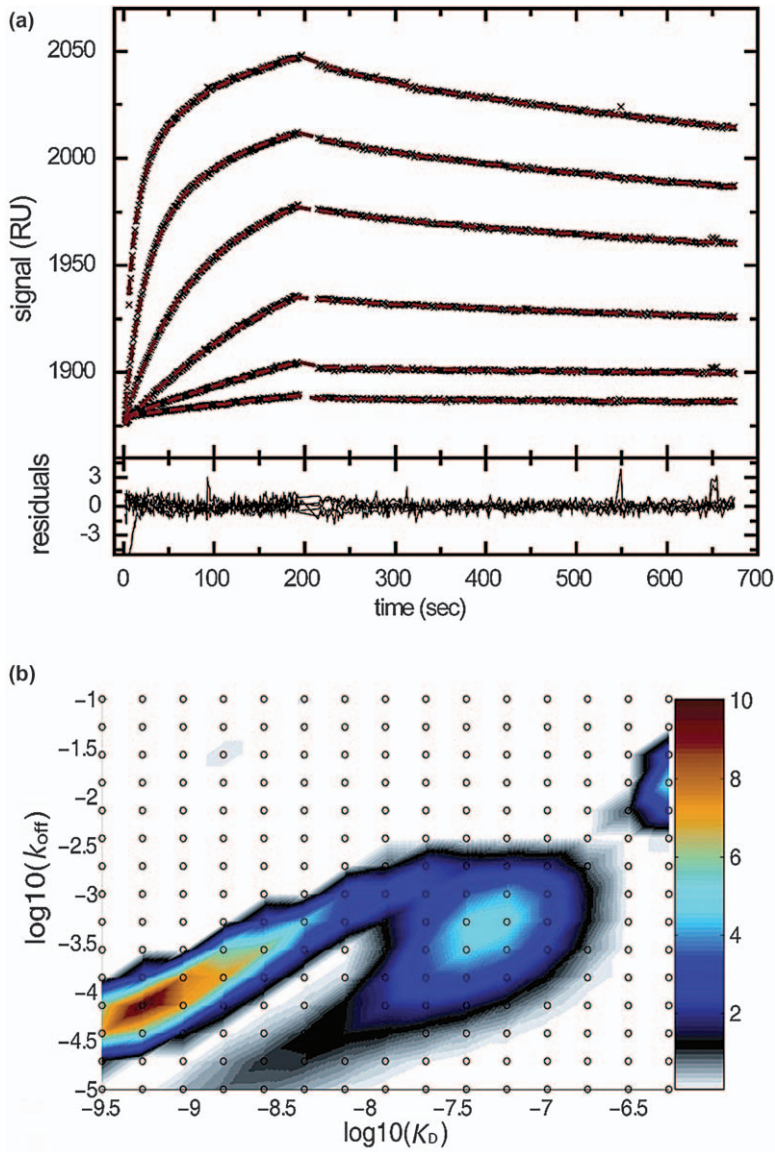


Figure 6.6 Distribution analysis of complex experimental surface binding kinetics of myoglobin binding to monoclonal antibody immobilized in the carboxymethyldextran matrix of a Biacore CM5 sensor chip. The two-dimensional rate and affinity constant distribution indicates heterogeneous binding sites with different affinities. This distribution analysis method is treated in Chapter 5.
Reprinted from J. Svitel, A. Balbo, R. A. Mariuzza, N. R. Gonzales and P. Schuck, Combined affinity and rate constant distributions of ligand populations from experimental surface binding kinetics and equilibria, *Biophys. J.*, **84**(6), 4062–4077. Copyright 2003, with permission from Elsevier.

View Online

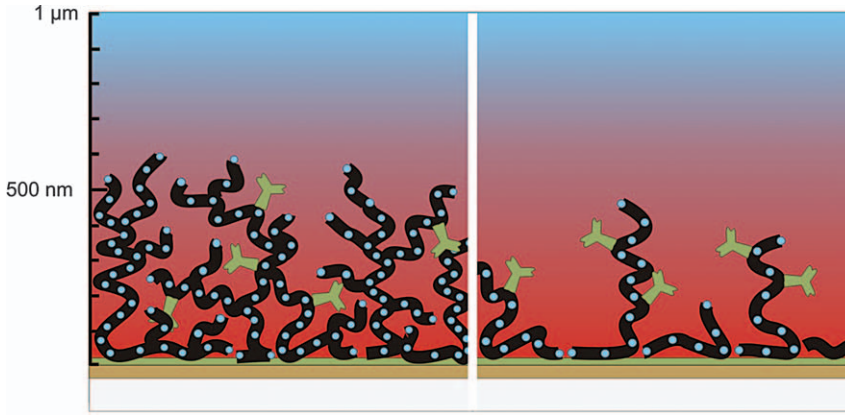


Figure 6.7 Low ligand density in a diluted hydrogel (right) *versus* reducing the immobilization density in a dense hydrogel matrix (left).

proportional to the analyte concentration in the sample, which is the prerequisite for a precise assay.

6.2 The Metal Layer of SPR Sensor Chips

As discussed in Chapter 2, SPR occurs in thin films of certain conducting materials deposited on transparent and usually dielectric substrates. More than a dozen metals, such as silver, copper, gold, aluminum, cadmium, and even iron,[6] along with some conducting metal oxides[7] show this phenomenon. To achieve a sharp SPR-dip, which is desirable because it usually results in a better signal-to-noise ratio, a high ratio $W = |\epsilon'|/|\epsilon''|$ between the real and imaginary parts of the material's complex refractive index $\epsilon = \epsilon' + i\epsilon''$ is preferred. Silver ($W = 37.96$), copper ($W = 20.38$), and gold ($W = 7.33$) give the highest ratios; however, only gold is used in practical applications as the chemical inertness of thin silver and copper layers is poor, causing them to corrode quickly in aqueous buffers containing oxygen and salt. Furthermore, with the most frequently employed weighted centroid method (see Section 2.3.6.2 in Chapter 2), a sharp resonance peak does not necessarily result in a higher signal-to-noise ratio; more significantly, gold has been shown to exhibit a higher refractive sensitivity[8] in today's dominant Kretschmann setups with angular interrogation.

Although the macroscopic appearance of a gold film deposited on a polished glass substrate suggests a smooth surface, the STM analysis of vacuum-deposited gold films reveals uneven topologies at the nanoscale (Figure 6.8).

Depending on the deposition method, the typical peak-to-peak roughness can easily reach 10 nm and more, which is significant considering that the thickness of a self-assembled monolayer (SAM) typically employed for the surface derivatization of biosensor substrates is around 1 nm.

Published on 24 May 2017 on http://pubs.rsc.org | doi:10.1039/9781788010283-00171

View Online

Published on 24 May 2017 on http://pubs.rsc.org | doi:10.1039/9781788010283-00171

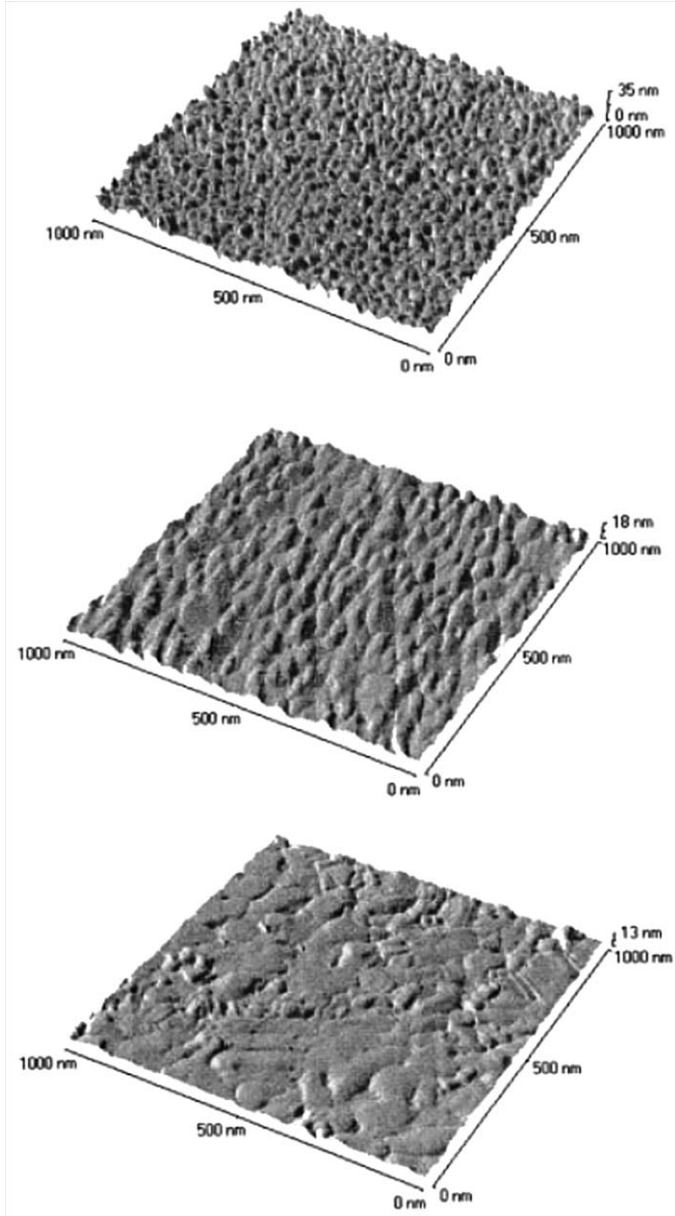


Figure 6.8 3D STM images of Au films deposited by thermal evaporation (top), magnetron sputtering (middle), and filtered arc deposition (bottom). Reprinted from A. Bendavid, P. J. Martin and L. Wieczorek, Morphology and optical properties of gold thin films prepared by filtered arc depoision, *Thin Solid Films*, **354**(1–2), 169–175. Copyright 1999, with permission from Elsevier.

View Online

Published on 24 May 2017 on http://pubs.rsc.org | doi:10.1039/9781788010283-00171

The refractive sensitivity does not depend on the thickness of the gold film;[9] however, to achieve a maximal resonance peak, gold film thicknesses from 40 to 55 nm are typically chosen. Thinner films give broader, asymmetric and deeper dips, and greater thicknesses give sharper and more symmetrical but less pronounced dips.

Sputtering yields dense, polycrystalline films with good adhesion properties, making it the preferred method. If thermal evaporation is used, an additional annealing step can slightly smooth the surface, resulting in a somewhat sharper dip and less long-term drift.[10]

Although high-energy deposition methods such as magnetron sputtering allow the direct deposition of gold on glass,[11] an additional adhesion layer is typically used because noble metals exhibit low adhesion to glass surfaces. The ideal adhesion promoter is highly transparent and does not damp the surface plasmons or decrease the reflectivity. Although non-metallic modifiers such as mercapto-functionalized silanes[12] or metal oxides are occasionally employed, chromium and titanium layers with thicknesses of a few nanometers are preferred owing to their chemical inertness and compatibility with the industrial equipment used to deposit thin films. Titanium has been reported to have slight advantages over chromium as its deposition process is more robust and its optical transmission is better.[13]

Recently, numerous approaches to improve the signal-to-noise ratio of SPR setups by modifying the metal layer and/or substrate material have been reported.[14] Enhancing the local field or the penetration depth is the most common method for enhancing the interaction integral in evanescent field sensing. Chip architectures that are able to excite long-range plasmons (LR-SPR), leading to an extended and more intense evanescent field, have been developed.[15] In the case of spectral interrogation, bimetallic silver–gold layers have been used to combine the superior optical characteristics of silver with the chemical inertness of gold.[16] Gratings were added on top of the metal layer, providing the required momentum to match to the incidence light and coupling it to the surface plasmons along with perturbing the propagation of the surface plasmons.[17]

More recently, considerable efforts have exploited localized SPs in metallic nanostructures. Localized SPR (LSPR) substrates in combination with wavelength interrogation result in the structure-dependent enhancement of the local evanescent field (Figure 6.9).

A wide variety of nanoparticle shapes have been proposed as LSPR sensors, such as rings, dots, stars, nanobottles, nanoprisms, nanocubes, and nanorice.[18] Depending on the nanoarchitecture chosen, the spectral sensitivity could be increased, and the bandwidth tuned within several orders of magnitude. Nanoholes, nanoslits, nanocircles, nanoarrays, and other nanoapertures have similar effects. In contrast to conventional SPR sensors, the phase-matching condition for exciting SPs in zero-order transmission can be tuned by the architecture of the holes, while prism coupling is not required.

View Online

Published on 24 May 2017 on http://pubs.rsc.org | doi:10.1039/9781788010283-00171

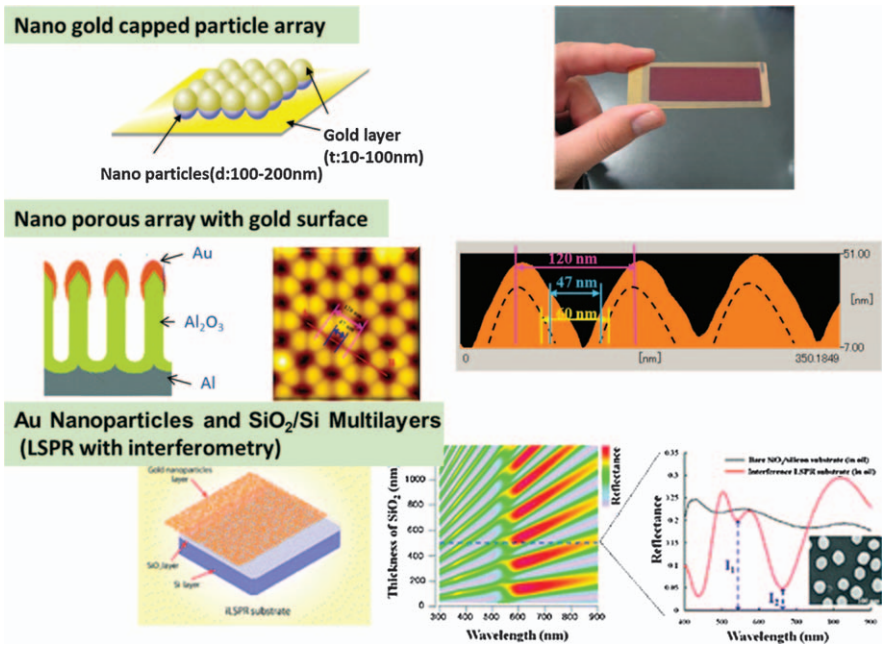


Figure 6.9 Plasmonic nanostructures for LSPR-based biosensor chips. Reprinted with permission from H. M. Hiep, H. Yoshikawa, M. Saito and E. Tamiya, An interference localized surface plasmon resonance biosensor based on the photonic structure of Au nanoparticles and SiO_2/Si multilayers, *ACS Nano*, 2009, **3**(2), 446–452. Copyright 2009 American Chemical Society, and from M. C. Vestergaard, K. Kerman, I. M. Hsing and E. Tamiya, *Nanobiosensors and Nanobioanalyses*, 2015, vol. 1, Copyright 2015 Springer Japan. With permission from Springer.

Notwithstanding, many issues related to the above developments remain to be addressed. For example, the reproducible and economical large-scale manufacturing of complex nanostructures that combine drastically enhanced sensitivities, tunable characteristics, highly localized sensing areas, and a relatively simple optical setup has the potential to form the basis for a new generation of miniaturized low-cost SPR devices that may find their way into diagnostics and related mass applications.

6.3 Adhesion Linking Layers for Noble Metals, Inorganic Dielectrics, and Plastics

As outlined in the previous section, it is necessary to protect the sensitive biomolecular ligands from the usually incompatible chip substrate material. In addition, suitable functional groups for ligand immobilization have to be introduced. This is usually achieved by coating the substrate with a bioinert layer that contains functionalizable groups, typically carboxylates. As one of

View Online

Published on 24 May 2017 on http://pubs.rsc.org | doi:10.1039/9781788010283-00171

the key characteristics of these layers – their hydrophilicity – makes them water soluble, they would be washed away without the use of an adhesion linking layer, which promotes adhesion to the substrate material. Therefore, a typical biochip coating contains at least three functional components: an adhesion linking layer, a bioinert matrix, and ligands coupled to the matrix. In this part, various aspects of the adhesion linking layer are discussed.

A good adhesion linking layer should not only provide a stable link between the substrate material and immobilization matrix, but also shield the substrate from the sample buffer with a dense and homogeneous film. With respect to the exponentially decaying structure of the evanescent field, this layer is preferably a close-shielding monolayer as thicknesses greater than 10 nm significantly decrease the sensitivity of the sensor and can lead to baseline drift due to swelling effects. On the other hand, thicknesses less than 1 nm usually result in unstable and inhomogeneous coatings; therefore, a good adhesion linking layer should form layers with thicknesses between 2 and 5 nm. Finally, the refractive index of the adhesion linking layer should be low, at least lower than that of the substrate material. Depending on the surface-exposed material of the biochip substrate – typically gold or glass – different routes are chosen to address the above requirements.

6.3.1 Adhesion Linking Layers for Noble Metal Surfaces

The surfaces of many transition metals are soft electron-pair acceptors and exhibit a strong affinity towards soft electron-pair donors such as thiols, disulfides, and thioethers. This allows the direct immobilization of biological ligands on noble metal surfaces *via* naturally present or subsequently introduced thiolated functional groups. However, as proteins tend to unfold and denature upon contact with metals and most other artificial substrates, these approaches are usually limited to more robust ligand–analyte systems such as nucleic acids. Advanced chip architectures efficiently stabilize the surface against non-specific interactions from the analyte matrix and screen the ligand and analyte from undesirable contact with the underlying metal, both of which require a more complex multilayer approach.

As shown in Figure 6.10, alkyl derivatives of the above-mentioned functional groups with chain lengths greater than 10 carbon atoms assemble spontaneously on such substrates and form SAMs with high packing densities.[19] Shorter thiols also assemble, but the SAMs are not well defined and are relatively unstable.[20]

Monofunctional mercaptoalkyls yield hydrophobic surfaces having contact angles greater than 100°. Bifunctional derivatives form monolayers with defined chemistries, which are useful intermediates for the covalent coupling of ligands or for further derivatization.[21] Typical examples of such compounds are 16-hydroxyhexadecane-1-thiol and the corresponding carboxylated version 15-carboxypentadecane-1-thiol. The adsorption of these long-chain thiols usually takes place in 1–5 mM ethanolic solutions

View Online

Published on 24 May 2017 on http://pubs.rsc.org | doi:10.1039/9781788010283-00171

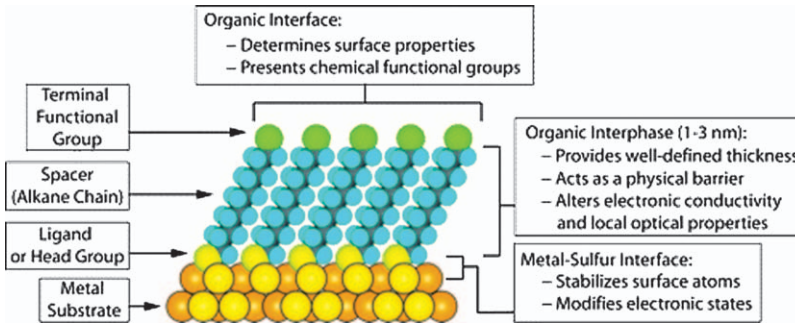


Figure 6.10 Schematic diagram of an ideal, single-crystalline SAM of alkanethiolates supported on a gold surface with a (111) texture. The anatomy and characteristics of the SAM are highlighted.
Reprinted with permission from J. C. Love, L. A. Estroff, J. K. Kriebel, R. G. Nuzzo and G. M. Whitesides, Self-assembled monolayers of thiolates on metals as a form of nanotechnology, *Chem. Rev.*, 2005, **105**, 1103–1169. Copyright 2005 American Chemical Society.

over 8–24 h. Although the formation of a monolayer is almost complete after a few minutes, the initially formed assembly is not well ordered and contains many *gauche* defects within the chains. Over time, the layer becomes more ordered and well packed. In addition to thiols, dithiols and thioethers are also suitable as these groups exhibit sufficiently high adsorption energies (typically in the range 40–50 kJ mol^{-1} or approximately 50% of the value for a C–C bond) on surfaces of group 7–12 metals. As discussed below in more detail, the stabilizing characteristics of the resulting surface (*i.e.* its inertness against the adsorption of proteins and other sample components) depend critically on the functionality of the surface exposed to the sample. However, the long-term stability of SAMs is limited as they show desorption after a few weeks of exposure to buffer or serum.[22] Stabilization through the adsorption of additional polymer layers increases the durability and can cover nanodefects.[23] A related but less common approach is the direct adsorption of positively charged or mercapto-derivatized polymers on the negatively charged metal surface. Owing to electrostatic attraction and the cooperative effect of several adsorption sites, stable monolayers can be formed.

An alternative way to modify the surface of a conducting material such as the gold interface of the SPR chip is through the electrodeposition of thin oligomeric or polymeric films from monomers in solution. Polypyrrole is probably the most intensively investigated and widely used conducting polymer for biosensing, mainly owing to its stability, conductivity, and biocompatibility. The intensive use of and interest in such interfaces for anchoring bioreceptors onto biosensor interfaces is driven mainly by the following factors: (i) the polymer films are uniform, (ii) their thickness can be readily controlled, and (iii) the surface modification is limited to the surface of the electrode. In addition, electrochemistry can be easily integrated with SPR measurements. Both methods are compatible in the sense

View Online

Published on 24 May 2017 on http://pubs.rsc.org | doi:10.1039/9781788010283-00171

that they both rely on a conductive substrate (for electrochemistry, the gold film of the SPR interface is the working electrode) without disturbing its use for the generation of surface plasmons.[24]

Yet another option for modifying the bare gold surface is the addition of a thin (a few nanometers) overcoating of SiO_2 or, more recently, carbon. The former can be deposited from the gas phase[25] or by sol–gel processes and allows for further modification using the well-characterized and robust silanization protocols described below. The drawbacks of this approach are the sensitivity of SiO_2 towards hydrolysis, limited adhesion to gold, and difficulties in controlling the deposition process. Although less frequently employed, carbon layers offer a more stable alternative. Graphene[26] and amorphous carbon are particularly interesting materials as, unlike diamond layers, they can be deposited at relatively low temperatures.[27] The modification of these surfaces follows straightforward protocols *via* either oxidation (see below) or the introduction of reactive groups from the gas phase.

6.3.2 Adhesion Linking Layers for Inorganic Dielectrics

The classic modification route for glass, ceramics, and other oxidic surfaces is treatment with silanes, which are able to form stable silyl ether links with exposed hydroxyl groups.[28]

A frequently used and versatile silane is glycidylpropyltrimethoxysilane (GPTMS), which is reactive towards amino, sulfhydryl, and hydroxyl groups and, alternatively, can be hydrolyzed to yield a vicinal diol or further oxidized to an aldehyde or carboxylate. Another example is aminopropyltriethoxysilane (APTES), which is useful for coupling activated carboxyls, aldehydes, or glycidyl moieties. Under optimal conditions, the silanes assemble on the surface of a thoroughly cleaned[29] substrate in a uniform monolayer[30] following the reaction scheme depicted in Figure 6.11. If properly prepared, such an arrangement allows the attachment of the bioinert matrix or the direct attachment of the biomolecular ligand in a similarly uniform fashion.

6.3.3 Adhesion Linking Layers for Plastics and Carbon Surfaces

Although gold and glass currently are the dominant chip surface materials used for direct optical biosensors, it is foreseeable that future low-cost devices will increasingly rely on injection-molded consumables made from, for example, poly(methyl methacrylate) (PMMA), polystyrene, polycarbonate, and cycloolefin copolymers. The surfaces of these materials are complex, heterogeneous mixes of amorphous and crystalline regions consisting of mostly hydrophobic polymer chains that often slowly migrate and rearrange over time. The modification of these kinds of substrates usually begins with an oxidative pretreatment, either *via* a wet-etching step[31] or, more

View Online

Published on 24 May 2017 on http://pubs.rsc.org | doi:10.1039/9781788010283-00171

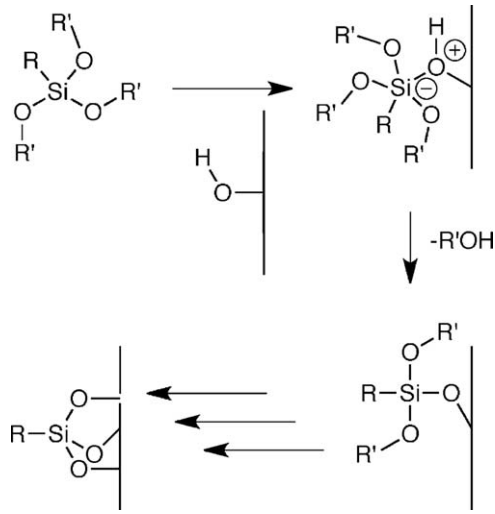


Figure 6.11 The silanization of glass substrates with trialkoxysilanes follows an addition–elimination mechanism and results in multiple surface-silane bonds.
Reproduced from ref. 129 with permission from the Royal Society of Chemistry.

reproducibly, oxygen plasma treatment.[32] The immobilization matrix can then be coupled either directly or *via* the subsequent adsorption of stabilizing polymer layers.[33]

Regardless of the substrate material, adhesion linking layers can be further applied *via* plasma deposition,[34] allowing the fast and simultaneous processing of large batch volumes, and can yield homogeneous coatings with different chemical functionalities at relatively low cost per unit. Typical methods for the preparation of thick films, such as dip or spin coating, are less suitable as the necessary coating thickness of a few nanometers is difficult to control reproducibly with these techniques.

6.4 Bioinert Matrices

Although the aforementioned adhesion mediators are optimized in terms of interaction with the substrate material, this characteristic induces a significant level of non-specific binding from the sample. Therefore, the addition of a bioinert topcoat or immobilization matrix is necessary.

6.4.1 Non-specific Adsorption of Biomolecules

The non-specific adsorption of heterogeneous macromolecules such as proteins or larger aggregates on surfaces is a central aspect in the design of biocompatible materials. However, the complex multi-step interaction

View Online

Published on 24 May 2017 on http://pubs.rsc.org | doi:10.1039/9781788010283-00171

process depends on the varying compositions and concentrations of potentially adhering components in the bulk and at the surface, which are still not fully understood. For example, the initial adsorption of plasma proteins is dominated by the smaller protein (albumin), which is present at a higher concentration in the bulk, whereas subsequent adsorption is dominated by larger proteins such as IgG and fibrinogen. This sequential adsorption is called the Vroman sequence[35] and explains the competitive adsorption of plasma proteins for a limited number of surface sites. The reorganization and stapling of biomolecules occur and are dependent on several factors and surface parameters.

Dynamically, adsorbing species undergo three phases:[36]

1. transport to the surface by convection and diffusion (see Figure 6.5);
2. reversible (labile) attachment on first contact; and
3. spreading and conformational rearrangement.

Whereas the transport rate is an effective means to control the extent of protein adsorption, the initial phase cannot be influenced by the surface functionality and structure. However, it is possible to tune the degree of protein attachment and subsequent processes by optimizing the nanoarchitecture and molecular-scale functional design of the surface. In this context, it should be stressed that the interaction of the surface and proteins with the solvent water plays an prominent role as the surrounding water molecules compete with potential attachment sites. The high internal energy of water (cohesion) favors the exclusion of low-energy sites (*i.e.* hydrophobic domains), which consequently tend to agglomerate *via* hydrophobic interaction, an entropic phenomenon related to the degree of organization of water molecules. This driving force leads to conformational changes after the adsorption of proteins to hydrophobic moieties. Proteins attached to poorly hydrated or attractive surfaces, regardless of whether they are nonspecifically attached or immobilize, undergo substantial deformation into a pancake-like structure.[37] This deformation process is typically irreversible and deactivates the protein. If the adsorbed proteins retain some lateral mobility, clustering can occur[38] as a secondary process, highlighting the drawbacks of models based upon simple Langmuir isotherms. Therefore, an essential prerequisite of a bioinert matrix is not simply hydrophilicity, but also a high degree of hydration. In general, the more hydrophilic the surface, the stronger is the surface–water interaction and the higher the degree of water molecule organization, and hence less chaotic behavior. Hydrophobic molecules will merely adsorb irreversibly on the hydrophilic surface (*e.g.* by unfolding hydrophobic sites that favor the increase in entropy of the total system upon binding). This primary interaction is the likely basis for two distinct types of response seen on hydrophobic and hydrophilic surfaces.[39] Moreover, at a hydrophobic surface, the hydrogen bonding among water molecules is disrupted, and significant surface dewetting that extends into bulk water is observed.

View Online

Published on 24 May 2017 on http://pubs.rsc.org | doi:10.1039/9781788010283-00171

In addition to hydrophilicity, the surface charge is an important factor. It is obvious that proteins will be attracted by oppositely charged structures. However, at medium and high ionic buffer strengths and physiological pH, ionic groups are usually surrounded by counterions; thus, if the charge density of the surface is not overly high, this effect is often less significant than expected. In this context, one should consider that the hydration spheres of ionized groups bind water molecules and therefore contribute to the bioinertness of the surface.

If not accompanied by irreversible secondary processes such as hydrophobic adsorption or covalent coupling, the electrostatic interaction is typically fully reversible at high ionic strength. If the underlying mechanism of protein adsorption is unknown, increasing the ionic strength is a useful approach to discriminate between ionic and hydrophobic interactions, as the latter are strengthened (*i.e.* are irreversible) under these conditions.

In addition to its reversible character, electrosorption is a relatively well-defined process and can be controlled by pH-induced charge shifts of adsorbates with defined p*I* values. Furthermore, electrosorption is self-terminated when electrostatic neutrality is reached. However, it should be noted that even proteins bearing the same charges on a strongly charged surface can show significant adsorption and override the net Coulombic force in low ionic strength solution.[40] Oppositely charged domains on a protein interacting with a homogeneously charged surface are likely to be a factor by driving out small counter-ions; this entropy-driven phenomenon is referred to as counter-ion evaporation.[41]

6.4.2 Functionalization Strategies for Ultralow-fouling Two-dimensional Surfaces

In accordance with the above, a molecular-level survey of the structure–property relationships of different functionalized surfaces[42] revealed that most surfaces that resist the adsorption of proteins incorporate groups that exhibit hydrophilicity and neutral overall charge. Another factor is the presence of hydrogen-bond donors and the absence of hydrogen-bond acceptors, indicating the role of hydrogen bonding as a third force that contributes significantly to biomolecular interactions. However, carbohydrate-based surfaces, many of which are highly protein resistant, do not follow this rule, indicating that not all aspects of surface–protein interactions are covered by this model. Again, water is likely to be the key in this observation as uncharged carbohydrates are reported to orient up to three layers of water.[43]

A popular and well-studied method of surface coating for reducing protein adsorption is derivatization with molecules containing poly(ethylene oxide), which are frequently called poly(ethylene glycol) (PEG) groups (*i.e.* the "pegylation" of the substrate).[44] Their ability to generate protein-resistant surfaces is often attributed to the fact that PEG chains are hydrated, neutral, highly mobile, and flexible. Many different strategies have been employed to obtain

View Online

Published on 24 May 2017 on http://pubs.rsc.org | doi:10.1039/9781788010283-00171

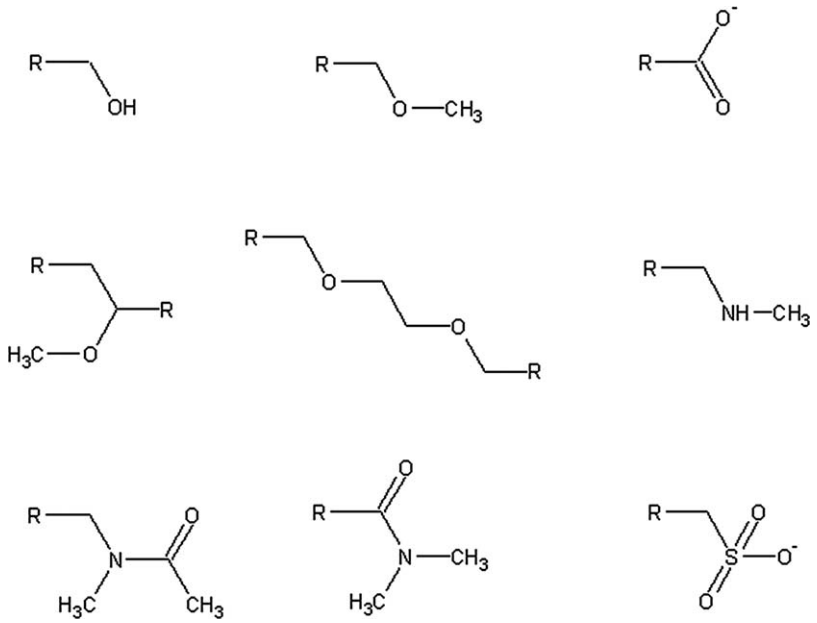


Figure 6.12 Selected protein-compatible functional groups.

PEG-containing surface coatings ranging from short-chain mixed SAMs[45] to long linear PEG chains[46,47] and multi-arm star-shaped polymers[48] (see Figure 6.12).

Despite their wide use, PEGs present some drawbacks since even at high densities, they are not able to eliminate protein adsorption completely; furthermore, they can be oxidized spontaneously or enzymatically in a physiological environment.[49,50]

More recently, various forms of zwitterionic surface derivatization have attracted increasing interest as these biomimetic, extremely hydrated although overall uncharged moieties can reduce non-specific binding to almost undetectable levels, even in full serum. As shown in Figure 6.13, common zwitterions are carboxy-, sulfo- and phosphobetaines, either as headgroups of a SAM or as part of a functionalized polymer.[51] A related approach is the use of so-called patterned peptides, gold affine SAMs that are terminally functionalized with short peptides comprising amino acids with opposite charges.[52] By adding appropriate chemical modifications, functional groups for further derivatization or ligand immobilization can be introduced.

With all of these approaches, one should keep in mind that owing to the relatively low density of attachment sites and layer thickness of a few nanometers, the ligand immobilization capacity of the presented chemistries is typically limited to a monolayer. Thus, the extent of non-specific binding must be extremely low to obtain an acceptable signal-to-background ratio.

Published on 24 May 2017 on http://pubs.rsc.org | doi:10

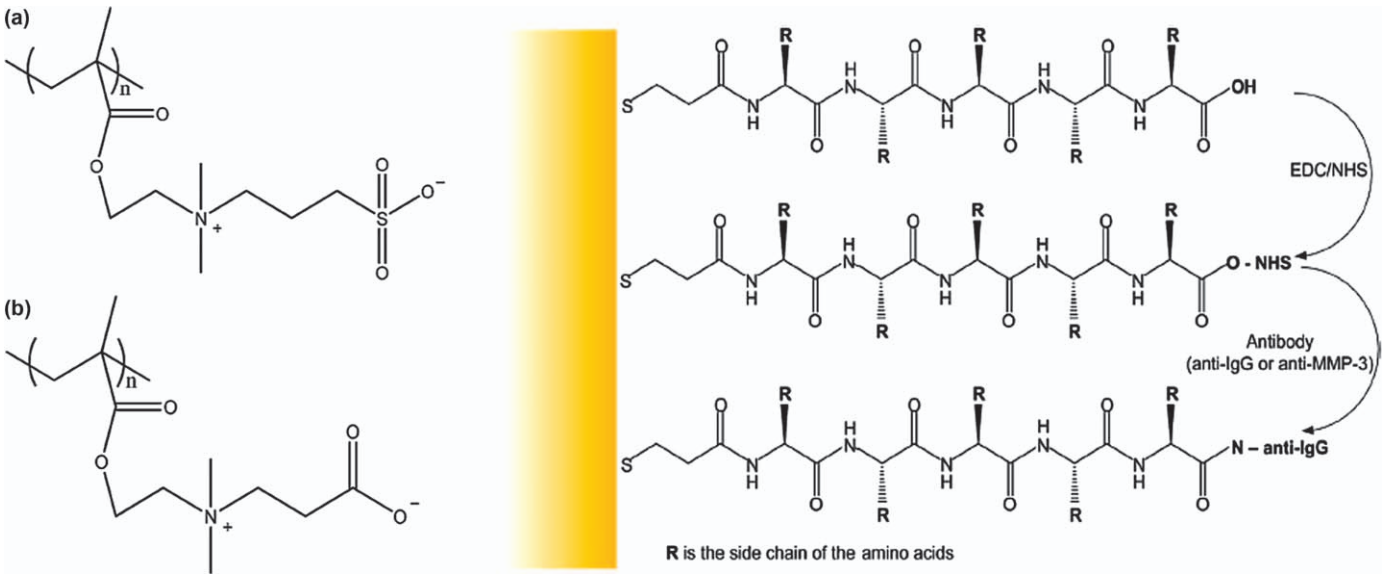


Figure 6.13 Left: sulfobetaine (a) and carboxybetaine (b) functional groups in a zwitterionic polymer. Right: EDC–NHS-mediated coupling of IgG to the C-terminus of a zwitterionic peptide coating.
Reprinted with permission from O. R. Bolduc, J. N. Pelletier and J.-F. Masson, SPR biosensing in crude serum using ultralow fouling binary patterned peptide SAM, *Anal. Chem.*, 2010, **82**(9), 3699. Copyright 2010 American Chemical Society, and from S. Jiang and Z. Cao, Ultralow-fouling, functionalizable, and hydrolyzable zwitterionic materials and their derivatives for biological applications, *Adv. Mater.*, **22**, 920–932. Copyright 2010 Wiley-VCH Verlag GmbH & Co. KGaA, Weinheim.

View Online

Published on 24 May 2017 on http://pubs.rsc.org | doi:10.1039/9781788010283-00171

6.4.3 Bioinert Hydrogels

In addition to choosing suitable functionalities at the molecular scale, the bioinertness of a surface can be controlled by structural means. Polymers grafted to the surface in a so-called hydrogel are an effective way to prevent the adsorption of proteins. As the amount of protein adsorbed is the result of the interplay between the bare surface–protein interactions, the competition between the proteins and the polymer chains to be in the vicinity of the surface, the polymer–protein interactions, and the conformational statistics of both the protein and polymer molecules, it is obvious that variations in the coating's nanoarchitecture result in different adsorption characteristics of the coated surface.

The surface stabilization by hydrogels is mainly due to two factors:

1. The enthalpic stabilization by tightly bound water around the polymer molecules. The more hydrated the polymer is, the more energy is needed to penetrate the hydration shell and interact with the polymer. Note that the underlying mechanism is the same, which also stabilizes 2D surfaces.
2. The decreasing degree of freedom of surface-bound polymer chains when a protein molecule approaches the coated surface. This leads to an energetically unfavorable entropic loss, causing the system to be more stable if dissolved macromolecular species do not interfere with the polymer layer.

The contribution of the enthalpic part is clearly larger, which can indirectly be attributed to the presence of highly stabilized planar surfaces that do not contain any hydrogels at all. On the other hand, this means that attractive forces between a macromolecular solute and a grafted, moderately hydrated polymer can override the entropic stabilization effect. Such a constellation can result in massive non-specific interactions several times greater in magnitude than on an uncoated substrate, which would be spontaneously covered by a dense protein monolayer.

Theoretical studies using mean-field theory[†53] demonstrate that branched and loop polymers are more effective than flexible linear chains in preventing protein adsorption[54] as they are somewhat more rigid and can provide a denser concentration of desired functional groups. For example, dendritic polyglycerols have shown good protein resistance and proven superior to dextran coatings used to reduce non-specific binding.[55] However, other features important for evanescent field biochips (*e.g.* immobilization

[†]A theory that describes the behavior of surface-grafted polymer chains. At moderate surface concentrations (semidilute regime), the statistical mechanical properties of the chains can be evaluated by analogy with the classical mechanics of a particle moving in a mean potential field. The analytical solutions of this theory provide a convenient way to explore the conformations and the interactions of such surfaces.

View Online

Published on 24 May 2017 on http://pubs.rsc.org | doi:10.1039/9781788010283-00171

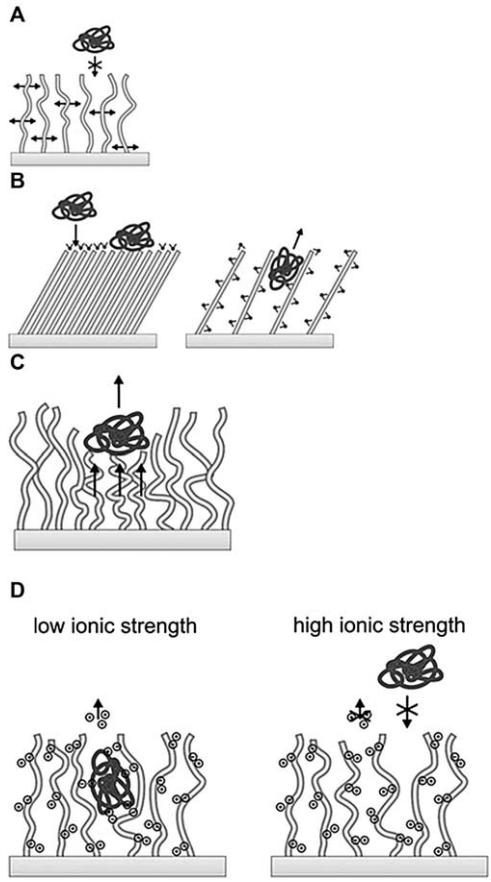


Figure 6.14 Schematic depiction of the different protein adsorption models. (A) Mobility model: ''wagging off'' of the protein molecules due to the high polymer chain mobility. (B) Water barrier model: tightly bound water on top of the layer or along the chains prevents interaction between polymer and protein. (C) Entropy model: protein adsorption is not favorable owing to a loss of entropy caused by the compression of the restricted volume of polymer chains by proteins. (D) Counter-ion release model: depending on the ionic strength of the surrounding medium, protein adsorption occurs.
Figure and text reproduced from ref. 130 with permission from the Royal Society of Chemistry.

capacity, nanoscale homogeneity, and diffusion characteristics) should also be considered, and these factors usually favor the use of more defined linear structures as the immobilization matrix (see Figure 6.14)

An additional feature of hydrogels for SPR-based biosensors is that the hydrogel can be tuned to fit the evanescent field. Ligands can be both coupled directly to the surface and immobilized in the evanescent volume, making higher ligand loading feasible. However, if the hydrogel becomes too

View Online

Table 6.2 Some hydrophilic, protein-compatible polymers.

Class	Polymer
Polysaccharides, natural	Dextran
	Alginic acid
	Hyaluronic acid
	Heparin
	Chitosan
	Pectin
Polysaccharides, modified	Carboxymethyldextran
	Carboxymethylcellulose
Polyalcohols	Poly(vinyl alcohol)
	Poly(hydroxyethyl methacrylate)
Polyalcohol and polyether	Polyglycerol (dendrimer)
Polyethers	Poly(ethylene glycol)
	Poly(propylene glycol)
	Poly(ethylene glycol)–polyacrylate
Polycarboxylates	Poly(acrylic acid)
Polyamines	Poly-L-lysine
Polyzwitterions	Poly(carboxybetaine methacrylate)
	Poly(sulfobetaine methacrylate)

Published on 24 May 2017 on http://pubs.rsc.org | doi:10.1039/9781788010283-00171

thick and dense, ligands and analyte molecules may not penetrate into the evanescent field. The quality of the bioinert hydrogel layer in combination with the type of ligand that should be coupled determines to a great extent the quality of the resulting biomolecular interaction. In Table 6.2, some hydrophilic, protein-compatible polymers are listed. An in-depth evaluation and properties of three-dimensional hydrogels are summarized in Section 6.5.2.

It can be concluded that good bioinert matrices can almost quantitatively eliminate non-specific binding, even from complex samples such as serum and fermentation broths, and increase the signal-to-background ratio by several orders of magnitude.

6.5 Choosing the Optimal Nanoarchitecture

As outlined above and in Section 6.6, the molecular-scale functionalities of sensor chip surfaces mediate the immobilization of ligands and are effective means to minimize non-specific binding. However, their proper selection alone is usually not sufficient to achieve a reliable sensorgram. In addition, structural characteristics in the sub-micrometer range must also be considered; in other words, the quality of the nanoarchitecture (*e.g.* hydrogel) determines the coupling efficiency and thus the accuracy of the rate and equilibrium constant measurements. A homogeneous distribution of binding sites and a homogeneous structure at the nanolevel are always desired and important when it comes to kinetic analysis. Furthermore, different immobilization capacities are required depending on the application, and extra features such as a filter functionality may be advantageous in some

View Online

cases. All of these issues are addressed by the design of the nanostructured coating or bioinert matrix.

Coatings for bioanalytical and biomedical devices are usually divided into two major groups: two-dimensional (2D) planar coatings and three-dimensional (3D) hydrogels. Both types are employed in SPR biosensor chips.

Published on 24 May 2017 on http://pubs.rsc.org | doi:10.1039/9781788010283-00171

6.5.1 Two-dimensional Surfaces

Two-dimensional surfaces are used for applications that require a low immobilization capacity (*e.g.* the kinetic analysis of medium to high molecular weight compounds). As the maximum density of an immobilized ligand is limited to one monolayer (1–2 $ng\,mm^{-2}$ for a typical protein), the depletion of the diffusion layer from the analyte during the interaction phase can hardly occur. In addition, the diffusion of analyte to and from the ligand is not hindered by an extended immobilization matrix. Both of these factors contribute to kinetically controlled binding. This free accessibility also minimizes the rebinding of dissociated analyte to free binding sites during the dissociation phase, which can occur in extended hydrogels and results in the measured dissociation rate constant (apparent k_{off}) being lower than the true k_{off}.

Furthermore, the absence of a 3D matrix makes this surface type well suited for the detection of particulate analytes such as viruses or even whole cells as a hydrogel would be inaccessible for such bulky species (*i.e.* keep them outside the evanescent field). For the same reasons and as a result of the higher field intensity close to the chip surface, 2D structures are good choices for the immobilization of high molecular weight ligands, cell fragments, and lipid mono- and bilayers (Figure 6.15).

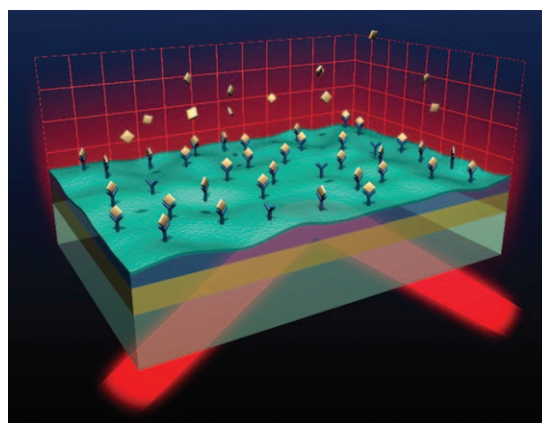


Figure 6.15 2D surface. Ligand molecules are immobilized on a thin (a few nanometers), planar immobilization matrix and are easily accessible to analyte molecules.

View Online

Published on 24 May 2017 on http://pubs.rsc.org | doi:10.1039/9781788010283-00171

Particularly for kinetic studies, homogeneous 2D coatings are essential as a narrow distribution of the immobilized ligand's activity and accessibility are prerequisites for an accurate fit of the resulting sensorgrams with the appropriate kinetic model. This can cause problems because the untreated surface of a sensor chip at the nanoscale is not a well-defined, homogeneous, two-dimensional plane. As pointed out in Section 6.2, most materials, including glasses, noble metals, and plastics, show an irregular nanotopology with a roughness well above 10 nm, corresponding to ~10 times the diameter of the immobilized ligand. The structure of the gold surface used in an SPR sensor depends on the deposition method; owing to the higher deposition energy, sputtered gold is denser and more homogeneous than vapor-deposited films, which consist of loosely adhered gold clusters. Nevertheless, as shown in Figure 6.8, the roughness is still significant. More problematic than this are molecular-scale inhomogeneities at the sub-micrometer level of an uneven structure, which can even be useful as they increase the surface area available for immobilization. Energetically, these steps, gaps, and tips represent discontinuities that can lead to pinhole defects in coatings, thus inducing local non-specific interactions and/or deactivating sensitive immobilized ligands (Figure 6.16). In this context, it should be noted that non-specific binding sites are of particular relevance for the aforementioned high-molecular weight molecules and aggregates because, owing to cooperative effects, a low percentage of such attachment points can be sufficient to induce the irreversible adsorption of larger species.

For these reasons, the frequently employed SAMs of long-chain mercaptoalkyls are not unproblematic, and it is advantageous to coat them with a second smoothing layer, ideally a thin polymeric layer. This second layer

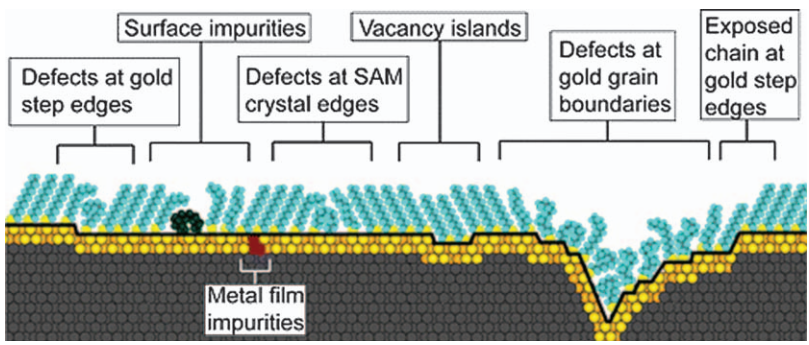


Figure 6.16 Schematic illustration of some of the intrinsic and extrinsic defects found in SAMs formed on polycrystalline substrates. The dark line at the metal/sulfur interface is a visual guide for the reader and indicates the changing topography of the substrate itself. Such defects can cause local non-specific interactions.
Reprinted with permission from J. C. Love, L. A. Estroff, J. K. Kriebel, R. G. Nuzzo and G. M. Whitesides, Self-assembled monolayers of thiolates on metals as a form of nanotechnology, *Chem. Rev.*, 2005, **105**, 1103–1169. Copyright 2005 American Chemical Society.

View Online

further increases the stability of the coating and can provide a spacer functionality, which is useful for increasing the accessibility of the immobilized ligand.

6.5.2 Three-dimensional Hydrogels

With a sufficiently sensitive detector, 2D surfaces are a good basis for many biomolecular interaction studies; however, numerous applications remain that require a ligand density greater than one monolayer, because either the analyte is relatively small (<2 kDa) or the optics are not sufficiently sensitive. A structurally flexible and strongly hydrated polymer brush is also useful for shielding the substrate and suppressing non-specific interactions. The enhanced accessibility of the ligand's binding sites and its increased mobility when immobilized through molecular spacers are further advantages. Hydrogels can also help to solubilize hydrophobic ligands that would otherwise tend to form insoluble aggregates on the chip surface and protect sensitive ligands against denaturation, especially in the dry state.

These obvious advantages led to the development of surface-grafted, typically brush-structured 3D hydrogels with thicknesses ranging from less than 10 to more than 1000 nm (see Figure 6.1). These structures provide an increased density of attachment sites and, more importantly, use a higher volume fraction of the evanescent field for the specific interaction, as is the case with 2D coatings. A welcome side effect of this approach is that the absolute influence of non-specific factors such as bulk shifts decreases proportionally with increasing occupation of the evanescent field volume by the ligand–analyte pair.

In principle, surface-grafted hydrogels can be made from any water-soluble polymer; however, in practice, polycarboxylates, polyethers, and polyols are preferred as they show significantly lower backgrounds than, for example, polyamines. In the early 1990s, the first commercial sensor chip coatings were derived from well-characterized, dextran-based solid phases for affinity chromatography. The most popular matrix material today is carboxymethylated dextran. Other carboxylated polysaccharides, such as alginate, pectin, carboxymethylcellulose, and hyaluronic acid, have occasionally been reported but are less common. Because these polymers are of natural origin, their structures are often not regular; that is, they can be more or less branched or form hyperstructures such as helices or suprafibers, thus contributing to heterogeneous binding site populations[5] (Figure 6.17). Furthermore, especially in the hydrated state, carbohydrates are relatively bulky molecules, occupying a considerable fraction of the evanescent field's volume that is then not available for the immobilization of ligand and hinders the free diffusion of analyte.

For these and other reasons, efforts have been made to replace polysaccharides with better defined synthetic polycarboxylates or zwitterionic polymers with lower backgrounds and smaller molecular footprints. In addition to reducing steric issues, coatings containing no hydroxyl groups

Published on 24 May 2017 on http://pubs.rsc.org | doi:10.1039/9781788010283-00171

View Online

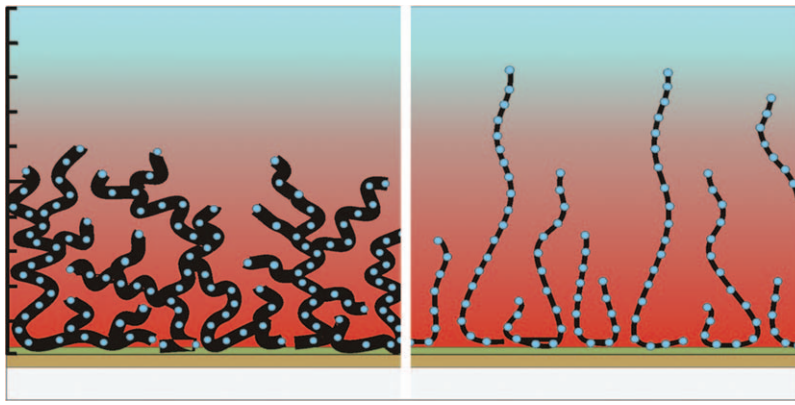


Figure 6.17 Structural differences between surface-grafted hydrogels based on polysaccharide (left) and synthetic polycarboxylate (right). See text for details.

Published on 24 May 2017 on http://pubs.rsc.org | doi:10.1039/9781788010283-00171

have the advantage that they cannot form ester crosslinks upon EDC [1-ethyl-3-(3-dimethylaminopropyl)carbodiimide]–NHS (*N*-hydroxysuccinimide) activation, a common side reaction with carboxymethylated carbohydrates. Furthermore, after activation, the NHS polyesters are moderately hydrophobic, which is a prerequisite for spotting ligand microarrays used for parallel detection with 2D SPR optics because if the surface is too hydrophilic, the spots run and merge. On the other hand (*i.e.* too much activation), the hydrophobicity can decrease the solubility of the NHS-activated polycarboxylate hydrogel; therefore, one should avoid over-activation.

Regardless of whether a natural polysaccharide or synthetic polymer is used, there are two main parameters that can be varied to control the immobilization capacity and diffusion characteristics of a 3D surface: the thickness and density of the hydrogel. The thickness depends on the molecular weight and structure of the polymer. Surface-grafted polymer monolayers with thicknesses from a few nanometers up to 2 μm with immobilization capacities ranging from 1 to >100 ng mm^{-2} can be realized. Using standard instrument configurations with angular detection, the maximum immobilization capacity achievable through hydrogels is ~150 mRIU (15°, 150 000 RU). Figure 6.18 shows that while the shift in resonance dip still lies within a (theoretically) detectable range, the peak flattens more and more until the minimum reflectivity becomes undetectable.

Typically, owing to the limited penetration depth of the evanescent field, thicknesses between 20 and 200 nm are employed; thicker hydrogels can be useful to achieve ultra-high immobilization densities for the detection of low molecular weight analytes. Hydrogels with thicknesses greater than 1 μm are also useful for keeping particulate contaminants and air bubbles outside the evanescent field, resulting in a very robust surface. Often, heavy diffusion limitation is observed in such structures, with a mean diffusion time of several seconds across the hydrogel.

In addition to controlling the thickness, the hydrogel's immobilization capacity can also be controlled by the hydrogel density. Moreover, variation

View Online

Published on 24 May 2017 on http://pubs.rsc.org | doi:10.1039/9781788010283-00171

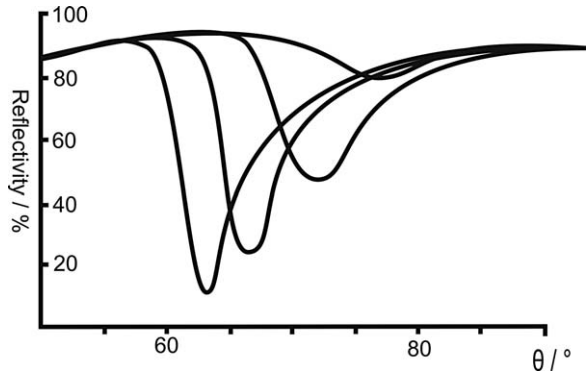


Figure 6.18 With increasing protein loading, the minimum reflectivity shifts to higher angles and flattens out until the SPR-dip completely disappears.

in the chain density can increase the selectivity as it can result in a filter effect, excluding macromolecules above a certain molecular weight. For mere detection or analyte quantification, it is advisable to choose relatively high density levels, as this not only maximizes the signal but also minimizes non-specific effects (see above). However, care must be taken to ensure that the hydrogel density is not too high, as analytes with molecular weights of 10 kDa or more can agglomerate in the upper layers of dense hydrogel matrices, clogging the pores and preventing subsequent analyte molecules from diffusing into the lower parts of the sensing layer. If the analyte carries hydrophobic domains, agglomeration and, in the worst case, the (partial) collapse of the hydrogel can occur. Irregularly shaped binding curves are typical indicators of this phenomenon. In addition, steric hindrance can result in heterogeneous immobilized binding sites shown in Figure 6.6.

It should be stressed that the above considerations apply only to medium and high molecular weight analytes. For low molecular weight (<1 kDa) compounds, a hydrogel with a maximum immobilization capacity should be chosen because these molecules are too small to be affected by high ligand densities and also diffuse fast enough to avoid mass transport limitations. Here, signal maximization and thus a maximum binding site density are the first priority; therefore, the hydrogel of choice for these applications should have a high thickness and medium to high density to permit high ligand loading on the hydrogel.

As an additional option for samples with particulate contaminants such as blood or crude fermentation broths, composite structures (*i.e.* hydrogels with additional filter layers) as depicted in Figure 6.19 can be advantageous. An unreactive, relatively thick hydrogel on top of the ligand-derivatized layer excludes particles and cells that might be present in the sample. These surfaces can also be used for assaying by acting as diffusion barriers so that most of the interaction takes place in a diffusion-controlled manner. The result is an extended linear slope of the binding curve, which is easy to fit and facilitates the calculation of analyte concentrations.

Irrespective of the surface structure, charge issues should also be considered when selecting chip coatings for a particular application. First, the surface

View Online

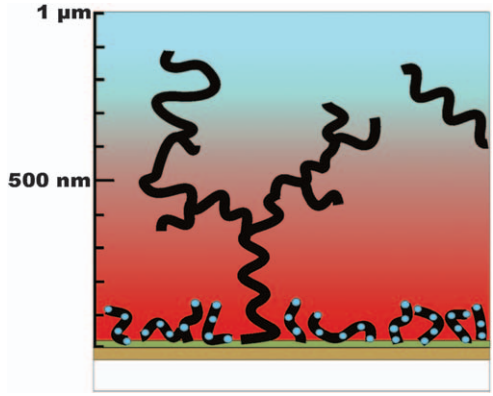


Figure 6.19 Schematic view of a hydrogel with an additional filter layer. Only the short polymer chains within the evanescent field are carboxyl functionalized and can immobilize ligands. The larger polymers do not carry ligands and prevent cells, cell debris, and particulate contaminants from entering the sensitive volume close to the chip surface.

Published on 24 May 2017 on http://pubs.rsc.org | doi:10.1039/9781788010283-00171

should be as uncharged as possible to minimize non-specific ionic interactions. Although most biomolecules are negatively charged and thus repelled by the usually anionic chip surfaces, numerous applications exist in which at least partially positively charged species that show significant adsorption to polycarboxylate surfaces are present. Biomedical serum-based systems are typical examples of such analyte matrices, and a low background is especially crucial in these systems as the analyte concentrations are often low.

A second critical aspect is the unwanted interaction of immobilized charged groups with either the ligand or the analyte. Although kinetic data obtained by SPR and homogeneous assays are usually comparable, a few cases have been reported in which the abundant carboxyl groups on a commercial carboxymethyldextran-coated sensor chip resulted in a K_D that is approximately two orders of magnitude different from that obtained by a solution-based reference assay. This effect could be significantly reduced by decreasing the negative charge density on the chip surface.[56]

As a certain amount of COOH groups is usually required for the electrostatic preconcentration of the ligand during the immobilization process and its covalent attachment, the carboxyl density has to be optimized in these cases. For dextran-based hydrogels, it was found that a reduction in the carboxymethylation level from one COOH group per anhydroglucose unit to one group per each four to eight units effectively reduces non-specific ionic interactions while maintaining a sufficient density of attachment sites.

On the other hand, situations may occur where the charge density (*i.e.* the strength of the carboxyl functionalities) is not sufficient. An example of such a situation is the immobilization of compounds with a p*I* below 4. Within the pH range of the typically applied preconcentration buffers, these molecules are still negatively charged, making their electrostatic accumulation in the hydrogel matrix difficult. Furthermore, below pH 4, an increasing

View Online

Published on 24 May 2017 on http://pubs.rsc.org | doi:10.1039/9781788010283-00171

percentage of the hydrogel-bound carboxylate groups is protonated (*i.e.* uncharged), thus enhancing this effect even more. Here, the introduction of strong acids such as sulfonate groups into the matrix is helpful as they remain unprotonated over the entire pH range and, at sufficiently low pH, can even attract relatively acidic species. A relatively straightforward way to introduce sulfo groups is activation with sulfo-NHS instead of the non-sulfonated compound. In Table 6.3, suitable nanostructures for various applications are presented.

Table 6.3 Suitable nanostructures for various applications.

Application	Suggested structure
Protein–protein, assay	Hydrogel, 100–500 nm, low to medium density. Linear polycarboxylate or carboxylated polysaccharide
Protein–protein, kinetics	Well-stabilized carboxylated 2D surface. Hydrogel, <50 nm, low density. Linear polycarboxylate
Protein–DNA or –polysaccharide	Hydrogel, 100–500 nm, low to medium density. Linear polycarboxylate
Protein–peptide or –small molecule	Hydrogel, >500 nm, high density. Linear polycarboxylate or carboxylated polysaccharide
Protein–cell, –virus, or –particle	Thin hydrogel, <20 nm, high density. Linear polycarboxylate or carboxylated polysaccharide. Well-stabilized carboxylated 2D surface
DNA–DNA, –small molecule or –peptide	Hydrogel, >300 nm, high density. Linear polycarboxylate.
DNA–protein	Hydrogel, 100–500 nm, low to medium density. Carboxylated (streptavidin-modified) polysaccharide
Cell, virus, particle, lipid bilayers–any species	Thin hydrogel, <20 nm, high density. Linear polycarboxylate or carboxylated polysaccharide, partially alkyl derivatized. 2D mercaptoalkyl-SAM.
Membrane proteins	Linear polycarboxylate or carboxylated polysaccharide, partially alkyl derivatized (for on-surface reconstitution). Hydrogel, 100 to 500 nm, low to medium density with linker molecules (when working with amphipoles).
Assays in serum or culture medium	Hydrogel, 100–500 nm, low to medium density. Polysaccharide with reduced carboxylation level
Ligand fishing from crude samples assays in whole blood	Hydrogel, 300–500 nm, low to medium density, optionally with filter layer
2D SPR microarrays, droplet-spotted Quantification assays	Hydrogel, >1000 nm, linear polycarboxylate
2D SPR microarrays, microflow-deposited	Application dependent. See above

View Online

6.6 Coupling Procedures for Ligand Immobilization

Coupling the ligand to the matrix on the sensor chip surface is one of the most critical steps when studying biomolecular interactions. The immobilization strategy should be chosen so that the immobilization level is sufficient and can be controlled. In addition, the activity and steric accessibility of the ligand must be preserved. In some cases (*i.e.* when the regeneration of the ligand–analyte pair is impossible or results in unacceptable ligand activity loss), the repeated removal and reimmobilization of the ligand is advantageous as it renders fresh ligand for each analyte binding cycle.

Generally, immobilization methods can be divided into adsorptive, covalent, ionic, and capture molecule-mediated coupling.

6.6.1 Adsorptive Immobilization

Adsorptive methods, typically immobilization to low-energy surfaces (*e.g.* plastics) *via* hydrophobic interactions, are the simplest and most popular approach in solid-phase assays as this process occurs spontaneously upon contact of a protein containing buffers with a hydrophobic surface.[57,58] A less common variant of this method is adsorption on noble metals such as gold or silver through strong thiol–metal bonds. Although this method is easy to perform and requires no prior surface preparation except thorough cleaning, huge portions of the adsorbed ligand are usually denatured owing to unavoidable structural changes.[59] Typically, less than 10% of the immobilized binding sites remain active and sterically accessible after such adsorption processes. Another disadvantage is the poor stabilization of the resulting surface against non-specific interactions and the impossibility of completely regenerating it after analyte binding. Therefore, such surfaces usually have to be blocked with suitable blocker proteins[‡] and can be used only once. As stable adsorption requires the cooperative forces of several surface-affine functional groups, the adsorbate must have a sufficient number of such residues and a molecular weight of at least 10 kDa. Therefore, this method is generally unsuitable for underivatized nucleotides, peptides, and small molecules.

6.6.1.1 Electrosorption

Electrostatic immobilization is a technique that is frequently used to attach oligonucleotides to polyamine-coated microarray substrates. As it is non-selective and results in considerable electrostatic forces towards the immobilized ligand, the drawbacks of this method are similar to those of adsorptive techniques (see Sections 6.3.1 and 6.5.1). Furthermore,

[‡]Typical examples are BSA and casein; further ready-made cocktails are commercially available.

Published on 24 May 2017 on http://pubs.rsc.org | doi:10.1039/9781788010283-00171

View Online

the non-specific background of the analyte matrix can be considerable as the typically positively charged surfaces are not well stabilized. Therefore, this method is suitable only for robust ligands and well-defined samples.

Published on 24 May 2017 on http://pubs.rsc.org | doi:10.1039/9781788010283-00171

Protocol 6.1 Electrostatic adsorption of DNA on (poly)amine-coated sensor chips

1. Prime amino-modified chip surface for 10 min with 0.1 M HCl.
2. Wash for 2 min with degassed 5 mM sodium acetate (pH 5.0)
3. Inject 1–100 μM DNA in degassed 5 mM sodium acetate (pH 5.0) for 5 min. A baseline increase between 3000 and 6000 μRIU (about 2000–4000 RU or 200–300 m°) should be observed.
4. Equilibrate for at least 15 min with the running buffer used for the interaction experiment. Depending on the ionic strength and pH, a certain fraction of the electrosorbed DNA is desorbed. NaCl (2 M) plus 10 mM NaOH results in quantitative desorption.
5. For a more stable immobilization, activate the surface with epichlorohydrin, as described in Protocol 6.10, and use amino- or sulfhydryl-derivatized DNA.
6. Start interaction analysis.

Notes:

- Free amines form carbamates with ambient CO_2, so amino-modified surfaces should either be prepared fresh or be used directly out of a sealed bag.
- Owing to the positive charges on these surfaces, significant non-specific binding can be observed, and regeneration is difficult. Therefore, the dry immobilization of amino-modified nucleotides on NHS-activated polycarboxylate surfaces is preferred for the immobilization of DNA.

6.6.2 Covalent Immobilization

Covalent coupling is the most frequently used immobilization method as it usually gives high coupling yields and forms stable covalent bonds between the ligand and a suitable biocompatible sensor chip coating. Therefore, it should be the first choice when evaluating different ways to immobilize biomolecules on a chip surface. One of its disadvantages is the randomly oriented coupling that occurs equally at the active and inactive sites of the ligand and hence can affect the affinity of at least a fraction of the immobilizate. In extreme cases, complete deactivation may even occur, particularly for small ligands (*e.g.* peptides). Non-uniform coupling of the ligand may lead to a heterogeneous distribution of rate and equilibrium constants, which can be determined using the distribution analysis method, as clearly described in Chapter 5.

View Online

Published on 24 May 2017 on http://pubs.rsc.org | doi:10.1039/9781788010283-00171

Regardless of which of the methods of covalent coupling described below is chosen, care must be taken to ensure that the ligand molecules come close enough to the reactive groups, otherwise no reaction can take place. This basic rule of "interaction before reaction" is an important prerequisite for good coupling yields, but it can be difficult to realize on highly stabilized surfaces, which are designed to suppress interaction. This obvious dilemma can be addressed in two ways, as described below.

6.6.2.1 *Electrostatic Preconcentration Prior to Covalent Coupling*

The pH of the coupling buffer is adjusted to below (for negatively charged surfaces) or above (for positively charged surfaces) the ligand's isoelectric point so that the net charge of the ligand is the opposite of the surface charge. If the ionic strength of the coupling buffer is sufficiently low (*i.e.* typically below 20 mM), and the p*I* of the ligand is close to or, better, above the p*I* of the surface, the electrostatic attraction between surface and ligand will override the hydrophilic (*i.e.* steric) stabilization. Under these conditions, the ligand accumulates at the surface until electrostatic neutrality is reached (the so-called preconcentration). Interestingly, because of the aforementioned counterion evaporation effect, electrosorption may also occur when the overall charge of the ligand is neutral or even the same as that of the surface. The preconcentration effect is drastic and independent of the ligand concentration; thus, it works until the coupling buffer is almost quantitatively depleted of ligand, even at concentrations as low as a few micrograms of ligand per milliliter. As the electrostatic forces work in a cooperative manner, the efficiency of the preconcentration is proportional to the molecular weight of the ligand. Achievable ligand densities depend mainly on the surface nanoarchitecture, including its dimensionality (2D *versus* 3D coatings) and, for 3D architectures, the thickness and density of the hydrogel. With hydrogels as thick as 1000 nm, high protein densities of well above 100 ng mm^2 (*i.e.* $>10^6$ RU or $>10^\circ$ SPR angle shift) can be achieved.

In addition to changing the ligand concentration and contact time, the ligand density is controlled by adjusting the ionic strength of the coupling buffer or varying the activation level. The latter is the preferred method as lowering the density of activated groups also avoids multi-site coupling, which can lead to unwanted crosslinking and ligand deactivation. In this context, it should be noted that preconcentration after activation is typically less effective than preconcentration of an underivatized surface. This is attributed to the partial conversion of charged groups into neutral and insoluble moieties, which results in a decrease in the overall charge density and a lower degree of hydrogel hydration. In turn, these factors can lead to shrinking effects (*i.e.* a reduction in the available volume for ligand immobilization).

View Online

Published on 24 May 2017 on http://pubs.rsc.org | doi:10.1039/9781788010283-00171

Protocol 6.2 Electrostatic preconcentration

Preparation of the coupling buffers:

The pH of the buffer should be at least 0.5 less than $pI_{Protein}$ to ensure a positive net charge of the protein, which is required for electrostatic interaction with the negatively charged surface. A low ionic strength is also essential. Prepare 5 mM buffers from formic, acetic, or maleic acid carefully titrated with 0.1 M NaOH, and avoid over-titration!

Buffer ranges:

pH 3.0–4.0: sodium formate
pH 4.0–5.5: sodium acetate
pH 5.5–6.0: sodium maleate

These buffers are subject to rapid microbial growth; therefore, after sterile filtration, aliquots should be frozen and stored until use and always used fresh. Do not add preservatives such as sodium azide, as azide interferes with later activation steps.

Procedure to check the electrostatic preconcentration:

1. Mount a carboxylated sensor chip in the instrument. Make sure that the liquid handling system is free from any protein contamination since even minor amounts of desorbed proteins will concentrate on the charged sensor surface.
2. *Optional:* To remove hydrophobically bound proteins from tubes, *etc.*, clean the flow system with an *easily desorbable* (avoid SDS) detergent solution followed by doubly distilled water. If SDS is used, wash with 5 M glycine · HCl afterwards.
3. Elute electrostatically adsorbed contaminants from the surface for 10 min with 2 M NaCl and 10 mM NaOH.
4. Check the baseline with coupling buffer. After 10–15 min, almost no drift should be observed.
5. Inject protein solution to verify the preconcentration conditions. If no interaction occurs, the ionic strength or pH should be lowered. Increasing the protein concentration is optional but usually not helpful. Repeat the last three steps until a sufficient preconcentration of the protein is observed on the sensor surface. *Note:* Some ligands contain significant salt contamination from previous purification steps or as preservative (*e.g.* ammonia salts, Tris, and sodium azide). These additives are often not stated on the product data sheet and can severely interfere with the preconcentration process and also quench the active groups. This results in a significantly reduced immobilization yield; therefore, the ligand should generally be microdialyzed into the coupling buffer.
6. Elute the protein from the surface for 2–5 min with elution buffer.
7. Wash with water until the baseline is stable.

View Online

Procedure to couple the ligand using the electrostatic preconcentration effect:

8. Prepare the buffer for the covalent activation of choice and activate the surface. See the paragraphs below for details.
9. Wash as quickly as possible with coupling buffer.
10. Inject the protein solution for 5–50 min. Since some of the carboxylate functionalities have been converted into uncharged groups by the matrix activation procedure, the preconcentration will usually be slower than that of the unactivated surface. The immobilization yield can be increased by repeated reinjection of the protein solution.
11. When working at low pH, inject water for 10 min to complete the coupling reaction, which proceeds slowly under these conditions.
12. Quench the remaining active groups, as described below.
13. *Optional:* Remove physisorbed proteins with regeneration buffer.
14. Wash with coupling buffer. The amount of covalently bound protein can now be determined by comparison with Step 4.
15. Switch to a suitable running buffer and start the interaction experiments.

Note: At least two analysis cycles (see next chapter) are required to equilibrate and stabilize the coating for reliable and accurate measurements of the rate and affinity constants.

Published on 24 May 2017 on http://pubs.rsc.org | doi:10.1039/9781788010283-00171

Sometimes, the ligand is too acidic for the above-described electrostatic preconcentration process. In such cases, the protein can be associated with a positively charged micelle (a cluster of oriented surfactant molecules). As shown schematically in Figure 6.20, the micelle–protein complex carries a positive net charge at neutral pH and is therefore attracted to the negative sensor surface. After the completion of the covalent immobilization process, the surfactant molecules are washed out.

6.6.2.2 *Dry Immobilization*

This method is less frequently employed and is useful when it is not possible to preconcentrate a ligand electrostatically onto the sensor chip surface. This is the case with ligands having p*I* values below 4, such as DNA, for relatively small and acidic compounds (*e.g.* some peptides), and for when the surface is not charged. In addition to bearing functionalities that are able to provide covalent coupling, the ligand to be immobilized must be robust enough to survive drying, which is necessary to bring it sufficiently close to the reactive groups at the sensor surface. Suitable sensor surfaces have to be preactivated offline following one of the protocols below. Alternatively, NHS-preactivated chips are commercially available. Care should be taken to ensure that the functional groups present on the surface cannot react with each other, as

View Online

Published on 24 May 2017 on http://pubs.rsc.org | doi:10.1039/9781788010283-00171

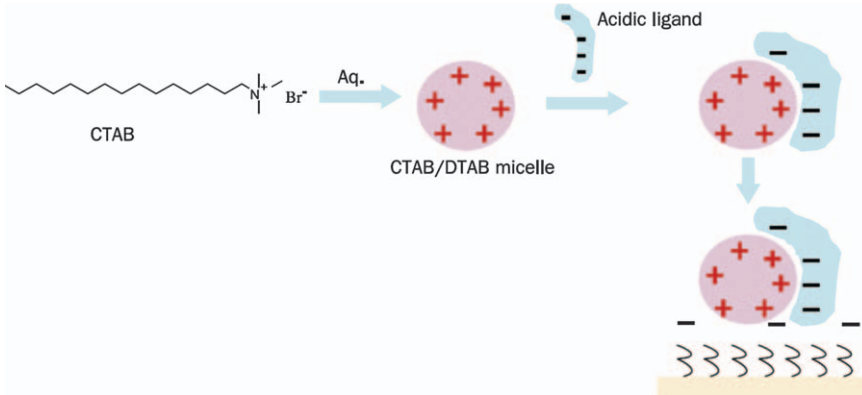


Figure 6.20 Hexadecyl-3-methylammonium bromide (CTAB)/dodecyl-3-methylammonium bromide (DTAB) micelle-mediated immobilization of acidic proteins. CTAB/DTAB forms positively charged micelles in aqueous solutions. The micelles bind electrostatically to the negatively charged sensor surface and may thus be used as carriers for acidic proteins. Reprinted from S. Löfås and A. McWhirter, The art of immobilization for SPR sensors, *Surface Plasmon Resonance Based Sensors*, 2006, vol. 4, p. 135. Copyright Springer-Verlag, Berlin, Heidelberg, 2006. With permission from Springer.

such self-quenching drastically reduces the coupling yield. For example, the commonly used carboxymethyldextran hydrogel surfaces are not suitable for dry immobilization because the NHS esters form esters with the abundant hydroxyl functionalities of the polysaccharide matrix, leading to deactivation and unwanted crosslinking, a side reaction that also occurs, although to a lesser extent, during standard wet activation. The advantages of dry immobilization are high coupling yields and the possibility of using less reactive coupling chemistries (*e.g.* epoxide activation) that require harsh reaction conditions such as elevated temperature.

Protocol 6.3 Dry immobilization (offline)

1. Place chips in a suitable receptacle and incubate the surface for 10 min with 2 M NaCl and 10 mM NaOH.
2. Wash thoroughly with doubly distilled (dd) water.
3. Prepare the buffer for covalent activation and activate the surface. See paragraphs below for details.
4. Wash thoroughly with dd water and remove liquid traces with a quick centrifuge spin or a sharp jet of clean compressed air/nitrogen. For reproducible drying, the optimal direction of the jet of air/nitrogen is 45° from the surface. It is essential that no droplets dry on the surface as even dd water leaves behind contaminants that may interfere with later processing steps.
5. Place chips in a dry and clean receptacle that is small enough to be placed in a vacuum desiccator.

View Online

Published on 24 May 2017 on http://pubs.rsc.org | doi:10.1039/9781788010283-00171

6. Manually spot 10–30 μL of a solution of at least 0.3 mg ligand mL^{-1} low ionic strength coupling buffer onto the chip surface so that the sensing area is entirely covered. Commercial spotters are preferable; contactless spotters may be used to produce a microarray to be measured with an SPR imaging instrument.[b] Dry as fast as possible in a vacuum desiccator without desiccant to avoid potential hydrolysis.

   Note: Some ligands come with significant salt contaminants from previous purification steps or as a preservative (*e.g.* ammonia salts, Tris, and sodium azide). These additives are often not stated on the product data sheet and can quench the active groups. As this results in a significantly reduced immobilization yield, the ligand should generally be microdialyzed into coupling buffer before spotting.
7. Incubate for 1–6 h depending on the activation employed. With less reactive functional groups and robust ligands, additional heating to elevated temperatures of up to 90 °C might be necessary.
8. If the chips are not used immediately, place them in a freezer at this stage of the process.
9. Dissolve unbound ligand for over 1 h with running buffer, wash with dd water, and dry as described above.
10. After at least two analysis cycles for equilibration and stabilization of the coating, the chips are now ready for interaction analysis.

[b]Commercial spotters usually spot 1 nL, and the spot diameter may vary between 50 and 300 μm and depends on the hydrophilicity of the surface. Be aware that the ligand concentration in $ng\,mm^{-2}$ should be recalculated from the spot size, concentration of ligand in the spotting liquid, and the coupling yield, which can vary between a few percent and 50%.

6.6.3 Covalent Activation Chemistries

Some activation chemistries commonly used to covalently immobilize the ligand on the chip surface are presented in the following sections. Most are based on carboxylic acid residues as this functional group is present on many bioinert immobilization matrices.

6.6.3.1 Amine Coupling via *Reactive Esters*

Owing to its flexibility, relative ease of use, high coupling yields, and robustness, this is the most frequently employed immobilization method (Figure 6.21). The reaction conditions to couple proteins, peptides, and small molecules to carboxylated chip surfaces are well characterized, and extensive optimization studies have been performed.[60] Typically, the surface-bound carboxyl groups are first activated by a carbodiimide and converted

View Online

Published on 24 May 2017 on http://pubs.rsc.org | doi:10.1039/9781788010283-00171

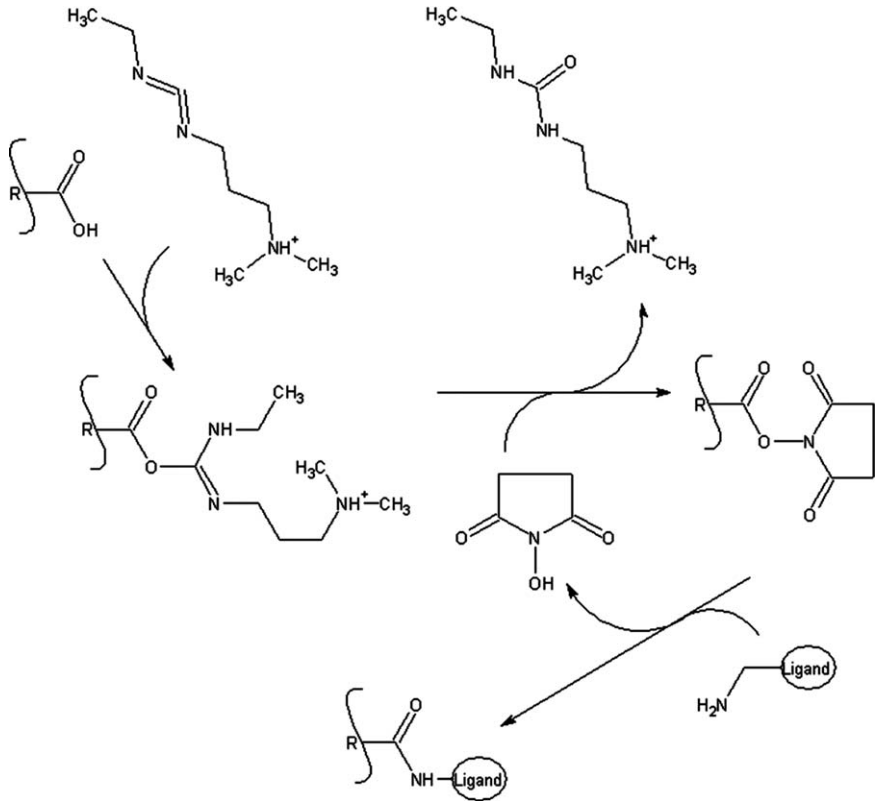


Figure 6.21 Reaction scheme of COOH activation with EDC–NHS and ligand coupling.

into active ester intermediates, which are then aminolyzed by lysines or the N-terminal NH_2 group of the ligand.

For more than 50 years, carbodiimides have been used to mediate the formation of amide bonds between carboxylates and primary or secondary amines.[61] Over time, a number of different reagents have been developed with the commonality that they all create reactive *O*-acylisourea intermediates with COOH groups, which are reactive towards nucleophiles such as primary and secondary amines, hydrazides, primary and some secondary alcohols, thiols, and, as important side reaction, water. In contrast, many carbodiimides such as dicyclohexylcarbodiimide (DCC) are insoluble in water and of limited use for bioconjugation; other variants are readily soluble in water and are therefore the reagents of choice for water-based activation methods.[62] 1-Ethyl-3-(3-dimethylaminopropyl)carbodiimide (EDC) is most frequently employed for conjugating biomolecules. The reagent itself along with the isourea reaction by-products are water soluble, facilitating activation and chip processing. EDC is usually supplied

View Online

Published on 24 May 2017 on http://pubs.rsc.org | doi:10.1039/9781788010283-00171

as a hydrochloride that is both hygroscopic and labile in the presence of water. It should be stored in a dry container at −20 °C and allowed to warm to room temperature before being opened to prevent water condensation, which will cause decomposition over time. For the same reason, EDC containing activation buffers should always be prepared fresh and not from stock solutions. Note that inactive EDC is among the most frequent reasons for failed immobilizations. EDC activation proceeds effectively from pH 4.5 to 7.5 in 2-(*N*-morpholino)ethanesulfonic acid or related buffers. Amine- and carboxylate-containing buffers should be avoided as they would react with the carbodiimide.

As the *O*-acylisourea intermediate hydrolyzes rapidly with a rate measured in seconds, it would not survive the time from activation until ligand injection. Therefore, it has to be converted into an active ester that is more stable. As depicted in Figure 6.21, this is achieved by adding water-soluble *N*-hydroxysuccinimide or its sulfonated derivative *N*-hydroxysulfosuccinimide to the activation mix. In contrast to the *O*-acylisourea, the thus formed (sulfo-)NHS ester intermediate has a half-life from minutes at pH 8–9 to many hours at pH 4–5. Although EDC–(sulfo)NHS-coupled reactions are highly efficient, one should be aware that side reactions (*e.g.* esterification with abundant hydroxyls of polysaccharide hydrogel coatings) can occur. The resulting esters are only partially quenched during the ethanolamine-capping step; however, they are subject to slow hydrolysis, as are the temporarily formed thioesters or acylated histidine side-chain nitrogens.[63] Aminolysis by the still available lysine functionalities of the immobilized ligand or bound analyte may also occur, the latter leading to incomplete regeneration during the first interaction cycles. Further, the high efficiency of the coupling reaction can result in multi-site coupling and crosslinking if larger ligands with many lysine residues are immobilized. Finally, the transesterification tendency of NHS esters should be noted as it can lead to the unwanted cross-activation of ligand carboxyl groups or carboxylate buffer components.

The aminolysis of (sulfo)NHS esters occurs smoothly at slightly alkaline pH (*i.e.* in carbonate or borate buffers of pH 8–10), where most amines are deprotonated. Therefore, this is the reaction condition of choice for the immobilization of small ligands and many peptides. For the immobilization of larger species (*e.g.* most proteins), it is advisable to create conditions in which only a small fraction of the lysine residues are reactive in order to prevent multi-site coupling and preserve the protein activity. A low pH between 4 and 6 is therefore recommended in these cases and is required to achieve the above-described electrosorption effect. As an additional advantage, coupling the amine terminus of the protein is favored over random immobilization through lysine residues by adjusting the pH of the coupling buffer to a lower value. The reason for this effect is the lower p*I* of N-terminal amines compared with lysine NH_2 groups. Such optimization of the pH can significantly increase the activity, especially for sensitive proteins.

View Online

Published on 24 May 2017 on http://pubs.rsc.org | doi:10.1039/9781788010283-00171

Protocol 6.4 The EDC–NHS coupling procedure

1. Prepare a solution of 0.1 M *N*-hydroxysuccinimide (NHS) in 50 mM 2-(*N*-morpholino)ethanesulfonic acid (MES) buffer (pH 6.0). Optionally, the NHS can be substituted by sulfo-NHS.
2. Prime a COOH-modified sensor chip according to the above-described procedure used to check the electrostatic preconcentration. Elute electrostatically adsorbed contaminants from the surface for 10 min with 2 M NaCl and 10 mM NaOH.
3. Check the baseline with coupling buffer. After 10–15 min, almost no drift should be observed.
4. Prepare a 5 to 500 mM solution of solid 1-ethyl-3-(3-dimethylaminopropyl)carbodiimide (EDC) in the NHS/MES buffer from Step 1. The optimal EDC concentration depends on the coating and the ligand. A low EDC concentration (around 20–50 mM) is recommended for linear polycarboxylate coatings and for the immobilization of larger ligands with abundant lysine residues. Planar coatings and carboxymethylated dextran hydrogels can be activated with higher EDC concentrations (up to 500 mM), especially if the ligand is small.
5. Inject this activation mix over the sensor chip for 1–20 min. Varying the incubation time allows the control of the activation level. To achieve a lower activation level, which, for example, is recommended for polycarboxylate hydrogels, the activation time should be <5 min.
6. For the standard wet immobilization protocol, wash briefly with water or slightly acidic coupling buffer and continue with ligand injection. For dry immobilization, wash with 5 mM acetic acid and dry according to Protocol 6.2.

In some cases, particularly with labile ligands or when preparing high-capacity surfaces for the analysis of low molecular weight compounds, the slight crosslinking of the immobilized ligand by injecting a short pulse of low-concentration EDC–NHS over the surface-bound protein can enhance the stability of the immobilized ligand. However, the applicability of such an additional crosslinking step should be tested empirically, as it comes with the risk of deactivating the ligand.

6.6.3.2 Amine Coupling Through Reductive Amination

Carbonyl groups such as aldehydes, ketones, and glyoxals can react with amines to form labile Schiff base intermediates that can be reduced to yield stable secondary amines. The formation of Schiff base is efficient at both low and high pH, and sodium borohydride and sodium cyanoborohydride are the most commonly used reduction reagents. The difference between them

View Online

Published on 24 May 2017 on http://pubs.rsc.org | doi:10.1039/9781788010283-00171

is that sodium cyanoborohydride is approximately five times milder[64] than sodium borohydride and does not reduce free aldehyde groups; hence cyanoborohydride leads to higher coupling yields by shifting the reaction equilibrium towards the product side.

The reductive amination of a Schiff base as shown in Figure 6.22 is a highly selective reaction that proceeds smoothly under mild conditions and, unlike coupling through amide bonds, preserves the positive charge of the reacted amine. Therefore, this reaction is an interesting alternative for the immobilization of sensitive ligands on polysaccharide surfaces that, after periodate oxidation, display a sufficient density of aldehyde groups in the form of cyclic hemiacetal structures.[65] Useful chip substrates for this method are coated with either non-derivatized dextran or carboxymethyldextran with a low degree of carboxymethylation. The latter has the advantage that it allows the electrosorptive preconcentration of protein (*i.e.* working with lower ligand concentrations in the immobilization buffer).

Protocol 6.5 Amine coupling through reductive amination

1. Prime the chip surface as described above (see Steps 2 and 3 in the EDC–NHS coupling Protocol 6.3).
2. Inject 10 mM sodium periodate in water for over 30 min. To control the density of aldehyde groups, the concentration and contact time may be varied.
3. If working without applying the electrosorption effect, inject the ligand at a concentration of at least 1 $mg\,mL^{-1}$ in phosphate, borate, or carbonate buffer at pH 7–10 plus 10 mM sodium cyanoborohydride (**caution:** extremely toxic). The optimal pH is 8–9, and other buffers may be used provided that they do not contain competing amines such as Tris. If protein ligands are electrostatically preconcentrated, a lower pH and lower ionic strength are required. As the reaction proceeds slowly under these conditions, long contact times of several hours should be chosen.
4. After completion of the coupling reaction, inject 0.5 M Tris or ethanolamine · HCl (pH 8.0) plus 10 mM sodium cyanoborohydride for 1 h. Alternatively, the excess aldehydes may be reduced by the injection of 50 mM sodium borohydride in 0.1 M sodium carbonate at pH 9.
5. Wash with a running buffer of choice until the baseline is stable and start the interaction analysis cycle.

In addition to coupling *via* active esters and reductive amination, several other amine-reactive chemistries exist; however, they are not described further here as their use in evanescent field-based biosensors is limited.

View Online

Published on 24 May 2017 on http://pubs.rsc.org | doi:10.1039/9781788010283-00171

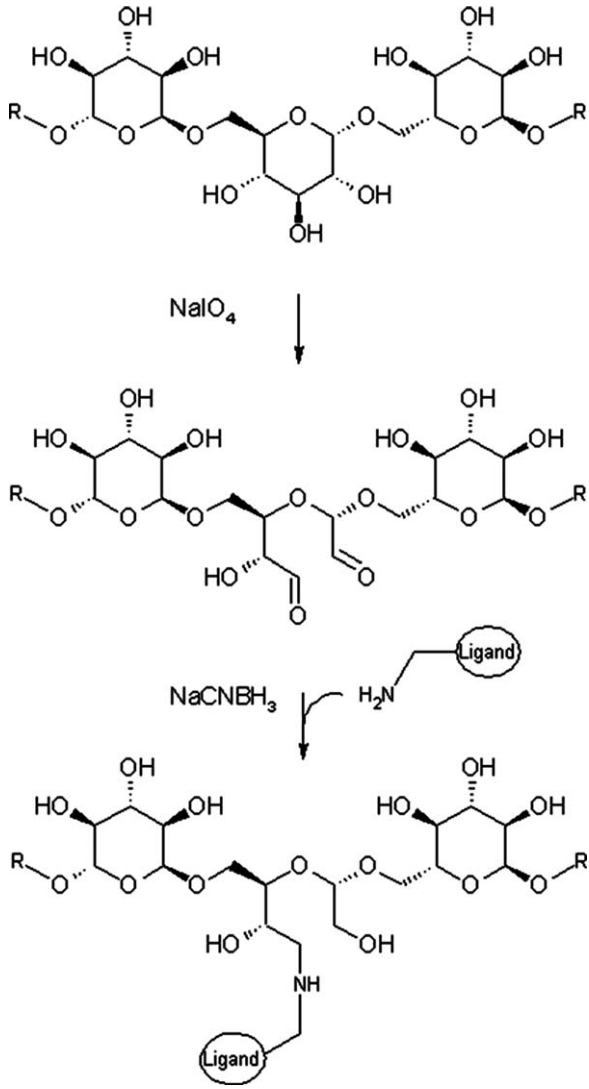


Figure 6.22 Oxidation of a polysaccharide hydrogel and immobilization of an amine-containing ligand through reductive amination.

6.6.3.3 Thiol Coupling via *Disulfide Exchange*

An alternative to coupling proteins through their amine functionalities is the use of thiol groups after the reduction of pendant disulfide bridges. Choosing this immobilization strategy makes sense if amines are not present, or if a sufficient number of disulfide groups located far enough from the protein's active site are available. In such cases, a higher activity of the immobilizate can be achieved compared with the more randomly oriented amine coupling.[66] Immobilization of the reduced proteins can occur either

View Online

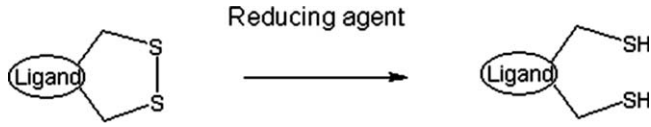


Figure 6.23 Reduction of disulfide-containing compounds.

Published on 24 May 2017 on http://pubs.rsc.org | doi:10.1039/9781788010283-00171

by the disulfide exchange using activated disulfides, nucleophilic substitution of haloacetyls, or alkylation of maleimides. The first method, the formation of disulfides, is reversible under reducing conditions, which makes it interesting for creating fully regenerable chip surfaces.[67] The last two methods yield stable bonds that cannot be cleaved again. Site-directed coupling can result in an immobilizate with higher activity, whereas the additionally introduced disulfide, acetyl, or maleimide residues can lead to slightly increased non-specific interactions.

Prior to thiol coupling, the protein of interest has to be reduced (Figure 6.23). This is usually effected using thiols containing compounds such as dithiothreitol (DTT) or dithioerythritol (DTE), 2-mercaptoethanol, 2-mercaptoacetic acid, and 2-mercaptoethylamine. For a more convenient purification of the reaction mixture after the reduction step, immobilized reducing agents may be used. The use of complexing additives is generally recommended to prevent reoxidation of the just reduced protein, which is catalyzed by traces of heavy metal ions.

Protocol 6.6 Protein disulfide reduction procedure

1. Add 0.5 mL of thiolated agarose to a column and equilibrate with 0.1 M phosphate buffer (pH 8.0).
2. Activate the column by adding 1 mL of 10 mM DTT in 0.1 M phosphate buffer (pH 8.0) containing 1 mM EDTA.
3. Wash the column with 20 column volumes of 0.1 M phosphate buffer (pH 8.0).
4. Add the protein to be reduced in 0.1 M phosphate buffer (pH 8.0) containing 1 mM EDTA. Recover fractions and collect all samples. Read the absorbance at 280 nm to determine which fractions contain the eluted protein. Pool these fractions, separate into aliquots, and freeze at –20 °C until analysis.

If using alternative protocols, make sure that no reducing reagents remain in the reduced protein solution.

During the thiol–disulfide exchange, the free thiol of the reduced ligand reacts with an activated disulfide on the chip surface and forms a new mixed disulfide upon the release of a leaving group (usually pyridyl sulfide). The latter is easily transformed into pyridine-2-thione, a non-reactive compound not capable of participating in further mixed-disulfide formation. As shown in Figure 6.24, only the surface-bound end of the mixed pyridyl disulfide has the potential to become attached to the sulfhydryl-containing ligand.

View Online

Published on 24 May 2017 on http://pubs.rsc.org | doi:10.1039/9781788010283-00171

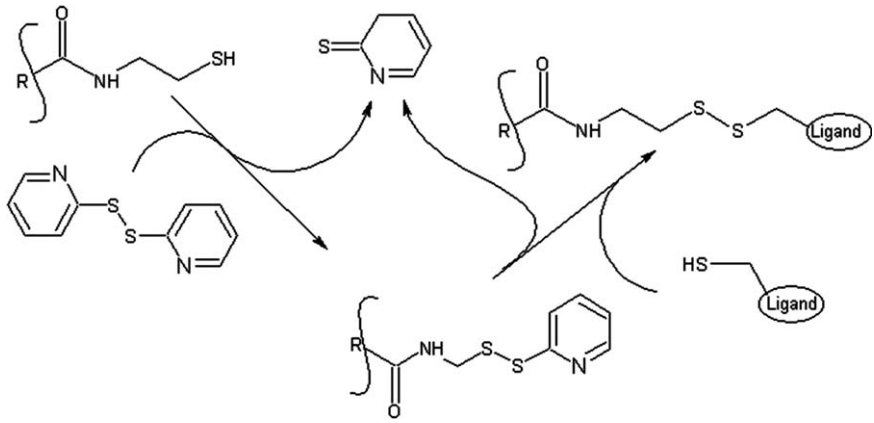


Figure 6.24 Pyridyl disulfide-mediated disulfide exchange.

This disulfide exchange reaction occurs over a broad pH range and in a variety of buffers, including in the acidic, low ionic strength conditions used for electrostatic ligand preconcentration.

As already mentioned, the resulting disulfide bond is cleaved under reducing conditions and is affected by thiol buffer additives.

Protocol 6.7 Thiol–disulfide exchange on thiol-modified surfaces

1. Prime a disulfide-derivatized chip (see Steps 2 and 3 in the EDC–NHS coupling Protocol 6.3).
2. Inject 100 mM DTT or other reducing agent in 0.1 M phosphate buffer (pH 8.0) for 20 min.
3. Wash for 5 min with running buffer.
4. Inject 10 mM pyridyl disulfide in 0.1 M phosphate buffer containing 20% ethanol for 20 min (*Note:* dissolve pyridyl disulfide in 100% ethanol before diluting to 10 mM with phosphate buffer–ethanol mixture).
5. Wash for 15 min with running buffer.
6. Switch to water as running buffer and wash the system for 10 min until the baseline is stable.
7. Inject 10–100 μg reduced protein mL^{-1} coupling buffer plus 1 mM EDTA for 10–20 min. Significant preconcentration should occur in this step.
8. Quench excess active disulfides with 1 mM mercaptoethanol in 0.1 M acetate buffer (pH 4.2) and 1 M NaCl for 30 min (prepare fresh).
9. Wash with running buffer of choice until the baseline is stable, then start the interaction analysis cycle.

View Online

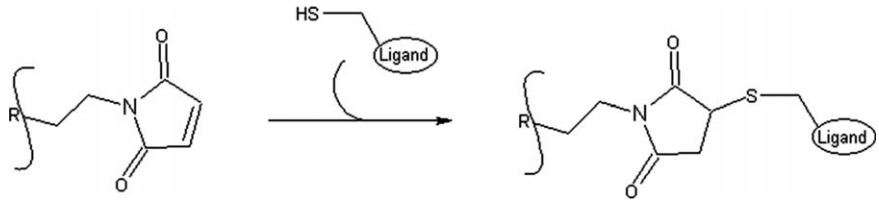


Figure 6.25 Maleimide coupling of sulfhydryl groups.

Published on 24 May 2017 on http://pubs.rsc.org | doi:10.1039/9781788010283-00171

Protocol 6.8 Thiol–disulfide exchange with PDEA on (poly)carboxylate surfaces

1. Scout the preconcentration conditions (Protocol 6.1) and prepare the ligand solution.
2. Prime and activate the surface slightly with EDC–NHS according to Protocol 6.3. A short activation time (1–3 min) is recommended.
3. Introduce disulfide groups by injecting 50 mM 2-(2-pyridinyldithio)ethanamine (PDEA) in 30 mM sodium borate (pH 8) for 5 min.
4. Immobilize the ligand by injecting the ligand solution for 6–7 min.
5. Quench excess reactive mixed pyridyldisulfide groups by injecting 50 mM cysteine–1 M NaCl in 50 mM sodium acetate buffer (pH 4.0) for 5 min.

6.6.3.4 *Thiol Coupling* via *Maleimides*

For irreversible immobilization *via* thiol groups, maleimide or haloacetyl coupling as shown in Figure 6.25 is the method of choice. The alkene groups of the maleimides undergo alkylation reactions with the sulfhydryls to form stable thioether bonds. The specificity of this coupling for sulfhydryl groups is high at neutral pH,[68] whereas some cross-reactivity with amino groups may occur at higher pH.[69] At pH 7, the reaction of maleimides with sulfhydryls is about 1000 times faster than with amines.[70] As a further side reaction, the maleimide group may undergo hydrolysis to an open form of maleamic acid both before and after the reaction with a sulfhydryl, especially at high pH.

Protocol 6.9 Maleimide coupling of sulfhydryl groups

Activate a carboxylated surface with EDC–NHS, as described in Protocol 6.3. The use of a 10-fold diluted activation mixture should be considered as such a reduced activation level is sufficient to obtain a good immobilization yield with most proteins.

1. Convert the active NHS esters into amino groups by injecting 1 M ethylenediamine hydrochloride (pH 6.0) for 10 min.

View Online

Published on 24 May 2017 on http://pubs.rsc.org | doi:10.1039/9781788010283-00171

2. Quench the remaining reactive groups with 1 M ethanolamine hydrochloride (pH 8.5) for 15 min.
3. Wash for 10 min with 0.1 M HCl.
4. Inject the heterobifunctional reagent *N*-γ-maleimidobutyryl-oxysuccinimide (20–50 mM) in HEPES-buffered saline (HBS) for 10 min.
5. Wash for 5 min with dd water.
6. Inject the reduced protein (Protocol 6.5) in a suitable coupling buffer (see Protocol 6.1) for 10 min.
7. Wash for 5 min with HBS.
8. Hydrolyze excess unreacted maleimido groups by exposing to 0.1 M NaOH for 10 min. Other, milder solutions may be used for inactivation but require a longer contact time.
9. Wash with running buffer of choice until the baseline is stable, then start the interaction analysis cycle.

Alternatively, maleimide-preactivated chips, which are commercially available, may be used. In this case, start with Step 6.

Note: As with most other protocols, at least two analysis cycles (see the next chapter) are needed to equilibrate and stabilize the coating for reliable and accurate measurements of the rate and affinity constants.

In addition to the maleimide method described here, sulfhydryl-containing ligands can also be immobilized through haloacetyl or epoxy activation. The latter is described in Section 6.6.3.6.

6.6.3.5 *Immobilization of Aldehydes Through Hydrazide Groups*

Aldehyde groups can be valuable reactive sites when immobilizing carbohydrates or glycoproteins.[71] In the case of carbohydrates, the anomeric aldehyde (*i.e.* the product of the mutarotation) is often used; otherwise, they can be created by the mild oxidation of sugar residues using sodium periodate. Alternatively, amino groups can be converted with glutaraldehyde (Figure 6.26). As carbohydrate groups are typically located at some distance from the ligand's binding site, immobilization through them might be considered as a useful method to retain the activity of immobilized glycoproteins. However, as immobilization using the EDC–NHS method can also be performed under mild conditions, the difference between the two methods is often smaller than expected; a comparative study of the antigen-binding capacities of immobilized monoclonal antibodies showed almost no difference between EDC–NHS- and hydrazide-mediated coupling.[72]

Hydrazide-derivatized sensor chips can be generated *in situ* by the EDC–NHS activation of carboxylated surfaces followed by reaction with hydrazine or the bifunctional and less toxic solution of adipic acid hydrazide. The activation level and thus the density of immobilized ligand can be controlled

View Online

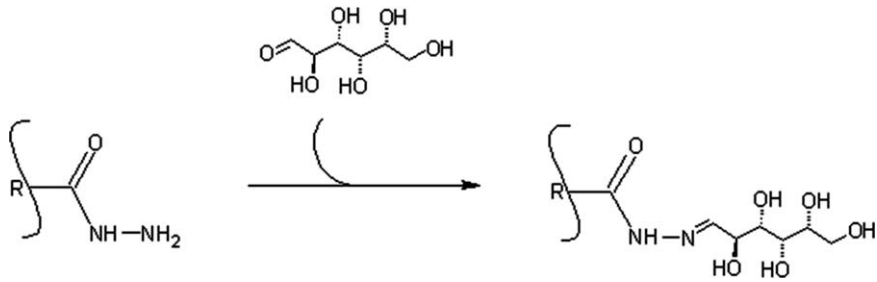


Figure 6.26 Hydrazide coupling of a carbohydrate through its anomeric aldehyde end group.

through the concentration and reaction time of the EDC–NHS mixture. To avoid the crosslinking of 3D surface structures, the concentration of the hydrazine (namely dihydrazide) should be sufficiently high. The coupling reaction itself proceeds best at slightly acidic pH and is therefore compatible with the conditions for electrostatic preconcentration. Small amounts of sulfate catalyze the reaction. The hydrazone bond is relatively stable at neutral and alkaline pH but somewhat labile in acidic buffers. Therefore, to avoid ligand leakage, it should be stabilized by reduction with cyanoborohydride.

Protocol 6.10 Glycoprotein oxidation

1. Dissolve the protein at a concentration of 3–10 mg mL^{-1} in 10 mM sodium phosphate and 0.1 M NaCl at pH 6.2.
2. From a freshly prepared stock solution of sodium periodate, add a sufficient volume to reach a final concentration of 5–10 mM.
3. Allow reaction for 30 min in the dark.
4. Immediately purify the oxidized protein into a slightly acidic immobilization buffer (see above) using a suitable column or spin column. Ensure that the purified protein contains no periodate contamination.
5. Pool protein fractions and dilute with immobilization buffer to a concentration of 30–300 μg mL^{-1}. Inject immediately (Step 5 in Protocol 6.11) because deactivation and precipitation may occur over time due to the intermolecular formation of Schiff base *via* self-polymerization. If solutions have to be stored, freeze them at −20 °C.

Protocol 6.11 Hydrazide activation of a carboxylated surface and coupling of aldehyde derivatized ligands

1. Prime the surface according to Steps 1–3 in Protocol 6.2.
2. Activate for 3 min with 0.2 M EDC and 0.05 M NHS. For lower ligand densities, dilute this activation mixture.
3. React with 0.1 M adipic acid hydrazide hydrochloride (pH 8.0).

Published on 24 May 2017 on http://pubs.rsc.org | doi:10.1039/9781788010283-00171

View Online

Published on 24 May 2017 on http://pubs.rsc.org | doi:10.1039/9781788010283-00171

4. Quench remaining NHS esters over 30 min with 1 M ethanolamine hydrochloride (pH 8.5).
5. Inject oxidized ligand according to Protocol 6.10 and react for at least 20 min.
6. Stabilize hydrazone bonds by reduction with 50 mM sodium cyanoborohydride (**Caution:** toxic! Prepare in a fume hood) in 0.1 M acetate buffer (pH 4.0) for 20 min.
7. Wash with running buffer of choice until the baseline is stable, then start interaction analysis.

Owing to their typically neutral-to-acidic nature, carbohydrates cannot be immobilized using the electrostatic preconcentration effect (Protocol 6.1). Therefore, they should either be injected at high concentrations of at least several tens of milligrams per milliliter or immobilized offline using the dry method according to Protocol 6.2.

6.6.3.6 Coupling Through Epoxy Groups

Epoxy-mediated immobilization is a long-used and robust method, especially for the immobilization of carbohydrate ligands in affinity chromatography.[73] With optical biosensors, this technique is relatively seldom employed as the commonly used carboxymethyldextran-based hydrogel coatings are difficult to activate, and the previously described alternative methods work under milder reaction conditions. However, for the coupling of carbohydrates along with the selective reaction with amine and sulfhydryl nucleophiles, epoxy coupling can be an interesting alternative (Figure 6.27), particularly because the positive amine charge, which is sometimes essential for the ligand's activity, is maintained. Note that crosslinking can occur as a side reaction.

Protocol 6.12 describes epoxy sensor chip activation and dry immobilization of carbohydrates. This protocol can be applied if the ligand is robust enough to survive drying and heating at strongly alkaline pH.

Protocol 6.12 Epoxy activation of chip surfaces and coupling of carbohydrates

1. Prime a hydroxyl- or amino-functionalized chip according to Protocol 6.3. Fully carboxymethylated dextran is difficult to epoxy activate and should not be used.
2. Activate for 15 min using 2% epichlorohydrin (**Caution:** toxic!) in 0.1 M potassium hydroxide. For a lower activation level (*i.e.* a lower ligand density), the pH and reaction time should be decreased.
3. Wash the chip thoroughly with water and dry according to Protocol 6.2.

View Online

4. Prepare 100 μL of a solution containing 10–100 mg ligand mL^{-1} and 10 mM NaOH and cover the sensing area of the chip with a few microliters of this solution so that it is totally covered by the liquid.
5. Dry thoroughly.
6. Heat at 70–90 °C for 30 min, ideally under an inert atmosphere. Lowering the reaction temperature is a way to decrease the coupling yield.
7. Wash for 2 h with running buffer.
8. Wash with water, dry as described in Protocol 6.2, and install the chip to start analysis cycles.

6.6.3.7 *Azlactone Coupling*

Azlactones are lactone-based functional groups that undergo ring opening in the presence of nucleophiles such as primary amines, thiols, and alcohols (Figure 6.28). Although studied in industry for many years by groups at 3M, Polaroid, and Rohm and Haas,[74,75] azlactones have only recently been used as a means to modify surfaces.

Incorporating the azlactone functionality into polymers is appealing because no activation or pretreatment is necessary for post-polymerization modification, they are more stable against hydrolysis than activated esters, and no small-molecule by-products are produced during functionalization.[76]

6.6.3.8 *Immobilization with Click Chemistry*

Recently, surface coatings incorporating alkyne terminal groups have become increasingly popular for the covalent linking of (mostly carbohydrate) ligands carrying azide functional groups using so-called click chemistry. Click chemistry is a generic term describing a range of chemical transformations characterized by high efficiency, selectivity, and tolerance to a variety of solvents and functional groups. The concept was introduced by Sharpless and co-workers[77] and is usually based on the copper(I)-catalyzed triazole formation through the classic Huisgen 1,3-dipolar cycloaddition between azides and alkynes. The reaction between these chemical moieties, which are both rare and generally inert in biological systems, forms a strong non-hydrolyzable triazole linkage. Additionally, azides are easy to incorporate synthetically in organic compounds and are used extensively as precursors to obtain amine-functionalized molecules, a feature that has resulted in large libraries of available carbohydrate azides. Such click coupling (Figure 6.29) has also been applied to immobilize carbohydrate azides in array formats to alkyne-functionalized microtiter plates, alkyne linkers on glass slides, and alkyne-functionalized gold surfaces.[78]

In a reversed approach, carbohydrate epitopes were immobilized on a carboxymethyldextran-coated sensor chip using Staudinger ligation chemistry. This was accomplished by first introducing azide functionalities to the

Published on 24 May 2017 on http://pubs.rsc.org | doi:10.1039/9781788010283-00171

View Online

Published on 24 May 2017 on http://pubs.rsc.org | doi:10.1039/9781788010283-00171

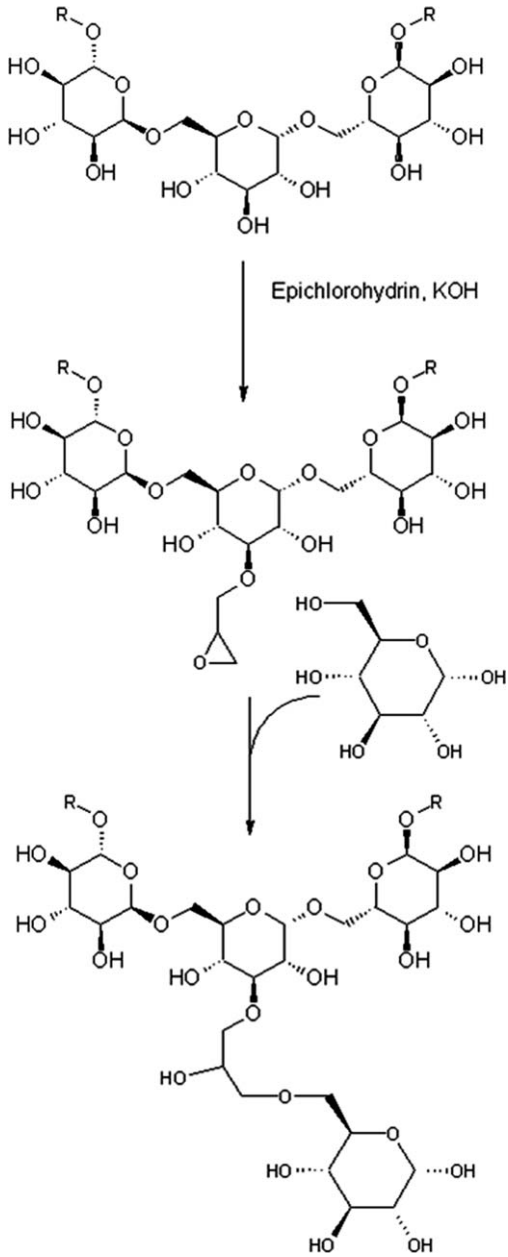


Figure 6.27 Epoxy activation of a dextran matrix and coupling of a carbohydrate.

carboxymethyldextran immobilization matrix followed by reaction with phosphane-modified carbohydrate ligands.[79] This coupling chemistry is extremely mild and can be adapted to different ligand types.

View Online

Published on 24 May 2017 on http://pubs.rsc.org | doi:10.1039/9781788010283-00171

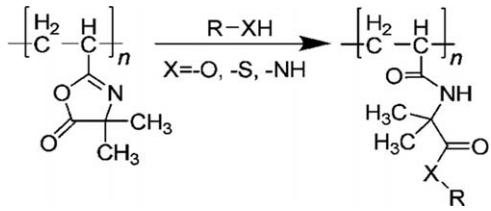


Figure 6.28 Reaction of nucleophilic residues with the azlactone ring.
Adapted with permission from S. P. Cullen, I. C. Mandel and P. Gopalan, Surface-anchored poly(2-vinyl-4,4-dimethyl azlactone) brushes as templates for enzyme immobilization, *Langmuir*, 2008, **24**, 13701–13709. Copyright 2008 American Chemical Society.

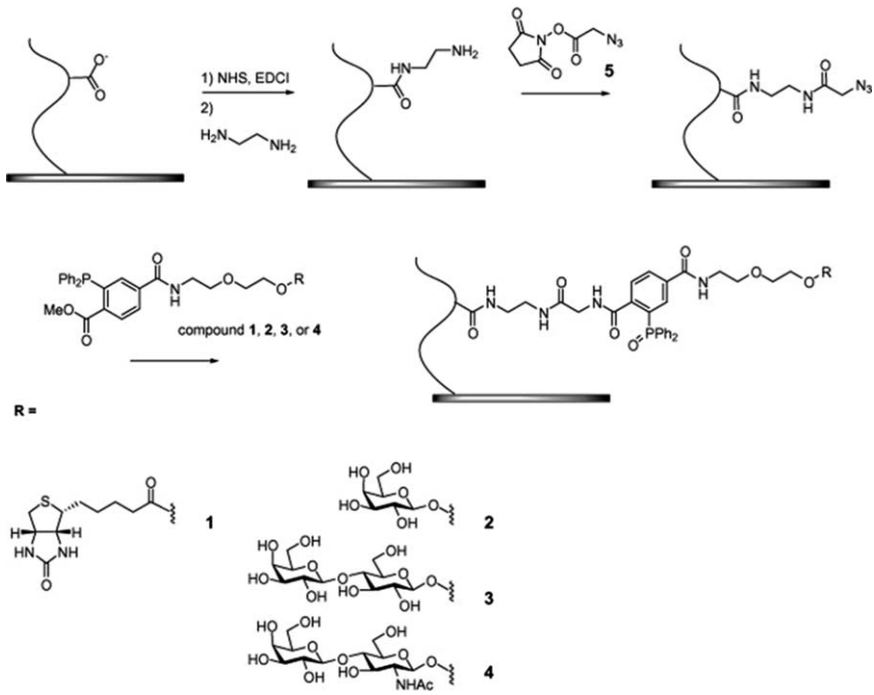


Figure 6.29 Conjugation of carbohydrate epitopes to a CMD (carboxymethyldextran) surface *via* a Staudinger click reaction.
Reprinted from R. S. Loka and C. W. Cairo, Immobilization of carbohydrate epitopes for surface plasmon resonance using the Staudinger ligation, *Carbohydr. Res.*, **345**(18), 2641–2647. Copyright 2010, with permission from Elsevier.

6.6.3.9 Coupling Through Photocrosslinking

In some proteins, nucleic acids and other organic molecules, primary amines, sulfhydryls, or carbohydrate groups are not readily available, are absent, or are necessary for functional reasons. For example, many naturally occurring small

View Online

Published on 24 May 2017 on http://pubs.rsc.org | doi:10.1039/9781788010283-00171

molecules, including terpenes, polyketides, peptides, alkaloids, and their conjugates, do not have a common "handle" for immobilization that can be easily designed and introduced onto each synthetic ligand.[80]

Surfaces derivatized with photoactivatable groups can immobilize any ligand through non-specific bond formation and thus overcome this obstacle. Photolabile functionalities such as arylazides, benzophenones, diazirines, and nitrobenzyl groups can be surface bound in order to allow protein immobilization upon UV light activation. They typically form highly reactive intermediates that have a low specificity for particular groups, which accounts for their non-specific nature. Such photoactivatable groups react with a variety of functionalities, including primary and secondary amines, sulfhydryls, and carbonyls. The highly reactive species formed upon photolysis can also attack C–H bonds, although its preference is for nucleophiles in heterologous systems.[107]

Photocrosslinking is particularly appealing for biosensor systems owing to the extremely simplified coupling protocol, the universality of the immobilization chemistry, and the technical simplicity incorporating irradiation elements into the SPR instrument hardware (Figure 6.30). With a suitable instrument in combination with prefunctionalized sensor chips, the immobilization can be performed fully automated and within a few minutes without the use of any activation buffers or related chemicals, which are usually required for covalent coupling. In addition, advanced features such as ligand density gradients can be easily prepared using an illumination gradient.[81]

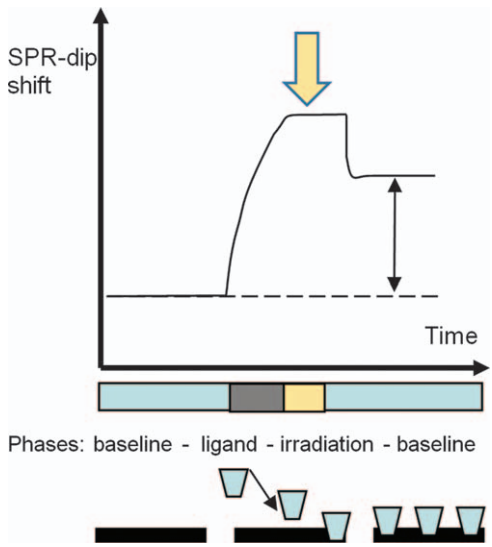


Figure 6.30 Sensorgram of a photoimmobilization cycle. The lack of activation and quenching steps significantly simplifies and shortens the immobilization procedure. Compare with Figure 6.2.

View Online

Published on 24 May 2017 on http://pubs.rsc.org | doi:10.1039/9781788010283-00171

A suitable photophore should be unreactive under ambient light but couple the ligand under mild conditions when irradiated. Therefore, wavelengths in and above the visible part of the light spectrum but below 300 nm are unsuitable because wavelengths below 300 nm can interact with tyrosine and tryptophan and can thus denature protein ligands. When exited, the crosslinker should be reactive towards as many functionalities of the ligand as possible and be able to immobilize pure hydrocarbon molecules with no heteroatom functionalities. Finally, the crosslinker should not be subject to non-specific interactions or expose reactive groups after the coupling is completed or the irradiation has been stopped.

Among other photoreactive groups, diazirines fulfil the above requirements and also form carbenes upon irradiation at 365 nm, which are more reactive than the reactive intermediates derived from other photolinkers. Accordingly, crosslinks to biomolecules are formed within short photo-irradiation times.[82]

Benzophenones, another popular group of photophores, are less reactive and require longer irradiation times. When exposed to 350 nm UV light, they become triplet-state intermediates, which also can immobilize various ligands (Figure 6.31). An advantage of this photophore is that activated benzophenone does not degrade readily, even when exposed to UV light, and is not involved in bond formation. As such, after UV exposure, unreacted benzophenone can be photolyzed again to form covalent bonds.[83,84]

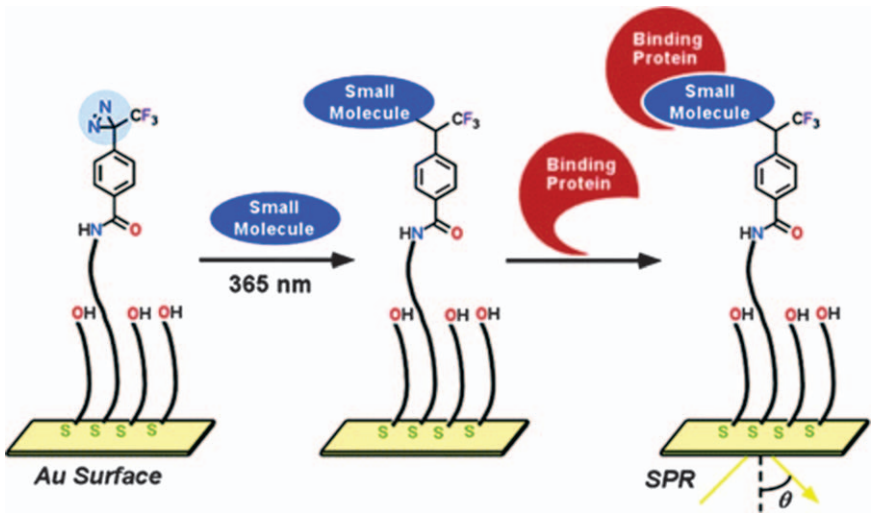


Figure 6.31 Photocoupling of small molecules to immobilized trifluoromethylaryldiazirine (TAD).
Reprinted with permission from N. Kanoh, M. Kyo, K. Inamori, A. Ando, A. Asami, A. Nakao and H. Osada, SPR imaging of photo-cross-linked small-molecule arrays on gold, *Anal. Chem.*, 2006, **78**(7), 2226–2230. Copyright 2006 American Chemical Society.

View Online

Published on 24 May 2017 on http://pubs.rsc.org | doi:10.1039/9781788010283-00171

As water quenches the reactive carbenes, and they also react with the organic immobilization matrix, adequate preconcentration is essential for good coupling yields. In addition, as the immobilization efficiency varies from ligand to ligand, different illumination times should be evaluated. Tests with commercially available photoactivatable hydrogel sensor chips[115] resulted in coupling ratios (covalently bound/electrostatically preconcentrated ligand×100) between 10 and 80% depending on the ligand and irradiation parameters. In accordance with published protocols, it may be advisable to immobilize dry, particularly when working with small, less-reactive ligands.[95]

The above-mentioned crosslinking chemistries are not exhaustive. Generally, most methods that are employed in bioconjugate synthesis or for the preparation of supports for affinity chromatograpy are also suitable for the derivatization of sensor chip coatings.

6.6.4 Immobilization *via* Molecular Linkers

Indirect immobilization through site-specific capture molecules on the chip surface can result in oriented coupling with retention of the ligand's activity and structure. The capturing groups can be proteins such as capture antibodies or protein A[85] along with smaller, more robust moieties such as streptavidin–biotin[37,86] or chelating groups such as NTA. Although such indirect methods appear to be more convenient, require no or little chemistry, and (at least theoretically) result in a higher percentage of active ligands after the immobilization process, one should be aware that bulky (protein) linkers occupy a significant fraction of the evanescent field's volume, which is then not available for ligand molecules (*i.e.* can result in smaller signals and might cause steric hindrance, especially in the case of high molecular weight analytes and hydrogel matrices). Furthermore, larger capture molecules can alter the affinity profile of the immobilized ligand or induce non-specific interactions.

An interesting feature of regenerable affinity-based ligand surfaces such as protein A and (poly)NTA is that the ligand can be removed together with the analyte during regeneration. This is advantageous when it is difficult to regenerate the ligand–analyte interaction.

6.6.4.1 Streptavidin–Biotin Coupling

Since the extraordinary affinity of biotin for avidin was recognized in 1941, the avidin–biotin system has become a standard coupling method owing to its versatility and relatively simple immobilization process. In recent decades, avidin was gradually replaced by the functionally related streptavidin, as streptavidin shows a lower non-specific background and binds biotin conjugates more stably than avidin.

When using biotinylated molecules, one should take into account that biotinylation is usually carried out with NHS-activated biotin derivatives, hence some lysine groups of the ligand will be randomly converted into

View Online

Published on 24 May 2017 on http://pubs.rsc.org | doi:10.1039/9781788010283-00171

uncharged amides. On the other hand, the covalent coupling of native ligand using the EDC–NHS method as the coupling chemistry is identical but usually gives higher immobilization yields. However, some ligands may be not amenable to the low-pH and low-salt conditions required for the pre-concentration step (typically, pH <5.0 in 10 mM sodium acetate) of the covalent coupling methods. It is also important to note that with covalent immobilization, the ligand may be coupled *via* more than one primary amine, resulting in surface heterogeneity. In these cases, coupling through minimal biotinylation offers advantages.

When biotinylating ligands, the biotinylation level should be as low as possible, ideally less than one biotin tag per ligand. Although the majority of the ligand molecules in the biotinylation mixture will not be biotinylated, multiple biotinylation (and thus crosslinks within the hydrogel surface) is safely avoided, and the ligand population becomes significantly more homogeneous.[87]

With the aim of a more defined biotinylation while preserving the ligand's activity, several site-specific methods have been developed. These *in vitro* or *in vivo* biotinylations rely on the sequence-specific action of enzymes such as biotin ligase[88,89] or intein-mediated protein splicing and introduction of a reactive C-terminal thioester/N-terminal cysteine.[90]

Another method utilizes the selective action of maleimide-activated biotin in the hinge region of antibodies. Preparations of both the intact antibody and the $F(ab')_2$ showed consistently enhanced detection capabilities that were 2.6 and 20 times that of the randomly biotinylated control, respectively.[91]

Protocol 6.13 Immobilization of biotinylated ligands on streptavidin-modified surfaces

1. Prepare a solution of ligand in a compatible buffer at a concentration of 1–20 $\mu g\,mL^{-1}$. The choice of buffer is not critical as the biotin–streptavidin interaction is strong ($K_D \approx 10^{-14}$) and takes place under a wide range of conditions. More important are the minor contaminants in free biotin that are often present with biotinylated biomolecules. As biotin is usually much smaller then the biotnylated ligand, it diffuses faster to the unoccupied binding sites and can drastically reduce the amount of bound ligand. Therefore, as a general precaution, one should excessively purify the biotinylated ligand in the corresponding buffer. Minicolumns are preferred over dialysis, as the latter is less efficient at completely removing biotin traces from the preparation.
2. Condition the streptavidin-derivatized sensor chip surface with 50 mM NaOH and 1 M NaCl for 10 min and then with immobilization buffer for 10–20 min until the baseline is stable.
3. Inject the ligand in immobilization buffer for 5–15 min. Although the binding itself proceeds rapidly, larger ligands generally require more time to reach the biotin binding pockets than smaller ones.

View Online

Published on 24 May 2017 on http://pubs.rsc.org | doi:10.1039/9781788010283-00171

The immobilization level can be controlled through the ligand concentration and incubation time. Interrupt the immobilization when the desired immobilization level is reached.

4. Run two or three test analysis cycles. Depending on the strength of the regeneration agent, a small fraction of loosely bound ligand may be desorbed. In this case, reinject the ligand solution over the chip and repeat the analysis cycles until a stable baseline is reached.

Unfortunately, one of the main characteristics of the biotin–streptavidin system, the extremely high affinity between the two binding partners, goes hand in hand with the irreversibility of the interaction.

Several approaches have been proposed to immobilize biotin-tagged ligands in a reversible manner:

- Replacing biotin by a related structure with lower streptavidin binding affinity. Examples are iminobiotin[92] and desthiobiotin.[93]
- Replacing (strept)avidin by a modified mutein with lower biotin binding affinity.[94]
- Immobilizing the streptavidin *via* complementary oligonucleotide strands that are covalently coupled to the immobilization matrix and to streptavidin (this method is discussed in Section 6.6.4.5).[130]

However, all of these alternatives either result in a lowered specificity of the bond or require a narrower range of conditions to work with, limiting the choice of ligand regeneration cocktails. Therefore, conditions under which the streptavidin–biotin interaction can be cleaved, thus rendering a reusable surface without the need to modify biotin or streptavidin, have been sought; two are as follows:

- Heating at 70 °C in water as running buffer. Although not yet employed for the regeneration of SPR sensor chips, this remarkably simple regeneration has been reported to release biotinylated ligands almost quantitatively while retaining the activity of streptavidin.[95]
- If a streptavidin surface is created through the reaction of immobilized biotin functionalities with tetrameric streptavidin, streptavidin can be irreversibly broken under highly denaturing conditions (*e.g.* 8 M guanidine · HCl at pH 1.5[97]) or similar cocktails. The robust biotin linker survives this treatment and is available for a new derivatization cycle with streptavidin.

6.6.4.2 Immobilization of His-tagged Ligands

For three decades, transition metals chelated by nitrilotriacetic acid (NTA) or other chelators have been successfully applied for the purification and detection of oligohistidine-tagged proteins, for immobilization on surfaces,

View Online

Published on 24 May 2017 on http://pubs.rsc.org | doi:10.1039/9781788010283-00171

and for tethering to lipid membranes. The fast dissociation of this interaction under mild conditions is readily achieved by adding competitors such as imidazole. Furthermore, the interaction may be switched by adding or removing the metal ion.[96] The (usually Ni^{2+}) complexes are relatively stable, although, interestingly, they are more sensitive to changes in conditions than NTA affinity columns. For total regeneration of the chip surface, these complexes can be cleaved by chelating agents such as EDTA.

Although the regenerability of the sensor surface is a highly practical feature, the K_D of the NTA–Ni^{2+}–His_6 complexes lies in the micromolar range and is therefore relatively weak. The lability of the immobilized complexes causes the continuous leaching of ligand, resulting in a drifting baseline. Furthermore, immobilized ligands are sensitive towards changes in ionic strength and/or pH along with the addition of chelating additives. Therefore, the use of this method is limited to biosensor-based experiments in which the regenerability of the ligand is of higher priority than a highly stable baseline. Small or low-affinity analytes are generally difficult to analyze using NTA-derivatized chip surfaces, as there is the risk that baseline drift and decreasing ligand density will compromise the integrity of the data set. The stability of the immobilizate is also critical when performing single-cycle kinetic experiments in which each analysis is performed in one long sample cycle.

Protocol 6.14 Immobilization of His_6-tagged ligands to (tris- or poly-)NTA surfaces

1. Mount the sensor chip derivatized with NTA or another suitable chelator.
2. Prepare the immobilization buffer using 10 mM HEPES, 0.15 M NaCl, and 0.005% Tween 20 (pH 6.4). Higher NaCl concentrations and higher pH lower the immobilization yield; lowering the pH to 6.9 increases it.
3. *Optional:* Microdialyze a 50–200 nM solution of ligand into immobilization buffer.
4. Condition the surface with 0.5 M Na EDTA (pH 8.5) for 5 min.
5. Wash for 2 min with immobilization buffer.
6. Inject 5 mM $NiCl_2$ in immobilization buffer for 2 min. Depending on the density of chelating groups, a baseline increase of 30–300 RU should be observed.
7. Wash for 2 min with immobilization buffer.
8. Inject 50–200 nM ligand in immobilization buffer for 2–5 min. In addition to changing the pH and ionic strength of the immobilization buffer, the amount of immobilized ligand can be controlled *via* the ligand concentration and contact time and should be relatively low as a certain number of unoccupied Ni complexes are required for stabilization (*i.e.* continuous rebinding of the weakly bound ($K_D < 10^{-6}$) His_6-tagged immobilizate). The binding is improved at low flow rates and high pH.

View Online

Published on 24 May 2017 on http://pubs.rsc.org | doi:10.1039/9781788010283-00171

9. Equilibrate with sample buffer until the baseline is stable. HEPES was found to give the best results, but PBS and Tris also work. Low concentrations (maximum = 50 μM) of EDTA in the sample buffer stabilize the assay as it scavenges contaminating metal ions.
10. Inject analyte in sample buffer and analyze the interaction.
11. Instead of regenerating the ligand–analyte interaction, the undissociated ligand–analyte pair can be quantitatively removed with a 3 min injection of 0.5 M Na EDTA at pH 8.5. If the surface is of good quality, about 100 such regenerations can be carried out without significantly affecting the surface capacity. This also means that the same chip can be used for many different proteins.

There are several ways to stabilize NTA-immobilized ligands and prevent leaching:

Lowering the ligand density

An efficient and simple approach is to decrease the ligand load. This provides a larger number of unoccupied NTA binding sites on the surface, which, in turn, increases the probability of rebinding dissociated ligands. A lower capture level can be obtained by adjusting the ligand concentration or by using a shorter contact time.[97]

Tris- and poly-NTA

As shown in Figure 6.32, only two out of the six His_6 tag histidines are coordinated in the Ni^{2+}–NTA complex. If more NTA groups are arranged in close vicinity of the remaining four histidines, a highly stable triple complex with a K_D of 10^{-9} is formed.

Such multiple complexation can be achieved either through three NTA groups linked with a suitable spacer geometry (tris-NTA)[102] or the self-organization of multiple NTA groups immobilized along a sufficiently flexible spacer backbone (poly-NTA).[98]

Although the affinity towards His_6 tags is three orders of magnitude higher compared with immobilization matrices with single NTA groups, resulting in stable immobilization, the regeneration conditions of standard and poly-NTA surfaces are identical (*i.e.* no harsh conditions are required).

Multiple and/or longer His_6 tags

Although studies with isolated hexahistidine tags suggest that they have high affinities with K_D in the nanomolar range, which cannot be further improved by increasing the number of histidines, the number and length of tags can affect the capture efficiency of His_x-labeled proteins. A test ligand tagged with decahistidine was more stably captured on an NTA sensor chip than the reference tagged with hexahistidine, and the best results were obtained with the double-histidine tag.[99] A hexa-spacer-deca histidine tag performed even better. The long-term stability of the immobilizate under continuous buffer flow was tested over 2 days, and the

View Online

Published on 24 May 2017 on http://pubs.rsc.org | doi:10.1039/9781788010283-00171

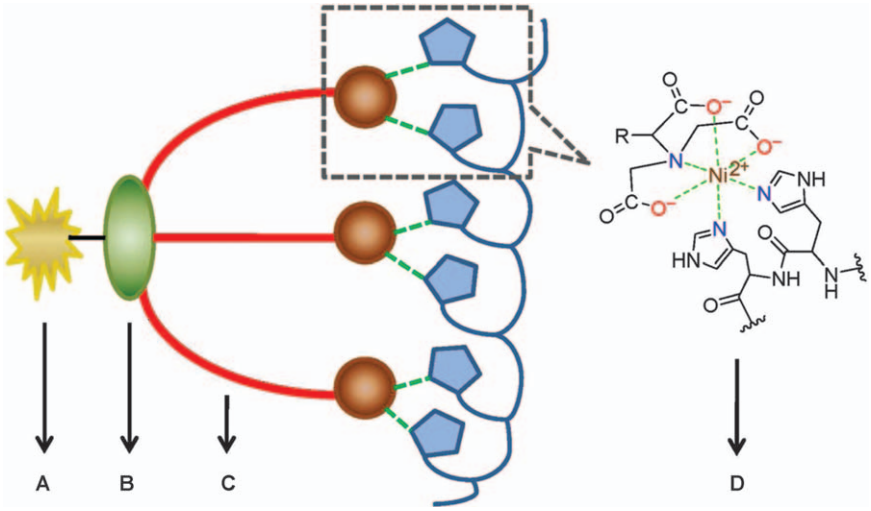


Figure 6.32 Schematic illustration of a tris-NTA–His_6 tag binding pair: (A) functional unit, (B) scaffold, (C) spacer, and (D) structure of NTA–Ni^{2+}–His_2. Reprinted with permission from Z. Huang, P. Hwang, D. S. Watson, L. Cao and F. C. Szoka, Jr, Tris-nitrilotriacetic acids of subnanomolar affinity toward hexahistidine tagged molecules, *Bioconjugate Chem.*, 2009, **20**, 1667–1672. Copyright 2009 American Chemical Society.

average baseline drift was only 2 RU min^{-1}, which is sufficiently low to be corrected for, even within a small-molecule binding experiment.[100]

Covalent stabilization

An alternative way to increase the capture stability on NTA-derivatized surfaces is to perform an amine coupling of the captured ligand.[101] The NTA groups are first chelated with nickel ions and, after activation with EDC–NHS, the ligand is injected and covalently bound. The nickel ions are then removed with EDTA. This immobilization method does not require preconcentration, and the ligand can be immobilized out of a crude sample. However, it should be kept in mind that the ligand on such surfaces is irreversibly bound, necessitating careful optimization of the regeneration conditions of the ligand–analyte interaction.

Anti-His_6 antibodies

As pointed out in Section 6.6.4.3, many ligands can be conveniently immobilized through specific IgGs. This is also the case with His_6 tags, and kits based on anti-His_6 antibodies are commercially available. The immobilization capacities of sensor chips prepared with these IgGs are roughly comparable to immobilization *via* NTA, but the stability of the resulting surfaces can vary from ligand to ligand.[104] Similarly, the non-specific background is case dependent; therefore, the optimal immobilization strategy for His_6-tagged ligands should be carefully evaluated during assay development.

View Online

Published on 24 May 2017 on http://pubs.rsc.org | doi:10.1039/9781788010283-00171

6.6.4.3 *Immobilization of and* via *Antibodies*

Regardless of the high cost, variable affinity, and short shelf-life, antibodies are ubiquitous tools for immobilizing various ligands. They are widely used in many diagnostic formats such as ELISA and lateral flow tests. In SPR-based applications, the specificity is highly critical because both specific and non-specific interactions contribute to the signal due to the label-free character and high sensitivity of direct optical biosensors. This is a major difference compared with assays using labels. Therefore, IgG selections, optimization results, and conclusions drawn from these formats should not be transferred to SPR-based applications without prior validation.

If properly selected, IgGs can be a flexible and straightforward means to immobilize almost any protein. However, one should keep in mind that owing to the size of the IgG molecules, significant non-specific binding can occur, and a considerable fraction of the evanescent field volume is occupied by the capture IgGs, thus limiting the maximum immobilization capacity for ligands and eventually resulting in steric effects that hinder undisturbed analyte binding.

Glutathione S*-transferase (GST) capture*
In addition to the aforementioned anti-His_6 system, GST tags are a prominent example of tags for indirect immobilization through capture antibodies. GST is a 26 kDa protein that binds glutathione with an affinity of 7.1 mM. The protein is widely used as a tag in protein expression to aid in purification and has been used to immobilize GST fusions on glutathione-functionalized substrates.[102] However, because the affinity towards glutathione is too low to immobilize GST fusion proteins with a stability sufficient for bioanalytical applications, IgG-based capture kits have been developed and are commercially available.

As outlined above, maximizing the specificity is key for successfully implementing antibodies in an SPR-based assay. Therefore, the immobilization method should be carefully selected.

There are two main approaches that can be used in the preparation of antibody-based sensor surfaces: random and site-directed antibody immobilization. Despite many publications reporting the benefits of site-directed antibody orientation on 2D surfaces, different antibody orientations on hydrogel matrices have been reported to result in only minor differences in specific activity.[103] In contrast, the significance of antibody orientation on a 3D support was shown in another publication.[104,122]

Figure 6.33 shows three popular site-directed immobilization methods. According to various literature reports, all of them seem to be superior to random immobilization, although no one method is significantly better than the others. Overall, antibody orientation usually improves the efficacy of the immunosensor, but it is closely related to and even dependent on the other aspects of the system (*e.g.* the nature of the antibody–antigen system,

View Online

Published on 24 May 2017 on http://pubs.rsc.org | doi:10.1039/9781788010283-00171

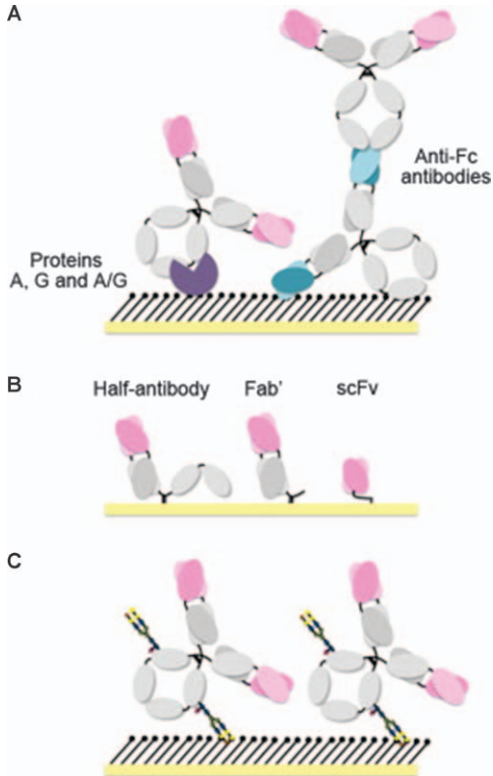


Figure 6.33 Schematic representation of site-directed antibody-immobilization: (A) *via* Fc binding proteins, (B) *via* antibody fragments, and (C) *via* oxidized oligosaccharide moieties.
Reprinted from A. Makaraviciute and A. Ramanaviciene, Site-directed antibody immobilization techniques for immunosensors, *Biosens. Bioelectron.*, **50**, 460–471. Copyright 2013, with permission from Elsevier.

the influence of steric hindrance, and non-specific interactions), the choice of regeneration conditions, and the assay format, not forgetting the stability and, of course, the cost.[122]

6.6.4.4 Protein A/G Surfaces for Antibody Immobilization

Both Protein G and protein A are well established as ligands in analytical and preparatory affinity chromatography. Protein G in particular has been shown to be useful in a variety of bioanalytical applications for the efficient capture and orientation of IgG antibodies for bacterial detection in kinetic studies and for IgG quantification in industrial applications.[105] Protein A and G surfaces are robust, allow the immobilization of IgG ligands in an oriented fashion, and can be regenerated several hundred times.[99] Therefore, they are a universal tool for the quick and straightforward preparation of various

View Online

IgG-capture surfaces, for building sandwich assays, and for fast antibody quantification.

Protocol 6.15 Immobilization of antibodies on surfaces modified with protein A or G

1. Equilibrate a protein A/G-modified sensor chip with sample buffer for 5 min until the baseline is stable. Alternatively, protein A can be immobilized on a carboxylated chip surface following Protocol 6.3.
2. Inject 5–50 μg IgG in physiological sample buffer for 3 min.
3. Wash for 2 min with sample buffer.
4. Inject the analyte sample and record the sensorgram.
5. *Optional:* Inject sample buffer and monitor dissociation.
6. Strip analyte together with ligand IgG with two 1 min pulses of 0.1 M HCl. The protein A/G surface is now ready for the immobilization of fresh IgG.

Not all antibodies bind equally well to protein A/G surfaces, hence the proper selection of the IgG affine protein and/or IgG is essential.

If a higher stability of the protein A/G with the bound IgG is desired, or if the captured IgG is precious or rare while the regenerability of the surface is less important, the complex can be stabilized by crosslinking with dimethyl pimelimidate.[106] This additional step makes the immobilizate more robust and prolongs the operational stability of the chip.

6.6.4.5 DNA-directed Protein Immobilization

The specific hybridization of single-stranded DNA (ssDNA) with the complementary DNA (cDNA) is a useful alternative method to immobilize proteins in a stable yet reversible and selective manner.[107,108] The ligand to be immobilized is first coupled to ssDNA, and the ssDNA that is linked to the protein is then hybridized to the surface, to which cDNA has been immobilized. An ssDNA tag may be attached to the protein *via* covalent linkage or a biotin–streptavidin linkage.[109] The spatially encoded DNA-directed protein immobilization has been derived from microarray technology;[110] thus, it is possible to immobilize multiple ligands in a multiplexed fashion.[125,126] Additional advantages are that the hybridized DNA acts as a spacer arm, and that the immobilization is reversible by increasing the temperature or by alkaline denaturation.[94,111]

The disadvantages of this method are the sensitivity of the immobilized ligand population towards conditions that destabilize DNA–DNA interactions, and the limited suitability for work with oligonucleotides, oligo-binding proteins, and oligo-degrading proteins. Furthermore, increased levels of non-specific binding have been reported, particularly for more complex samples such as serum or plasma.[112]

Published on 24 May 2017 on http://pubs.rsc.org | doi:10.1039/9781788010283-00171

View Online

Published on 24 May 2017 on http://pubs.rsc.org | doi:10.1039/9781788010283-00171

6.6.4.6 *Immobilization of and Through Aptamers*

Aptamers are oligonucleotide bioaffinity capture reagents that have attracted increasing attention in recent years. Nucleic acid sequences, which show the highest affinity towards a target protein, are selected from a synthetic, combinational nucleotide library called SELEX (systematic evolution of ligands by exponential enrichment).[113] Aptamers are smaller than antibodies, hence a higher density of capture agents can be coated on surfaces to yield a high binding capacity for target proteins and exploit better the volume of the evanescent field. Compared with antibodies, particularly polyclonal antibodies, aptamers are produced *in vitro*, eliminating the need for animals in production. In addition, aptamers are reported to have a longer shelf-life and are less sensitive to environmental change. Detailed reviews of aptamers in microfluidics were presented by Xu *et al.*[114] and Mosing and Bowser[115] and of aptamers for protein immobilization by Nakanishi *et al.*[94,116]

As the physicochemical characteristics of aptamers are comparable to those of oligonucleotides, the immobilization strategies are similar. In addition to the direct chemisorption of thiol-modified sequences on bare gold, which is less favorable owing to the considerable level of non-specific interactions, amino-modified aptamers were coupled to carboxyl-derivatized sensor surfaces using the already described EDC–NHS coupling method. Although this chemistry is a robust standard method, one should keep in mind that aptamers usually have a very low p*I* (*i.e.* the electrostatic preconcentration step does not work). Therefore, non-covalent methods such as the immobilization of biotinylated aptamers to streptavidin-modified chip surfaces and the hybridization of partially complementary ssDNA at aptamer with an oligonucleotide immobilized on the sensor chip surface should be considered and might yield improved coupling yields.[117]

6.6.5 Immobilization of Membrane Proteins

Membrane-associated proteins such as G protein-coupled receptors (GPCRs) are the targets for more than 50% of currently available drugs and remain the principal subject for new drug discovery. Characterizing the functions of these structures at the molecular level and their interactions with the associated signaling machinery is therefore of considerable interest. Label-free chip-based biosensors are a suitable detection platform to study these interactions because, biophysically, the surface of a sensor chip is a good model for the surfaces of cells or other particulate species, especially when modified with suitable functionalities.[118,119]

Most membrane proteins denature when removed from the lipid bilayer membrane and, if not stabilized with detergents, require a more or less intact membrane environment to display their normal functionality. This can be achieved (see Figure 6.34) by either first integrating the transmembrane species into vesicles (namely liposomes), which are then fused on a hydrophobic surface or on an amphiphilic hydrogel,[120,121] or by first

View Online

Published on 24 May 2017 on http://pubs.rsc.org | doi:10.1039/9781788010283-00171

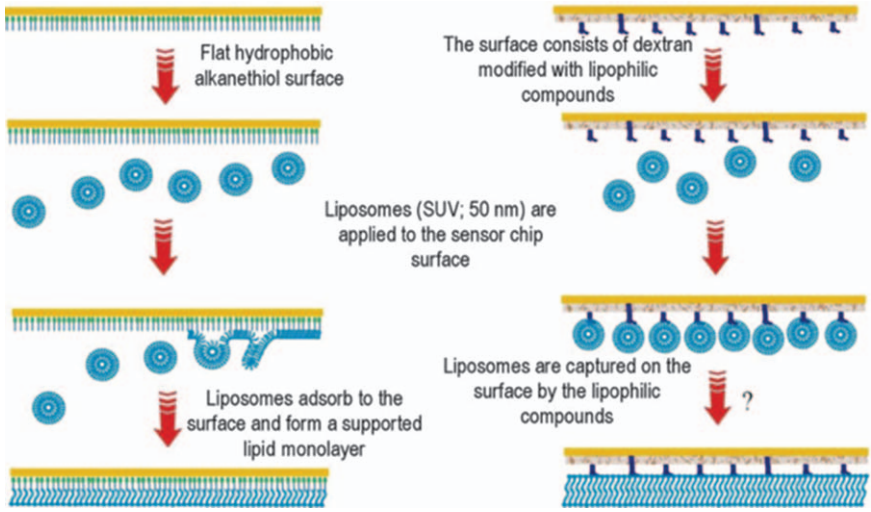


Figure 6.34 Preparation of monolayer and bilayer model membrane systems on a planar alkyl-SAM (left) and a hydrogel cushion modified with hydrophobic anchor molecules (right).
Reproduced with permission from H. Mozsolits, W. G. Thomas and M.-I. Aguilar, Surface plasmon resonance spectroscopy in the study of membrane-mediated cell signaling, *J. Pept. Sci.*, 2003, **9**(2), 77–89. Copyright 2003 European Peptide Society and John Wiley & Sons, Ltd.

immobilizing the membrane protein on a partially alkyl-derivatized hydrogel sensor chip followed by on-chip reconstitution with a lipid–detergent mixture.[122] The ligand immobilization can be covalent through capture tags or *via* antibodies; the latter allows the specific on-chip purification of particular ligands from crude cell lysates.[123]

Three surface types are suitable for the preparation of supported lipid layers:

- Hydrophobic alkyl-SAMs. Liposomes adsorb on such surfaces to form lipid **mono**layers.
- Hydrogel surfaces functionalized with lipophilic anchor molecules. These alkyl anchors penetrate the walls of vesicles, which then spread and fuse into lipid **bi**layers.
- Untreated SiO_2 surfaces. Vesicles spread spontaneously and form lipid **bi**layers.[124]

The approach using an underlying hydrogel cushion has the advantage that the lipid bilayer is supported by a hydrated structure, better resembling the natural environment of a cell wall. Transmembrane proteins lose their activity when immobilized in a hydrophobically supported lipid monolayer; hence, a fluid bilayer structure is mandatory. Furthermore, the preparation process is more robust (*i.e.* not as easily affected by the contaminants that immediately adsorb on strongly hydrophobic surfaces and require rigorous

View Online

cleaning of the liquid handling system prior to an experiment). However, for the preparation of lipid monolayers as linking interfaces for the immobilization and interaction analysis of extracellular matrix components, planar alkyl-SAMs are a well-defined and straightforward choice.

Published on 24 May 2017 on http://pubs.rsc.org | doi:10.1039/9781788010283-00171

Protocol 6.16 Preparation of mixed micelles[125]

1. Prepare a lipid film by pipetting a small volume of solution containing 10 mM lipid into a chloroform-washed round-bottomed glass tube and drying this solution under a nitrogen stream (fume hood). Slight heating in a 30 °C water bath accelerates the drying process.
2. Evacuate for at least 2 h in a vacuum desiccator to remove solvent traces.
3. Add 25 mM of the detergent octylglucoside in 9 mM HEPES at pH 6.4 and 135 mM NaCl to yield a 3.3 mM lipid solution. If other detergents are used, the volume of the detergent solution should be adjusted such that the ratio ([detergent]-$cmc_{detergent}$)/[lipid] is between 2 and 3.5. Note that the optimum ratio depends on the lipid and the detergent and must be empirically identified from case to case.
4. Shake every 10 min for at least 45 min at room temperature and check for turbidity.

Protocol 6.17 On-surface reconstitution of lipid bilayers without and with immobilized receptor protein[125]

Priming the surface:

1. Mount a partially alkyl derivatized carboxylated hydrogel-coated sensor chip.
2. Wash the surface for 5 min with 20 mM CHAPS.

Optional immobilization of receptor protein:

3. Activate the surface for 7 min with 0.2 M *N*-ethyl-*N*-dimethylaminopropylcarbodiimide and 50 mM *N*-hydroxysuccinimide.
4. Inject 10–100 μg receptor protein in a suitable coupling buffer (see Protocol 6.1) plus 20 mM octylglucoside or other suitable detergent for 10 to 20 min.
5. Quench remaining active groups for 15 min with 1 M ethanolamine (pH 8.5) plus 20 mM octylglucoside.

Formation of lipid bilayer and reconstitution of receptor protein:

6. Inject the mixed micelles (prepared as described in Protocol 6.11.) for 2 min at a slow flow rate.
7. Wash with running buffer and start the interaction experiments.

View Online

Note: The lipid bilayer can be completely removed by two 2 min injections of 20 mM CHAPS. The flow system was delayed for 2 min after injection. Lipid deposition quantity data were collected for 100 s after the end of injection. The sensor surface was regenerated by two 1 min injections of 20 mM CHAPS or optimally 50 mM octylglucoside.

Published on 24 May 2017 on http://pubs.rsc.org | doi:10.1039/9781788010283-00171

Alternatively, liposomes or cell fragments can be modified with suitable tags such as biotin, oligonucleotides, or His_6, which are then specifically bound by the corresponding capture molecules immobilized on a hydrophilic surface (Figure 6.35). The ligand (receptor protein) density can be controlled either *via* the lipid/transmembrane protein ratio during vesicle preparation or, when using the on-chip reconstitution protocol, by varying the NHS activation level (Protocol 6.17, Step 3).

The above-described immobilization in lipid bilayers mimics the natural environment of membrane proteins but with an abundance of hydrophobic domains on the surface. This can be problematic because hydrophobic domains are subject to non-specific interactions, especially when the injected

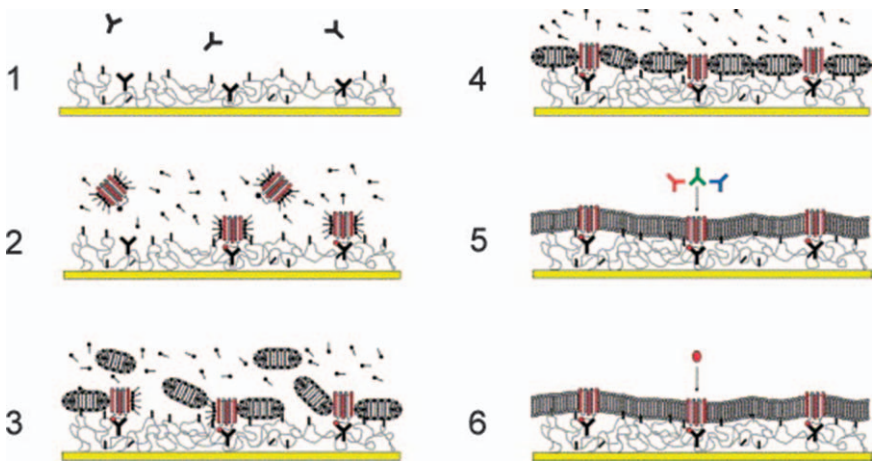


Figure 6.35 Schematic illustration of the capture and reconstitution of GPCRs on a sensor surface. (1) A capturing molecule that recognizes the GPCR at a position distant from the ligand binding site (in this case, 1D4 monoclonal antibody) is immobilized on a sensor chip that has a dextran surface containing hydrophobic alkyl groups. (2) A detergent-solubilized GPCR is captured by the immobilized antibody. (3) The captured GPCR is reconstituted in a lipid bilayer by injecting lipid–detergent mixed micelles in the analyte flow stream. (4) The surface is washed with buffer to remove detergent molecules, leaving behind a lipid bilayer. (5) The functional activity of the lipid-reconstituted GPCR is tested by binding conformation-dependent antibodies. (6) The binding of small-molecule ligands by the captured and reconstituted GPCR can then be tested. Reprinted from P. Stenlund, G. J. Babcock, J. Sodroski and D. G. Myska, Capture and reconstitution of G protein-coupled receptors on a biosensor surface, *Anal. Biochem.*, **316**(2), 243–250. Copyright 2003, with permission from Elsevier.

View Online

Published on 24 May 2017 on http://pubs.rsc.org | doi:10.1039/9781788010283-00171

analytes are hydrophobic, a typical situation during the screening of drug candidates. In addition, the solubilization of membrane proteins (including the screening of appropriate detergents), removal of the detergents, and integration into vesicles can be tedious and time-consuming tasks.

Therefore, alternative methods have been explored in order to simplify these processes, increase the ligand's stability, and make the assay more specific. Three such methods are as follows:

- Stabilizing the membrane-associated ligands by genetic point mutations so that they remain active outside the cell membrane without detergents. At the same time, tags for purification may be introduced, which can also be used for directed immobilization.[118]
- Immobilizing the solubilized ligand to standard hydrogel-coated surfaces and adding detergent to the running buffer. A membrane protein may not always have to be in a membrane or lipid environment to retain its analyte binding activity; if carefully optimized, the solubilization in detergent may be sufficient.[125]
- As above, but replacing detergents by more stable amphipoles (APols). APols are short amphipathic polymers developed to keep membrane proteins soluble as individual complexes in aqueous solution in the absence of detergent. The polymer consists of highly polar groups that separate hydrophobic chains along the polymer.[126,127] These polymers can be further modified to contain linker groups for attachment to the sensor surface (see Figure 6.36).

Some APols that have been synthesized and characterized include biotinylated APols (BAPols), polyhistidine- and imidazole-tagged APols (HistAPols and ImidAPol), and oligodeoxynucleotide-derivatized APols (OligAPols). As the chemistries of APols are versatile, it should not be problematic to add almost any desired functionality to these polymers.

6.6.6 Overview and Selection of Immobilization Chemistries

Although ongoing efforts strive to simplify and standardize immobilization protocols, there is still no ideal, general-purpose immobilization strategy, and the optimum choice depends on the experimental approach along with the natures of the ligand, analyte, and sample buffer. Generally, it is desirable that the immobilization chemistry does not interfere with the ligand's binding characteristics, and that the ligand's activity is affected as little as possible by the link to the sensor chip surface. In most cases, the straightforward covalent methods give good results. As a rule of thumb, it is advisable to begin experiments with standard amino coupling chemistry combined with low- to medium-density hydrogels (see below) and, if not successful, to try alternative, site-directed immobilization strategies.

As can be seen in Figure 6.37, owing to its robustness and good immobilization yield, standard amino coupling is the most popular method, followed by directed immobilization of biotinylated ligands. However, when

View Online

Published on 24 May 2017 on http://pubs.rsc.org | doi:10.1039/9781788010283-00171

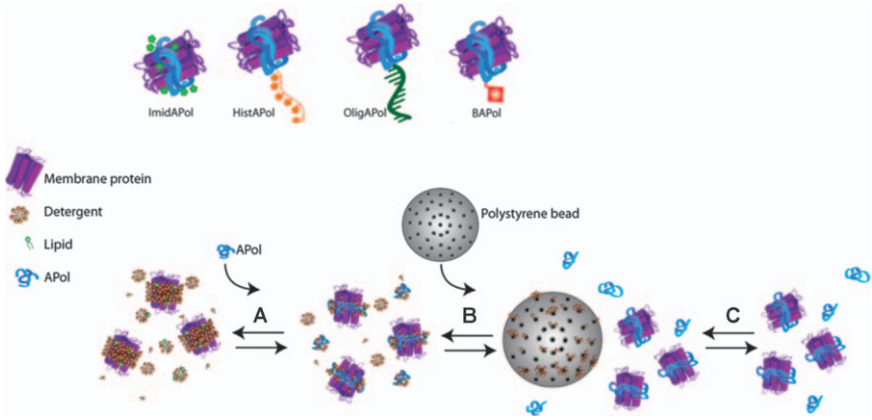


Figure 6.36 Some tagged APols and workflow for trapping membrane proteins (MPs) in APols. First, MPs are extracted from the membrane by a detergent and are optionally purified. (A) APols are added, and mixed APol–detergent–MP complexes are formed. (B) Detergent is removed by adsorption on polystyrene beads. (C) After detergent removal, the MP–APol complexes are soluble in detergent-free solutions.
Reprinted from E. A. Della Pia, R. W. Hansen, M. Zoonens and K. L. Martinez, Functionalized amphipols: a versatile toolbox suitable for applications of membrane proteins in synthetic biology, *J. Membr. Biol.*, **247**, 815–826. Copyright 2014, with permission from Elsevier.

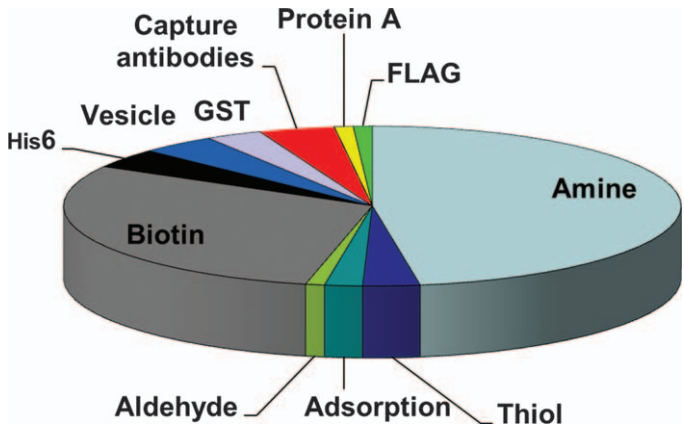


Figure 6.37 Relative usage of different immobilization techniques in 2003. Data from ref. 131.

analyzing such statistics, one should keep in mind that the use of different immobilization methods is significantly constrained by the commercial availability of suitable sensor chip surfaces.

Table 6.4 might be helpful in identifying immobilization methods for the most common ligands, but note that not every method is suitable in each specific case.

Published on 24 May 2017 on http://pubs.rsc.org | doi:10

Table 6.4 Suitable immobilization strategies for different ligands: the recommended methods are listed first, and Protocol numbers are given in parentheses.

Ligand	Immobilization method	Remarks
Proteins, general	EDC–NHS (6.4) Thiol exchange, maleimide (6.6, 6.7, 6.8, 6.9) Reductive amination (6.5) Ni^{2+}/His_6 (6.14) Biotin–streptavidin (6.13) Direct adsorption Epoxide coupling (6.12) Azlactone Oligonucleotide linkers Aptamers Photocoupling	Dry coupling or micelle-mediated immobilization may be necessary if pI <4, as preconcentration becomes difficult
Membrane proteins	On-surface reconstitution (6.17) Amphipoles (optionally tagged) Incorporation into labeled micelles	Requires labeled lipids
Antibodies	EDC–NHS (6.4) Protein A/G (6.15) Secondary antibodies Thiol exchange, maleimide (6.6, 6.7, 6.8, 6.9) Ni^{2+}/His_6 (6.14) Hydrazide (6.11) Biotin–streptavidin (6.13) Epoxide coupling (6.12) Azlactone Oligonucleotide linkers Aptamers Photocoupling	Obey different affinities After oxidation of glycosyl residues
Antibody fragments, affibodies	EDC–NHS (6.4) Thiol exchange, maleimide (6.6, 6.7, 6.8, 6.9) Biotin–streptavidin (6.13) Epoxide coupling (6.12) Azlactone Oligonucleotide linkers Aptamers Photocoupling	
Glycoproteins	EDC–NHS (6.4) Hydrazide (6.11)	

Published on 24 May 2017 on http://pubs.rsc.org | doi:10

	Thiol exchange, maleimide (6.6, 6.7, 6.8, 6.9)	
	Biotin–streptavidin (6.13)	
	Epoxide coupling (6.12)	
	Azlactone	
	Photocoupling	
Peptides	EDC–NHS (6.4, 6.3)	Dry coupling may be necessary as preconcentration is difficult
	Reductive amination (6.5)	
	EDC–NHS-activated peptides to amines	Dilute sample to avoid crosslinking
	Biotin–streptavidin (6.13)	
	Ni^{2+}/His_6 (6.14)	
	Epoxide coupling (6.12)	
	Azlactone	
	Click chemistry	
	Photocoupling	
Small molecules	EDC–NHS (6.4, 6.3)	Chemistry depends on ligand functional groups. Dry coupling may be necessary due to the lack of preconcentration effect
	Reductive amination (6.5)	
	Biotin–streptavidin (6.13)	
	Hydrazide (6.11)	
	Reverse EDC–NHS to amino surface	
	Epoxide coupling (6.12)	
	Click chemistry	
	Photocoupling	
DNA	EDC–NHS, dry (6.4, 6.3)	EDC–NHS and epoxy coupling require amino-modified oligonucleotides but give higher immobilization yields
Oligonucleotides	Epoxide coupling (6.12)	
	Biotin/streptavidin (6.13)	
	Photocoupling	
DNA, native	Electrosorption (6.1)	Combine with epoxy activation
	EDC–NHS, dry (6.4, 6.3)	
PCR products	Photocoupling	
Carbohydrates	Hydrazide (6.11)	
	Epoxide coupling (6.12)	
	Click chemistry	
	Photocoupling	
Cells, cell fragments	Specific capture antibodies	
	Electrosorption to 2D amine surfaces	
	Lectins	
	Biotin–streptavidin (6.13)	If biotinylation possible
Viruses, fragments	Specific capture antibodies	
	Electrosorption to amine surfaces	

View Online

6.7 Considerations for Spatially Resolved Immobilization

Multiplexed and label-free protein analysis offers tremendous potential for drug discovery as it provides a versatile means for the high-throughput assays required for target and lead identification and also diagnostics and functional screening for personalized medicine. However, the development of efficient, universal, and protein-compatible immobilization techniques is a demanding task. In addition, not every deposition method that works well for DNA microarray production is suitable for delicate and often costly protein ligands. Further, ensuring the functional integrity of proteins on surfaces remains challenging, particularly for membrane proteins, the most important class of drug targets.

Several critical issues with protein microarrays have been identified: (1) inconsistent printed microspot morphologies and uniformities; (2) low signal-to-noise ratios due to factors such as complex surface capture protocols, contamination, and static or no-flow mass transport conditions; (3) inconsistent quantification of captured signal due to spot uniformity issues; (4) non-optimum protocol conditions (*e.g.* pH and temperature), which promote variability in assay kinetics; and (5) poor protein (*e.g.* antibody) printing, storage, and/or shelf-life compatibility with common microarray assay fabrication methods, which are directly related to microarray protocols.[128]

The key factors involved in overcoming these problems [namely a homogeneous ligand distribution within a spot, sufficient density of active ligand, and long-term (storage) stability of the ligand] are directly correlated with the chip surface nanoarchitecture, the coupling chemistry, and the interplay with the deposition method employed.

Figure 6.38 shows different methods for the fabrication of protein microarrays (also see Table 6.5). Today, only direct deposition techniques (*i.e.* contact and non-contact printing) have practical relevance. This might be due to the evolution from DNA microarray printing, where a wide range of adaptable instrumentation along with the related know-how has been developed over the last two decades. The reasonable throughput, compatibility with existing infrastructure, and relative simplicity of these approaches might be additional factors favoring the use of direct printing.

It makes sense to start the selection of the optimum coupling chemistry and nanostructure with the intended application of the corresponding array and divide SPR microarrays in two major groups:

- *Arrays for individual research.* Such arrays may be analytical or functional, and their setups span the entire range of SPR assay formats known today. IgG ranking, drug screening, epitope binning, and biochemical pathway mapping are typical applications. These arrays and their surface requirements are so diverse that their greatest commonality is that they are custom manufactured in relatively small runs, often

Published on 24 May 2017 on http://pubs.rsc.org | doi:10.1039/9781788010283-00171

View Online

Published on 24 May 2017 on http://pubs.rsc.org | doi:10.1039/9781788010283-00171

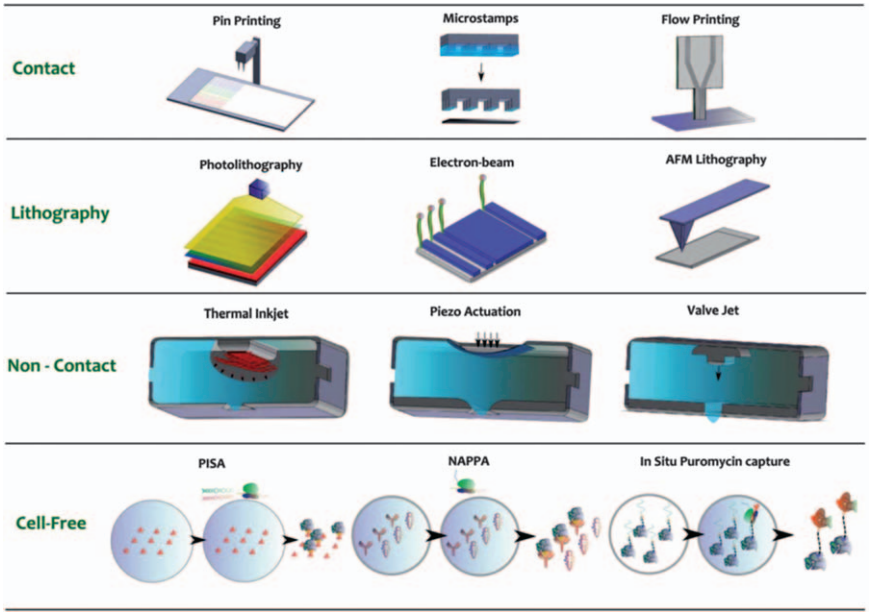


Figure 6.38 Summary of various technologies for the fabrication of protein arrays. Reprinted from ref. 128 with permission from the Royal Society of Chemistry.

by the end user immediately before the interaction experiment. Throughput and long-term stability are therefore not a primary concern. With this in mind, microfluidic flow (CFM) printers should be the first choice for the small-scale production of such arrays as these devices are based on the proven and defined concept of micro-flow cells (the same principle as applied in standard SPR instruments for 25 years). Their disadvantage of limited scalability is not relevant for small batches, and the ability to transfer known protocols from other SPR instruments to the microarray scale is an invaluable advantage that saves time and resources during method development. In line with the above, practically any surface and coupling chemistry listed in this chapter is compatible with these printers.

- *Analytical microarrays for assaying analyte concentrations.* Until now, such assays have been the domain of indirect methods such as ELISA or various dipstick lateral flow tests. Owing to the drastically reduced complexity, higher accuracy, and shorter processing time combined with the elimination of cross-reactivity issues, which can be a real problem in multiplexed, microarray-based protein analysis, direct assays offer significant advantages over these traditional formats. Typical application areas for such arrays are diagnostics, environmental/food analysis, and protein mapping. Microarrays of this group are manufactured in high numbers, and many applications are cost sensitive.

Published on 24 May 2017 on http://pubs.rsc.org | doi:10

Table 6.5 Side-by-side comparison of different protein microarray fabrication methods. Reproduced from ref. 127 with permission from the Royal Society of Chemistry.

	Throughput	Spot quality	Array fabrication flexibility (ability to print different biomolecules: cells, antibodies, proteins, lipids *etc.*)	Maintenance	Special requirements[a]
Pin printing	++++	++	+++	+++	++ ε, η, ↑, δ
Microstamping	+++	+++	+++	++++	+++ ς, ε
Photolithography	+++	+++	+++	++++	+++ ς, ε
DPN	++	+++	+++	+++	++ ε, η, ↑, δ
E-beam	++	+++	+++	+++	++ ς, ε
Thermal InkJet	+++	+++	++++	++	++ ε, η, ↑, δ
Piezo Actuation	+++	+++	++++	++	++ ε, η, ↑, δ
Valve jet	+++	+++	++++	++	++ ε, η, ↑, δ
Microfluidics	+	++++	++++	++++	++++ υ
PISA cell free	++	+++	++	N/A	+++
NAPPA cell free	++	+++	++	N/A	+++
Ratings criteria					
++++	1000's spots per second	Consistent inter and intra spot morphology	Can be used to generate arrays employing a very large and diverse number of biomolecules	Very little maintenance, can be performed by the user	Very few external and internal factors need to be controlled. Samples can be printed straight out of the box or as directed
+++	100's spots per second	Usually consistent requiring very little adjustment	Can be used to generate arrays using a number of different biomolecules	Maintenance is required however user can be guided to fix most issues	A few variables with need to be controlled. Some modification of protocols is necessary to insure effective printing
++	10's spots per second	Some inconsistency in morphology, requiring consistent user readjustment	Is limited to printing a small amount of biomolecules	Maintenance requires outside expertise	A large number of external or internal factors will need to be accounted for
+	<1 spot per second	Inconsistent spot morphology	Can effectively array a certain type of biomolecule	Intricate maintenance, requires outside expertise, with potentially long machine downtimes	Samples need to be modified in order to be used with the system. Most variables will need to be controlled

[a] υ = viscosity, ε = ongoing expenses, η = humidity, ↑ = temperature, δ = buffers, ς = clean room conditions.

View Online

Therefore, pin or microjet spotters, which can achieve high throughputs, are the first choice for the large-scale production of SPR microarrays for multiplexed analyte quantification.

With the latter droplet-deposition formats (either contact or non-contact), the choice of the appropriate surface and coupling chemistry is absolutely crucial for homogeneous spots, high activities, low intra-ligand variation, and long-term stability.

Ideally, the substrate should be coated with a thick hydrogel brush having a high immobilization capacity. Such coatings immediately absorb spotted droplets and fix the liquid evenly, resulting in a homogeneous spot morphology and a low inner- and intra-spot coefficient of variation (CV). Thin coatings are less suitable, as the spotted liquid is subject to microconvection and spreading, resulting in donut effects, smeared and/or merged spots, and other unwanted artifacts (see Figure 6.39).

As described in Section 6.1.2, thick hydrogels with high ligand densities result in a more or less pronounced diffusion-controlled analyte binding. Although in a typical biomolecular interaction analysis experiment one usually tries to avoid such a regime, diffusion limitation is the perfect prerequisite for analyte quantification because the initial slope of the then linear sensorgram is directly correlated with the analyte concentration, which can be easily calculated with simple and automated software algorithms (Figure 6.40).

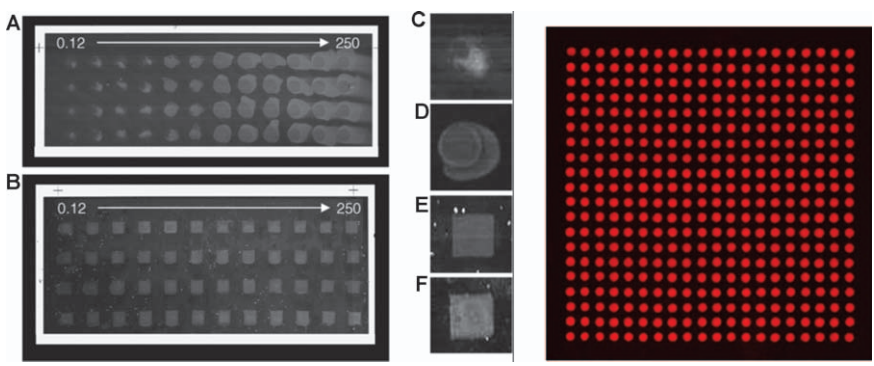


Figure 6.39 Left: printing of different concentrations of test protein on a 2D surface (bare gold) using a pin (A) and a microfluidic spotter (B). Uneven distribution and spot smearing appear with the pin spotting but not with CFM printing. Right: test array produced with a pin spotter on a 1–2 μm polycarboxylate hydrogel brush. (HC1500M, XanTec). In contrast to the 2D surface, the spots are homogeneous and no artifacts are observed. Reprinted from S. Natarajan, P. S. Katsamba, A. Miles, J. Eckman, G. A. Papalia, R. L. Rich, B. K. Gale and D. G. Myszka, Continuous-flow microfluidic printing of proteins for array-based applications including surface plasmon resonance imaging, *Anal. Biochem.*, **373**, 141–146. Copyright 2007, with permission from Elsevier.

Published on 24 May 2017 on http://pubs.rsc.org | doi:10.1039/9781788010283-00171

View Online

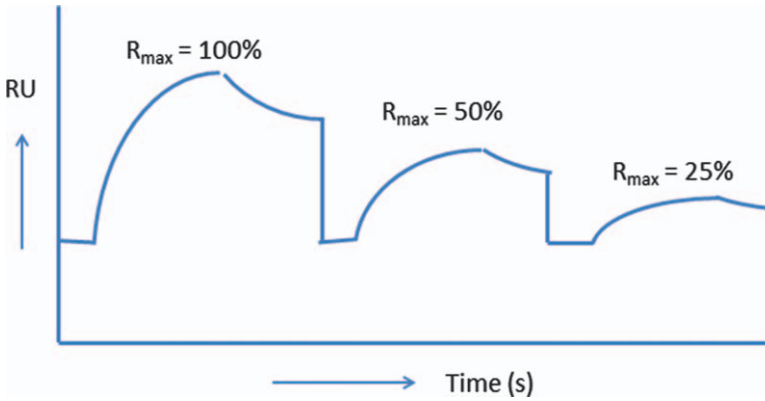


Figure 6.40 Decrease in R_{max} value.

In addition, the stability of most protein ligands, especially those in the dry state, is significantly increased when they are embedded in a protein-friendly microenvironment rather than being exposed to the ambient atmosphere, as would be the case on thin hydrogels or even 2D structures.

In addition to the surface nanostructure, the coupling chemistry should also be adapted to the requirements of dry immobilization. The good news is that the often problematic electrostatic preconcentration plays a minor role, as the drying process forces the ligand onto the surface anyway. Incubation times are also less critical because once printed, the chips can easily be incubated for hours or longer and even at slightly elevated temperature or under irradiation if necessary. On the other hand, overly reactive coupling chemistry might be partially deactivated (hydrolyzed) before the spotting run has been completed, or undesired side reactions might occur. For example, NHS-activated carboxymethyldextran, the standard matrix used in most SPR experiments, is not suitable for dry spotting because the reactive NHS esters crosslink with the carboxy groups of the sugar moieties, which contain abundant hydroxyl functionalities. This results in the formation of an impenetrable, hard resin and the almost complete loss of the highly hydrated, 3D structure. Protein-compatible, pure polycarboxylates, which are not based on polysaccharides, are the clearly superior alternative, as their NHS-activated forms do not undergo such side reactions.

In addition to the well-known NHS coupling, the less reactive epoxy and azlactone chemistries are suitable and, at least in the case of epoxy coupling, have a long history of immobilization on affinity chromatography resins and protein microarrays. Unlike NHS esters, they do not hydrolyze quickly, making the spotting process more robust.

Photocoupling (see Section 6.6.3.9) might play a particularly interesting role in the production of microarrays. The unselective, random attack of the highly reactive intermediate allows the immobilization of any ligand, regardless of its chemical structure, even for ligands that cannot be immobilized at all using conventional chemistries. The resulting standardization,

Published on 24 May 2017 on http://pubs.rsc.org | doi:10.1039/9781788010283-00171

View Online

better process control, and compatibility with existing equipment further add to the advantages of this simple and straightforward coupling protocol.

6.8 Conclusions and Outlook

Published on 24 May 2017 on http://pubs.rsc.org | doi:10.1039/9781788010283-00171

This chapter gives an overview of the surface technology for SPR and related biosensors. A few key factors (namely composition and nanostructure of the immobilization matrix) determine the performance and characteristics of the sensor chip and should be used to optimize the system for particular applications. As a direct consequence of the increasing variety of ligand–analyte interactions that can be analyzed by SPR, different immobilization methods have been developed in recent years, and the most important ones are presented here.

At the end of this chapter, it can be concluded that the data quality delivered by optical biosensors is only as good as the surface of the biochip, making it necessary to select carefully the optimum nanostructure and coupling chemistry for a particular application. Because SPR is a very sensitive yet unselective method, artifacts caused by defective or suboptimal surfaces are immediately visible, stressing the requirement for a highly inert immobilization matrix and rigorous optimization.

A highly dynamic, recently evolved field is the development of nanostructured transducer layers. Such chips not only boost the sensitivity of standard SPR setups, but also form the basis for low-cost detection platforms with drastically simplified optics. The coming years will show if the considerable potential of these new approaches will materialize into innovative analytical tools.

Amphipoles are poised to revolutionize the field of membrane proteins. This new class of polymers holds the potential to simplify and standardize drastically the currently tedious immobilization protocols, further increasing the robustness of the assays.

Despite the enormous progress in the fields of bionanotechnology and surface science in recent years, the design of surfaces for analytical and biomedical devices remains a challenge. The interplay among multifunctional macromolecules, ions, and other dissolved species and water molecules at interfaces results in a complex scenario that is difficult to describe with theoretical models. Therefore, several phenomena and processes at the molecular scale remain incompletely understood. As time passes, these last knowledge gaps in surface science are slowly disappearing, resulting in chip surfaces with increased signal-to-noise ratios and more homogeneous binding site distributions. As predicted in the previous edition of this book, polysaccharide matrices of microbial origin, which are inhomogeneous on the nanoscale but are still frequently employed, are being replaced more and more by better defined synthetic polymers with optimized functionalities and structures. In addition, intense research on 2D surfaces has led to functionalized coatings that are nearly quantitatively bioinert.

View Online

Published on 24 May 2017 on http://pubs.rsc.org | doi:10.1039/9781788010283-00171

In addition to further minimizing the non-specific background and optimizing surface homogeneity, there is still a clear demand for more universal and easily performed immobilization techniques that are standardized and can be used for any ligand regardless of its chemistry, size, and structure. Photochemistry might represent a step in this direction, although it is too early to judge the suitability of this approach for SPR. In the future, we envision relatively simple protocols that allow the efficient and fully automated immobilization of the most frequently employed ligand classes.

As pointed out in the last part of this chapter, the surfaces and deposition methods for SPR microarrays are another area of ongoing development as the large number of ligands to be immobilized in parallel combined with additional requirements demand adaptable and process-compatible protocols for the deposition, immobilization, and long-term stabilization of ligand arrays.

6.9 Questions

1. Try to scale the dimensions roughly by drawing perpendicular to the surface (1) the gold layer thickness of an SPR device, (2) the antibody coating, (3) the evanescent field, and (4) the stagnant layer in mass transport-controlled kinetics if we use a flow cell height of (5) two white blood cells.
2. Recently, several SPR transducers have been developed that utilize localized surface plasmons. What are the differences from the standard Kretschmann configuration? Discuss the pros and cons of such setups.
3. A protein with a p*I* of 4.8 is to be covalently immobilized on a polycarboxylate hydrogel-coated sensor chip using EDC–NHS coupling. A coupling buffer of pH 4.5 and ionic strength 10 mM after activation with 50 mM EDC–NHS is used, but unfortunately, the immobilization yield is poor.
   A. Discuss potential reasons for this observation. How would it be possible to discriminate whether the electrostatic preconcentration or the covalent coupling step cause the low immobilization level?
   B. When discussing the problem in your laboratory, several proposals came up for how to improve the immobilization yield:
      i. increasing the concentration of the ligand;
      ii. increasing the EDC concentration;
      iii. lowering the pH of the immobilization buffer;
      iv. lowering the ionic strength of the immobilization buffer;
      v. using sulfo-NHS instead of NHS;
      vi. purifying (dialyzing) the ligand.
   C. Sort these measures by their effectiveness for the two possibilities that
      a. the electrostatic interaction, or
      b. the covalent coupling is the reason for the low immobilization yield.

View Online

Published on 24 May 2017 on http://pubs.rsc.org | doi:10.1039/9781788010283-00171

4. Draw a typical sensorgram of three analysis cycles if the ligand is decoupled after each regeneration step (*e.g.* 50% loss of ligand after a regeneration step).
5. The immobilization of His_6-tagged ligands on NTA-derivatized sensor chips usually results in drifting baselines. Why?
   a. How can this problem be addressed?
   b. Discuss potential pros and cons of these methods.
6. A common observation with affinity biosensors is the dependence of the electrostatic adsorption (preconcentration) and thus the immobilization capacity on the flow rate of the liquid handling system. Would you expect a higher or lower capacity with increasing flow rate? Explain the phenomenon.
7. Concerning immobilization:
   a. Small ligands or oligonucleotides are frequently immobilized *via* biotin–streptavidin interaction. Why?
   b. An alternative can be the direct immobilization through reactive groups. What should be obeyed in this case?
   c. Discuss the advantages and disadvantages of indirect *versus* direct immobilization.
8. Usually, microflow spotters give higher immobilization densities and more homogeneous spots. Why? Despite these advantages, there are a few applications where droplet spotting is preferred. Which applications are these, and why?

References

1. B. Alberts, D. Bray, J. Lewis, M. Raff, K. Roberts and J. D. Watson, *Molekularbiologie der Zelle*, VCH, Weinheim, 2nd edn, 1990.
2. J. Israelachvili, *Intermolecular and Surface Forces*, Academic Press, San Diego, 2nd edn, 1992.
3. P. Schuck, L. F. Boyd and P. S. Andersen, Measuring protein interactions by optical biosensors, in *Current Protocols in Protein Science*, John Wiley & Sons, New York, 1999, pp. 20.2.1–20.2.21. (Annual Report 1 Z01 OD 010485).
4. J. Svitel, A. Balbo, R. A. Mariuzza, N. R. Gonzales and P. Schuck, *Biophys. J.*, 2003, **84**, 4062–4077.
5. H. Zhao, I. I. Gorshkova, G. L. Fu and P. Schuck, *Methods*, 2013, **59**, 328–335.
6. J. Sadowski, J. Lekkala and I. Vikholm, *Biosens. Bioelectron.*, 1991, **6**, 439–444.
7. C. Rhodes, S. Franzen, J.-P. Maria, M. Losego, D. N. Leonard, B. Laughlin, G. Duscher and S. Weibel, *J. Appl. Phys.*, 2006, **100**, 054905-1–054905-4.
8. J. Homola, I. Koudela and S. S. Yee, *Sens. Actuators, B*, 1999, **54**, 16–24.
9. S. Ekgasit, C. Thammacharoen, F. Yu and W. Knoll, *Appl. Spectrosc.*, 2005, **59**(5), 661–667.

View Online

Published on 24 May 2017 on http://pubs.rsc.org | doi:10.1039/9781788010283-00171

10. B. A. Snopok, K. V. Kostyukevich, S. I. Lysenko, P. M. Lytvyn, O. S. Lytvyn, S. V. Mamykin, S. A. Zynyo, P. E. Shepeliavyi, S. A. Kostyukevich, Y. M. Shirshov and E. F. Venger, *Semicond. Phys., Quantum Electron. Optoelectron.*, 2001, **4**, 56–69.
11. H. Neff, W. Zong, A. M. N. Lima, M. Borre and G. Holzhüter, *Thin Solid Films*, 2006, **496**, 688–697.
12. C. A. Goss, D. H. Charych and M. Majda, *Anal. Chem.*, 1991, **63**(1), 85–88.
13. B. A. Sexton, B. N. Feltis and T. J. Davis, *Sens. Actuators, A*, 2008, **141**, 471–475.
14. A. Shalabney and I. Abdulhalim, *Laser Photonics Rev.*, 2011, **5**(No. 4), 571.
15. A. W. Wark, H. J. Lee and R. M. Corn, *Anal. Chem.*, 2005, **77**, 3904–3907.
16. S. A. Zynio, A. V. Samoylov, E. R. Surovtseva, V. M. Mirsky and Y. M. Shirshov, *Sensors*, 2002, **2**, 62–70.
17. C. J. Alleyne, A. G. Kirk, R. C. McPhedran, N. A. Nicorovici and D. Maystre, *Opt. Express*, 2007, **15**(13), 8163–8169.
18. *Nanobiosensors and Nanobioanalyses*, ed. M. C. Vestergaard, K. Kerman, I.-M. Hsing and E. Tamiya, Springer, Tokyo, 2015.
19. J. C. Love, L. A. Estroff, J. K. Kriebel, R. G. Nuzzo and G. M. Whitesides, *Chem. Rev.*, 2005, **105**, 1103–1169.
20. C. Pale-Grosdemange, E. S. Simon, K. L. Prime and G. M. Whitesides, *J. Am. Chem. Soc.*, 1991, **113**, 12–20.
21. C. D. Bain, J. Evall and G. M. Whitesides, *J. Am. Chem. Soc.*, 1989, **111**, 7155–7164.
22. N. T. Flynn, T. N. T. Tran, M. J. Cima and R. Langer, *Langmuir*, 2003, **19**, 10909–10915.
23. *Multilayer Thin Films: Sequential Assembly of Nanocomposite Materials*, ed. G. Decher and J. B. Schlenoff, Wiley-VCH, Weinheim, 2006.
24. E. Wijaya, C. Lenaerts, S. Maricot, J. Hastanin, S. Habraken, J.-P. Vilcot, R. Boukherroub and S. Szunerits, *Curr. Opin. Solid State Mater. Sci.*, 2011, **15**, 208–224.
25. S. Szunerits, Y. Coffinier, S. Janel and R. Boukherroub, *Langmuir*, 2006, **22**, 10716–10722.
26. (a) L. Wu, H. S. Chu, W. S. Koh and E. P. Li, *Opt. Express*, 2010, **18**, 14395; (b) O. Salihoglu, O. Balci and C. Kocabas, *Appl. Phys. Lett.*, 2011, **100**, 213110; (c) A. Penezic, G. Deokar, D. Vinaud, E. Pichonat, P. Subramanian, B. Gašparovi, R. Boukherroub and S. Szunerits, *Plasmonics*, 2014, **9**, 677.
27. M. R. Lockett, S. C. Weibel, M. F. Philips, M. R. Shortreed, B. Sun, R. M. Corn *et al.*, *J. Am. Chem. Soc.*, 2008, **130**, 8611.
28. P. Van der Voort and E. F. Vansant, *J. Liq. Chromatogr. Relat. Technol.*, 1996, **19**, 2723–2752.
29. J. J. Cras, C. A. Rowe-Taitt, D. A. Nivens and F. S. Ligler, *Biosens. Bioelectron.*, 1999, **14**, 683–688.
30. P. Silberzan, L. Leger, D. Aussere and J. J. Benattar, *Langmuir*, 1991, **7**, 1647–1651.

View Online

Published on 24 May 2017 on http://pubs.rsc.org | doi:10.1039/9781788010283-00171

31. S. R. Holmes-Farley, R. H. Reamey, T. J. McCarthy, J. Deutch and G. M. Whitesides, *Langmuir*, 1985, **1**, 725–740.
32. U. Lappan, H.-M. Buchhammer and K. Lunkwitz, *Polymer*, 1999, **40**, 4087–4091.
33. A. Delcorte, P. Bertrand, E. Wischerhoff and A. Laschewsky, *Langmuir*, 1996, **13**, 5125–5136.
34. S. Liu, M. M. L. M. Vareiro, S. Fraser and A. T. A. Jenkins, *Langmuir*, 2005, **21**, 8572.
35. L. Vroman, J. S. Mattson and C. A. Smith, *Science*, 1974, **184**, 585–586.
36. M. A. C. Stuart, *Surfactant Sci. Ser.*, 1998, **75**, 1–25.
37. P. Billsten, M. Wahlgren, T. Arnebrandt, J. McGuire and H. Elwing, *J. Colloid Interface Sci.*, 1995, **175**, 77–82.
38. S. Ravichandran and J. Talbot, *Biophys. J.*, 2000, **78**, 110–120.
39. P. Vadgama, *Annu. Rep. Prog. Chem., Sect. C: Phys. Chem.*, 2005, **101**, 14–52.
40. A. Wittemann, B. Haupt and M. Ballauff, *Phys. Chem. Chem. Phys.*, 2003, **5**, 1671–1676.
41. C. Czeslik, R. Jansen, M. Ballauff, A. Wittemann, C. A. Royer, E. Gratton and T. Hazlett, *Phys. Rev. E: Stat., Nonlinear, Soft Matter Phys.*, 2004, **69**, 021401.
42. E. Ostuni, R. G. Chapman, R. E. Holmlin, S. Takayama and G. M. Whitesides, *Langmuir*, 2001, **17**, 5605–5620.
43. P. M. Claesson, in *Biopolymers at Interfaces*, ed. M. Malmsten, Marcel Dekker, New York, 1998, vol. 75, pp. 281–320.
44. K. L. Prime and G. M. Whitesides, *Science*, 1991, **252**(5009), 1164–1167.
45. D. Schwendel *et al.*, *Langmuir*, 2001, **17**, 5717–5720.
46. Z. H. Yang, J. A. Galloway and H. U. Yu, *Langmuir*, 1999, **15**(24), 8405–8411.
47. S. J. Sofia, V. Premnath and E. W. Merrill, *Macromolecules*, 1998, **31**(15), 5059–5070.
48. J. Groll *et al.*, *Langmuir*, 2005, **21**(5), 1991–1999.
49. C. D. Walkey and W. C. W. Chan, *Chem. Soc. Rev.*, 2012, **41**, 2780–2799.
50. F. Kawai, T. Kimura, M. Fukaya, Y. Tani, K. Ogata, T. Ueno and H. Fukami, *Appl. Environ. Microbiol.*, 1978, **35**, 679–684.
51. S. Jiang and Z. Cao, *Adv. Mater.*, 2010, **22**(9), 920–932.
52. O. R. Bolduc, J. N. Pelletier and J.-F. Masson, *Anal. Chem.*, 2010, **82**, 3699–3706.
53. S. I. Milner, T. A. Witten and M. E. Cates, *Europhys. Lett.*, 1988, **5**, 413–418.
54. I. Szleifer, *Phys. A*, 1996, **244**, 370–388.
55. C. Siegers, M. Biesalski and R. Haag, *Chem. – Eur. J.*, 2004, **10**, 2831–2838.
56. A. W. Drake, M. L. Tang, G. A. Papalia, G. Landes, M. Haak-Frendscho and S. L. Klakamp, *Anal. Biochem.*, 2012, **429**, 58–69.
57. B. W. Morrisey and C. C. Han, *J. Colloid Interface Sci.*, 1978, **65**, 423–431.
58. C. J. Van Oss and J. M. Singer, *J. Reticuloendothelial Soc.*, 1966, **3**, 29–40.

View Online

Published on 24 May 2017 on http://pubs.rsc.org | doi:10.1039/9781788010283-00171

59. J. E. Butler, L. Ni, R. Nessler, K. S. Joshi, M. Suter, B. Rosenberg, J. Chang, W. R. Brown and L. A. Cantarero, *J. Immunol. Methods*, 1992, **150**, 77–90.
60. B. Johnsson, S. Löfås and G. Lindquist, *Anal. Biochem.*, 1991, **198**, 268–277.
61. D. G. Hoare and D. E. Koshland, *J. Am. Chem. Soc.*, 1966, **88**, 2057–2058.
62. J. C. Sheehan and J. J. Hlavka, *J. Org. Chem.*, 1956, **21**, 439–441.
63. P. Cuatrecasaes and I. Parikh, *Biochemistry*, 1972, **11**, 2291–2299.
64. L. Peng, G. J. Calton and J. W. Burnett, *Appl. Biochem. Biotechnol.*, 1986, **14**, 91–99.
65. S. P. Massia and J. Stark, *J. Biomed. Mater. Res.*, 2001, **56**, 390–399.
66. B. Renberg, I. Shiroyama, T. Engfeldt, P. Nygren and A. E. Karlström, *Anal. Biochem.*, 2005, **341**, 334–343.
67. D. J. O'Shanessy, M. Brigham-Burke and K. Peck, *Anal. Biochem.*, 1992, **205**, 132–136.
68. D. G. Smyth, O. O. Blumenfeld and W. Konigsberg, *Biochem. J.*, 1964, **91**, 589–595.
69. C. F. Brewer and J. P. Riehm, *Anal. Biochem.*, 1966, **18**, 248–255.
70. G. Gorin, P. A. Martin and G. Doughty, *Arch. Biochem. Biophys.*, 1966, **115**, 593–597.
71. D. J. O'Shannessy and R. H. Quarles, *J. Appl. Biochem.*, 1985, **7**, 347–355.
72. B. Johnsson, S. Löfås, G. Lindquist, A. Edström, R.-M. Müller Hillgren and A. Hansson, *J. Mol. Recognit.*, 1995, **8**, 125–131.
73. L. Sundberg and J. Porath, *J. Chromatogr.*, 1974, **90**, 87–98.
74. S. M. Heilmann, J. K. Rasmussen and L. R. Krepski, *J. Polym. Sci., Part A: Polym. Chem.*, 2001, **39**, 3655–3677.
75. M. E. Buck and D. M. Lynn, *Polym. Chem.*, 2012, **3**, 66–80.
76. R. M. Arnold, N. E. Huddleston and J. Locklin, *J. Mater. Chem.*, 2012, **22**, 19357–19365.
77. H. C. Kolb, M. G. Finn and K. B. Sharpless, *Angew. Chem., Int. Ed.*, 2001, **40**, 2004–2021.
78. O. Norberg, L. Deng, T. Aastrup, M. Yan and O. Ramström, *Anal. Chem.*, 2011, **83**(3), 1000–1007.
79. R. S. Loka and C. W. Cairo, *Carbohydr. Res.*, 2010, **345**(18), 2641–2647.
80. R. E. Dolle, *J. Comb. Chem.*, 2005, **7**, 739–798.
81. I. Caelen, H. Gao and H. Sigrist, *Langmuir*, 2002, **18**, 2463–2467.
82. M. Hashimoto and Y. Hatanaka, *Eur. J. Org. Chem.*, 2008, 2513–2523.
83. G. T. Hermansson, *Bioconjugate Techniques*, Academic Press, San Diego, 2nd edn, 2008.
84. D. Kim and A. E. Herr, *Biomicrofluidics*, 2013, **7**, 041501.
85. J. Quinn, P. Patel, B. Fitzpatrick, B. Manning, P. Dillon, S. Daly, R. O'Kennedy, M. Alcocer, H. Lee, M. Morgan and K. Lang, *Biosens. Bioelectron.*, 1999, **14**, 587–595.
86. P. Nilsson, B. Persson, M. Uhlén and P. A. Nygren, *Anal. Biochem.*, 1995, **224**, 400–408.
87. G. Papalia and D. Myszka, *Anal. Biochem.*, 2010, **403**(1–2), 30–35.

View Online

Published on 24 May 2017 on http://pubs.rsc.org | doi:10.1039/9781788010283-00171

88. J. E. J. Cronan, *Biol. Chem.*, 1990, **265**, 327–333.
89. E. Boer, P. Rodriguez, E. Bonte, J. Krijgsveld, E. Katsantoni, A. Heck, F. Grosveld and J. Strouboulis, *Proc. Natl. Acad. Sci. U. S. A.*, 2003, **100**, 7480–7485.
90. R. Y. P. Lue, G. Y. J. Chen, Y. Hu, Q. Zhu and S. Q. Yao, *J. Am. Chem. Soc.*, 2004, **126**(4), 1055–1062.
91. I.-H. Cho, E.-H. Paek, H. Lee, J. Y. Kang, T. S. Kim and S.-H. Paek, *Anal. Biochem.*, 2007, **365**, 14–23.
92. M. D. Savage, G. Mattson, S. Desai, G. W. Nielander, S. Morgensen and E. J. Conklin, 1994, *Avidin-Biotin Chemistry: A Handbook*, 2nd edn, Pierce Chemical Co., Rockford, USA.
93. J. D. Hirsch, L. Eslamizar, B. J. Filanoski, N. Malekzadeh, R. P. Haugland and J. M. Beechem, *Anal. Biochem.*, 2002, **308**, 343–357.
94. S.-C. Wu and S.-L. Wong, *J. Biol. Chem.*, 2005, **280**(24), 23225–23231.
95. A. Holmberg, A. Blomstergren, O. Nord, M. Lukacs, J. Lundeberg and M. Uhlén, *Electrophoresis*, 2005, **26**, 501–510.
96. S. Lata, A. Reichel, R. Brock, R. Tampe and J. Piehler, *J. Am. Chem. Soc.*, 2005, **127**, 10205–10215.
97. Biacore Application note 29-0079-29 AA, 2011, GE Healthcare UK Ltd, Little Chalfont, Buckinghamshire, UK.
98. http://www.xantec.com/products/spr_sensorchips.php.
99. F. Khan, M. He and M. J. Taussig, *Anal. Chem.*, 2006, **78**, 3072–3079.
100. M. Fischer, A. P. Leech and R. E. Hubbard, *Anal. Chem.*, 2011, **83**, 1800–1807.
101. R. L. Rich, J. Errey, F. Marshall and D. G. Myszka, *Anal. Biochem.*, 2011, **409**(2), 267–272.
102. C. M. Kolodziej, C.-W. Changx and H. D. Maynard, *J. Mater. Chem.*, 2011, **21**, 1457–1461.
103. B. Johnsson, S. Lofas, G. Lindquist, A. Edstrom, R. M. M. Hillgren and A. Hansson, *J. Mol. Recognit.*, 1995, **8**(1–2), 125–131.
104. R. Patel and B. A. Andrien, *Anal. Biochem.*, 2010, **396**(1), 59–68.
105. G. Bergström and C. F. Mandenius, *Sens. Actuators, B*, 2011, **158**(1), 265–270.
106. B. Catimel, M. Nerrie, F. T. Lee, A. M. Scott, G. Ritter, S. Welt, L. J. Old, A. W. Burgess and E. C. Nice, *J. Chromatogr. A*, 1997, **776**, 15–30.
107. H. Schroeder, M. Adler, K. Gerigk, B. Müller-Chorus, F. Goütz and C. M. Niemeyer, *Anal. Chem.*, 2009, **81**, 1275.
108. R. C. Bailey, G. A. Kwong, C. G. Radu, O. N. Witte and J. R. Heath, *J. Am. Chem. Soc.*, 2007, **129**, 1959.
109. F. Rusmini, Z. Zhong and J. Feijen, *Biomacromolecules*, 2007, **8**, 1775.
110. R. Wacker and C. M. Niemeyer, *ChemBioChem*, 2004, **5**, 453.
111. S. Laib and B. D. MacCraith, *Anal. Chem.*, 2007, **79**, 6264.
112. Laboratory Guideline 28-9615-80 AB, 11/2011, GE Healthcare UK Ltd, Little Chalfont, Buckinghamshire, UK.
113. D. H. Bunka and P. G. Stockley, *Nat. Rev. Microbiol.*, 2006, **4**, 588.
114. Y. Xu, X. Yang and E. Wang, *Anal. Chim. Acta*, 2010, **683**, 12.

View Online

115. R. K. Mosing and M. T. Bowser, *J. Sep. Sci.*, 2007, **30**, 1420.
116. K. Nakanishi, T. Sakiyama, Y. Kumada, K. Imamura and H. Imanaka, *Curr. Proteomics*, 2008, **5**, 161.
117. L. Zhou, M.-H. Wang, J.-P. Wang and Z.-Z. Ye, *Chin. J. Anal. Chem.*, 2011, **39**(3), 432–438.
118. V. Z. Slepak, *J. Mol. Recognit.*, 2000, **13**(1), 20–26.
119. H. Mozsolits, W. G. Thomas and M. I. Aguilar, *J. Pept. Sci.*, 2003, **9**(2), 77–89.
120. P. A. Ohlsson, T. Tjärnhage, E. Herbai, S. Löfås and G. Puu, *Bioelectrochem. Bioenerg.*, 1996, **38**, 137–148.
121. M. A. Cooper, A. Hansson, S. Löfås and D. H. Williams, *Anal. Biochem.*, 2000, **277**, 196–205.
122. O. P. Karlsson and S. Löfås, *Anal. Biochem.*, 2002, **300**, 132–138.
123. P. Stenlund, G. J. Babcock, J. Sodroski and D. G. Myszka, *Anal. Biochem.*, 2003, **316**, 243–250.
124. C. A. Keller, K. Glasmästar, V. P. Zhdanov and B. Kasemo, *Phys. Rev. Lett.*, 2000, **84**(23), 5443–5446.
125. I. Navratilova, J. Sodroski and D. G. Myszka, *Anal. Biochem.*, 2005, **339**, 271–281.
126. E. A. Della Pia, R. W. Hansen, M. Zoonens and K. L. Martinez, *J. Membr. Biol.*, 2014, **247**, 815–826.
127. M. Zoonens and J.-L. Popot, *J. Membr. Biol.*, 2014, **247**, 759–796.
128. V. Romanov, S. N. Davidoff, A. R. Miles, D. W. Grainger, B. K. Galeabd and B. D. Brooks, *Analyst*, 2014, **139**, 1303–1326.
129. C. A. Schlecht and J. A. Maurer, *RSC Adv.*, 2011, **1**, 1446–1448.
130. A. Wörz, B. Berchtold, K. Moosmann, O. Prucker and J. Rühe, *J. Mater. Chem.*, 2012, **22**, 19547–19561.
131. R. L. Rich and G. Myszka, *J. Mol. Recognit.*, 2005, **18**, 1–39.

Published on 24 May 2017 on http://pubs.rsc.org | doi:10.1039/9781788010283-00171

Published on 24 May 2017 on http://pubs.rsc.org | doi:10.1039/9781788010283-00255

CHAPTER 7

Fragment and Low Molecular Weight Compound Analysis

ROBERT KARLSSON,* O. KARLSSON AND P. BELCHER

GE Healthcare Life Sciences, Björkgatan 30 Box 605, SE 75125, Uppsala, Sweden
*Email: robert.karlsson@ge.com

7.1 Introduction

Surface plasmon resonance (SPR) is firmly established as an essential tool in fragment screening and characterization of low molecular weight (LMW) compounds during the hit to lead process in drug discovery. In fragment screening, compounds are typically in the molecular weight range from 150 to 300 Da,[1–4] whereas small-molecule drugs (Figure 7.1) cover a wider range. Notably, more than 70% of approved drugs appear in the molecular weight range 200–500 Da with a peak between 300 and 400 Da.

In fragment screening, SPR allows the direct detection of compounds with low affinity and rapid off rates. Binding can be confirmed by using competition assays and by testing compounds over a wide range of concentrations. In later phases, kinetic analysis is used to guide development towards compounds with preferred off rates, affinity, and selectivity. This chapter discusses low molecular weight analysis from methodology and workflow perspectives. Direct binding assays, competition formats, and key points in assay development, assay setup, and data analysis are described. Examples with drug targets of different classes, including G protein-coupled receptors (GPCRs) and kinases, are provided and typical workflows in fragment screening and hit to lead processes are discussed.

Handbook of Surface Plasmon Resonance, 2nd Edition
Edited by Richard B. M. Schasfoort
© The Royal Society of Chemistry 2017
Published by the Royal Society of Chemistry, www.rsc.org

View Online

Published on 24 May 2017 on http://pubs.rsc.org | doi:10.1039/9781788010283-00255

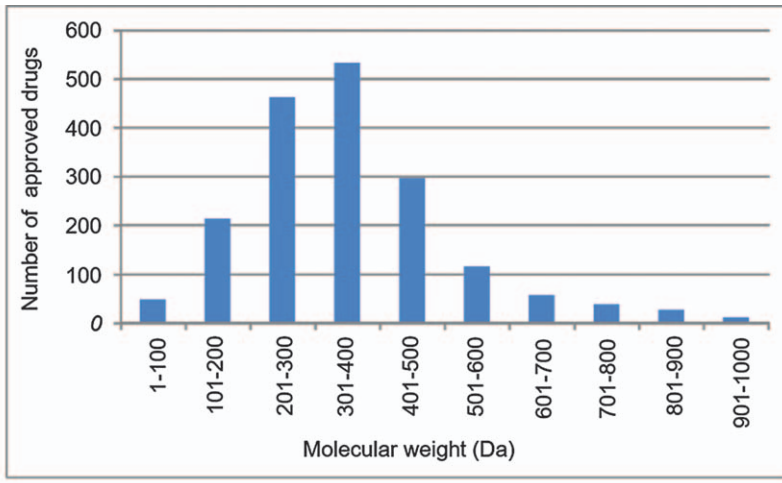


Figure 7.1 Molecular weight distribution of approved small-molecule drugs. Source: Drug Bank 5.0 (http://www.drugbank.ca).

7.2 Assay Formats for Low Molecular Weight Analysis

SPR experiments typically involve immobilization of a target molecule followed by injection of an LMW analyte. This assay format is called a direct binding assay (DBA). Immobilization of the target makes this assay amenable for screening of libraries of LMW compounds. With this format, binding is detected but the binding site is not identified. Site-specific information can be obtained by competitive assays, such as the inhibition in solution assay (ISA) and the surface competition assay (SCA). These assays complement each other and are often run in sequence.

In the following examples, four small molecules A, B C, and D with the same molecular weight but with different kinetic properties are used to illustrate DBA, ISA, and SCA formats.

7.2.1 Direct Binding Assay (DBA)

In a DBA, the target molecule is immobilized or captured on the sensor surface and the analyte is tested for binding to the target. A target molecule can have several binding pockets. Depending on the complementarity between analyte and binding pocket structures, analytes can bind to the target with differing speeds and strengths.

In Figure 7.2, analytes A and D fit in pockets 1 and 2, respectively, analyte B may not bind at all, and analyte C binds weakly to pocket 2.

Published on 24 May 2017 on http://pubs.rsc.org | doi:10

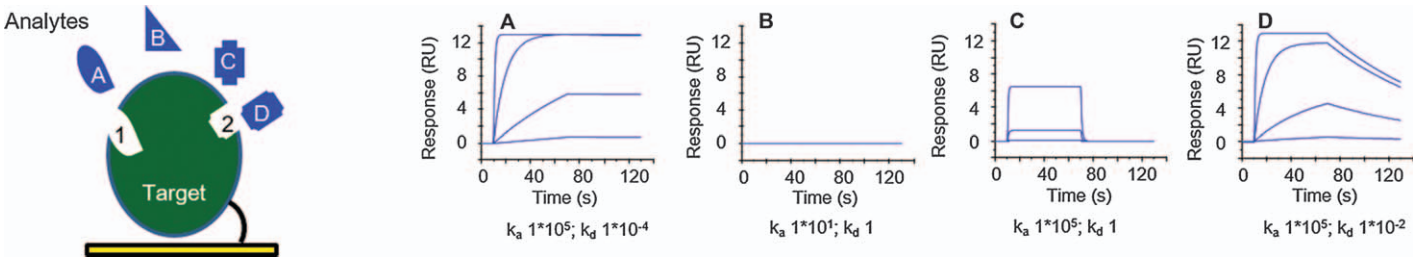


Figure 7.2 Analytes A–D bind to a target molecule with hypothetical binding curves obtained with 10 nM to 10 μM concentrations and with association rate constants k_a and dissociation rate constants k_d as indicated.

View Online

Published on 24 May 2017 on http://pubs.rsc.org | doi:10.1039/9781788010283-00255

7.2.2 Solution Competition or Inhibition in Solution Assay (ISA)

The solution competition assay is often referred to as an inhibition assay. A molecule that specifically binds to a certain binding pocket on the target is immobilized on the sensor surface. Analytes are added to the target outside the instrument to allow target molecules and analytes to react. After a few minutes, the solution is injected over the sensor surface. If an analyte molecule has bound to the binding pocket of interest, a drop in the signal level is observed compared with the situation when target alone is injected, as shown in Figure 7.3C and D. The red curve is the uninhibited signal. The concentration at which inhibition becomes visible, *i.e.* where the signal starts to drop, reflects the affinity of interaction between the target and the compound in solution.

7.2.3 Surface Competition Assay (SCA)

The SCA involves simultaneous injection of two compounds that react with the immobilized target as shown in Figure 7.4. One compound has been selected as a probe for a specific binding pocket. If the second compound reacts with another pocket, the curves are additive. If the compounds react with the same site, the resulting response will reflect the kinetics and molecular weight of each compound. This format is particularly useful if the two competing compounds have different dissociation properties, as this will result in a change in the curve shape. There are several variants of this assay where binding occurs sequentially instead of in parallel.[5]

7.2.4 Selection of Assay Format

Although all three assay formats can be used for screening,[6] they differ with respect to assay setup and to the information that can be obtained (Table 7.1).

The direct binding assay is the only assay that can provide high-resolution kinetic data and where it is possible to observe binding to all binding pockets. It is relatively easy to perform as standard chemistries or capture can be used for immobilization. The requirement on instrument sensitivity for LMW compounds is higher than for protein analysis and solvent correction is often needed for LMW analysis.

An ISA may be more difficult to set up but has distinct advantages. The readout of the assay is straightforward and solvent correction is not required; signal levels are often higher than in a DBA and surfaces can be very stable. Affinity data can be obtained for both high- and low-affinity binders. The lack of kinetic data may not be important in fragment screening, where on and off rates may be too rapid for kinetic analysis, but otherwise limit the usefulness of the ISA format.

Published on 24 May 2017 on http://pubs.rsc.org | doi:10

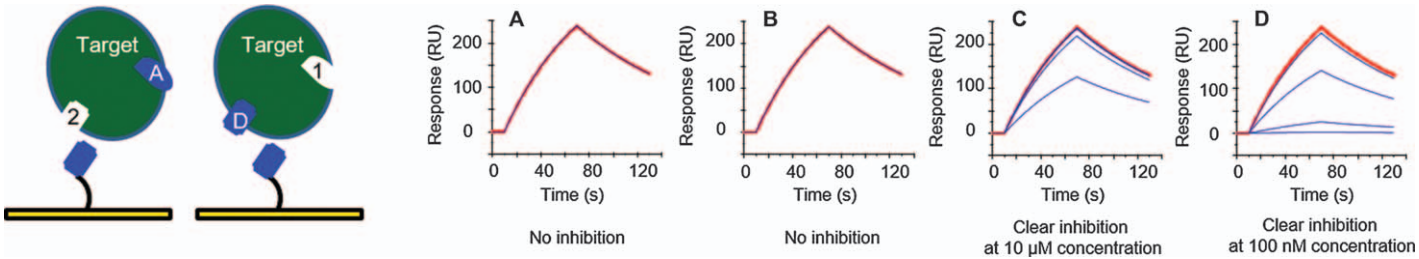


Figure 7.3 Analytes A–D first bind to the target in solution. The target is at a constant concentration of 50 nM and analyte concentrations are varied from 10 nM to 10 μM. No inhibition occurs with analytes A and B. The affinity of compound C is lower than that of D. Therefore, a higher concentration is required to observe inhibition for compound C than for D. The red curve corresponds to target injection in the absence of samples.

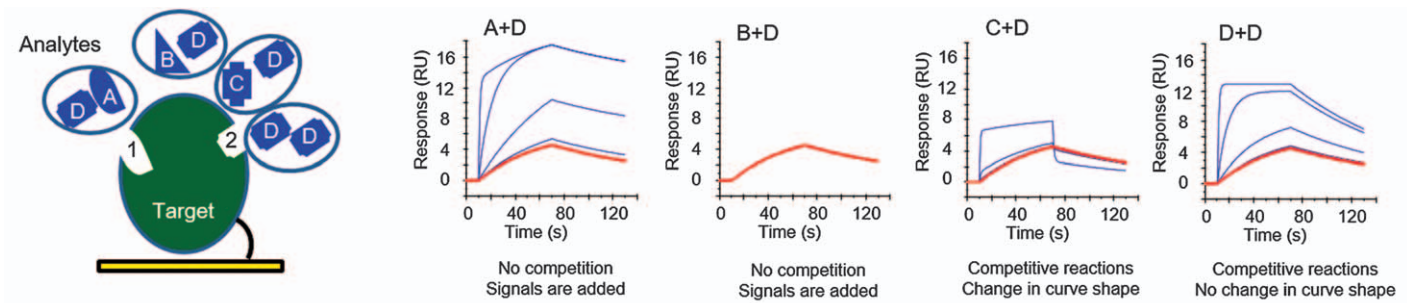


Figure 7.4 Analyte D reacts with binding pocket 2 and is kept at a constant concentration of 100 nM (red curve). In the competition experiment, D is injected together with 10 nM to 10 μM concentrations of compounds A–D. When compounds C and D compete, a change in curve shape is observed and during the dissociation phase the signal is lower compared with the situation where compound D is injected alone.

View Online

Table 7.1 Comparison of assay formats.

Parameter	DBA	ISA	SCA
Immobilization partner	Target	A compound that identifies a specific binding pocket	Target
Immobilization	Standard protocols	Chemical modification may be necessary	Standard protocols
Expected response levels	Low	Intermediate to high	Low
Solvent correction needed	Yes	No	No if the response is read from the dissociation phase. Otherwise yes
Stability of immobilized molecule	May be sensitive: mild regeneration conditions may be required	High: harsh regeneration conditions can often be used	May be sensitive: mild regeneration conditions may be required
Can provide kinetic data	Yes	No	Sometimes
Can provide affinity data	Yes	Yes	Sometimes
Response related to all binding pockets	Yes	No	Yes
Response related to a specific binding pocket	No	Yes	No
Throughput	High	High	Intermediate

Published on 24 May 2017 on http://pubs.rsc.org | doi:10.1039/9781788010283-00255

The SCA is typically not the primary assay format but shares target and target immobilization procedures with the DBA.

The DBA is the most versatile assay. It can be used in all stages of research from fragment screening to lead optimization, which has contributed to its popularity. However, site-specific information is required in many cases, for instance with protein–protein interaction (PPI) targets where one is trying to find binders to sites where no functional assay exists.[7] It is also used to identify allosteric binders to kinases, as such binders may improve kinase selectivity.[8] The interest in allosteric binders is not restricted to kinases and is much broader, as many targets have several binding sites.[9] ISA or SCA can be used here to complement the information from a DBA. The SCA is a natural complement to the DBA as it can be performed on the same sensor surface.

ISA is sometimes used as a primary assay[10] for the detection of site-specific analytes. In later stages of development a switch to the DBA can be considered in order to generate kinetic data for a few selected binders.

View Online

Published on 24 May 2017 on http://pubs.rsc.org | doi:10.1039/9781788010283-00255

7.3 Methodology

When the first Biacore system was introduced in 1990, direct binding of small molecules could not be observed. The increased sensitivity of SPR instrumentation now allows the direct detection of small-molecule binding irrespective of the molecular weights of LMW compounds and targets. Furthermore, kinetic studies can be carried out with excellent resolution of kinetic profiles with as little as 1 RU response. One example of these high-resolution data (Figure 7.5) shows how melagatran (430 Da) binds to immobilized thrombin. The association rate constant determined from this experiment was very high, 3.3×10^{7} L mol^{-1} s^{-1}. By using high data acquisition rates, it is now also possible to differentiate between dissociation rate constants lower than 2 s^{-1} (Figure 7.6). Clearly, the performance of SPR systems is available for the detection and characterization of small-molecule binding to immobilized targets.

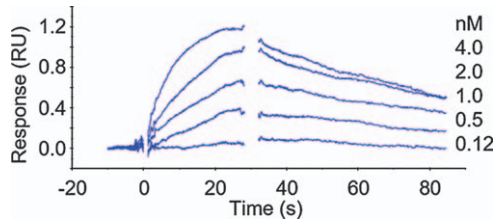


Figure 7.5 Melagatran (MW 430 Da) binds to immobilized thrombin. Binding curves obtained with concentrations from 0.12–4.0 nM are resolved within 1 RU.

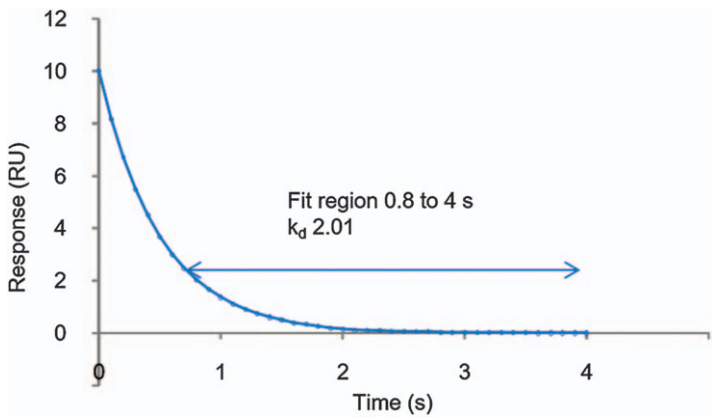


Figure 7.6 Noise structure from Biacore S200 overlaid with theoretical binding curve with $k_d = 2.0$. Refit of data between 0.8 and 4.0 s returns the expected rate constants. The first 0.8 s was excluded from the fit to mimic a real experiment where some disturbances can be expected when blank-subtracted data are used.

View Online

Published on 24 May 2017 on http://pubs.rsc.org | doi:10.1039/9781788010283-00255

7.3.1 Immobilization of Proteins

A protein can be immobilized using a variety of immobilization and capture procedures (see Chapter 6). Coupling *via* the amine group is a popular choice for covalent coupling through the N-terminus or protein lysines. The reactivity of the N-terminus is often higher than that of lysines, in particular when coupling occurs at low pH where the amines are partly protonated. Amine coupling may thus occur preferentially through the N-terminus to give an oriented coupling. Owing to the abundance of lysine groups, the protein may be attached through multiple linkages. In Figure 7.7, three lysines are present and one of them in the active site involved in LMW binding. By coupling the protein in the presence of an excess of an LMW compound that blocks the binding site, it can be protected and the binding activity of the protein can thus be maintained. As a rule of thumb, the concentration of the LMW compound should be 10 times the K_D concentration (at the coupling pH) to protect 90% of the binding sites.

For antibody–antigen or other protein–protein interactions very little protein has to be immobilized, but with LMW analytes high immobilization levels are still required, in particular for large protein targets. When targets approach 400 kDa, surface capacities may not be sufficient.

Table 7.2 lists theoretical immobilization levels required to observe a response of 10 RU for a 150 Da molecule and indicates useful immobilization procedures. In practice, higher levels can be required if some target molecules are inactive.

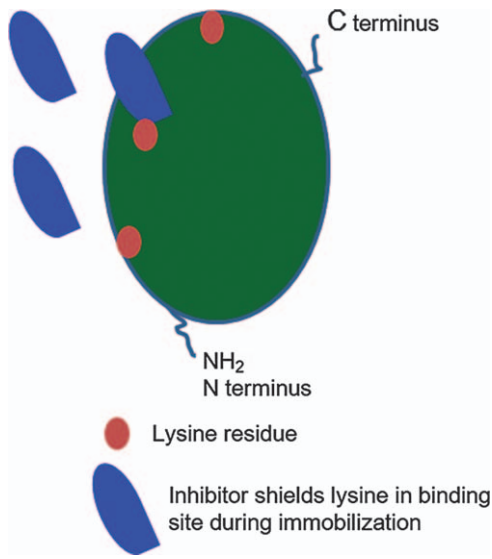


Figure 7.7 An excess of inhibitor is used during immobilization: it shields the lysine in the active site and prevents immobilization in the active site.

View Online

Published on 24 May 2017 on http://pubs.rsc.org | doi:10.1039/9781788010283-00255

Table 7.2 Target immobilization levels and means for immobilization.

Target MW	Target immobilization (RU)	Amine and thiol coupling	Capture on NTA surface	Capture using antibodies or streptavidin
10 000	667	×	×	×
25 000	1667	×	×	×
50 000	3333	×	×	×
100 000	6667	×	×	–
200 000	13 333	×	–	–
400 000	26 667	?	–	–

Table 7.3 Equilibrium responses (RU) for a 1 mM binder at different binding capacities and screening concentrations.

	Analyte/screening concentration (mM)				
R_{max} (RU)	0.1	0.2	0.5	1.0	2.0
10	0.9	1.7	3.3	5.0	6.7
20	1.8	3.3	6.7	10.0	13.3
40	3.6	6.7	13.3	20.0	26.7

The immobilization levels in Table 7.2 assume that all molecules are capable of binding and are calculated using the equation

$$\text{target immobilization} = \text{LMW response} \times \frac{\text{target MW}}{\text{LMW compound MW}}$$

The use of a molecular weight of 150 Da is relevant for fragment screening. The saturation response level required will depend on the affinity between the compound and the target: 10 RU can be sufficient for micromolar binders when the screening concentration is 1 mM, but millimolar binders may require additional binding capacities as illustrated in Table 7.3.

A maximum binding level of 10 RU for a fragment of 150 Da will generally be too low for the detection of a millimolar binder even when high concentrations are used. With a screening concentration of 500 μM, a saturation response of 30–40 RU would be appropriate for the detection of a 1 mM binder. This would lead to response levels around 10 RU.

In later stages of development where compounds are larger and when kinetic analysis becomes more important, up to 5–10 times lower levels of immobilization can be used.

7.3.1.1 Covalent Coupling or High-capacity Capture

For fragments, covalent (amine or thiol) coupling and capture on a nitrilotriacetic acid (NTA) surface can provide sufficient binding capacity even for targets with molecular weights exceeding 100 kDa. To reduce the dissociation of the target from NTA or anti-histidine antibody surfaces (Figure 7.8),

Published on 24 May 2017 on http://pubs.rsc.org | doi:10

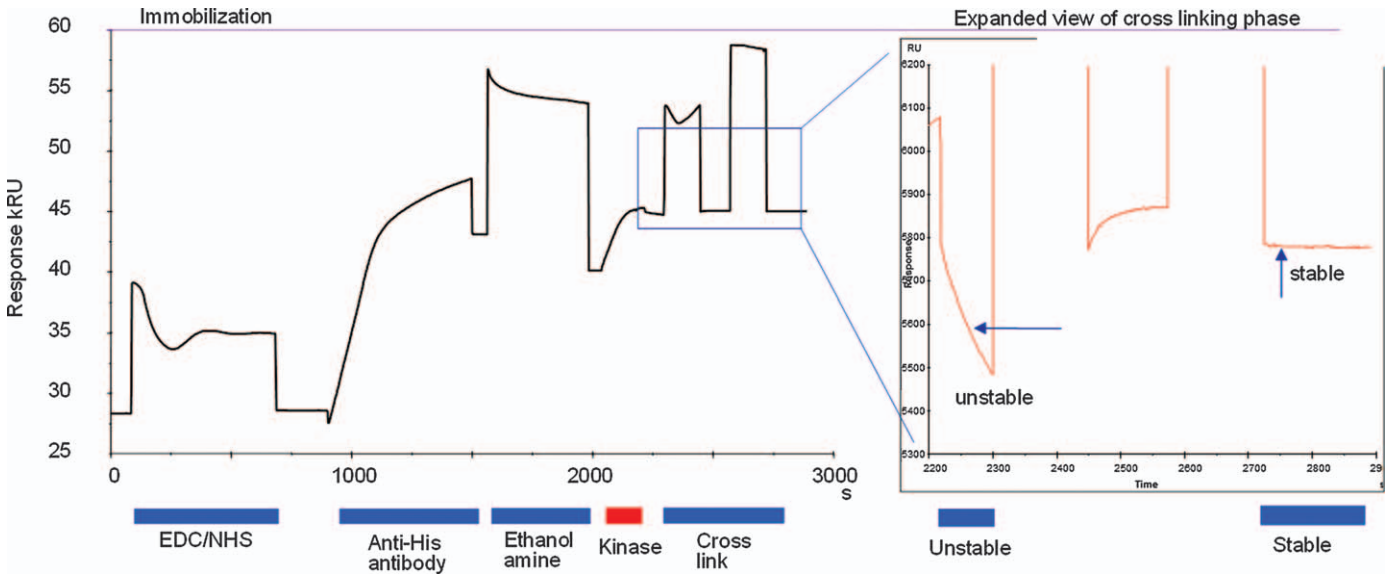


Figure 7.8 Anti-histidine antibody immobilization followed by capture of a histidine-tagged kinase. Crosslinking with EDC–NHS after capture of the histidine-tagged kinase improves stability.

View Online

Published on 24 May 2017 on http://pubs.rsc.org | doi:10.1039/9781788010283-00255

crosslinking or capture to an EDC–NHS-activated surface can be used to improve stability.[11–13] Crosslinking has also been used to stabilize covalently immobilized proteins.[6]

Sensor Chip CM7 from GE Healthcare provides additional binding capacity (Figure 7.9)[14,15] and is useful for the direct immobilization of high molecular weight targets and for targets with low percentage activity.

7.3.1.2 Capture Approaches

With targets in the molecular weight range 10–40 kDa, capture technologies can also be used for screening. For kinetic analysis, capture is compatible also with larger targets and here capture is often the preferred choice. Capture can typically be performed at neutral pH. This makes capture a popular approach, especially in situations where the target is unstable at the low pH that is often required for direct immobilization. Figure 7.10

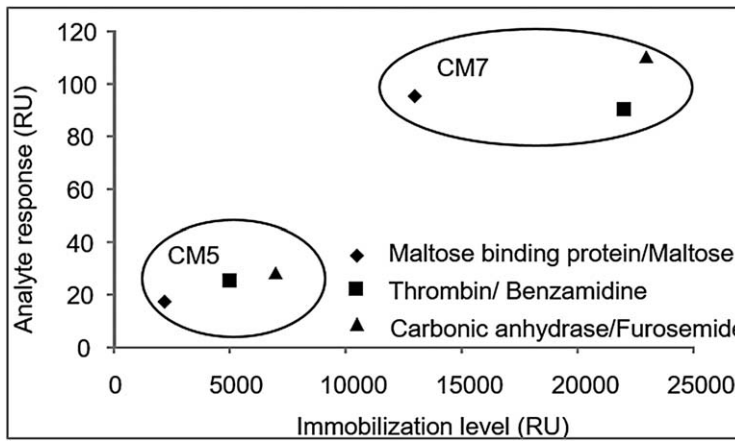


Figure 7.9 Standard amine coupling of three proteins on Sensor Chips CM5 and CM7 followed by LMW binding demonstrates a threefold increase in binding capacity with Sensor Chip CM7.

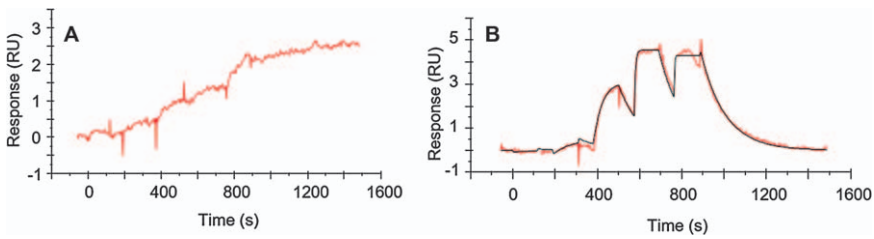


Figure 7.10 Comparison of amine coupling (A) and biotin capture (B). When an LMW analyte was injected over the amine-coupled surface, no meaningful data were obtained. In contrast, biotin capture gave LMW binding that could be fitted to a one-to-one interaction model.

View Online

Published on 24 May 2017 on http://pubs.rsc.org | doi:10.1039/9781788010283-00255

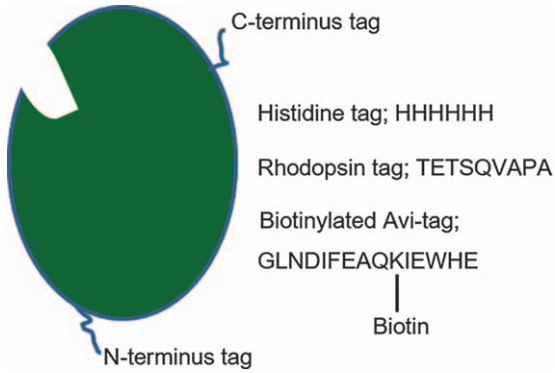


Figure 7.11 Peptide tags such as histidine tags, rhodopsin tags and Avi tags can be attached to N- or C-termini to achieve oriented capture to sensor surfaces.

illustrates how a shift from amine coupling to biotin capture resulted in a working assay for LMW compounds reacting with an enzyme.

If the amino or carboxy terminus is distant from the binding site, the protein can be tagged using peptide tags such as hexa- or decahistidine tags, rhodopsin tags or Avi tags (Figure 7.11). A histidine tag can be used for capture on NTA surfaces or on surfaces with immobilized anti-histidine antibody. Rhodopsin tags are often used for membrane proteins and proteins are captured on 1D4 antibody surfaces.[16] Biotin can be enzymatically attached to the Avi tag to provide site-directed biotin coupling to streptavidin. Capture provides orientation and can reduce assay development efforts as the regeneration conditions are known. Antibody capture can be used, but with both antibody and target proteins on the surface there is a risk of additional non-specific binding.

7.3.2 Immobilization of Small Molecules

In ISA, a target definition molecule has to be immobilized, and this is often a small molecule. Small-molecule immobilization typically involves amine, thiol, aldehyde, carboxylic or hydroxyl groups. Small-molecule immobilization can be straightforward. Binding activity may be lost, however, if immobilization involves parts of the molecule that are required for target binding. For covalent coupling, the concentration of the LMW compound needs to be higher than with proteins, and is typically in the range 1–50 mM. The reason for this is that electrostatic preconcentration may not be used. The pH of coupling is normally higher than for proteins.

There is still relatively little general information available on the immobilization of small molecules on sensor surfaces. We recommend a discussion with an organic chemist in cases where immobilization is not immediately feasible.

View Online

A recently described isocyanate chemistry[17] intended for glass slide microarrays may potentially be adapted to SPR surfaces as this chemistry is broadly reactive. Here, water stability of reagents and dry chemistry need to be considered for flow cell-based SPR systems.

Published on 24 May 2017 on http://pubs.rsc.org | doi:10.1039/9781788010283-00255

7.3.3 Protein Activity

The activity of the immobilized protein can be controlled by performing saturation experiments and by calculating the stoichiometry of binding. The protein is saturated when the steady-state level becomes independent of analyte concentration (see, for instance, the last two injections in Figure 7.10B). The apparent stoichiometry is obtained from the relation

$$\text{apparent stoichiometry} = \frac{\text{analyte response}}{\text{analyte MW}} \Big/ \frac{\text{target immobilization level}}{\text{target MW}}$$

The reason for the word ''apparent'' is that small molecules and proteins may not give the same response per gram (see Section 7.3.5).

If an LMW compound can be immobilized, the target activity in solution can be measured using calibration-free concentration analysis (CFCA).[18] This is a convenient way to check and compare the activity of expressed proteins and involves injection of analyte at two flow rates (Figure 7.12). The resulting binding curves can be fitted with a variant of the one-to-one interaction model whereby the active concentration of the target protein is calculated. CFCA may reveal if the total protein (A_{280}) and active (binding) protein concentrations differ.

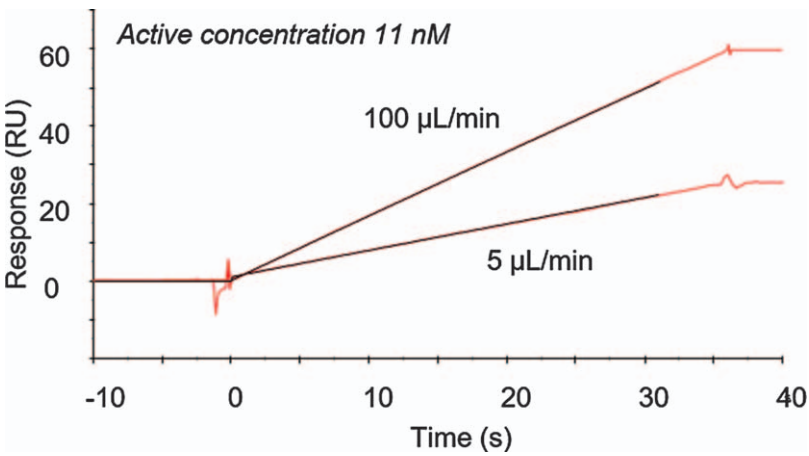


Figure 7.12 Calibration-free concentration analysis. Overlay plot of experimental and fitted data. Analyte injected at flow rates of 5 and 100 µL min^{-1} exhibit different binding rates. Sensorgrams fitted to 11 nM concentration.

View Online

By comparing apparent stoichiometry data with active concentration data, a potential effect of immobilization on protein activity can be inferred.

7.3.4 Compound Solubility and Concentrations in Screening

In fragment screening, libraries are often designed with solubility in mind. The calculated *c*log*P*, *i.e.* the partition coefficient between *n*-octanol and water, for compounds in a fragment library are typically below 3 and trending to be lower than 2.5.[1,3] This in contrast to commercial drugs, where close to 50% of all drugs have *c*log*P* values in the range of 3–6.[19]

Poor solubility may lead to precipitation on the sensor surface,[20] leading to disturbed sensorgrams (Chapter 5, Figure 5.13). For lead compounds and drugs that are of higher affinity and can be tested at lower concentrations, water solubility may be less of an issue. Compound solubility in the high micromolar to millimolar range ensures that screening can be performed at high concentrations.

The analyte concentration used in screening experiments effectively determines the range of affinities that can be detected. If the main interest is to identify micromolar binders, micromolar concentrations are recommended. If millimolar binders are of interest, then millimolar concentrations should be used.

7.3.5 Compound Refractive Index Increment

SPR systems measure changes in refractive index. The specific signal (RU g^{-1}) obtained from a binding event is related to the refractive index increment, d*n*/d*c*, where d*n*/d*c* is how much the refractive index of a solution varies with a given increment in concentration, expressed as $g\,mL^{-1}$. For proteins, the refractive index increment is narrowly distributed[21] and typically varies by less than 10%. It is therefore reasonable to assume that most proteins will give the same specific signal. For small molecules, the distribution is wider and d*n*/d*c* values can vary twofold or more.[22] This makes stoichiometry data more uncertain and will impact the interpretation of acceptable binding levels in screening. As a rule of thumb, a fragment or compound that gives R_{max} values above five times the theoretical R_{max} can be considered as superstoichiometric and can be disregarded. With R_{max} values larger than three times the theoretical R_{max}, the compound can often be selected for inspection. Compounds with R_{max} values up to three times the theoretical R_{max} can often be accepted as hits.

7.3.6 Buffer Selection

The choice of buffer can be critical. Phosphate, Tris, and HEPES buffers are frequently used in SPR experiments.

The choice of buffer substance and buffer additives can make the difference between success and failure (see Section 7.4). The concentration of the

Published on 24 May 2017 on http://pubs.rsc.org | doi:10.1039/9781788010283-00255

View Online

Published on 24 May 2017 on http://pubs.rsc.org | doi:10.1039/9781788010283-00255

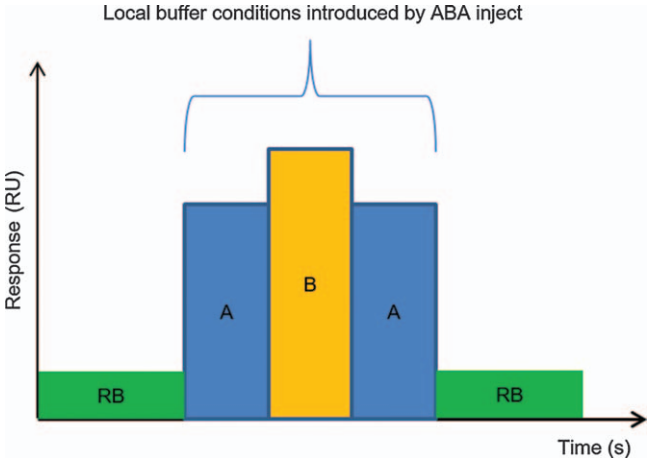


Figure 7.13 The ABA inject protocol allows a temporary change of buffer conditions. RB is the running buffer. In the first A segment of the ABA inject protocol, a new buffer condition is established. In the B segment, binding of analyte in the new buffer is monitored, and in the second A segment, dissociation is monitored, again in the new buffer condition. After the ABA inject is finished, RB flows over the sensor surface.

buffer substance is also important and unwanted binding of small molecules to the sensor surface can be reduced simply by increasing the buffer strength from 10 to 50 mM.

By spending a few hours on searching the literature for guidance or on testing different buffers and buffer additives, data quality can be drastically improved. Design of experiments (DOE) has been useful in other areas to improve the sensitivity of Biacore assays.[23] A DOE approach in which several parameters are varied within a design space may also prove useful for optimizing LMW–target interactions.

The ABA-inject software is an excellent tool for buffer scouting A single running buffer can be maintained during a run, and new buffer conditions are introduced with the ABA-inject (Figure 7.13). This means that test solutions can be placed directly in well plates, and buffer scouting can be performed in high-throughput mode as there is no need to change buffer flasks.

7.3.7 Sample Preparation

LMW compounds are typically obtained as powder or in DMSO stock solutions. A powder is first dissolved in DMSO and the solution is then diluted to a suitable working concentration. Compound stability in DMSO–water solutions can be poor[24,25] and even repeated freeze–thawing of DMSO stock solutions can lead to compound degradation if water creeps into the solutions.

DMSO in the assay buffer improves solubility but too high a DMSO concentration may be harmful to the protein. A final DMSO concentration of

View Online

Published on 24 May 2017 on http://pubs.rsc.org | doi:10.1039/9781788010283-00255

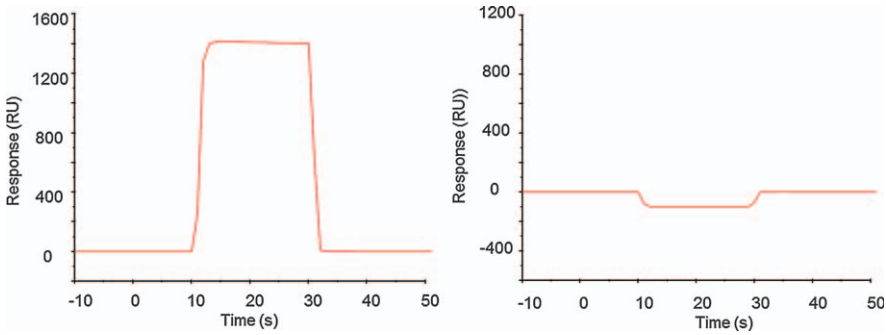


Figure 7.14 A difference in DMSO concentration of 1% between sample and running buffer (left) typically gives a refractive index change of 1500 RU. If samples are matched more closely to the running buffer, the refractive index signal will be lower (right). Normal reference subtraction works well for refractive index differences of up to a few hundred RU, but with larger differences solvent correction is necessary.

2–5% is typically used. At this stage, ensure that well plates, tips, filters, *etc.*, used in the assay and to prepare samples are compatible with DMSO. During sample preparation, mixing should be thorough and the DMSO content of sample solution and running buffer should be matched as closely as possible to avoid large differences in refractive index (Figure 7.14).

7.3.8 Solvent Correction

Solvent correction[26] aims to improve the quality of binding data by reducing the effect of DMSO buffer mismatches. If the running buffer contains 2% DMSO, a sample may contain lower or higher DMSO concentrations depending on how the sample is diluted.

The preparation of solvent correction solutions is described in Tables 7.3 and 7.4. Here the starting solutions are 1.02×PBS and 100% DMSO. Buffers with 1.5 and 2.8% DMSO are prepared (Table 7.4). Next, these solutions are mixed in a second step to obtain a series of solvent correction solutions (Table 7.5).

Four to eight solvent correction solutions are recommended. It is not necessary to know the exact DMSO concentration in each solution but it is important that the solutions cover the sample DMSO range. These solutions are injected over active and reference surfaces. Binding levels from the reference-subtracted curve (active – reference) is plotted *versus* binding levels on the reference surface (Figure 7.15A and B). In Figure 7.15A, the reference-subtracted data are close to 1 RU irrespective of the signal on the reference curve. In this case, solvent correction may not be needed.

In Figure 7.15B, signals on the reference-subtracted curve range from −13 to 7 RU. Ideally, the signal should be zero, but differences in signal linearity on different flow cells and excluded volume effects due to immobilization generate an offset.

View Online

Published on 24 May 2017 on http://pubs.rsc.org | doi:10.1039/9781788010283-00255

Table 7.4 Preparing solvent correction solutions: part 1.

Start	1.5% DMSO	2.8% DMSO
1.02× PBS (μL)	9800	9800
100% DMSO (μL)	150	280

Table 7.5 Preparing solvent correction solutions: part 2.

	1	2	3	4	5	6	7	8
DMSO concentration (%)	2.8				→			1.5
1.5% DMSO (μL)	0	200	400	600	800	1000	1200	1400
2.8% DMSO (μL)	1400	1200	1000	800	600	400	200	0

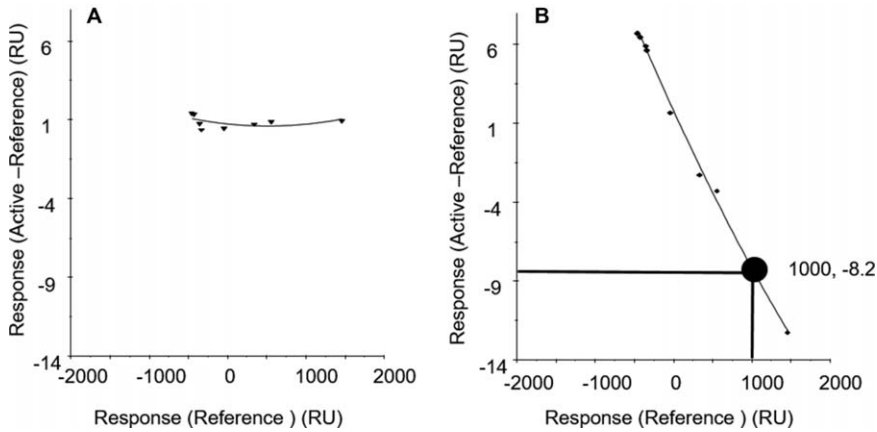


Figure 7.15 Solvent correction curves. Reference-subtracted (active – reference) response plotted *versus* reference response. The signal on the reference varies from −500 to 1500 RU. In (A) the reference-subtracted data are independent of the reference data. In (B) the reference-subtracted data range from −13 to 7 RU. For a sample with a response of 1000 RU on the reference surface, the reference-subtracted value is at −8.2 RU. Therefore, to obtain a zero active – reference signal, 8.2 RU is added to the response.

For solvent correction, the signal obtained with the sample on the reference surface is measured. The corresponding response on the solvent correction curve is read and the correction factor is found from the *y*-axis as illustrated in Figure 7.15B. For a sample with a 1000 RU signal on the reference curve, 8.2 RU is added to the reference-subtracted data to eliminate refractive index effects.

7.3.9 Z', Positive and Negative Controls

Positive and negative controls are useful for validating an assay and to ensure consistent data quality over time. They should be run several times

View Online

during longer runs. A positive control is a compound that is known to bind to the target. Ideally, it should be of the same type as the samples, *i.e.* use a small molecule if samples are small molecules, and not a protein or peptide.

Positive controls can be run at intermediate or saturating concentrations. A negative control can consist of a DMSO sample that has been prepared in the same way as fragment samples. The use of running buffer as the source of negative controls is not recommended as the running buffer is prepared in a different manner.

By calculating a Z' value,[27] the quality of an assay can be estimated:

$$Z' = 1 - \frac{3 \times \mathrm{SD(positive\ control)} + 3 \times \mathrm{SD(negative\ control)}}{\mathrm{average\ of\ positive\ control} - \mathrm{average\ of\ negative\ control}}$$

If positive and negative controls are well separated and standard deviations (SD) are low, the Z' value will be high. Generally, an assay with a Z' factor >0.8 is considered as very good, and a Z' factor >0.6 is good. For Z' factors <0.5, the assay is not robust enough to be used for primary screening.[28]

As Z' values are based on the response from positive and negative controls, it can be established during assay development. A high Z' value indicates that the assay is ready for sharp runs.

For this conclusion to be valid for a fragment screen, the signal from the positive control needs to be adjusted for the molecular weight range of fragments. If the molecular weight of the positive control is larger than the fragments and the response is used directly, Z' values will be artificially high.

The use of the response from the positive control to estimate fragment response levels is highly recommended. When this is combined with estimates of target occupancy [based on assumed affinities and the concentration used in screening (Section 7.3.1)], the quality of the assay can be predicted. In our experience, such estimates can often replace Z' analysis.

7.4 Target Considerations

A recent estimate from the target database[29] indicates that more than 2500 drug targets have been investigated. By using drug[30] and target databases, it is possible to obtain detailed information about targets and their link to disease. GPCRs and kinases are two important drug target classes where SPR has been used extensively.

7.4.1 GPCRs

Close to 800 seven transmembrane (7TM) receptors have been identified.[31] These proteins are expressed as a single polypeptide chain that passes through the membrane seven times. Ligands typically bind to the N-terminus, to extracellular parts of the TM regions, but also inside the TM region.[32] For SPR studies, the receptors are typically solubilized and captured on

Published on 24 May 2017 on http://pubs.rsc.org | doi:10.1039/9781788010283-00255

View Online

Published on 24 May 2017 on http://pubs.rsc.org | doi:10.1039/9781788010283-00255

NTA-modified dextran surfaces[12,33] or a more hydrophobic surface where the protein can be embedded in a lipid bilayer.[16,34] Running buffers include both Tris and HEPES buffers in the pH range 7.4–7.8 and with 1–5% DMSO. Maltoside detergents such as 0.1% *n*-dodecyl-β-D-maltopyranoside are typically added to the running buffer to ensure solubility of receptors. However, other detergents such as CHAPS, cholesteryl hemisuccinate and lauryl maltose neopentyl glycol have also been used.

7.4.2 Kinases

The catalytic domain of kinases consists of about 250–300 amino acids. Kinase inhibitors can be ATP competitors or non-ATP or allosteric competitors.[8] The allosteric inhibitors are of great interest as they may prove to be more specific than the ATP competitors.

Early studies of kinase inhibitor binding[11] showed (Figure 7.16) that the buffer conditions used in biochemical assays had to be modified to obtain acceptable results. Drift and questionable responses were obtained when ATP was injected in HEPES buffer (Figure 7.16A). Phosphate and Tris buffers worked much better. In this case (Figure 7.16B and C) Tris buffer was used as Mn^{2+} was needed for kinase activity. Phosphate buffer that also worked satisfactorily was abandoned to avoid any precipitation of Mn.

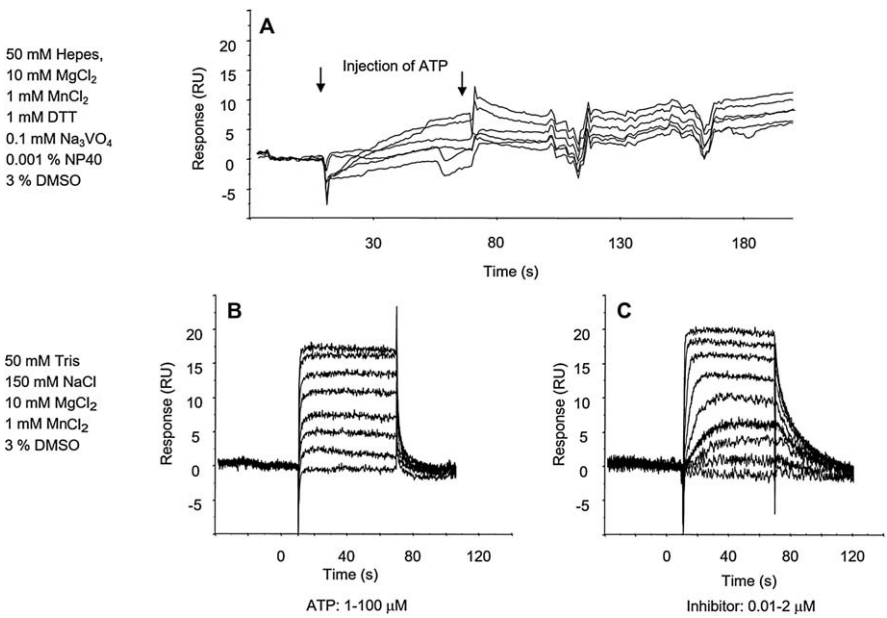


Figure 7.16 Binding of ATP and a kinase inhibitor to an immobilized kinase. No binding activity and drift were observed with HEPES buffer (A), but both ATP and inhibitor bound in a concentration-dependent manner when Tris buffer was used (B and C).

View Online

7.5 Fragment Screening Workflow

SPR is now frequently used along with NMR and X-ray crystallography in the fragment screening process.[4,35] In contrast to NMR and X-ray crystallography SPR does not provide structural information but is used to select fragments for further structural characterization. An advantage with SPR is that it requires less protein than either NMR or X-ray crystallography and a sufficient throughput without the need to pool compounds. Without pooling there is no risk of compound–compound interferences. With a direct binding assay, fragments that bind to the target are identified. Site specificity can be determined with a competition assay and can potentially reveal allosteric binders. Based on affinity measurements and K_D values, ligand efficiency (LE) or log *P*/LE (LELP) can be calculated.[36] These data can later be combined with structural information for prioritization of scaffolds for fragment growing.[2,3]

7.5.1 Fragment Libraries

Fragment libraries typically consist of compounds with molecular weights in the range 150–300 Da and with *c*log *P* values <3. The size of commercial libraries and libraries used by contract research organizations varies from 100 to over 125 000 with a median size of 1500 compounds.[4] Libraries have evolved with filters for Pan Assay INterference compoundS (PAINS)[37] to reduce the number of false positives and are being developed to contain both planar and 3D fragments[3] suitable for a broad range of targets.

The SPR workflow as implemented in Biacore systems consists of several steps (Figure 7.17), where each step has a defined purpose. This workflow or parts of it are widely used.[28,38–40] The order of steps may vary and affinity analysis can sometimes be performed prior to binding site analysis. In other cases, fragments are first identified using other screening methods and fragments may enter the workflow at the affinity analysis step.[41–43]

7.5.2 Clean Screen

A library can be tested once to identify and remove compounds that bind to the sensor surface. We recently tested a commercial library with 2740 compounds for binding to sensor chips CM5, CM7 (both dextran surfaces), and SA (streptavidin). Compounds were injected at 1 mM concentration in a phosphate buffer containing 2% DMSO. Compounds that raised the baseline from one cycle to another by more than 10 RU were identified as sticky binders (Figure 7.18). Eleven fragments bound to sensor chip CM5, 16 to sensor chip CM7 and 37 to sensor chip SA. Three fragments bound to all three surfaces and were general binders. Eight fragments bound to two surfaces and were selective binders. Poorly behaving compounds may impact subsequent cycles where their behavior can mask a well-behaved (but weak) binder. With a clean screen, these compounds can be removed from

Published on 24 May 2017 on http://pubs.rsc.org | doi:10.1039/9781788010283-00255

View Online

Published on 24 May 2017 on http://pubs.rsc.org | doi:10.1039/9781788010283-00255

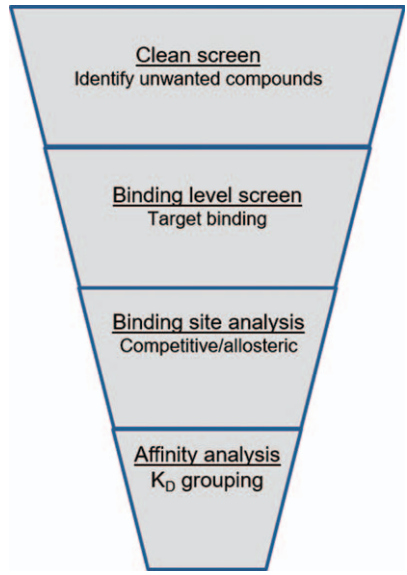


Figure 7.17 The fragment screening workflow. The objective is to identify a few hits with structural diversity that can be grown into more high-affinity compounds.

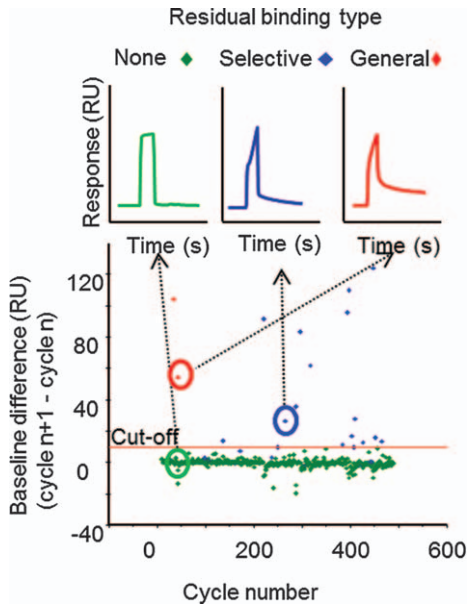


Figure 7.18 In a clean screen, sticky fragments are identified by inspection of changes in baseline. Sticky compounds give rise to elevated baselines and can be removed or placed at the end of a screen. With this simple precaution, disturbances from sticky compounds can be reduced.

View Online

or injected last in the screening experiment. For the same reasons and with the same actions, a clean screen with immobilized proteins is also recommended.

7.5.3 Binding Level Screen

In a binding level screen, target binding is tested. Assay conditions have been developed and target activity has been measured with positive controls binding to the site of interest. For a binding level screen, the positive control should ideally be a weak LMW binder (not a peptide or a protein) with visible but rapid dissociation. Visible dissociation allows verification of solvent correction by inspection of how well the association and dissociation phases are connected. Rapid dissociation ensures that the assay can be performed without regeneration.

A typical vial and plate setup for the Biacore S200 is shown in Figure 7.19. Samples and controls are placed in a 384-well plate and wash solutions and solvent correction samples are placed in vials. After at least three start-up cycles to equilibrate the system, a solvent correction cycle is run followed by samples and positive and negative controls. During the run, controls are typically repeated every 30 cycles to monitor the assay performance and solvent correction is repeated every 50 cycles.

Samples are typically injected for 20–30 s with a dissociation time of 0 s using a flow rate of 30 $\mu L\,min^{-1}$. With this setup, the required sample volume for a Biacore S200 system is 64 μL. The wash solution, 50% DMSO, is used to wash the flow system (but not the surface) between injections.

During setting up, the molecular weight of each fragment is entered and will be used later during data analysis.

An assay set up in this way will consume about 250 mL of buffer and will be ready in just under 12 h. A common mistake in setting up the assay is to remove control steps, such as solvent correction, wash steps, and positive/negative controls to increase ''throughput.'' This strategy is often counterproductive, as any potential time savings are negated by increased analysis of complex data and revalidation of ''hits.''

7.5.4 Data Analysis – Report Points and Curve Shapes

There are several SPR systems and software solutions on the market, but irrespective of what system was used there are common issues that have to be addressed during analysis. How can a cut-off level be established? What type of binding curves will be regarded as hits? How can these ''early'' hits be prioritized and selected for further analysis? In this section, we consider some tools that are available in Biacore systems.

As a working hypothesis, an ideal fragment is expected to bind with a rapid approach to the steady state followed by rapid dissociation. Slow-binding, slow-dissociation, and very high-level binders are typically disregarded as they are associated with potential problematic behaviors

Published on 24 May 2017 on http://pubs.rsc.org | doi:10.1039/9781788010283-00255

View Online

Published on 24 May 2017 on http://pubs.rsc.org | doi:10.1039/9781788010283-00255

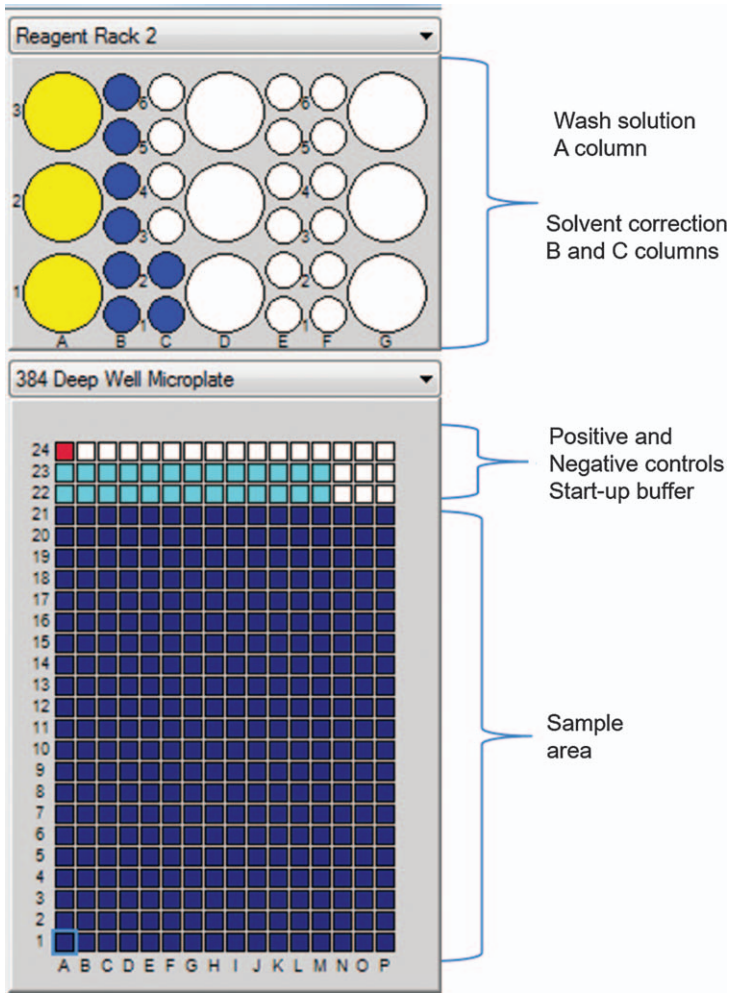


Figure 7.19 Setup of well plates and vials with samples, controls, solvent correction, and wash solutions.

(superstoichiometry, off-site binding, aggregation, *etc.*).[20] The expected binding behavior can be checked using report point data or by direct inspection of sensorgrams.

7.5.4.1 Report Point Analysis

Four report points are associated with every sample (Figure 7.20): baseline prior to injection, binding early and binding during injection, and stability after injection. A significant difference in response values for report points binding early and binding indicates slow or irregular binding. If the stability level is higher than the baseline level there may be a slow

View Online

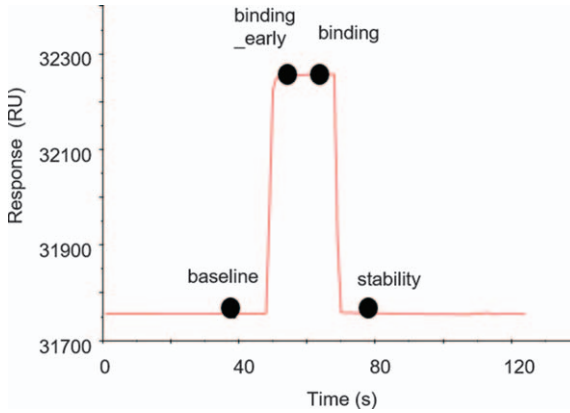


Figure 7.20 Four report points associated with sample injection: baseline, binding early, binding, and stability. These report points are used to identify slow-dissociating fragments and fragments that deviate from steady-state binding.

dissociation or the fragment sticks to the target. Based on the report points, sensorgrams can be grouped into three categories using curve markers: no issues, slow dissociation, or multiple issues.

Data analysis with the Biacore S200 proceeds through a number of steps:

1. Calculate and inspect solvent correction curves.
2. View auto QC plots of baseline, binding, and stability and exclude obvious outliers.
3. Plot the reference-subtracted and solvent-corrected response for report point binding early *versus* cycle number.

The plot in step 3 will display samples and positive and negative controls together with a table that gives response values for each cycle. The plot will automatically highlight fragments with unwanted binding behavior. These are indicated as curve markers and colored differently from the samples.

A cut-off level is automatically set so that 10% of all binders are above the threshold by default. From this stage, a user has several options to continue with data analysis. The user can adjust the threshold and identify binders without further considerations. Alternatively, tools for blank subtraction, molecular weight adjustments, capture adjustment, adjustment for trends in positive and negative controls, and median filtering can be applied:

- Blank subtraction can remove systematic errors at the sensorgram level by subtracting a blank sensorgram for which buffer was injected instead of sample.
- With the molecular weight adjustment tool, the response is divided by the molecular weight of the analyte, which allows a better comparison of small and large fragments.

Published on 24 May 2017 on http://pubs.rsc.org | doi:10.1039/9781788010283-00255

View Online

Published on 24 May 2017 on http://pubs.rsc.org | doi:10.1039/9781788010283-00255

- Adjustment for capture can be performed to compensate for variations in capture level.
- Adjustments to controls can be performed if the response from positive and negative controls varies over time. Remember to check that the assay has sufficient resolution even at lower levels of the positive control or higher levels of the negative control before performing this adjustment.
- Median filtering allows the user to set upper and lower limits (*y*-axis) for fragments that are not considered as hits and to set a window (*x*-axis) with a defined cycle width for median filtering. Filtering can reduce trends, waves, and offsets based on the report points of the non-binders. A drawback of this procedure is that it sometimes effects trends observed in the positive control and can change a trend from being negative in other plots to being positive. In such cases, median filtering is not recommended.

Blank subtraction and molecular weight adjustments should be considered in most cases. The other tools make data look better but this should be justified, as looking better is not always the same as being better.

In the example in Figure 7.21, blank subtraction was performed (Figure 7.21A) followed by molecular weight adjustment (Figure 7.21B). After molecular weight adjustment, the cut-off was set to (average +3SD) of the negative control as indicated by the red line.

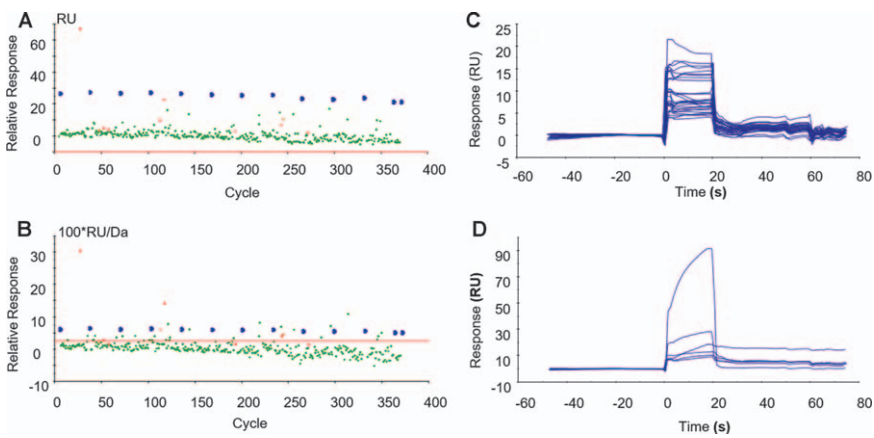


Figure 7.21 Report point analysis of a binding level screen (A and B) and sensorgrams obtained with selected (C) and deselected (D) fragments. In (A), report point values have been blank subtracted; there is a large difference between the positive control that has a higher molecular weight (437 Da compared with the average fragment MW of 161 Da). In (B), data have been adjusted for differences in molecular weight and a cut-off has been set using average + 3SD of negative controls. The sensorgrams above the cut-off were inspected to identify unwanted curve shapes and superstoichiometric binders. This resulted in the selection of 28 ''good'' fragment (8.3%).

View Online

Published on 24 May 2017 on http://pubs.rsc.org | doi:10.1039/9781788010283-00255

After removal of fragments with curve markers, 28 sensorgrams (Figure 7.21C) remained. Some of these sensorgrams still had a slightly elevated baseline and in some cases there was a decrease in signal level during the injection. The sensorgrams above the cut-off (Figure 7.21D) demonstrated increasing binding during injection and higher binding levels both during and after injection.

For this data set, capture was not used as the target was covalently immobilized. The decrease in response for positive controls (blue markers) was considered acceptable, and median filtering was not applied.

If the same library is used over and over again, it can be useful to keep track of compounds with curve markers. With this annotation, the quality of the library can be reviewed and improved by removing these compounds.

7.5.4.2 Sensorgram Analysis

The sensorgram comparison tool[44] in Biacore T200 evaluation software v.3.0 allows a direct comparison of curve shapes. This functionality can also be applied for the analysis of screening data. The case illustrated below was run on Biacore T200 and it is not the same data set as presented above.

Similarly to report point analysis, a user can first perform solvent correction and inspect QC plots to exclude obvious outliers.

The sensorgram comparison tool is opened and the user starts to select sensorgrams with the desired curve shape. These sensorgrams can be collected from several different runs and will be selected as ''standards'' (Figure 7.22A). Sensorgrams are routinely blank subtracted. To focus on curve shapes rather than signal levels, each sensorgram is normalized by re-scaling it between 0 and 100. The baseline is used as the zero level and the maximum response during injection as 100. A comparison window is obtained by using minimum and maximum sensorgrams (Figure 7.22B).

Sample sensorgrams (red) that have also been normalized are displayed in an overlay plot with the sensorgrams that make up the comparison window (blue). The user decides if the sample sensorgram meets the criterion of being similar to the standard (Figure 7.22C) or not (Figure 7.22D). The decision is noted in a results table. With a binding level cut-off of 5 RU, this procedure resulted in the selection of compounds in Figure 7.22E and deselection of compounds with curve shapes in Figure 7.22F.

To strengthen further the selection of appropriate binders, an apparent stoichiometry can be calculated. In this way, curve shapes and stoichiometry data can be combined to support the selection of fragments that will be subjected to further analysis.

The analysis of binding level screens can thus be supported with different tools. Report point analysis can handle larger data sets than sensorgram analysis but is less visual. In sensorgram comparisons, all data points and not only report points are used for the analysis. A further advantage is that a user can use the same set of standard sensorgrams for every screen that is

View Online

Published on 24 May 2017 on http://pubs.rsc.org | doi:10.1039/9781788010283-00255

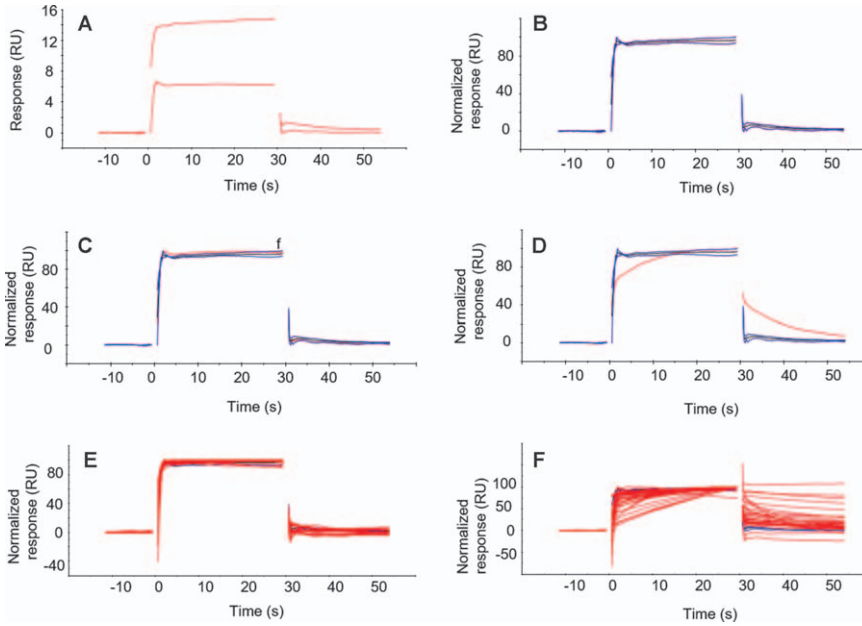


Figure 7.22 Sensorgram comparison for analysis of binding level screen. In (A), fragments with preferred curve shape have been identified. In (B), these curves have been normalized and a comparison window has been established. In (C), a fragment sample (red curve) falls very close to the comparison window. In (D), a fragment with deviating shape is displayed in an overlay plot with the comparison window. In (E), fragments with preferred curve shape are shown, and in (F), curves with unwanted curve shapes are displayed.

performed in the same way, *i.e.* with the same injection times. The standard shapes can be independent of the target.

Decisions taken during analysis are at least partly subjective. In particular, it will be important to describe how the cut-off level was decided as this to a large extent governs the number of hits. This number is later reduced as some compounds may give rise to irregular curve shapes. With these approaches, the cut-off setting should be regarded as a prioritization of the best candidates rather than actual identification of hits.

If the number of hits is considered to be too high, other filters based on apparent stoichiometry or fragment diversity can be used to obtain a reasonable number of hits that can be handled downstream.

7.5.4.3 Summary

- Establish the assay with positive and negative controls.
- Strive for a response of at least 10 and preferably 20 RU for a 150 Da fragment.

View Online

- Look for binding curves characterized by an almost immediate approach to the steady state and with rapid dissociation.

7.5.5 Affinity Screen

K_D estimates are important for several reasons. First, a dose–response relation is established, and second, K_D values are used to calculate LE and LELP. These metrics are used to track the optimization of the fragment through the medicinal chemistry program.

Fragments identified in a primary screen can be validated by affinity analysis. Fragments identified by NMR or other screening techniques can enter the SPR workflow at this stage. For such fragments, the SPR assay has to be developed from the start. Assay development here follows the same steps as outlined earlier in this chapter.

If a binding level screen has already been performed with SPR, the same assay can often be used directly for affinity analysis. In an affinity screen, a dose–response curve is generated by testing a compound over a wide range of concentrations. Injection and dissociation times can be kept short (20–30 s) and regeneration is "never" required. Include a positive control to ensure consistent data quality. If possible, include an R_{max} control, *i.e.* a compound for which binding levels approach target saturation. With this, R_{max} can be estimated or obtained from a fitting procedure. Knowledge or R_{max} for one compound of known molecular weight will simplify data analysis, as R_{max} values for different molecular weights can then be estimated.

On the Biacore S200, affinity analysis can be performed with both multi-cycle and single-cycle kinetic setups. Single-cycle kinetics here supports up to nine sample injections in a single cycle.

7.5.6 Affinity Analysis

Affinity analysis of eight fragments identified in a binding analysis screen is illustrated in Figure 7.23. These binding sets are, in our opinion, good representatives of low-affinity fragments.

The fragments were tested with concentrations from 900 to 79 μM (1.5-fold dilutions). The molecular weight and the estimated R_{max}, $R_{Max_est,}$ are shown for each fragment. R_{Max_est} was calculated by scaling the saturation response obtained with the R_{max} control to the individual molecular weight of each fragment. The saturation response for the R_{max} control was 47.2 RU and the molecular weight of the control was 437 Da.

Most fragments yielded response values that were much lower than the expected saturation responses, indicating weak affinities. There were two exceptions. In subset F, the estimated saturation response was almost reached at 900 μM concentration, and in subset H, the response was double the expected response.

There are some disturbances in the sensorgrams, but steady-state levels are reasonably well established except for subsets D and H, where secondary

Published on 24 May 2017 on http://pubs.rsc.org | doi:10.1039/9781788010283-00255

Published on 24 May 2017 on http://pubs.rsc.org | doi:10

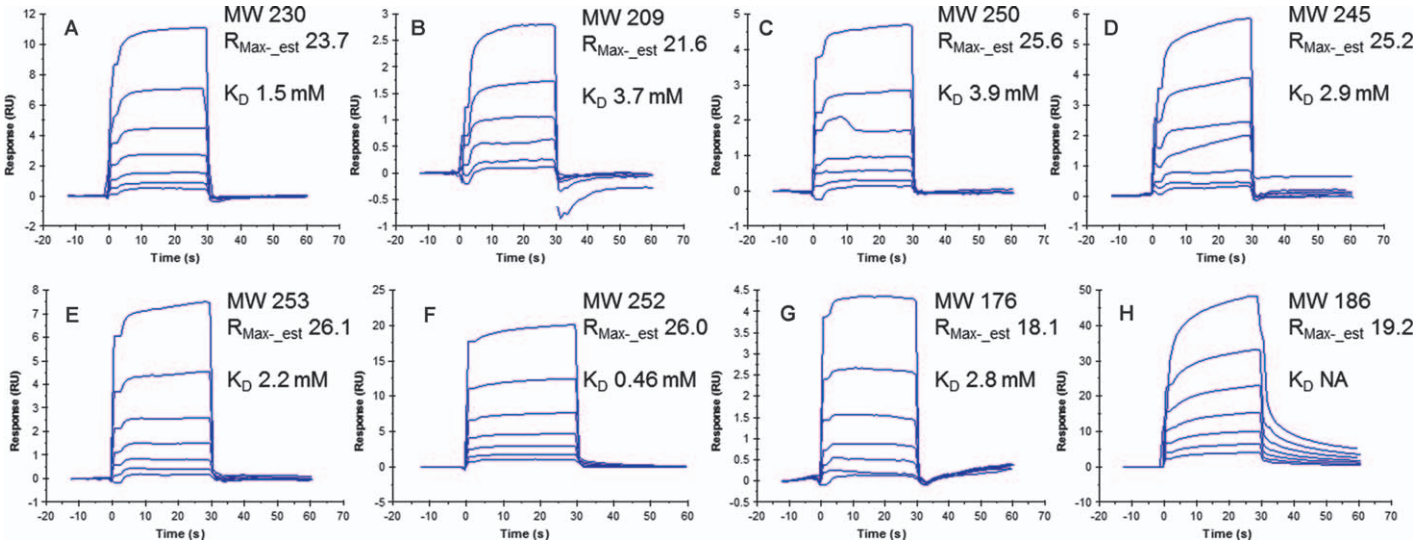


Figure 7.23 Binding curves 900–79 μM for affinity analysis. In each subset panel the molecular weight, the estimated value, $R_{\text{Max_est}}$, and the K_D determined by fitting data to a steady-state model with constant R_{max} are shown.

View Online

Published on 24 May 2017 on http://pubs.rsc.org | doi:10.1039/9781788010283-00255

binding effects can be seen. The K_D values shown in the panels were obtained by fitting the data to an affinity model where R_{Max_est} was entered as a constant. In cases where secondary binding events are obvious, a response from report point binding early is typically used for K_D analysis to reduce the impact of such events.

The rationale for this analysis procedure is illustrated in Figure 7.24, where two ways to determine the affinity for fragment F are compared.

At 900 μM, this fragment is almost at saturation so it would be reasonable to find a K_D value close to 500 μM where the target is half saturated. When the data are fitted to the regular steady-state model with R_{max}, K_D, and offset as floating parameters (Figure 7.24A), the result is quite different and unexpected. A K_D of 6 M and an R_{max} of 139 kRU are reported. Clearly, this fitting algorithm is not capable of resolving K_D and R_{max} values. When the data are fitted with the estimated R_{max} entered as a constant (Figure 7.24B), the curve shape is locked by this value and K_D is as expected at 460 μM.

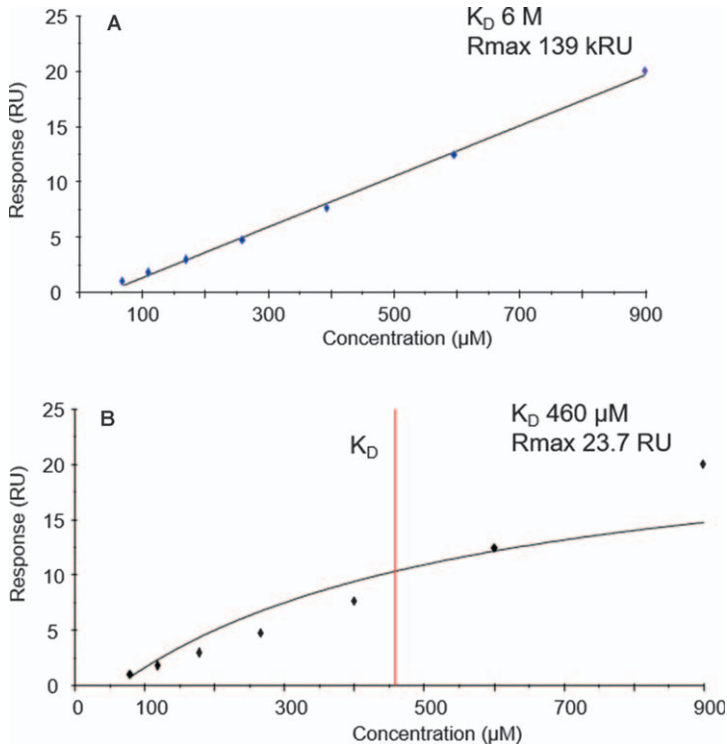


Figure 7.24 Data fitted to a steady-state model. In (A), both R_{max} and K_D were obtained from the fitting procedure, and in (B), the estimated R_{max} value was entered as a constant and K_D was calculated, Note the unexpected values for K_D and R_{max} in (A) and the more realistic values in (B).

View Online

Published on 24 May 2017 on http://pubs.rsc.org | doi:10.1039/9781788010283-00255

Fitting with a constant R_{max} improves the reliability of the results and works in many but not all cases. The estimated R_{max} is still an approximation. A better estimate may be obtained if the data are also corrected for differences in refractive index increment.

Summary:

- Expect weak affinities with response values below or far below target saturation.
- Include a compound as R_{max} control and calculate/estimate control-based R_{max} values for each fragment.
- Fit the data to a steady-state model with the estimated R_{max} as a constant.
- Use the data for ranking of affinities and view K_Ds as estimates of affinity.

7.5.7 Site Specificity – Use of Blocked or Saturated Targets

The direct binding assay detects available binding sites irrespective of site specificity. An investigator may be interested in binders to a specific site but also in discovering secondary sites that may be exploited for the development of inhibitors. ISA and SCA can be used to determine site specificity as described previously. There are, however, other alternatives.

In Figure 7.25, the active site of the target has been blocked and binding is tested on both active and blocked target. The target can be blocked by changing the active[28] site, by covalent attachment of a compound to the active site,[6] or by saturating the site with a slowly dissociating compound.[45] Under these circumstances, binding to the blocked target indicates the existence of a secondary site.

A blocked target will not always be available. However, the same principles can be applied when a site-specific binder of high affinity or at high concentration is added to the running buffer and to all samples. The binding site will be saturated by the specific binder. During injection, the sample and the specific binder will compete for the binding site. If the concentration and affinity of the specific binder are high enough, it will continue to occupy

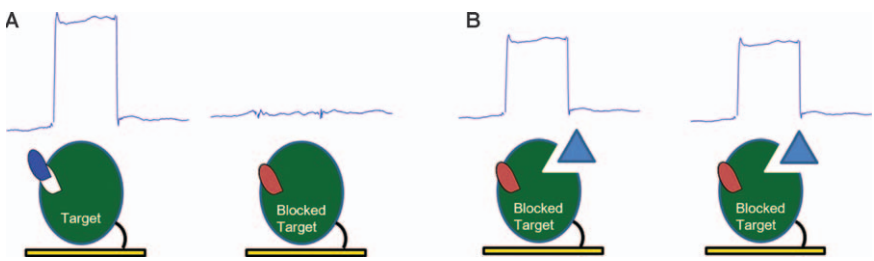


Figure 7.25 (A) Absence of binding on blocked target indicates competitive binding. (B): Binding to blocked target demonstrates the existence of a secondary site, non-competitive binding.

View Online

the site. If a binding event is detected under such circumstances (Figure 7.26), it indicates that the sample binds to a second binding site. This approach may require large quantities (in some cases up to gram quantities) of the inhibitor, as it is added to the running buffer.

Published on 24 May 2017 on http://pubs.rsc.org | doi:10.1039/9781788010283-00255

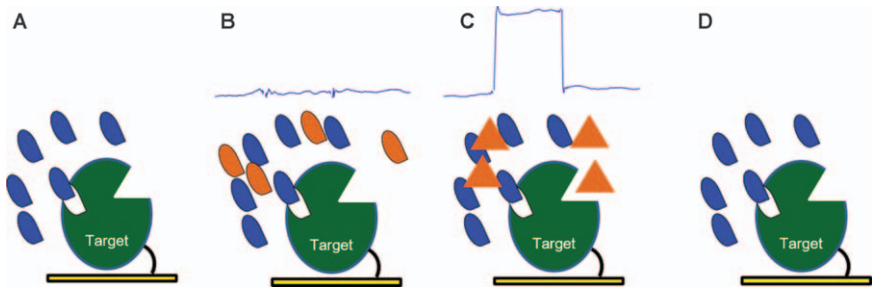


Figure 7.26 (A) A known inhibitor is added to the running buffer and saturates the binding site. (B) Injection of competing sample mixed with known inhibitor. No signal is observed as the target continues to be occupied by the inhibitor. (C) Injection of a new sample mixed with inhibitor. A binding event is observed as this sample recognizes and binds to a second binding site. (D) After every sample injection, running buffer with inhibitor ensures that the target remains blocked.

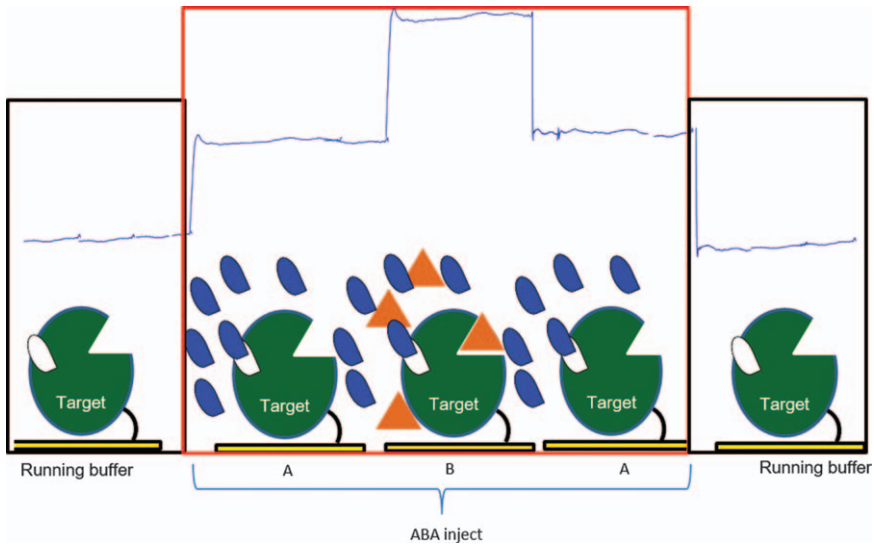


Figure 7.27 Running buffer and ABA inject. A baseline is established by the running buffer. During the first A part of the injection a known inhibitor saturates and blocks the binding site. During the B part sample and inhibitor are injected. Here the sample binds to a second site and a binding curve is observed. During the second A part the analyte dissociates and the known inhibitor continues to block the site. When the ABA inject is ready, the signal returns to the baseline as running buffer flows over the sensor surface.

View Online

Published on 24 May 2017 on http://pubs.rsc.org | doi:10.1039/9781788010283-00255

The results may not always be as clear as presented here. If the sample is of high affinity and injected at a high concentration, it may effectively replace the known inhibitor on the target. Depending on the molecular weights of sample and inhibitor, a positive or negative signal can then be observed, In this case, a positive signal cannot be interpreted as a demonstration of a second binding site.

To reduce the amount of inhibitor that is required for this type of experiment, the ABA inject available on the Biacore S200 and Biacore 8K can be used as shown in Figure 7.13. The ABA inject is a continuous injection system with three injection zones. In the first A zone, a target-specific binder is injected. The concentration of this compound should be high enough that the target is saturated during this part of the injection. In the second zone, B, a mixture of sample and target-specific binder is injected. To complete the injection, the target-specific binder is again injected on its own in the second A zone (Figure 7.27). The requirements on affinity and concentration for the site-specific binder are the same as when it is added to the running buffer and the binder must also be able to saturate the binding site during the first A zone of the injection. With this approach, it is also possible to perform competition experiments with different inhibitors within the same experiment to facilitate mapping of binding sites.

7.6 Hit to Lead Workflow

Target-based drug development from identification and validation of targets to the start of clinical trials (Figure 7.28) includes a number of decision points.

Fragment and high-throughput screening is part of the hit selection process. Prioritized fragments can be grown into more high-affinity compounds and these, along with hits from high-throughput screening campaigns, are developed further into lead compounds. As compounds evolve, selectivity, target occupancy,[46] and pharmacokinetic properties come more into focus. Here, SPR technology can be used to obtain kinetic and thermodynamic data, guide structure–activity studies, and thereby support the selection of candidates that enter clinical studies.

7.6.1 Off-rate Screening

Historical data[2] demonstrate that hits from a fragment screen on average grow from 15 to 28 atoms to become more lead like. Affinity may increase gradually and is often associated with more stable binding. To reduce the need for sample clean-up from organic synthesis and to measure effects as



Figure 7.28 Questions and decision points in the drug development workflow.

View Online

Published on 24 May 2017 on http://pubs.rsc.org | doi:10.1039/9781788010283-00255

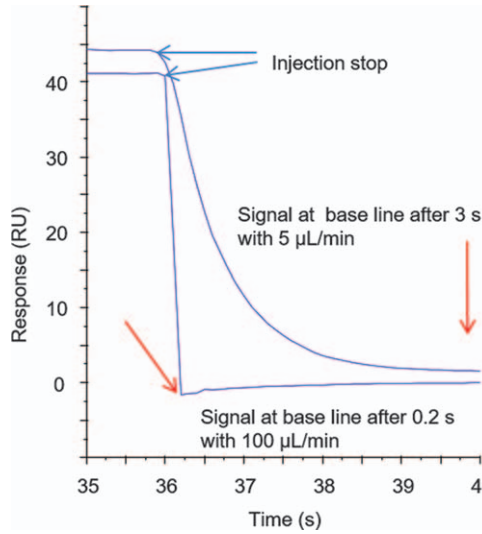


Figure 7.29 By using a high flow rate and using signals directly without reference or blank subtraction, dissociation data can be collected 0.2 s after the end of the injection. With this approach it may be possible to obtain better resolution of off-rates.

soon as possible, off-rate screening was introduced.[47] Fragments were grown using a range of chemistries and two test procedures were compared. In one procedure the new compound was purified and tested for binding and in the other the reaction mixture was evaporated, redissolved in DMSO and diluted into running buffer. Dissociation rate constants determined by these two procedures were in good agreement with each other, indicating that the synthesis and testing workflow can be simplified.

The initial off-rate screening was performed at 25 °C, but if solubility is not an issue lower temperatures may potentially offer additional information. Off rates are temperature dependent, with slower off rates at lower temperatures. To maximize the possibility of quantitating off rates, high flow rate, high data acquisition rate, and the use of non-referenced data can also be tried. High flow rates reduce the rise and fall times of the SPR signal, high data acquisition rates reduce the loss of valid data points, and with non-referenced data time alignment artifacts can be eliminated. Under optimum conditions (Figure 7.29), valid off-rate data may be collected 0.2 s after injection stop when a flow rate of 100 µL min^{-1} is used.

7.6.2 Lead Optimization

The first report of LMW analysis with SPR sensors was published in 1995[48] and the k_a/k_d plot for visualization of large kinetic data sets was introduced 7 years later in 2002[49] (Figure 7.30). During that period, SPR was added as a new element in the growing biophysical toolbox[50] that was used in drug

View Online

Published on 24 May 2017 on http://pubs.rsc.org | doi:10.1039/9781788010283-00255

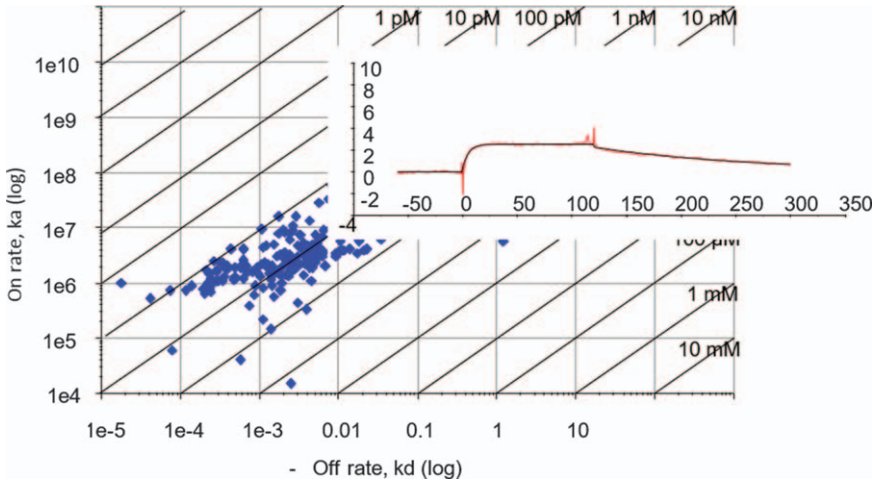


Figure 7.30 Plot of k_a *versus* k_d on a logarithmic scale. Dashed lines are isoaffinity lines. By clicking a point in the plot result, details including the sensorgram(s) and sample identifications are shown. The plot provides easy access to the distribution of kinetic properties even for very large data sets.

discovery and development. The value of kinetics started to be recognized and kinetic analysis of LMW–target interactions is now commonplace. Over the years, technical developments leading to increased sensitivity (Figure 7.5) and throughput and improved methodology and data display methods have made it easier to obtain and validate kinetic data for LMW compounds.

With the improved throughput and sensitivity of new instrumentation, analysis can now also keep up with compound generation where a medicinal chemist can generate 50–100 new compounds per week.

The impact of kinetics on the drug discovery process is perhaps best understood by listing the titles of some recent publications and by the observation that the term *structure–kinetic relation* (SKR) now exists in parallel with the more common structure–activity relation (SAR):

- When structure–affinity relationships meet structure-kinetics ….[51]
- Structure–kinetic relationships – an overlooked parameter in hit-to-lead optimization.[52]
- Structure–affinity relationships (SARs) and structure–kinetics relationships (SKRs) of Kv11.1 blockers.[53]
- On-rate based optimization of structure–kinetic relationship – surfing the kinetic map.[54]
- Design strategies to address kinetics of drug binding and residence time.[46]
- The role of binding kinetics in GPCR drug discovery.[55]

View Online

With these observations, the case for kinetic analysis in lead optimization will need no further justification.

7.7 Tips

LMW compound analysis and LMW kinetics have traditionally been seen as very challenging, but this may no longer be the case as systems, methods, software, and knowledge have all improved. Still, some help may occasionally be needed.

In this section we list 16 brief tips, not necessarily in a logical order, that we hope readers will find useful;

- Use a direct binding assay.
- Estimate how much you need to immobilize.
- Check protein activity with a positive/R_{max} control.
- Use buffer scouting to find/improve binding conditions if necessary.
- Select the screening concentration according to what you want to detect – millimolar or micromolar binders.
- If you use DMSO, make sure all equipment (tips, plates, filters, *etc.*) is compatible with organic solvents (no polystyrene).
- Prepare negative controls in the same way as other samples – do not use the running buffer as a negative control.
- Make sure samples are mixed thoroughly – poor mixing can give rise to strange sensorgram shapes.
- Test that the assay is good for purpose before starting extended runs with many samples.
- If capture is to be used, allow the signal to stabilize prior to sample injection.
- Keep the controls and run solvent correction and positive and negative controls throughout the assay.
- In fragment screening, prioritize fragments with a ''square-wave'' appearance.
- Strive for R_{max} values between 1 to 10 RU for the characterization of lead compounds.
- Try different temperatures – temperature may have a huge impact on binding characteristics.
- If you are stuck, try something else.
- Learn by doing.

7.8 Questions

1. You have determined k_a and k_d values for an LMW analyte as shown in Table 7.6. You are interested in the detection of fragments with affinities in the millimolar range. Can this surface be used for screening of a fragment library with compounds in the 150–275 Da range?

Published on 24 May 2017 on http://pubs.rsc.org | doi:10.1039/9781788010283-00255

View Online

Published on 24 May 2017 on http://pubs.rsc.org | doi:10.1039/9781788010283-00255

2. The 45 kDa ligand previously used in capture experiments (Table 7.6) was immobilized using amine coupling at pH 5.5. The activity was tested using the same analyte as in the capture experiment. Based on the saturation response the activity was now 22%. What was the activity of the ligand in capture mode? Suggest at least two ways to improve the activity of the immobilized ligand.
3. Positive and negative controls in a fragment screen gave the results in Table 7.7. The molecular weight of the positive control was 235 Da. The fragment screen was performed with fragments at 1 mM concentration and with fragments in the MW range from 150 to 275 Da. What cut-off level in RU can be used for identification of a ''hit'' during screening? Can fragments with a K_D of 1 mM be detected?
4. K_D values were determined for 14 fragments using an estimated R_{max} value during the fitting procedure. The K_D values (mM) in Table 7.8 were obtained. When these fragments were allowed to compete with a known inhibitor, the binding curves shown in Figure 7.31 were obtained. The blue curve is the known inhibitor and the red curves represent injections of a mixture of the known inhibitor and the fragments. Are any of these fragments an allosteric (non-competitive) binder? In what way did the K_D values support the design of the competition experiment?
5. The ligand efficiencies for the fragments in Table 7.8 ranged from 0.20 to 0.29 kcal mol^{-1} K^{-1}. Given the uncertainties in K_D values, how would you use these values?

Table 7.6 k_a and k_d values determined for an LMW analyte.

Ligand molecular weight (Da)	45 000
Capture level (RU)	1500
Analyte molecular weight (Da)	516
k_a (L mol^{-1} s^{-1})	3.2×10^{6}
k_d (s^{-1})	1.3×10^{-3}
R_{max}	13.2

Table 7.7 Results of a fragment screen of positive and negative controls.

Cycle number	5	35	65	95	125	155	185	215	245
Positive control (RU)	29.2	29.7	28.1	27.3	26.8	25.7	25.0	24.1	22.3
Cycle number	3	33	63	93	123	153	183	213	243
Negative control (RU)	1.3	1.8	2.0	1.7	1.6	2.2	1.8	1.7	1.9

Table 7.8 K_D values determined for 14 fragments.

Fragments 1–7	1.01	1.68	2.41	2.56	3.24	3.70	4.46
Fragments 8–14	4.46	4.57	4.81	5.23	5.49	5.53	5.69

View Online

Published on 24 May 2017 on http://pubs.rsc.org | doi:10.1039/9781788010283-00255

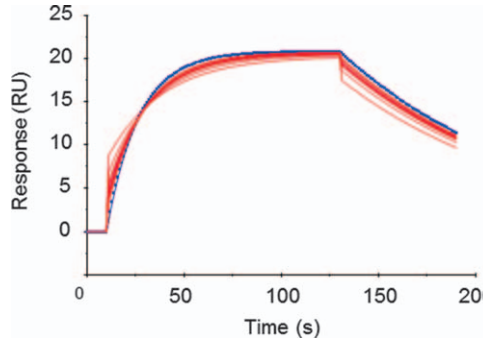


Figure 7.31 Typical binding curves for fragment interactions competing with an inhibitor.

References

1. M. Baker, *Nat. Rev. Drug Discovery*, 2013, **12.1**, 5–7.
2. D. A. Erlanson, S. W. Fesik, R. E. Hubbard, W. Jahnke and H. Jhoti, *Nat. Rev. Drug Discovery*, 2016, **15**(9), 605–619.
3. H. Jhoti, G. Williams, D. C. Rees and C. W. Murray, *Nat. Rev. Drug Discovery*, 2013, **12**(8), 644.
4. G. M. Keseru, D. A. Erlanson, G. G. Ferenczy, M. M. Hann, C. W. Murray and S. D. Pickett, *J. Med. Chem.*, 2016, **59**(18), 8189–8206.
5. A. Chavanieu and M. Pugnière, *Expert Opin. Drug Discovery*, 2016, **11.5**, 489–499.
6. R. Karlsson, M. Kullman-Magnusson, M. D. Hämäläinen, A. Remaeus, K. Andersson, P. Borg, E. Gyzander and J. Deinum, *Anal. Biochem.*, 2000, **278.1**, 1–13.
7. Y. Bai, S. Tashiro, S. Nagatoishi, T. Suzuki, D. Yan, R. Liu, K. Tsumoto, M. Bartlam and T. Yamamoto, *Protein Cell*, 15, **6**(12), 924–928.
8. J. Blanc, R. Geney and C. J. Menet, *Anti-Cancer Agents Med. Chem.*, 2013, **13.5**, 731–747.
9. R. F. Ludlow, M. L. Verdonk, H. K. Saini, I. J. Tickle and H. Jhoti, *Proc. Natl. Acad. Sci.*, 2015, **112.52**, 15910–15915.
10. J. S. Albert, N. Blomberg, A. L. Breeze, A. J. H. Brown, J. N. Burrows, P. D. Edwards, R. H. A. Folmer, S. Geschwindner, E. J. Griffen, P. W. Kenny, T. Nowak, L.-L. Olsson, H. Sanganee and A. B. Shapiro, *Curr. Top. Med. Chemistry*, 2007, **7.16**, 1600–1629.
11. H. Nordin, M. Jungnelius, R. Karlsson and O. P. Karlsson, *Anal. Biochem.*, 2005, **340.2**, 359–368.
12. R. L. Rich, J. Errey, F. Marshall and D. G. Myszka, *Anal. Biochem.*, 2011, **409.2**, 267–272.
13. R. Chu, D. Reczek and W. Brondyk, *Sci. Rep.*, 2014, **4**, 1–9.
14. Data file 28-9681-84 AA, *G. E. Healthcare*, 1–6.
15. S. Kortagere *et al.*, *J. Virol.*, 2012, **86.16**, 8472–8481.

View Online

Published on 24 May 2017 on http://pubs.rsc.org | doi:10.1039/9781788010283-00255

16. P. Stenlund, G. J. Babcock, J. Sodroski and D. G. Myszka, *Anal. Biochem.*, 2003, **316.2**, 243–250.
17. C. Zhu, X. Zhu, J. P. Landry, Z. Cui, Q. Li, Y. Dang, L. Mi, F. Zheng and Y. Fei, *Sensors*, 2016, **16.3**, 378.
18. E. Pol, H. Roos, F. Markey, F. Elwinger, A. Shaw and R. Karlsson, *Anal. Biochem.*, 2016, **510**, 88–97.
19. Log *P* distribution among drugs, http://www.organicchemistry.org/prog/peo/cLogP.html?_sm_au_=icVSvrntSm0rtq3H.
20. A. M. Giannetti, B. D. Koch and M. F. Browner, *J. Med. Chem.*, 2008, **51.3**, 574–580.
21. H. Zhao, P. H. Brown and P. Schuck, *Biophys. J.*, 2011, **100.9**, 2309–2317.
22. T. M. Davis and W. D. Wilson, *Anal. Biochem.*, 2000, **284.2**, 348–353.
23. A. Moberg, A. Lager, M. D. Hämäläinen and T. Jarhede, *J. Pharm. Biomed. Anal.*, 013, **78**, 224–232.
24. B. A. Kozikowski *et al.*, *J. Biomol. Screening*, 2003, **8.2**, 205–209.
25. X. Cheng, J. Hochlowski, H. U. A. Tang, D. Hepp, C. Beckner, S. Kantor and R. Schmitt, *J. Biomol. Screening*, 2003, **8.3**, 292–304.
26. Å. Frostell-Karlsson, A. Remaeus, H. Roos, K. Andersson, P. Borg, M. Hämäläinen and R. Karlsson, *J. Med. Chem.*, 2000, **43.10**, 1986–1992.
27. J. H. Zhang, T. D. Chung and K. R. Oldenburg, *J. Biomol. Screening*, 1999, **4.2**, 67–73.
28. S. Perspicace, D. Banner, J. Benz, F. Müller, D. Schlatter and W. Huber, *J. Biomol. Screening*, 2009, **14.4**, 337–349.
29. H. Yang, C. Qin, Y. H. Li, L. Tao, J. Zhou, C. Y. Yu, F. Xu, Z. Chen, F. Zhu and Y. Z. Chen, *Nucleic Acids Research*, 2016, **44.D1**, D1069–D1074.
30. V. Law *et al.*, *Nucleic Acids Research*, 2014, **42.D1**, D1091–D1097.
31. M. Almén, K. J. Nordström, R. Fredriksson and H. B. Schiöth, *BMC Biol.*, 2009, **7.50**, 1.
32. B. K. Kobilka, *Biochim. Biophys. Acta, Biomembr.*, 2007, **1768.4**, 794–807.
33. N. Robertson, A. Jazayeri, J. Errey, A. Baig, E. Hurrell, A. Zhukov, C. J. Langmead, M. Weir and F. H. Marshall, *Neuropharmacology*, 2011, **60.1**, 36–44.
34. O. P. Karlsson and S. Löfås, *Anal. Biochem.*, 2002, **300.2**, 132–138.
35. J. Renaud, C. Chung, U. H. Danielson, U. Egner, M. Hennig, R. E. Hubbard and H. Nar, *Nat. Rev. Drug Discovery*, 2016, 1–20. Advance on line publication.
36. A. Kuglstatter, M. Stahl, J. U. Peters, W. Huber, M. Stihle, D. Schlatter, J. Benz, A. Ruf, D. Roth, T. Enderle and M. Hennig, *Bioorg. Med. Chem. Lett.*, 08, **18.4**, 1304–1307.
37. J. B. Baell, L. Ferrins, H. Falk and G. Nikolakopoulos, *Aust. J. Chem.*, 2014, **66.12**, 1483–1494.
38. M. S. Chimenti, S. L. Bulfer, R. J. Neitz, A. R. Renslo, M. P. Jacobson, T. L. James, M. R. Arkin and M. J. S. Kelly, *J. Biomol. Screening*, 2015, **20.6**, 788–800.

View Online

39. T. Christopeit, T. J. O. Carlsen, R. Helland and H. K. S. Leiros, *J. Med. Chem.*, 2015, **58.21**, 8671–8682.
40. J. A. Christopher, J. Brown, A. S. Dore, J. C. Errey, M. Koglin, F. H. Marshall, D. G. Myszka, R. L. Rich, C. G. Tate, B. Tehan, T. Warne and M. Congreve, *J. Med. Chem.*, 2013, **56.9**, 3446–3455.
41. A. Kohlmann *et al.*, *J. Med. Chem.*, 2013, **56.3**, 1023–1040.
42. S. G. Zech *et al.*, *J. Med. Chem.*, 2016, **59.2**, 671–686.
43. X. Wu *et al.*, *ACS Chem. Biol.*, 2015, **10.6**, 1476–1484.
44. R. Karlsson, E. Pol and Å. Frostell, *Anal. Biochem.*, 2016, **502**, 53–63.
45. C. A. Shepherd, A. L. Hopkins and I. Navratilova, *Prog. Biophys. Mol. Biol.*, 2014, **116.2**, 113–123.
46. K. P. Cusack, Y. Wang, M. Z. Hoemann, J. Marjanovic, R. G. Heym and A. Vasudevan, *Bioorg. Med. Chem. Lett.*, 15, **25.10**, 2019–2027.
47. J. B. Murray, S. D. Roughley, N. Matassova and P. A. Brough, *J. Med. Chem.*, 2014, **57.7**, 2845–2850.
48. R. Karlsson and R. Stahlberg, *Anal. Biochem.*, 1995, **228.2**, 274–280.
49. P. O. Markgren, W. Schaal, M. Hämäläinen, A. Karlén, A. Hallberg, B. Samuelsson and U. H. Danielson, *J. Med. Chem.*, 2002, **45.25**, 5430–5439.
50. H. J. Boehm, M. Boehringer, D. Bur, H. Gmuender, W. Huber, W. Klaus, D. Kostrewa, H. Kuehne, T. Luebbers, N. Meunier-Keller and F. Mueller, *J. Med. Chem.*, 2000, **43.14**, 2664–2674.
51. M. Vilums, A. J. M. Zweemer, F. Barmare, A. M. F. van der Gracht, D. C. T. Bleeker, Z. Yu, H. de Vries, R. Gross, J. Clemens, P. Krenitsky, J. Brussee, D. Stamos, J. Saunders, L. H. Heitman and A. P. IJzerman, *Eur. J. Med. Chem.*, 2015, **93**, 121–134.
52. M. Vilums, A. J. M. Zweemer, Z. Yu, H. de Vries, J. M. Hillger, H. Wapenaar, I. A. E. Bollen, F. Barmare, R. Gross, J. Clemens, P. Krenitsky, J. Brussee, D. Stamos, J. Saunders, L. H. Heitman and A. P. IJzerman, *J. Med. Chem.*, 2013, **56.19**, 7706–7714.
53. Z Yu, J. P. D. van Veldhoven, J. Louvel, I. M. E. 't Hart, M. B. Rook, M. A. G. van der Heyden, L. H. Heitman and A. P. IJzerman, *J. Med. Chem.*, 2015, **58.15**, 5916–5929.
54. A. Schoop and F. Dey, *Drug Discovery Today: Technol.*, 2015, **17**, 9–15.
55. D. C. Swinney, B. A. Haubrich, I. Van Liefde and G. Vauquelin, *Curr. Top. Med. Chem.*, 2015, **15.24**, 2504–2522.

Published on 24 May 2017 on http://pubs.rsc.org | doi:10.1039/9781788010283-00255

Published on 24 May 2017 on http://pubs.rsc.org | doi:10.1039/9781788010283-00295

CHAPTER 8

Combined Antibody Characterization: High-throughput Ranking, Binning, and Mapping

KOEN WAGNER

AIMM Therapeutics, Meibergdreef 59, 1105 BA Amsterdam, The Netherlands
Email: kwagner@aimmtherapeutics.com

8.1 General Introduction

In recent years, antibody-based therapeutics has made remarkable advances in the clinical landscape.[1] Since the approval of mouse antibody OKT3 (proprietary name: Orthoclone OKT3) in 1992, an ever-increasing number of antibodies have come into clinical use for the treatment of infectious disease, cancer, and autoimmune disease.[2,3] So far, 60 antibodies have been clinically approved (www.imgt.org), and an even greater number are in clinical trials.[3] In addition to their therapeutic potential, antibodies are also widely used as diagnostic tools, both in the clinic and in research.[4]

Given the demand for functional antibodies, there is increasing interest in methods that allow the selection of promising antibody leads from large screening pools, at high throughput. Typically, antibody screening is performed by selecting binding antibodies from libraries with end-point assays [*e.g.* enzyme-linked immunosorbent assay (ELISA) or fluorescence-activated cell sorting (FACS)] that supply basic information about binding kinetics or

Handbook of Surface Plasmon Resonance, 2nd Edition
Edited by Richard B. M. Schasfoort
© The Royal Society of Chemistry 2017
Published by the Royal Society of Chemistry, www.rsc.org

View Online

Published on 24 May 2017 on http://pubs.rsc.org | doi:10.1039/9781788010283-00295

antibody epitopes. After the initial screening rounds, a large pool of antibodies is obtained that needs to be characterized further before selecting leads. Therefore, the development of suitable reliable, high-throughput methods to define the binding kinetics and epitopes of antibodies (which are ideally performed on a single instrument) will greatly speed up the discovery process.

This chapter describes the high-throughput functional characterization of antibodies by means of affinity ranking, antibody binning, and epitope mapping surface plasmon resonance (SPR) imaging. In the first experiment, the affinity ranking experiment categorizes antibodies based on their binding kinetics, and in the second experiment antibodies that bind overlapping epitopes are defined through epitope binning. In the third experiment, the exact epitope of the antibody is defined through epitope mapping. These three setups combined supply the information that is required to identify the most promising antibodies.

To allow high-throughput measurements, we used the IBIS MX96 SPR imaging instrument (IBIS Technologies, Enschede, The Netherlands) for our experiments, as this instrument allows the measurement of up to 96×96 (9216) interactions in a single run.

8.2 Affinity Ranking

Affinity ranking is the characterization of a pool of (mutant) proteins solely on their binding kinetics (k_a, k_d, K_D) for their binding partner(s). In this section, we describe affinity ranking using antibodies and their antigens as examples. However, of course, the affinity ranking method is valid for all kinds of biomolecular interactions (*e.g.* protein–protein binding, protein–DNA binding). Multiplex SPR instrumentation allows the rapid measurement of a large number of interactions in real time, and this stands out from other high-throughput analysis methods, which are discussed below.

ELISA is a frequently used method to obtain affinity data with high throughput. However, ELISA is an end-point method (giving K_D only). Furthermore, in ELISA, ligands are frequently passively immobilized (“coated”) on a well-plate surface. During the coating step (which is typically carried out overnight), the ligand structure is converted from a 3D solution structure to a 2D surface-bound structure, which could lead to a loss of epitopes that have a defined 3D structure.[5] In SPR, ligands are chemically immobilized on a sensor surface, which typically consists of a chemically activated dextran layer (but other sensor surfaces are also available). Chemical immobilization is a much quicker process than passive immobilization and, with standard methods, takes ~30 min to complete. Also, the dextran coating of the SPR sensor surface is not a flat structure (such as the bottom of a well plate) and allows for hydration of the immobilized ligand, which contributes to preserving the 3D structure. However, the use of a dextran-layered SPR sensor surface does not guarantee that the structure of the ligand is retained after immobilization, and this should always be tested experimentally.

View Online

Published on 24 May 2017 on http://pubs.rsc.org | doi:10.1039/9781788010283-00295

Another popular high-throughput affinity ranking method is FACS, which, like ELISA, is an end-point measurement and yields only a K_D value.[6] FACS is mainly used for affinity ranking with live cells as ligand and (fluorescent) antibodies/proteins as analyte (coated beads could be a suitable alternative ligand in FACS). Although *per se* FACS is a good method to obtain reliable binding data, the use of live cells does come with some disadvantages. First, a cell culture sample is never homogeneous and, from one cell to the next, there could be great variation in the expression of the target ligand. Also, cells could express receptors that engage non-specifically with the analyte of choice, and these need to be blocked before starting the experiment (*e.g.* many cell lines express antibody-binding receptors, Fcγ and FcRn, that bind to the invariant Fc-tail of an antibody).[7] Furthermore, as FACS detects binding events on live cells (and not on purified ligand), the outcome does not specify which ligand on the cell the analyte had bound, allowing for false positives. Therefore, to verify the (less-specific) results obtained on live cells, it is important to combine FACS with a method that measures the interaction of pure analyte and ligand alone. On the other hand, the use of live cells as ligand has one important advantage: many binding targets of antibodies (or other proteins) are membrane-associated proteins or *trans*-membrane proteins. Membrane proteins are usually difficult to purify and, when purified, may be difficult to use *in vitro*. Then, FACS is a suitable alternative to obtain affinity data. However, given the recent advances in cell profiling with SPR, it very likely that in the near future SPR will be also utilized to measure antibody–cell interactions.[8,9]

To set up an affinity ranking experiment with multiplex SPR, several aspects need to be considered before starting (which sensor surface to use; how many interactions to measure; which controls to include; how to immobilize the antibodies on the sensor). These questions will be illustrated by discussing two examples of affinity ranking experiments.

8.2.1 Experiment 1: Affinity Ranking of Human IgG Binding Hepatitis C Virus E2 Protein

8.2.1.1 Introduction

This experiment involves affinity ranking of a large pool of antibodies, all of which bind the hepatitis C virus (HCV) E2 protein, with capture SPR.

Hepatitis C is one of the major global public health problems, with around 180 million people chronically infected and 350 000 deaths every year from hepatitis C-related complications.[10] To assist the development of a vaccine, better understanding of the immune response in individuals that spontaneously clear the infection is needed. Spontaneous clearance of the primary HCV infection occurs in 25–40% of individuals.[11–13] A broadly neutralizing antibody response against HCV E1E2 glycoproteins at the early phase of infection has been associated with clearance.[14,15] Identifying epitopes on the HCV E1 and E2 glycoproteins that are associated with viral

View Online

Published on 24 May 2017 on http://pubs.rsc.org | doi:10.1039/9781788010283-00295

clearance is highly relevant to vaccine development, and therefore we set out to identify new antibodies that bind the HCV E2 glycoprotein and demonstrate broad neutralizing capacity.

A pool of 88 human immunoglobulin G (IgG) antibodies, all of which are specific to the HCV E2 protein, was obtained by screening immortalized B cells for HCV pseudoparticle infection neutralizing activity.[16] Binding to HCV E2 protein was confirmed with ELISA. Because the purification of 88 different antibodies, without further information on neutralization activity or antibody sequence, would be a tortuous effort at this point, we decided to use the raw material (*i.e.* supernatant from B-cell cultures) in an affinity ranking experiment. In combination with neutralization and sequence data, the outcome of the ranking experiment decides which B-cell clones would be selected for the next round of selection.

8.2.1.2 Setting Up the Experiment

The optimal setup for an affinity ranking experiment is to immobilize all antibodies in similar orientations, at similar densities. To ensure that all antibodies are captured at the same density (RU), it is important that all antibody samples have similar concentrations. The amount of immobilized ligand (RU) depends on both the immobilization method and the ligand concentration.[17,18] Therefore, to compare reliably the affinities of many different antibodies in a single experiment, it is important that both the antibody concentration and the immobilization efficiency are the same for all antibodies in the array.

To ensure that all the antibodies are immobilized in equal amounts, a SensEye anti-human IgG-coated SPR sensor (gel type) was chosen (all antibodies are of the IgG class). For this experiment, we specifically chose to use a capture sensor rather than a chemically activated non-coated SPR sensor (*e.g.* SensEye Easy-2-Spot). Chemical immobilization of ligands on activated sensors relies on coupling of exposed primary amines (present on lysine residues) to *N*-hydroxysuccinimide (NHS) esters on the dextran layer. This reaction forms a covalent bond between the dextran and the ligand. As reactive lysine residues may be present at, or close to, the binding domains of the ligand (*i.e.* the variable domains of the antibody), coupling of these residues could potentially disrupt the ligand structure. Therefore, there is always a chance that some antibodies in the pool lose activity during chemical immobilization. Furthermore, because many primary amines are present in antibodies (on average, an antibody has ~40 lysine residues), there is a high degree of randomness in the product of the immobilization reaction, and this in turn could also have consequences for the activity of the immobilized antibody and the amount of antibody that will be immobilized (owing to variations in antibody p*I* and structure, some antibodies are immobilized more efficiently than others). For these reasons, precoated capture sensors are more suitable for affinity ranking experiments. This experiment uses a pre-made anti-human IgG-Fc sensor (other available SensEye capture sensors are anti-His, anti-human IgM, anti-human IgA, anti-human IgG

View Online

CH1, anti-multi-species IgG-Fc, and streptavidin-coated), but even if no capture sensors are available for the ligand of choice, it is possible to prepare one's own sensors and use these in the affinity ranking experiment (this option is discussed in Experiment 2).

Published on 24 May 2017 on http://pubs.rsc.org | doi:10.1039/9781788010283-00295

8.2.1.3 CFM Spotting

In the first affinity ranking experiment, samples of 88 human IgG antibodies were captured simultaneously on a gel-type anti-hu-IgG-Fc SensEye sensor. Using a continuous flow microspotting (CFM) spotter equipped with a 4×12 printhead, up to 96 antibodies can all be characterized in a single experiment using the 2×4×12 layout. Note that, when using this layout, not all samples are spotted at the same time: first the top half (4×12) of the sensor is spotted, and then the bottom half (4×12). This could, potentially, lead to drying effects, hence it is recommended to include (at least) one control sample that is spotted on both the top and bottom halves, to ensure that the spotting procedure does not influence the outcome of the ranking experiment.

A good capture sensor does not require a high sample concentration to capture a sufficient amount of ligand. In this experiment, samples containing 0.1 $\mu g\,mL^{-1}$ human IgG were spotted on the anti-hu-IgG-Fc SensEye sensor (0.1 $\mu g\,mL^{-1}$ is the recommended concentration, but likely lower concentrations may also be used). These samples were non-purified medium samples (containing 2% ultra-low IgG fetal calf serum, HyClone), diluted in system buffer (PBS + 0.05% Tween 20 + 0.01% sodium azide). After spotting the ligands, the sensor should be used immediately. Figure 8.1 shows the anti-hu-IgG-Fc sensor directly after spotting with 88 B-cell supernatants plus controls.

8.2.1.4 Affinity Ranking: Analysis and Interpretation

After the capture of ligands on the sensor surface has been verified, affinity ranking can be initiated. Since the antibody-immobilized ligands may not be regenerated (low-pH regeneration would not only remove the analyte, but also remove the captured ligands from the sensor), affinity ranking is performed with a kinetic titration. In a kinetic titration setup, a series of injections with increasing concentration of analyte is performed. During the kinetic titration, analyte binds on the ligand-captured spots until the spots are saturated with analyte. The spots, on which the binding of analyte is detected at the lowest concentrations, are likely to contain the highest-affinity ligands. In our pilot experiment, the binding curves of kinetic titrations of the anti-HCV E2 antibodies with HCV E2 protein clearly showed the different binding properties of the immobilized antibodies (Figure 8.2).

To allow the fitting of kinetic constants from the binding curves, the fitting procedure needs to be modified to compensate for the accumulation of signal response with each new injection step. For this, an adapted version of

View Online

Published on 24 May 2017 on http://pubs.rsc.org | doi:10.1039/9781788010283-00295

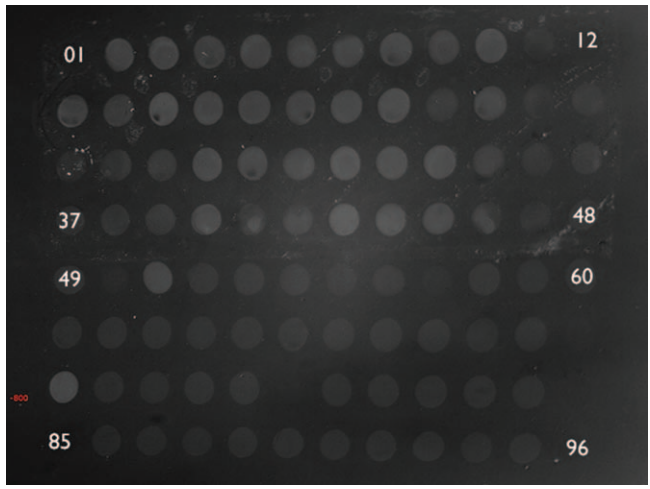


Figure 8.1 Image of anti-hu IgG SenseEye Chip after CFM spotting with B-cell supernatants. Ninety-six samples (88 B-cell supernatants + 8 controls) were immobilized in two 4×12 arrays. Spot numbers are indicated on the image. Positions 1, 12, 72, 84, 85, and 96 were spotted with system buffer without adding B-cell supernatant.

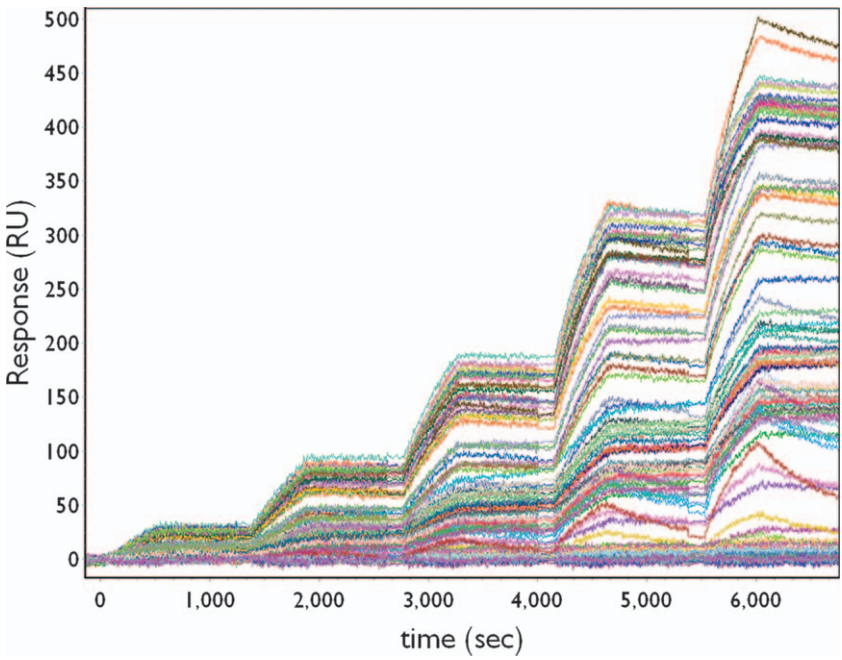


Figure 8.2 Binding of immobilized B-cell IgG to soluble HCV E2 protein. A concentration series of five concatenated injections with HCV E2 protein (0.05–1.0 μg mL^{-1}) were injected over a chip on which 88 different anti-HCV E2 human B cell IgG were immobilized. Based on their binding curves, high-affinity antibodies are readily discriminated from low-affinity antibodies.

View Online

Published on 24 May 2017 on http://pubs.rsc.org | doi:10.1039/9781788010283-00295

Scrubber2 is used, to apply a so-called "floating align point" fitting. In a kinetic titration experiment, after each dissociation phase the next association phase starts with an increased RU signal (as illustrated in Figure 8.2). Therefore, the align point is not equal to the injection point but needs to be set back in time to compensate for the non-zero RU at the starting point. Instead, the association phases are globally fitted simultaneously to an optimal value for the injection point, to compensate for accumulation due to previous injections (see the example in Figure 8.3).

Thus, we determined the kinetic constants for all HCV E2 binding antibodies in this experiment. Table 8.1 lists the kinetic constants of nine antibodies that were selected from the pool of 88 (curve fits are shown in Figure 8.4). The binding kinetics of these nine antibodies illustrate the

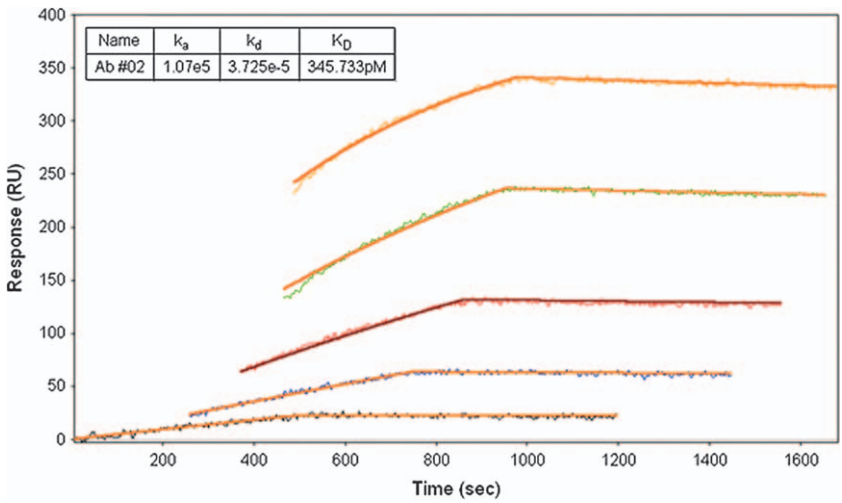


Figure 8.3 Example fitting of kinetic titration binding curves with the "floating align point" method. The injection point is set as variable, to compensate for the non-zero starting point. This explains the different starting point of each curve.

Table 8.1 Binding constants of nine selected HCV E2-binding antibodies.[a]

Clone	k_a (10^4 L mol^{-1} s^{-1})	k_d (10^{-5} s^{-1})	K_D (pM)
01	3.02	32.0	10 600
02	10.7	3.73	346
03	8.44	5.46	652
04	2.47	0.69	284
05	2.25	33.7	15 000
06	4.67	0.1[b]	21.4
07	2.39	0.1[b]	41.9
08	4.65	39.1	8410
09	7.42	0.1[b]	13.5

[a]All antibodies were measured on only one spot; no error could be determined.
[b]When no dissociation rate could be fitted, a value of 0.1×10^{-5} was used.

Published on 24 May 2017 on http://pubs.rsc.org | doi:10

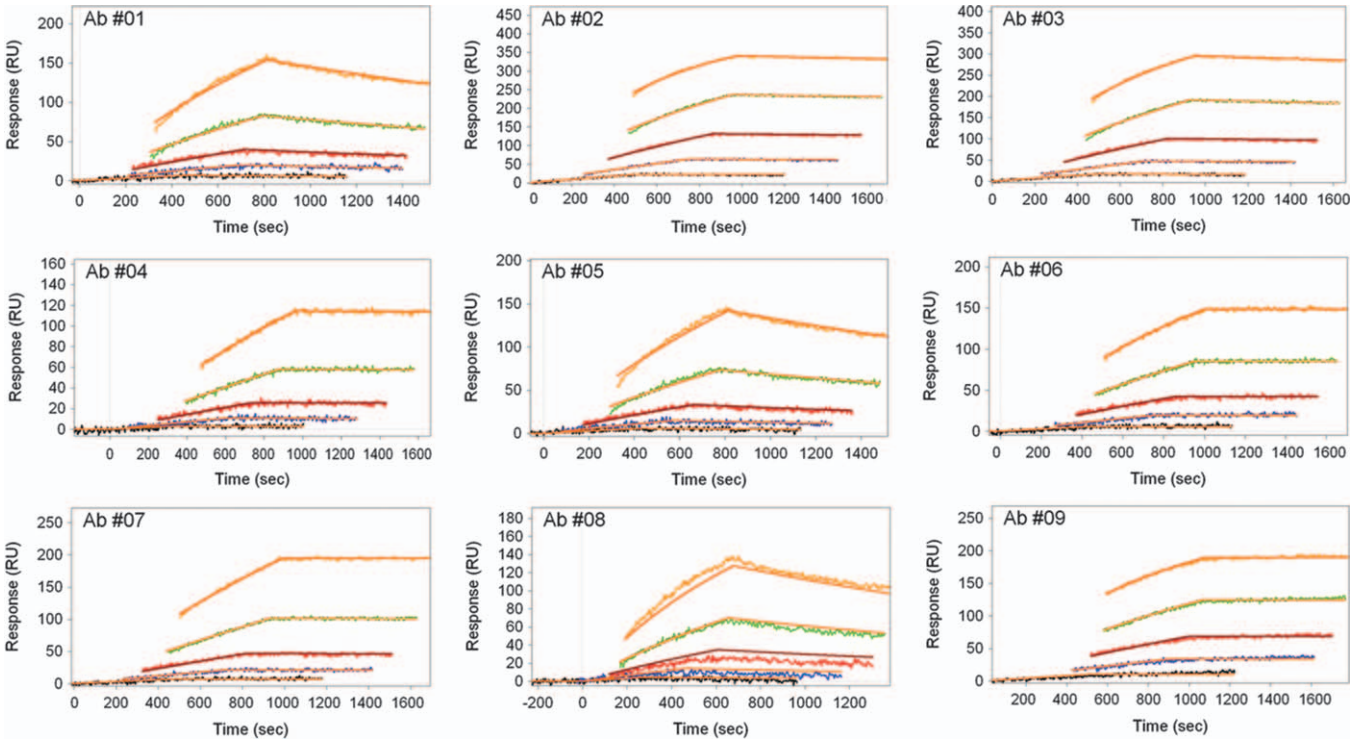


Figure 8.4 Curve fits for antibodies described in Table 8.1. SPR curves were fitted to a 1 : 1 binding model using Scrubber2 software.

View Online

Published on 24 May 2017 on http://pubs.rsc.org | doi:10.1039/9781788010283-00295

diversity of the antibody pool, showing K_D values ranging from 10 to 10 000 pM. Based on the binding kinetics, the antibodies can be divided into three groups: **high-affinity binders**, with a slow on-rate and a slow off-rate (K_D: 10–100 pM), **intermediate affinity binders**, with a fast on-rate, but also a fast off-rate (K_D: 100 pM–1 nM), and **weak affinity binders**, with a slow on-rate and a fast off-rate (K_D: 1–10 nM). Note that, as this experiment consists of a single run of injections, and no duplicate injections can be made in this setup, the binding constants found should by no means be regarded as the ''true and definitive binding constants'' of the tested ligands. Affinity ranking experiments are performed to compare large sets of antibodies in a single run, and not to define exact binding constants.

8.2.2 Experiment 2: Affinity Ranking of Rabbit IgG Binding MHC–Peptide Complexes

8.2.2.1 Introduction

This experiment involves affinity ranking and measuring the binding specificity of rabbit antibodies, binding the major histocompatibility complex (MHC), with capture SPR on a laboratory-made anti-rabbit-capture SPR sensor.

The MHC complex is the natural substrate for T-cell receptors.[19] MHC complexes are present on the surface of cells and consist of two subunits (α and β) plus a variable peptide. This peptide is then visible (''presented'') to the immune system, as it is a potential binding site for T-cell receptors. In the absence of intruders, the peptides that are presented by MHC complexes are degradation products of the host-cell proteins. However, for example, when a virus infects a cell, the cell will instead present degradation products of viral proteins on their MHC complexes, thus harnessing T cells to direct a response to the threat.[20] The same process also occurs in cancer. As tumor cells have protein expression profiles that differ greatly from those of healthy cells and express tumor-association antigens, MHC complexes on those cells will then present peptides that are specific to tumor cells.[21] Indeed, on multiple occasions, MHC–peptide complexes were detected that are presented on a wide variety of tumors.[22,23] Antibodies directed against these tumor-associated MHC–peptide complexes have high therapeutic potential, as these are agents that are highly selective to tumor cells and may direct the patient immune system to the tumor cells.[24]

In this experiment, we performed affinity ranking with a pool of 40 antibodies obtained from rabbits that were immunized with a specific MHC class I–peptide complex, here denoted ''complex A'' (MHC class I is one of the two MHC classes, each of which presents a different set of peptides and engages with different T-cell subsets).

A pool of rabbit antibodies was analyzed for affinity and specificity to the MHC–peptide complex. Antibodies were captured of a laboratory-prepared anti-rabbit-coated SPR sensor and then three kinetic titrations were

View Online

Published on 24 May 2017 on http://pubs.rsc.org | doi:10.1039/9781788010283-00295

performed. First, a titration was carried out with monomeric MHC–peptide complex A (the natural substrate). This was followed by titration with a non-specific MHC complex, which presents a different peptide ("complex B"). This was done to assess the specificity of the antibodies for complex A. To enhance the responses of complex B binding, MHC complex tetramers were injected instead of monomers. Following the injection of complex B tetramers, now complex A tetramers (the complex used for immunization) were titrated. Thus, antibodies were ranked on their affinity for the native, monomeric MHC–peptide complex, and also assessed on their specificity to the presented peptide (by comparing binding to complex A and complex B tetramers). In the experiment, the analytes for non-specific binding (here MHC–peptide complex B) were always titrated in before the specific analytes (here MHC–peptide complex A). Also, the lower affinity analytes (here MHC complex A monomers) were always titrated in before the higher affinity analytes (here MHC multimers). Thus, saturation of the captured ligands was minimized; as the captured ligands cannot be regenerated, the complete titration with all three analytes needs to be performed in a single concatenated injection and no duplicate injections can be made. Therefore, in this experiment, the focus was on observing the binding **specificity** of the captured ligand, and finding the exact **affinity** was secondary (of course, the ligands may still be ranked based on these data, but this is considerably less accurate owing to possible saturation effects).

8.2.2.2 Preparing a Capture Sensor

To perform a kinetic titration of a panel of rabbit antibodies, we decided to prepare an anti-rabbit-coated SPR capture sensor. Antibodies were immobilized on an Easy-2-Spot SensEye sensor; this could be carried out in the IBIS MX96 so that the progress of the immobilization reaction could be followed. For our anti-rabbit sensor, we chose an anti-rabbit IgG H + L antibody (Bethyl). For preparing capture sensors, it is important to select an antibody that has a very low off-rate for its target, thus maximizing the stability of the capture antibody–target antibody complex. Before preparing a laboratory-made ligand capture sensor, it is best first to compare the binding kinetics of multiple capturing ligands; the best capture ligand would be the one with the lowest off-rate (k_d).

After coupling the capture ligands, antibodies are spotted on the sensor in a similar manner to that on a precoupled antibody capture sensor. The capturing of antibodies is readily detected when imaging the sensor inside the IBIS MX96 instrument (Figure 8.5).

8.2.2.3 Performing Multiple Kinetic Titrations in a Single Run on a Laboratory-made Sensor

In this experiment, 40 rabbit IgG samples in medium (IgG concentration: $\sim 0.1\ \mu g\,mL^{-1}$) were spotted in duplicate. After insertion in the IBIS MX96 instrument, the sensor was briefly washed with system buffer before

View Online

Published on 24 May 2017 on http://pubs.rsc.org | doi:10.1039/9781788010283-00295

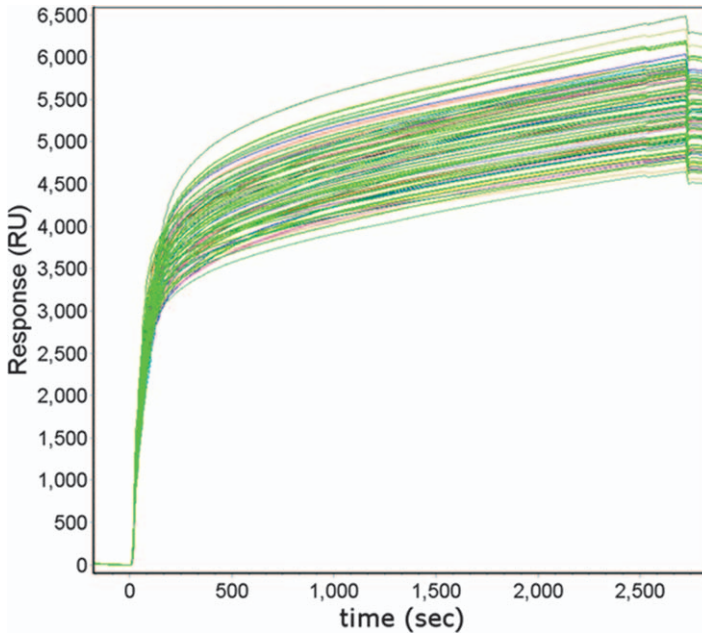


Figure 8.5 SPR responses during chip coupling. An Easy-2-Spot SensEye chip is coupling with anti-rabbit H + L (25 $\mu g\,mL^{-1}$). Shown are responses on 96 positions during the injection of antibody, demonstrating the cross-linking of antibody on the chip. Antibody was injected for 45 min, in coupling buffer (10 mM MES, pH 4.5 + 0.05% Tween 20); prior to coupling, the chip was washed three times with coupling buffer.

starting the experiment. The first injections were performed with system buffer, to stabilize the sensor. Then, a sample of concentrated rabbit IgG ($\sim$20 $\mu g\,mL^{-1}$) was injected; this was done to saturate any empty binding sites on the sensor. Specifically the reference spots need to be saturated, as these spots have not captured any ligand during the spotting procedure; therefore, to obtain proper reference curves, it is important to saturate the sensor with antibody before starting the experiment. As, during the experiment, the captured antibody will dissociate from the sensor, it is important that there is no difference in this dissociation reaction between signal and reference spots, otherwise the dissociation of analyte will be overestimated, as then there is no proper reference for the dissociation of the captured antibody. This becomes especially important when working with self-made sensors, as these sensors are typically less stable, and more captured antibody may dissociate from these sensors during an experiment.

After saturating the sensor with antibody, three more system buffer injections were carried out to stabilize the sensor once more. Then, a concentration series of three different analytes was applied, in the following order of injection: (1) MHC–peptide complex A monomers, (2) MHC–peptide complex B tetramers, and (3) MHC–peptide complex A tetramers. Between

View Online

each concentration series, the sensor was injected three times with system buffer, to remove bound analyte (this does not always work with low off-rate interactions).

Published on 24 May 2017 on http://pubs.rsc.org | doi:10.1039/9781788010283-00295

8.2.2.4 *Binding Specificity + Ranking: Analysis and Interpretation*

In this experiment, antibodies that bind non-specifically to MHC–peptide complex (''MHC binders'') are clearly distinguished from those that only bind MHC–peptide complex A (Figure 8.6). Some antibodies are not 100% specific to MHC–peptide complex A, but do show a clear preference for complex A over complex B (examples are indicated in Figure 8.6). Notably, the binding curves clearly show that the antibodies have a weaker affinity for MHC–peptide monomers than for the tetrameric complexes, and this is independent of antibody specificity. Specifically, the tetrameric complexes show a much lower off-rate (k_d) than the monomers; this is likely due to the antibody being able to engage the same tetramer with both variable domains simultaneously, which greatly increases the stability of the complex. Owing to their multivalency, the tetramers also are likely to have higher rebinding rates.

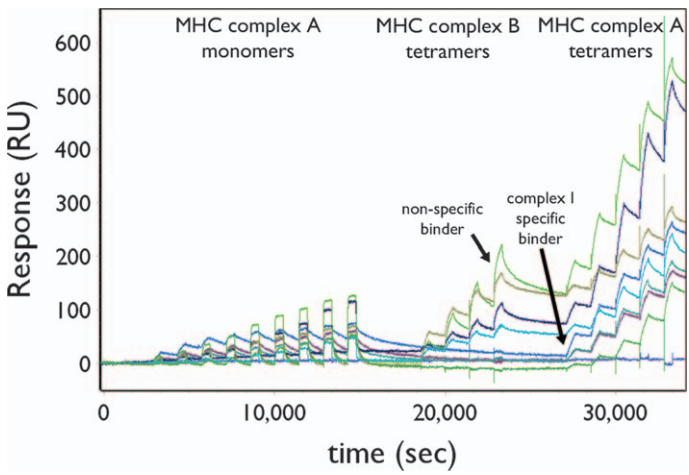


Figure 8.6 Binding of captured rabbit IgG to MHC–peptide complexes. From all 40 captured antibodies, eight antibodies are highlighted as examples. First, a concentration series of nine concatenated injections with MHC–peptide complex A monomers (0.10–25.6 $\mu g\,mL^{-1}$) were injected, and then a concentration series of four concatenated injections with MHC–peptide complex B tetramers (0.375–3.0 $\mu g\,mL^{-1}$), followed by a concentration series of six concatenated injections with MHC–peptide complex A tetramers (0.275–8.75 $\mu g\,mL^{-1}$). Examples of specific and non-specific binders are indicated with arrows.

View Online

Table 8.2 Binding constants to MHC–peptide complexes.[a]

Clone	K_D (pM) Monomer A	Tetramer A	Tetramer B	Specificity[b]
01	67 100	1300	–	"infinite"[c]
02	1890	804	3420	4.25
03	1470	764	–	"infinite"
04	903	327	1150	3.52
05	20 700	1360	211	0.16
06	102 000	2670	336	0.13
07	1960	626	–	"infinite"
08	62 800	1880	–	"infinite"

[a]All antibodies were measured on only one spot; no standard error could be determined.
[b]Binding specificity for complex I is defined as K_D(complex B tetramers)/K_D(complex A tetramers). A specificity value close to 1 indicates that the antibody binds both complexes with similar K_D value; such an antibody likely binds the MHC part of the complex and not the presented peptide.
[c]An "infinite" specificity value is attributed to antibodies that do not bind complex B.

Similarly to what was found for the HCV binding panel, a great variation in antibody K_D was observed (ranging from 900 to 100 000 pM for complex A monomers and from 300 to 3000 pM for the tetramers) (Table 8.2). The binding specificity was evaluated by calculating K_D(complex B)/K_D(complex A) (using tetramer binding kinetics) (Table 8.2). Based on their specificity, the antibody pool is divided into three groups: a group of MHC binders showing specificity of ~1, a group that have a preference for complex A (specificity 3–10), and a group that binds exclusively to complex A (specificity from >100 to ∞). Notably, high-affinity (K_D in the pM range) binders are found in each of the three groups, suggesting no immediate correlation between affinity and peptide (non-)specificity.

8.2.3 Conclusions on Affinity Ranking and Outlook

With these two experiments, we have shown how we can obtain important data on antibody affinity and specificity with one quick high-throughput SPR experiment. In the next two sections, we demonstrate how information on antibody epitopes can be obtained using high-throughput SPR techniques.

8.3 Epitope Binning

Epitope binning is the categorization of, for example, antibodies based on their binding site ("epitope"). Defining the epitope of an antibody is of interest for scientific and therapeutic reasons, as it provides important information about its mechanism of action.[25,26] Furthermore, because the antibody epitope is innate, it cannot be altered through genetic engineering. Therefore, there is a high demand for reliable methods to define antibody epitopes at high throughput.

Published on 24 May 2017 on http://pubs.rsc.org | doi:10.1039/9781788010283-00295

View Online

Published on 24 May 2017 on http://pubs.rsc.org | doi:10.1039/9781788010283-00295

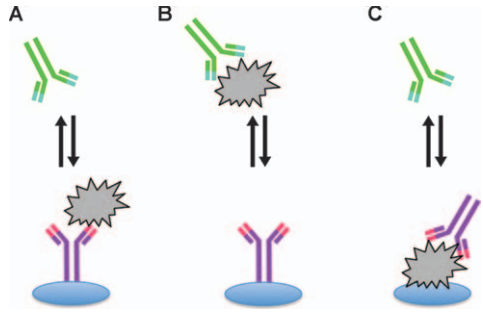


Figure 8.7 Strategies for epitope binning. (A) Antibody sandwich. A second antibody is injected over an antibody–antigen complex. The antibody can only bind if its epitope is not occupied by the first (immobilized antibody). (B) Premix. Antibody and antigen are first incubated together and then injected on the immobilized antibody. The immobilized antibody can only bind if the premixed antibody does not occupy the epitope of the immobilized antibody. (C) Tandem blocking. Antigen is immobilized and then injected with antibodies. After the binding of the first antibody, the second antibody can only bind if its epitope is not occupied by the first. Adapted from Y. N. Abdiche, D. S. Malashock, A. Pinkerton and J. Pons, Exploring blocking assays using Octet, ProteOn, and Biacore biosensors, *Anal. Biochem.*, 2009, **386**, 172.

Through binning, antibodies epitopes are revealed indirectly, by re-injecting a second antibody (ideally with a known epitope) over previously formed antibody–analyte complexes (Figure 8.7). If this second antibody binds a preformed antibody–analyte complex, then those two antibodies have different epitopes (and if the second antibody does not bind, the two antibodies likely have overlapping epitopes).[27] In some cases, the second antibody may even demonstrate enhanced binding, for example if, as a consequence of the first binding event, the epitope of the second is exposed or stabilized. These stimulated interactions could indicate synergy between two antibodies, and this could be relevant to combination therapy or vaccine development.

Different setups exist to perform epitope binning (illustrated in Figure 8.7): antibody ''sandwich'' binning (injecting a second antibody over antibody–antigen complex), premix binning (injecting antibody–antigen complex over antibodies), and tandem blocking (injection antibodies in sequence over immobilized antigens).[27–29] Each of these methods has advantages and disadvantages, which were discussed in great detail in Abdiche *et al.*[27] Briefly, the premix and tandem blocking methods are very applicable to bin antibodies that bind antigens with repeating epitopes, whereas antibody sandwiches are very practical for high-throughput experiments (as many combinations can be made on a single sensor).[27]

In this section, we describe one example experiment to illustrate the strength of epitope binning with multiplex SPR. In this experiment, we used the antibody sandwich binning setup.

View Online

Published on 24 May 2017 on http://pubs.rsc.org | doi:10.1039/9781788010283-00295

8.3.1 Experiment 3: Epitope Binning of Antibodies Binding the Respiratory Syncytial Virus (RSV) Glycoprotein

8.3.1.1 Introduction

Respiratory syncytial virus (RSV) is a leading cause of respiratory disease in young children and risk-group adults.[30,31] Furthermore, RSV is one of the first infectious diseases for which an antibody drug, palivizumab (Synagis), which binds the RSV fusion (F) protein, is available for active treatment and passive immunization of individuals at risk.[32] The G glycoprotein (G protein) is the second surface antigen of the RSV virus, apart from the mentioned F protein. In turn, the RSV G protein is a clinically relevant target for antibodies as well; antibodies directed against this antigen were shown to reduce RSV pathogenesis in mice.[33–35] Because they bind a different target in the RSV virus, anti-G protein antibodies could, in combination with palivizumab, allow for a more effective treatment.[34,36] Therefore, the finding of novel epitopes in the RSV G protein is relevant to the development of improved vaccines and new antibody-based drugs against RSV.

We selected a panel of 13 antibodies, all binding RSV G protein that we isolated from immortalized human B cells. In addition, the previously described murine antibody 131-2G was included as a control.[36,37] Antibody 131-2G is a potent binder of the RSV G protein, and shows anti-infective activity *in vivo*.[34,36,37]

8.3.1.2 Setting Up the Experiment

The optimal setup for an epitope binning experiment is to immobilize the antibodies directly on the sensor, as in this setup non-specific binding of the secondary antibody should be eliminated (or reduced as much as possible). For this reason, it is less recommended to use a capture or capture-crosslinked sensor because, unless the capture sensor is completely saturated, there is always the chance that a secondary antibody may bind unoccupied sites on the capture sensor rather than bind exposed ligand epitopes. If continuing with the use of a capture or capture-crosslinked sensor, it must be ensured that the capture sensor remains saturated by co-injecting a non-binding ligand for the capture sensor with each analyte injection (*i.e.* when binning RSV G-protein binding IgG on an anti-IgG sensor, non-binding IgG should be added to each RSV G injection, and also to each secondary antibody injection). Another approach is to add a non-binding ligand to the system buffer in order to saturate the sensor surface before injecting the antigen and specific antibody.

Direct chemical immobilization of antibodies on the sensor, however, may compromise their activity (as discussed in Section 8.2.1.2), hence it is recommended to perform binning experiments only after obtaining initial affinity data (for example, with a kinetic titration ranking experiment). Of course, if the antibodies are stable when directly immobilized and remain active after repeated regeneration, the binning experiment may very well be combined with an affinity measurement. Similarly, antibodies that are not

View Online

Published on 24 May 2017 on http://pubs.rsc.org | doi:10.1039/9781788010283-00295

active when directly immobilized may still be of use when injected as a secondary antibody. Because of all the mentioned restrictions of directly immobilized antibodies, in principle, epitope binning should more be regarded as a "Yes or No" experiment rather than a detailed affinity study.

An epitope binning experiment typically consists of repeated cycles of two concatenated injections: first an injection with binding analyte is made and then a second injection with a secondary antibody. Ideally, all of these secondary antibodies should also be present on the sensor. When binning large antibody panels, many injections need to made, and the experiment will take a considerable amount of time (runs of several days are not an exception). Therefore, it is recommended to include a "blank" secondary injection, without antibody (or with a non-binding antibody), after every 10 injections, to measure the binding response of the coupled antibodies. This response is then used as a standard for normalizing the signals for comparing the responses of the secondary antibodies.

8.3.1.3 Epitope Binning: Analysis and Interpretation

A panel of 13 antibodies binding the RSV G protein, with antibody 131-2G antibody included as a positive control, was immobilized on a gel type Easy-2-Spot SensEye SPR sensor. Not all antibodies were active when directly immobilized (Figure 8.8).

Most antibodies, when injected as secondary antibodies, bound antibody + G protein complexes, and only two antibodies in the panel (AT61 and AT64) did not bind.

When analyzing the epitope binning experiment, we found that binding of 131-2G to RSV G glycoprotein does not block AT33, and *vice versa* (Figure 8.9B).

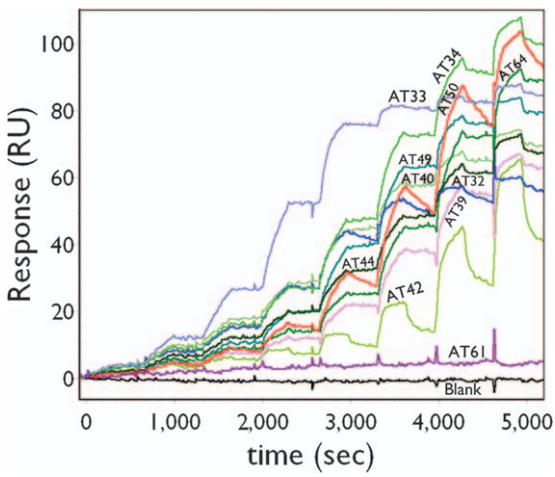


Figure 8.8 Kinetic titration of RSV G glycoprotein binding antibodies. Eight concatenated injections with increasing RSV A2 G-protein concentration (0.02–2.25 $\mu g\,mL^{-1}$) were carried out on an anti-IgG sensor surface with an array of captured antibodies. Responses of binding antibodies are highlighted. Blank: response on an "empty" spot, without immobilized antibody.

View Online

Published on 24 May 2017 on http://pubs.rsc.org | doi:10.1039/9781788010283-00295

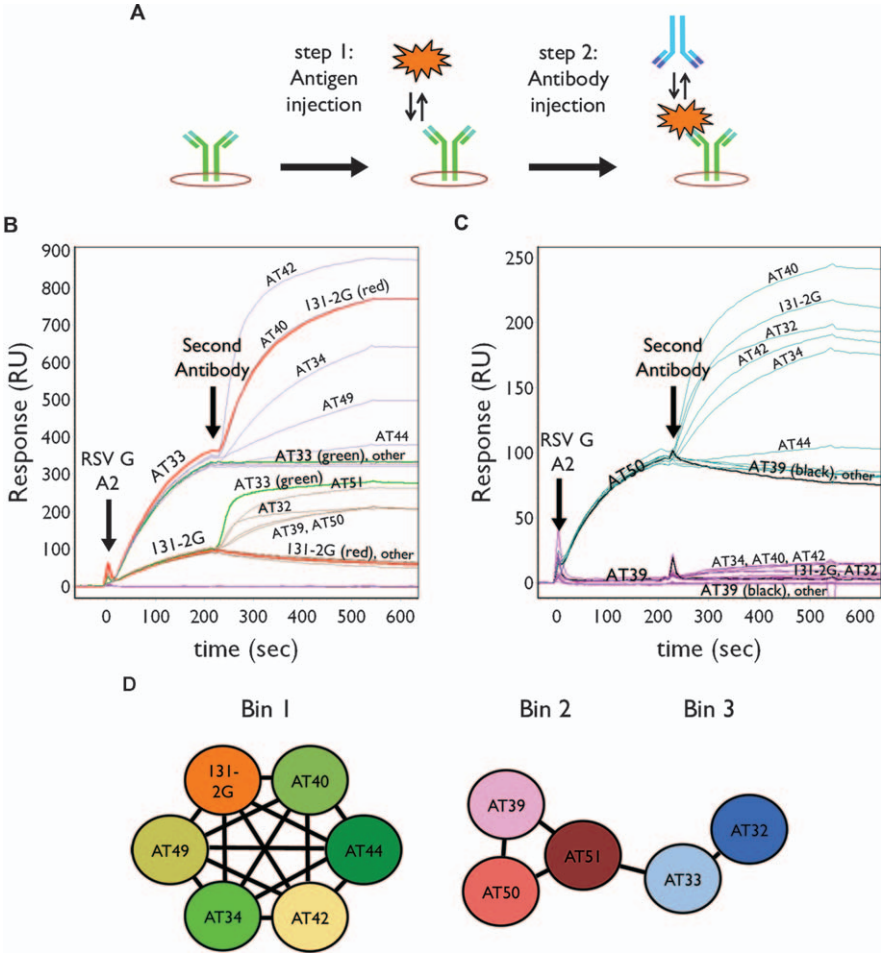


Figure 8.9 Epitope binning of RSV G glycoprotein-binding antibodies. (A) Experimental setup (''antibody sandwich''). First, immobilized antibodies bind the antigen (step 1), then a second antibody is injected (step 2). The second antibody can only bind if its epitope is not blocked by the first antibody (*i.e.* the antibody immobilized on the sensor). An array of immobilized antibodies results in a multiplex data set with up to 96×96 sensorgrams. (B) Epitope binning responses of immobilized antibodies AT33 and 131-2G. (C) Epitope binning responses of immobilized antibodies AT39 and AT50. Antibodies are covalently linked to an amino-functionalized SPR sensor surface. RSV A2 G protein (1.6 nM) was injected, followed by injection of a second anti-RSV G antibody (2.0 $\mu g\,mL^{-1}$). Responses of the second antibody injections show the competing or non-competing behavior with respect to the epitope. Responses of AT33 (green) and 131-2G (red), when injected as second antibody, are highlighted in **bold**. (D) Node plot of RSV G binding antibodies, constructed from epitope binning results. Antibodies binding overlapping epitopes are connected with black lines.

View Online

Published on 24 May 2017 on http://pubs.rsc.org | doi:10.1039/9781788010283-00295

Apparently, these two antibodies have different, non-overlapping epitopes. Furthermore, when AT33 was injected as second antibody, no response was observed on AT33-bound RSV G glycoprotein complexes (and the same was observed upon injecting 131-2G over 131-2G-bound RSV G) (Figure 8.9B). These results indicate that the antigen is not multimeric, and that both antibodies bind a single, non-repeating, epitope.

On the other hand, binding of AT32 and AT51 is blocked after AT33 binds RSV G, suggesting that these two antibodies have epitopes that overlap with that of AT33 (Figure 8.9B). Similarly, antibodies AT34, AT40, AT42, AT44, and AT49 are blocked by 131-2G (Figure 8.9B), suggesting that this group of antibodies also binds an epitope similar to that of 131-2G. Notably, two other antibodies, AT39 and AT50, are not blocked by either AT33 or 131-2G, indicating that these antibodies bind yet another epitope (Figure 8.9B). On injecting AT39 as secondary antibody, the antibody does not bind to AT50-bound glycoprotein, suggesting that the epitopes of AT39 and AT50 overlap (Figure 8.9C). Furthermore 131-2G and AT32 are not blocked by AT39 or AT50, confirming that these antibodies bind different epitopes (Figure 8.9C).

From the epitope binning data, a node plot was constructed, dividing the antibodies into three separate bins (Figure 8.9D). Bin 1 contains all antibodies with epitopes that overlap with 131-2G (these are AT34, AT40, AT42, AT44, AT49, and 131-2G itself). Notably, all antibodies within this subgroup bind the glycoproteins from both the RSV A2 and B substrains, suggesting that their epitopes are conserved between both strains. The other antibodies, which bind only the G protein of RSV strain A2, are divided over two more bins: bin 2 consists of AT39, AT50, and AT51, and bin 3 contains antibodies AT32 and AT33. These two subgroups both recognize different epitopes that are not conserved between the G glycoproteins of the two substrains. Note that binding of AT33 is blocked by AT50 and AT39, but AT33 does not block AT39 and AT50 *vice versa*; therefore, we placed AT33 in a different bin from AT39 and AT50. AT51 is blocked by both members of bin 2, but by only one member of bin 3 (AT33); therefore, we tentatively placed AT51 in bin 2 (this placement was later confirmed with epitope mapping results).

8.3.2 Conclusions on Epitope Binning and Outlook

The epitope binning experiment shows that with the IBIS MX96 SPR imaging instrument, a large antibody panel can be effectively binned into epitope groups. In the same experiment, we identified which antibodies within our panel bind to a known epitope (that of 131-2G), and which ones bind other, previously unidentified, epitopes.

However, the limitation of the binning experiment is that although it does define the exact identity of the antibody epitopes, it only reveals which antibodies share overlapping binding sites (and which do not). Within each bin, a large variation in epitopes could still exist and, moreover, it is not unlikely that two antibodies that block each other may bind largely different, but overlapping, epitopes.

View Online

Published on 24 May 2017 on http://pubs.rsc.org | doi:10.1039/9781788010283-00295

To identify the exact epitope of each antibody, at the amino acid level, further detailed studies will be necessary, which could be more elaborate (*e.g.* co-crystal structure analysis). A useful tool to map the exact epitope, which was also used here to compare the anti-RSV G antibodies, would be to look for strain or species specificity. Since many, but not all, epitopes are conserved between different strains or species, identifying the strain/species specificity of an antibody gives useful clues about its binding site. Here, we have shown that the antibodies belonging to bins 2 and 3 bind only the A-substrain of the RSV virus, indicating that these antibodies bind to a portion of the G protein that is not conserved between the A and B substrains, thereby excluding a large (conserved) portion of this protein.[38]

In the next section, we demonstrate how the potential of high-throughput SPR can be harnessed to map antibody epitopes with amino acid resolution.

8.4 Epitope Mapping

Epitope mapping is defined as the identification of the exact binding site of an antibody at the molecular level. Ideally, the antibody epitope is defined by a co-crystal structure of the antibody with its antigen, but this method is low throughput and relatively costly, as it requires large amounts of highly pure antibodies and antigens, and these may not always be readily available. Various epitope mapping methods have been described extensively in the literature that are less labor intensive (*e.g.* peptide array ELISA or Western blotting, mutational scanning analysis, and H/D exchange mass spectrometry), but these methods are not always of practical use for high-throughput analysis.[39,40] Moreover, as the discovery of novel antibodies with potential clinical relevance typically involves the screening of a large panel of candidates, there is a high demand for high-throughput epitope mapping methods.

Here, we describe epitope mapping methods for high-throughput SPR imaging. Two different setups, ''amino-acid skipping'' and ''alanine scanning'' epitope mapping, are described, each of which is illustrated in a separate experiment. Both experiments rely on immobilizing a peptide library to an SPR sensor, over which an array of antibodies is then injected. The antibody epitope is then a product of the peptides that the antibody binds (and does not bind). Thus, using high-throughput SPR imaging, a large panel of up to 100 antibodies can be mapped in a single experiment, in a fast and reproducible manner.

8.4.1 Experiment 4: Epitope Mapping of Anti-RSV G Antibodies Using a Library of Overlapping Peptides

8.4.1.1 Introduction

Amino acid skipping is mapping antibody epitopes by injection over a library of immobilized peptide oligomers, which together compromise the entire antigen sequence (or a large portion thereof). To validate this method, we

View Online

chose to map the exact epitopes of the same 13 antibodies, directed against the RSV G-protein, that were used in the epitope binning experiment (Section 8.3). Our library consisted of 40 biotinylated, 12-meric peptides that comprise amino acids 149–199 of the RSV G glycoprotein from substrain A2 (Table 8.3).

Published on 24 May 2017 on http://pubs.rsc.org | doi:10.1039/9781788010283-00295

Table 8.3 Peptides used for peptide mapping of RSV G-protein binding antibodies.[a]

No.	Sequence
1	KQRQNKPPSKPN
2	QRQNKPPSKPNN
3	RQNKPPSKPNND
4	QNKPPSKPNNDF
5	NKPPSKPNNDFH
6	KPPSKPNNDFHF
7	PPSKPNNDFHFE
8	PSKPNNDFHFEV
9	SKPNNDFHFEVF
10	KPNNDFHFEVFN
11	PNNDFHFEVFNF
12	NNDFHFEVFNFV
13	NDFHFEVFNFVP
14	DFHFEVFNFVPC
15	FHFEVFNFVPCS
16	HFEVFNFVPCSI
17	FEVFNFVPCSIC
18	EVFNFVPCSICS
19	VFNFVPCSICSN
20	FNFVPCSICSNN
21	NFVPCSICSNNP
22	FVPCSICSNNPT
23	VPCSICSNNPTC
24	PCSICSNNPTCW
25	CSICSNNPTCWA
26	SICSNNPTCWAI
27	ICSNNPTCWAIC
28	CSNNPTCWAICK
29[b]	SNNPTCWAICKR
30	NNPTCWAICKRI
31	NPTCWAICKRIP
32	PTCWAICKRIPN
33	TCWAICKRIPNK
34	CWAICKRIPNKK
35	WAICKRIPNKKP
36	AICKRIPNKKPG
37	ICKRIPNKKPGK
38	CKRIPNKKPGKK
39	KRIPNKKPGKKT
40	RIPNKKPGKKTT

[a]All peptides are biotinylated at the N-terminus. Biotin is linked to the N-terminus *via* coupling of biotin-XX-SSE (Invitrogen) to the N-terminal amino acid.
[b]Peptide 29 was incorrectly synthesized and could not be used.

View Online

Published on 24 May 2017 on http://pubs.rsc.org | doi:10.1039/9781788010283-00295

This portion of the RSV G glycoprotein contains a highly immunogenic extracellular domain and includes the epitope of antibody 131-2G.[41] In our peptide library, the peptides are overlapping 12-mers with an offset of one amino acid (*i.e.* peptide 1 consists of amino acids 149–160, peptide 2 of amino acids 150–161, and so on, until peptide 40, which consists of amino acids 188–199). The library of biotinylated peptides was immobilized on a streptavidin-coated SensEye SPR sensor using CFM in such a way that each peptide was spotted on a specific position on the sensor. After spotting the peptides, antibodies were injected and, based on which peptides the antibodies bind, their epitopes will be revealed.

8.4.1.2 Setting Up the Mapping Experiment

The first step in designing an epitope mapping experiment is to synthesize a peptide library. Our peptide library consists of 12-meric peptides; the peptide size is not entirely arbitrary, but generally the peptide should be large enough to accommodate the entire epitope, plus at least one or two flanking residues. For this purpose, we recommend a length of a least 10 amino acids. Furthermore, if it is likely that the epitope contains amino acid modifications (*e.g.* glycosylation, phosphorylation), it is recommended to include these in the library. To allow immobilization on SPR sensors, we chose to incorporate a biotin moiety, as this allows quick immobilization on streptavidin-coated sensors and, furthermore, because the biotin–streptavidin interaction is stable under low-pH conditions, the chip may be regenerated. Biotin is attached to the N-terminus of the peptides *via* a double aminohexanoic acid linker; the long linker is inserted to ensure that the peptide is sufficiently far away from the streptavidin to allow optimal exposure to the binding antibodies.

The peptides were efficiently immobilized 40 min after spotting with a 2.0 μM peptide solution, diluted in capture buffer (PBS + 0.05% Tween 20 + 0.05% sodium azide). Also, on the same sensor, several spots were coupled with a biotinylated anti-human IgG antibody. These spots were used to verify the activity and concentration of the anti-RSV antibodies. The activity of these antibodies was determined by injecting RSV G glycoprotein after each antibody injection. Any anti-RSV G antibodies captured on spots coated with anti-IgG will bind the RSV G glycoprotein, and thus generate a response on these spots. Hence we can validate the activity of the injected antibody, even when it does not bind any of the immobilized peptides.

On completion of the immobilization, some peptide aggregates were visible in the sample tray, but they were not seen on the coated sensor; instead, the immobilization of biotinylated peptides could be readily detected on the SensEye surface (Figure 8.10). All peptides coupled to the streptavidin-coated SensEye, except for peptide 29; however, this was due to an incorrect synthesis of this peptide.

Before injecting any antibody sample over the peptide-coated sensor, we first performed several injections with system buffer + 0.1 mg mL^{-1} bovine

View Online

Published on 24 May 2017 on http://pubs.rsc.org | doi:10.1039/9781788010283-00295

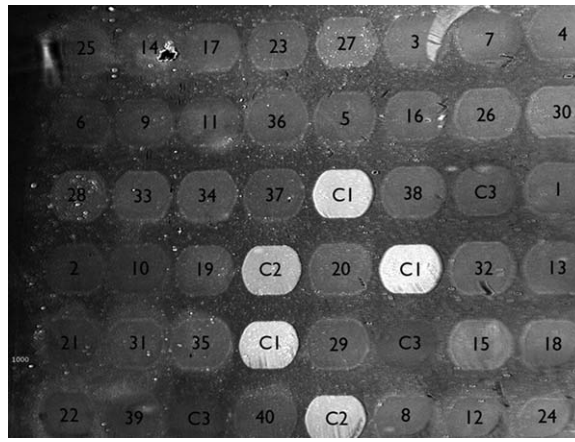


Figure 8.10 SPR image of a streptavidin-coated SPR sensor, after spotting biotinylated peptides and controls. The peptide number is indicated on each spot; C1 = biotinylated anti-IgG, C2 = biotinylated mouse IgG (anti-IL21), C3 = system buffer (PBST + 0.01% BSA). The SPRi image was taken at a camera angle of +1000 m°. The camera image is inverted and the contrast is enhanced.

serum albumin (BSA), to reduce non-specific interactions of antibodies with particularly ''sticky'' peptides. In our peptide library, we observed that peptides 11, 37, 38, 39, and 40 particularly show non-specific binding to BSA. The non-specific binding response decreased with each sample injection, suggesting that spots coated with these peptides slowly become saturated with BSA (Figure 8.11).

After the sensor surface has become stable, and non-specific interactions are minimized (in this experiment we performed five cycles of injections with ''empty'' system buffer), injection with peptide-binding antibodies may commence. In this epitope mapping experiment, cycles of two concatenated injections were performed. In the first of the two injections per cycle, antibody was injected, in the second injection RSV G-protein was injected (as discussed above, RSV G-protein is injected to verify antibody activity), then the chip was regenerated and a second cycle was started. Example results on anti-IgG spots are shown in Figure 8.12.

8.4.1.3 Epitope Mapping: Results and Interpretation

Most antibodies in our panel, including antibodies that showed poor activity in the antigen binding assays (*e.g.* AT61 and AT64), bound multiple peptides in the library, with responses that were clearly higher than in non-specific binding (Figure 8.13). Only antibodies AT42 (Figure 8.13F) and AT49 (Figure 8.13I) did not bind any of the peptides; likely these antibodies recognize a conformational epitope that, as suggested from the binning

View Online

Published on 24 May 2017 on http://pubs.rsc.org | doi:10.1039/9781788010283-00295

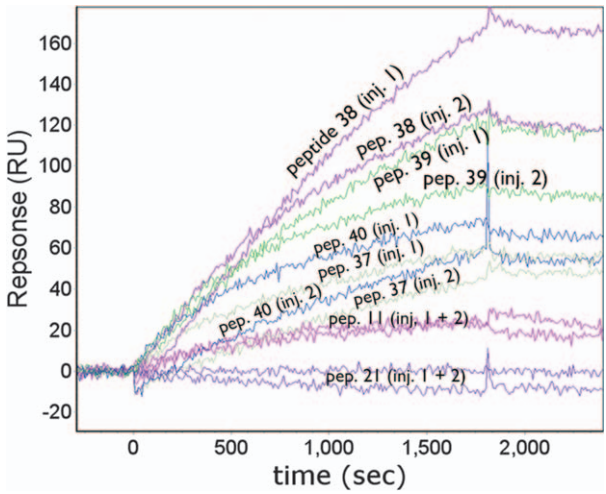


Figure 8.11 Non-specific binding of BSA to peptides coupled to a streptavidin sensor. Biotinylated peptides were immobilized on a streptavidin-coated SPR sensor. PBS + 0.05% Tween 20 + 0.1 mg mL^{-1} BSA was injected twice. In this figure, the peptides with the highest non-specific binding responses are shown.

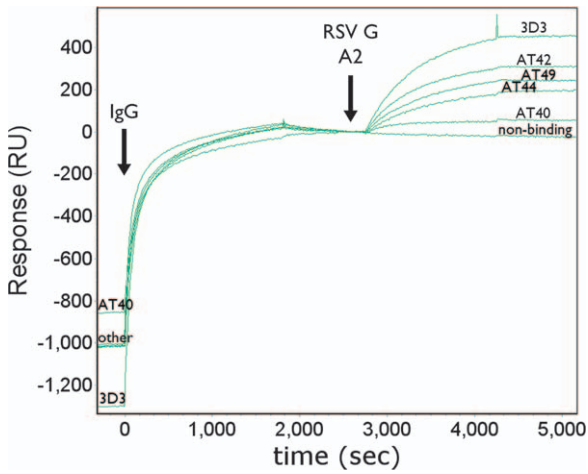


Figure 8.12 Anti-IgG captured antibodies binding RSV G protein. Biotinylated anti-IgG was captured on a streptavidin-coated sensor. RSV G-binding antibodies (3.0 μg mL^{-1}) or a non-binding antibody (here 3.0 μg mL^{-1} rituximab) were injected, followed by injection of RSV A2 G protein (0.5 μg mL^{-1}). This experiment was carried out simultaneously with epitope mapping, to verify the activity of the injected antibodies.

experiments, overlaps with the epitope of 131-2G. Antibodies AT33 (Figure 8.13B) and 131-2G (Figure 8.13N), for which we have shown that they bind non-overlapping epitopes, clearly bind a different subset of

View Online

Published on 24 May 2017 on http://pubs.rsc.org | doi:10.1039/9781788010283-00295

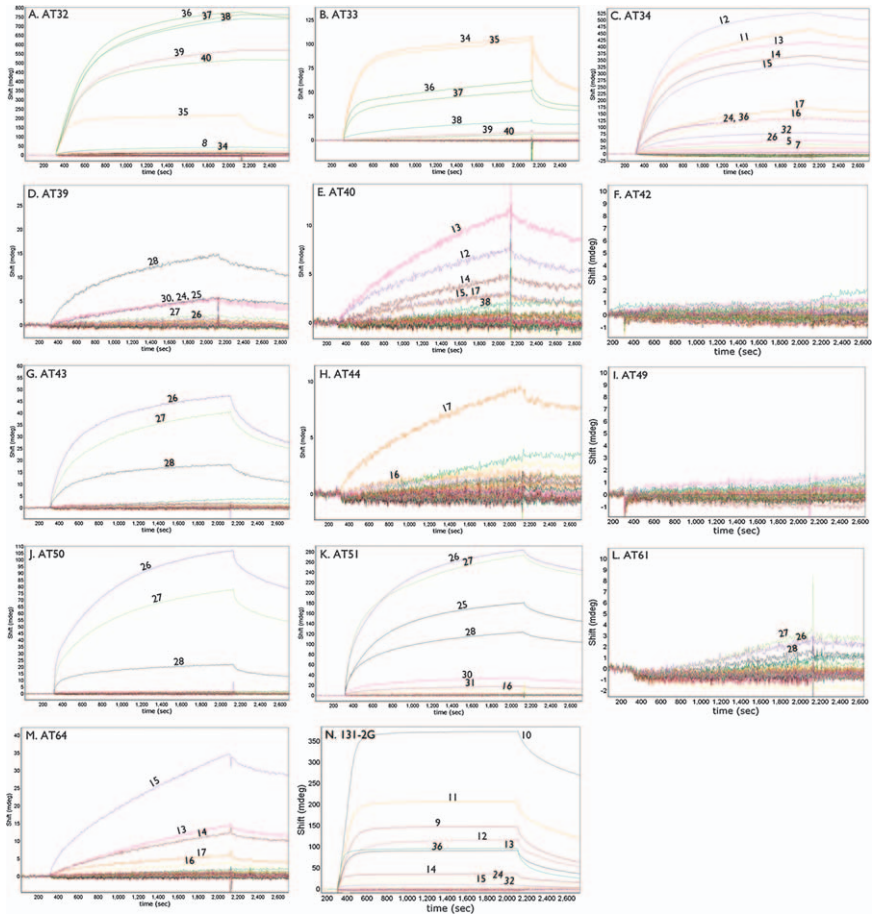


Figure 8.13 Binding of antibodies to the immobilized peptide library. Shown are binding curves of antibody (3.0 $\mu g\,mL^{-1}$) injected on peptide-immobilized spots. Responses are shown in m° (1 millidegree = 10 RU). Binding curves resulting from non-specific interactions are indicated with italics.

peptides, with 131-2G binding peptides 9–19 and AT33 binding peptides 34–40.

In order to compare the epitopes of all antibodies in our panel, we plotted the maximal response on each peptide (in RU) against the peptide number (Figure 8.14). This plot clearly shows that the three different subgroups within our panel each bind a different set of peptides, confirming the epitope binning results. The antibodies belonging to bin 1 bind peptides 9–17, bin 2 antibodies bind peptides 24–31, and the third group recognizes peptides 34–40. The mapping results also immediately suggest that the binding site of AT51 overlaps with AT39 and AT50 (and not with AT33), confirming its

View Online

Published on 24 May 2017 on http://pubs.rsc.org | doi:10.1039/9781788010283-00295

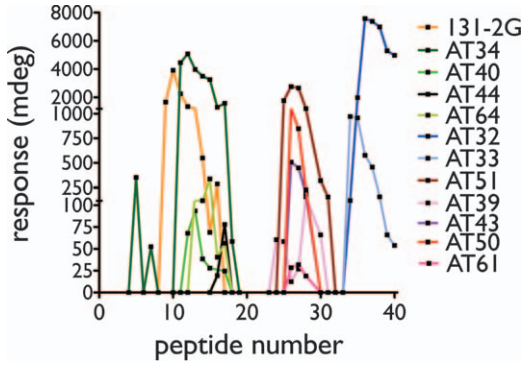


Figure 8.14 Epitope mapping of RSV G binding antibodies. Shown is the maximum binding response of each antibody (average of two injections) *versus* peptide number. Antibodies AT42 and AT49 did not bind any of the immobilized peptides (see Figure 8.13). In this plot, three epitope bins are identified, each shown in a different color.
Adapted from B. Cortjens, E. Yasuda, K. Wagner, Y. B. Claassen, A. Q. Bakker, J. B. M. van Woensel and T. Beaumont.[38] Copyright © American Society for Microbiology, *Journal of Virology*, 2017, DOI:10.1128/JVI.02357-16.

placement with AT39 and AT50 (this was not directly evident from the epitope binning experiment).

Notably, peptides 24–40 all consist of sequences that are poorly conserved between RSV substrains A and B.[42] The poor conservation of their epitopes suggests why the antibodies in bin 2 (AT39, AT50, AT51, and AT61) and bin 3 (AT32 and AT33) only bind the glycoprotein of human RSV substrain A2, and not that of substrain B. The epitope of bin 1 antibodies (AT34, AT40, AT42, AT44, AT64, and 131-2G), on the other hand, is part of the region (amino acids 164–176) that is highly conserved between RSV substrains.[42] This finding explains the binding of bin 1 antibodies to RSV G proteins from both substrains.

To define the exact epitope of each antibody, we first defined which amino acids are essential for binding; these are the amino acids that are shared by all peptides to which the antibody binds. These amino acids are defined as the ''core epitope'' of each antibody. For example, 131-2G binds peptides 9–16 (Figure 8.13N). These eight peptides share the five amino acid sequence HFEVF, and this sequence forms the ''core'' epitope of 131-2G. This result is in agreement with earlier epitope mapping studies carried out with conventional techniques.[36,37]

When comparing the binding responses on each individual peptide, we observed that each antibody shows a large variation in the magnitude of the binding response between different peptides (for example, antibody AT33 shows a response of ~1000 RU on peptides 34 and 35, but a lower response of only ~100 RU on peptide 38; Figure 8.13B). This variation in signal suggests that, even though many peptides contain the core epitope, the

View Online

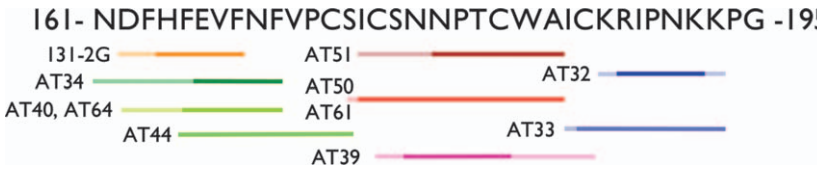


Figure 8.15 Epitopes of RSV G binding antibodies. Epitopes are defined from the epitope mapping results. Residues that are essential for binding (''core epitope'') are indicated with dark lines. Context residues that enhance binding are indicated with light lines.
Adapted from B. Cortjens, E. Yasuda, K. Wagner, Y. B. Claassen, A. Q. Bakker, J. B. M. van Woensel and T. Beaumont.[38] Copyright © American Society for Microbiology, *Journal of Virology*, 2017, DOI:10.1128/JVI.02357-16.

affinity of an antibody for a peptide does not depend on the presence of its core epitope alone. Likely, the amino acids adjacent to the essential core epitope or so-called ''context'' enhance binding. Together with the core epitope, these enhancing adjacent residues form the ''complete epitope'' of the antibody. Thus, we have defined a ''core epitope'' and ''complete epitope'' for the 11 antibodies in our panel and the two controls (Figure 8.15).

Furthermore, our epitope mapping results show that the epitopes of antibodies belonging to the same bin may vary at the amino acid level. For example, antibody AT44 binds only two peptides (16 and 17), suggesting that AT44 has a relatively large core epitope that consists of the five C-terminal amino acids of the 131-2G-core epitope plus the next six amino acids on the C-terminal side (Figure 8.15). Apparently, to bind its target, AT44 needs to make contact with more residues than, for example, 131-2G, and this could be the cause of the relatively low affinity of antibody AT44. These kinds of variations are also observed for antibodies belonging to the other bins (Figure 8.15) and indicate that, even when binning studies demonstrate that antibodies have overlapping epitopes, there may still be significant differences in the epitope at the amino acid level, which in turn may have consequences for antibody affinity or the mechanism of action.

This experiment illustrates the potential of high-throughput SPR imaging for epitope mapping experiments. In one experiment, the epitopes of 13 antibodies mapped at single amino acid resolution. In a second experiment, another epitope mapping method (*e.g.* alanine scanning) was also tested for use in high-throughput SPR imaging.

8.4.2 Experiment 5: Mapping the Epitope of Anti-human Parecho Virus Antibody AM18 with Alanine Scanning SPR

8.4.2.1 Introduction

This experiment was intended to perform epitope mapping of antibody AM18, recognizing the RGD motif in the human parechovirus VP1

Published on 24 May 2017 on http://pubs.rsc.org | doi:10.1039/9781788010283-00295

View Online

Published on 24 May 2017 on http://pubs.rsc.org | doi:10.1039/9781788010283-00295

protein. Human parechoviruses (HPeV) are single-stranded, positive-sense RNA viruses in the genus *Parechovirus* within the family Picornaviridae.[43] Since it was first recognized in 2004 that HPeV are a significant cause of central nervous system and neonatal sepsis, their clinical importance, primarily in children, has started to emerge.[44,45] Intravenous immunoglobulin treatment is the only treatment available in such life-threatening cases and has given moderate success; indicating direct inhibition of parechovirus infection using monoclonal antibodies is a potential treatment.

The HPeV genome is about 7300 bases in length, enclosed in an icosahedrally symmetric capsid of 60 copies of each of the three capsid proteins VP0, VP3, and VP1.[43,46] HPeV1 contains an arginine–glycine–aspartic acid (RGD) motif close to the C-terminus of VP1.[43] The RGD motif is found in a number of viral capsid proteins that recognize integrin receptors to gain entry into host cells, *e.g.* coxsackievirus A9 (CVA9), echovirus (EV) 9 (Echo9), and foot-and-mouth disease virus.[47–49] The RGD motif has also been shown to be an important antigenic site. Diluted antiserum raised against a peptide containing the RGD motif neutralized 51% of HPeV1 infections in a plaque assay.[50] An HPeV-neutralizing antibody, AM18, with reactivity against HPeV1, -2, -4, -5, and -6, was isolated by screening libraries of immortalized B cells.[51] With peptide scanning, the epitope of AM18 was localized to the C-terminal portion of HPeV VP1, containing the RGD motif.[52] In this experiment, we chose to map the exact epitope antibody AM18 with alanine scanning.

Alanine scanning is an epitope mapping method in which residues in a target protein are systematically substituted for alanine and assayed for function. Substitution with alanine eliminates side-chain interactions without altering the main-chain conformation or introducing steric or electrostatic effects, and therefore is often the preferred choice for defining the roles of specific side chains in antibody–antigen interactions, while preserving the native structure of the antigen.[53]

Alanine scanning can be directly translated to the peptide epitope mapping method described in Section 8.4.1, substituting residues within peptides that contain antibody epitopes for alanine. Specifically with alanine scanning, it can be defined which residues within an epitope contribute most to binding (this question is more difficult to address using a library of overlapping peptides). In this experiment, AM18 was tested on a library of six peptides: a ''wild-type'' peptide containing the RGD motif + five alanine mutants. The ''wild-type'' 14-mer peptide, with sequence VTSSRAL**RGD**MANL, is derived from the C-terminal portion of HPeV1 VP1 (Table 8.4).

The alanine scanning experiment was performed using a similar setup to that in Section 8.4.1. First, the antibody was injected, then antibody activity was measured by injecting purified VP1 protein. As a negative control, we used the non-RGD-binding anti-HPeV1 VP1 antibody AM28.[51]

View Online

Published on 24 May 2017 on http://pubs.rsc.org | doi:10.1039/9781788010283-00295

Table 8.4 Peptides used for alanine scanning of anti-HPeV VP1 antibody AM18.[a]

No.	Sequence
TB1-1	VTSSRAL**RGD**MANL
TB1-2	VTSSRAL**AGD**MANL
TB1-3	VTSSRAL**RAD**MANL
TB1-4	VTSSRAL**RGA**MANL
TB1-5	VTSSRA**AAA**MANL
TB1-6	AAAAAGA**RGD**AGAA

[a]All peptides are biotinylated at the N-terminus. Biotin is linked to the N-terminus *via* coupling of biotin-XX-SSE (Invitrogen) to the N-terminal amino acid.

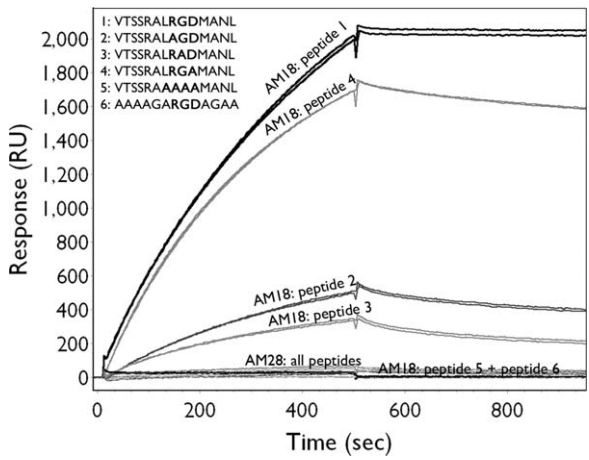


Figure 8.16 Alanine scanning of anti-HPeV VP1-protein antibody AM18. Purified AM18 (5.0 $\mu g\,mL^{-1}$) was injected over a peptide-immobilized chip. AM18 binds the complete peptide (peptide 1) with the highest response; responses are reduced on alanine-replaced peptides. Purified antibody AM28 (5.0 $\mu g\,mL^{-1}$), not binding the RGD epitope, was injected as a negative control.
Adapted from S. Shakeel, B. M. Westerhuis, A. Ora, G. Koen, A. Q. Bakker, Y. Claassen, *et al.*, *Virology*, 2015, **89**, 9571. Copyright 2015, American Society for Microbiology.

8.4.2.2 Alanine Scanning: Results and Interpretation

AM18 has the highest response on the wild-type peptide (peptide 1), and shows only a slightly reduced response on peptide 4 (however, dissociation in increased on peptide 4); the maximal responses on peptides 2 and 3 are much lower (Figure 8.16).

This result suggests that the first two amino acids in the RGD motif contribute most to binding, and the final aspartic acid contributes less to

View Online

Published on 24 May 2017 on http://pubs.rsc.org | doi:10.1039/9781788010283-00295

binding but stabilizes the antibody–epitope complex, as substituting the aspartic acid increases antibody dissociation. The large effect of substituting glycine for alanine is unexpected, as these amino acids differ by only one methyl group. Likely, the more flexible glycine residue makes an important contribution to the structure of the epitope. As expected, deleting the complete RGD-motif (peptide 5) completely removes binding.

Notably, AM18 did not bind peptide 6, which consisted of the RGD motif flanked by a series of alanine and glycine (Figure 8.16), demonstrating that the RGD motif alone does not suffice for binding. Apparently, the residues flanking the RGD motif are also essential for forming the epitope. Alanine scanning of the residues flanking the RGD motif would reveal which residues are required for AM18 binding.

To summarize the experiment, we have demonstrated with alanine scanning that AM18 binds the RGD motif of HPeV1 VP1. For each residue within this motif, a different role could be assigned. The arginine and glycine residue are important for AM18 association, and specifically the more flexible glycine contributes greatly to the epitope structure. The C-terminal aspartic acid stabilizes the antibody–epitope complex.

8.4.3 Conclusions on Epitope Mapping and Outlook

High-throughput epitope mapping SPR is a powerful tool for mapping epitopes of large sets of antibodies. We have demonstrated epitope mapping of anti-RSV G antibodies with single amino acid accuracy, finding that, even for antibodies within a bin group, epitopes may vary greatly at the amino acid level. Our analysis suggests that antibody epitope ''core'' residues exist that are essential for binding. These core residues are flanked by ''context'' residues that enhance binding. Together, the core and context residues form the complete epitope. With alanine scanning, we have demonstrated that anti-HPeV VP1 antibody AM18 binds the RGD motif of VP1. Our analysis also suggested that residues flanking RGD are essential for AM18 binding.

In these two experiments, we have mapped the epitopes of antibodies against RSV G-protein and HPeV VP1. One limit of the use of linear peptide libraries is that only antibodies recognizing a linear epitope are efficiently mapped. Antibodies binding a conformational epitope (*e.g.* AT42 and AT49 in the anti-RSV-G panel) are less efficiently mapped with linear peptides. Conformational epitopes may be mapped with libraries of mutated target protein, performing alanine scanning on the complete protein rather than a peptide, or by using libraries of structurally constrained peptides.[54,55] In principle, these methods are also transferable to high throughput, providing that mutated protein, or constrained peptide libraries can be immobilized on SPR sensors.

Furthermore, the direct measurement of antibody binding and dissociation with SPR allows for a more elaborate analysis than with end-point

View Online

measurement (*e.g.* ELISA) or structural data. With SPR imaging, as demonstrated for AM18, the roles of individual residues within epitopes can be assigned immediately from the binding curves.

8.5 General Conclusions and Outlook

We have shown, with five different experiments, how high-throughput SPR can accelerate antibody discovery, and at the same time provide in-depth analysis of antibody–antigen interactions and their epitopes. All experiments were performed on the same SPR imaging instrument (IBIS MX96), demonstrating its unique versatility.

At AIMM Therapeutics, we apply high-throughput SPR to validate our screens, to categorize our binders based on their epitopes, to select high-affinity candidates, to identify target-specific and non-specific antibodies, and to find antibodies that bind unique epitopes. Because only a minimal amount (0.1 $\mu g\,mL^{-1}$) of antibody is required, these experiments can be carried out at an early stage in the discovery process and have significantly improved our lead selection.

At present, the limitations of high-throughput SPR imaging lie mostly in the number of samples that may be processed in a single experiment. The current version of the CFM spotter prints up to 96 different samples on a single SensEye, and the IBIS MX96 has positions for up to 96 different samples. Analyzing larger sample pools would require a change in the instrumentation hardware, to permit the use of, for example, 384 or 1536 samples (these numbers correspond to existing well-plate formats) in a single experiment.

8.6 Questions

1. In Section 8.3.1.2, we discussed the issues of epitope binning on a capture-crosslinked sensor (*i.e.* a capture sensor, on which ligands are captured, that is later crosslinked so that it may be regenerated). How would you set up your experiment to circumvent these issues? What consequences would your setup have on your data?
2. Epitope mapping works best on antibodies with a linear epitope. Which experiments could you try in order to define whether your antibody has a linear epitope?
3. How can you reduce the effects of ligand (*i.e.* antibody) density variations on the outcome of your affinity ranking experiment?
4. Construct a node plot from Figure 8.17. Shown are injections of five secondary antibodies (A, B, C, D, and E) after antigen E2 was injected over spots with the same five antibodies.
5. Alanine scanning is discussed in Section 8.4.2. What are the key differences between alanine scanning epitope mapping and mapping by amino acid skipping? How would you address these experimentally?

Published on 24 May 2017 on http://pubs.rsc.org | doi:10.1039/9781788010283-00295

View Online

Published on 24 May 2017 on http://pubs.rsc.org | doi:10.1039/9781788010283-00295

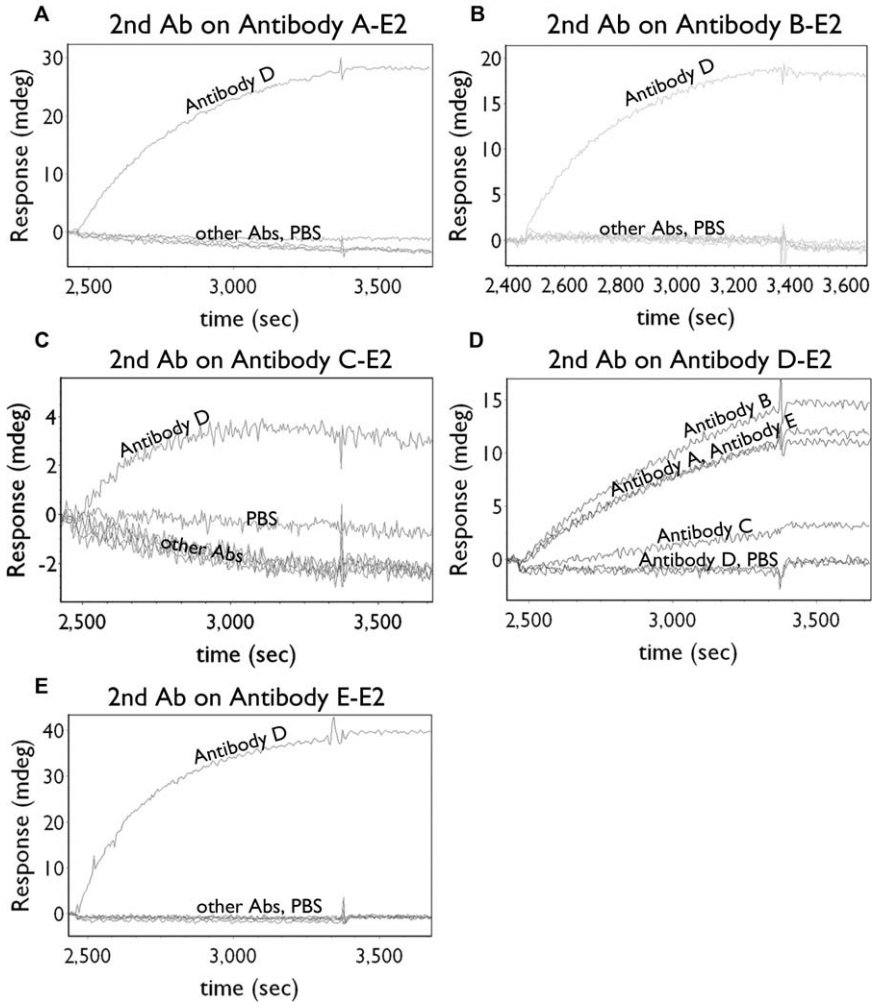


Figure 8.17 Sandwich binning of five antibodies binding HCV E2 antigen. Adapted from S. J. Merat, R. Molenkamp, K. Wagner, S. M. Koekoek, D. van de Berg, E. Yasuda *et al.*, *PLoS One*, 2016, **11**, e0165047.

References

1. A. L. Nelson, E. Dhimolea and J. M. Reichert, *Nat. Rev. Drug Discovery*, 2010, **9**, 767.
2. K. Maggon, *Curr. Med. Chem.*, 2007, **14**(18), 1978.
3. J. Reichert, *mAbs*, 2016, **8**, 1.
4. C. A. Borrebaeck, *Antibodies Diagn.*, 2000, **21**(8), 379.
5. J. Gervay and K. D. McReynolds, *Curr. Med. Chem.*, 1999, **6**(2), 129.
6. M. Brown and C. Wittwer, *Clin. Chem.*, 2000, **46**(8B), 1221.

View Online

Published on 24 May 2017 on http://pubs.rsc.org | doi:10.1039/9781788010283-00295

7. J. V. Ravetch and S. Bolland, *Annu. Rev. Immunol.*, 2001, **19**, 275.
8. R. B. M. Schasfoort, A. E. H. Bentlage, I. Stojanovic, A. van der Kooi, E. van der Schoot, L. W. M. M. Terstappen *et al.*, *Anal. Biochem.*, 2013, **439**, 4.
9. I. Stojanovic, Y. van Hal, T. J. G. van der Velden, R. B. M. Schasfoort and L. W. M. M. Terstappen, *Sensing Bio-Sensing Res.*, 2016, **7**, 48.
10. J. P. Messina, I. Humphreys, A. Flaxman, A. Brown, G. S. Cooke, O. G. Pybus *et al.*, *Hepatology*, 2015, **61**, 77.
11. J. M. Micallef, J. M. Kaldor and G. J. Dore, *J. Viral Hepatitis*, 2006, **13**, 34.
12. C. H. B. S. van den Berg, B. P. X. Grady, J. Schinkel, T. van de Laar, R. Molenkamp, R. van Houdt *et al.*, *PLoS One*, 2011, **6**, e27555.
13. J. Grebely, K. Page, R. Sacks-Davis, M. S. van der Loeff, T. M. Rice, J. Bruneau *et al.*, *Hepatology*, 2013, **59**, 109.
14. J. M. Pestka, M. B. Zeisel, E. Bläser, P. Schürmann, B. Bartosch, F.-L. Cosset *et al.*, *Proc. Natl. Acad. Sci. U. S. A.*, 2007, **104**, 6025.
15. W. O. Osburn, A. E. Snider, B. L. Wells, R. Latanich, J. R. Bailey, D. L. Thomas *et al.*, *Hepatology*, 2014, **59**, 2140.
16. S. J. Merat, R. Molenkamp, K. Wagner, S. M. Koekoek, D. van de Berg, E. Yasuda *et al.*, *PLoS One*, 2016, **11**, e0165047.
17. R. B. M. Schasfoort, W. de Lau, A. van der Kooi, H. Clevers and G. H. M. Engbers, *Anal. Biochem.*, 2012, **421**, 794.
18. R. B. M. Schasfoort, K. C. Andree, N. van der Velde, A. van der Kooi, I. Stojanovic and L. W. M. M. Terstappen, *Anal. Biochem.*, 2016, **498**, 8.
19. M. M. Davis and P. J. Bjorkman, *Nature*, 1988, **334**, 395.
20. J. A. Weidanz and W. H. Hildebrand, *Expert Rev. Proteomics*, 2006, **3**, 641.
21. R. B. Alexander, F. Brady, M. S. Leffell, V. Tsai and E. Cellis, *Urology*, 1998, **51**, 150.
22. Y. T. Chen, M. J. Scanlan, U. Sahin, O. Tureci, A. O. Gure *et al.*, *Proc. Natl. Acad. Sci. U. S. A.*, 1997, **94**, 1914.
23. T. Dao, S. Yan, N. Veomett, D. Pankov, L. Zhou, T. Korontsvit *et al.*, *Sci. Transl. Med.*, 2013, **5**, 176ra33.
24. J. A. Weidanz, O. Hawkins, B. Verma and W. H. Hildebrand, *Int. Rev. Immunol.*, 2011, **30**, 328.
25. G. Sautto, A. W. Tarr, N. Mancini and M. Clementi, *Clin. Dev. Immunol.*, 2013, 450963.
26. J. Ivanyi, *Front. Immunol*, 2014, **5**, 107.
27. Y. N. Abdiche, D. S. Malashock, A. Pinkerton and J. Pons, *Anal. Biochem.*, 2009, **386**, 172.
28. Y. N. Abdiche, K. C. Lindquist, D. M. Stone, A. Rajpal and J. Pons, *J. Immunol. Methods*, 2012, **382**, 101.
29. V. Towne, Q. Zhao, M. Brown and A. C. Finnefrock, *J. Immunol Methods*, 2013, **388**, 1.
30. W. W. Thompson, D. K. Shay, E. Weintraub, L. Brammer, N. Cox, L. J. Anderson and K. Fukuda, *J. Am. Med. Assoc.*, 2003, **289**, 179.
31. C. B. Hall, G. A. Weinberg, M. K. Iwame, A. K. Blumkin, K. M. Edwards, M. A. Staat *et al.*, *N. Engl. J. Med.*, 2009, **360**, 588.

View Online

Published on 24 May 2017 on http://pubs.rsc.org | doi:10.1039/9781788010283-00295

32. S. Johnson, C. Oliver, G. A. Prince, V. G. Hemming, D. S. Pfarr, S. C. Wang *et al.*, *J. Infect. Dis.*, 1997, **176**, 1215.
33. E. J. Collarini, E. H. Lee, O. Foord, M. Park, G. Sperinde, H. Wu *et al.*, *J. Immunol.*, 2009, **183**, 6338.
34. L. M. Haynes, H. Caidi, G. U. Radu, C. Miao, J. L. Harcourt, R. A. Tripp and L. J. Anderson, *J. Infect. Dis.*, 2009, **200**, 439.
35. H. Caidi, J. L. Harcourt, R. A. Tripp, L. J. Anderson and L. M. Haynes, *PLos One*, 2012, **7**, e51484.
36. L. J. Anderson, J. C. Hierholzer, Y. O. Stone, C. Tsou and B. F. Fernie, *J. Clin. Microbiol.*, 1986, **23**, 475.
37. L. J. Anderson, P. Bingham and J. C. Hierholzer, *J. Virol.*, 1988, **62**, 4242.
38. B. Cortjens, E. Yasuda, K. Wagner, Y. B. Claassen, A. Q. Bakker, J. B. M. van Woensel, T. Beaumont, *J. Virol.*, 2017, DOI: 10.1128/JVI.02357-16.
39. J. M. Gershoni, A. Roitburd-Berman, D. D. Siman-Tov, N. Tarnovitski Freund and Y. Weiss, *BioDrugs*, 2007, **21**, 145.
40. J. Sharon, M. J. Rynkiewicz, Z. Lu and C. Y. Yang, *Immunology*, 2014, **142**, 1.
41. J. J. Gorman, J. L. McKimm-Breschkin, R. S. Norton and K. J. Barnham, *J. Biol. Chem.*, 2001, **276**, 38988.
42. W. M. Sullender, *Clin. Microbiol. Rev.*, 2000, **13**, 1.
43. T. Hyypiä, C. Horsnell, M. Maaronen, M. Khan, N. Kalkkinen, P. Auvinen *et al.*, *Procl. Natl. Acad. Sci. U. S. A.*, 1992, **89**, 8847.
44. K. S. Benschop, J. Schinkel, R. P. Minnaar, D. Pajkrt, L. Spanjerberg, H. C. Kraakman *et al.*, *Clin. Infect. Dis.*, 2006, **42**, 204.
45. M. A. Verboon-Maciolek, T. G. Krediet, L. J. Gerards, L. S. de Vries, F. Groenendaal and A. M. van Loon, *Pediatr. Infect. Dis. J.*, 2008, **27**, 241.
46. J. Seitsonen, P. Susi, O. Heikkilä, R. S. Sinkovits, P. Laurinmäki, T. Hyypiä and S. J. Butcher, *J. Virol.*, 2010, **84**, 8509.
47. M. Roivainen, L. Piirainen, T. Hovi, I. Virtanen, T. Riikonen, J. Heino and T. Hyypiä, *Virology*, 1994, **203**, 357.
48. A. Berinstein, M. Roivainen, T. Hovi, P. W. Mason and B. Baxt, *J. Virol.*, 1995, **64**, 2664.
49. B. Nelsen-Salz, H. J. Eggers and H. Zimmermann, *J. Gen. Virol.*, 1999, **80**, 2311.
50. P. Joki-Korpela, V. Marjomäki, C. Krogerus, J. Heino and T. Hyypiä, *J. Virol.*, 2001, **75**, 1958.
51. B. M. Westerhuis, K. S. Benschop, G. Koen, Y. Claassen, K. Wagner, A. Q. Bakker *et al.*, *J. Virol.*, 2015, **89**, 7457.
52. S. Shakeel, B. M. Westerhuis, A. Ora, G. Koen, A. Q. Bakker, Y. Claassen *et al.*, *Virology*, 2015, **89**, 9571.
53. K. L. Morrison and G. A. Weiss, *Curr. Opin. Chem. Biol.*, 2001, **5**, 302.
54. H. Lamdan, J. V. Gavilondo, Y. Muñoz, A. Pupo, V. Huera, A. Musacchio *et al.*, *Mol. BioSyst.*, 2013, **9**, 2097.
55. V. Chico, A. Martinez-Lopez, M. Ortega-Villaizan, A. Falco, L. Perez, J. M. Coll and A. Estepa, *J. Virol.*, 2010, **84**, 7140.

Published on 24 May 2017 on http://pubs.rsc.org | doi:10.1039/9781788010283-00328

CHAPTER 9

Treating Raw Data: Software for SPR Applications

NOAH T. DITTO* AND JOSHUA ECKMAN

Wasatch Microfluidics, 800N 300W C309, Salt Lake City, UT 84103, USA
*Email: nditto@microfl.com

9.1 Introduction

With the release of the first commercially available SPR biosensor over 25 years ago, there inevitably has been a need for software tools capable of addressing the requirements of both automated data collection and analysis of real-time binding data. Around the time that BIAcore (now Biacore, a division of GE Healthcare) launched its first commercial platform, processor speeds were around 16 MHz, with 2 MB of RAM and 60 MB hard drives common for entry-level desktops.[1] Today, standard desktops routinely have processor speeds of around 3 GHz, 8 GB of RAM, and 1 TB hard drives, collectively enabling personal computers to handle substantially more complex data sets and sophisticated software packages. This exponential growth in computing power has facilitated the development of advanced software tools for many analytical instruments, including surface plasmon resonance (SPR) biosensors.

Data files generated by label-free biosensors can be significant in terms of memory requirements owing to the real-time nature of data collection, as opposed to technologies that only record a final endpoint value. In addition to the data-rich nature of SPR, demand for additional applications and throughput has pushed the complexity of instrumentation to include highly varied fluidics and detector configurations (see Chapter 2). The advantages of having biosensors with capabilities to monitor ever-increasing numbers of

Handbook of Surface Plasmon Resonance, 2nd Edition
Edited by Richard B. M. Schasfoort
© The Royal Society of Chemistry 2017
Published by the Royal Society of Chemistry, www.rsc.org

View Online

Published on 24 May 2017 on http://pubs.rsc.org | doi:10.1039/9781788010283-00328

ligand–analyte interactions has further pushed the requirements of computing resources to collect real-time binding data for hundreds of interactions simultaneously. Whereas early SPR platforms had, for example, four flow cell locations, of which three were active and one was used for referencing, commercial platforms utilizing SPR array imaging or biolayer interferometry (BLI) (see Chapter 10) today can have hundreds of active sensing surfaces. This has increased the number of surfaces being monitored per injection by several orders of magnitude. Additionally, liquid handling and robotics interfaces have simplified the execution of high numbers of analysis cycles in a fully automated fashion. Hence the increase in data generation capabilities can be attributed to both higher numbers of samples being injected across sensor surfaces *via* improved liquid handling automation and also increased sensor surface capacities.

In conjunction, data analysis tools have evolved to handle the increasing numbers of interactions measured per study. Software for the analysis of SPR data has grown to encompass a diverse range of tools from simple, spreadsheet-based solutions to advanced multicomponent software packages capable of handling thousands of binding sensorgrams. The niche for basic, lower throughput biosensors still exists in many laboratories, but market demands and advances in computing technologies have led to improvements in instrument software to the point that most commercially available systems now implement at least semiautomated software for acquiring and processing data. Although fully automated data processing would greatly reduce the hands-on requirements of using SPR, there are many aspects of data processing and curation that still require human interpretation for validation.

9.2 Software Tools for Designing and Executing Experiments

9.2.1 General Considerations

Simplified instrument control interfaces and hardware have made SPR a fairly accessible technology. While it can be relatively straightforward for biosensor users to obtain binding signals in their assays, thoughtful experimental design and careful analysis are crucial for achieving high-quality data (see Chapter 5). Tools for the analysis of SPR data are very limited in their ability to correct for poorly designed studies. Using SPR, both good and bad data can be equally easy to acquire, but the latter often entail misinterpretation of observed behaviors and/or the need for follow-up experiments to achieve more suitable conditions.

Several aspects of assay design are important not only for achieving high-quality data but also for reducing experimental complexity and maximizing the efficient use of reagents. Table 9.1 lists some relevant considerations to keep in mind.

The applicability of these factors will vary between platforms, mainly as a consequence of differences in hardware. For example, the volume of analyte

View Online

Table 9.1 Experimental considerations that impact the quality of SPR data.

Reagent factors	Analyte/ligand purity and active concentration
	Valency of analyte/ligand
	Non-specific binding
	Running buffer composition
	Regeneration conditions
	Reference surface composition
Hardware factors	Data collection rate
	Flow rate
	Sample deck temperature
	Flow cell temperature
	Sample loop volume, if applicable
	Detector sensitivity
Study design factors	Purpose of data
	Assignment of active/reference surfaces
	Dissociation time
	Association time
	Required analyte titration range
	Appropriate ligand density

Published on 24 May 2017 on http://pubs.rsc.org | doi:10.1039/9781788010283-00328

injection required in order to reach a certain level of binding response is often an important consideration. Traditional SPR platforms maintain flow directionality in a single orientation and necessitate matching desired contact time and flow rate with available sample capacities. Fortunately, these systems often have built-in calculators for determining analyte volumes as a function of flow rate, contact time, and dead volume. There are systems, however, that recirculate or maintain bidirectional flow of analyte during an injection, for which the injection volume is largely a fixed parameter, requiring less analyte in order to achieve a specific response.

Another example is the assignment of reference surfaces, which is important for removing experimental artifacts from data and increasing the ease of data analysis. For systems with a single monitored surface per flow cell, at least one separate flow cell must often be assigned for referencing and should ideally be located in close proximity to the surface from which it will be subtracted. In contrast, instruments with multiple monitored surfaces residing within the same flow cell typically maintain reference locations immediately adjacent to active surfaces, so the reserving of surfaces that could be otherwise used for active binding is not necessary.

Despite differences based on hardware configurations, several aspects of assay design and execution are largely universal across all SPR platforms. One common feature is ensuring that analytes are well matched to the system running buffer to avoid sensorgram shifts due to buffer mismatching. Data analysis tools do allow for some level of correction for these bulk shift effects, but it is in the best interest of the user to mitigate the issue before the experiment is under way. Similarly, regeneration of analyte from the

View Online

Published on 24 May 2017 on http://pubs.rsc.org | doi:10.1039/9781788010283-00328

sensor surface at the end of a cycle can play a critical role in the success of an SPR study. Although a small percentage of ligand inactivation or incomplete regeneration can be acceptable under certain circumstances, greater levels often preclude meaningful data analysis.

For experiments focused on measuring dissociation rates, consideration must be given to how much of a dissociation phase can be accommodated by the instrument run time and other factors such as buffer consumption. Also, the dissociation time must be sufficiently long to meet the 5% rule, such that from the start to the end of dissociation, the decay in signal must be at least 5% in order to measure the off-rate accurately.[2,3] Although the objective of SPR studies is often to measure kinetic rate constants for ligand–analyte interactions that have not been previously characterized, it is possible to run some preliminary studies prior to a full experiment, in order to gain a better understanding of the system in question. Some software interfaces even allow for dynamic extension of cycle times, so that particularly slow dissociating interactions may be allowed to more time to separate from the surface.

9.2.2 Pre-assay Studies

When possible, evaluating experimental conditions such as ligand density, analyte binding responses, and regeneration efficiency prior to a full SPR study is an excellent way to improve data quality for eventual analysis. If the pre-assay work can be performed using only a subset of the available sensor surfaces, then it may be possible to carry out the full study on the same sensor using the remaining surfaces. A few antigen injections across the surface(s) provide valuable data for estimating appropriate analyte titration ranges and dissociation times. Additionally, interactions that are difficult to regenerate efficiently may necessitate changes in experimental strategy, such as the use of a capture surface or injection of analyte using the single-cycle kinetics approach (see Chapter 4, Section 4.5.4). Time spent ascertaining correct conditions, and avoiding deleterious ones, can avoid complications in data analysis and/or repetition of the experiment.

9.2.3 Software Tools for Pre-assay Planning

In the initial stages of assay development and optimization, tools such as KD-Assistant, SPR-Simulation, and BiaCalculations are platform-independent packages that can, among other things, plot theoretical response curves and time to equilibrium, and calculate analyte titrations necessary to achieve desired R_{max} values.[4] These tools also allow the importation of injection response data, such as those from pre-assay studies, in order to model contact times and titration ranges. Software tools have also been developed to enhance the ease of assay design. BiaMethodWriter, for example, was

View Online

developed as a more user-friendly way of building experiments for earlier BIAcore instruments and also giving the user a simple means of calculating sample volumes and experiment run times.[4] These tools are freely available, allowing the opportunity to explore assay design in more detail, particularly for laboratories with limited budgets and/or platforms lacking in machine-specific software.

Commercial software packages that are offered by a variety of instrument manufacturers also make available features such as fit simulation using kinetic constants. In addition to simulation features, such software has calculations built in for estimation of required running buffer, sample volumes, and total experimental run time that greatly aid in planning an experiment effectively. Table 9.2 provides some examples of software packages available as standalone systems or in conjunction with an instrument.

Published on 24 May 2017 on http://pubs.rsc.org | doi:10.1039/9781788010283-00328

Table 9.2 Examples of biosensor control/set-up and data analysis software packages.

Control/setup software	Analysis software	Instrument(s)	Manufacturer
BiOptix 404pi Console	BiOptix Analysis	4004pi	BiOptix
System Control Software-M1R/ M2R	Analyzer AR2	MASS-1, MASS-2, SPR-2, SPR-2/4	Sierra Sensors
SPR-2/4 Control Software R2			
Reichert Control	Scrubber	Reichert4SPR	Reichert
BI Control	BI Data Analysis		Biosensing Instruments
Data Acquisition	Kinetic Evaluation	Esprit, Twingle, Springle	Kinetic Evaluation Instruments
Biacore Control	Biacore Evaluation	1000, 2000, 3000, T200, A100, 4000, S200	GE Lifesciences
EzView	EzAnalysis, EzFit	OpenPlex, XelPlex	Horiba
IBIS Data Acquisition	SPRint, Epitope Binning 2.0, Scrubber	MX96	IBIS/Wasatch Microfluidics
Octet Data Acquisition	Octet Data Analysis	Octet RED, HTX	FortéBio
Proteon Manager	Proteon Manager	Proteon XPR36	Bio-Rad
SPR Navi Control	SPR Navi DataViewer	Ilves, Naali, Vasa, Otso	BioNavis
KD Assistant	NA	NA	NA
BiaMethodWriter	NA	NA	NA
Curve Simulation	NA	NA	NA
BiaCalculations	NA	NA	NA
NA	CLAMP	NA	University of Utah
NA	Scrubber	NA	BioLogic Software
NA	Screener	NA	Genedata
NA	EvilFit		NIH (see Chapter 5)

View Online

Published on 24 May 2017 on http://pubs.rsc.org | doi:10.1039/9781788010283-00328

9.2.4 Takeaways for SPR Study Design and Execution

High-quality SPR data come from proper experimental planning.[5] This includes consideration of hardware strengths and weaknesses and understanding of the analyte and ligand system in question. Additionally, the assay design should be fit-for-purpose, as data-quality attributes should reflect experimental objectives. As an example of high-quality kinetics, maintaining a low level of ligand density is essential to avoid many of the pitfalls with kinetics assays (see Chapter 4, Section 4.6). Conversely, for studies in a higher throughput screening context, increased ligand density may be necessary in order to achieve robust activity of ligands over the course of the many injections. Both instances highlight the balance of rigor and speed. With this approach in mind, data analysis can focus more on the interactants and less on challenges associated with assay non-ideality.

9.3 Data Analysis

9.3.1 Data Output

As discussed earlier, technological advances and evolving trends in research have led to a broad range of SPR platforms becoming available. Different injection schemes and active/reference surface configurations have expanded the diversity of data collection options. Collectively, these various configurations mean that database structures do not necessarily follow a standard format. In spite of this, at its core, SPR data are still a measure of binding signal *versus* time.

As SPR is a real-time method, data collection rates play an important role in how SPR studies are designed and the type of data quality derived. Data collection rates are primarily limited by the speed at which detection can be performed across all surfaces in an experimentally reasonable time, relating to hardware and software capabilities. Most systems perform data collection somewhere in the range 1–10 Hz. For example, limits on data collection rates largely drive the upper bounds of association rates that can be accurately measured by SPR. These higher data collection rates are typically most valuable for kinetic experiments where rapid changes in signals need to be monitored with sufficient detail in order to represent accurately binding behaviors for fitting. Lower data collection rates are best used for non-critical aspects of a cycle such as the regeneration phase, in order to reduce the size of data files.

9.3.2 Data Analysis Software Packages

Owing to the range of instrument configurations and to some extent usage restrictions imposed by manufacturers, many of the software tools in use for the analysis of SPR data are platform specific. Data analysis programs primarily exist independent of instrument control and data collection software,

View Online

Published on 24 May 2017 on http://pubs.rsc.org | doi:10.1039/9781788010283-00328

with the benefit that data analysis can be performed while an experiment is being actively run. Output from instruments can be in proprietary file formats and therefore preclude direct use of third-party software for data analysis. However, many platforms have features for exporting data in simple text format that largely allows for import into additional analysis tools, although restructuring of the data tables may be required. Several analysis programs also allow viewing of data analysis from the result file as it is being written, although some database configurations prohibit data analysis until the experiment is complete.

Although many software tools are preconfigured to an instrument, third-party software can also be adapted to an instrument's specific hardware and database format. Detailed below are Scrubber (BioLogic), CLAMP (University of Utah), TraceDrawer (Ridgeview Instruments), and Screener (Genedata), which are examples of analysis tools that are instrument independent and can be adapted to a number of different commercial platforms.[6]

Scrubber performs both initial data ''scrubbing'' steps and fitting routines for steady-state affinity and global kinetic analysis. Scrubber was developed to simplify SPR data processing and fitting, particularly for kinetics, at a time when tools for such purposes were not very user friendly. It was initially designed for the four flow cell format, common to earlier BIAcore instruments. Since then, it is has been expanded to accommodate data formats for higher throughput platforms, but the core features and layout remain consistent between versions. Later in this chapter, an example data set is processed using a higher throughput version of Scrubber. Although Scrubber does fit global kinetics, is it restricted to a 1 : 1 Langmuir binding model, with the option to include a mass transport term.

The CLAMP program is focused on global kinetic fitting of SPR data sets. Although it has some features for removal of spike and bulk refractive shifts, it relies mostly on preprocessing of data using other tools such as Scrubber. CLAMP does offer additional binding models beyond simple 1 : 1 interactions. Additionally, features are available for users to create their own model. The application of more complex models to data sets should be avoided, however, unless the binding mechanisms are well understood.

TraceDrawer is a tool for organizing and fitting SPR data. The software is generalized for any data set that is time resolved, but has integrated tools that are specific to the needs of SPR, such as normalization and referencing. Versions have been developed specifically for platforms such as the BioNavis SPR Navi 200 and Sierra Sensors SPR-2. Additionally, the software can also handle text import, allowing flexibility with most database structures.

Another universal software package that can process SPR data is Screener, which can handle text files of real-time binding data and calculate kinetics and affinities. All routine SPR data processing features are also available. A unique advantage of Screener is that in larger research environments, it can accommodate data from a number of different analytical techniques into a single software package. The scalability of the software also can be used to match the throughput capabilities of certain SPR platforms.

View Online

Published on 24 May 2017 on http://pubs.rsc.org | doi:10.1039/9781788010283-00328

Many core features are common to SPR data processing software, such as signal correction using surface referencing and blank injection subtraction. Certain software features, however, target particular applications and capabilities of an instrument. As an example, for instruments having sensitivity sufficient for small-molecule analysis, tools are made readily available to correct for the high refractive indices of running buffers needed for solubilization of these compounds (see Chapter 7, Section 7.3.7). Software packages for platforms without applications for small-molecule analysis will typically not have these specific processing features in place. It should be cautioned that inclusion of software features is not a guarantee of an easily implemented application. Although demonstrable under ideal conditions, some applications can be less robust in real-world usage. The user should remain knowledgeable regarding the hardware and software limitations of an instrument.

9.4 Fundamental Data Processing Techniques

9.4.1 Introduction

Data from an SPR experiment require specific processing routines prior to interpretation of results and there are several factors relating to optical and fluidics phenomena that must be corrected, which have been extensively detailed elsewhere.[3,5,7–9] Fortunately, all steps in data processing can be conducted through specialized software tools that allow the user to understand the data better and distinguish good results from bad in a streamlined fashion. Table 9.3 highlights many of these features.

9.4.2 Normalization/Calibration

In order to correct for differences in measured responses across sensing locations on sensor surfaces, normalization or calibration routines are commonly applied to sensor data. Injections of diluted glycerol are typically used to standardize surface responses, owing to the inertness of glycerol towards most surfaces and its much higher refractive index in comparison with water or physiological buffers. Corrections for response sensitivity are applied primarily for a specific sensor to establish a relative correction, although for some instruments the correction is meant to normalize response to a fixed value based on the injected solution, independent of the sensor. Normalization routines are embedded in the control and analysis software for most platforms, so that following an instrument's guidelines on normalization solution preparation and application to data sets is fairly straightforward.

9.4.3 Excluded Volume Correction

Similarly to how normalization corrects for response sensitivities, excluded volume (EV) correction focuses on correcting response behaviors of surfaces

View Online

Table 9.3 Key features for software used to analyze SPR data.

General data processing features	Normalization
	Local and global referencing
	Blank subtraction
	Zeroing
	Despiking
	Cropping
Kinetics/affinity features	Kinetic and steady-state fitting
	Local/global fitting
	Calculation of bound responses
	Fitting of all or subset of analytes simultaneously
	Affinity in solution
	Thermodynamics
	DMSO correction (small molecules)
	Binding model options
	Floating of select parameters during fitting
Concentration analysis	Fitting of response curves
General binding/competition studies	Calculation of differential responses
	Graphical representation of competitive relationships
	Integration of secondary data
	Assignment of report points
Data maintenance	File saving
	Tracking of processing steps
	Exporting of calculated constants and curves
	Exporting of time-resolved signals

Published on 24 May 2017 on http://pubs.rsc.org | doi:10.1039/9781788010283-00328

in the presence of various levels of ligand. This commonly arises in studies with small molecules, which typically have small magnitudes of responses, and require solubilization with DMSO, which has a very high refractive index. The combination of high ligand density and potentially low R_{max} values causes differences in EV to materially impact binding responses. Correction of EV is carried out using titration of DMSO and most instruments with suitable sensitivity for small-molecule work have software routines that specifically address this issue. More information on EV correction using DMSO can be found in Chapter 7, Section 7.3.8.

9.4.4 Referencing

A core processing step in all SPR studies is surface referencing, which is achieved by subtraction of responses observed on a reference surface from those on an active surface. Referencing corrects for bulk shift phenomena and minor non-specific binding (NSB). An ideal reference has a composition similar to that of the active surface, but depending on the assay design can simply be a non-reacted surface or one that has been activated/deactivated but with no ligand present. Positioning of references adjacent to active surfaces is preferred, and subtraction using these locations is termed local referencing. Selection of a single surface or the average of multiple surfaces

View Online

as a reference, to be applied against all reaction surfaces, is termed global referencing. Different surfaces can often be chosen for use as a reference. The SPR platform and analysis packages largely dictate which surfaces can be used for referencing.

Published on 24 May 2017 on http://pubs.rsc.org | doi:10.1039/9781788010283-00328

9.4.5 Blank Subtraction

Blank subtraction, also commonly referred to as double referencing, can be used to remove baseline drift, such as signal drifts that may occur due to matrix effects from high-salt or pH extremes of regeneration solutions. Blank subtraction is accomplished by injecting buffer solutions, matched to the sample diluent and running buffer, at various points in an experiment in place of an analyte injection and using the same injection parameters. These blank injection responses are then subtracted from the analyte injection responses. Importantly, blank subtraction is not a substitute for EV corrections in small-molecule studies. Blank injections used for subtraction are ideally positioned close in experimental time to analyte injections and after initial warm-up cycles are completed, when baselines begin to stabilize. Inclusion of properly matched blanks in an experiment is a user responsibility and during data analysis software interfaces typically allow high flexibility in terms of which injection will be used for blank subtraction.

9.4.6 *x*-Scale Alignment

Depending on flow rate, injector format, and flow cell geometry in an SPR system, there can be modest delays in the time that it takes for an injection to reach all surfaces. To correct for this, *x*-scale alignment tools are available in many software packages. Alignment is commonly done by manually defining when an injected sample actually reaches the monitored surface and causes a shift in signal. For kinetics in particular, consistent start times across a series of injections is important for data fitting.

9.4.7 *y*-Scale Zeroing

As its name implies, *y*-scale zeroing adjusts binding signals to zero on the *y*-axis response scale. Although software tools often allow flexibility regarding where on the time scale zeroing will take place, it is usually an average of data points in the baseline prior to analyte injection. Although not necessary for all forms of data analysis, it does establish a uniform starting point for calculation of response, including R_{max}. The use of software report points, consisting of predefined points or ranges on the *x*-axis embedded in the data acquisition method, is an option on certain platforms that allows automated zeroing of signals. For data sets without report point tracking, zeroing windows can be manually assigned during data analysis.

View Online

9.5 Example of Competitive Epitope Binning Data Analysis

9.5.1 Introduction

Published on 24 May 2017 on http://pubs.rsc.org | doi:10.1039/9781788010283-00328

The increasing level of throughput available today in many commercial platforms has expanded applications of label-free biosensors to include, among other things, epitope binning of monoclonal antibodies (mAbs). Epitope binning is a pairwise, competitive assay that finds relationships among antibodies that bind to similar regions or ''epitopes'' on an antigen.[10]

The establishment of antibodies as a major class of therapeutic modalities to treat disease and infection has driven the need for analytical tools capable of discriminating nuanced binding behaviors. Label-free real-time biosensors are routinely used analytical tools for antibody characterization, enabling a breadth of applications, such as binding kinetics, affinity, and specificity determinations. The limited throughput of traditional biosensors has resulted in epitope characterization being carried out on only small subsets of candidate antibodies following preliminary screening by other methods. With recent advances in hardware configurations (Chapter 2) and data analysis tools, epitope characterization of much larger antibody panels is now possible.[10–13]

In conjunction with the enhanced capabilities of modern high-throughput biosensors, there is a growing pressure to identify novel antibodies that can engage targets in a manner that is both therapeutically superior and also distinct in terms of intellectual property.[14] The lack of routine processes for engineering mAbs towards a specific epitope means that candidate selection dictates screening of large panels to identify desirable attributes among a smaller subset.

Beyond therapeutic antibody candidates, competitive epitope binning can also be implemented in understanding immunological responses. Screening of antibodies from sera can identify response profiles to vaccine candidates or characterize anti-drug antibody (ADA) responses in individuals treated with therapeutic antibodies.[15,16] In both instances, the real-time nature and high throughput of modern biosensors can provide an extensive understanding of antibody binding profiles using relatively limited amounts of precious clinical samples.

Competitive epitope binning is conducted using one of three assay formats[10] (Figure 9.1). In the classical (sandwich) format, an array of ligand mAbs is immobilized on a sensor surface. A monovalent antigen is then injected and captured by the ligand mAbs, immediately followed by the injection of a second mAb (analyte) across the entire array to assess competition for antigen epitopes. In the premix format, an antigen, which may be mono- or multivalent, is mixed with a molar excess of mAb and injected across a surface of immobilized mAbs to determine whether the ligand and analyte mAbs recognize overlapping or non-overlapping epitopes. For tandem binning experiments, one mAb is injected across a surface-bound

View Online

Published on 24 May 2017 on http://pubs.rsc.org | doi:10.1039/9781788010283-00328

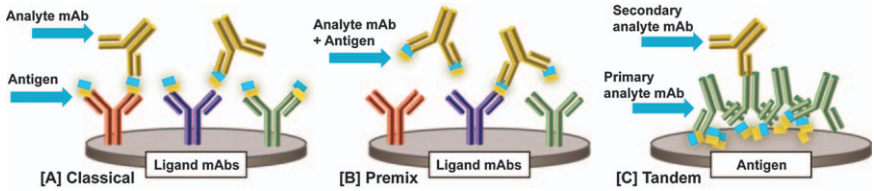


Figure 9.1 Illustration of the three competitive epitope binning formats.[10] (A) Classical – two injections: (1) antigen followed by (2) mAb analyte. (B) Premix – single injection of antigen premixed with saturating levels of mAb analyte. (C) Tandem – two injections: (1) primary/saturating mAb followed by (2) secondary/competing mAb.

antigen until saturation is achieved, then another mAb is injected to identify competition for antigen binding. Ideally, each mAb is represented both as a ligand and as an analyte (or, in the case of the tandem assay, as the primary and secondary mAb injection) in order to maximize confidence in competition profiles, since some mAbs may be better suited than others in certain roles (*e.g.* a weak affinity mAb may perform poorly as the capture mAb, but give detectable sandwiching responses upon reversing the assay and using it as the analyte).

The choice of assay format is largely driven by the valency of the antigen, the affinities of the antibody panel, and the injection and/or fluidics configuration of the biosensor. Both the premix and tandem assay formats require saturation of binding sites by mAbs, whereas the classical format does not. The classical format, however, cannot be used when the antigen is multivalent. Additionally, the tandem format requires either repeated capture of antigen on the biosensor surface or identification of suitable regeneration conditions for covalently bound antigen. The premix and classical formats commonly utilize covalently immobilized mAbs, which generally present less of a challenge for regeneration owing to the low pH tolerance of most mAbs. These multiple assay formats enable epitope binning to be adapted to a variety of workflows and biosensor platforms,[10] facilitating its routine implementation.

9.5.2 Epitope Binning Experimental Design

In the example provided here, we proceed through the data analysis for a classical epitope binning experiment. The experiment was designed such that each mAb was represented in the assay both as a ligand and as an analyte. In addition to adding more confidence to the blocking relationships observed, analyzing mAbs in both orientations can also identify competitive relationships that are dependent on order of addition and may represent more dynamic aspects of binding such as changes in antigen confirmation.

In brief, 42 mAbs were coupled using a continuous flow microspotter (Wasatch Microfluidics) to discrete locations on a carboxymethylated

View Online

Published on 24 May 2017 on http://pubs.rsc.org | doi:10.1039/9781788010283-00328

dextran (CMD) surface using EDC [1-ethyl-3-(3-dimethylaminopropyl)carbodiimide]–NHS (*N*-hydroxysuccinimide) amine coupling chemistry. The sensor prism was then docked in an MX96 SPR imager (IBIS) and remaining active sites were quenched using ethanolamine. Using a flow cell format that encompasses all ligand locations into a single fluidic chamber, a monomeric 32 kDa antigen was injected across the array for 5 min, followed by mAb for 5 min, then the surface was regenerated using 10 mM glycine (pH 2.0). Each mAb that was printed as a ligand was also injected in this format, in order for each mAb to compete fully against all others in the panel. Injections of antigen followed by buffer only were included throughout the experiment to monitor ligand activity over the course of the study. Reference data were collected using interspot locations positioned immediately adjacent to active surfaces. At the conclusion of the binning experiment, a titration of glycerol was injected across the array to calibrate (normalize) binding signals for differences in surface responses.

9.5.3 Preprocessing of Data Using SPRint

Figure 9.2 is an unprocessed serial sensorgram view, in the SPRint (IBIS) software analysis tool, of ligand locations for all injections across the duration of the study. In this particular workflow, SPRint is well suited to calibrate, locally reference, blank subtract, and zero the entire data set rapidly prior to more detailed analysis with software dedicated to epitope binning.

Note that regeneration pulses run between cycles were removed from this data view for clarity. Active surfaces are represented as colored sensorgrams, with interspot reference surfaces denoted in green.

As the MX96 utilizes imaging-based SPR, an image is shown of the 42 printed mAb locations in Figure 9.3, taken during the experiment by the

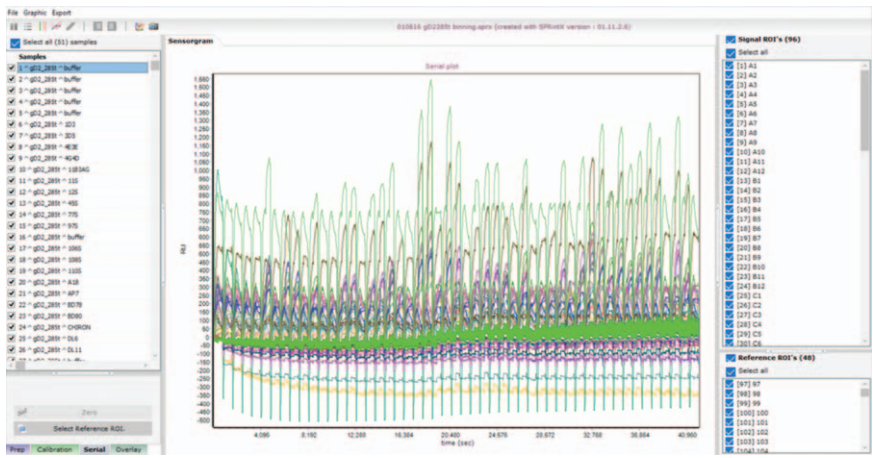


Figure 9.2 Serial view of epitope binning sensorgrams in SPRint software prior to calibration. Green sensorgrams are reference surfaces.

View Online

Published on 24 May 2017 on http://pubs.rsc.org | doi:10.1039/9781788010283-00328

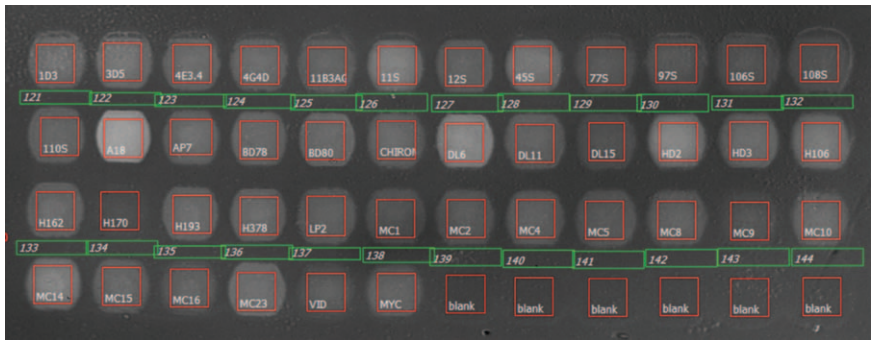


Figure 9.3 Camera view of 42 mAb array immobilized on CMD sensor prism surface.

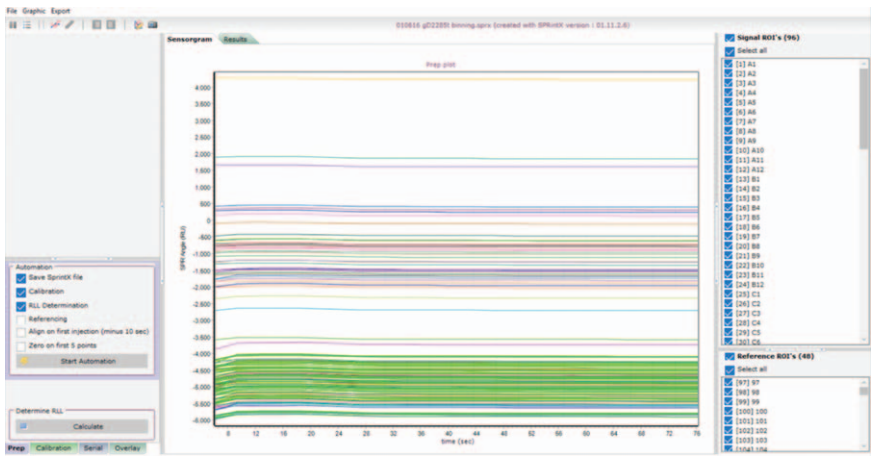


Figure 9.4 Selection of calibration and response of local ligand (R_{LL}) processing functions. Other processing functions shown, including referencing, zeroing, and alignment, will be reflected in subsequent steps.

data acquisition software. Lighter, square-like locations indicate the presence of printed mAbs, with the darker background comprising the CMD matrix. Red boxes highlight active (mAb) locations and green rectangles dictate where references signals will be monitored. While mAbs were concentration normalized for printing, different levels of contrast for ligand locations reflect differing degrees of immobilization efficiency for each mAb.

For this SPR platform, the first step in the data processing routine is to apply glycerol calibration to the sensor surfaces to adjust for differences in response sensitivities. Figure 9.4 shows functions in the software for applying a calibration routine to the data set and also for calculating the response of local ligand (R_{LL}) values, which use calibration data to estimate the density of immobilized ligand on active surfaces.

View Online

Published on 24 May 2017 on http://pubs.rsc.org | doi:10.1039/9781788010283-00328

Calibrated data are shown in Figure 9.5. Indicated adjacent to the ligand locations on the right side of the interface in parentheses are the R_{LL} values, in RU. Following calibration, the sensorgram data are inspected for evidence of antigen binding to references. In Figure 9.6, a single ligand location and its adjacent reference surface are shown for an injection of antigen followed by running buffer. The sensorgram profile indicates no evidence of antigen appreciably binding to the reference. Lack of reference binding by the antigen was also consistent for other active/reference locations in this assay and the reference signals were then subtracted from the active surface signals.

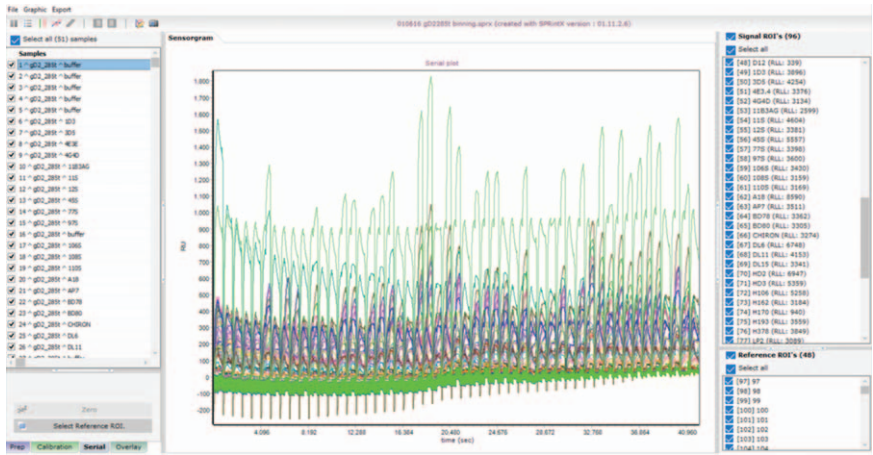


Figure 9.5 Serial sensorgrams following calibration. Note R_{LL} values (in RU) listed in the right-hand ligand column.

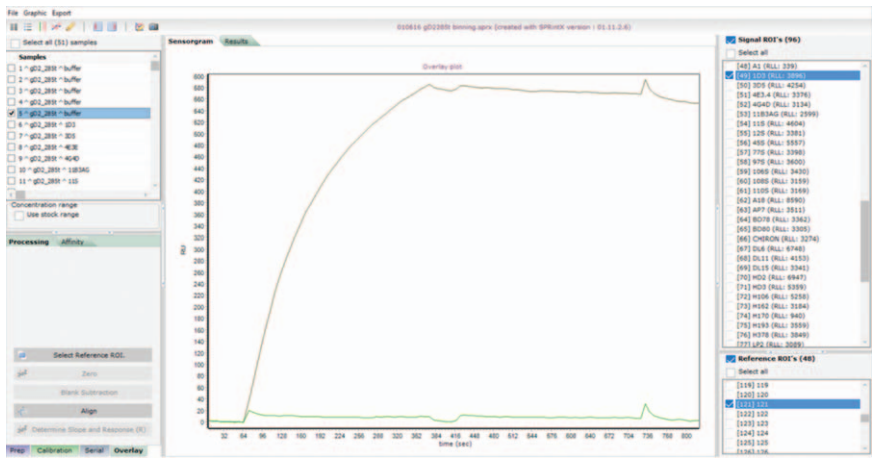


Figure 9.6 Selection of a single active surface (brown) and its corresponding local reference (green). Note the lack of binding by antigen to the reference.

View Online

Published on 24 May 2017 on http://pubs.rsc.org | doi:10.1039/9781788010283-00328

Following inspection of the calibrated surfaces for evidence of NSB, local reference locations were subtracted from active surfaces (Figure 9.7).

Lastly, the data were aligned on the *x*-scale to account for the delay in injection reaching all surfaces and zeroed using an average of baseline signal at the start of each cycle as shown in Figure 9.8. Zeroing of the data is critical for calculation of binding responses during epitope binning data analysis.

Following zeroing and alignment, the epitope binning data file is exported as a format suitable for Epitope Binning 2.0 software (Wasatch Microfluidics).

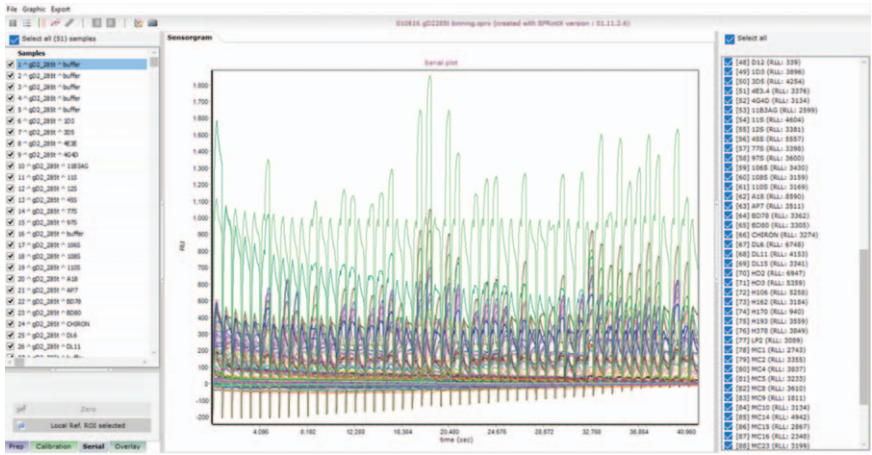


Figure 9.7 Sensorgram profiles following subtraction of local references.

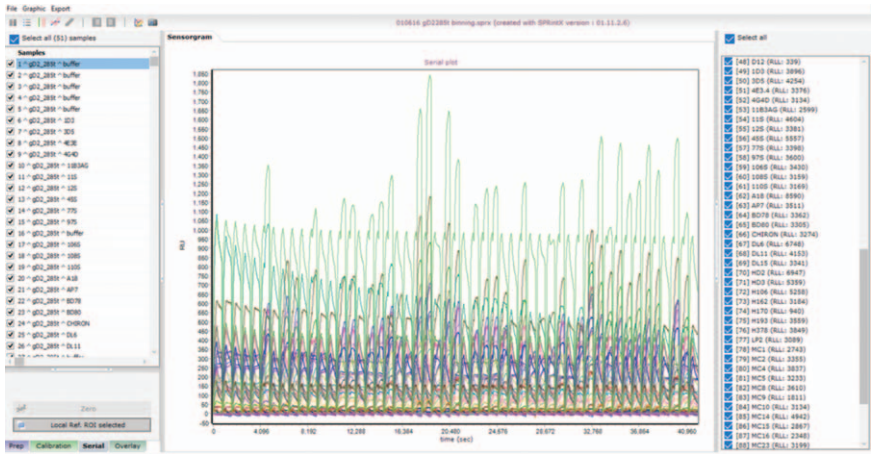


Figure 9.8 Sensorgram profiles following *x*-scale alignment and zeroing of injections.

View Online

Published on 24 May 2017 on http://pubs.rsc.org | doi:10.1039/9781788010283-00328

9.5.4 Epitope Characterization Using Epitope Binning 2.0

Upon import of the calibrated, double-referenced, and zeroed data file, the interface displays all ligand and analytes as individual columns, in addition to a ''unique mAb'' column, listing all samples to be included in the analysis (Figure 9.9).

Right clicking of analytes or ligands at this point also allows adjustment of sample names and inclusion/exclusion of samples from further data analysis. After selecting Continue, the user is taken to the Binning tab, where criteria for responses indicative of sandwiching or blocking are defined (Figure 9.10).

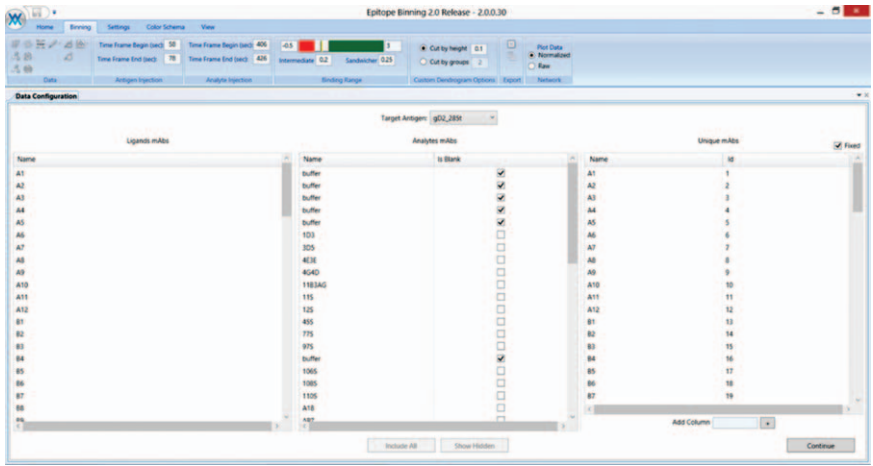


Figure 9.9 View of ligand and analyte information after import into Epitope Binning 2.0 software.

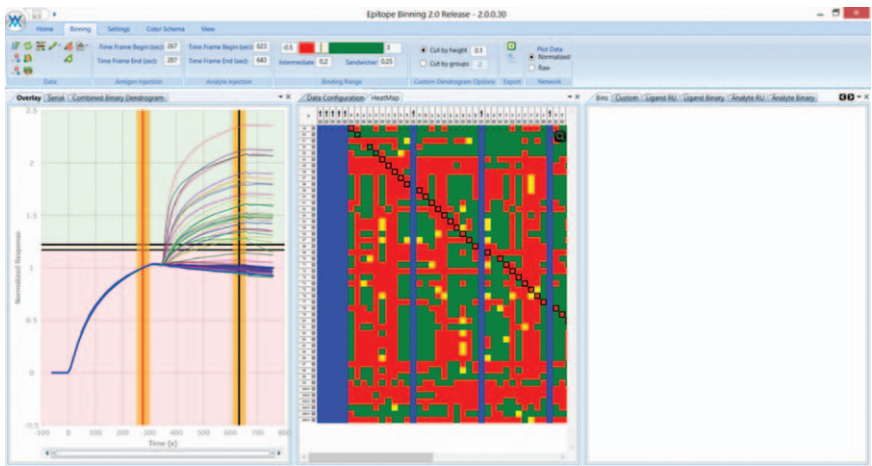


Figure 9.10 Adjustment of antigen normalization and measured response bars in sensorgram Overlay window. Thresholds are then set for sandwiching/intermediate/blocking responses.

View Online

Published on 24 May 2017 on http://pubs.rsc.org | doi:10.1039/9781788010283-00328

The Overlay window on the left side of the software interface displays sensorgram data for the ligand locations selected. Additionally, there are tabs to display the sensorgrams in a serial fashion, which is particularly useful for evaluating signal response trends over the course of the experiment. Dragging the left-most vertical bar to the end of the antigen injection phase in the Overlay window identifies the time point where the data will be normalized on a per ligand basis, in order to correct for differences in antigen binding capacities for each ligand across the duration of the experiment, as seen in Figure 9.10. The right-most vertical bar is then moved near the end of the mAb injection phase and will be used to calculate sandwiching responses of analyte mAbs binding to antigen prebound on ligand mAbs, relative to the signal of antigen alone.

In the heat map (center window), ligands are represented as rows and analyte injections are represented as columns. After the time points for ligand normalization and sandwiching have been defined, ranges specifying responses as sandwiching (green cells), blocking (red cells), or intermediate (yellow cells) can be adjusted. Intermediate values allow for highlighting of responses that are not clearly sandwiching or blocking and may require more investigation. For analysis steps subsequent to the heat map, however, intermediate are treated as sandwichers. Threshold values can be adjusted globally by making adjustments to the Binding Range values at the top of the software window in Figure 9.10. Adjustments can also be made locally to individual ligands by selecting a ligand row and then manually dragging the cutoff bars in the overlay window to the desired location. Locally adjusted ranges are denoted with a black dot next to that ligand in the heat map.

To remove ligand mAbs that display insufficient antigen biding, an example of which is shown in Figure 9.11, these mAbs are first selected using the Highlighting dropdown and then any ligand with insufficient antigen

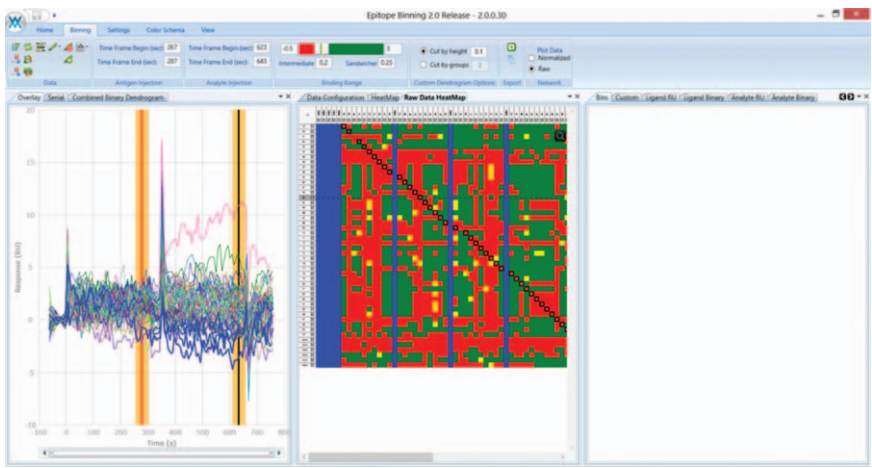


Figure 9.11 An example of a ligand with sensorgrams showing no appreciable binding to antigen.

View Online

binding is eliminated from the analysis, as shown in Figure 9.12. Similar processes are available to remove mAbs that fail to exhibit self/self-competition and analytes that appear inactive in the assay.

Once assignments of sandwiching, blocking, and intermediate behaviors is complete and poorly behaved ligands and analytes have been removed, the heat map is sorted. Sorting of heat map matrices can be carried out using a number of routines; in this case, an advanced binary routine is applied to group competitively similar mAbs in the heat map and also display self/self-competitive cells along the diagonal. Figure 9.13 displays the heat map post-sorting.

Published on 24 May 2017 on http://pubs.rsc.org | doi:10.1039/9781788010283-00328

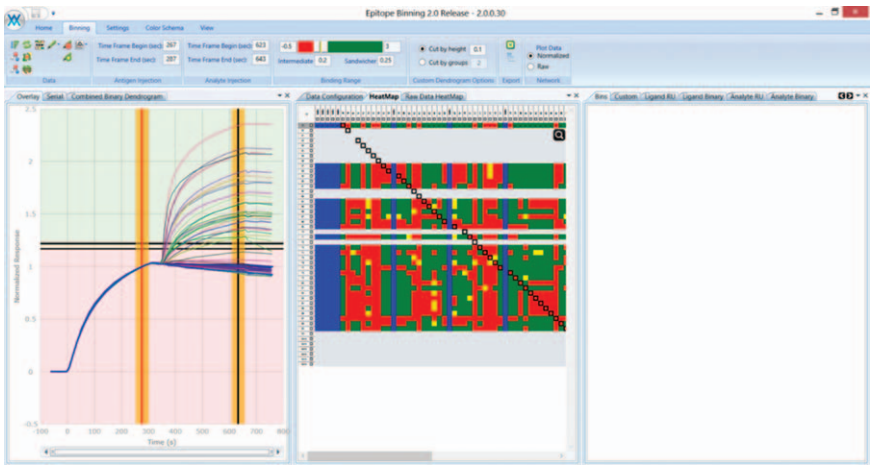


Figure 9.12 Heat map with inactive ligands and negative control ligands removed (gray rows).

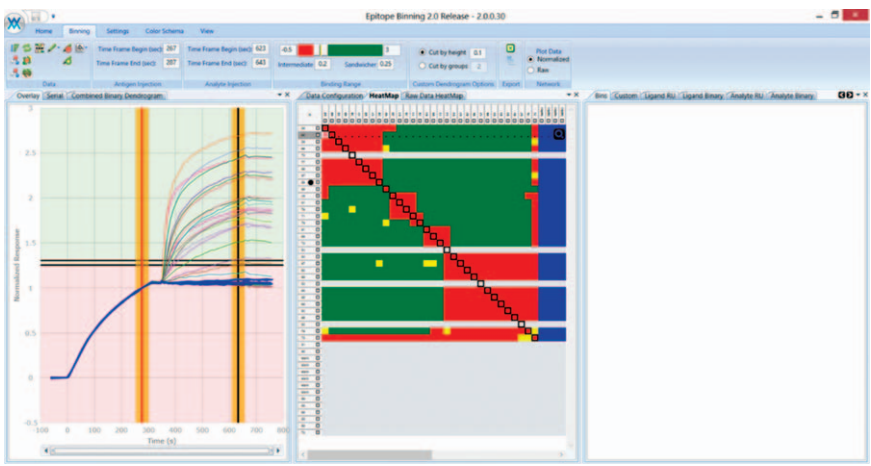


Figure 9.13 Sorted heat map.

View Online

Published on 24 May 2017 on http://pubs.rsc.org | doi:10.1039/9781788010283-00328

From the sorted heat map, dendrograms are developed using hierarchical clustering routines. These dendrograms display trends for both signal response and competitive relationships for ligands and analytes. The combined binary dendrogram, representing the competitive behaviors of the analytes and ligands, is shown in Figure 9.14. While the individual ligand and analyte dendrograms are useful for investigating behaviors in a particular orientation, the combined binary dendrogram represents the overall competitive dynamics from the binning study while taking into account the behavior of mAbs in both orientations, and is a starting point in developing network plots. The right-most window in Figure 9.14 illustrates a community network plot.

The network plot is a representation of blocking relationships between the mAbs that were tested in the experiment. Each mAb is represented by a node, and mAbs that block one another are connected by a chord. A solid line denotes a blocking interaction in both orientations, whereas a dotted line denotes a blocking relationship in one orientation and a sandwiching relationship in the other orientation, also known as an asymmetry. It is important to note that the network plot depiction is appropriate when all of the mAbs represented in the set as ligands are also tested as analytes, to form a symmetrical heat map. If this is not the case, then the absence of a connection between mAbs in the network plot that were not tested against one another in a full pairwise fashion cannot be interpreted as a lack of blocking relationship between those mAbs, and the visualization is therefore incomplete. In the case where ligands and analytes are not tested fully against one another in a pairwise fashion, the network plots should not be used. Instead, ligand or analyte clustering *via* dendrogram analysis should be performed, grouping rows with like rows, and columns with like columns.

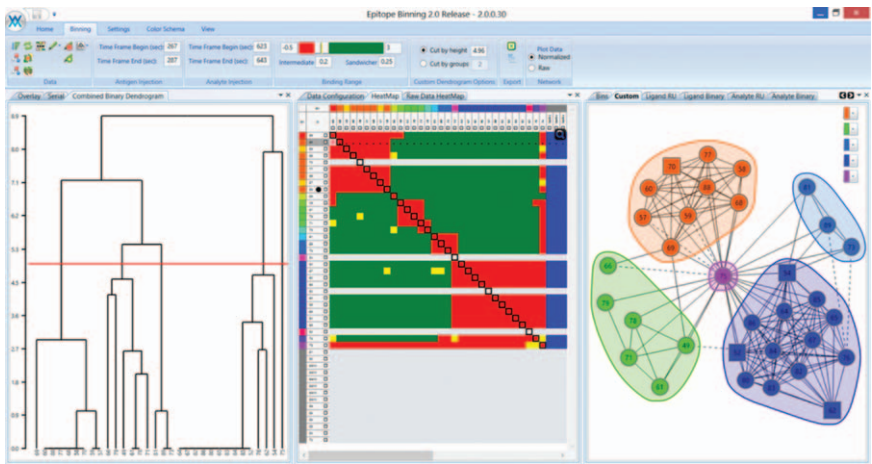


Figure 9.14 Dendrograms (left window) derived using hierarchical clustering from the heat map. In the right window is a community network plot based on the cut height (red line) set on the dendrogram.

View Online

Published on 24 May 2017 on http://pubs.rsc.org | doi:10.1039/9781788010283-00328

The network can be used to visualize ''bin'' and community ''group'' relationships within the set. An epitope bin is defined as a grouping of mAbs that behave in the same way in the epitope binning experiment. To belong to a bin, all members must exhibit *exactly* the same blocking and sandwiching behaviors as other mAbs in that bin. Hence the bins representation is the most restrictive way of organizing mAbs into like-behaved species. When a user desires to group the mAbs from a less restrictive vantage point, community detection algorithms can be used to organize the blocking networks groups of like-behaved species, rather than by exactly the same behavior of bins.

The origins of both the bin network and community network plots are based on the combined binary dendrogram structure. At the lowest, leaf portions of the dendrogram, the binning network is represented. Moving up the *y*-scale of the dendrogram transitions to the community network representation. Using community networks, mAbs can be organized into groupings that ignore minor differences in competition profiles. This allows the analyst to see much more broadly conserved behaviors and avoid some of the challenges associated with the aforementioned intermediate responses. At the same time, the discrete, binary data reprinted as bins are still close at hand.

Once the networks are established, the analyst has the opportunity to integrate data from other assays into the network plots. Data can arise from a diverse number of sources, including expression yields, kinetics/affinity, and functional assays. In Figure 9.15, functional assay data are populated in a data column and then selected for display on the community network plot. The network view now describes the functional relationships of these mAbs in the context of epitope in a visually simplified way.

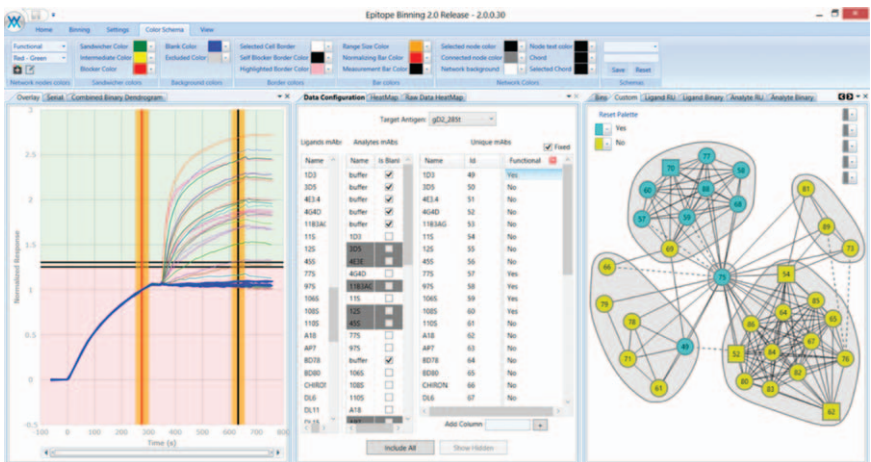


Figure 9.15 Functional yes/no assay data imported and overlaid on top of community networks.

View Online

At this point, the data file can be saved and sensorgram profiles, heat maps, bin/community lists, and network plots can all be exported.

9.6 Example of Kinetic Data Analysis

9.6.1 Introduction

In this section, an example of data analysis is presented for a kinetics study. More detailed aspects of principles of design and analysis of kinetics assays can be found in Chapter 4. The ability to determine kinetic rate constants and their utilization for the calculation of binding affinity have been core applications for biosensors for many years.[17–22] Although software tools for evaluating SPR binding kinetics differ in their layouts, they share very similar data processing functions, including referencing, blank subtraction, and fitting tools for determining rate constants. This workflow should provide the reader with an opportunity to see the basic methodology surrounding the processing of kinetic data that can be applied to many other analysis programs.

9.6.2 Experimental Design

For the experiment illustrated here, 96 discrete replicates of a single mAb were arrayed on a CMD sensor chip by EDC–NHS chemistry using a continuous flow microspotter (CFM). Following printing of the mAb array, the sensor prism was docked in an MX96 SPR imager and remaining active sites were quenched with an injection of ethanolamine. The flow cell of the MX96 encompasses all ligand locations, so that each injection sees all ligand surfaces simultaneously. A 66 kDa antigen was prepared in PBS plus Tween-20 running buffer at four dilutions from 300 to 11 nM. Following warm-up cycles of buffer-only injections, the antigen series was injected from lowest to highest concentration. Between cycles, 50 mM glycine (pH 2.0) was used to regenerate the sensor surface back to baseline. Interspot regions of non-activated CMD were used as references. At the conclusion of the experiment, glycerol injections were made using an automated routine in order to calibrate the response across all sensing regions.

9.6.3 Preprocessing of Data Using SPRint

Although Scrubber can be used as a standalone tool for data analysis, initial processing of the data was carried out in the SPRint software as it is designed specifically to handle the data format from this instrument. Descriptions of processing steps using SPRint can be found in the section on epitope binning (Section 9.5), but in brief the sensorgram signals were calibrated, locally referenced, blank subtracted, aligned, and zeroed (SPRint allows one to ''CRAZE'' the data: Calibrate, Reference, Align, Zero, and Export). Particular attention was paid to evidence of non-specific binding and

Published on 24 May 2017 on http://pubs.rsc.org | doi:10.1039/9781788010283-00328

View Online

regeneration efficiency. Once all of the initial processing steps were complete, the data were exported for kinetic fitting using Scrubber.

9.6.4 Global Kinetic Analysis in Scrubber 2.0 HT

When the file is first opened in Scrubber, the left window displays a table view of ligands (rows) and injections (columns). Sensorgrams for all cycles are overlaid in the right-hand window, as seen in Figure 9.16. There are many options in Scrubber, detailed as tabs across the top of the active windows, although not all will be necessary for a given study. For example, zeroing was previously done in SPRint and for this example it will therefore not be needed.

Columns and rows in the data table not required for kinetic fitting can be excluded from analysis by right clicking and choosing Hide; in this experiment, adjacent buffer-only injections were excluded from the fitting routine using this process. Next, antigen titration order, starting concentration, and dilution factor are assigned in the Stock Conc and Dilution Factor fields. In the data table, numerical assignment of antigen injection order is carried out by highlighting each column and labeling the highest concentration as 1, the second highest as 2, and so on. In this example, 300 nM was the maximum antigen concentration and was diluted threefold, so 300 n (n being an abbreviation of nM and u for μM) and 3 are placed in their respective fields. It is advantageous to use this automated calculation of

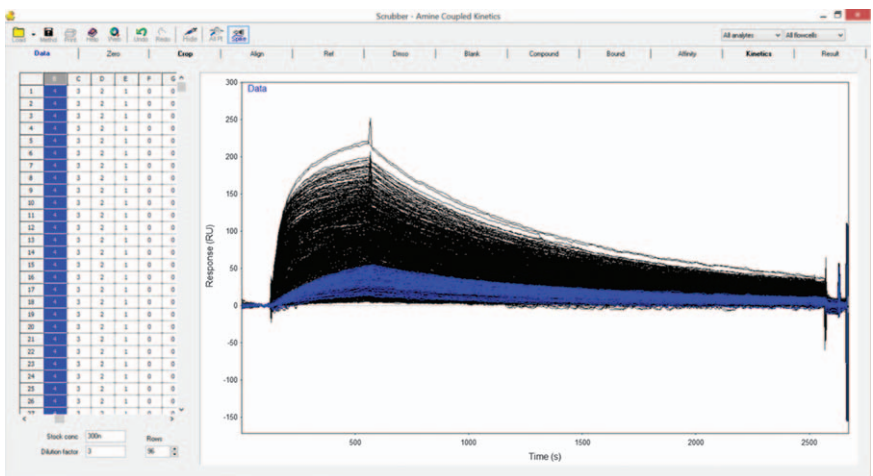


Figure 9.16 Data table view of mAb:antigen kinetic experiment in the Scrubber 2.0 HT. Columns in the left panel denote injections and rows indicate ligand locations. Numbering of columns in a low to high orientation dictates the titration order of antigen injections, with concentration and dilution factor values assigned below. The right panel displays an overlapped view of all sensorgrams in the experiment.

Published on 24 May 2017 on http://pubs.rsc.org | doi:10.1039/9781788010283-00328

View Online

Published on 24 May 2017 on http://pubs.rsc.org | doi:10.1039/9781788010283-00328

titration points as it reduces the chance of an individual concentration being incorrectly entered.

The next processing step is to remove regions of data not required for fitting. In the Crop tab, vertical bars can be adjusted to bound data for inclusion (Figure 9.17). All data points outside these bars are removed from the analysis going forward. Data for removal would be, for example, sensorgram profiles for the regeneration step. Lastly, there is an option for Despiking, which is primarily for very short-term data artifacts such as minor air spikes.

After cropping, the data are now ready for kinetic fitting under the Kinetics tab (Figure 9.18). In this tab, the k_d radio button is selected to display a list of ligands in the left-hand window and the corresponding overlaid sensorgrams on the right. The green vertical bar identifies the start of the injection, the blue vertical bar is moved to denote the end of the injection phase, and then Fit is selected to find a global fit of k_d for each ligand titration series. Fits are displayed in red. Once the global fitting routine for k_d is complete, these fits are fixed by selecting the k_d column and choosing Fix.

Fixing the off-rates allows the software to make a better initial approximation of the k_a values by not factoring variable k_d values into the model. The k_a/k_d radio button is next selected and Fit is chosen to first fit the k_a values. Once k_a/k_d fitting is complete, the k_d column is selected and Float is chosen in order for the model to find a solution in the context of both k_a and k_d (Figure 9.19). Fitting for k_a and k_d in other software tools can be done similarly to this workflow, although in some tools k_a/k_d fitting is a single selection and does not require separate k_d fitting prior to k_a.

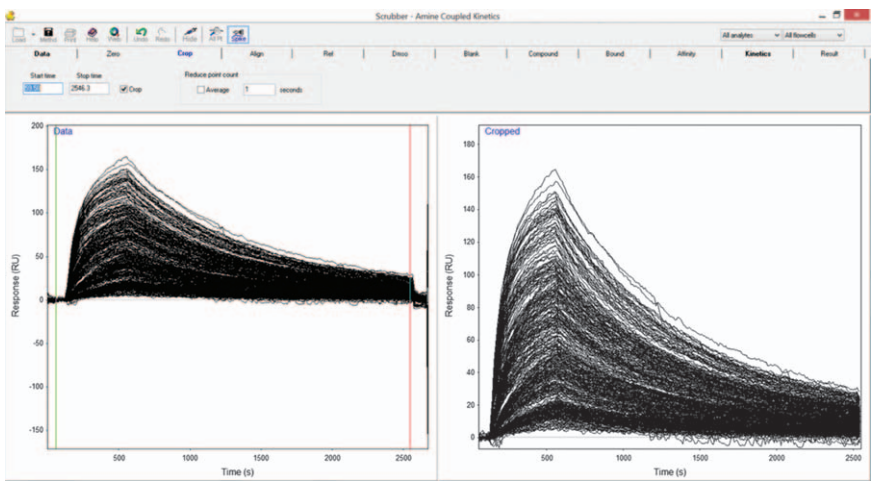


Figure 9.17 View of sensorgrams pre- (left panel) and post-cropping (right panel). In this example, additional baseline prior to antigen injection and refractive index shifts resulting from injection of regeneration solutions were removed.

View Online

Published on 24 May 2017 on http://pubs.rsc.org | doi:10.1039/9781788010283-00328

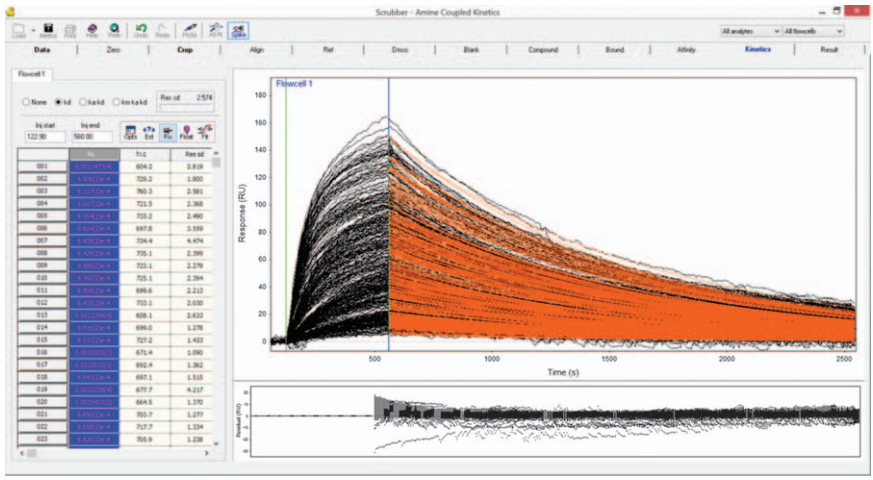


Figure 9.18 Initial fit of off-rates in the Kinetics tab. After fitting is completed, the k_d column is highlighted and Fixed prior to fitting of k_a using the k_a/k_d radio button.

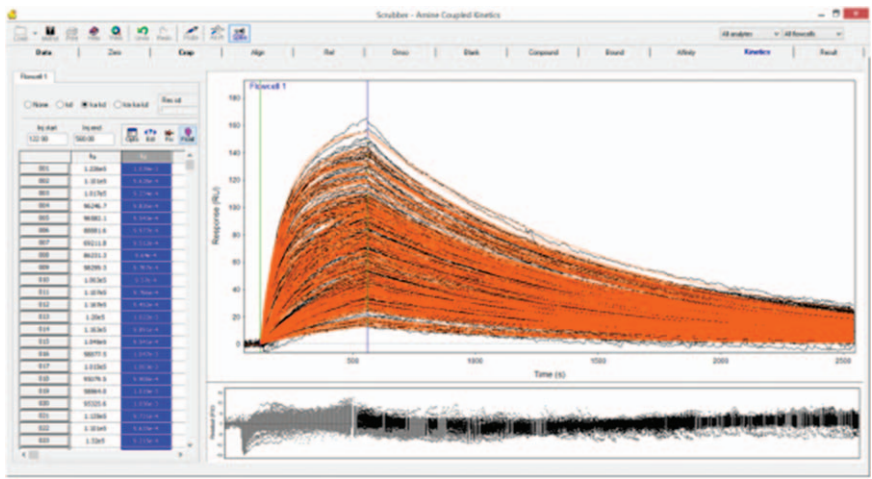


Figure 9.19 After initially fitting the data set for k_a, the k_d column is selected and allowed to Float so that a solution for both variables can be simultaneously obtained.

The fitting routine in Scrubber uses a 1 : 1 Langmuir model. Other software programs may provide additional models, but caution should be used in applying these to a kinetic fit unless the interaction has been well characterized.

On the Results tab, experimental sensorgrams and kinetic fits are plotted in a tiled view on a per ligand basis, by selection of the Anlyt and Sim icons on the right side of the interface (Figure 9.20). This particular footprint corresponds to each well (A1 through H12) of the 96-well source plate used

View Online

Published on 24 May 2017 on http://pubs.rsc.org | doi:10.1039/9781788010283-00328

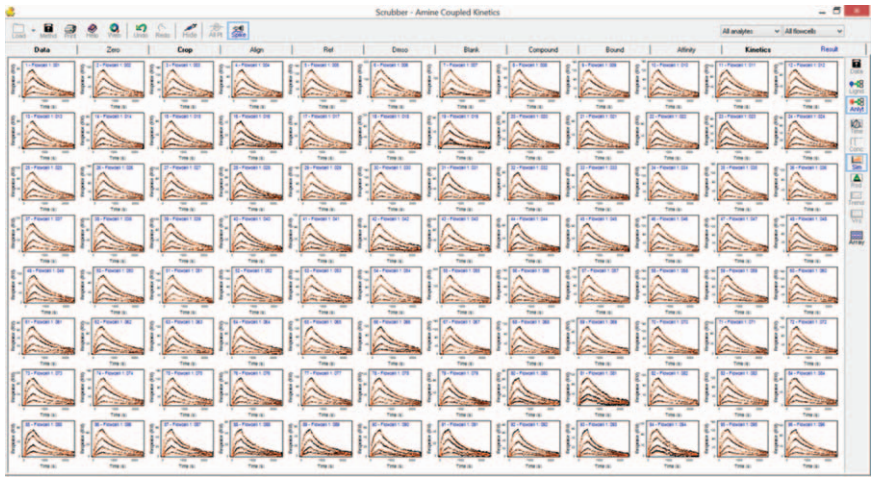


Figure 9.20 In the Results tab, tiled view of all 96 ligand replicates printed in the array. The layout corresponds to positions in the micro-well source plate used for printing.

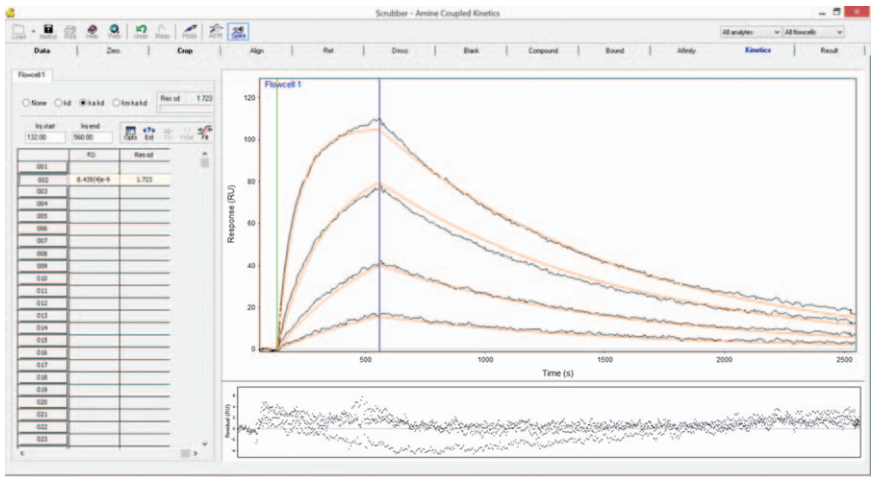


Figure 9.21 Kinetics tab view with individual ligand selected and corresponding sensorgrams displayed. After inspection of fits, data can be copied from this table for further analysis.

for printing the mAb array. This can be an excellent way to scan a large panel quickly for any discrepancies in fitting.

To follow up on specific ligands, the user can return to the Kinetics tab (Figure 9.21) and curves can be inspected individually by selecting specific ligands in the table and observing profiles and residuals. Right clicking on the table allows for export of all pertinent data including k_a, k_d, R_{max}, K_D, and the standard deviation of residuals (Res SD).

View Online

9.7 Conclusions

Software tools have become indispensable in real-time label-free biosensor workflows. In conjunction with hardware advances, they are redefining the role of biosensors, particularly in life science research. Although software can greatly simplify assay design and data analysis, it does not replace a thorough understanding of the principles fundamental to quality biosensor data. Additionally, the breadth of biosensor applications dictates that there is not a one-size-fits-all approach to study design and analysis. Fortunately, with attention to these key principles, the implementation of software tools can greatly expand the accessibility and versatility of biosensors in research.

9.8 Questions

1. Which software package can be used for building a script to execute an experiment?
   A. BiaMethodWriter.
   B. TraceDrawer.
   C. Scrubber.
   D. CLAMP.
2. Prior to running a full experiment, what information could be derived by injection of an analyte across a newly prepared ligand surface?
   A. Ligand activity.
   B. Analyte titration range.
   C. Regeneration efficiency.
   D. Experimental dissociation times.
   E. All of the above.
3. What data processing step is specific for studies involving small molecules?
   A. Local referencing.
   B. Blank subtraction.
   C. Excluded volume correction.
   D. Cropping.
4. What is competitive epitope binning primarily used for?
   A. Determining rate constants.
   B. Clustering of mAbs based on shared antigen binding sites.
   C. Antigen concentration analysis.
   D. Biomarker screening.
5. What are the three types of competitive epitope binning formats?
   A. Classical, premix, tandem.
   B. Premix, tandem, complex.
   C. Classical, tertiary, premix.
   D. None of the above.
6. What kinetic fitting model does Scrubber use?
   A. Heterogeneous analyte.
   B. Bivalent analyte.
   C. Two-state.
   D. One-to-one.

Published on 24 May 2017 on http://pubs.rsc.org | doi:10.1039/9781788010283-00328

View Online

Acknowledgements

The authors acknowledge the Cohen–Eisenberg laboratory at the University of Pennsylvania for their support in providing the example data used here. Research reported in this chapter was supported by the NIH National Institute of Allergy and Infectious Diseases under award number R44AI127039.

Published on 24 May 2017 on http://pubs.rsc.org | doi:10.1039/9781788010283-00328

References

1. Advertisement. *PC Computing* 54–55 (1990).
2. P. Schuck and Minton, *Trends Biochem Sci.*, 1996, **21**, 458–460.
3. A. Onell and K. Andersson, *J. Mol. Recognit.*, 2005, **18**, 307–317.
4. SPR Pages. *Software* (2016). Available at: http://www.sprpages.nl/downloads/software.
5. D. G. Myszka, *J. Mol. Recognit.*, 1999, **12**, 279–284.
6. D. G. Myszka and T. Morton, *Trends Biochem Sci.*, 1998, **23**, 149–150.
7. R. L. Rich and D. G. Myszka, *Curr. Opin. Biotechnol.*, 2000, **11**, 54–61.
8. R. Karlsson and A. Fält, *J. Immunol. Methods*, 1997, **200**, 121–133.
9. D. G. Myszka, T. A. Morton, M. L. Doyle and I. M. Chaiken, *Biophys. Chem.*, 1997, **64**, 127–137.
10. Y. N. Abdiche, D. S. Malashock, A. Pinkerton and J. Pons, *Anal. Biochem.*, 2009, **386**(2), 172–180.
11. Y. N. Abdiche *et al.*, *J. Immunol. Methods*, 2012, **382**(1–2), 101–116.
12. Y. N. Abdiche *et al.*, *PLoS One*, 2014, **9**(3), e92451, DOI: 10.1371/journal.pone.0092451.
13. P. Estep *et al.*, *MAbs*, 2013, **5**, 270–278.
14. B. D. Brooks, A. R. Miles and Y. N. Abdiche, *Drug Discovery Today*, 2014, **19**, 1040–1044.
15. F. Ylera, S. Harth, D. Waldherr, C. Frisch and A. Knappik, *Anal. Biochem.*, 2013, **441**, 208–213.
16. M. Wadhwa, I. Knezevic, H.-N. Kang and R. Thorpe, *Biologicals*, 2015, **43**, 298–306.
17. P. S. Katsamba *et al.*, *Anal. Biochem.*, 2006, **352**, 208–221.
18. G. A. Canziani, S. Klakamp and D. G. Myszka, *Anal. Biochem.*, 2004, **325**, 301–307.
19. A. Gertler *et al.*, *J. Biol. Chem.*, 1996, **271**, 24482–24491.
20. D. Altschuh *et al.*, *Biochemistry*, 1992, **31**, 6298–6304.
21. R. Karlsson, A. Michaelsson and L. Mattsson, *J. Immunol. Methods*, 1991, **145**, 229–240.
22. A. W. Drake, D. G. Myszka and S. L. Klakamp, *Anal. Biochem.*, 2004, **328**, 35–43.

Published on 24 May 2017 on http://pubs.rsc.org | doi:10.1039/9781788010283-00356

CHAPTER 10

Biolayer Interferometry (Octet) for Label-free Biomolecular Interaction Sensing

DAVID O. APIYO

Pall FortéBio, 47661 Fremont Boulevard, Fremont, CA 94538, USA
Email: david_apiyo@pall.com

10.1 Introduction to Biolayer Interferometry (BLI)

Label-free biosensing technologies have been growing in popularity ever since the introduction of the first Biacore instrument [surface plasmon resonance (SPR)]-based systems in 1990.[1] They are systems that convert biological responses into signals without the use of a fluorescent label. These systems are used to perform biomolecular kinetic analysis, to measure the presence and concentration of biomolecules, and to determine the strength of interactions between two molecules, amongst other things. By virtue of having been the first label-free technology to become commercially available, GE Health Sciences SPR technology, as demonstrated by the Biacore family of instruments, is currently the dominant technology in the market. However, FortéBio, a division of Pall Corporation that produces and markets the biolayer interferometry (BLI) technology, has seen a rapid rise in the introduction of its Octet family of instruments into the market. The Octet is currently the fastest growing label free technology and accounts for approximately 28% of the label-free instruments market.[2] It is also the leading non-SPR label-free technology and offers a variety of advantages over SPR.

Handbook of Surface Plasmon Resonance, 2nd Edition
Edited by Richard B. M. Schasfoort
© The Royal Society of Chemistry 2017
Published by the Royal Society of Chemistry, www.rsc.org

View Online

Published on 24 May 2017 on http://pubs.rsc.org | doi:10.1039/9781788010283-00356

BLI is a label-free technique used for monitoring the interaction between two different biological molecules[3] with one, the ligand, either pre-immobilized onto a biosensor surface or immobilized during the assay, while the other, the analyte, is kept in solution. It is an optical analytical technique that utilizes the changing interference pattern of white light obtained from a tungsten lamp and shone over a reflective biosensor surface with the immobilized ligand and analyte in solution interacting. The binding between the ligand and the analyte produces an increase in optical thickness on the tip of the biosensor that can be measured as a wavelength shift from the reference surface and is a direct measure of the change in thickness of the biological layer.

Interferometry assumes thin reflective surfaces. The shift of the signal to longer wavelengths is due to the second reflective surface (Figure 10.1) moving away from the first reflective surface.

In BLI, the second surface becomes thicker and there is an effective location of the reflective surface. In Octet instruments that utilize the BLI technology, the measured spectral shift is directly related to the optical thickness change. This is an outcome of the wavelength range and sensor geometry. The optical thickness change may, however, be affected by the conformational presentations of the bound molecule on the biosensor

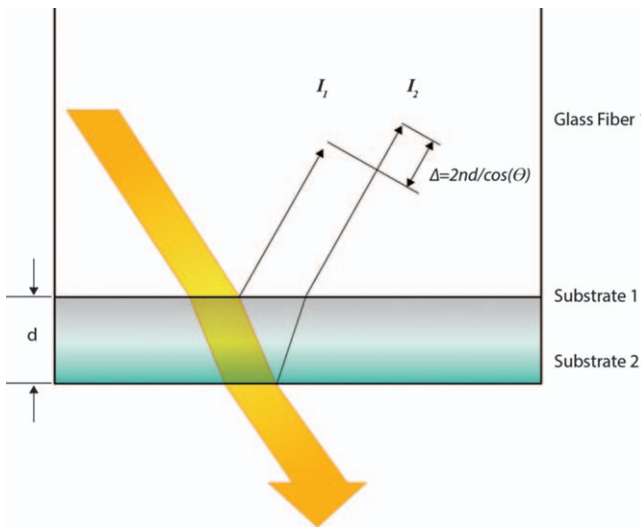


Figure 10.1 Schematic of the interference layer in BLI. Incident white light from the detector situated above the biosensor (glass fiber) results into two reflection patterns, I_1 and I_2. I_1 is the intensity reflected from substrate 1 (surface 1) and I_2 is the intensity reflected from the bottom of the surface that includes substrate 2 and the interaction with biological molecules at the tip of the biosensor surface. The two reflection intensities are correlated with the refractive index of the layer and a fixed phase shift reflection to obtain a reflectance signal as a function of wavelength.

View Online

Published on 24 May 2017 on http://pubs.rsc.org | doi:10.1039/9781788010283-00356

surface. Only molecules binding to or dissociating from the biosensor surface can shift the interference pattern and generate a response profile. Unbound molecules, changes in the refractive index of the surrounding medium, or changes in flow rate do not affect the interference pattern. This is a unique characteristic of BLI, and extends its capability for application to crude samples used in protein–protein binding, quantitation, affinity, and kinetics applications. Owing to the robust nature of the instrumentation and the ease with which crude samples can be measured, Octet systems can be used with minimal training by laboratory personnel. A typical training time of 2 h is sufficient for the independent operation of the system by most users. Octet systems have increased strongly in popularity in biopharmaceutical production and characterization applications in the last few years.

The direct measurement of biomolecular interactions plays a critical role in determining the rate of complex formation and stability. The determined affinity of an interaction is a predictive measure of the dose at which a given biopharmaceutical reagent is effective and is therefore a necessary requirement in drug development. Kinetic analysis of the interaction between biological molecules is also critical to the characterization of their functional properties and is an essential analytical step in development and production. There are endpoint methods for performing kinetic analysis, such as enzyme-linked immunosorbent assay (ELISA), that have traditionally been used for this purpose. However, the real-time capabilities of label-free technologies such as SPR and BLI offer unique insights into kinetic measurements. These techniques can provide kinetic details such as k_a and k_d values (association and dissociation rates, respectively) that offer further information on interaction mechanisms, and also affinity constants (K_D). An affinity constant measures how tightly a ligand binds to its analyte and is therefore a good indicator of the concentrations required to achieve efficacy during drug development.

10.2 BLI Platforms

BLI platforms are based on the simple format of ''Dip and Read.'' In this format, sample handling relies on the movement of the disposable fiber optic-based tips containing the sensing surface into samples presented either in the standard plate-based formats or in a sample compartment. This sampling method is advantageous over SPR-based techniques in that it allows for the specific analysis of target molecules within a crude sample such as cell culture supernatants, serum, or even plasma without the need to purify the sample, as sample clogging is not an issue. Moreover, as a result of the detection method, sample viscosity and changing refractive index concerns upon biomolecular interactions are not a major concern. BLI is therefore more robust to organic solvents and viscous media such as glycerol or poly(ethylene glycol) than would be expected in other label-free techniques; which are largely fluidics based.

View Online

Published on 24 May 2017 on http://pubs.rsc.org | doi:10.1039/9781788010283-00356

The BLI platforms include the relatively high-throughput Octet systems and the single-channel Blitz instrument. The flagship of the Octet systems is the 96-channel HTX instrument, which is capable of analyzing up to 96 samples simultaneously and utilizes both 96- and 384-well microtiter plates. The Octet 384 and Octet Red96 instruments are lower throughput than the HTX but are still capable of analyzing 16 and eight samples simultaneously, respectively. The Octet 384 utilizes both 96- and 384-well microtiter plates whereas the Octet Red96 is compatible with a 96-well microtiter plate. In addition to these high-throughput instruments, there is also the relatively low-throughput Octet K2, which is a two-channel instrument that utilizes a 96-well microtiter plate and that is designed to allow users to analyze a maximum of two samples at a time; potentially with one channel assigned to the binding chemistry while the other channel analyzes the negative control for purposes of referencing. Although it lacks the automation capability of the Octet instruments, the Blitz; the lowest throughput instrument in FortéBio's BLI family of instruments, is nevertheless just as versatile. It is a one-channel instrument that uses a sample drop compartment or Eppendorf tubes for sample loading and that has the advantage of a sample compartment requiring as little as 4 μL of sample; a simple single drop of sample is needed for the rapid analysis of the presence or absence of the target protein during a bioprocess in a yes-or-no analysis format. It is also capable of performing full kinetic characterization of most molecules. The features and capabilities of each of these instruments are summarized in Table 10.1.

10.3 BLI Biosensors

Biosensors are analytical sensing devices that can indicate the presence and/or amount of biological materials in a sample with which they come into contact by generating a signal response. The signal can be one of many physical means – potentiometric, electrical, capacitive, thermal, optical, acoustic, resonator, and others. Examples of biosensors abound in research and commercial literature, from pregnancy tests to glucose monitors, to label-free optical biosensors. Many commercial organizations provide access to optical biosensors for the analysis of biopharmaceuticals.[4] The information provided by each biosensor is similar; however, the flexibility of operation, data analysis, and throughput are significantly different. Unlike techniques that measure the change in refractive index following the interaction between biological molecules, such as SPR, BLI utilizes a biosensor composed of a fiber optic material functionalized at the tip (Figure 10.2A).

The biosensor has a proprietary biolayer at the tip that creates the reference surface of the light interference pattern. When a molecule binds to this biosensor surface, a second interference pattern is registered by the detector. This second interference pattern depends on the optical density created. BLI measures the difference in the reflection light wavelength between these two surfaces (Figure 10.2B) and reports the response in nanometers in real time.[5]

Published on 24 May 2017 on http://pubs.rsc.org | doi:10

Table 10.1 Specifications and capabilities of BLI platform instruments.

Property	BLItz	Octet QKe	Octet QK384	Octet RED96	Octet RED384	Octet HTX
Molecular weight range (Da)	>10 000	>5000	>5000	>150	>150	>150
No. of spectrometers	1	1	2	8	16	16
No. of channels per read	1	1–8	1–16	1–8	1–16	1–96
Microplate positions	N/A	1	2	1	2	2
Biosensor reracking	N/A	Yes	Yes	Yes	Yes	Yes
Robot compatible	No	No	Yes	No	Yes	Yes
Sample vessel formats	Drop holder or 0.5 mL tube	96/96 HA	96/96 HA 384/384 TW	96	96/96 HA 384/384 TW	96/96 HA 384/384 TW
Minimum sample volume	4 μL	80 μL per well	40 μL per well	180 μL per well	40 μL per well	40 μL per well
Affinity range (approximate)	1 μM to 0.1 nM	0.1 mM to 10 pM	0.1 mM to 10 pM	0.1 mM to 10 pM	0.1 mM to 10 pM	0.1 mM to 10 pM
Sample usage	Non-destructive and recoverable					
Temperature control	None	4 °C above ambient to 40 °C				
21 CFR Part 11 compliance	Available as option for all systems					

View Online

Published on 24 May 2017 on http://pubs.rsc.org | doi:10.1039/9781788010283-00356

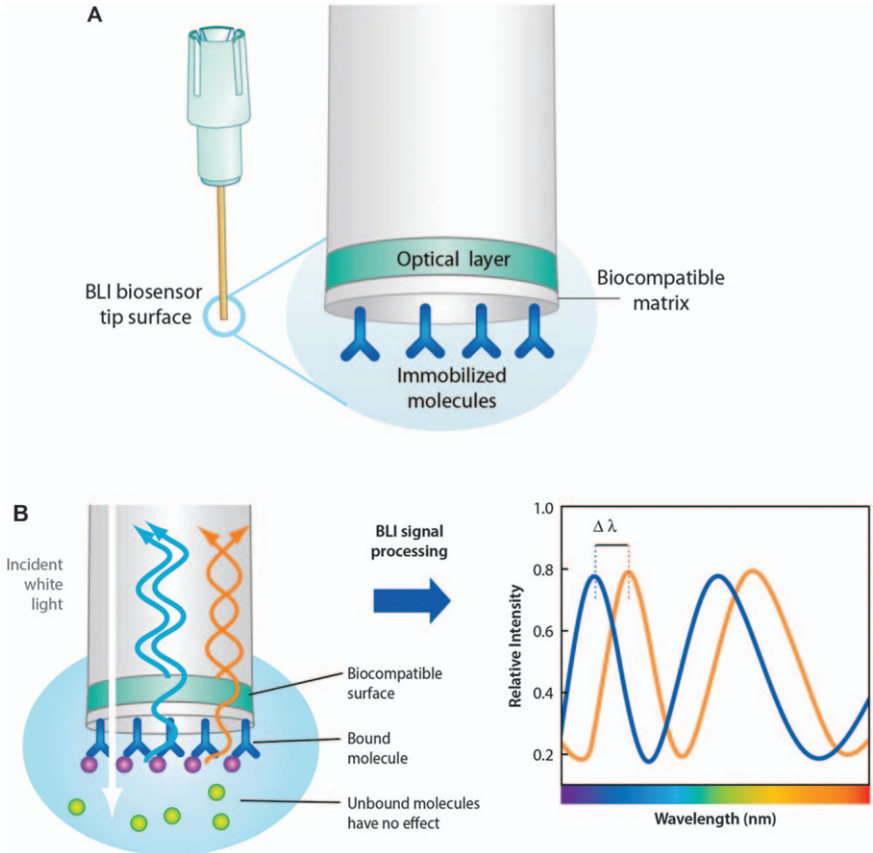


Figure 10.2 (A) BLI biosensor surface showing optical layer with the functionalized surface. Reproduced with permission from A.T. Renee, and K. Sriram, *FortéBio Application Note 14: Biomolecular Binding Kinetics Assays on the Octet Platform*, 2014. (B) Relative intensity of the light reflection pattern from the two surfaces on the biosensor. The BLI systems measure the difference in reflected light wavelength ($\Delta\lambda$) between the two surfaces. Reproduced with permission from T. Renee and M. Weillei *FortéBio Application Note 19: Analysis of FcRn–Antibody Interactions on the Octet Platform*, 2016.

This means that the SPR unit RU = μRIU that corresponds to refractive index changes and is calibrated, *e.g.*, with glycerol concentrations cannot be applied directly to BLI technology.

10.3.1 Biosensor Selection

FortéBio's BLI technology comes with a wide selection of biosensor surfaces. The biosensors are coated with a proprietary biocompatible matrix that is uniform and non-denaturing with minimal non-specific binding. The tips

View Online

Published on 24 May 2017 on http://pubs.rsc.org | doi:10.1039/9781788010283-00356

are derivatized and are available in a number of preconfigured chemistries that are tailored for use in measuring the concentration of biopharmaceuticals and contaminants present in biopharmaceutical preparations. The selection of a biosensor should be based on its intended use, kinetics or quantitation. The biosensors are therefore categorized into three groups: kinetics (K), quantitation (Q) and both kinetics and quantitation (K and Q) biosensors. The classification is based on the potential stability of the immobilized molecule on the biosensor for kinetics assays and on the biosensors reproducibility for quantitation assays. For kinetics assays, the most commonly used surface is streptavidin. With this surface, the ligand is first biotinylated to allow for immobilization through the formation of a biotin–streptavidin bond. Since streptavidin has a very high affinity for biotin,[7] this is the recommended surface when investigating high-affinity interactions – typical molecules that bind with sub-nanomolar affinities. In addition to streptavidin biosensors, the second-generation amine reactive biosensors (AR2G) are also suitable for use in high-affinity characterization. Since both biosensors use chemistries that target the primary amino groups in biological molecules (N-terminal and epsilon primary amino groups), such as can be found in lysine residues, it is critical that the ligand be purified (for specificity) and be devoid of any competing primary amino groups such as are usually found in some buffers or in preservative reagents. Both biosensor surfaces are recommended for biomolecular interaction studies where purified ligand is available and where tight affinity is expected. For non-purified ligands, the BLI systems require capture-based biosensors such as anti-human capture (AHC) and anti-mouse capture (AMC). These biosensors have the added advantage that they can be easily regenerated with the appropriate regeneration conditions and can therefore be reused many times. Regenerated biosensors are quality controlled to be reused approximately 10 times and should be processed according to FortéBio's recommendations for proper storage if the reuse is not immediate.

Biosensor surfaces such as Ni-NTA biosensors can be used for both kinetics and quantitation assays. Others, such as protein A or protein G biosensors, can only be used for quantitation assays. In selecting a biosensor surface for a quantitation experiment, it is important to keep in mind the quantitation dynamic range for the selected biosensor (Table 10.2). It may be necessary in some cases to establish this dynamic range in an optimization study as the range may be different for different samples and in different media. Table 10.2 gives general guidelines for the dynamic range for each biosensor surface.

Although FortéBio classifies the biosensor surfaces for kinetics, quantitation or kinetics and quantitation use, it is important to keep in mind that these classifications are based purely on the stability of the ligand on the biosensor upon immobilization and the expected affinities to the analyte for the kinetics biosensors. If the expected affinity is relatively weak (weaker than that of the ligand to the derivatized biosensor), then it is

Published on 24 May 2017 on http://pubs.rsc.org | doi:10

Table 10.2 Biosensors classified by applications.

Biosensor type	K, Q, K & Q	Application	Quantitation dynamic range	Regeneration
Aminopropylsilane (APS)	K	Binding measurement of lipids, liposomes, hydrophobic proteins that do not have other methods of surface attachment	N/A	Protein and analyte dependent, users should validate their own assays
Amine-reactive 2G (AR2G)	K	Covalently immobilizing any molecule with a terminal amine group for all kinetic analyses	N/A	Protein dependent
Super streptavidin (SSA)	K	Small molecule and fragment analyses only, should not be used for large-molecule measurements	N/A	Analyte compounds can be washed off during dissociation in buffer since most have fast off-rates
Anti-human Fc capture (AHC)	K	Capturing human IgGs or human Fc fusion proteins for kinetic analysis with various analytes	N/A	Yes for K
Anti-mouse Fc capture (AMC)	K	Capturing mouse IgGs or mouse Fc fusion proteins for kinetic analysis with various analytes	N/A	Yes for K
Streptavidin (SA)	K	Immobilizing biotinylated molecules for all kinetic analyses	N/A	Protein dependent
High-precision streptavidin (SAX)	K & Q	Immobilizing biotinylated molecules for high precision quantitation and kinetic measurements	N/A	Protein dependent
Ni-NTA (NTA)	K & Q	Quantitation of His-tagged proteins in buffer or diluted matrix, capturing of His-tagged proteins for kinetic analyses with various analytes	Protein dependent, typically 0.5–1000 $\mu g\,mL^{-1}$	Yes for K, no for Q

Published on 24 May 2017 on http://pubs.rsc.org | doi:10

Table 10.2 (*Continued*)

Biosensor type	K, Q, K & Q	Application	Quantitation dynamic range	Regeneration
Anti-human Fab-CH1 (FAB)	K & Q	Quantitation of human IgG and Fab and $F(ab')_2$, capturing of human IgG and Fab and $F(ab')_2$ for kinetic analyses with various analytes	Analyte dependent, typically 0.5–1000 $\mu g\,mL^{-1}$	Yes for K, yes for Q (5× in a narrower dynamic range, 5–500 $\mu g\,mL^{-1}$)
Anti-GST (GST)	K & Q	Quantitation of GST-tagged proteins, direct capturing of GST-tagged proteins for kinetic analyses with analytes	Protein dependent, typically 0.1–2000 $\mu g\,mL^{-1}$	Yes for K, no for Q
Anti-penta-His (HIS1-K)	K & Q	Quantitation of His-tagged proteins in matrix and capturing His-tagged proteins for kinetic analysis	Protein dependent, typically 0.1–500 $\mu g\,mL^{-1}$	Yes for K
Anti-human IgG Fc (AHQ)	Q	Quantitation measurements of human IgGs or human Fc fusion proteins	0.025–200 $\mu g\,mL^{-1}$	No
Anti-murine IgG Fv (AMQ)	Q	Quantitation measurements of mouse IgGs or mouse $F(ab')_2$	0.1–200 $\mu g\,mL^{-1}$	No
Anti-His (HIS2)	Q	Quantitation of HIS-tagged proteins in crude matrices or buffer	Protein dependent, typically 0.1–200 $\mu g\,mL^{-1}$	Protein dependent
Protein A (ProA)	Q	Quantitation of IgGs of various species	0.025–2000 $\mu g\,mL^{-1}$	Yes
Protein G (ProG)	Q	Quantitation of IgGs of various species	0.025–2000 $\mu g\,mL^{-1}$	Yes
Protein L (ProL)	Q	Quantitation of IgGs of various species *via* the kappa light chain	0.05–2000 $\mu g\,mL^{-1}$	Yes

View Online

Published on 24 May 2017 on http://pubs.rsc.org | doi:10.1039/9781788010283-00356

possible to use a quantitation classified biosensor for a kinetics experiment such as in yes/no binding investigations or screening experiments. For quantitation however, reproducibility and precision are the key factors, hence these must be taken into consideration when selecting the appropriate biosensors.

The amine-reactive, streptavidin, aminopropylsilane, and other capture biosensors are generic surfaces that can be derivatized with appropriately modified biomolecules to create customized biosensors.

10.3.2 Regeneration of Biosensors

Regeneration of the Octet is the process of removal of either the immobilized ligand–analyte complex from the biosensor surface or the analyte from the immobilized ligand. Successful regeneration allows for the reuse of the biosensor either through a fresh immobilization or through the use of a different sample of analyte to the retained immobilized ligand. The key requirement is that the regeneration reagents do not compromise the quality of the biosensor surface or the functional integrity of the immobilized ligand. Octet biosensor surface regeneration is dependent on the capture or immobilization chemistries and the affinities and on assay requirements. Regeneration for quantitation applications must be more complete than for kinetics assays since quantitation assays are more dependent on the surface capacity of the biosensor. For example, a 20% decrease in surface capacity over 10 regeneration cycles will not affect rate constants but would affect precision of quantitation by 10–20%. Optimal regeneration conditions should completely clear the biosensor surface of the target removal molecule without compromising the biosensor's functional chemistry. Capture-based biosensors typically require the use of low-pH glycine buffer for regeneration whereas the regeneration conditions for the other biosensors often depend on the properties of the analyte in use and the affinity of binding. However, commonly used regeneration reagents include low-pH buffers, detergents, SDS, and high ionic strength buffers. The Octet platform's high-throughput sample plate format provides users with the ability to scout quickly for optimal regeneration conditions in simple design of experiment (DoE) formats where different reagents are combined or varied in concentration while monitoring their ability to deplete a bound analyte. Although most Octet biosensors can be regenerated a minimum of 10 times, the number of regeneration cycles should be investigated for each type of assay. Figure 10.3 shows regeneration cycle evaluation results for IgG binding to protein A biosensors in a quantitation assay.

The data show that no significant differences are observed between the successive cycles over the 11 cycles studied. Similarly, in a kinetics assay, where anti-human capture (AHC) biosensors were used to perform an affinity characterization of an antigen molecule towards an immobilized human IgG over several cycles (Figure 10.4), with regeneration of the biosensors using low-pH glycine buffer (pH 1.7) between cycles, the observed

Published on 24 May 2017 on http://pubs.rsc.org | doi:10

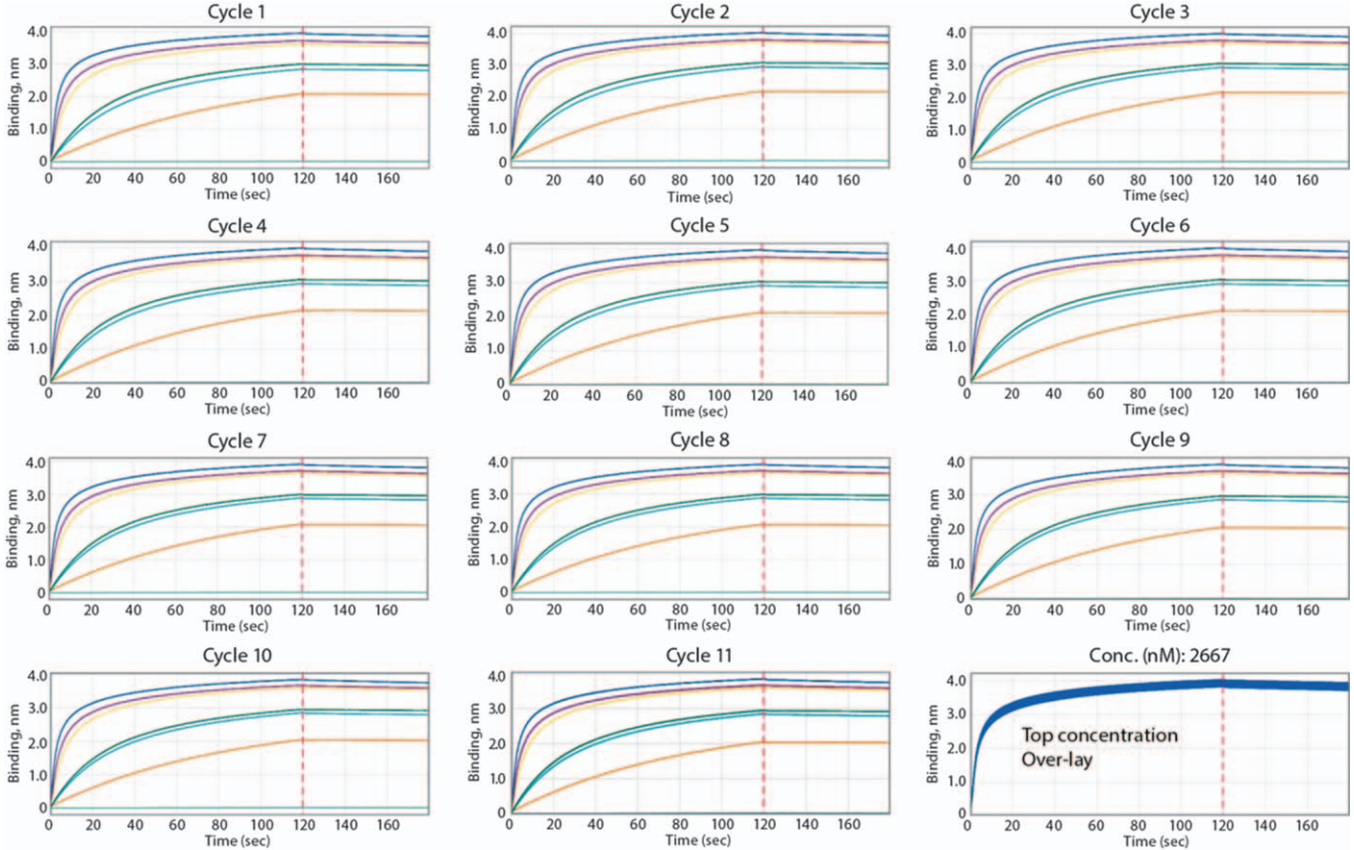


Figure 10.3 Different cycles of IgG titer determination using Octet protein A biosensors with regeneration between each cycle. Regeneration was performed using three cycles of biosensor dips into 10 mM glycine buffer (pH 1.7) for 5 s followed by biosensor dips into neutral PBS buffer (pH 7.4). The binding profiles indicate that the top concentration signals decrease from 4.0 to 3.81 nm, well within the acceptable specification of 4.03–3.61 nm for this data set.

View Online

Published on 24 May 2017 on http://pubs.rsc.org | doi:10.1039/9781788010283-00356

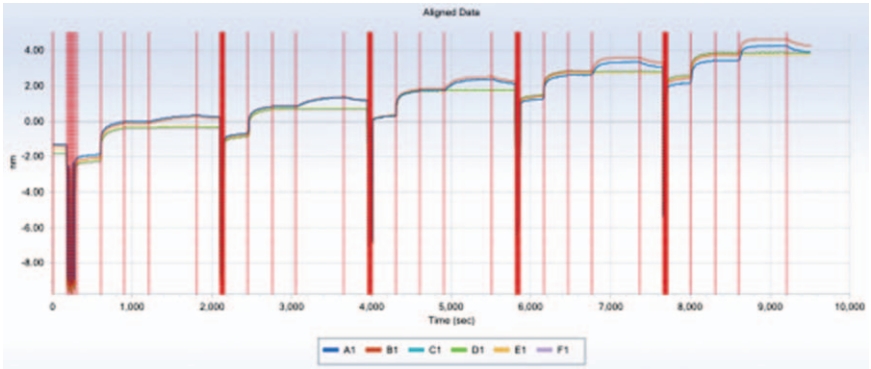


Figure 10.4 Full kinetics assay showing four cycles of immobilization of human IgG and binding of a serial dilution of the analyte followed by regeneration (thick vertical lines between each cycle).

on- and off-rates were virtually identical for the four cycles studied (Figure 10.5).

Furthermore, a global fit analysis of the data using a 1 : 1 model resulted into no differences in K_D values (Table 10.3), despite the slight reduction in signal amplitudes with successive cycles.

The two studies (quantitation and kinetics) suggest that the Octet biosensors are robust to regeneration and the maximum number of potential regeneration cycles should be evaluated on a case-by-case basis.

10.4 Basics of Binding Kinetics Using BLI

Kinetics experiments using BLI begin by binding a ligand to the surface of a biosensor tip. The ligand-bound biosensor tip is then dipped into a solution containing the analyte (association) and then the running buffer (dissociation). Measurements are taken in real time, generating binding association and dissociation curves from which the kinetic parameters k_a, k_d, and K_D are extracted.

The k_a, k_d, and K_D values are calculated by fitting the association and dissociation curves using mathematical equations. The simplest model to describe the interaction between two biomolecules is

$$A + L \underset{k_d}{\overset{k_a}{\rightleftharpoons}} AL$$

where the binding model assumes a 1 : 1 interaction between one molecule of ligand (L) bound to the biosensor surface and one of the analyte (A in solution). Complex formation in a 1 : 1 binding model follows pseudo-first-order kinetics. The rate of complex (AL) formation is dictated by the association rate constant and the concentrations of unbound ligand and analyte. The equation used to fit the association is an integration of a differential

Published on 24 May 2017 on http://pubs.rsc.org | doi:10

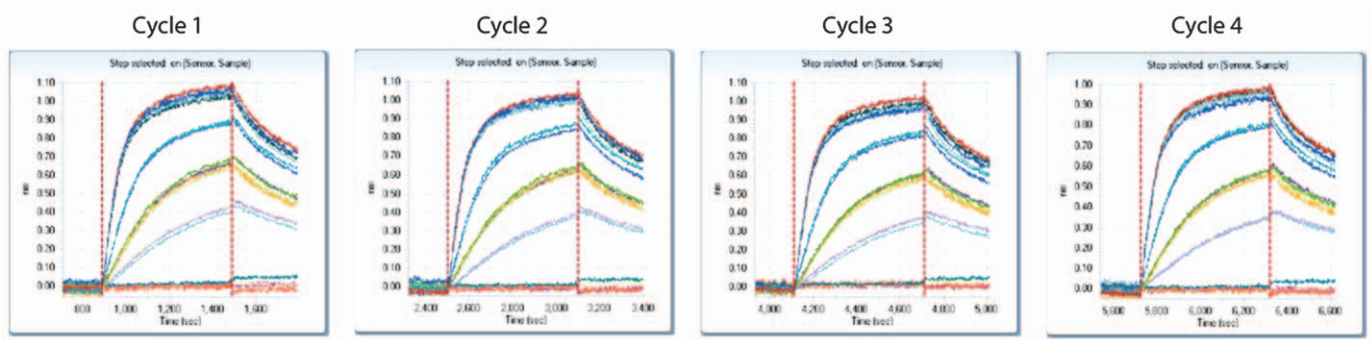


Figure 10.5 Four cycles of affinity characterization of immobilized human IgG binding to analyte in a dose-dependent manner with regeneration between each cycle. AHC biosensors were used. Despite an ~10% loss of signals by the third cycle, no significant change was observed in the association or dissociation steps of the assay.

View Online

Table 10.3 Comparison of dissociation constant (K_D) values obtained using regenerated AHC biosensors: the expected K_D of 3.66×10^{-9} M is shown at the top in bold followed by the K_D values from the successive cycles 1–4.

K_D (M)	K_{on} (L mol^{-1} s^{-1})	K_{dis} (s^{-1})
3.66×10^{-9}	**3.97×10^{5}**	**1.45×10^{-3}**
(1) 3.45×10^{-9}	4.06×10^{5}	1.40×10^{-3}
(2) 3.75×10^{-9}	3.89×10^{5}	1.46×10^{-3}
(3) 3.94×10^{-9}	3.84×10^{5}	1.51×10^{-3}
(4) 3.99×10^{-9}	3.77×10^{5}	1.50×10^{-3}

Published on 24 May 2017 on http://pubs.rsc.org | doi:10.1039/9781788010283-00356

equation showing that the rate of association is a function of the decreasing concentration of unbound ligand molecules as analyte binding occurs:

$$Y = Y_0 + A[1 - \exp(-k_{obs}t)]$$

where Y = level of binding, Y_0 = binding at start of association, A is an asymptote, t = time, and k_{obs} is the observed rate constant. At the same time as the AL complex is forming, it also decays back to A and L. The term k_{obs} reflects the overall rate of the combined association and dissociation of the two binding partners. When biosensors are dipped into buffer solution that is free of analyte, the complex begins to decay at a rate that is a function of the dissociation rate constant and the concentration of ligand–analyte complex. The equation used to fit dissociation is

$$Y = Y_0 + A[\exp(-k_d t)]$$

where Y_0 is binding at start of dissociation and k_d is the dissociation rate constant. This equation reflects the decline of the dissociation rate over time as the concentration of bound complexes on the surface decreases. The term k_d measures the stability of the complex, or the fraction of complexes that decay per second, and is expressed in units of s^{-1}. By solving the above equations for k_{obs} and k_d, the association rate constant k_a can then be calculated with the equation

$$k_a = \frac{k_{obs} - k_d}{[\text{analyte}]}$$

The association rate constant, k_a, represents the number of AL complexes formed per second in a 1 M solution of A and L. The term k_a is expressed in L mol^{-1} s^{-1}. K_D is the affinity constant, or equilibrium dissociation constant. It represents the ratio of the on-rate to the off-rate and corresponds to the concentration of analyte at which 50% of ligand binding sites are occupied at equilibrium, or the concentration at which the number of ligand molecules with analyte bound equals the number of ligand molecules without analyte bound. There is an inverse relationship between K_D and affinity. The smaller the affinity constant, the tighter is the interaction between the ligand and the analyte. In order to calculate K_D and k_a, the concentration of the analyte must be known; k_d, however, is independent of concentration.

View Online

The larger is k_d, the faster is the rate of dissociation Since k_d can be determined without knowing how much analyte is present, it is useful for screening applications such as ranking sets of unpurified binders in complex matrices.

Published on 24 May 2017 on http://pubs.rsc.org | doi:10.1039/9781788010283-00356

10.4.1 Relationship Between R_{eq}, R_{max}, and K_D

If the analyte association phase is left to run long enough, eventually the binding interaction will reach a point where the rates of association and dissociation are equal. At this point, the curve flattens out and has reached the equilibrium binding signal, or R_{eq}. Since there is a fixed amount of ligand on the surface of the biosensor, there is a maximum amount of analyte that can be bound. When the highest possible analyte binding has been reached, it is considered the maximum binding signal, or R_{max}. The value of R_{eq} relative to R_{max} depends on the analyte concentration relative to K_D. For example, if the analyte concentration is equal to K_D, then R_{eq} will occur at 50% of R_{max}.

During the association step of an assay, the rate of complex (AL) formation is a function of k_a, expressed in L mol^{-1} s^{-1}. When the biosensor is dipped into the running buffer for dissociation, the AL complex dissociates back to A and L giving k_d, which is expressed in s^{-1}. The k_d value measures the stability of the complex interaction; the larger is k_d, the less stable is the complex.

K_D is represented in mol L^{-1}, and is the ratio of the on- and off-rates. It measurers how tightly bound an analyte is to a ligand, according to

$$K_D = \frac{[A][L]}{[AL]} = \frac{k_d}{k_a}$$

For k_a and K_D to be calculated, the analyte concentration is therefore required to determine certain parameters. However, k_d is independent of concentration and the constant can be calculated without concentration.[6]

10.5 Data Acquisition and Analysis on the Octet

10.5.1 Data Acquisition on the Octet

The Octet systems come with data acquisition software that allows the user either to customize their assay setup or to use already inbuilt templates to run an experiment. The templates can also be modified to suit the user's intended assay design. The instrument has to be turned on at least 1 h prior to use to allow the lamp to warm up. After starting the Octet system hardware and the Octet data acquisition software, the following steps should be followed sequentially when designing and running an assay:[8]

1. Select the type of experiment you intend to run in the ''Experiment Wizard'', *i.e.* ''New Kinetics Experiment'' or ''New Quantitation

View Online

Published on 24 May 2017 on http://pubs.rsc.org | doi:10.1039/9781788010283-00356

Experiment.'' Within the ''New Kinetics Experiment,'' the user can select either ''Basic Kinetics'' or ''Epitope Binning,'' whereas within the ''New Quantitation Experiment,'' the user has further choices of either ''Basic Quantitation,'' ''Basic Quantitation with Regeneration,'' or ''Advanced Quantitation.'' The user can then move onto the next tab in the software by either clicking the move forward arrow or by using the menu at the top of the page.

2. Define a sample plate or import a sample plate definition from a previously designed experiment. Note that the Octet instruments are compatible with both 96- and 384-well microtiter plates, depending on the version. In addition, the higher throughput instruments can be configured to use different read heads: 8- or 16-channel read head for the Octet 384 instrument and 8-, 16-, 32-, 48-, or 96-channel read head for the Octet HTX instrument. The selected read head allows the user to define the sample plate in a compatible manner.
3. If running kinetics experiments, click on the next tab on the menu at the top of the page, ''Assay Definition.'' This window allows the user to design the assay. In this step, create a library of possible assay steps. A typical kinetics assay includes a baseline step, a loading step (ligand immobilization), another baseline step, an association step (analyte binding), and a dissociation step (dissociation of analyte depends on its affinity to the ligand). In Octet's ''Dip and Read'' plate format, since there is no laminar flow of the sample and since samples can sometimes be diffusion limited if not ''flowed'' over the chemistry surface at a sufficient flow rate, the diffusion-limited phenomenon is compensated for by shaking the sample plate to create a ''turbulent'' flow of samples around the biosensor surface. This sample plate shake speed should be set at 1000 rpm in kinetics assays but can be varied in quantitation assays.
4. Select the ''Sensor Assignment'' tab at the top of the menu. The software automatically assigns the required number of sensors for the assay based on the plate design. By default, the software requires the sensors to be placed in the first column of the biosensor tray. However, this can be customized by the user based on the actual physical position of the biosensors on the sensor plate. It is also important to instruct the software in this window on whether sensors would be reused or not when running a quantitation experiment.
5. The next tab in the acquisition software allows the user to review the experimental design and to confirm the intended setup.
6. Finally, the ''Run Experiment'' tab allows the user to assign the data storage drive and to start the experiment. In the Octet, the user is advised to use the delayed start option, which allows the system to equilibrate samples at the desired temperature for $\sim$10 min prior to starting the experiment. This is an especially useful feature when using reagents that may not be stable at low temperatures.

View Online

Published on 24 May 2017 on http://pubs.rsc.org | doi:10.1039/9781788010283-00356

10.5.2 Data Analysis on the Octet

10.5.2.1 Quantitation Data Analysis

Quantitation experiments allow the user to determine sample concentration using a reference set of standards. After an experiment has been run, the data analysis session is started by clicking on the Data Analysis software icon. A data analysis session can be used to load and analyze an experiment or to reanalyze an experiment. Analyzing a quantitation experiment can be performed with the following procedures:[9]

1. Once the data analysis software is opened, right click the experiment folder in the workstation directory and select ''Load a Folder.'' The experiment is added to the Loaded Data directory.
2. In the Loaded Data directory, click the experiment name to open it. The binding curves, sample plate, and sample plate table should appear on the screen in the data selection tab. The Octet system Data Analysis allows the user to edit sample designations. The user can exclude samples from analysis if they do not meet the sample R^2 or residual threshold. The user can also correct standard samples input concentrations if necessary before analysis. An unknown sample can also be changed to a standard sample and *vice versa*. These are done by right clicking the sample well on the sample plate and selecting the desired command. If a blank sample was run, the blank sample binding curve is subtracted from all the other curves by check marking the reference subtraction box.
3. Click on the ''Results'' tab from the menu at the top of the window to proceed to the data analysis window.
4. The first step in the data analysis window is for the user to choose the appropriate standard curve equation to use for analysis and to generate a standard curve from the standard samples used in the experiment. The unknown samples are automatically extrapolated from the generated standard curve. The standard curve equations include:
   (i) Linear Point to Point – The Octet System Data Acquisition software connects the points of the standard curve with straight line segments.
   (ii) Dose Response-4PL (Default; Unweighted) – A symmetrical dose–response curve. No points are weighted during the curve fitting.
   (iii) Dose Response-4PL (Weighted Y2) – A non-symmetrical dose–response curve with weighting applied as 1/Y2.
   (iv) Dose Response-4PL (Weighted Y) – A non-symmetrical dose–response curve with weighting applied as 1/Y (as Y increases, weighting decreases).
   (v) Dose Response-5PL (Default; Weighted Y2) – A non-symmetrical dose–response curve with weighting applied as 1/Y2.
   (vi) Dose Response-5PL (Unweighted) – A symmetrical dose–response curve. No points are weighted during the curve fitting.

View Online

Published on 24 May 2017 on http://pubs.rsc.org | doi:10.1039/9781788010283-00356

(vii) Dose Response-5PL (Weighted Y) – A non-symmetrical dose–response curve with weighting applied as 1/Y.

5. The next step in the analysis is to select the appropriate binding rate equation, the curve-fitting equation that models the binding data. Two options exist depending on the type of assay run:
   (i) Initial Slope – calculates the initial slope of the acquired quantitation data (nm s^{-1}). Choose this equation for a basic quantitation or basic quantitation with regeneration experiment.
   (ii) R equilibrium – this equation is recommended for an advanced quantitation experiment that includes amplification. This equation uses the calculated equilibrium, not the initial slope, to model the data.
6. The user has the option to change the default parameters for the zero concentration and the low concentration threshold:
   (i) Zero Conc. Threshold – Calculated binding rates less than the zero concentration threshold are reported as zero in the results table.
   (ii) Low Conc. Threshold – Clicking ''Calculate Binding'' rate causes the initial rate to be calculated using both a linear and an exponential equation. The low-concentration threshold determines which value is reported in the results table. If the result from a linear fit is below the low-concentration threshold, then the value from the linear fit is reported in the analysis table. If the result from a linear fit is greater than the low-concentration threshold, then the value from the exponential fit is reported in the analysis table. Changing this threshold can improve the precision for low-concentration samples.
7. Finally, click ''Calculate Binding Rate.''

Useful information generated from an Octet quantitation data analysis includes the following:

1. Sample ID – The name of the sample entered in the Octet System Data Acquisition software.
2. Group Type – The well designation (Standard, Unknown, Reference, or Control).
3. Binding Rate – The rate of sample binding to the biosensor computed by the Octet System Data Acquisition software using the binding rate equation specified.
4. Dilution Factor – The dilution factor used to prepare the assay sample. The dilution factor is multiplied by the well concentration to determine the *calculated concentration*.
5. Known Conc. – The user-specified standard concentration that was entered during sample plate definition.
6. Well concentration – The concentration of the analyte determined from the standard curve. The well concentration is multiplied by the dilution factor to determine the *calculated concentration*.

View Online

Published on 24 May 2017 on http://pubs.rsc.org | doi:10.1039/9781788010283-00356

7. Calc. Conc. – The sample concentration computed from the standard curve.
8. Replicate Group – A set of replicate values organized as a set to facilitate calculation of statistics.
   (i) BR AVG – The average binding rate of the replicate group.
   (ii) BR SD – The standard deviation of the binding rate of the replicate group.
   (iii) BR CV – The coefficient of variation of the binding rate of the replicate group.
   (iv) Concentration avg – The average concentration of the replicate group.
   (v) Concentration SD – The standard deviation of the concentration of the replicate group.
   (vi) Concentration CV – The coefficient of variation of the concentration of the replicate group.
9. Residual (%) – Residual = [(expected standard concentration – calculated standard concentration)]/expected standard concentration.
10. r2 (COD) – The r^2 of the curve fit used to determine the binding rate.
11. Cycle – Number of biosensor regeneration cycles.

10.5.2.2 Basic Kinetics Data Analysis

A basic kinetics experiment enables the user to determine the association and dissociation rates of a molecular interaction; required information for the determination of the affinity constant. After an experiment has been run, start a data analysis session by opening the data analysis software similarly to the procedure in quantitation assay analysis.

1. Click on the experiment folder to open it. A window will be displayed that shows the user the experiment summary as setup in the Data Acquisition software. Before continuing with the analysis, the user must remember that a kinetics experiment requires a baseline step followed by association and then dissociation, in that order. The software allows the user to edit step types in the first window to conform to this format if not originally designated as such. The steps must, however, have been run as such during data acquisition.
2. Click on the ''Processing'' tab to process the data. The ''Processing'' window provides tools for correcting binding curves using different reference subtraction and alignment options. Reference subtraction is performed based on the assay setup. Reference subtraction is optional and is not required for all applications. There are two types of references used in Octet experiments:
   (a) Reference biosensors – Used as a reference throughout the entire assay; for example, biosensors without active capture molecules.
   (b) Reference wells – Contain only assay buffer and are used to measure system drift.

View Online

Published on 24 May 2017 on http://pubs.rsc.org | doi:10.1039/9781788010283-00356

If an experiment includes reference biosensors and reference wells, the Octet System Data Acquisition software offers multiple reference subtraction methods for data processing:

(i) Reference Wells – Corrects binding data for system drift. For example, drift is measured by the interaction of the immobilized biosensors with the assay buffer. This method requires at least one row of reference wells in the sample plate. If more than one row of reference wells is selected (checked), the signals are averaged and the average signal is subtracted from the samples.

(ii) Parallel Reference Sensors – Corrects data for system artifacts or non-specific binding of the sample to the biosensor surface. This method requires one reference biosensor for each ligand biosensor.

(iii) Double Reference – Corrects the binding data for signal due to system artifacts, non-specific binding, and system drift. This method requires one reference biosensor per ligand biosensor and one or more rows of reference buffer in the sample plate.

(iv) Average Reference Sensors – Corrects the binding data using either a single reference biosensor or the average signal of multiple biosensors.

3. Click on the ''Align *Y*-axis'' option to allow for the alignment of the data to a common point on the *Y*-axis (alignment along the *X*-axis is achieved during the assay due to the parallel movement of all biosensors). Specify both a time and assay step from which to execute the alignment. The time range from the specified step will be used to calculate an average. The calculated average will be set to $y = 0$ for all curves.
4. Perform an ''Inter-step Correction'' – Allows for the correction of a misalignment between two steps due to system artifacts. Note that for the most effective inter-step correction, the baseline and dissociation steps of an assay cycle must be performed in the same microplate well. The software accords the user three options for inter-step correction:
   (a) Align to Association – Moves the baseline step on the *Y*-axis to align the end of the baseline with the beginning of the adjacent step.
   (b) Align to Dissociation – Moves the association step on the *Y*-axis to align the end of the association step with the beginning of the adjacent dissociation step.
   (c) Align to Baseline – Moves the association step on the *Y*-axis to align the beginning of the association with the end of the adjacent baseline step.
5. Click Process Data.
   The processed data effects the changes made with software creating a panel with raw data, subtracted data, and aligned data. Processing parameters can be saved at this point or the user can click on the ''Analysis'' tab in the menu at the top of the window to proceed with

View Online

Published on 24 May 2017 on http://pubs.rsc.org | doi:10.1039/9781788010283-00356

data fitting. In the analysis window, two types of kinetics analysis are available:

(a) Curve fitting – Determines the kinetic constants k_a and k_d and the affinity constant K_D by fitting the data to a specified binding model.
(b) Steady-state analysis – Determines the affinity constant K_D from the calculated or measured equilibrium response.

Curve Fitting – To analyze the processed kinetic data, specify the curve fitting options including steps to analyze, curve fitting model, type of fitting algorithm to apply (local or global), and step time to analyze.

6. Select the step(s) to include in the analysis: association, dissociation, or both:
   (a) Association only – Generates k_{obs}.
   (b) Dissociation only – Generates k_{dis}.
   (c) Association and dissociation – Generates k_{obs}, k_{on}, k_{dis}, and K_D.
7. Select the model – The mathematical model that is used to generated the fitted view:
   (a) 1 : 1 Model – Fits one analyte in solution binding to one binding site on the surface.
   (b) 2 : 1 (HL) Model – Fits the binding of one analyte in solution to two different binding sites on the surface. Kinetic parameters are calculated for two interactions (k_{on1}, k_{on2}, k_{dis1}, k_{dis2}, K_{D1}, K_{D2}).
   (c) 1 : 2 Bivalent Analyte Model – Fits the binding of one bivalent analyte to a monomeric immobilized ligand. Kinetic parameters are calculated for two interactions (k_{on1}, k_{on2}, k_{dis1}, k_{dis2}, K_{D1}, K_{D2}). The model is available in the ''Analysis'' tab – ''Model'' menu – in ''Kinetics'' mode.
   (d) Mass Transport – A heterogeneous ligand model that fits the binding of the analyte taking into account two steps: (1) transport of the analyte from the bulk solution to the surface and (2) molecular interaction of the analyte with the ligand.
8. Select the fitting algorithm. Fitting-Local – If this option is selected, the Octet System Data Acquisition software computes kinetic constants for each curve. The constants that are calculated depend on the steps that are analyzed (association only, dissociation only, or association and dissociation). Fitting-Global (Full) – If this option is chosen, an analysis includes all of the binding curve data in the group and the Octet System Data Acquisition software generates kinetic constants for the entire group. The kinetic constants that are calculated depend on the model selected. Data can be grouped by sensor or by color:
   (a) By Sensor – Groups all data from one biosensor (for example, Biosensor A1) together and applies a global fit to the group.
   (b) By Color – Groups all data that are the same color and applies a global fit to that group.

   Global fitting is generally performed using either R_{max} unlinked option – the theoretical response maximum (R_{max}) is calculated by assuming equivalent surface capacity between biosensors (R_{max} linked)

View Online

Published on 24 May 2017 on http://pubs.rsc.org | doi:10.1039/9781788010283-00356

or non-equivalent surface capacity between biosensors (R_{max} unlinked). The R_{max} unlinked option is selected when biosensors used are different for each sample in the group. R_{max} linked, on the other hand, is used when the same biosensor is used, typically in experiments where the analyte binds with a relatively fast off-rate.

Steady-State Analysis – Allows the user to analyze data based on reaction equilibrium and is especially useful with systems generating very fast on-rates or off-rates and where rate-based analysis may not suffice. There two ways to analyze kinetics data using the steady-state option:

(a) *R* equilibrium – Fits the binding curve to a 1 : 1 model and uses the calculated R_{eq} to determine the steady-state affinity. If this option is selected, you first must perform a curve-fitting kinetic analysis.
(b) Response – Takes the average response from the user-specified time window and uses it to calculate the steady-state affinity constant.

10.5.2.3 Kinetics Data Analysis Definitions

1. Color – The color of the biosensor binding curve in the Fitting and Residual view.
2. Conc (nM) – The molar concentration of the sample used in the association step. The molar concentration is entered by the user or computed by the molarity calculator during experiment setup.
3. Response – Response calculated from the time window entered in the Steady-State Analysis section.
4. K_D (M) – Affinity constant. For the 2 : 1 and 1 : 2 models, the Octet System Data Acquisition software computes two K_D values.
5. k_{on} (L mol^{-1} s^{-1}) – Rate of association. For the 2 : 1 and 1 : 2 models, the Octet System Data Acquisition software computes two k_{on} values.
6. k_{on} Error – Standard error of the rate of association.
7. k_{dis} (s^{-1}) – Rate of dissociation. For the 2 : 1 and 1 : 2 models, the Octet System Data Acquisition software computes two k_{dis} values.
8. k_{dis} Error – Standard error of the rate of dissociation.
9. R_{max} – The maximum response determined from the fit of the binding data.
10. R_{max} Error – The standard error of R_{max}. For the 2 : 1 and 1 : 2 models, the Octet System Data Acquisition software computes two R_{max} values.
11. k_{obs} (s^{-1}) – Observed binding rate. For the 2 : 1 and 1 : 2 models, the Octet System Data Acquisition software computes two k_{obs} values.
12. k_m – The mass transport rate constant.
13. k_m Error – The standard error of the mass transport rate constant.
14. R_{eq} – The calculated response at equilibrium that is determined from a fit of the binding data.
15. R_{eq}/R_{max} (%) – Ratio of R_{eq} to R_{max}.

View Online

Published on 24 May 2017 on http://pubs.rsc.org | doi:10.1039/9781788010283-00356

16. Full X2 – A measure of the goodness of curve fitting (not directly related to a parameter estimate). It is the sum of squared deviations, where *deviation* is the difference between the actual data point and the fitted curve. There is one value for each curve-fit. Values close to zero indicate a good curve fit.
17. Full R2 – R^2 is the coefficient of determination (COD). It is an estimate of the goodness of the curve fit and is not directly related to the estimate of a specific parameter. Values close to 1.0 indicate a good curve fit.
18. SSG K_D – The steady-state group K_D value. Use this feature to view quickly the steady-state-derived K_D values of groups defined within grouped view (not replicate groups). The column is populated by opening Grouped view, selecting up to three grouping parameters and activating Steady-State under additional graphs. The SSG K_D value is reported for the set of data within each pane of the Grouped view. Replicate grouping and global analysis are not used to determine this value.
19. SSG R_{max} – The steady-state group R_{max} value.

10.6 Determination of Affinity Constants Using BLI

10.6.1 Ligand Surface Immobilization

The characterization of a binding interaction on BLI to derive an affinity constant starts with the optimal immobilization of a ligand molecule onto the biosensor surface. Two approaches are used for ligand immobilization on a BLI biosensor: either a direct immobilization (Figure 10.6A) or a capture-based immobilization (Figure 10.6B).

Direct immobilization is used with both streptavidin or amine-reactive biosensors, which have the advantages that they produce very stable surfaces, are compatible with most proteins, and can generally be regenerated

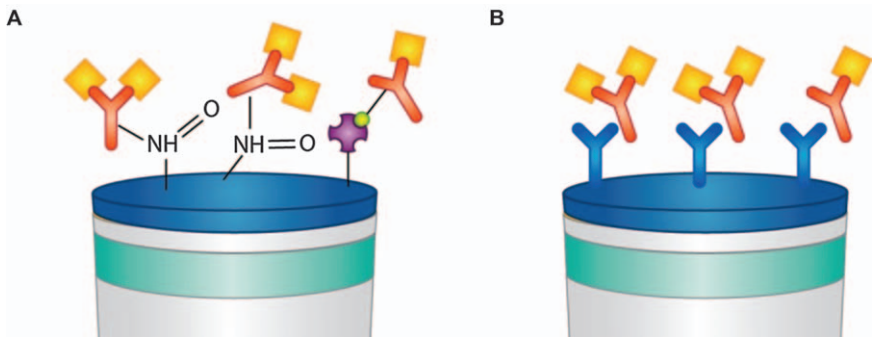


Figure 10.6 Schematics of (A) direct and (B) capture-based ligand immobilization on the biosensor surface.

View Online

Published on 24 May 2017 on http://pubs.rsc.org | doi:10.1039/9781788010283-00356

at the analyte binding step. The main disadvantages are that they require purified proteins and can create heterogeneous surfaces that may result in complex binding. In this type of immobilization, the ligand can be biotinylated and then immobilized onto a streptavidin biosensor, or an amine-reactive biosensor could be used. Amine-reactive biosensors provide a surface with a high density of carboxylic acids and a low propensity for non-specific interactions. The carboxylic acids are activated by reaction with EDC [1-ethyl-3-(3-dimethylaminopropyl)carbodiimide hydrochloride] and NHS (*N*-hydroxysulfosuccinimide) to generate highly reactive NHS esters. The esters react rapidly with the primary amines of biomolecules such as proteins and peptides to form highly stable amide bonds. The irreversible immobilization is stable in a wide range of pH conditions, from pH 0.5 to 11, and in up to 5 M salt concentration. The capture immobilization method, on the other hand, utilizes biosensors precoated with high-affinity anti-mouse or anti-human antibodies. The advantages of this approach include the fact that immobilization can be carried out with crude and non-purified samples. The method presents a capture epitope specificity through known points of immobilization, resulting in a more homogeneous surface. The biosensors can also be regenerated and reused. The main disadvantage is that the sensor surface is not as stable as would be the case for direct immobilization, which typically involves the formation of covalent bonds. As a result, this approach may not be optimal for very high-affinity interactions. Immobilization of the ligand on the biosensor surface to an optimal density is critical to obtaining good kinetic data. Whereas too low a density may lead to low analyte response, too much ligand on the biosensor can lead to data artifacts as a result of potential steric hindrance and ligand aggregation on the biosensor surface. Over-saturation may also lead to non-specific interactions from higher analyte concentrations. These artifacts may significantly impact the observed binding kinetics. A typical immobilization concentration on BLI instruments should be in the range 50–100 nM over a 300 s period. For expensive reagents where high sample concentration may not be available, lower concentrations may be used while proportionally increasing the immobilization time.

10.6.2 Binding Kinetics

Once an optimal immobilization of the ligand has been obtained, the next step in the affinity characterization is to monitor the binding of the analyte to the immobilized ligand to allow the extraction of an on-rate and a dissociation rate from which the affinity constant can be calculated. It is important to note that for an affinity constant to be calculated, the binding systems must be at equilibrium. Equilibrium will be achieved when the formation of the binding complex and the molecules dissociating after the complex formation are equal so that the net change is zero.[11]

View Online

Published on 24 May 2017 on http://pubs.rsc.org | doi:10.1039/9781788010283-00356

10.6.3 Setting Up Kinetics Assays Using BLI

It is fairly simple to set up kinetics assays using BLI systems. As with other label-free techniques, the appropriate choice of a biosensor surface chemistry and knowledge of optimal experimental conditions together with proper assay techniques and high-quality active reagents are critical to determining accurate affinity and kinetic constants and should be the first considerations.

Examples are given below of considerations for developing kinetics assays in various formats, with suggestions for designing an effective assay, optimizing each step, and minimizing potential artifacts that could arise from non-specific binding (NSB).

Biosensors come ready to use with standard binding agents such as streptavidin and amine-reactive groups, allowing for irreversible attachment of proteins essentially to create custom biosensor surfaces. Alternatively, capture agents such as anti-mouse IgG Fc capture or Ni-NTA provide a means for highly specific capture of antibodies or recombinant proteins even from unpurified samples. The most important consideration for biosensor selection is choosing a format that best maintains the structure and activity of the immobilized ligand while presenting an accessible analyte binding site. In addition, the presence of a tag such as His-tag for immobilization of the ligand may aid in the choice of whether to use a capture or a direct immobilization biosensor such as streptavidin.

Direct immobilization of a target protein to a biosensor can be accomplished by the creation of a covalent bond to free lysine residues *via* an amine-reactive biosensor (AR2G) or *via* biotin interaction with streptavidin. This method results in stable, non-reversible coupling of a molecule to the biosensor with minimal dissociation. The method is compatible with most proteins and allows the creation of a ''custom'' biosensor surface with virtually any protein, and is typically regenerable to the level of the immobilized ligand. The main constraints with this method, however, is that the ligand has to be purified for the covalent chemistries, performed under optimal buffer and pH conditions, to be effective. In addition, there is a potential for loss of ligand activity due to steric hindrance, especially when the biosensor surface is overly saturated.

The following considerations are important when performing amine coupling:

1. The ligand must be pure, must not contain any extraneous amines, or be diluted in amine-containing buffer.
2. The ligand must also be prepared in low-salt buffer and at a pH just below its p*I* value to maintain a balance between creating enough charge to attract it to the biosensor and retaining as much un–protonated lysines as possible.
3. If the ligand has been lyophilized from buffer, it may be necessary to perform a desalting or dialysis step to reduce the buffer ionic strength.

View Online

Published on 24 May 2017 on http://pubs.rsc.org | doi:10.1039/9781788010283-00356

Key considerations when performing biotinylation for use with streptavidin biosensors are as follows:

1. Biotinylation should be performed in a solution at neutral pH, typically in PBS buffer after dialysis of the sample to remove potential competing free amines.
2. The ratio of biotins per target molecule should be controlled with the aim of producing conjugates at a 1 : 1 biotin : protein ratio.
3. A long-chain linker such as EZ-Link NHS-PEG4-Biotin (Thermo, part no. 21329) or NHS-PEG12-Biotin (Thermo, part no. 21312) should be used to minimize steric hindrance effects.

10.6.3.1 Optimization of Ligand Immobilization

Achieving the optimal density of immobilized ligand on the surface of a biosensor is critical to obtaining good-quality kinetic data. Unlike in SPR, where the amount of immobilization signal required for good kinetics may be predetermined based on ligand molecular weight and percent activity, in BLI, maximum occupation of biosensor active sites by the ligand, ligand size, and conformation dictate the immobilization signal amplitude. However, an excess of ligand bound to the biosensor can lead to data artifacts due to crowding, steric hindrance, and possible aggregation on the biosensor surface. Oversaturation of the biosensor may also promote weaker non-specific interactions at higher analyte concentrations, or analyte ''walking'' or ''rebinding'' effects at lower analyte concentrations. These artifacts may significantly impact the observed binding kinetics. On the other hand, if insufficient ligand is immobilized, the analyte binding signal during the association step may be too low to detect. It is therefore critical to scout for the optimal immobilization concentration and time by loading different ligand concentrations onto the microtiter plate and screening them against binding to a constant concentration of analyte before performing full kinetics.

When performing the immobilization step in a kinetics assay, slow capture for a longer time is preferable to rapid ligand immobilization. Ideally, the binding curve in the immobilization step will show a gradual increase in signal and should not be allowed to reach saturation. A steep, fast, initial increase in signal may lead to uneven immobilization that may result in assay artifacts. A typical immobilization concentration for a ligand molecule is 50–100 nM. If the ligand concentration is low, *e.g.* below 50 nM, a longer time may be required to achieve sufficient immobilization signal. A zero-ligand biosensor should also be run as a control for determining whether the analyte binds non-specifically to the biosensor surface or not. The immobilization concentration to select for an assay should be the lowest concentration of immobilized ligand that yields an acceptable signal in the analyte association step.

View Online

Published on 24 May 2017 on http://pubs.rsc.org | doi:10.1039/9781788010283-00356

10.6.3.2 *Example of Affinity Characterization on the Octet*

As an example of a kinetics assay on the Octet instrument, an affinity characterization of the binding between the prostate-specific antigen (PSA) and an anti-human PSA mouse monoclonal antibody is presented. The following were used to run the assay: FortéBio's streptavidin biosensors, biotinylated anti-PSA antibody, human PSA antigen (30 kDa), 10 mM PBS buffer spiked with 0.1% BSA and 0.01% Tween 20. Two 96-well, black, flat-bottomed, polypropylene microtiter plates (Greiner Bio-One, part no. 655209) were used, one for the hydration of the biosensors and the other for sample filling. Samples were filled into each well at 200 μL as shown in Figure 10.7.

The stock antibody was immobilized at 12.5 $\mu g\,mL^{-1}$ for each well and into five wells to be immobilized to five biosensors. The antigen was subjected to a twofold serial dilution, resulting in six different dilutions including a zero concentration using assay buffer. The assay was run as follows:[10]

1. Baseline (buffer dip) for 60 s.
2. Antibody immobilization onto the biosensors for 600 s.
3. Baseline 2 (buffer dip) for 120 s.
4. Antigen binding (association) for 300 s.
5. Dissociation (buffer dip) for 900 s.

Note that when performing any type of affinity charaterization assay, it is important to use sample concentrations that are likely to achieve some sort of curvature in the association phase. Typical top concentrations are approximately 10–20 times the estimated K_D. When the K_D is unknown, it is advisable to start with high sample concentrations. The dissociation step time should be set based on the expected affinity constant, with longer times being used for very tight binders.

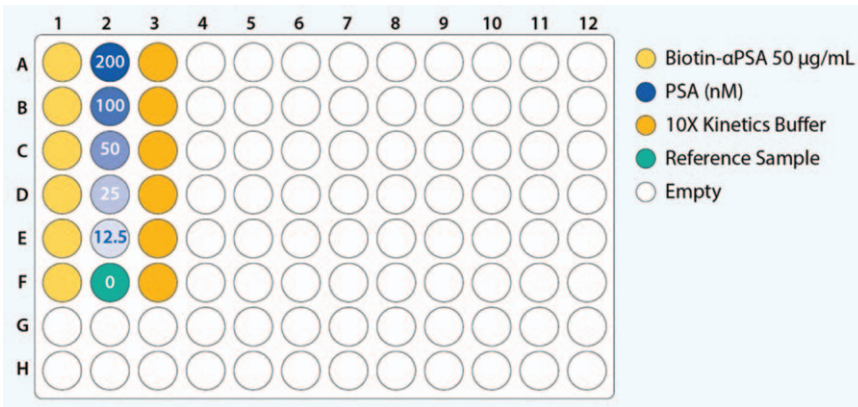
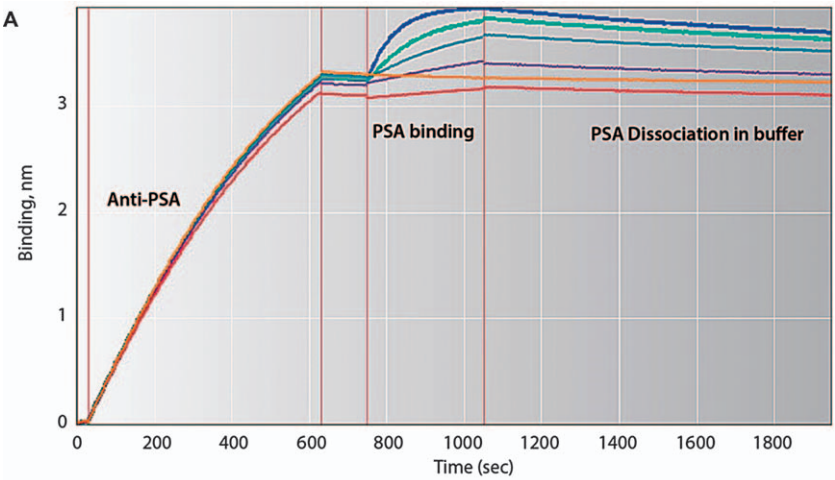


Figure 10.7 Sample plate configuration for the assay steps and sequence for anti-PSA antibody-binding PSA antigen.

View Online

Published on 24 May 2017 on http://pubs.rsc.org | doi:10.1039/9781788010283-00356



K_D (M)	k_{on}(1/Ms)	k_{dis}(1/s)
5.14E-09	6.72E+04	3.45E-04

Figure 10.8 (A) Raw data curves showing all the steps for the anti-PSA antibody–PSA antigen binding assay on the Octet. Reproduced with permission from T. Renee, *Fortebio Technical Note 38*, 2013, 2–3. (B) Anti-PSA–antibody binding to PSA antigen in a dose-dependent manner. Data were fitted to a global 1 : 1 fit. Reproduced with permission from T. Renee, *FortéBio Technical Note 38*, 2013, 2–3.

Figure 10.8A and B show the raw data and the processed and analyzed curves, respectively, for the dose dependent binding of PSA to anti-PSA antibody. Data were analyzed using a global fit with a 1 : 1 model. The 1 : 1 binding model assumes that there are two binding partners, neither of which undergoes a binding-induced conformational change or participates in cooperative binding. The first step in the data analysis is to use eqn (10.1) (Table 10.4) to fit the ''Dissociation'' step data from the Octet to solve for k_d.

An assumption is made when using the ''Full Dissociation'' option that, given infinite time, all molecules bound will dissociate and Y will therefore

View Online

Table 10.4 Octet equations used in a 1 : 1 fit model for extracting kinetic parameters.

Equation no.	Equation
Eqn (10.1)	$Y = Y_0 + A\exp(-k_d t)$ $Y =$ nm shift $A =$ amplitude of total binding $t =$ time (s), x-axis value of data $Y_0 = Y$ value at the start of the association step
Eqn (10.2)	$Y = Y_0 + A[1 - \exp(-k_{obs} t)]$
Eqn (10.3)	$k_a = (k_{obs} - k_d)/M$ $M =$ molar concentration of binding protein in solution
Eqn (10.4)	$K_D = k_d/k_a$

Published on 24 May 2017 on http://pubs.rsc.org | doi:10.1039/9781788010283-00356

eventually reach a value equivalent to that prior to binding (*i.e.* as $t \rightarrow$ infinity, then $Y \rightarrow Y_0$). The curve fit is performed using non-linear least-squares regression. Once k_d has been determined, it is used in conjunction with eqn (10.2) (Table 10.4) to fit the ''Association'' step data and solve for k_{obs}. This is also performed by non-linear least-squares regression. Using the calculated k_d and k_{obs}, eqns (10.3) and (10.4) (Table 10.4) are used to calculate k_a and K_d, respectively.

10.6.4 Protein Quantitation on the Octet

Accurate protein quantitation is critical to the selection of expression strains for the development and optimization of bioreactor titers in production. Traditional analytical methods for protein quantitation include ELISA, HPLC, UV–Vis spectroscopy and biochemical methods such as the Bradford assay. These methods have drawbacks, however, such as long analysis times, lack of specificity, labor-intensive protocols, and imprecision. Label-free assays can differentiate between conformationally active and inactive proteins and generally do not require highly purified samples. Quantitation assays on BLI platforms enable the user to determine sample concentrations using a set of sample standards and have many similarities to ELISA. They utilize capture molecules immobilized to the biosensor surface while the analyte is bound from solution in the sample plate. The signal reported from the assay is either directly or inversely proportional to the analyte bound. Quantitation is performed in a similar manner as a kinetics assay except that data are analyzed only from the association phase. Data analysis for quantitation assays is performed using binding rate equations that analyze either the initial slope of binding (direct quantitation) or the equilibrium endpoint of binding (indirect quantitation–sandwich assays). The assays can either be a one-step assay such as in the case of IgG titer analysis or a multi-step assay such as in traditional ELISA or immunogenicity assays.

View Online

Published on 24 May 2017 on http://pubs.rsc.org | doi:10.1039/9781788010283-00356

10.6.4.1 ELISA Conversion on the Octet

ELISA has been in use since the early 1970s in analyte concentration measurements in solution. ELISAs typically involve the immobilization of a ligand onto a protein-adsorbing sample plate followed by the binding of an analyte and finally a detection antibody with washes in between the addition of each reagent. The detection antibody can be covalently linked to an enzyme that can react with a substrate resulting in a color change at the end of the reaction. This color change should be directly proportional to the amount of analyte present in solution and is compared with a standard curve to extract the analyte concentration. Quantitation assays on the Octet platform have many similarities to ELISA. Both are performed on a solid support on which the capture molecule is immobilized and the analyte is bound from solution. The signal reported in the assay is either directly or inversely proportional to the amount of bound analyte. As a result, Octet quantitation assays can be considered automated forms of ELISA that have major advantages over ELISA and HPLC, including significant time savings (Figure 10.9). The octet platform allows the user to choose from a variety of assay formats (direct, sandwich, sandwich followed by signal amplifications), detect low-affinity analytes that are often missed in ELISA assays[12]

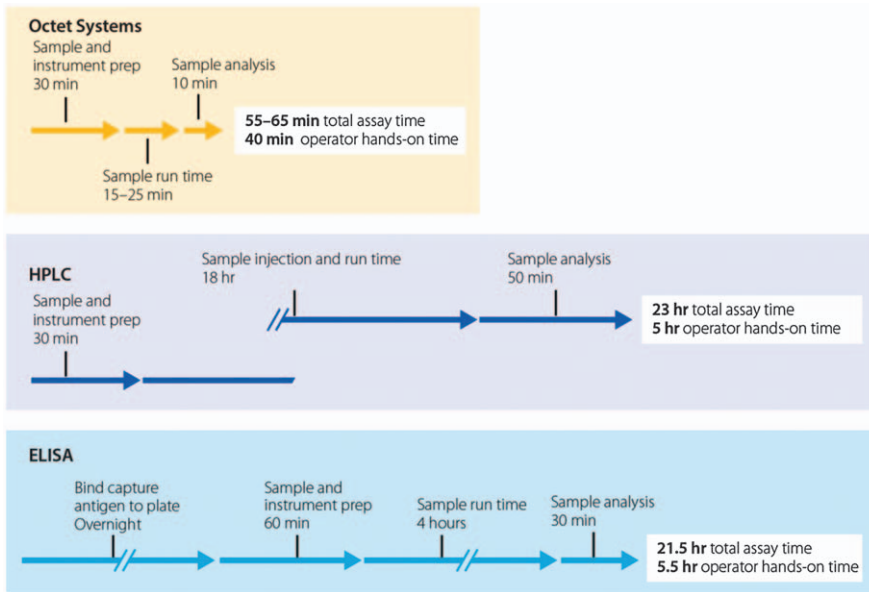


Figure 10.9 Protein quantitation assay time comparison between Octet, ELISA, and HPLC.
Reproduced with permission from T. Rashi and K. Sriram, *FortéBio Application Note 10: Developing a Robust Quantitation Assay for Monoclonal Antibodies and Other Proteins on the Octet Platform*, 2013, 2–3.

View Online

owing to the requisite wash steps, and minimize handling *via* automation, hence reducing variability, all while monitoring data in real time. The conversion to an Octet assay often involves simply reoptimizing and/or validating the conditions and configurations of the already existing ELISA assay. However, in some cases where the minimum essential requirements are stringent, more development work is required.

Published on 24 May 2017 on http://pubs.rsc.org | doi:10.1039/9781788010283-00356

10.6.4.2 *Setting Up Concentration Measurement Assays on the Octet*

The Octet platform provides a convenient and reliable analytical method for measuring antibody and protein concentrations through various stages of drug discovery and development. Octet systems can enable informed decisions to be made earlier in both drug and process development – particularly when chromatography and other critical separation steps are needed. The simple ''Dip and Read'' approach permits streamlined workflows and rapid quantitation of 96 samples in as little as 20 min or 384 samples in 70 min.

In a typical quantitation assay, biosensors coated with capture molecules are dipped into samples in the sample plate and the on-rate is measured in real time. The measured on-rate is then used to determine the concentration of the target protein. This is effected by comparing the binding signals obtained from a set of known analyte concentrations that are used to generate a standard curve with the signals from the unknown samples.

Similarly to setting up kinetics experiment, concentration measurements in BLI also start with the selection of the appropriate biosensor surface and the relevant assay format to be used. In so doing, one must consider the presence of an epitope on the analyte that binds to an immobilized ligand on the biosensor surface. When the estimated concentration of the analyte is in the dynamic range for the selected biosensor as determined from Table 10.2, then the direct quantitation method in which the analyte binds directly to the immobilized biosensor surface should be used. On the other hand, if the expected concentration is lower than the limit of detection, then a multi-step or indirect quantitation method with a signal amplification step should be used.

10.6.4.3 *Best Practices for Direct Quantitation Assay Setup*

1. Hydrate biosensors for at least 10 min prior to use. Biosensors should be hydrated in a biosensor tray assembly with a hydration plate underneath containing at least 200 μL of hydration media at corresponding locations. The hydration media should be identical with the media of the samples to be measured.
2. Biosensors should be hydrated only for immediate use. Once biosensors have been hydrated, they must not be allowed to dry and

View Online

Published on 24 May 2017 on http://pubs.rsc.org | doi:10.1039/9781788010283-00356

should be inserted into the instrument's biosensor compartment with the hydration tray in place. They may be stored at 4 °C, with the tips of the biosensors submerged in hydration media for up to 1 day, with the understanding that the storage time is determined by the stability of the proteins on the biosensors.

3. Determine the useful standard curve concentration range for the analyte, and work in the linear section of the standard curve.
4. The default settings of a 400 rpm shaking speed and a 2 min read time is sufficient for analyte concentrations in the range 0.5–2000 $\mu g\,mL^{-1}$; however, if higher sensitivity is desired, then the shaking speed and read time should be increased to 1000 rpm and 5 min, respectively.
5. Ensure that the standards are diluted in the same buffer matrix as the unknown sample(s).
6. During standard curve generation and testing of unknown samples, perform reference subtraction if non-specific binding is observed. A reference sample should be run that matches the matrix of the unknown but is devoid of the analyte of interest.
7. The sample(s) being analyzed should be run neat or diluted to bring the concentration within the linear dynamic range of the standard curve.
8. Both standard samples and unknown samples should be assayed in replicate to allow for the calculation of coefficients of variation and to test the robustness of the assay.
9. In Octet data analysis, previously saved standard curves can be imported into new data sets and used for the analysis, implying that the standard curve does not always have to be run. However, validate the accuracy of calculated concentrations using saved standard curves against freshly generated standard curves.
10. When regenerating and reusing the biosensors, ensure that the sensors are preconditioned in order to achieve the best consistency between different regeneration cycles. In preconditioning, the biosensors are subjected to the regeneration conditions prior to first-time usage to ensure that all cycles of the quantitation process use similar biosensor conditions.

As an example of a direct quantitation assay on the Octet, human IgG samples of known concentrations, ranging from 1 to 700 $\mu g\,mL^{-1}$ were used to generate a typical Octet quantitation standard curve.[13] The binding curves (Figure 10.10) show dose-dependent behavior with higher concentrations resulting into higher signal response. The data were fitted using the binding rate from the initial slope (30 s of the assay) and generated the standard curve shown in Figure 10.11. This standard curve can then be used to quantify unknown sample concentrations provided that the unknown samples are treated in an identical manner as the standard samples.

View Online

Published on 24 May 2017 on http://pubs.rsc.org | doi:10.1039/9781788010283-00356

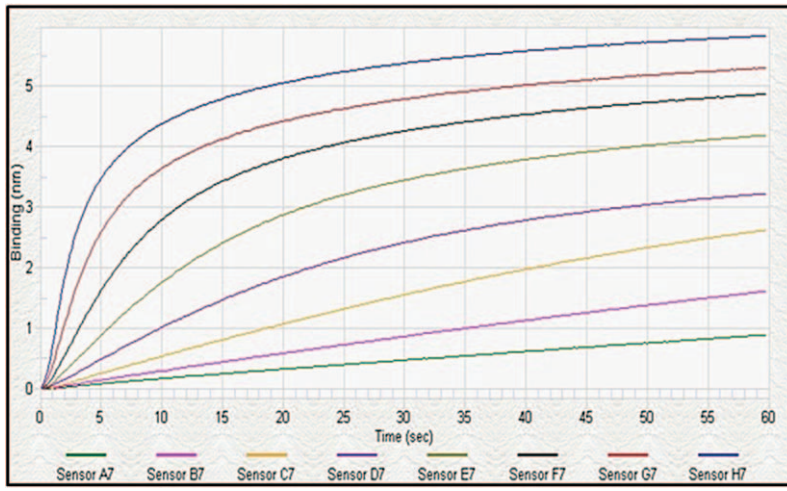


Figure 10.10 Octet binding curves for human IgG standard samples ranging from 1 to 700 μg mL^{-1} and analyzed using protein A biosensors. Each sample concentration was assayed in duplicate.
Reproduced with permission from Z. Sydney, T. Rashi and K. Sriram, *FortéBio Application Note 12: Validated Quantitation and Activity Assay of Antibody Fragment Molecules (Fab)*, 2013, 3–4.

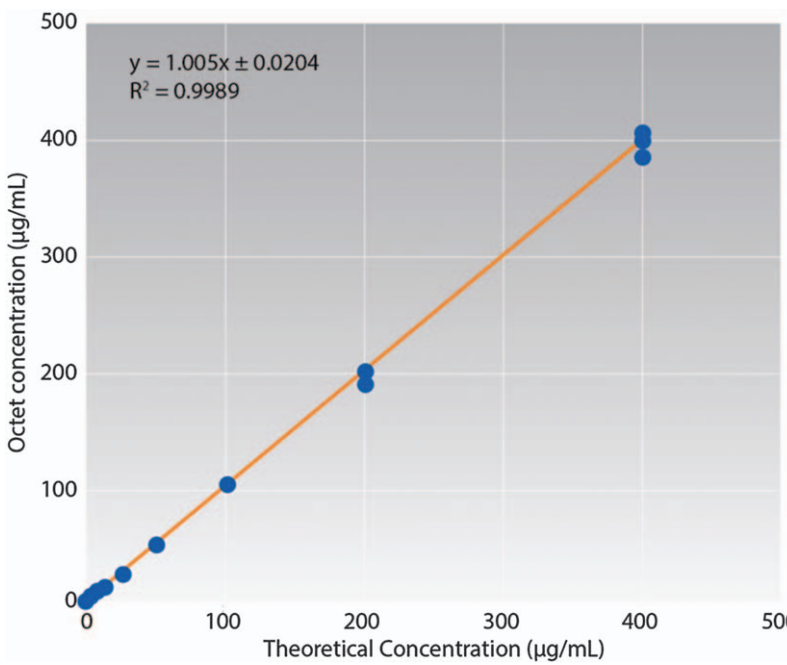


Figure 10.11 Standard curve generated from the initial slope binding rate as a function of IgG concentration.
Reproduced with permission from Z. Sydney, T. Rashi and K. Sriram, *FortéBio Application Note 12: Validated Quantitation and Activity Assay of Antibody Fragment Molecules (Fab)*, 2013, 3–4.

View Online

Published on 24 May 2017 on http://pubs.rsc.org | doi:10.1039/9781788010283-00356

10.7 Emerging Applications

10.7.1 Octet Use in Epitope Binning

An epitope is a molecular region on the surface of an antigen capable of eliciting an immune response and of combining with the specific antibody produced by such a response. Epitope binning is the classification of a given population of monoclonal antibodies according to *how* and *where* they interact with the antigen. It refers to the use of competitive binding assays to identify pairs of antibodies that bind to the same or to overlapping epitopes on an antigen. Families of antibodies (or bins) having the same binding specificity can be used to define specific epitopes on the antigen.

The goal of a typical epitope binning or cross-blocking experiment is to identify antibodies that bind to different or identical epitopes on the antigen. Antibodies are tested two at a time for competitive binding to one antigen. By competing antibodies against one another in a pairwise and combinatorial format, antibodies with distinct blocking behaviors can be discriminated and assigned to ''bins.'' The end result is matrix of pairwise binders and blockers.

The Octet's high-throughput capability makes it a convenient analytical tool for performing epitope binning experiments. Assay orientation is an important consideration when designing epitope binning experiments, with three different formats possible depending on sample cost and availability. A combination of any two of the formats may be necessary to confirm ambiguous results. Prior to performing a binning experiment, verification of binding between the test antibodies and the antigen must be done to allow for proper data interpretation when there is lack of binding during the binning experiment. The three formats (Figure 10.12) are as follows:

1. *In-tandem epitope binning.* Here, the antigen is immobilized onto a biosensor surface either through a tag such as His-tag while using Ni-NTA biosensors or by first biotinylating the antigen and then immobilizing onto the biosensor surface using a streptavidin (SA) biosensor. This is followed by the binding of the first antibody; the saturating antibody. An increase in response signals should be observed as a result of the binding of the two molecules. Next, the biosensor is dipped into a solution of the second antibody; the competing antibody. If binding is observed, there would be another increase in response signals. This would signify binding to an unoccupied epitope on the antigen by the second antibody, implying that the saturating antibody is non-blocking, hence the two antibodies belong to different bins.
2. *Premix epitope binning.* In this format, the antigen is initially mixed with the first antibody off-line in an equilibrium experiment. The antibody must be in excess of the antigen to allow for saturation of its

View Online

Published on 24 May 2017 on http://pubs.rsc.org | doi:10.1039/9781788010283-00356

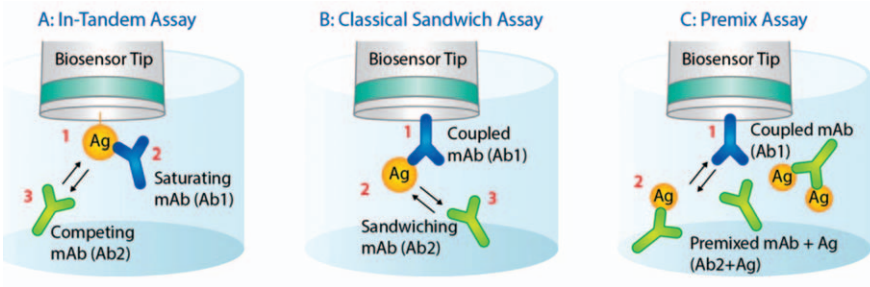


Figure 10.12 In the in tandem format (A), biosensor-immobilized antigen is presented to two antibodies in consecutive steps. The classical sandwich assay (B) involves biosensor immobilization of the Ab1, followed by incubation with the antigen, and then an Ab2[14] (referred to as the sandwiching antibody). In the premix format (C), antigen is premixed with a large molar excess of the first antibody, and subsequently presented to a biosensor loaded with the Ab2.

antigen binning epitope. The mixture is then immobilized onto the biosensor, where a signal response increase should be observed. The biosensor is then dipped into a solution of the second antibody, where an increase in signal response would signify binding and would imply that the two antibodies bind to different epitopes and therefore belong to different bins.

3. *Sandwich epitope binning.* The sandwich binning format takes the form of a traditional sandwich assay in which the first antibody is immobilized onto the biosensor to a saturating level. In this format, the antibody is immobilized onto an antibody-based biosensor such as an anti-human capture (AHC) or anti-mouse capture (AMC) biosensor or could first be biotinylated to be immobilized onto an SA biosensor followed by the binding of the antigen and finally the binding of the second antibody. At each binding step of the assay, an increase in signal response signifies binding whereas the lack of an increase in signal signifies no binding. As is the case with the first two assays, binding of the second antibody implies that the two antibodies are non-competing and belong to different bins.

On the Octet, epitope binning experiments are run as kinetic experiments with many repeating steps in the Octet Data Acquisition software.

The epitope binning data analysis feature on the Octet software provides easier visualization of larger data sets that use biosensor regeneration. Results are placed in a 2D matrix that allows further cross-blocking data analysis. Typical epitope binning or cross-blocking analysis focuses on comparing cycles of repeating association steps, with monitoring of baselines or dissociation steps for binding stability. An example of epitope binning data from an Octet instrument is shown in Figure 10.13.

View Online

Published on 24 May 2017 on http://pubs.rsc.org | doi:10.1039/9781788010283-00356

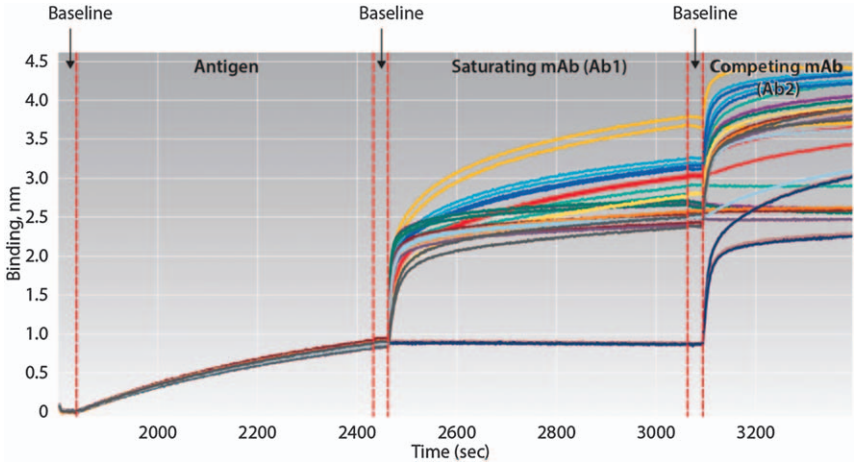


Figure 10.13 Fast binning of antibodies accomplished by in-tandem binning. Reproduced with permission from T. Rashi, Y. Amrita, S. Liao-Chan, T. Jan Willem and K. Sriram, *FortéBio Application Note 16: Cross-Competition or Epitope Binning Assays on the Octet HTX System*, 2013, 4–7.

10.7.2 Octet in Virus Titer Studies

A fast and accurate determination of vaccine titer during vaccine manufacture is important in understanding vaccine development process performance and for correctly scaling each process step. Traditionally, single radial immunodiffusion (SRID) assays have been the most commonly used technique for vaccine titer determination. However, SRID is time consuming and generally exhibits poor precision. ELISA has been the alternative method but tends to exhibit lower precision, partly due to inherent operator-introduced errors. ELISA also typically exhibits a low dynamic range. Alternative assays that can speed up the analysis process and provide accurate and precise potency data on different vaccine strains have therefore been desirable.

The Octet's ''Dip and Read'' format with its high-throughput capability and a simpler and more direct vaccine/antigen–antibody binding measurement method provides process development groups with a robust and easy-to-use alternative to the SRID and ELISA methods. It reduces the assay time from days to just a few hours for a 96-well plate of samples. The Octet has been successfully used in the study of viruses such as Zika, Ebola,[15] and the pandemic influenza virus, among others. For example, for the influenza virus, the relative standard deviation and dynamic range of the vaccine titer assay were tested using the Octet and found to be better than those obtained with SRID, with sample preparation reduced to a simple dilution using FortéBio's sample diluent. Samples can be analyzed in their natural state without the use of detergents, and so the method does not directly measure

View Online

Published on 24 May 2017 on http://pubs.rsc.org | doi:10.1039/9781788010283-00356

hemagglutinin (HA) content as in SRID, but instead measures the amount of whole virus present. The assay has been applied successfully to various sample types, including inactivated, split virion, and recombinant hemagglutinin vaccine samples. The Octet system can also be used in a vaccine stability test to assess vaccine stability through the use of heat-stressed vaccine samples.

10.7.2.1 Octet Study Example: Influenza Vaccine Titer

10.7.2.1.1 Materials and Reagents. Samples of inactivated virus and antibody standards were purchased from NIBSC (South Mimms, UK). Split virion vaccine samples were provided by Sanofi Pasteur (Lyon, France), and recombinant hemagglutinin vaccine samples and antibodies by Protein Sciences (Meriden, CT, USA). Sample diluent (part no. 18-1048) and protein A and G biosensors (part nos 18-5010 and 18-5082, respectively) were provided by FortéBio. Black polypropylene 96-well sample plates from Greiner Bio-One (part no. 655209) (Sigma Aldrich M9685) were used.

10.7.2.1.2 Method. The assay is based on the binding of the vaccine to polyclonal antibodies that recognize the influenza epitopes presented by the vaccine. The polyclonal antibody is bound to protein G- or protein A-derivatized biosensors directly from crude sample such as sera antibodies.

1. Hydrate the required number of biosensors to be used.
2. Determine the optimal concentration of antibody to be immobilized onto the biosensor (this should be done for every strain of virus) by performing a serial dilution of the antibody and immobilizing each sample for 300 s (Figure 10.14).
3. Dip the antibody-immobilized biosensors into the vaccine samples at a fixed concentration to determine a response at each dilution of the antibody.
4. The lowest antibody concentration that gives maximum vaccine binding response signals should be selected for the virus titer studies.

For influenza virus, the sample binding step is typically 300 s except for split virion analysis, where the step should take less than 30 s as virus heterogeneity can occur with time. To determine the titer, a standard curve is required and is generated using a titration of standard samples of known concentrations.[16] The response signals (Figure 10.15) obtained from the standard samples are analyzed by calculating the binding rate for the initial slope of the binding curve.

The virus standard was tested over the range 1–140 $\mu g\,mL^{-1}$ based on the HA concentration provided by NIBSC. The linear range was established to be between 5 and 75 $\mu g\,mL^{-1}$ with a linear regression value of 0.9951, as shown

View Online

Published on 24 May 2017 on http://pubs.rsc.org | doi:10.1039/9781788010283-00356

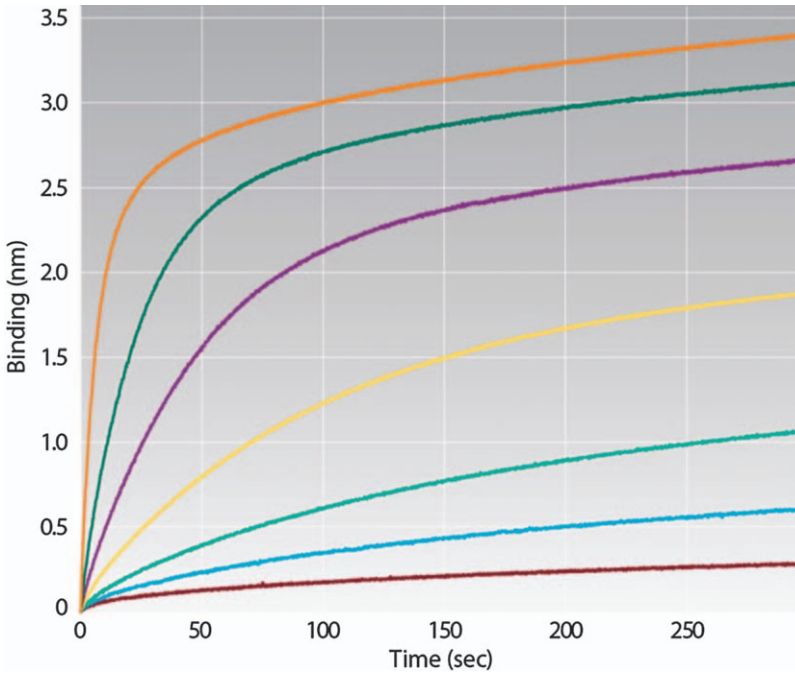


Figure 10.14 Sera antibody – A/California/7/2009(H1N1) was immobilized onto protein A biosensors in a twofold serial dilution starting from a 10-fold dilution.
Reproduced with permission from W. David, S. Debby, J. Kyle and A. David, *FortéBio Application Note 20: A Fast and High Precision Influenza Vaccine Potency Assay*, 2016, 2–3.

in Figure 10.16. Once the linear range and antibody loading concentration have been determined, the assay is ready to be used for sample titer determination.

10.7.3 Analysis of FcRn–Antibody Interactions Using the Octet

The Octet is rapidly becoming a highly suitable approach for the analysis of Fcγ receptors and neonatal Fc receptor (FcRn) molecules binding to IgGs. Here we present the example of the use of Octet in FcRn–antibody interactions analysis. The Fc region of human IgG contributes to a number of beneficial biological and pharmacological characteristics of therapeutic antibodies. One of the most important is the prolonging of plasma half-life, due to its unique, pH-dependent interaction with FcRn. Because altered FcRn binding can increase or decrease the serum half-life of Fc-containing therapeutics, thereby impacting drug efficacy, FcRn binding interactions are increasingly being assessed at multiple stages of biological drug development. FcRn–Fc activity and binding assays are performed as part of

View Online

Published on 24 May 2017 on http://pubs.rsc.org | doi:10.1039/9781788010283-00356

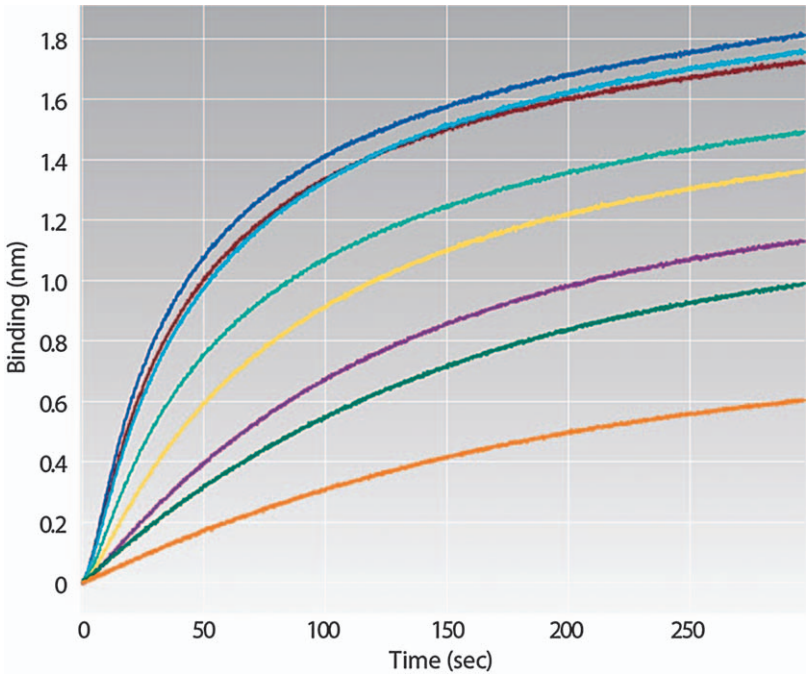


Figure 10.15 Response curves for dose-dependent binding of standard inactivated influenza A/H1NI virus samples to optimal A/California/7/2009 (H1N1) antibody immobilized onto protein A biosensors.

characterization studies to enhance overall product understanding and demonstrate comparability in the development of biosimilar materials. FcRn typically binds to IgGs with low affinity, hence an instrument capable of measuring weak binding and an optimal assay orientation is desirable.

10.7.3.1 Biosensor Selection and Assay Orientation

In selecting the optimal biosensor and assay format, several factors are considered; sample stability, the size of each molecule, and the potential for avidity should all be factored in. FcRn receptor itself is a major histocompatibility complex (MHC) class I-like heterodimer that binds to the CH2–CH3 hinge region of both heavy chains of antibody Fc, resulting in a 2 : 1 binding stoichiometry.[17] It can be immobilized *via* biotinylation and captured onto SA biosensors, or it can be captured *via* polyhistidine (HIS) tag onto anti-penta-HIS (HIS1K) biosensors. In each of these approaches, IgG remains in solution as the analyte. However, since a single IgG can bind to two FcRn molecules, there is potential for avidity to affect kinetic rates when FcRn is used as the immobilized ligand. When analyte bridging occurs, dissociation kinetics can be altered and result in an artificially low dissociation rate constant (k_d).

View Online

Published on 24 May 2017 on http://pubs.rsc.org | doi:10.1039/9781788010283-00356

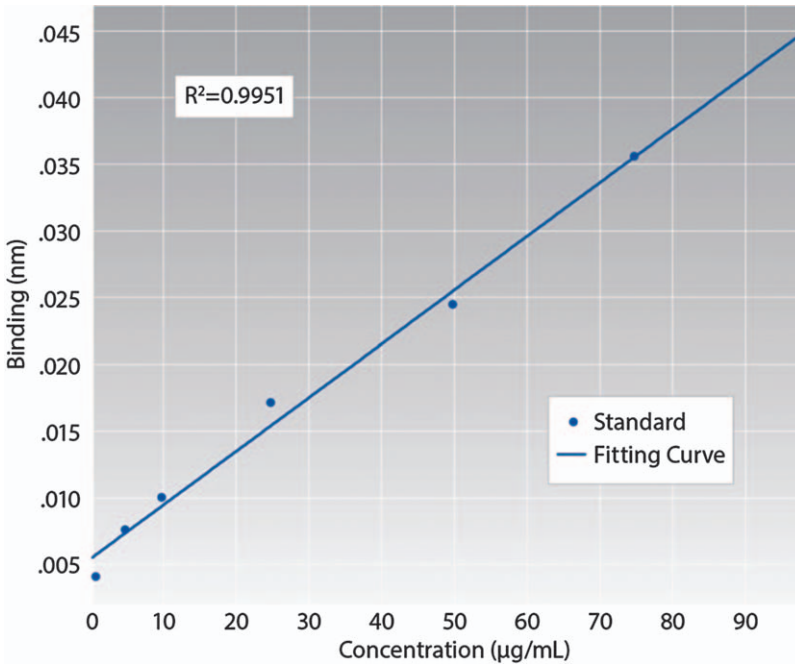


Figure 10.16 Linear range of the standard curve of A/H1N1 virus samples obtained using an initial slope binding rate analysis from data in Figure 10.15. Reproduced with permission from W. David, S. Debby, J. Kyle and A. David *Fortebio Application Note 20: A Fast and High Precision Influenza Vaccine Potency Assay*, 2016, 2–3.

Two different strategies can be utilized to minimize avidity in a biosensor assay where one binding partner is multivalent: (1) a significantly reduce ligand (FcRn) loading density or (2) reversal of the assay orientation. If FcRn is immobilized as described above using SA or HIS1K biosensors, the effective surface density of the FcRn ligand must be low enough that adequate spacing results between receptor molecules to prevent analyte bridging. This lowered density can be accomplished either by reducing the concentration of FcRn used in the loading step or by shortening the time of the loading step, or both. However, fewer ligand molecules on the surface means fewer available sites for analyte binding, thus reducing the assay sensitivity. Maintaining an adequate assay signal can limit how much FcRn immobilization can be minimized.[18]

The second and more reliable strategy is to reverse the assay orientation so that the bivalent molecule (IgG) is immobilized on the biosensor instead of the FcRn. The biosensor format that we recommend for the most accurate analysis of FcRn–IgG interactions is capture of IgG on anti-human Fab–CH1 biosensors. These biosensors come pre-immobilized with a high-affinity ligand that is specific for the CH1 region of human IgG Fab. This capture

View Online

Published on 24 May 2017 on http://pubs.rsc.org | doi:10.1039/9781788010283-00356

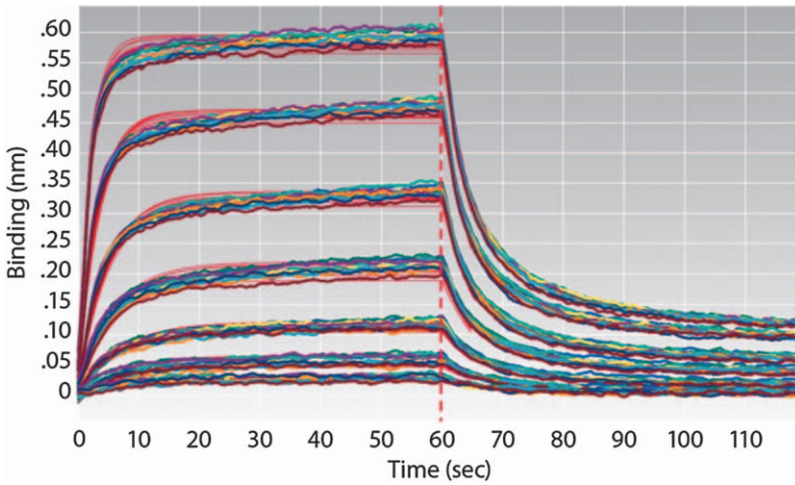


Figure 10.17 Overlay of several replicates of the FcRn–IgG association/dissociation step. The assay was performed by immobilizing the receptor onto anti-FAB biosensors. Curve fitting of data traces was performed using a 1 : 1 model with global fitting and a 5 s dissociation step (fit lines are in red).
Reproduced with permission from T. Renee and M. Weillei, *FortéBio Application Note 19: Analysis of FcRn–Antibody Interactions on the Octet Platform*, 2016, 10–11.

method is highly specific and reliable for characterizing FcRn–hIgG kinetics with all four subclasses of human IgG, and has the advantage of being more conducive to use as a platform approach when testing multiple IgGs against FcRn and other Fc receptors. Capture of IgG is oriented, creating a more homogeneous surface on the biosensor with the Fc region exposed for receptor binding. An example of an IgG–FcRn receptor binding optimized kinetics assay is shown in Figure 10.17.

10.8 Questions

1. Why is it advisable to start with a high concentration of analyte when investigating affinity constants where the estimated K_D is unknown?
2. In establishing assay step times, what are the critical requirements for the association and dissociation steps?
3. Why is the biosensor-immobilized ligand stability an important consideration when running a kinetics assay?
4. Besides molecular weight, what other physical property of the ligand or analyte should be taken into consideration when predicting response signals in BLI?
5. Why does sample plate shaking speed matter when running both kinetics and quantitation assays?

View Online

Published on 24 May 2017 on http://pubs.rsc.org | doi:10.1039/9781788010283-00356

References

1. P. Säfsten, S. L. Klakamp, A. W. Drake, R. Karlsson and D. G. Myszka, *Anal. Biochem.*, 2006, **353**(2), 181–190, DOI: 10.1016/j.ab.2006.01.041.
2. SDI Market Forecasts 2013–2018: Global Assessments Report, 13th edition.
3. J. Concepcion, K. Witte, C. Wartchow, S. Choo, D. Yao, H. Persson, J. Wei, P. Li, B. Heidecker, W. Ma, R. Varma, L.-S. Zhao, D. Perillat, G. Carricato, M. Recknor, K. Du, H. Ho, T. Ellis, J. Gamez, M. Howes, J. Phi-Wilson, S. Lockard, R. Zuk and H. Tan, *Comb. Chem. High Throughput Screening*, 2009, **12**, 791–800.
4. S. Kumaraswamy, in *Biopharmaceutical Production Technology*, ed. G. Subramanian, Wiley-VCH Verlag GmbH & Co. KGaA, Weinheim, Germany, 2012, ch. 13, vol. 1 & 2, pp. 447–471, DOI: 10.1002/9783527653096.ch13.
5. A. T. Renee and K. Sriram, *FortéBio Application Note 14: Biomolecular Binding Kinetics Assays on the Octet Platform*, 2014.
6. T. Renee and M. Weillei, *FortéBio Application Note 19: Analysis of FcRn-Antibody Interactions on the Octet Platform*, 2016. http://www.FortéBio.com/literature.html.
7. N. M. Green, *Adv. Protein Chem.*, 1975, **29**, 85–133, DOI: 10.1016/S0065-3233(08)60411-8.
8. Octet Data Acquisition User Guide version 9.0, 2015, 47–61.
9. Octet Data Analysis User Guide version 9.0, 2015, 38–143.
10. R. L. Rich and G. G. Myszka, *Anal. Biochem.*, 2007, **361**, 1–6, DOI: 10.1016/j.ab.2006.10.040.
11. T. Renee, *FortéBio Technical Note 38*, 2013, 2–3.
12. T. Rashi and K. Sriram, *FortéBio Application Note 10: Developing a Robust Quantitation Assay for Monoclonal Antibodies and Other Proteins on the Octet Platform*, 2013, 2–3.
13. Z. Sydney, T. Rashi and K. Sriram, *FortéBio Application Note 12: Validdated Quantitation and Activity Assay of Antibody Fragment Molecules (Fab)*, 2013, 3–4.
14. T. Rashi, Y. Amrita, S. Liao-Chan, T. Jan Willem and K. Sriram, *FortéBio Application Note 16: Cross-competition or Epitope Binning Assays on the Octet HTX System*, 2013, 4–7.
15. D. Corti, J. Misasi, S. Mulangu, D. A. Stanley, M. Kanekiyo, S. Wollen, A. Ploquin, N. A. Doria-Rose, R. P. Staupe, M. Bailey, W. Shi, M. Choe, H. Marcus, E. A. Thompson, A. Cagigi, C. Silacci, B. Fernandez-Rodriguez, L. Perez, F. Sallusto, F. Vanzetta, G. Agatic, E. Cameroni, N. Kisalu, I. Gordon, J. E. Ledgerwood, J. R. Mascola, B. S. Graham, J.-J. Muyembe-Tamfun, J. C. Trefry, A. Lanzavecchia and N. J. Sullivan, *Science*, 2016, **351**(9279), 1339.
16. W. David, S. Debby, J. Kyle and A. David, *FortéBio Application Note 20: A Fast and High Precision Influenza Vaccine Potency Assay*, 2016, 2–3.
17. W. L. Martin and P. J. Bjorkman, *Biochemistry*, 1999, **38**(39), 12639.
18. T. Renee and M. Weillei, *FortéBio Application Note 19: Analysis of FcRn-Antibody Interactions on the Octet Platform*, 2016, 10–11.

Published on 24 May 2017 on http://pubs.rsc.org | doi:10.1039/9781788010283-00398

CHAPTER 11

Strategies for Building Protein–Glycosaminoglycan Interaction Networks Combining SPRi, SPR, and BLI

SYLVAIN D. VALLET,[a] LISETTE DEDDENS,[b] ARNAUD VONARBURG,[b] ROMAIN SALZA,[a,†] CLÉMENT FAYE,[a,‡] ATTILA ARANYOS,[b] NICOLAS THIERRY-MIEG[c] AND SYLVIE RICARD-BLUM*[a]

[a] Institut de Chimie et Biochimie Moléculaires et Supramoléculaires, UMR 5246 CNRS – Université Lyon 1, 69622 Villeurbanne, France; [b] Pall FortéBio; [c] TIMC-IMAG, UMR 5525 CNRS – Université Grenoble Alpes, La Tronche, France
*Email: sylvie.ricard-blum@univ-lyon1.fr

11.1 Introduction

The extracellular matrix (ECM) is a structural scaffold contributing to the organization and mechanical properties of tissues[1,2] and is a key player in tissue failure.[3] The ECM modulates cell behavior *via* several receptors and

[†]Present address: Histalim, Montpellier, France.
[‡]Present address: Colcom, Clapiers, France.

Handbook of Surface Plasmon Resonance, 2nd Edition
Edited by Richard B. M. Schasfoort
© The Royal Society of Chemistry 2017
Published by the Royal Society of Chemistry, www.rsc.org

View Online

Published on 24 May 2017 on http://pubs.rsc.org | doi:10.1039/9781788010283-00398

this dynamic structure constantly undergoes remodeling,[4] which leads to diseases if uncontrolled.[5] Understanding these mechanisms is essential for finding novel therapeutic targets and designing strategies for regenerative medicine.[4,6] ECM molecules are therefore important targets for pharmacotherapy.[7] The structure and functions of the intricate 3D ECM network rely on numerous interactions, and the identification of key interactions for ECM assembly and cell interplay is a prerequisite to determining how they are disturbed in diseases.

The human ECM is comprised of 274 proteins forming the core matrisome (*e.g.* collagens, laminins, fibronectin, elastin, and proteoglycans) and of 747 matrisome-associated proteins, which are secreted factors, ECM regulators (degradation and crosslinking enzymes), and ECM-affiliated proteins (*e.g.* semaphorins, galectins, mucins).[8,9] The ECM is a source of bioactive fragments (matricryptins), which are released from extracellular proteins by proteolysis, and have biological activities of their own.[10–12] Endostatin, a C-terminal proteolytic fragment of collagen XVIII, is one of the most studied matricryptins. It is both anti-angiogenic and anti-tumoral,[10,13] has ATPase activities,[14] and contributes to host–pathogen interactions.[15] In addition to proteins, the ECM contains five sulfated glycosaminoglycans (GAGs), chondroitin sulfate, dermatan sulfate, keratan sulfate, heparin, and heparan sulfate, which are covalently linked to proteins to form proteoglycans,[16] and hyaluronan, a non-sulfated GAG.

GAGs are complex, linear polysaccharides made of repeating disaccharide units comprising a hexuronic acid (or a galactose for keratan sulfate) and a hexosamine. Heparin (HP) and heparan sulfate (HS) share the same disaccharide unit and are extensively modified by several enzymes during and after their synthesis.[17] They both have tremendous structural diversity and 23 HS disaccharides have been identified *in vivo*[18] out of the 48 theoretically possible HS disaccharides.[19] Heparan sulfate is less sulfated than heparin and is organized into highly sulfated domains and *N*-acetylated domains interspersed with domains of intermediate sulfation. Heparin and heparan sulfate interact with at least 435 proteins,[20,21] including ECM proteins, growth factors, chemokines, enzymes, and receptors such as integrins.[22] These interactions are involved in numerous biological processes such as development, angiogenesis, tumor growth, host–pathogen interactions, inflammation, ECM assembly, cell–matrix interactions, and signaling. The identification of the sulfate groups involved in protein recognition, the determination of the minimal size of heparin required for binding to its partners, and the calculation of their association rate to, and dissociation rate from, their partners together with the affinity are required to decipher the molecular mechanisms underlying their biological roles at the individual level.[22] However the building of GAG–protein interaction networks is required to determine how these individual interactions influence each other *in vivo*, form networks in various biological processes, and are altered in diseases.

View Online

11.2 A Roadmap to Build Protein–Glycosaminoglycan Interaction Networks

Published on 24 May 2017 on http://pubs.rsc.org | doi:10.1039/9781788010283-00398

Protein–GAG interaction networks are built from experimental data and from manual curation of the literature. The interaction database developed in our laboratory, MatrixDB[23–25] (http://matrixdb.univ-lyon1.fr), focuses on interactions involving at least one extracellular matrix protein or GAGs and is one of the very few databases, if any, reporting protein–GAG interactions and thus giving the possibility for users to build not only protein–protein interaction networks but also GAG–protein interactomes as described below. MatrixDB belongs to the International Molecular Exchange consortium (www.imexconsortium.org), and follows the consortium curation rules to report interaction data.[26] We perform literature curation through the interface developed by another interaction database, IntAct[27] (www.ebi.ac.uk/intact). Interaction data curated by MatrixDB and the other IMEx consortium databases are freely available and can be downloaded from their websites. We have developed a roadmap comprising the following steps to build and analyze protein–protein and protein–GAG interaction networks:

1. Identification of biomolecular interactions by screening about 100 potential interactors spotted in triplicate onto a gold surface by surface plasmon resonance imaging (SPRi) in a Biacore Flexchip system (GE Healthcare). This instrument is based on grating-coupled SPR sensor chips consisting of a plastic optical grating coated with a thin (~80 nm) layer of gold onto which biomolecules are spotted[28] and is described in Section 11.3.
2. Calculation of kinetic parameters (association and dissociation rates) and equilibrium dissociation constant (K_D) by SPR (Biacore T100/T200, GE Healthcare) and/or Bio-Layer Interferometry (BLI) (Octet RED96, Pall FortéBio). These parameters are used to prioritize interactions within a network and to evaluate the half-lives of the interactions.[22] Binding sites are either identified experimentally through site-directed mutagenesis and binding assays performed with mutants or predicted *in silico* by molecular modeling when possible.
3. Visualization of the interaction networks either with MatrixDB iNavigator[25] (http://matrixdb.univ-lyon1.fr) or with Cytoscape (www.cytoscape.org), an open-source software platform,[29] which is also used to calculate the metrics of the networks (*e.g.* shortest path, diameter, betweenness) and to contextualize the networks by integrating kinetics, affinity, biological pathways, and transcriptomic and proteomic data when available.
4. Enrichment analyses are performed either with Cytoscape apps or with the Functional Enrichment analysis tool FunRich[30] (www.funrich.org), which displays the results of the analyses in the form of tables and charts. We have used this roadmap to build and analyze the interaction networks of the ECM bioactive fragment

View Online

Published on 24 May 2017 on http://pubs.rsc.org | doi:10.1039/9781788010283-00398

endostatin,[31] the ECM protein procollagen C-proteinase enhancer-1,[32] proteoglycans,[33] a subnetwork of heparin/heparan sulfate interactions regulating angiogenesis in the pericellular matrix,[22] and ECM–parasite interactomes.[15]

11.3 Identification of Biomolecular Interactions by Surface Plasmon Resonance Imaging

SPRi is useful for screening several hundred potential interactions.[34] We have used the Biacore Flexchip system (GE Healthcare) to monitor up to 300 binding events between one analyte injected in buffer flow and recirculated over the array and 70–100 biomolecules spotted in triplicate on a 1 cm^2 gold surface. The protocol used does not require any chemical modification of the proteins or GAGs prior to spotting and relies on their physical adsorption on bare gold.

SPRi assays were performed as described previously.[31,32,35,36] Glycosaminoglycans and proteins were spotted in triplicate at concentrations of 0.06–1 mg mL^{-1} on a bare gold chip (Gold Affinity chip (GE Healthcare) (Figure 11.1A and B) using a non-contact microarraying system (Piezorray,

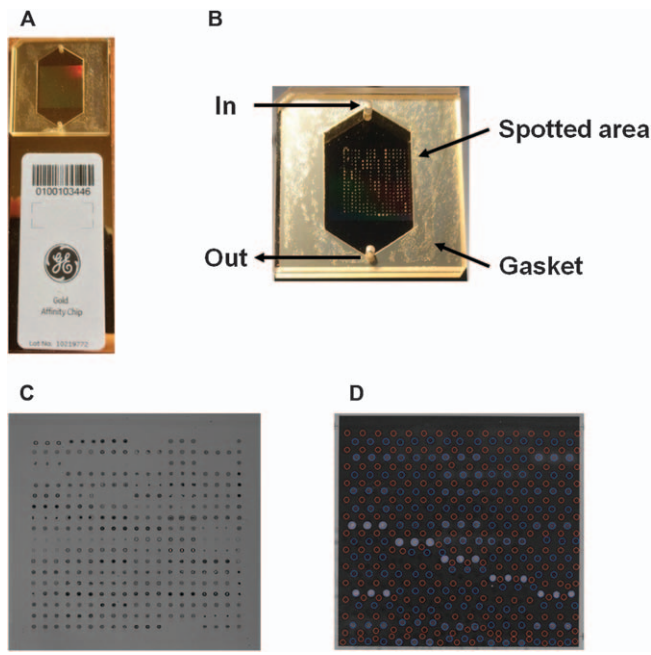


Figure 11.1 (A) Flexchip Gold Affinity chip. (B) Flow cell of the Flexchip Gold Affinity chip (1 cm^2 spotted matrix, 19×18 spots, flow cell volume 46 µL). (C) Flexchip Gold Affinity chip visualized by the CCD camera after spotting. (D) Definition of the regions of interest (spotted biomolecules, blue circles; reference spots, red circles).

View Online

Published on 24 May 2017 on http://pubs.rsc.org | doi:10.1039/9781788010283-00398

PerkinElmer Life Sciences or sciFlexarrayer S3, Scienion) creating a matrix of 225–342 spots (250–300 μm diameter). This non-contact system was selected to avoid damaging the gold-coated plastic grating chip. The spotted chips (Figure 11.1C) were dried and stored under vacuum at 4 °C for 3–4 weeks. The gasket window was sealed over the array to create a unique flow cell of 46 μL (Figure 11.1B). The regions of interest (ROIs), corresponding to the spots of biomolecules, were then defined. Each ROI has four reference spots to correct for bulk refractive index and non-specific binding of the analyte to the surface of the chip (Figure 11.1D).

Tutorial Aspects of SPRi

The Flexchip system does not include a spotting system but several types of arrayers are commercially available. Visual inspection of the spotted arrays is mandatory to check the quality of the spots, which may affect the signal and hence the quality of interaction data.

- The shape of the spots should be regular.
- The spots should be homogeneous.
- The spotted amount should be reproducible.
- The spots should be regularly distributed on the gold surface.

These parameters may be affected by the nature, the molecular weight, and the viscosity of spotted biomolecules, by the buffer used, and by evaporation/drying after spotting.[37]

The experiments were performed at 25 °C. After spotting, the chip surface was blocked five times in a buffer containing mammalian proteins (Biacore Flexchip blocking buffer, GE Healthcare) for 5×5 min and equilibrated with phosphate-buffered saline, 0.05% (v/v) Tween 20 (Sigma) at 500 μL min^{-1} for 90 min. The analyte was diluted in the same buffer at 500 nM, flowed over the chip surface and recirculated for 20 min at 300–500 μL min^{-1}. The spontaneous dissociation in buffer flow of the complex formed between the spotted ligand and the injected analyte was monitored for 40 min. Data collected from reference spots (bare gold regions and tag spots) were subtracted from those collected on spotted proteins and GAGs to obtain specific binding curves. The chips were used only once because it was difficult to find appropriate conditions to dissociate simultaneously all the complexes formed on the chip surface. Response levels at selected time points were used to rank interactants. In addition, kinetic parameters and equilibrium dissociation constants can be calculated by the Flexchip Evaluation Software 2.1.

The Flexchip system, which has been discontinued by GE Healthcare, had limitations. A single experiment required a large volume of analyte (1.6 mL) and the instrument did not allow the normalization of bulk refractive index

View Online

Published on 24 May 2017 on http://pubs.rsc.org | doi:10.1039/9781788010283-00398

ranks for each signal spot and its four reference spots. In addition, physical adsorption of biomolecules on bare gold may lead to uncontrolled drift in the course of experiments, affecting the kinetics and affinity of interaction (see surface chemistries in Chapter 6). The Flexchip instrument was not designed to perform kinetic titration experiments but it has been successfully used to calculate the kinetics and affinity of antigen–antibody interactions.[34,38,39] However, it is really appropriate for screening purposes and for the identification of new biomolecular interactions between a single analyte injected over hundreds of ligands (''yes/no'' answer), which are used to build comprehensive protein–protein and protein–GAG interaction networks. Furthermore, it is possible to inject whole cells over the arrays to monitor their binding to spotted ligands, as shown for intact, live parasites.[15]

11.4 Building and Functional Analysis of Protein–Glycosaminoglycan Interaction Networks

We built GAG–protein interaction networks using the interaction data we collected by SPRi in a Biacore Flexchip system and by manual curation of the literature. They were stored in the interaction database MatrixDB that we have developed[23–25] (http://matrixdb.univ-lyon1.fr). MatrixDB is a member of the International Molecular Exchange consortium (IMEx) (www.imexconsortium.org) and follows the curation rules of this consortium. The curation process is performed *via* the curation interface of the IntAct database[26] (www.ebi.ac.uk/intact), which is also a member of the IMEx consortium. To take into account the fact that numerous extracellular proteins such as collagens and laminins are multimeric and to discriminate interaction data obtained with multimers from those obtained with individual, isolated, polypeptide chains, we used the identifiers of the complex portal for multimers[40] (www.ebi.ac.uk/intact/complex) and UniProtKB accession numbers for monomeric proteins and the chains of multimers. We built a global GAG–protein interaction network by querying the MatrixDB database for interactions established by heparin (HP), heparan sulfate (HS), chondroitin sulfate (CS), dermatan sulfate (DS), and hyaluronan (HA) with proteins. No interaction of keratan sulfate was available in the MatrixDB database. The interaction network comprised five GAGs, 135 proteins, and 211 interactions (Figure 11.2).

A number of GAG-binding proteins are able to bind to several GAGs (Figure 11.3), showing that the GAG–protein interaction network is highly connected. Heparin has the highest number of protein partners that specifically bind to it. In contrast, all the DS-binding proteins are able to interact with other GAGs (Figure 11.3). Heparan sulfate also has a very small

Published on 24 May 2017 on http://pubs.rsc.org | doi:10

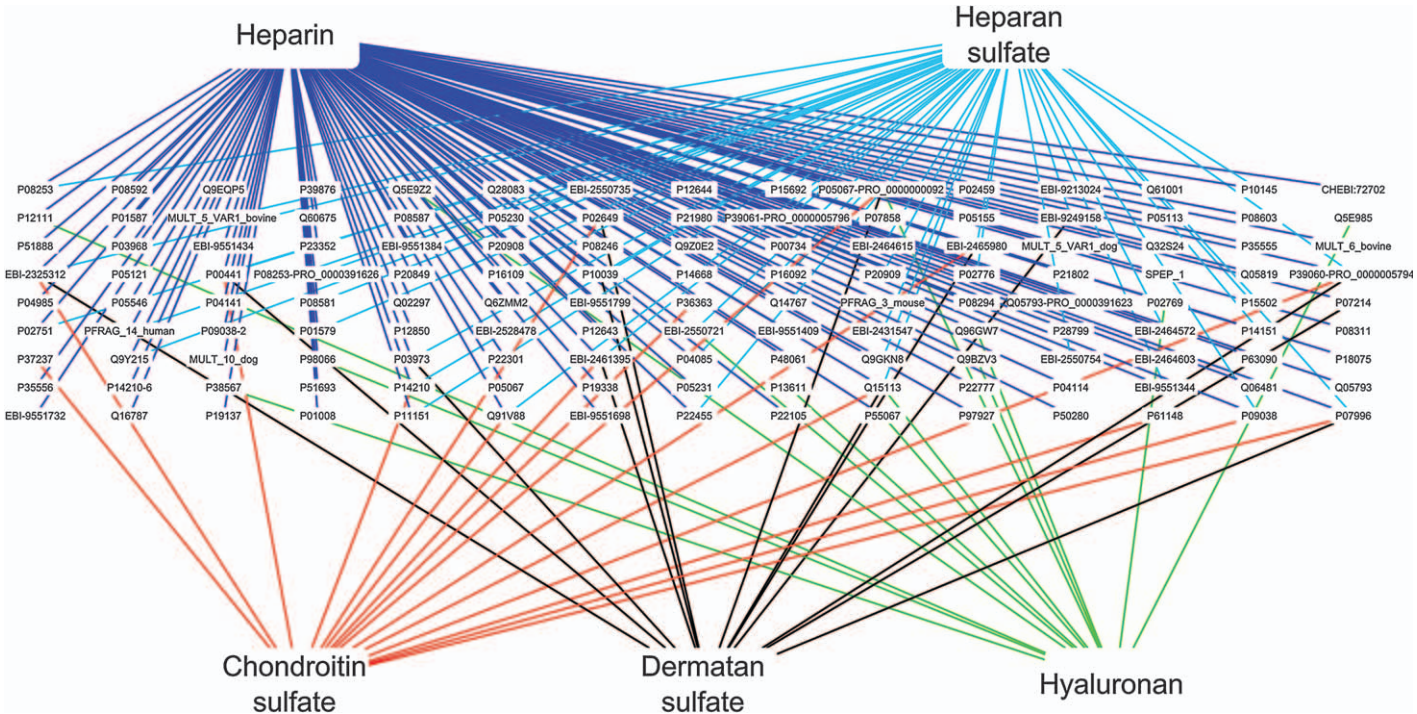


Figure 11.2 Interaction network of the major glycosaminoglycans (CS, DS, HA, HP, and HS) with proteins. Interaction data were collected from MatrixDB[25] and the protein–GAG network was built with Cytoscape.[29] Black, interactions of dermatan sulfate; blue, interactions of heparin; light blue, interactions of heparan sulfate; green, interactions of hyaluronan; red, interactions of chondroitin sulfate. Monomeric proteins are represented by their UniProtKB accession numbers and multimeric proteins by their complex portal identifiers. Bioactive fragments (matricryptins) are labeled by their UniProtKB profeature.

View Online

Published on 24 May 2017 on http://pubs.rsc.org | doi:10.1039/9781788010283-00398

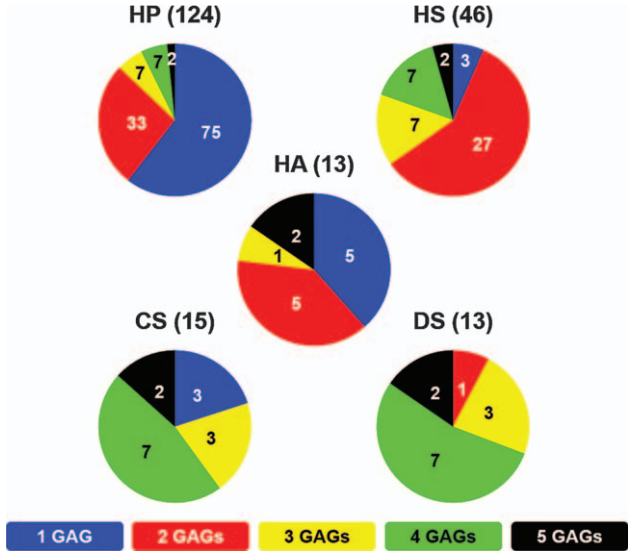


Figure 11.3 The number of proteins interacting with one (blue), two (red), three (yellow), four (green), and five (black) GAGs are indicated for each glycosaminoglycan (HP, heparin; HS, heparan sulfate; CS, chondroitin sulfate; DS, dermatan sulfate; HA, hyaluronan). These data come from the interaction network displayed in Figure 11.2.

number of specific protein partners. This might be because it has the same disaccharide unit as heparin, although the extent and clustering of post-synthetic modifications vary between both GAGs, and also heparin is more widely used than heparan sulfate for interaction studies.

We used the functional enrichment analysis tool FunRich[30] (www.funrich.org) to analyze the GAG–protein interaction network described above. The reference dataset was the human FunRich database.

The enrichment analysis of the term ''Cellular component'' shows that most GAG-binding proteins are located within the extracellular matrix (Figure 11.4A), which was expected given that GAGs are mostly located within the extracellular matrix and at the cell surface, although some of them have been identified in the nucleus.[41] Seven percent of GAG-binding proteins are located in basement membranes. Regarding ''Molecular function,'' 37% of the GAG-binding proteins are annotated as ''extracellular matrix structural constituent,'' which indicates that they play a role in ECM structural assembly and architecture (Figure 11.4B). In addition, some GAG partners display growth factor activity (7%), cytokine activity (8%), and cell adhesion molecule activity (7%). These functions are significantly enriched over the reference dataset ($p < 0.01$). A total of 39% of GAG-binding partners participate in cell growth and/or maintenance and ~30% in cell communication and signal transduction, but the enrichment in signal

View Online

Published on 24 May 2017 on http://pubs.rsc.org | doi:10.1039/9781788010283-00398

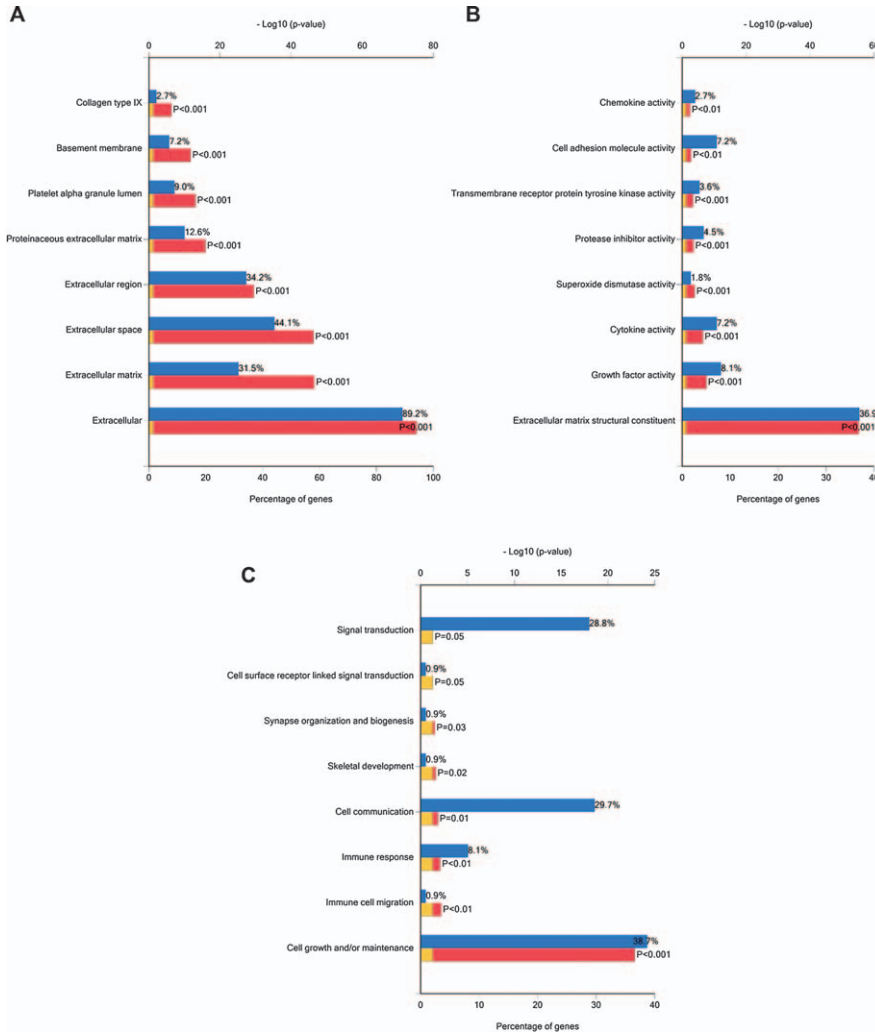


Figure 11.4 Enrichment analyses of the proteins binding to the major glycosaminoglycans (CS, DS, HA, HP, and HS). Interaction data were collected from MatrixDB[25] and enrichment analyses of (A) ''Cellular Component,'' (B) ''Molecular Function,'' and (C) ''Biological Process'' were performed with FunRich.[30] Blue bars, percentage of genes/proteins annotated with a term; red bars, p value; yellow, statistical threshold ($p = 0.05$).

transduction does not reach statistical significance ($p = 0.05$) (Figure 11.4C). In summary GAG-binding proteins identified by querying MatrixDB mostly contribute to the assembly and architecture of the extracellular matrix. In addition to this structural role, one-third of them regulate cell growth and cell communication.

View Online

Published on 24 May 2017 on http://pubs.rsc.org | doi:10.1039/9781788010283-00398

11.5 Contextualization of the Interaction Network with Kinetic Parameters and Affinity

11.5.1 Kinetic and Affinity Data Available in Interaction Databases

These parameters were collected from MatrixDB[25] and from ref. 22. SPR binding assays are widely used to characterize GAG–protein interactions and most values of equilibrium dissociation constants (63%) and association/dissociation rates (60%) stored in the MatrixDB database for heparin/heparan sulfate–protein interactions have been calculated using SPR. Indeed, we used SPR binding assays to characterize the interactions of heparin/heparan sulfate with several ECM proteins, including the matricryptin endostatin,[42] collagens I[43] and V,[43,44] procollagen C-proteinase enhancer-1,[45] angiopoietin like-4,[46] and integrin receptors.[47] For these experiments, biotinylated heparin or heparan sulfate was captured on streptavidin covalently immobilized on CM4 sensor chips and proteins were used as analytes.[43–47]

Kinetic parameters and affinity were used to rank and prioritize interactions within interaction networks. We included only heparin and heparan sulfate in this part of the work because few parameters were available for CS, DS, and HA. Edges of the HP/HS–protein interaction network were color-coded according to the values of the equilibrium dissociation constant (Figure 11.5A) and association rates (Figure 11.5B). The dissociation rates were coded using dots and dashes (Figure 11.5B). Five out of the eight partners of HP and HS bound to both GAGs with similar affinity according to the ranges we defined. The three other partners bound with a higher affinity to HP than to HS (Figure 11.5B). The association rates to HP and HS were in the same range for the three proteins with available data but only one protein dissociated at a similar rate from HP and HS. The two other proteins formed a more stable complex with HP than with HS.

11.5.2 Kinetics and Affinity Calculated by Bio-Layer Interferometry

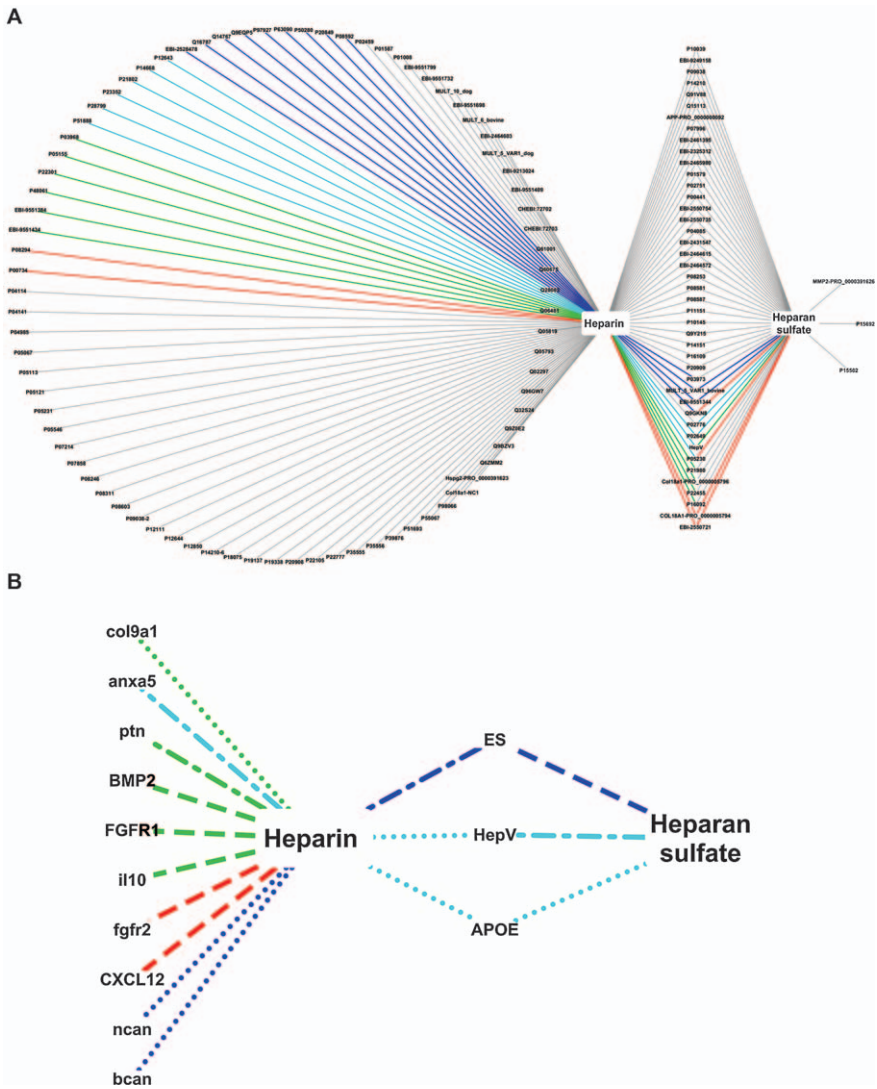
Bio-Layer Interferometry (BLI) assays were performed to characterize interactions of heparin with three ECM proteins. Collagen I (a triple-helical protein, MW 300 kDa), endostatin, a fragment of collagen XVIII[11,12] (MW 21 kDa), enriched in β-sheets,[48] and the propeptide of the extracellular enzyme lysyl oxidase[49] (MW ~30 kDa) were used as analytes. Collagen I is a rod-like molecule (300 nm in length and 1.5 nm in diameter), the propeptide of lysyl oxidase is intrinsically disordered and thus has an extended conformation, whereas endostatin is a globular protein. The three proteins are basic (p*I* 9.3 for endostatin, 9.6 for collagen I, and 11.8 for the propeptide of lysyl oxidase). Collagen I extracted from human placenta was obtained

View Online

Published on 24 May 2017 on http://pubs.rsc.org | doi:10.1039/9781788010283-00398

from Sigma-Aldrich (C7774). Human endostatin[31] and the propeptide of human lysyl oxidase were both expressed as recombinant proteins in human embryonic kidney cells with the octapeptide FLAG (DYKDDDDK) at their N-terminus and C-terminus, respectively. Both recombinant proteins were expressed and purified in the laboratory by affinity chromatography (Anti-FLAG M2 Agarose; Sigma-Aldrich, A2220).

BLI binding assays were performed with the Octet RED96 (Pall FortéBio) in black 96-well plates at 25 °C in a working volume of 200 μL under orbital agitation at 1000 rpm. This system is described in detail in Chapter 10. Biotinylated heparin was captured *via* streptavidin covalently immobilized



View Online

Published on 24 May 2017 on http://pubs.rsc.org | doi:10.1039/9781788010283-00398

on different streptavidin sensors coated with a proprietary polymer. Prior to each assay, tips were prewetted in 200 μL of HEPES-buffered saline (HBS) for at least 10 min. Streptavidin (SA; designed for immobilization of biotinylated proteins >1 kDa for protein–protein interaction), High Precision Streptavidin (SAX; designed for drug discovery and quality control), and Super Streptavidin (SSA; designed for immobilization of proteins, peptides, and nucleic acids and for small-molecule interactions) sensors were equilibrated in HBS, loaded with 10 or 100 $\mu g\,mL^{-1}$ biotinylated heparin (Sigma-Aldrich, H3393, 16 kDa)[42] in HBS, washed in HBS and equilibrated in HBS-P^+ (endostatin and propeptide of lysyl oxidase) or HBS (collagen I). Binding curves were analyzed using the FortéBio Data Analysis 9.0 software, with a global 1 : 1 model fitting set.

The equilibrium dissociation constant of collagen I–heparin interaction displayed a 1.4-fold increase when calculated from BLI experiments performed on an SA sensor compared with the value determined by SPR experiments carried out on a CM4 sensor chip, but both values are in the low nanomolar range (4.8 nM by BLI *versus* 3.4 nM by SPR[43]) (Table 11.1). The equilibrium dissociation constant of the endostatin–heparin interaction varied by 1.5-fold when calculated from data collected on SSA, which allows a high immobilization density, and SAX sensors. Both the association and dissociation rates were decreased by 2.3- and 1.7-fold, respectively, on an SSA sensor compared with an SAX sensor, but the measurements performed on the SAX sensor had a large standard deviation (Table 11.1). The nature of the sensor surface coating influences the value of the equilibrium dissociation constant and of the kinetic parameters of HP–endostatin interactions.

We then investigated the binding of the propeptide of lysyl oxidase to heparin using an SSA sensor (Figure 11.6). The curves displayed negative shifts and were flipped to calculate kinetic parameters and affinity. Flipping of the data can be performed because the responses were proportional to the analyte concentration, and values of kinetic parameters were validated to be

Figure 11.5 Heparin/heparan sulfate–protein interaction networks contain 124 and 46 proteins, respectively, and share 43 partners. Proteins binding to both GAGs are displayed in the center. (A) Edges connecting GAGs and GAG-binding proteins were color-coded according to the value of the equilibrium dissociation constants (K_D). Gray, no data available; blue, 0.3–10 nM; cyan, 10.5–20 nM; green, 36–400 nM; red, 1140–10 000 nM. (B) Edges connecting GAGs and GAG-binding proteins were color-coded according to the value of the association rate (blue, 2.23–9.04×10^3 $M^{-1}\,s^{-1}$; cyan, 1.9–7.6×10^4 $M^{-1}\,s^{-1}$; green, 1.4–6.6×10^5 $M^{-1}\,s^{-1}$; red, 2.1–2.16×10^6 $M^{-1}\,s^{-1}$). For the dissociation rate the code was the following: dotted, 2.3–6.6×10^{-4} s^{-1}; dashed-dotted, 1.2–4.3×10^{-3} s^{-1}; dashed, 1–8.3×10^{-2} s^{-1}). Kinetic and affinity data were extracted from MatrixDB database.[25] The interaction network was built with Cytoscape.[29] Monomeric proteins were labeled according to their gene name. Multimeric proteins were labeled with their Complex Portal identifiers and bioactive fragments (matricryptins) by their UniProtKB profeature. ES, endostatin; HepV, a fragment of the collagen α_1(V) chain.

View Online

Published on 24 May 2017 on http://pubs.rsc.org | doi:10.1039/9781788010283-00398

Table 11.1 Kinetic parameters and equilibrium dissociation constant of heparin–protein interaction calculated from BLI experiments performed in HBS-P^+ with Super Streptavidin (SSA) or High Precision Streptavidin (SAX) sensors or in HBS with streptavidin (SA) sensors for collagen I. Collagen I, 0.26–67 nM; endostatin, 0.16–10 μM; propeptide of lysyl oxidase, 0.22–14 μM. Data were fitted to a 1 : 1 model.

Collagen I	SA	
Association rate ($M^{-1}\,s^{-1}$)	$2.8 \pm 0.6 \times 10^{5}$	
Dissociation rate (s^{-1})	$1.3 \pm 0.5 \times 10^{-3}$	
K_D (nM)	4.8 ± 2.9	
Endostatin	**SSA**	**SAX**
Association rate ($M^{-1}\,s^{-1}$)	3.0×10^{3}	$7.0 \pm 5.2 \times 10^{3}$
Dissociation rate (s^{-1})	9.8×10^{-5}	$1.7 \pm 1.6 \times 10^{-4}$
K_D (nM)	31.8	21.3 ± 7.2
Propeptide of lysyl oxidase	**SSA (HP 16 kDa)**	**SSA (HP 6 kDa)**
Association rate ($M^{-1}\,s^{-1}$)	2.1×10^{2}	1.9×10^{2}
Dissociation rate (s^{-1})	2.1×10^{-4}	3.6×10^{-5}
K_D	1.0 μM	190 nM

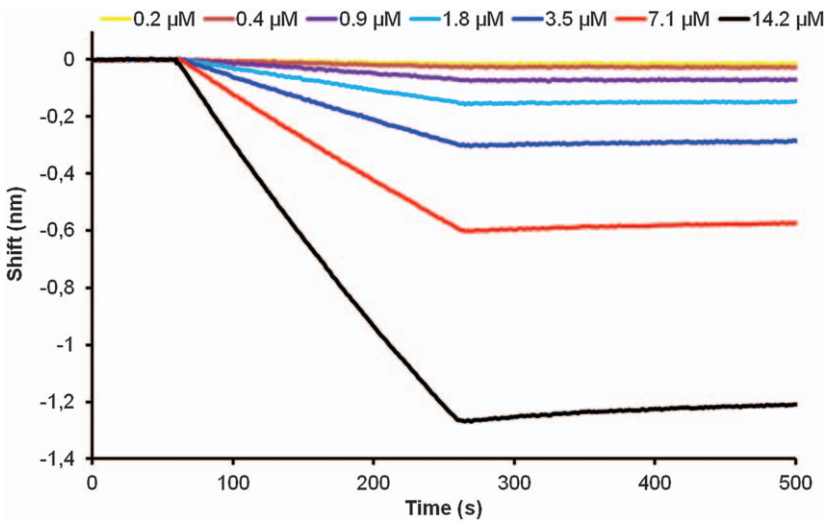


Figure 11.6 Bio-Layer Interferometry analyses of the binding of the propeptide of lysyl oxidase (0.2–14.2 μM) to heparin from porcine intestinal mucosa (H3393) biotinylated as described[42] and captured on an SSA sensor. The data were flipped as described in ref. 50.

independent of the magnitude of the nm shift.[50] A negative signal can occur when the optical thickness decreases upon binding. This can be due either to the release of a cofactor or when a more closely packed structure is obtained by a conformational change of the ligand.

View Online

Published on 24 May 2017 on http://pubs.rsc.org | doi:10.1039/9781788010283-00398

Last, we determined the influence of heparin size (6 and 16 kDa) on kinetics and affinity calculated for the heparin-LOX propeptide on a SSA sensor. The propeptide bound to both heparins at a similar rate but dissociated faster from full-length heparin, leading to a 5-fold decrease in the value of the equilibrium dissociation constant for 6-kDa heparin (Table 11.1). The propeptide bound with a higher affinity to 6-kDa heparin than to 16-kDa heparin.

Tutorial Aspects of BLI (see BLI features and benefits in Chapter 10)

- For accurate measurements, be aware of reflections from the bottom of the well plate causing jumps in the response curves. There are protocols to prevent this (see Chapter 10, Section 10.5.2.2).
- SPR applies a boost of the evanescent field by a factor of ~30 (see Chapter 2, Section 2.3.4) and is intrinsically more sensitive than BLI.
- Why do we need to flip the interaction curves and what is the reason that these negative responses are measured? See answer to question 2 at the end of this book.

11.6 Conclusion

We have set up a roadmap for building and analyzing GAG–protein interaction networks, for integrating kinetics and affinity into these networks, and for analyzing them by performing functional enrichment analyses. Label-free interaction analysis is a crucial tool for calculating the binding strength and kinetics of the interactants in the networks. Screening of potential interacting pairs was performed by SPRi in a Biacore Flexchip system, whereas the association and dissociation rates and the equilibrium dissociation constants were determined by either SPR or BLI. We studied the binding of heparin with three proteins by BLI using three different streptavidin sensors and showed that these surfaces influence the calculated values of equilibrium dissociation constant, and the association and dissociation rates of heparin–protein interactions. These changes are associated at least in part with the conformation, the isoelectric point, and the post-translational modifications (*e.g.* glycosylation) of the proteins and are likely to be protein dependent. The molecular mechanisms underlying the biological functions of the biomolecular interaction networks can be revealed using a combination of instruments based on SPRi, SPR, and BLI and bioinformatic tools as shown in this chapter.

11.7 Abbreviations

BLI Bio-Layer Interferometry
CS chondroitin sulfate

View Online

DS	dermatan sulfate
ECM	extracellular matrix
EDC	1-ethyl-3-(3-dimethylaminopropyl) carbodiimide hydrochloride
GAG	glycosaminoglycan
HA	hyaluronan
HBS	HEPES-buffered saline
HEPES	4-(2-hydroxyethyl)-1-piperazineethanesulfonic acid
HP	heparin
HS	heparan sulfate
MW	molecular weight
NHS	*N*-hydroxysulfosuccinimide
RU	resonance unit
SPR	surface plasmon resonance
SPRi	surface plasmon resonance imaging

Published on 24 May 2017 on http://pubs.rsc.org | doi:10.1039/9781788010283-00398

11.8 Questions

1. The Biacore Flexchip instrument is very useful for identifying protein and glycosaminoglycan partners. Why do we need a combination of instruments based on different approaches (SPRi, SPR, and BLI), as also discussed in Chapter 12, Section 12.2?
2. Why do we need to flip the BLI interaction curves (see Figure 11.6) and what is the reason why negative responses are measured as a result of biomolecular binding?

Acknowledgements

The authors used the SPR and SPRi systems of the Protein Science Facility (UMS 3444/US8, SFR Biosciences, Lyon, France). They thank Loïc Blum and Christophe Marquette (UMR 5246 CNRS, Université Lyon 1, France) and AXO Science (Villeurbanne, France) for access to the spotter. This work was supported in part by a grant from the Fondation pour la Recherche Médicale (DBI20141231336) to S.R.-B. and N.T.-M. and by a grant from the Institut Français de Bioinformatique (ANR-11-INS-0013, Glycomatrix project) to S.R.-B. and N.T.-M.

References

1. C. Frantz, K. M. Stewart and V. M. Weaver, *J. Cell Sci.*, 2010, **123**, 4195–4200.
2. A. D. Theocharis, S. S. Skandalis, C. Gialeli and N. K. Karamanos, *Adv. Drug Delivery Rev.*, 2016, **97**, 4–27.
3. M. A. Karsdal *et al.*, *Assay Drug Dev. Technol.*, 2013, **11**, 70–92.
4. P. Lu, K. Takai, V. M. Weaver and Z. Werb, *Cold Spring Harbor Perspect. Biol.*, 2011, **3**, a005058.

View Online

Published on 24 May 2017 on http://pubs.rsc.org | doi:10.1039/9781788010283-00398

5. T. R. Cox and J. T. Erler, *Dis. Models & Mech.*, 2011, **4**, 165–178.
6. B. N. Brown and S. F. Badylak, *Transl. Res. J. Lab. Clin. Med.*, 2014, **163**, 268–285.
7. H. Järveläinen, A. Sainio, M. Koulu, T. N. Wight and R. Penttinen, *Pharmacol. Rev.*, 2009, **61**, 198–223.
8. R. O. Hynes and A. Naba, *Cold Spring Harbor Perspect. Biol.*, 2012, **4**, a004903.
9. A. Naba, K. R. Clauser, H. Ding, C. A. Whittaker, S. A. Carr and R. O. Hynes, *Matrix Biol.*, 2016, **49**, 10–24.
10. S. Ricard-Blum and R. Salza, *Exp. Dermatol.*, 2014, **23**, 457–463.
11. S. Ricard-Blum and S. D. Vallet, *Biochimie*, 2016, **122**, 300–313.
12. S. Ricard-Blum and S. D. Vallet, *Front. Pharmacol.*, 2016, **7**, 11.
13. A. Walia *et al.*, *Biochim. Biophys. Acta*, 2015, **1850**, 2422–2438.
14. S. Wang, X.-A. Lu, P. Liu, Y. Fu, L. Jia, S. Zhan and Y. Luo, *Mol. Cancer Ther.*, 2015, **14**, 1192–1201.
15. M. Fatoux-Ardore, F. Peysselon, A. Weiss, P. Bastien, F. Pratlong and S. Ricard-Blum, *Infect. Immun.*, 2014, **82**, 594–606.
16. R. V. Iozzo and L. Schaefer, *Matrix Biol.*, 2015, **42**, 11–55.
17. J.-P. Li and M. Kusche-Gullberg, *Int. Rev. Cell Mol. Biol.*, 2016, **325**, 215–273.
18. J. D. Esko and S. B. Selleck, *Annu. Rev. Biochem.*, 2002, **71**, 435–471.
19. R. Sasisekharan, Z. Shriver, G. Venkataraman and U. Narayanasami, *Nat. Rev. Cancer*, 2002, **2**, 521–528.
20. A. Ori, M. C. Wilkinson and D. G. Fernig, *J. Biol. Chem.*, 2011, **286**, 19892–19904.
21. D. Xu and J. D. Esko, *Annu. Rev. Biochem.*, 2014, **83**, 129–157.
22. F. Peysselon and S. Ricard-Blum, *Matrix Biol.*, 2014, **35**, 73–81.
23. E. Chautard, L. Ballut, N. Thierry-Mieg and S. Ricard-Blum, *Bioinformatics*, 2009, **25**, 690–691.
24. E. Chautard, M. Fatoux-Ardore, L. Ballut, N. Thierry-Mieg and S. Ricard-Blum, *Nucleic Acids Res.*, 2011, **39**, D235–D240.
25. G. Launay, R. Salza, D. Multedo, N. Thierry-Mieg and S. Ricard-Blum, *Nucleic Acids Res.*, 2015, **43**, D321–D327.
26. S. Orchard *et al.*, *Nat. Methods*, 2012, **9**, 345–350.
27. S. Orchard *et al.*, *Nucleic Acids Res.*, 2014, **42**, D358–D363.
28. J. M. Brockman and S. M. Fernandes, *Am. Lab.*, 2001, **33**, 37–41.
29. P. Shannon *et al.*, *Genome Res.*, 2003, **13**, 2498–2504.
30. M. Pathan *et al.*, *Proteomics*, 2015, **15**, 2597–2601.
31. C. Faye, E. Chautard, B. R. Olsen and S. Ricard-Blum, *J. Biol. Chem.*, 2009, **284**, 22041–22047.
32. R. Salza *et al.*, *Biochem. J.*, 2014, **457**, 137–149.
33. F. Peysselon, M. Fatoux-Ardore and S. Ricard-Blum, in *From Binary Interactions of Glycosaminoglycans and Proteoglycans to Interaction Networks*, Matrix Biology Institute, Edgewater, New Jersey, USA, ed. Endre A. Balazs, 2012, **5**, 277–298.
34. R. L. Rich *et al.*, *Anal. Biochem.*, 2008, **373**, 112–120.

View Online

35. S. Symoens *et al.*, *Biochem. J.*, 2011, **433**, 371–381.
36. C. Bonod-Bidaud *et al.*, *J. Invest. Dermatol.*, 2012, **132**, 1841–1849.
37. R. Wellhausen and H. Seitz, *J. Biomed. Biotechnol.*, 2012, **2012**, 831347.
38. D. Wassaf *et al.*, *Anal. Biochem.*, 2006, **351**, 241–253.
39. R. L. Rich *et al.*, *Anal. Biochem.*, 2009, **386**, 194–216.
40. B. H. M. Meldal *et al.*, *Nucleic Acids Res.*, 2015, **43**, D479–D484.
41. M. D. Stewart and R. D. Sanderson, *Matrix Biol.*, 2014, **35**, 56–59.
42. S. Ricard-Blum *et al.*, *J. Biol. Chem.*, 2004, **279**, 2927–2936.
43. S. Ricard-Blum, M. Beraud, N. Raynal, R. W. Farndale and F. Ruggiero, *J. Biol. Chem.*, 2006, **281**, 25195–25204.
44. S. Ricard-Blum, L. L. Peel, F. Ruggiero and N. J. Freeman, *Anal. Biochem.*, 2006, **352**, 252–259.
45. T. Weiss, S. Ricard-Blum, L. Moschcovich, E. Wineman, S. Mesilaty and E. Kessler, *J. Biol. Chem.*, 2010, **285**, 33867–33874.
46. C. Chomel, A. Cazes, C. Faye, M. Bignon, E. Gomez, C. Ardidie-Robouant, A. Barret, S. Ricard-Blum, L. Muller, S. Germain and C. Monnot, *FASEB J.*, 2009, **23**, 940–949.
47. C. Faye, C. Moreau, E. Chautard, R. Jetne, N. Fukai, F. Ruggiero, M. J. Humphries, B. R. Olsen and S. Ricard-Blum, *J. Biol. Chem.*, 2009, **284**, 22029–22040.
48. Y. H. Ding, K. Javaherian, K. M. Lo, R. Chopra, T. Boehm, J. Lanciotti, B. A. Harris, Y. Li, R. Shapiro, E. Hohenester, R. Timpl, J. Folkman and D. C. Wiley, *Proc. Natl. Acad. Sci. U. S. A.*, 1998, **95**, 10443–10448.
49. S. R. Vora, Y. Guo, D. N. Stephens, E. Salih, E. D. Vu, K. H. Kirsch, G. E. Sonenshein and P. C. Trackman, *Biochemistry*, 2010, **49**, 2962–2972.
50. B. Heidecker, K. Witte and W. McGinn-Straub, *Octet Appl. Note*, 2011, **3**, 1–8.

Published on 24 May 2017 on http://pubs.rsc.org | doi:10.1039/9781788010283-00398

Published on 24 May 2017 on http://pubs.rsc.org | doi:10.1039/9781788010283-00415

CHAPTER 12

Future Trends in SPR Technology

RICHARD B. M. SCHASFOORT

Medical Cell BioPhysics Group (MCBP), MIRA Institute, University of Twente, P.O. Box 217, 7500 AE Enschede, The Netherlands
Email: r.b.m.schasfoort@utwente.nl

12.1 Introduction

In 2016, surface plasmon resonance (SPR) technology is still the gold standard in direct biomolecular interaction sensing, as predicted 10 years ago. However, the dominance of SPR over other label-free technologies is tending to come more into balance with other technologies, *e.g.* biolayer interferometry (BLI) (see Chapter 10). In the 1990s and early 2000s, a single company (Biacore) mainly dominated the market (~90%) for high-quality SPR systems, including optics, liquid handling, and sensor chips. As highlighted in Chapter 3, with currently 26 SPR-related companies, the market is now more open than ever before and competition between companies is taking place in several aspects of SPR technology and other evanescent field-based optical label-free sensing systems. A forecast has been given of the global SPR market revenue for 2015, 2020, and 2025.[1] Key features of this forecast are the analysis of the SPR market by region, product, and application, and a revenue forecast in terms of absolute dollars. It is estimated that the global market for SPR devices will account for over US$1 billion by the end of 2025, owing to increasing application in the drug discovery segment.

The customers for SPR instruments will profit from the competition between the providers of the technology, offering more flexibility, innovation,

Handbook of Surface Plasmon Resonance, 2nd Edition
Edited by Richard B. M. Schasfoort
© The Royal Society of Chemistry 2017
Published by the Royal Society of Chemistry, www.rsc.org

View Online

Published on 24 May 2017 on http://pubs.rsc.org | doi:10.1039/9781788010283-00415

and cost-effectiveness. The field of clinical analysis is expected to undergo an evolutionary change with the introduction of new multianalyte diagnostic label-free systems where point-of-care (POC) devices for specific applications are the ultimate objective. Mainly the combination of SPR imaging (SPRi) and dedicated microfluidics may drive the technology to another level of commercialization.

The main aspects of the future trends were already covered in the first edition of this Handbook in 2008, but in 2016 decisive trends could be observed in the development of instrumentation in the market (Figure 12.1). First, there is an enormous need for high-throughput analysis and, since the introduction of the Octet system of FortéBio (now part of Pall Life Sciences) in 2005, this technology had a huge impact. FortéBio was, and still is, the fastest growing company in the label-free technology market and the BLI technology (Octet) cannot be neglected any longer (see Chapter 10).

Further in this chapter, anticipated trends regarding label-free detection applications are highlighted. Necessarily, as can be observed with the trends as identified and described in the first edition, this may have a speculative character. The too academic trends in the first edition are discarded in this chapter, and new trends are highlighted based on progressive personal

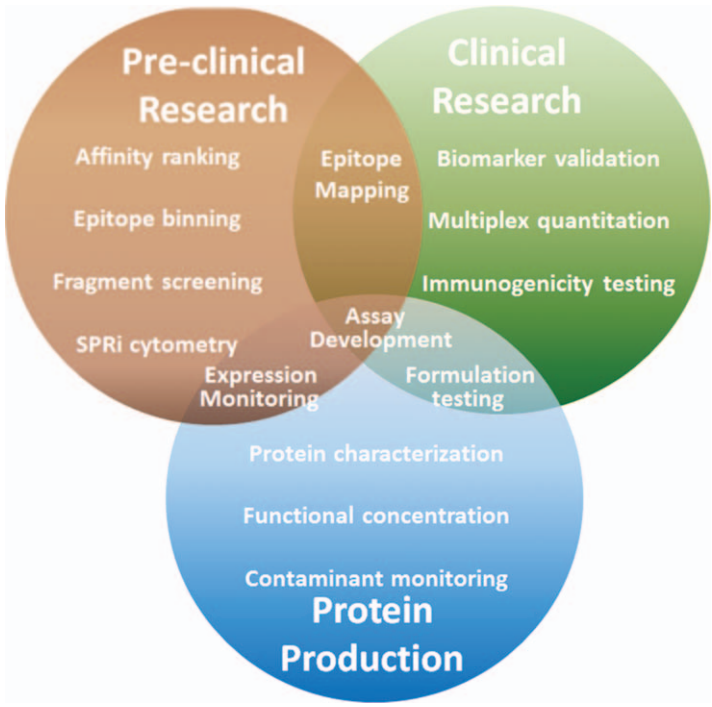


Figure 12.1 SPR is gaining impact in various applications in life sciences. SPRi cytometry is a new field in preclinical research. Each application field needs high-throughput analysis.

View Online

Published on 24 May 2017 on http://pubs.rsc.org | doi:10.1039/9781788010283-00415

insight. Such an attempt may be regarded as biased to some extent by the interests and perspectives of the author. However, it is hoped that this chapter will, at the minimum, provide a description of some exciting prospects for the coming decade in the main areas of SPR development and instrumental applications. It is structured according to the three essential units that make up SPR instruments: (1) the detection instrumentation, (2) the fluidics, and (3) sensor surfaces/chips. These units are complementary to each other and all critical for the quality and performance of the overall SPR biosensor system.

Special attention is devoted to the field of SPR cytometry (Section 12.8) as an upcoming application field and one can already identify five different application areas where label-free detection in combination with living cells is appealing. The McSPRinter technology is considered the most promising commercial platform to meet the demands of researchers in the field of selection of cells for excretion products both in quality and quantity. In the following sections, the author's perception of the trends in each of these fields is discussed.

12.2 Trends in SPR Instrumentation

Although the improvements in and functionality of the Biacore line of instruments during the past 25 years of SPR technology are impressive, new trends of niche applications in segmented parts in the market are definitely appearing. The recombinant protein area demands the screening of a large number of analytes in complex samples, exceeding by far the currently readily available number of 4–20 channels and single-needle injections. Multianalyte parallel monitoring of kinetic parameters is desired and the introduction of the Octet HTX by Pall Life Sciences in 2014 meets this demand. Additionally, the high multiplex power of the IBIS MX96/CFM technology (IBIS Technologies, Enschede, The Netherlands) is the answer for screening many biomolecular interactions simultaneously for epitope binning and affinity ranking applications (Figure 12.2). Over the next 5 years it is foreseen that hundreds to thousands of simultaneous biomolecular interactions should be measured for screening the quality of the binders. SPR imaging technology followed the protein microarray technology, and the kinetic parameters of hundreds of interactions can be determined in a parallel manner. The eight-needle Biacore 8K is GE Healthcare's answer to the high-throughput needs of pharmaceutical companies who demand screening power for highly sensitive fragment and low molecular weight compound analysis.

12.2.1 Nanoparticle-based Localized SPR (LSPR)

SPR phenomena are not restricted to planar multilayers as discussed in this book: for metal particles, usually gold, with dimensions much smaller than the wavelength of the interacting light, surface plasmon effects can be much

View Online

Published on 24 May 2017 on http://pubs.rsc.org | doi:10.1039/9781788010283-00415

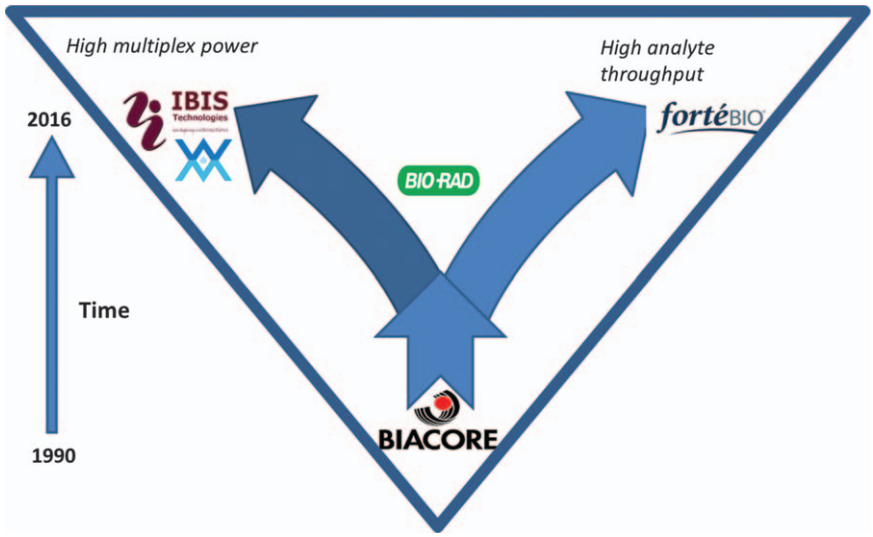


Figure 12.2 The triangle of high-end instruments installed at many pharmaceutical companies. ''One size fits all'' does not work any longer but the companies need the triangle of instruments for the various projects in the discovery of new therapeutic lead candidates.

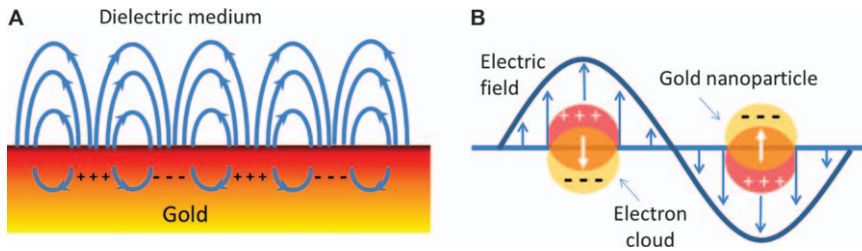


Figure 12.3 Schematic illustration of the physical phenomenon of planar and nanoparticle SPR: (A) SPR and (B) LSPR.

more prominent.[2] Nanostructured surfaces, such as nanoholes, can also be applied to exploit surface plasmon/plasmonic effects for sensing biomolecular interactions.

LSPR occurs in metal nanoparticles that are much smaller than the incident wavelength. Here the induced polarization oscillates locally around the nanoparticle at a certain frequency (Figure 12.3). The LSPR wavelength and peak width of the nanoparticles are extremely sensitive to nanoparticle composition, size, shape, dielectric environment, and proximity to other nanoparticles.[3]

The new nanoparticle LSPR trend is unequivocally relevant and some instrumentation manufacturers already apply the principle in their instruments (see Chapter 3, Section 3.5.2). The use of metal nanoparticles as a surface plasmon-assisted field can also be exploited in intrinsic refractive index (RI) sensors, analogous to the more familiar planar SPR experiments

View Online

Published on 24 May 2017 on http://pubs.rsc.org | doi:10.1039/9781788010283-00415

(for a review, see ref. 4). The physical basis of this application is light extinction (absorption due to a local surface plasmon resonance effect and scattering), which is heavily dependent on the nanoparticle's dielectric constant, size, and geometry, and also on the dielectric constant of the surrounding medium. The principle is now crystallized for sensing applications as LSPR as described by Haes and van Duyne[5] for the first time. A nanoparticle-based LSPR sensor yields sensitive biomolecular interaction detection with extremely simple, small, light, robust, and low-cost instrumentation. Haes and Van Duyne used this LSPR spectroscopy method to detect from less than 1 pM up to micromolar concentrations of biological molecules. Gold nanoparticles of defined dimensions can be coated on a substrate in order to allow the easy exchange of liquids similar to flat SPR instruments, and we can now observe commercial instruments in the market that exploit this LSPR technology. As described in Chapter 3, Section 3.5.2, the instruments of Nicoya (OpenSPR) and Affinité Instruments (P4SPR) apply the LSPR principle in affordable instruments. Hong and Kao[6] developed such a gold nanoparticle-coated film to achieve highly spatially resolved biosensing that is based on LSPR. It has been described that unlike the planar gold film employed for conventional SPR sensing, the gold nanoparticle film relies exclusively on shifting the peak extinction wavelength for the detection of biomolecular interactions, and it does not depend critically on the angle of incidence. However, it turned out that wavelength shifts of the SPR-dip cannot be detected as sensitively as with the Kretschmann-operated SPR instruments with angular resolution. Further complicating factors are the quality control (size, distribution, layer thickness) of the ''rough'' nanoparticle surface and functionalization, which determines the accurate measurement of reliable kinetic parameters. An LSPR device that is able to measure low molecular weight compounds and meet the Biacore standards, as described in Chapter 7, needs, in the author's opinion, at least a decade of further development.

12.2.2 SPR Imaging

SPR imaging has the ability to provide a microscopic view of the sensor surface and define certain regions of interest for the measurement of many biomolecular interactions at the same time. Some instruments fit in the full multiplex mode whereas others (*e.g.* from Sierra Sensors) apply the imaging principle to measure many analytes simultaneously (*e.g.* eight using the hydrodynamic isolation principle; see Chapter 3, Section 3.5.4.6). Reference spots, positive and negative controls to determine the non-specific binding and/or cross-over interactions, and also triplicates or higher replicates of identical interactions for checking the variability of the sensor surface are helpful for obtaining reliable, accurate, and valid data. Common mode effects caused by temperature changes, bulk RI shifts, or flow direction shifts can be compensated using these local reference spots. For every spot, the shift of the SPR-dip should be followed to permit subtraction and referencing. The data should not include an instrumental artifact but should

View Online

show the real kinetic data of the parallel interaction process. The development of SPR imaging is not in its end stage, as it can be seen that the sensitivity of SPR imaging instruments does not yet meet the standards of, *e.g.*, the Biacore S200 instrument.

It is foreseen that in due course the further improvements in SPR imaging will be enormous as a result of huge improvements in hardware and better digital camera specifications with high-speed frame grabbing and extremely low pixel noise.

Published on 24 May 2017 on http://pubs.rsc.org | doi:10.1039/9781788010283-00415

12.3 Trends in Fluidics

Microfluidic approaches instead of cuvette systems turned out to be the most powerful technology for the controlled, accurate, and reliable binding to the SPR surface for maximum sensitivity and intrinsic kinetic rate and affinity control and obtaining thermodynamic properties of the molecules under study. Attractive features in advanced microfluidic cartridges are low sample consumption and the potential for relatively high mass transfer when high flow rates and thin channels are used. As described already in Chapter 3, Section 3.4.2 and Figure 3.3, flow channels are formed, in principle, by pressing a grooved surface against the sensor chip. Biacore introduced a microfluidic cartridge (the IFC; interfluidics cartridge) for sample delivery in 1990, with incorporated pneumatic values that allow specific channels to be closed off, thereby providing control over the flow paths. This allowed the sample or buffer liquid volumes to be directed to different surface areas. Also integrated was an (HPLC-like) injection loop in this microfluidic cartridge that allowed a fixed sample volume to be chased by running buffer and flowed over the surface.

Although this technology has shown to be fairly powerful and far superior with regard to stability in comparison with simple cuvette-based systems, some improvements were addressed in different designs. For example, the constraints of the injection loop with finite fixed sample volumes allowing only limited sample contact times and flow rates were overcome with the oscillatory flow technique reported by Lokate *et al.*[7] This permits the use of sample plugs of smaller volume, yet allowing simultaneously very long contact times while maintaining high flow rates and mass transfer. This can be very important when working with limited sample volumes, for characterizing better the kinetic binding parameters by permitting the binding progress to reach a steady state, and to be utilized to improve the sensitivity for analyte detection at low concentrations.

To improve the usage of each sensor flow channel, Biacore introduced the option of hydrodynamically addressing different spots within a channel, thus multiplexing the use of each sensor flow channel as shown in Section 3.6 (Biacore A100/4000) and Figure 3.31. A different microfluidic design was implemented in the commercial ProteOn system by Bio-Rad, where a criss-cross pattern of microfluidic channels allows the binding of a series of several samples to several different sensor spots to be measured in parallel – a design particularly suitable to SPR imaging (see Figure 3.23). The latter

View Online

Published on 24 May 2017 on http://pubs.rsc.org | doi:10.1039/9781788010283-00415

multianalyte detection permits experimental designs that do not require surface regeneration. However, Bio-Rad discontinued the production of the ProteOn XPR36 instruments and the supply of disposables and services will stop in 2019. The integrated high-end ProteOn XPR36 possessed both higher analyte (6×) and higher multiplex (6×) throughput, but it turned out that different instruments show either much higher analyte (Octet HTX) or much higher multiplex (IBIS MX96) throughput as shown in the triangle in Figure 12.2. A one-technology-fits-all approach as developed in the ProteOn XPR36 for the various projects in pharmaceutical screening campaigns is no longer valid and the higher analyte (6×) and higher ligand channels (6×) appeared to be a too mediocre improvement over the standard four-channel Biacore instruments.

12.3.1 Microarray Spotting on SPR Sensor Chips

With the introduction of protein microarrays in the late 1990s, there was tremendous excitement about the potential of protein arrays to improve further our understanding of protein expression, function, and structure on a scale approaching the number of proteins in the proteome. However, there was also from the beginning some hesitancy by many scientists to adopt a technology that is often still perceived as unstable and irreproducible. Protein microarrays were developed largely by extending technologies used for gene chips.[8] Most protein arrays as currently developed rely on detection technologies that apply fluorescent tags. Fluorescence detection methods are definitely successful for gene biochips, but much less convenient with protein chips owing to the heterogeneity of proteins, the variability of affinity of binding, difficulties in the synthesis of conjugates, and the potential for non-specific binding. Also, signal-producing reactions in solution catalyzed by commonly used enzyme-linked antibodies are difficult to implement in an immunoassay microarray format, where the product will diffuse away from the surface, diminishing the potential for the discrimination of spots. However, Robert Corn and colleagues applied an enzymatic amplification method as described for SPR sensing in the first edition of this Handbook, Section 8.3, which applied a localized non-soluble precipitate, which was detected by SPR. This principle of enzymatic amplification is applied in the Genalyte POC device using evanescent field-based ring resonator technology (see Section 12.6.1).[9]

A major challenge is how to spot the ligands on the SPR sensor surface. Several commercial array systems have been developed for printing target DNA on microscope slides, which were adapted to create protein microarrays. In short, every arrayer consists of an XYZ robot, the printhead of which travels between a microtiter plate, containing the ligand, and the sensor surface, which is a standard 3×1 inch microscopic glass slide. In total 16 spots per mm^2 (4×4) can be printed when spots have a pitch width of 250 μm, so a 3×1 inch glass slide can easily contain 20 000 spots. The differences between the available systems are mainly based on the structure of the printhead: there are several different ways of picking up a small

View Online

amount of ligand solution and printing small amounts of this solution in an orderly and systematic way on the sensor surface. Examples of arrayer methodologies include piezo technology (inkjet dispensers), quills (split-pen), and ''pen and ring'' systems, which are described in a review paper.[10] As a consequence, the systems differ considerably in reliability, accuracy, capacity, and the required (starting) volume of sample. For SPR imaging, printing technology problems are now solved with the technology developed and commercialized by Wasatch Microfluidics (Salt Lake City, UT, USA) (see Figure 12.4).

The continuous flow microspotter (CFM) has a patented microfluidic printing technology to deposit up to 384 different ligands on a sensor surface

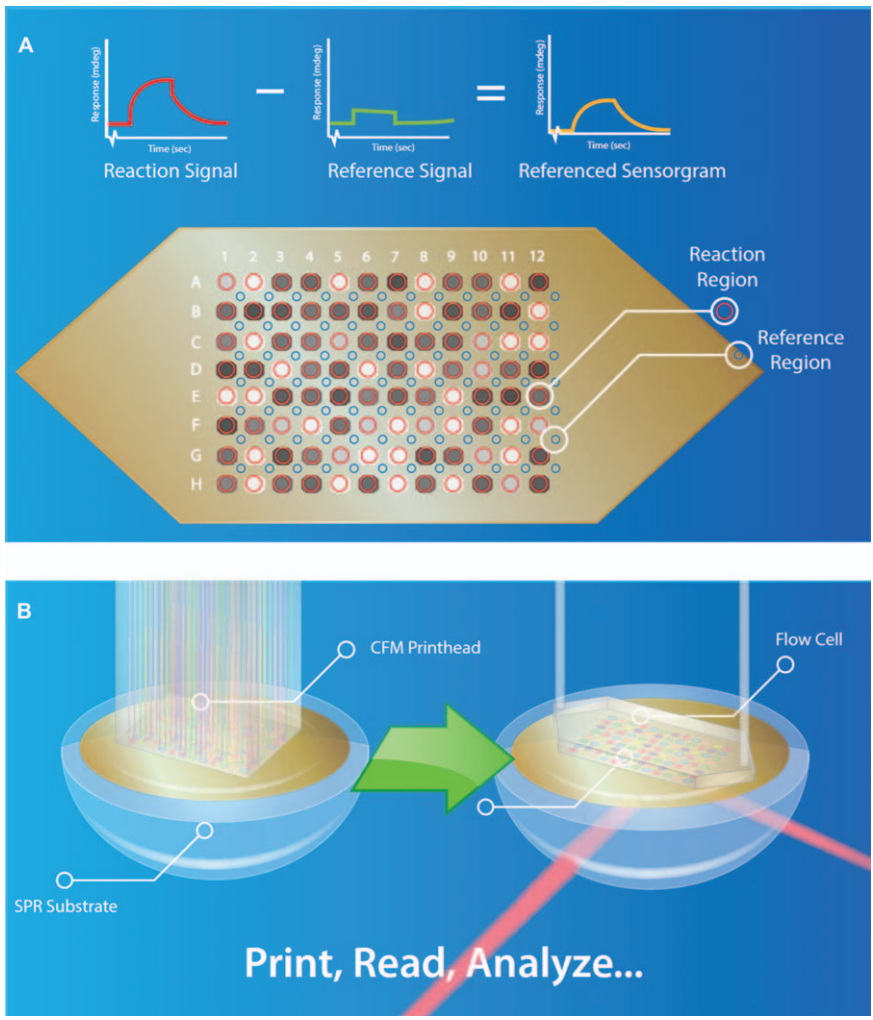


Figure 12.4 (A) Analyte exposed to a 96-plex array in an SPR imager flow cell. (B) Printing of 96-plex array (CFM) followed by monitoring of analyte interactions in an SPR imager.
Reused with permission from Josh Eckman.

Published on 24 May 2017 on http://pubs.rsc.org | doi:10.1039/9781788010283-00415

View Online

Published on 24 May 2017 on http://pubs.rsc.org | doi:10.1039/9781788010283-00415

in an array of distinct spots. Unlike other systems that deposit droplets of material ''*en masse*'', the CFM uses flow to cycle molecules back and forth over the surface, yielding optimal binding from crude or dilute solutions. As a result, the CFM enables up to 10 000-fold enhancements in sensitivity to be achieved and printing at concentrations 1000-fold more dilute than in competing technologies. Hence printing using flow is attractive and greatly improves the quality of sensing the biomolecular interaction of interest.

Recent improvements[11] include the deposition of ligands using a novel dash printhead of up to 384 spots. Figure 12.5 shows (A) the SPR reflectivity image of a 384-spot array and (B) the tiled overlay of 384×8 sensorgrams in a

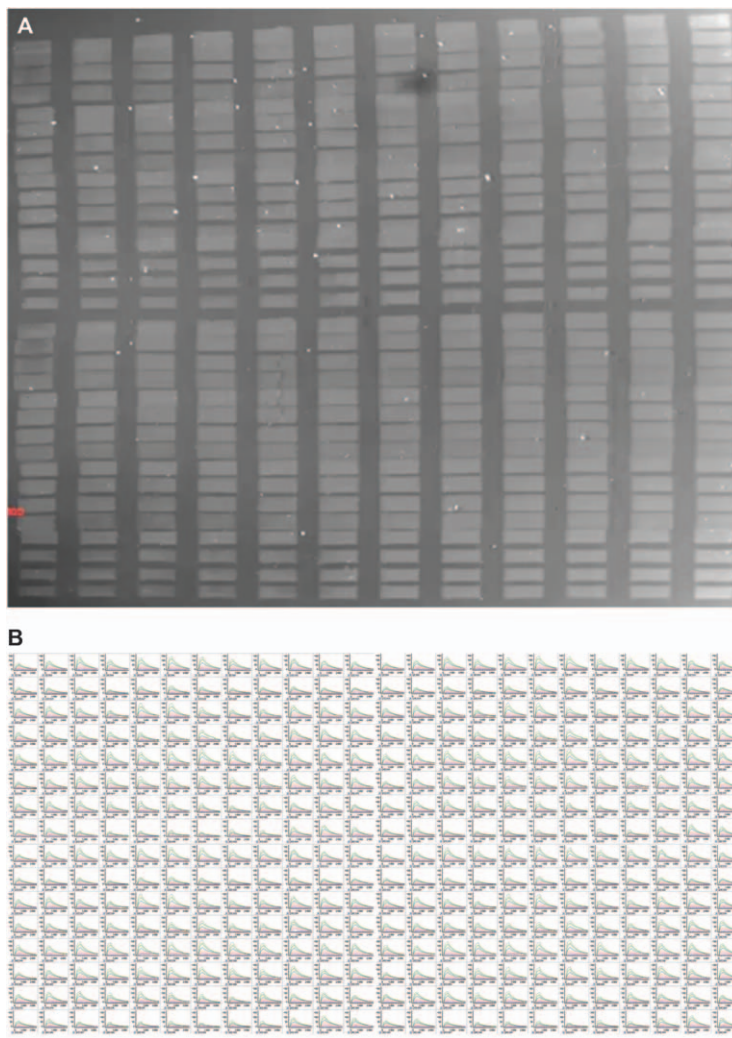


Figure 12.5 (A) The 384 dash printed SPR reflectivity image in the IBIS MX96 and (B) tiled overlay sensorgrams of eight analyte injections exposed to 384 spots. Reused with permission from Josh Eckman.

View Online

Table 12.1 Dimensions of the CFM printhead (in μm) (2016).

Type	Spot height	Spot width	Pitch height	Pitch width	Head height	Head width
6×8	500	830	780	970	4680	7760
4×12	390 (150 dash)	540	600	660	2400	7920

Published on 24 May 2017 on http://pubs.rsc.org | doi:10.1039/9781788010283-00415

quality comparison study shown. In Table 12.1, the dimensions of the CFM printhead are given.

12.3.2 Gradient Printing for Multiplex Sensing

Gradient chemistry strategies are attractive in combination with SPR imaging. In SPR imaging instruments, the optimal degree of coupling can be spatially resolved. An example of the gradient chemistry strategy was published by the group of Paul Yager, who also contributed to Chapter 10 of the first edition of this Handbook. Gradients can also be created by timely contact of a ligand with the sensor chip. A microfluidic device is necessary to create the gradients on the sensor surface. Because of the individual control of CFM-produced spots, the CFM also can be used to create a discrete ligand density series of spots (see Section 12.3.1).

The optimal degree of coupling and reduction of non-specific binding (for, *e.g.*, POC devices) can be spatially resolved in the redundant biomolecular interactions when multiplex detection using SPR imaging is applied. Several papers have described the importance of tuning the ligand density for affinity determinations (see Section 12.7). For example, in Biacore instruments an operator has to tune the ligand density (R_{max} values between 50 and 100 RU) for accurate affinity constant calculations. In Chapter 5, the importance to the distribution of surface sites of analyzing the kinetic parameters of biomolecular interactions is described.

Spatially resolved gradients can be created using a polydimethylsiloxane (PDMS) device by timely contact of a ligand with the sensor chip, which is shown schematically in Figure 12.6. This idea was already published in the first edition of this Handbook (Chapter 12).[12]

At the sensing lane area of Figure 12.5, ligands are measured on certain regions of interest (ROIs). At the non-specific binding section, the capture ligand will bind non-specifically to the surface, while the ligand was not in contact with this section, hence ligands are not present on the surface. At the common mode rejection (clean) section, the capture ligand did not contact the surface and the area can be used for common mode rejection compensation for bulk RI shifts of buffer or regeneration liquids, or for temperature correction. Not only defined areas of sensing lane, non-specific binding section, or common-mode rejection section, but also a gradient of contact times of ligands and/or capture ligands should be created in the microfluidic device.

View Online

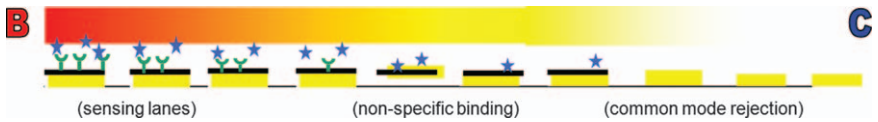


Figure 12.6 A sample can be injected slowly at point B and reversed after a certain exposure to the sensor spots. The diffusion rate of the compounds and the contact time determine the spatial resolved accumulation or gradient of ligands and analytes. Because the supply of ligand and analyte in the sample is only from one side (B) to the other (C), there is a gradual contact time difference of the sample with the sensing areas on the left (red) and right side (yellow to blank). Here the ligand coating solution (green antibody) was reversed at the fourth spot. The capture analyte (blue stars) is reversed at the seventh spot. The final three spots as indicated here in this linear flow channel will never be exposed to the ligand- or analyte-containing solution. Accurate syringe pumping should be applied.
Reproduced from ref. 12 with permission from The Royal Society of Chemistry.

Published on 24 May 2017 on http://pubs.rsc.org | doi:10.1039/9781788010283-00415

Although the lateral resolution of SPR imaging is limited by the propagation length of the surface plasmon wave (*e.g.* ~10 μm), a huge potential for writing lanes is available for current SPR imaging instruments. In the first edition of this Handbook, a future trend suggested was a DNA codon self-assembly printing principle. However, currently this technology is still in its infancy, perhaps owing to complicated protein–DNA codon conjugate mixture manufacture and the advanced protocols needed for validation of these mixtures. Alternatively, the CFM, with 384 unique addressable spots, is superior and covers the need to develop such microfluidic DNA codon technology. Again, quality counts and the individual addressable CFM-produced spot turned out to be outstanding with respect to control of the relevant spotting parameters such as contact time, concentration of the ligand in the spotter, the degree of EDC–NHS activation of the hydrogel, the pH for each individual spot, the ionic strength, and the buffer content.

The physical dimensions of the array chip are defined by the channel width and pitch of a line channel printhead. Lines (channels) of 50 μm in microfluidic devices can easily be created and ideally when a line printer is available then in criss-cross fashion 2304 crossings (48×48 lines) can be written on the SPR sensor chip surface. The 4×4 criss-cross was already applied in the 1990s by Berger *et al.*[13] and later Bio-Rad developed the principle for the Proteon XPR36 (6×6 criss-cross).

A (not commercially available) line printer based on PDMS replicates allows the fabrication of an even higher density multi-ligand array (up to ultimately 300×400 lines = 120 000 spots!) that fits in the current SPR imaging window, but this huge number placed limitations on the data processing and real-time monitoring of all these interactions simultaneously. For example, the IBIS MX96 is able to independently address ROIs of 10×10 pixels (= 55×55 μm), so a 4096 array is currently feasible in the SPR imager.

View Online

Published on 24 May 2017 on http://pubs.rsc.org | doi:10.1039/9781788010283-00415

A line printer can meet this demand by *multiplying* in criss-cross fashion, *e.g.* 32×32×4 (2× double print), while the CFM of Wasatch Microfluidics has been developed by *adding* 48 spots×8 dash-prints = 384 spots (using a dash flow printhead) on a single SensEye sensor. By applying automated injection schemes in, *e.g.*, a 16-line printer, a 4096 criss-cross array can be built in a limited number of only eight line printing steps. Dedicated printheads in combination with control of flow will gain potential for the study of biomolecular interactions in various applications.

12.4 Trends in Sensor Surfaces

Although dimensionally extremely small, the quality of the sensor chip surface coating has a tremendous influence on the performance of an SPR biosensor. It has been clearly demonstrated that the gold surface needs to be shielded from the influence of complex samples. The modification of surfaces is necessary to tailor surface properties such as the adsorption behavior of ligands, wettability, and biocompatibility. For example, a polystyrene microtiter plate for ELISA measurements was mimicked in an SPR setup by spincoating or spraying of a polystyrene polymer dissolved in toluene solution.[14] However, hydrophobic surfaces are prone to poor wettability, ligand desorption due to physical attachment, and the adsorption of air bubbles, detrimental for signal reproducibility. A hydrophilic coating is more stable and preferred in SPR biosensors. The hydrogel-based carboxymethylated dextran layer of Biacore's CM5 sensor chips is the most popular matrix for SPR biosensors owing to its high coupling yields, the perfect volume match with the evanescent field, reliability towards covalent ligand immobilization, and reducing non-specific binding. The reaction conditions for coupling proteins, peptides, and small molecules to carboxymethylated dextran surfaces are well characterized and extensive optimization studies have been performed.[15]

SPR imaging of an area of 1 cm^2 of various high-quality sensor chips shows defects in more than 50% of the sensor chips, leading to potential affected sensorgrams and artifacts. For instance, irreproducible drying effects, caused, for example, by adsorbed air bubbles, often show cauliflower images of the surface. Further, submicron dust particles that are always present in the air can be irreversibly adsorbed on the surface. Elimination of air bubbles in the liquid handling system and protection of the sensor surface by proper packaging will reduce these issues. The imaging feature reveals the quality of the sensor surface and inhomogeneous coatings can be visualized by inspection of the SPR reflectivity image. The operator of the imaging instrument is able to reject suspicious sensor areas. The homogeneity of the nano-architecture of the sensor surface can be checked with a reflectivity image where the SPR angle is set in the inflection point of the left-hand flank of the SPR curve. For instance, in the IBIS MX96 system of IBIS Technologies, either an SPR image can be measured with improved contrast or the SPR image can be transposed further to an artificial color image. In

View Online

order to avoid contamination, it is extremely important to expose the uncovered sensor chip to the open atmosphere as briefly as possible. Biacore introduced in 1990 a cassette for the sensor chip that is opened automatically only inside the Biacore instrument.

Published on 24 May 2017 on http://pubs.rsc.org | doi:10.1039/9781788010283-00415

12.4.1 SensEye®† Sensor: Easy2Spot

The SensEye Easy2Spot of Ssens (Enschede, The Netherlands) belongs to the sensor category for covalent ligand immobilization. For this type of immobilization, traditionally sensors with a layer containing carboxylic acid groups are selected (*e.g.* SensEye COOH sensors, Biacore CM5). For example, proteins or peptides can be immobilized on the sensor surface *via* a primary amine functionality on the molecules, after activation of the carboxylic acid groups on the sensor surface using EDC and (sulfo-)NHS.

The ready-to-use SensEye Easy2Spot was developed for covalent immobilization of ligand (arrays) *without* the need for prior sensor activation. This SensEye contains a hydrophilic layer of active esters that react readily with (primary) amine groups of the ligand, resulting in covalent bonding *via* stable amide bonds. No additional chemistry is involved, and surface activation is not required. Like the immobilization of ligands *via* EDC–NHS chemistry, the ligand immobilization on an Easy2Spot surface results in random ligand immobilization.

In comparison with the standard sensors for covalent ligand immobilization, SensEye Easy2Spot sensors have several major benefits:

- Easy2Spot sensors are time and reagent saving, as no activation is required.
- Optimal for spotting of ligand arrays.
- Highly reproducible ligand immobilization.
- Very low lot-to-lot variation.

For covalent immobilization, purified ligands are required, as all molecules presented to the sensor surface will be immobilized. Double printing of ligands (sequential printing of two ligand arrays on the same sensor surface) is not recommended, as the activated sensor surface is sensitive to hydrolysis when exposed to air. This will result in reduced immobilization during the second print.

The sensor has proven to be very suitable for direct printing of ligand arrays, for instance, by using the CFM (see Section 12.3.1). The typical capacity of human serum albumin immobilization onto the G-type of this SensEye is 2000–4500 RU, depending on the ligand immobilization conditions selected. For the P-type SensEye Easy2Spot, this capacity is 750–2000 RU.

†SensEye® is a registered trademark of Ssens BV, Enschede, The Netherlands.

View Online

After ligand immobilization, the remaining active esters can be quenched in a standard ethanol amine procedure, in which ethanol amine is covalently attached to the remaining activated esters. However, to preserve the non-fouling characteristic of the background surface, a non-residual quenching procedure is recommended. Ssens provides SensEye Quench, a set of two quench solutions that convert the residual active esters into the corresponding carboxylic acid groups.

Published on 24 May 2017 on http://pubs.rsc.org | doi:10.1039/9781788010283-00415

12.4.2 SensEye Protein A/G, SensEye Anti-IgG, and Fixit Protocol

The SensEye pA/G belongs to the category of direct ligand capturing, with a surface that has protein A/G affinity for the Fc part of IgGs. Unlike most covalent immobilization strategies that result in random ligand immobilization, the use of a SensEye pA/G results in an oriented immobilization of the IgG *via* its Fc region. The pA/G sensor has a non-fouling background surface that allows the direct capturing of human IgGs from complex samples such as crude cell lysates, human serum, plasma, or whole blood.

This SensEye can be used for cover coupling of a ligand by capturing from different types of solutions, but can also be combined with a protein spotter, thus capturing an array of different IgGs. This array can subsequently be used for the characterization of the captured IgGs. When this characterization involves multiple, sequential interactions and surface regeneration, captured IgG will be lost during regeneration. For example, when an array of captured mAbs are applied for a binning application, a regeneration step is necessary, with the consequence that the captured mAbs elute from the surface. To overcome this drawback, Ssens developed a fixation procedure that stabilizes the protein A/G–IgG interaction without loss of IgG affinity. This so-called FixIt protocol can be performed directly after IgG capture in the spotting device. It should be noted that the FixIt protocol may affect the amount of captured IgG and the IgG's affinity if not performed under optimal conditions. These conditions will depend on the application and have to be verified.

Rabbit anti-human serum albumin IgG (aHSA) was captured on a SensEye protein A/G, the FixIt protocol was applied, and multiple interactions with HSA and subsequent regeneration (10 mM glycine, pH 2) were performed. The effectivity of the FixIt procedure is illustrated in Figure 12.7A, which shows the HSA binding of 14 sequential incubation–regeneration cycles and demonstrates that regeneration results in the removal of bound HSA only, without loss of sensor binding capacity. Without the FixIt procedure, the captured aHSA is completely removed from the sensor during the regeneration of the first cycle (see Figure 12.7B).

The SensEye protein A/G, like all ligand-capturing SensEyes, has a protective coating to maintain a high-affinity surface during storage, and to ensure reproducible double printing. This coating can be removed before

View Online

Published on 24 May 2017 on http://pubs.rsc.org | doi:10.1039/9781788010283-00415

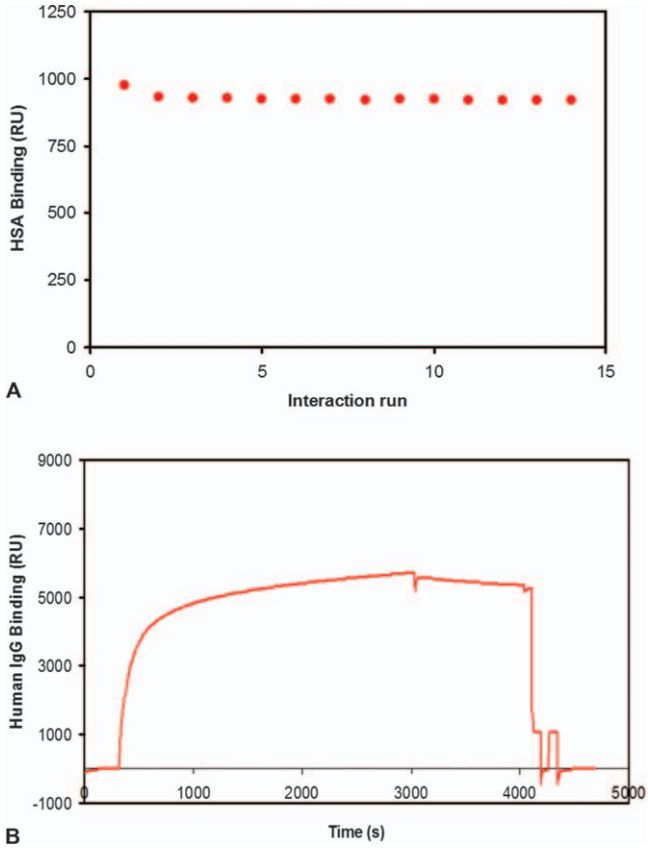


Figure 12.7 (A) Rabbit anti-HSA was captured onto a SensEye protein A/G and subsequently fixed by the FixIt procedure. Multiple cycles of interactions with HSA and subsequent regeneration were performed, demonstrating removal of bound HSA only and a constant SensEye response indicating a stable sensor. (B) Typical interaction of human IgG from human AB serum (0.25% in PBS) with the SensEye a-hu-IgG-Fc: association, dissociation, and complete regeneration without sensor fouling.

spotting by performing a prespotting rinse in the spotter. It should be noted that during double printing, the ligands of the first print are exposed to air. The effect of drying/air exposure on the captured ligands of the first print has to be verified. Reuse of a regenerated sensor for printing is not recommended.

The SensEye anti-human IgG Fc (a-hu-IgG-Fc) also belongs to the category of direct ligand-capturing SensEyes and has a surface with a high affinity for the Fc part of human IgGs. The use of a SensEye a-hu-IgG-Fc results in an oriented immobilization of human IgGs *via* their Fc region. By using a spotter such as the CFM from Wasatch, an array of human IgGs can be spotted on this sensor. The sensor surface is very robust, and can be

View Online

Published on 24 May 2017 on http://pubs.rsc.org | doi:10.1039/9781788010283-00415

regenerated numerous times without affecting the IgG binding capacity of the sensor surface.

The SensEye a-hu-IgG-Fc is designed for direct, reversible binding of human IgG, binding of ligands containing a human IgG-Fc tag, human IgG concentration measurements, and interaction analysis. The SensEye a-hu-IgG-Fc shares some characteristics with the SensEye pA/G. As for the SensEye pA/G, the surface has a non-fouling background, which allows the direct capture of human IgGs from crude samples such as cell lysates, human serum, plasma, and whole blood, and has a protective coating to maintain a high-affinity surface during sensor storage, and to allow reproducible double printing. Furthermore, the sensor is very suitable for direct, irreversible/covalent binding of human IgG in combination with the SensEye FixIt procedure.

The SensEye a-hu-IgG-Fc has a very high IgG binding capacity, but the sensor also performs very well in applications that require (very) low capture levels. Furthermore, this SensEye can be applied in kinetic titration, binning, and epitope mapping experiments. The SensEye a-hu-IgG-Fc shows that human IgG from human AB serum results in about 10 000 RU of captured human IgG.

12.5 Hyphenated SPR Technology

In the last 10 years, new developments in the combination of SPR with complementary technologies, also referred to as ''hyphenated'' SPR, have been explored. Often, these technologies are off-line and should be used serially, but they share the SPR sensor device, which can be installed in the SPR instrument and also inspected with the other hyphenation techniques.

12.5.1 SPR-MS

Krone *et al.*[16] first combined SPR and mass spectrometry (MS), which created a unique approach for protein investigations. This technique was subsequently adapted and modified in several laboratories[17,18] and some of the commercial instruments are now also equipped with basic analyte recovery capability for MS. The basic idea is to follow up the characterization of interactions between proteins and surface-immobilized ligands by SPR with the determination of the identity of the bound proteins or peptides using MS. This has applications in protein interaction discovery in proteomics, and also in the characterization of protein modifications critical for the interaction. Considering the SPR sensor surface as a miniaturized chromatographic matrix, SPR-MS is reminiscent also of the traditional affinity chromatographic purification preceding MS in protein discovery, but obviously with added real-time quantification of the capture and elution process, and also exhibiting different elution behavior due to the much smaller scale matrix. Several fundamentally different interface approaches

View Online

Published on 24 May 2017 on http://pubs.rsc.org | doi:10.1039/9781788010283-00415

have been developed by different groups, for example: (1) direct use of the SPR chip surface for MS by mounting the preloaded SPR chip on a matrix-assisted laser desorption/ionization (MALDI) platform[19] or analyzing the surface with a SELDI protein chip reader;[20] (2) on-chip digestion followed by microfluidic elution, recovery in a reversed-phase microcapillary column, and ESI/MS/MS sequencing of peptides from the digest;[21] and (3) analyte dissociation, microfluidic elution, and collection followed by external digestion and MALDI-TOF sequencing. Recent progress in SPR-MS includes improved methods and operations, increased limits of detection, multi-protein analysis, and protein-complex delineation. With the subsequent design of SPR protein arrays, SPR-MS entered the field of high-throughput protein interaction discovery and miniaturized diagnostics.

As illustrated by Gilligan *et al.*,[22] the manipulation of small, distinct liquid volumes in microfluidics with reversible and oscillatory flow patterns[23] can provide significantly increased amounts of recovered material and controlled washing conditions. In this approach, small liquid plugs containing the loading sample, washing buffers, and elution solution are separately transferred to the sensor surface such that multiple cycles of loading, washing, and recovery can take place, enriching the eluent concentration in the same plug of recovery buffer. Further, by virtue of the oscillatory flow pattern, once the specific liquid volumes are covering the flow cells, the contact times can be extended (while maintaining high mass transfer to the capturing molecules at the surface) until the slow binding kinetics arising from the low antigen concentration has achieved a plateau. The latter sample handling technique has been applied, for example, to minimize sample consumption and optimize detection efficiency in an SPR-based assay for the detection of anti-idiotypic antibodies in patient sera.[24] Another effective approach for improved recovery from the SPR surface is the use of a larger surface.[25] An overview of combined SPR-MS was presented by Bellon *et al.*[26]

12.5.2 Other Hyphenated SPR Techniques

A way to enhance sensitivity and to push the limit of detection (LOD) to lower surface coverages is the use of fluorescent chromophores covalently attached to the analyte molecules. In this so-called surface plasmon fluorescence spectroscopy (SPFS), the resonantly excited surface plasmon waves excite the fluorophores,[27] and their emitted photons can be monitored by a detection unit attached to a conventional SPR setup.[28] In Chapter 9 in the first edition of this Handbook, the features and benefits of such an SPR excited fluorescence instrument were described. However, there appears to have been no commercialization of this technology since 2006. Perhaps this is due to the complicated instrumentation while the biomolecular interaction is not longer detected label free. As described in Section 12.6.1, nanoparticle enhancement technology applied directly to SPR instruments also has the

View Online

benefit of a dramatic improvement of the sensitivity but also the selectivity of detection because sandwich antibodies can be applied. Although it is no longer intrinsically label free, the benefit is that the greatly enhanced sensitivity can be applied in a wide range of multiplex diagnostic applications.

SPR optics in the Kretschmann configuration requires the assembly of optical components only at the prism side, hence approaching the instrument at the wet side with flow cells in microfluidic cartridges, cuvettes for a microscope, and ''lab-on-a-chip'' devices is in principle feasible. The implementation of lab-on-a-chip devices is discussed below in Section 12.5.3. However, the combination of a lab-on-a-chip device with SPR sensing is in its infancy, and the trend suggested in the first edition of this Handbook did not evolve as foreseen.

The lateral resolution of SPR, which is equal to the propagation length of the plasmon wave (*e.g.* for a wavelength of 680 nm it is of the order of 10 μm), is sometimes unacceptably large for the imaging of small features, such as ligand clusters, aggregates, or fibrils with sub-micrometer dimensions. If a higher lateral resolution is needed, then other combinations of instruments or hyphenated SPR technology are required. A combination of atomic force microscopy (AFM) and SPR[29] seemed in principle a very interesting approach, but commercial SPR imaging combinations with AFM, STM,[30] SPM, Raman spectroscopy, *etc.*, have not entered the market since the first edition of this Handbook in 2008.

12.5.3 Implementation of ''Lab-on-a-Chip'' Devices for SPR Systems

In 1990, Biacore introduced a fully automated pneumatic valve-operated microfluidic cartridge for biospecific interaction analysis, which at that time was the most high-tech and advanced fluidic system developed in a commercial instrument. However, since the introduction in 1990 by Manz *et al.*[31] of miniaturized total analysis systems (μ-TAS), enormous research efforts[32,33] have been expended in the area of miniaturized or lab-on-a-chip devices, with tens of thousands of papers up to 2016. It may once have seemed a utopian dream to create highly parallel and automated microfabricated devices for SPR systems and in the academic field many attempts have been reported. Ouellet *et al.*[34] described an integrated microfluidic array using soft lithography techniques for high-throughput SPRi-based detection. The device consists of 264 element-addressable chambers isolated by microvalves. The resulting 700 pL chamber volumes, combined with a serial dilution network for simultaneous interrogation of up to six different analyte concentrations, allow further shortening of detection times. The development of high-throughput protein analytic measurements is a critical technology for systems approaches to biology and medicine. However, the quality and reliability of commercial systems and many issues regarding the vulnerable microfluidic valve switching need to be solved before such

Published on 24 May 2017 on http://pubs.rsc.org | doi:10.1039/9781788010283-00415

View Online

Table 12.2 Lab-on-a-chip building blocks for SPR devices as described in the literature.

Lab-on-a-chip building block	Description
Channel	Formed by dry/wet etching, molding, or soft lithography, *e.g.* polydimethylsiloxane (PDMS)[35]
Pump	Permits fluid transport that can be driven electro- or hydrodynamically[36]
Mixer	Splitting or coiling of a laminar flow[37]
Separator	Based on capillary electrophoresis (CE) or free-flow electrophoresis (FFE)[38]
Collector	Using hydrodynamic addressing/isolation or address flow[39]
Spotting	Line, criss-cross, or flow spotting (Wasatch)[40]
Detector	Functionalized gold SPR surface (Chapter 6)

Published on 24 May 2017 on http://pubs.rsc.org | doi:10.1039/9781788010283-00415

systems can penetrate the market. Over the last 10 years, new microfluidic trends for SPR systems have evolved significantly and the multichannel hydrodynamic isolation principle (Sierra Sensors) and the fluidics of the Biacore 8K were the outcome of highly advanced fluidics for new SPR instruments achieving more parallel and automated microanalyses for biological phenomena.

Table 12.2 contains a compilation of some potential building blocks for lab-on-a-chip devices that are useful in combination with SPR detection. In the following section just a few of these building blocks are described in detail.

12.5.3.1 Pumping Liquids Using Electroosmotic Flow in Microfluidic Devices with Gold Layers

Although in the past 10 years only pressure-driven pumping has been applied in commercial SPR systems, features and benefits of electroosmotic flow pumping could be attractive in microfluidic networks. The principle of electroosmotic flow is as follows. When an electric field is applied in the longitudinal direction of a charged surface (substrate) or capillary, the cations close to the wall move towards the cathode (Figure 12.8). Wrapped in the layer of cations, the bulk solution is transported in the direction of the cathode. The only plane of friction is between the stationary layer at the capillary wall and the layer of cations, which is in motion. As illustrated in Figure 12.8, unlike in pressure-driven systems with a parabolic flow profile (Poiseuille flow), the velocity of the bulk is constant, resulting in a flat flow profile (plug flow). The stagnant diffusive layer of, *e.g.*, 2 μm (see Chapter 6, Figure 6.5.) is reduced to the thickness of the double layer (~10 nm), which is dependent on the ionic strength of the buffer solution. This may result in improved mass transport of the analyte to the immobilized ligand. The velocity of the electroosmotic flow (v_{EOF}) is given by the following equation[41]:

$$v_{EOF} = (\varepsilon_0 \varepsilon / 4\pi\eta)\zeta E$$

View Online

Published on 24 May 2017 on http://pubs.rsc.org | doi:10.1039/9781788010283-00415

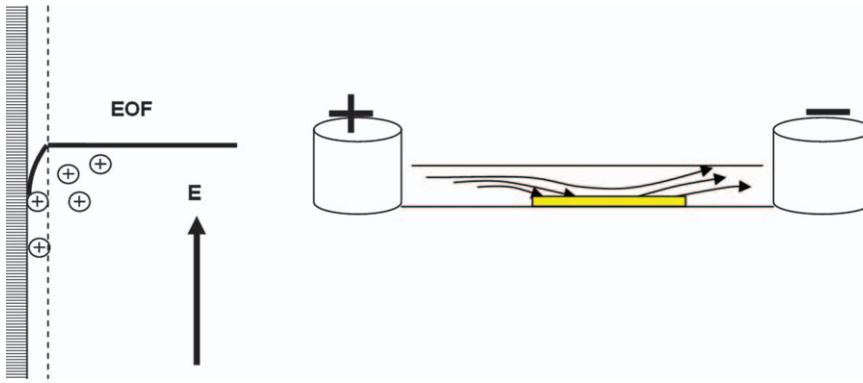


Figure 12.8 The electroosmotic flow profile is plug flow, whereas hydrodynamic pumping gives a laminar flow profile. The electric field (E) will drag cations in the double layer of the wall (~10 nm) to the cathode (negative electrode). If a conducting gold layer is deposited on the glass surface, the electric field will be short-circuited and affected by the gold through reduction and oxidation processes at the gold surface. The gold layer can then be considered as a bipolar electrode.
Reproduced from ref. 12 with permission from The Royal Society of Chemistry.

where ε_0 and ε are the dielectric constants of vacuum and the buffer, respectively, ζ is the zeta-potential, the potential of the first moving layer at the capillary wall, η is viscosity, and E is the lateral electric field. In order to modify the magnitude and direction of the EOF, either E or ζ should be modified. The principle of modifying or even reversing the EOF inside a capillary has been presented before, including the control of flows in integrated devices.[42] As the EOF is generated at the channel wall, the viscosity at the wall is one of the determining factors for the flow velocity. If a conducting gold layer is deposited on the glass surface, the electric field in the lateral direction will be influenced, and changes in the EOF arise.

The gold patches for SPR sensing are not directly connected to a power supply but are floating. A lateral field is over the gold layer and the equipotential of the gold is considered to be the average between the potentials in the electric field in the liquid at both sides of the gold electrode. Under conditions where the voltage difference is low ($\ll$1 V), no reactions occur, no electrical current will flow, and the double layer of the metal/electrolyte interface behaves as an insulator. In contrast, when the voltage difference over the electrodes becomes too large, an electric current will flow through the metal, and at both ends electrochemical processes or even electrolysis of the liquid will occur, resulting in bubble generation.

12.5.4 Electrochemical SPR (E-SPR) Application

If, on the other hand, the gold electrode is connected in an electronic circuit, then a changed potential of the electrode will modify the charge distribution

View Online

Published on 24 May 2017 on http://pubs.rsc.org | doi:10.1039/9781788010283-00415

near the metal surface, and hence alter the ionic distribution in the double layer. A potentiostat enables the potential of the gold surface to be maintained with respect to a reference electrode. Also, the current can be controlled and the working electrode in the three-electrode configuration makes it possible to apply various electrochemistry principles (*e.g.* cyclic voltammetry, electrochemical impedance spectroscopy, amperometry, conductometry). In principle, these ionic changes will also be measured with SPR, because changes in the ionic concentration in the electrical double layer will alter the RI in the evanescent field. This so-called electrochemical SPR or E-SPR phenomenon depends on the ionic composition of the electrolyte and the potentials in the liquid with respect to the electrode. This E-SPR principle has been developed in various commercial SPR instruments, including instruments from Reichert and KE Instruments. As described in the literature,[43] in a first approximation, the RI of the double layer can be considered to vary with the change in the charge of the double layer. Lioubimov *et al.*[44] described a combination of oscillating electric potential and SPR measurement. Tadjeddine[45] presented a multilayer model of the electrochemical interface in combination with SPR phenomena. Physical, surface, and polymer chemists have found particular utility for this type of application. While the electrochemistry experiment is being run, SPR data are also being generated simultaneously. SPR is used to understand what is happening at the gold electrode when these induced electrochemical phenomena occur.

12.6 Prospects for SPR-based Point-of-care Devices

Already from the beginning of the introduction of SPR technology, one goal was the use of SPR for point-of-care (POC) diagnostics, but several attempts were not successful. Why is this development of POC SPR devices so problematic? Is it the sensitivity, which should compete with other immunochemical tests (*e.g.* dipsticks) using labels? Or are SPR-based POC instruments still very costly and utilize an expensive disposable, therefore hindering introduction into this competitive market? Developing a diagnostic POC test is one thing, but bringing it to the market while taking into account the product's value for different stakeholders is a very different task. While clinicians might estimate the value of a test by its impact on the patient, many more factors influence the success of a diagnostic product. All stakeholders, from caregivers to patients, to manufacturers, to payers, and to policy-makers, expect different benefits from a product, and only if the diagnostic tool meets the criteria of all of these groups will it thrive in the market. Convincing doctors, patients, and payers of these benefits is usually more difficult for a diagnostic product than for a therapeutic product. In addition, insurance companies and governments who pay the healthcare bills fear that more diagnostic tools will lead to higher use of therapeutics. This is an important misconception, since diagnostics aim to remove the

View Online

Published on 24 May 2017 on http://pubs.rsc.org | doi:10.1039/9781788010283-00415

trial-and-error workflow of treatment options. However, that is another discussion and is outside the scope of this book.

Technically, SPR can become an important POC diagnostic tool, but then POC devices should have the specifications of the high-end instruments in the market. Additionally, the device should be small, accurate, reliable, robust, inexpensive (<€5), and disposable, and should compete with dipstick technology or should allow a multiplex measurement from a drop of body fluid. This is not a sinecure, as shown in the next section, but in the author's opinion it is not impossible. A huge market demands that these devices should be developed urgently and is willing to pay enormous amounts of money, as already shown in 2014.

12.6.1 Point-of-care Theranostics

Clinicians are beginning to use POC testing of compact (in terms of size and weight) and flexible clinical chemistry testing devices suitable for use close to the patient. For example, Theranos (Palo Alto, CA, USA) developed a blood-testing device named Edison, and indicated that the microfluidic device uses a few drops of blood obtained *via* a finger-prick, rather than vials of blood obtained *via* traditional venipuncture.[46] By the summer of 2014, its founders had raised over $400 million from investors, valuing the company at $9 billion. In October 2015, a report in the *Wall Street Journal* raised concerns about the accuracy of its Edison device. An independent US government review by the Centers for Medicare and Medicaid Services reported inaccurate testing results and multiple deficiencies in sample handling. Subsequently, in 2016, Theranos was under criminal investigation by federal prosecutors and the Securities and Exchange Commission. The Theranos debacle shows how valuable POC technology is in a commercial setting, but also how important it is that it meets the current standards of analytical accuracy, robustness, and reliability. These analytical devices are designed to move diagnostic testing out of central laboratories into sites closer to the patient. Miniaturization of devices will offer advantages when rapid and selective monitoring is required, *e.g.* of cardiac markers for diagnosing acute myocardial infarction[47] or whole blood chemistry relevant to intensive care medicine.[48,49]

Although not label free or SPR, Philips (Eindhoven, The Netherlands) announced in May 2016 the launch of a new handheld blood test, the Minicare I-20 system, for the rapid diagnosis of a heart attack at the point-of-care. The new test is being introduced in selected countries in Europe, including the UK, Germany, The Netherlands and Belgium. As a result, patients with chest pain presenting at the emergency department are set to benefit from this major innovation, which Philips has recently CE marked for compliance with the European *in vitro* diagnostic medical devices directive. The handheld Minicare I-20 system measures the level of cardiac troponin I (cTnI), a protein that is excreted by the heart muscle into the blood following a heart attack. It delivers test results, comparable to those

View Online

Published on 24 May 2017 on http://pubs.rsc.org | doi:10.1039/9781788010283-00415

obtained by laboratory testing, in less than 10 min near the patient, reducing the time for a physician to decide on the appropriate treatment pathway.

Why are POC SPR devices not yet available in the market? We can identify the following five reasons:

1. SPR-based concentration measurement is never as sensitive as with labeled techniques because of the intrinsic and inherent drawback of SPR: the detection of non-specific binding interferes with the specific binding signal intended to be measured. In contrast, an immunoassay that detects only the label will not be susceptible to signal interference from non-specific binding of unlabeled proteins.
2. For POC analysis, there is still not yet the absolute necessity to detect kinetic rate equilibrium constants of biomolecular interactions, which are the unique features of SPR sensing.
3. Current SPR instruments are still bulky and expensive and are not in an acceptable state for production intended for high-volume markets. The integrated SPREETA chip of Texas Instruments was the ultimate configuration for POC SPR devices but this application has not developed as successfully as expected. However, the SPREETA chip is applied in a research instrument by Seattle Sensors.
4. The advantages of direct detection and the speed of SPR appeared to be not (yet) the crucial factor making it suitable for POC devices and giving it a decisive advantage, *e.g.* over dipstick tests, which seem to be fast enough for current applications.
5. The cost aspect of sensor chips with respect to conjugate labeling is the remaining argument to replace labeled tests for POC SPR devices. The POC SPR chip and the instrument are too costly and cannot compete with disposable dipstick tests (<€5).

If POC tests can be designed in which the kinetics of the biomolecular interaction determine the outcome of a multiplex test, then POC SPR devices will be attractive for the market and can be developed with a great intrinsic advantage. Although in the academic community one may observe new POC SPR initiatives, commercially it is still in its infancy. For example, Feltis *et al.*[50] reported a fully self-contained, handheld SPR device that is capable of duplicating many laboratory-based tests with a sensitivity range similar to those of many commercial ELISA-based immunoassays.

12.6.2 Signal Enhancement Cascade for Boosting the Dynamic Range

One of the great challenges in the diagnostics of complex, multifactorial diseases is the multiplex detection of biomarkers in small volumes of complex body fluids. It has become increasingly clear that the assessment of a single biomarker, with few exceptions, is insufficient for diagnosis,

View Online

Published on 24 May 2017 on http://pubs.rsc.org | doi:10.1039/9781788010283-00415

selection of treatment, and prognosis. There is a clear and pressing medical need for sophisticated diagnostic devices that can assess the patient's condition in an early phase of the disease process, which can assist the treating physician in selecting patient-specific treatment. Since patients do not present clinical symptoms, only small amounts of body fluids are available for analysis that can be isolated with minimal discomfort for the patient, for example by venipuncture, collection of urine, and in osteoarthritis, for example, from a small synovial fluid aspirate. The current state-of-the-art of nanotechnology permits the miniaturization of detection systems on a chip and has the promise to allow the development of the next generation of diagnostic devices. However, until recently, multiplex detection with high sensitivity and specificity in a broad dynamic range of concentration in such miniaturized devices was unresolved, but the first commercial approaches are now being made.

Bailey and co-workers developed the Maverick instrument, commercialized by Genalyte (San Diego, USA) (www.genalyte.com) since 2007. Genalyte announced that it had completed a $44M Series C financing round on 18 August 2015. The company intends to utilize the funding to refine the existing Maverick platform to a POC device for the physician office setting and to perform the clinical studies required to prove the accuracy of the device and suitability for use in a near-patient setting. With the application of a single drop of blood to a silicon microchip, Genalyte's Maverick detection system can offer a complete panel of 128 diagnostic test results in 15 min and it follows the Theranos strategy, but alternatively on a platform that is similar to detection using the evanescent field principle of SPR. A signal enhancement protocol is used by enzymatically forming a precipitate that is proportional to the bound analyte as initially developed by Robert Corn (see Chapter 8 in the first edition of this Handbook). Hopefully in the future Genalyte will meet the required standards of accuracy, robustness, and reliability and will learn from the failures of Theranos.

Hence particularly challenging is the need to detect potential biomarkers in a wide range of concentrations simultaneously in the same sample (tens of $ng\,mL^{-1}$ for abundant to as low as a few $pg\,mL^{-1}$ for poorly expressed biomarkers). Commonly used detection systems usually have a linear detection range of approximately 2–3 logs. In pilot experiments by the MCBP group (Prof. Dr L. W. M. M. Terstappen) in cooperation with Developmental Bioengineering (Prof. Dr H. B. J. Karperien) of the University of Twente, a new strategy for signal enhancement was tested that could allow the simultaneous detection of low- and high-abundance biomarkers in a few microliters of synovial fluid. The procedure is shown in Figure 12.9. The experiment showed that each enhancement step resulted in a linear amplification of the signal. Without amplification, high-abundance biomarkers (tens of $ng\,mL^{-1}$) could be reproducibly quantified. With maximum amplification, low-abundance biomarkers in the range of a few $pg\,mL^{-1}$ could be reproducibly quantified, extending the linear detection range from 2–3 logs to 6 logs. These promising results demonstrate the feasibility of an

View Online

Published on 24 May 2017 on http://pubs.rsc.org | doi:10.1039/9781788010283-00415

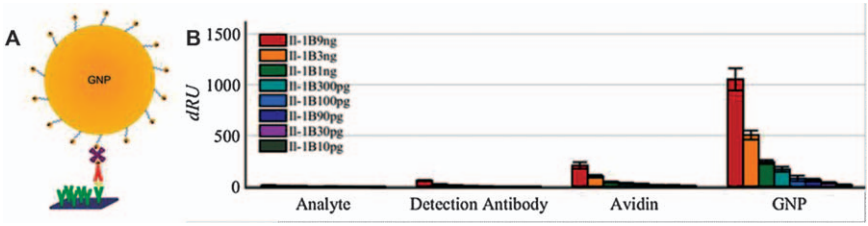


Figure 12.9 Linear enhancement of SPR signal. (A) Schematic illustration of the enhancement cascade using refractive index labels. (B) Enhancement of the SPR signal of a 96-plex measurement using the IBIS MX96.

SPR-based readout of a miniaturized multiplex assay for assessing patient diseases. This patent pending principle of using labels on a label-free detection platform is a breakthrough in simultaneous multiplex testing of complex body fluids in an extremely broad dynamic range from high-abundance to very low-concentration analytes.

As shown in Figure 12.9, in the first step, a custom-designed chip coated with an antibody against IL1B (panel A, green) is incubated with 100 μL of analyte in a concentration range from 10 $pg\,mL^{-1}$ up to 9 $ng\,mL^{-1}$. Subsequently, the chip is incubated with a second biotinylated IL1B antibody (red; first enhancement), (neutr)avidin (purple; second enhancement), and a biotinylated gold nanoparticle (GNP) (third enhancement). At each step the SPR signal is recorded over time and after a limited time exposure the following step is initiated. The IBIS MX96 allows a fully automated detection protocol. Without an amplification step, analyte concentrations between 1 and 100 $ng\,mL^{-1}$ can be easily detected. With full amplification using gold nanoparticles (GNP), analyte concentrations of <1 $pg\,mL^{-1}$ could be detected. When signals are enhanced, background noise, as observed in unamplified interactions, is reduced to almost zero and specific signals are easily obtained. Amplification is linear over the tested concentration range.[51] Thus, after the first injection of the cascade of injections, the report point for concentration of the higher abundance biomarker can be quantified. The second injection of a specific biotinylated anti-biomarker compound covers a second window of dynamic range. After concatenated injections up to maximum amplification, low-abundance biomarkers in the region of a few $pg\,mL^{-1}$ could be reproducibly quantified, extending the detection range from 2–3 logs to 6 logs.

12.7 Trends in Measuring Reliable Kinetic Parameters

Generally in complex media (patient samples, *e.g.* serum, urine, synovial fluid) non-specific binding will often result in false positives because abundant proteins other than the analyte interact (at lower affinity) with the sensor surface and ligand molecules. A general strategy applied in diagnostic

View Online

Published on 24 May 2017 on http://pubs.rsc.org | doi:10.1039/9781788010283-00415

tests is that the ratio of specific to non-specific binding can be tuned by both the degree of sample dilution and the ligand density. In label-free POC devices, the concentration should preferably be measured in the mass transport-limited regime because in this way the fastest results are obtained instead of incubating to depletion or equilibrium (as in ELISA). The causes of non-specific binding and the influence on the binding kinetics can be grouped as follows:

1. Parallel binding processes and/or cross-reactivity and formation of multi-assembly complexes.
2. Rebinding of dissociating molecules (this results in an apparent slower off-rate).
3. Steric hindrance and/or ''avidity'' effects (apparent slower on-rate).
4. Ligand immobilization artifacts and heterogeneity of surface binding sites (distribution of constants).
5. Mass transport limitation effects (*e.g.* analyte depletion of the layer close to the immobilized ligand surface).
6. Additional interfering effects that do not fit into one of these groups, such as complex reactions (*e.g.* induced fit, allosteric conformational change).

Surface binding measurements, as facilitated by SPR and illustrated in this book, provide unique opportunities, among them small sample volumes,[52] high-affinity measurement with signal-to-noise ratio independent of K_D, and micropurification for interaction discovery[53] and multi-protein binding studies.[54] However, this comes at the price of immobilizing one binding partner to the surface. For proteins, this raises the possibility that its conformational ensemble may be skewed or even significantly altered, even when using chemically and/or structurally uniform attachment strategies. Further, although in free solution all molecules experience the same environment, the microenvironment at the surface may be strongly variable depending on the location on the surface (*e.g.* from surface roughness), or depending on the location within an inhomogeneous matrix (*e.g.* from the obligate density distribution perpendicular to the surface of grafted polymers,[55,56] or from ligand gradients perpendicular or parallel to the surface created during immobilization[57]). In solution, the conformational ensemble usually exchanges rapidly enough for the binding thermodynamics to be well described by single values, but as a result of the immobilization and localization to the surface, this is frequently not the case any longer for the surface sites.

12.7.1 Affinity Ranking with the Interpolation Method

The values of the affinity constants (k_d, k_a, and K_D) that are determined by label-free interaction analysis methods are thus affected by the ligand density and how the ligand has been immobilized. This section outlines an SPR imaging method that yields high-throughput globally fitted affinity ranking values using

View Online

Published on 24 May 2017 on http://pubs.rsc.org | doi:10.1039/9781788010283-00415

a 96-plex array. A kinetic titration experiment without a regeneration step was applied for various coupled antibodies binding to a single antigen. Globally fitted rate (k_d and k_a) and dissociation equilibrium (K_D) constants for various ligand densities and analyte concentrations are exponentially interpolated to the K_D at the $R_{max} = 100$ RU response level (K_D^{R100}).[58]

For multiple applications, the quality of binding, expressed as the dissociation equilibrium constant (K_D), is of great importance. The K_D value (in mol L^{-1}) in a 1 : 1 Langmuir model is the analyte concentration at which in equilibrium 50% of the ligand molecules are specifically bound with analyte molecules (see Chapter 1, Section 1.4.4). Since K_D is used for the determination of the effective dosage levels of biomolecules that are applied as drugs, the determined K_D should reflect the K_D in solution. However, the constants that are derived from current, immobilized ligand-based assays are affected by the immobilized state of the ligand. This causes the thus determined apparent constants to deviate from the true ''solution'' constants owing to interfering effects that result from the immobilization of the ligand.[59] These interfering effects include rebinding effects, mass transport limitation, non-specific binding, and deviation from the 1 : 1 model binding.[60] The higher the ligand density, the more pronounced these interfering effects become, and it is generally accepted that the ligand density should be applied just above the limit of detection of the biosensor instrument.[61] The same holds for the analyte concentration – interfering effects will occur when multiple analyte molecules compete for interaction with a single immobilized ligand molecule.

A so-called K_D^{R0} method for the determination of affinity constants was published in 2011[62] in which the contribution of interfering effects is minimized or theoretically zeroed, so that the constants are a better estimate of the true constants of biomolecular interactions in solution. This method is based on the extrapolation of the number of immobilized ligand and analyte molecules to zero, thus mimicking the interaction in which only one ligand and one analyte molecule are involved, allowing a true 1 : 1 binding model with theoretically no interfering effects.

Recognized practical effects are additional ligand immobilization artifacts and heterogeneity of surface binding sites. The method will not compensate for this and the alternative route is by capturing ligands followed by the target interaction. Further, owing to a harsh regeneration step, the R_{max} value will decrease after the subsequent injections of the analyte concentrations and can again affect the kinetic affinity constants. Preferably any regeneration step of the surface should be avoided and this is achieved using kinetic titration.[63]

As already indicated in Chapters 4 and 5, the calculation of the ''true'' affinity equilibrium constant will become more reliable at lower densities, preferably at a ''density'' of only a single immobilized ligand molecule acting as a free ligand. Then the contribution of the interfering effects will theoretically be very low. In practice, this condition cannot be applied and by decreasing the ligand density the more noisy and less reliable the

View Online

Published on 24 May 2017 on http://pubs.rsc.org | doi:10.1039/9781788010283-00415

sensorgrams become. Additionally the quality of fits to noisy curves cannot be judged adequately. It should be noted that immobilization artifacts and heterogeneity of surface binding sites should further be reduced.

As proof of principle for interpolating the affinity values to a fixed R_{max} value, an experimental ranking test of eight monoclonal antibodies directed against the epithelial cell adhesion molecule was performed.[64] The analysis of such a kinetic titration experiment with a ''floating align point fitting'' was embedded in the analysis software for 96-plex interaction analysis (see also Chapter 8, Section 8.2.1.4 and Figure 8.3). Floating align point fitting means that the subsequent injections of the antigen will be fitted without having the align point equal to the injection time point. During the measurement, the antigen interaction will generate an increasing signal and each new baseline level in the kinetic titration is the result of the accumulated analyte bound to the ligand molecules (Figure 12.10). Hence the align point that is used for the fit calculations is not equal to the injection time zero, but always earlier in the concatenated series. The amount of

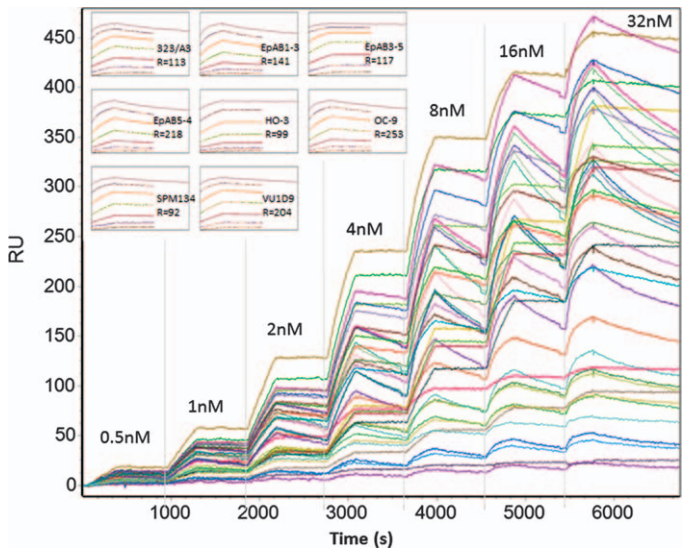


Figure 12.10 Serial view of the rEpCAM ranking experiment over 48 spots consisting of concatenated injections of rEpCAM (concentrations from 0.5 to 32 nM as indicated) without regeneration. In total six spots per antibody $\times 8$ Abs resulted in $48 \times 7 = 336$ sensorgrams. Top left insets: results in tile view are shown for the eight different mAbs of the injections in overlay per spotted antibody (auto-scaled). The R_{max} values are shown per spot in the inserted tiled overlay. The sensorgrams in overlay were globally fitted (red lines in the tiled overlay) using the floating align point fitting procedure in Scrubber2 software.[64]
Reprinted from R. B. M. Schasfoort, K. C. Andree, N. van der Velde, A. van der Kooi, I. Stojanović and L. W. M. M. Terstappen, Interpolation method for accurate affinity ranking of arrayed ligand–analyte interactions, *Anal. Biochem.*, **500**, 21–23. Copyright 2016 Elsevier Inc. All rights reserved.

View Online

Published on 24 May 2017 on http://pubs.rsc.org | doi:10.1039/9781788010283-00415

immobilized protein will cause a shift of the SPR-dip as measured by the R_{LL} value (response of local ligand density) that can be considered as the total protein density per spot, whereas the amount of *functional ligand* is related to the fitted R_{max} value.

Affinity ranking information was obtained by injections of the various antigen concentrations over the high-affinity coupled antibodies without a regeneration step. This kinetic titration method with global fits to the on- and off-rates for various levels of R_{max} showed a significant improvement in reliability when *interpolation* to R_{max} = fixed value is applied. Although theoretically correct as an academic exercise, in practice, exponential *extrapolation* to R_{max} = zero may lead to deviated ranking values when different ranges of R_{max} are measured. Extrapolation to $R_{max} = 0$ of these different ranges will result in less comparable ranking values and the unreliable lower values contribute highly to how the exponential extrapolation intersects the *Y*-axis at $R_{max} = 0$. Generally, practical ranking of many antibodies simultaneously can be performed when the R_{max} ranges of all these antibodies overlap, which is the case in this biomolecular interaction test with $R_{max} = 100$ RU (see Figure 12.11). Then an R_{max} = fixed value can be

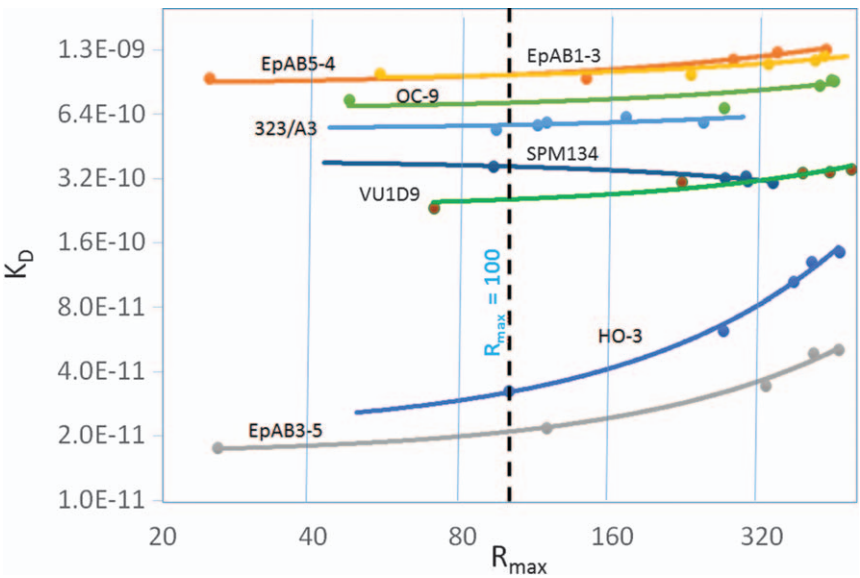


Figure 12.11 Equilibrium dissociation constant K_D (*y*-axis) as a function of R_{max} (*x*-axis) of rEpCAM to antibody EpAb3-5, HO-3, VU1D9, SPM134, clone 323/A3, OC-9-1, EpAB5-4, and EpAB1-3. Each point is the result of global fitting of six injections of the kinetic titration experiment. An exponential fit to $R_{max} = 100$ RU was applied for the different ligand density spots.[64]
Reprinted from R. B. M. Schasfoort, K. C. Andree, N. van der Velde, A. van der Kooi, I. Stojanović and L. W. M. M Terstappen, Interpolation method for accurate affinity ranking of arrayed ligand–analyte interactions, *Anal. Biochem.*, **500**, 21–23. Copyright 2016 Elsevier Inc. All rights reserved.

View Online

Published on 24 May 2017 on http://pubs.rsc.org | doi:10.1039/9781788010283-00415

chosen so that these values can be better ranked with respect to each other and R_{max} values lower than 20 RU can be discarded.

As the ligand density of an antibody captured on the sensor surface is tuned in Biacore instruments to obtain affinity values at $R_{max} = 50–100$, these values with proper fits of the curves are considered to be reliable. In SPR imaging instruments, the non-tunable range of ligand densities after off-line spotting can be used to calculate the accurate ranking affinity value of multiple antibodies by interpolating to $R_{max} =$ fixed. A rule of thumb regarding low ligand densities but acceptable noise levels using SPR imaging instruments is to interpolate various ligand densities to a fixed value of $R_{max} \approx 100$ RU. Further, it is important that the functional concentration, as applied in the fitting routine, is determined accurately for calculation of the absolute affinity values of K_D and k_a. The calibration-free concentration analysis (CFCA) method recently introduced by Karlsson and Roos[65] (see Chapter 1 Section 1.4.2) further improves the accuracy of the kinetic values. However, ranking values (with respect to each other) from different immobilized antibodies can be determined without knowing the exact functional analyte concentrations. Hence the best practical ranking affinity value for comparing many antibodies with the target can be obtained by interpolating the globally fitted affinity values to $R_{max} = 100$ RU. Additionally, the quality of the ranking result can be checked further with the distribution analysis of surface sites as outlined in the next section.

12.7.2 Affinity Ranking with the Interpolated Distribution Analysis Method

As described in Chapter 5 and Figure 5.5, the heterogeneous distribution of surface sites can be analyzed with the software tool EvilFit. By calculating the rate and affinity constants from a panel of antibodies, it is important that the functional ligand density and surface chemistry are similar for all antibodies. The interpolation method as described in Section 12.7.1 calculates the affinity constants by interpolating to $R_{max} = 100$ RU, but the distribution of surface sites is not checked for the antibody panel. EvilFit software should be extended to measure multiplex data from many spots with a variation in ligand densities. In Figure 12.12, a distribution analysis result is shown of a cross-reactivity pair of BSA (ligand) to anti-HSA (analyte) with an apparent nanomolar affinity. In theory, it is incorrect to calculate the affinity of such a polyclonal showing cross-reactive ultimate biphasic interaction, but sometimes ranking of polyclonals should be carried out and an inappropriate 1 : 1 model should be used to rank the affinity of various polyclonals. When the ligand density is varied by serial dilution of the ligand and exposing the dilution series to the sensor surface using the CFM (see Section 12.3.1), then various ligand density spots are exposed to a concatenated dilution series of injections of the analyte. Each spot can be analyzed separately and in Figure 12.12A–F the result is shown for six spots with increasing ligand

View Online

Published on 24 May 2017 on http://pubs.rsc.org | doi:10.1039/9781788010283-00415

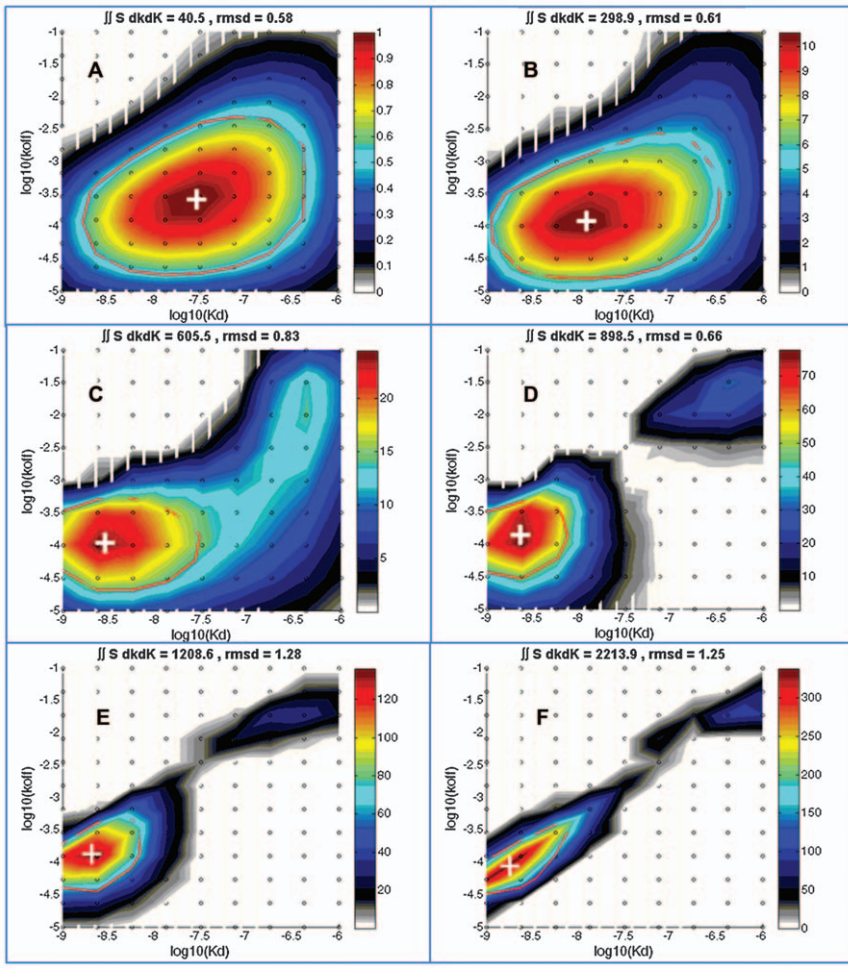


Figure 12.12 Distribution analysis result for the same ligand–analyte interaction with, from (A) to (F), an increasing functional ligand density [R_{max} value in (A)–(F) = 40, 299, 665, 899, 1209, and 2214 RU, respectively]. The white + is the global fitted value as calculated in Scrubber2 software (1 : 1 model). Data were generated in the IBIS MX96 instrument and show a huge effect of the ligand density on the affinity constants. Higher R_{max} results in a lower apparent affinity. (A) and (B) shows- a broad distribution due to lower signal to-noise ratio levels, in (C) and (D) two phases of the interaction can be clearly observed, and in (E) and (F) this is masked by the dominating lower affinity phase of the biphasic interaction.

density. The ligand density effect on the affinity parameters is huge when such a biphasic interaction is calculated using EvilFit software taking the distribution effect into account. The $\log_{10}K_D$ value shifts by a factor of

View Online

Published on 24 May 2017 on http://pubs.rsc.org | doi:10.1039/9781788010283-00415

20 from −7.5 to −8.8 (32 to 1.6 nM) and the off-rate $\log_{10}k_d$ by a factor of 4 from −3.5 to −4.1 (3.2×10^{-4} to 8×10^{-5} s^{-1}).

Hence for the screening of the quality of antibodies in comparison studies, it is not reliable to make decisions from high-quality globally fitted affinity values only. The experimental and boundary conditions for all studies should be similar and modern software tools such as EvilFit can help to find the proper design of experiment (DoE) conditions. It is foreseen that more scientists will adopt these analysis tools in affinity screening programs for large panels of antibodies. When, for example, a 384-spot array (Figure 12.4) is used, many ligand densities can be printed and, from the contour plots in EvilFit, similar conditions can be found for various antibodies in the panel. Fortunately, no additional experiments are needed, but more multiplex power gives improved quality in comparison studies to rank the affinity of a target to many antibodies in a panel.

12.8 SPRi Cytometry

In various publications,[66–69] it has been successfully shown that SPR can be used to give added value to cell analysis by measuring viable cells or the products of viable cells label free in a multiplex manner.[70] It became apparent that SPRi cytometry should still be developed intensively in order to reveal its potential fully and provide added value in cellular analysis. In this section, recent developments in SPRi cytometry are described and its future potential is highlighted.[71–73]

The field of SPRi cytometry covers at least the following applications:

- Detection of cell membrane antigens.
- Quantifying the ratio of surface antigens per cell population.
- Vesicle monitoring using SPRi.
- Affinity ranking of cell surface antigens on living cells.
- Quantifying the production rate of molecules per individual cell.
- Selection of individual cells using SPRi: the McSPRinter.

An outline of this SPRi cytometry section is as follows. In Section 12.8.1, SPRi cytometry for the presence and absence of cell surface antigens is described for red blood cell (RBC) monitoring. In Section 12.8.2, not only the presence or absence of cell membrane antigens is being measured, but also the ratio of the number of various cell membrane antigens for at least 44 different cell surface antigens. In Section 12.8.3, detection of extracellular vesicles is described. In Section 12.8.4, a feasible strategy is shown to rank the avidity of RBCs to FcγR interactions, including affinity screening of peptide-HLA to T-cell receptor (TCR) interactions.

Further, the SPRi cytometry field includes the monitoring of the cellular excretion of cellular products (*e.g.* antibodies) by living cells (*e.g.* hybridomas). The production rates of antibodies by single cells were successfully quantified including a simulation using Comsol Multiphysics modeling as described in Section 12.8.5. In line with excretion product

View Online

Published on 24 May 2017 on http://pubs.rsc.org | doi:10.1039/9781788010283-00415

monitoring, it was possible to detect apoptosis/necrosis in cells while being monitored in real time.[74] First, captured cells on top of the sensor surface were treated with paclitaxel. Then, after a few hours, a binding signal of cytochrome *c* (an apoptosis marker) on the attached cells could be measured.

Finally, in the McSPRinter described in Section 12.8.6, not only can the monitoring of the cellular excretion of thousands of cells be monitored but also it enables one to isolate the individual cells of interest. The relatively simple protocol allowed us to monitor, track, and quantify the excretion of antibodies label free and in real time from individual cells by SPRi in combination with microwell MEMS technology.

12.8.1 Label-free Cell Membrane Antigen Profiling

Studies focusing on retrieving qualitative and quantitative information on cell membrane antigens are relevant for various applications.[75] The most widely used technologies for cell surface antigen determination are flow cytometry and fluorescence microscopy. For both techniques, antibodies targeting the cell membrane antigens are fluorescently labeled and the fluorescence signals obtained from the cells correspond to the density of the antigens. To assess multiple antigens simultaneously, antibodies are labeled with different fluorochromes. In this manner, multiplexing of at least six antigens can be performed routinely, which is too small for detailed antigen screening of RBCs. Multiplex typing is also possible using a genotyping approach; however, these methods are hampered by null-alleles, resulting in false-positive results and, similarly to cytometric methods, are accompanied by relatively high costs. Therefore, the inexpensive agglutination-based methods are still being used for RBC typing to assure safe blood matching between donors and transfusion recipients.

The use of a label-free method such as SPR imaging may overcome these issues. Multiplexing can be achieved by spotting the various antibodies on the surface of an SPRi sensor at different positions. Previous attempts to achieve this, using either stationary live cells or soluble RBCs, have not resolved how to accomplish massive parallel cellular analysis or how to realize it quickly in a matter of minutes.

This section describes a new SPR imaging detection method for typing RBCs[76] using a critical sedimentation followed by a wash step of antibody spots recognizing RBC antigens on a sensor surface. Although label-free analysis of biomolecular interactions by SPR is widely used for determinations of binding kinetics, the label-free binding of cells to ligand-spotted surfaces has not been intensively studied for several reasons:

1. Suspended cells under certain shear rate conditions are bounced from the wall and will not interact with the sensor surface because of the size of the cell in relation to the thickness of the stagnant layer under laminar flow conditions.

View Online

Published on 24 May 2017 on http://pubs.rsc.org | doi:10.1039/9781788010283-00415

2. For practical reasons, most commercial SPR instruments are configured with optics on top of the fluidics to avoid leakage of liquid into the optical compartment of the instrument. In these instruments, cell sedimentation will occur at the surface opposite to that of the SPR sensor.
3. Cells and particles clog valves and tiny channels in microfluidic cartridges.
4. Cells should first be homogeneously suspended, *e.g.* using back-and-forth flow, before injection of the cells in the label free sensing area. Many systems allow one direction of flow only.
5. A cell is many times ($>20\times$) larger than the penetration depth of the evanescent field ($\sim 0.5\lambda$ of incident light), so only a small part of the cell is within the decaying evanescent sensing field (see Figure 12.13).
6. Cell interactions to immobilized antibodies/antigens do not show 1 : 1 binding kinetics because of the multiple antigens present on a cell. Avidity-based models using serial dilutions of the ligand densities should be applied for the number of interactions and for qualifying the affinity of the cell antigen–antibody interaction.
7. Responses due to cell adhesion will depend on the orientation and packing density of bound cells (see Figure 12.14). A non-linear response is expected close to saturation levels of the surface area.

Here we report a method for how specific interactions of RBCs with an array of anti-RBC antibodies spotted on a sensor can be achieved and used for antigen typing of RBCs – a method that can in principle be used for any cellular detection in a label-free manner. The IBIS MX96 instrument (IBIS Technologies, Enschede, The Netherlands) was used because it is capable of simultaneous label-free SPR measurements of 48–96 spots, and has the resolving power to tackle antigen typing. It contains reversed optics and back-and-forth flow fluidics, allowing for sedimentation and controlled-flow mixing of cells. Valveless injection of samples and wide (1 mm internal diameter) tubing allow smooth aspiration of cell suspensions without clogging.

In the IBIS MX96, samples were exposed to all spots at the same time and interactions with all 48 spots were monitored in real time. The sensor surface can be used many times using a regeneration process in which the RBCs are removed from the covalently coupled ligands, keeping assay costs low.

Prior to injection of the cells, the diluted RBC suspension (20×10^6 cells mL^{-1}, obtained from 5 μL of blood) was both mixed (by repeated aspirating and



Figure 12.13 The evanescent field of an SPR device will only partly fill the sedimented cell.

View Online

Published on 24 May 2017 on http://pubs.rsc.org | doi:10.1039/9781788010283-00415

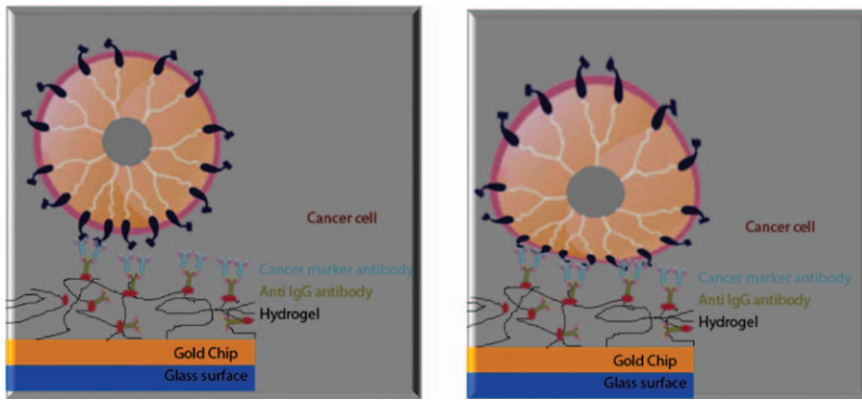


Figure 12.14 Cells sediment and penetrate into the evanescent field and will be detected. The cell surface antigens will bind to specific ligands and will deform the cell, generating more signal to specific spots.

dispensing) and transported from a microtiter plate (200 μL) using the built-in autosampler by *XYZ* positioning of the needle *via* Teflon tubing into the flow chamber. Mixing was necessary to homogenize a pellet of cells in the microtiter plate well. The flow chamber contained the array of spotted ligands. A total volume of 800 μL was aspirated into the tubing and a cell suspension of 200 μL was passed into and through the flow chamber at a flow rate of 120 μL s^{-1}. After stopping the flow, a slow accelerated increase in response was observed while RBCs sedimented onto the complete sensor surface, including the reference spots. However, after resuming the flow after 3 min of sedimentation, at 20 μL s^{-1} in the backward direction, unbound cells and superfluous cells were washed from the surface (Figure 12.15).

Although the kinetic curves during sedimentation showed a non-exponential binding curve, a delay in response was always observed after stopping the flow. The response then slowly increased on all spots, and also negative control spots, in direct relation to the number of cells that landed on the surface (Figure 12.15). The cells landed during the sedimentation phase in a region of interest (ROI) with a size smaller than a ligand spot, encompassing as large a surface area of the spot as possible. The method therefore monitors the average interaction of all cells that land within the ROI (see Figure 12.15, inset), changing the RI in the evanescent field and resulting in a signal increase. This sedimentation response (S) can then be recorded for all spots (Figure 12.15). After resuming the flow, washing away unbound cells, a downward signal to the baseline was observed on reference spots, or if the cell was negative for antigen-specific spots, caused by flushing of the sedimented cells. However, an upward signal was observed for spots with antibodies recognizing antigens on the cell surface. For some spots, the upward signal can be three times the S response >15 000 RU. We observed some unequal distribution of RBCs over the whole chip, with some spots having less RBC sediment and therefore a lower S signal. Importantly, the magnitude of the specific total response (T, Figure 12.15)

View Online

Published on 24 May 2017 on http://pubs.rsc.org | doi:10.1039/9781788010283-00415

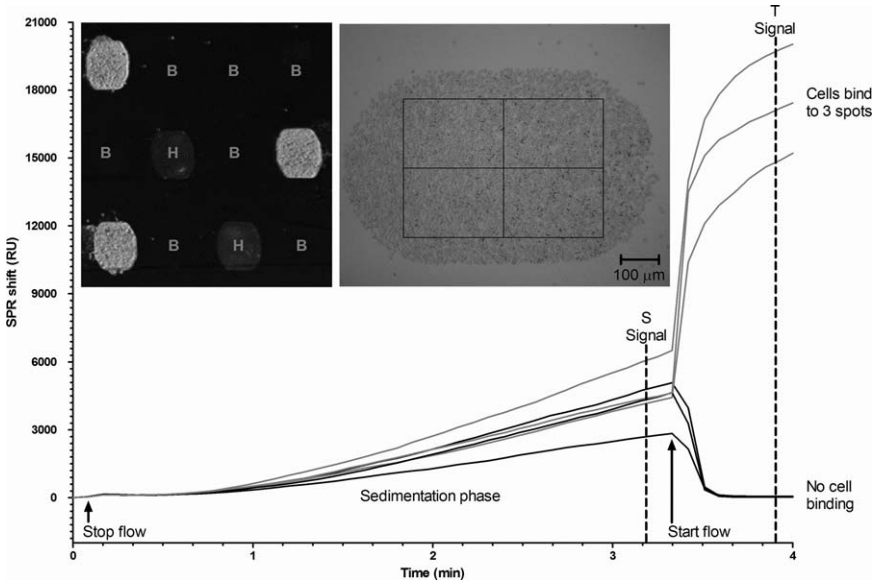


Figure 12.15 The sensorgram shows binding of RBCs to three specific spots with anti-A and three reference spots without ligands. After stopping the flow, the cells sediment on the sensor surface non-specifically and a sedimentation signal (*S*) was observed for all spots. After restarting the flow, washing away unbound cells, an upward signal (*T*) was measured for cells that bind specifically to selected spots, whereas control spots return to the baseline level. The top left inset is an SPR image (reflectivity) of the sensor surface showing three specific anti-A spots with RBCs and some reference, or blanco, spots (B) are visible, whereas the spotted protein (HSA: H) is visible on some spots. The top right inset is a microscopic view of a single spot with four quadrants of ROIs showing M+ RBCs bound to an anti-M spot.[69] Reprinted from R. B. M. Schasfoort, A. E. H. Bentlage, I. Stojanovic, A. van der Kooi, E. van der Schoot, L. W. M. M. Terstappen and G. Vidarsson, Label-free cell profiling, *Anal. Biochem.*, **439**(1) 4–6. Copyright © 2013 Elsevier Inc. All rights reserved.

was directly related to the sedimentation response (*S*, Figure 12.15), allowing for normalization of the data between spots and between experiments ($n > 100$) by expressing the specific response as a ratio T/S (Figure 12.16). Only cells expressing an antigen corresponding to an antibody on a spot (ROI) gave a specific response with $T/S > 1$, allowing for accurate detection of the expressed blood group (Figure 12.16B).

From these observations, the kinetic process of cell binding has at least two typical features:

- First, after injecting the cells, a delay of the response signal is observed after stopping the flow. This typical delay is only observed when large

View Online

Published on 24 May 2017 on http://pubs.rsc.org | doi:10.1039/9781788010283-00415

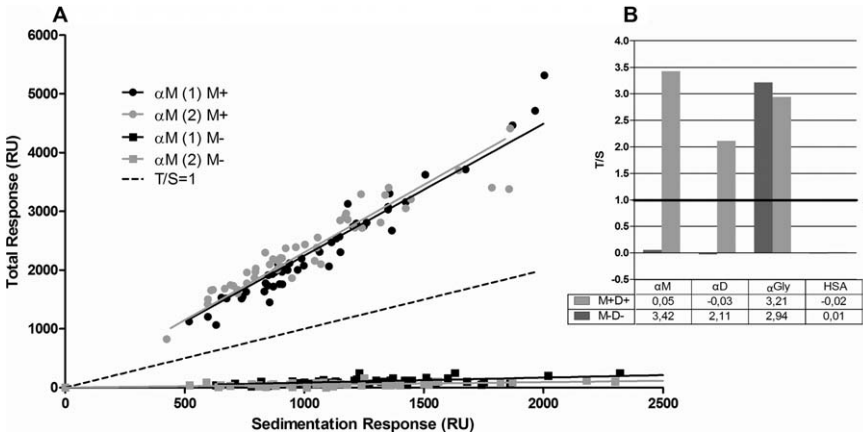


Figure 12.16 SPR sensors (1 and 2) were spotted with anti-M to type RBCs (typed with standard agglutination methods), and the signals ($n > 100$) are measured as explained in Figure 12.15. The total response (T) on anti-M spots was plotted against the sedimentation response (S), resulting in a highly significant correlation ($p < 0.0001$) for M+ cells with respect to M− cells. Therefore, the response (T/S) was used as a normalized response value. SPR sensors were then spotted with anti-M, anti-rhesus D (anti-D), anti-glycophorin A (anti-Gly, positive control), or HSA (negative control) to type RBCs (typed as M + D + or MD with standard agglutination methods), and the signals were measured and expressed as normalized T/S, reliably typing the cells as either D or M positive or negative. The columns and error bars represent means and standard errors of means, respectively.[69]
Reprinted from R. B. M. Schasfoort, A. E. H. Bentlage, I. Stojanovic, A. van der Kooi, E. van der Schoot, L. W. M. M. Terstappen and G. Vidarsson, Label-free cell profiling, *Anal. Biochem.*, **439**(1) 4–6. Copyright © 2013 Elsevier Inc. All rights reserved.

particles (cells) are applied, and never when, *e.g.*, an antibody sample is injected.

- Second, cells that bind specifically to the immobilized ligand molecules will show an upward response after starting the flow again, whereas a downward response is observed from reference spots or other spots that do not bind cells. If the shear rate is below a certain critical value of disruption, the response is stable and the cells will stay on the spots and no off-rate is observed.

These typical effects can be explained as follows:

1. While cells flow in tubing and flow chambers, the laminar flow will deplete the stagnant layer of cells close to the wall. In other words, after lateral transport of the cell suspension over the sensor surface, cells are not in direct contact with surfaces because of shear forces,

View Online

Published on 24 May 2017 on http://pubs.rsc.org | doi:10.1039/9781788010283-00415

but will stay in the middle of the stream. Therefore, the RBCs will first enter the cell-free stagnant layer before settling in the evanescent field of the sensor and hence a delay of sedimentation response is observed.

2. When cells are bound to specific spots of the sensor surface, the flow will induce a reorientation, repacking, or pressing down of the bi-concave RBCs to the surface. Energetically, it is more beneficial that cells are pressed closer to the surface induced by the flow. This results in a larger part of the specifically bound cells that is localized in the evanescent field and an upward response is observed. In contrast, sedimented cells that are not recognized by the coated antibodies (and reference spots) will be washed away and the response will return to the baseline. However, when the flow is too high (data not shown), the shear forces on the cells will also increase and the cells will disrupt from the surface. Hence discrimination can be made between weak/non-binding cells compared with specific bound cells by adjusting the flow rate in the backward direction after the sedimentation phase. This observation led to a strategy to qualify avidity of cell interactions as described in Section 12.8.3.

Label-free cell profiling measurements could be repeated more than 100 times using a single sensor surface. To summarize: label-free cell profiling of RBCs has been outlined using an SPR array imaging method. RBCs were injected in a flow chamber on top of a spotted sensor surface. Spots contained antibodies to various RBC membrane antigens. A typical sensorgram showed an initial response corresponding to cell sedimentation (*S*) followed by a specific upward response (*T*) corresponding to specific binding of cells during a critical wash step. The full analysis cycle for RBC profiling was less than 6 min. The sensor surface could be regenerated at least 100 times, allowing the label-free determination of the cell surface antigen profile of RBCs.

12.8.2 Quantifying the Ratio of Surface Antigens per Cell Population

Rapid multiplex cell surface marker analysis can expedite investigations in which a large number of antigens need to be analyzed. Flow cytometry is the gold standard for the analysis and quantification of antigen expression on cells. Simultaneous analysis of multiple cell surface antigens at the same level of sensitivity is limited, however. In this section, an SPRi-based technique is introduced for multiplex (44-plex) parameter analysis in less than 20 min using a single sample. The expression of 44 antibodies including four negative controls on cells from five different cancer cell lines by SPRi was measured and compared with flow cytometry. The results showed that SPRi can be used for rapid quantitative multiplex cell surface marker analysis (Figure 12.17).

View Online

Published on 24 May 2017 on http://pubs.rsc.org | doi:10.1039/9781788010283-00415

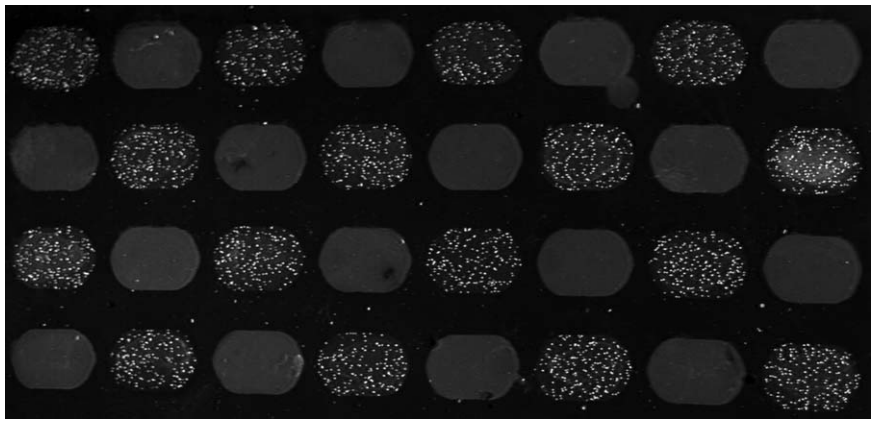


Figure 12.17 T-lymphocytes are visible in the SPR image on a checkerboard of anti-CD3 spots and BSA spots. Specific cell binding is observed on anti-CD3 spots after the flow started and non-bound cells are washed away.

In recent years, the desire for high-throughput multiplex cell analysis has grown. This stems from the fact that diseases such as cancer often involve complex cell surface antigen expression patterns. Several techniques, such as fluorescence microscopy and flow cytometry, have proven to be useful for multiplex cell analysis, but they are time consuming and multiplexing is limited by the available stains and filters of the respective setup. A 19-parameter flow cytometry setup was reported,[77] but its difficulty of use and complexity of data interpretation and presentation make the method unattractive for practical use. In addition, the fluorochromes used in multiparameter flow cytometric analysis cannot detect the antigens with the same sensitivity. It should be taken into account that flow cytometry measures individual cells whereas with other techniques an average of a population of cells is detected.

An alternative technique for multiplex cell analysis is proposed here: surface plasmon resonance imaging (SPRi). Stojanović *et al.*[78] reported the ability of SPRi to detect consistently epithelial cell adhesion molecule (EpCAM) expression on various cancer cells. The cells still being alive could be detected individually in real time and label free. The simultaneous label-free detection of 44 antigens on viable cells could be achieved in less than 20 min. In addition, the ease of use of the system and the simple sample preparation are improvements over more laborious and complex cell analysis alternatives. Flow cytometry was used as the reference technique for comparing the SPRi output. Antigen expression was quantified using QuantiBRITE phycoerythrin (PE) beads and the relative expression ratio of each cell surface marker for each cell line was compared with the resonance unit (RU) output of SPRi (IBIS MX96). The fluidics technology in the IBIS MX96 has been designed such that the sample does not pass any valve. The standard 100 μm (height) flow cell in the IBIS MX96 was replaced with a

View Online

Published on 24 May 2017 on http://pubs.rsc.org | doi:10.1039/9781788010283-00415

300 μm flow cell to obtain better sample homogeneity and less shear force in the flow cell upon injection of the cell sample. The homogeneous cell sample injection and larger volume of culture medium obtained improve the cell viability over time. ROIs were used to define the signal and reference surface area. Each signal ROI had its own dedicated reference ROI; after data collection, the responses from the reference ROIs can be subtracted from each signal ROI in order to obtain referenced output data.

For immobilizing various anti-cell receptor ligands on the sensor surfaces, the Wasatch Microfluidics CFM spotter was used.[79] Ligand immobilization buffer was used to prime the CFM system and to dilute the desired ligands. The immobilization protocol lasted 30 min. The CFM spotter has the ability to spot up to 48 different ligands onto the sensor in a single run simultaneously under back-and-forth confined flow (or 96–384 ligands if a repeated printing protocol is used). The confined back-an-forth flow increases the efficiency of the spotting and avoids the risk of evaporation for contact and non-contact droplet-based spotting methods.

Easy2Spot preactivated G-type SensEye sensors (Ssens) were used as SPR sensor surfaces. The sensors have a 100 nm hydrogel-like layer on gold and are preactivated for easy immobilization without EDC–NHS activation required by the user (see Section 12.4.1).

Antibodies were selected based on expected differences in expression levels between cells of the five cell lines. The antibodies that were used belong to three different categories, providing information on the cell of origin, recognizing antigens involved in cell adhesion, and potential drug targets. Anti-human EpCAM/CD326, Her2, and EGFR antibody were kindly provided by Immunicon (Huntingdon Valley, Philadelphia, PA, USA). Anti-human CD3, CD8a, CD11c, CD14, CD19, CD20, CD25, CD33, CD45, CD56, CD61, CD66b, CD105, CD123, CD140a, CD146, CD235a, CD71, CD117, CD221, CD227, CD261, CD262, CD309, Her3, CD24, CD44, CD49a, CD49b, CD49c, CD49d, CD49e, CD49f, CD103, CD104, CD106, CD113, CD144, CD166, CD324, and CD334 antibodies were purchased from Biolegend (San Diego, CA, USA), anti-human CD113 from Santa Cruz Biotechnology, (Santa Cruz, CA, USA), and anti-human CD103 from BD Biosciences (San Jose, CA, USA). Anti-human serum albumin antibody was used as a negative control in the SPRi experiments and was purchased from Sigma-Aldrich (Steinheim, Germany). Anti-mouse IgG PE was purchased from Abcam (Cambridge, UK) and was used for staining of unlabeled antibodies in flow cytometry and as a negative control in the SPRi experiments.

Cells from the following cell lines were used: breast cancer cell lines MCF7 (ATCC HTB-22) and SKBR3 (ATCC HTB-30), the acute myelogenous leukemia cell line KG1a (ATCC CCL-246.1), the osteosarcoma cell line MG-63 (ATCC CRL-1427), and the large cell lung cancer cell line NCI-H460 (ATCC HTB-177). The cells were cultivated in their appropriate complete culture medium and were harvested using trypsin (except KG1a), after which they were resuspended in complete culture medium to obtain a concentration of 1.0 million cells mL^{-1}.

View Online

Published on 24 May 2017 on http://pubs.rsc.org | doi:10.1039/9781788010283-00415

A 10 mM solution of immobilization buffer at pH 4.5 was prepared using anhydrous sodium acetate (Sigma-Aldrich) and acetic acid (Merck Schuchardt, Hohenbrunn, Germany).

A 1% solution of bovine serum albumin (BSA) (Sigma-Aldrich) in sodium acetate immobilization buffer was used as a deactivation agent. A stock solution of 2-aminoethanol (MP Biomedicals, Illkrich, France) was used to prepare a 100 mM 2-aminoethanol solution with a pH of 8 and used as an extra sensor deactivation step after the initial BSA deactivation.

When viable cells were analyzed in the SPRi apparatus, the system buffer was the complete culture medium. For spotting the antibodies, the stock solutions were diluted in ligand immobilization buffer in order to achieve an end concentration of 5 $\mu g\,mL^{-1}$. Of forty-eight wells of a 96-well plate, 44 were filled with an anti-cell receptor antibody and four were used as negative controls. The well plate and SPR sensor were then inserted in the CFM spotter, after which it was set up to print the ligands during 30 min (30 cycles of 1 min). After completion of the printing, the sensor was inserted in the MX96 and sensor deactivation was performed with the two deactivation buffers (1 min each). After deactivation, the analysis script and times were programmed into the MX96. The cells were flowed over the sensor surface using a custom-made ''cell analysis script'' in which the sample plug containing the cells was flushed over the entire surface and after which the flow was switched off, allowing the cells to sediment and interact with the ligands. Cells were allowed to interact with the ligands for 1000 s (16.7 min), and after this association phase the back flow of fresh medium started again.

To validate the data acquired by SPRi, a comparison was made using flow cytometry analysis as described elsewhere.[7,80]

Figure 12.18 shows an SPR sensorgram illustrating the expression of all tested markers on cells from the breast cancer cell line MCF7 and Figure 12.19 an SPR sensorgram illustrating the expression of HER2 on cells from the five different cell lines. The higher the SPR response then the higher the cell surface expression of the antigen will be. An explanation is that cells with high-abundance surface markers will insert faster and deeper in the gel layer, whereas cells without interaction will lie on top of the hydrogel and are not ''visible'' in the evanescent field. The sensorgrams clearly show a great divergence of expression of the markers on MCF7 cells, and likewise different levels of HER2 expression on cells of the five cell lines are seen. The SPR RU endpoint values were recorded after 900 s as indicated with a dashed line in Figures 12.18 and 12.19. The SPR RU values obtained from each cell line and each antibody are shown in Figure 12.20. All data was collected at the same time ($t = 900$ s) and the RU values show differences in responses per cell line injected at 1 million cells mL^{-1} and per marker. Some markers also show negative SPR responses. The SPRi values were color coded in Figure 12.20, all values at or below the isotype PE control were colored red and the values above were gradually colored from red, though yellow to green (red tones representing the low-expressed markers and green tones representing the highly expressed markers). Anti-human serum albumin

View Online

Published on 24 May 2017 on http://pubs.rsc.org | doi:10.1039/9781788010283-00415

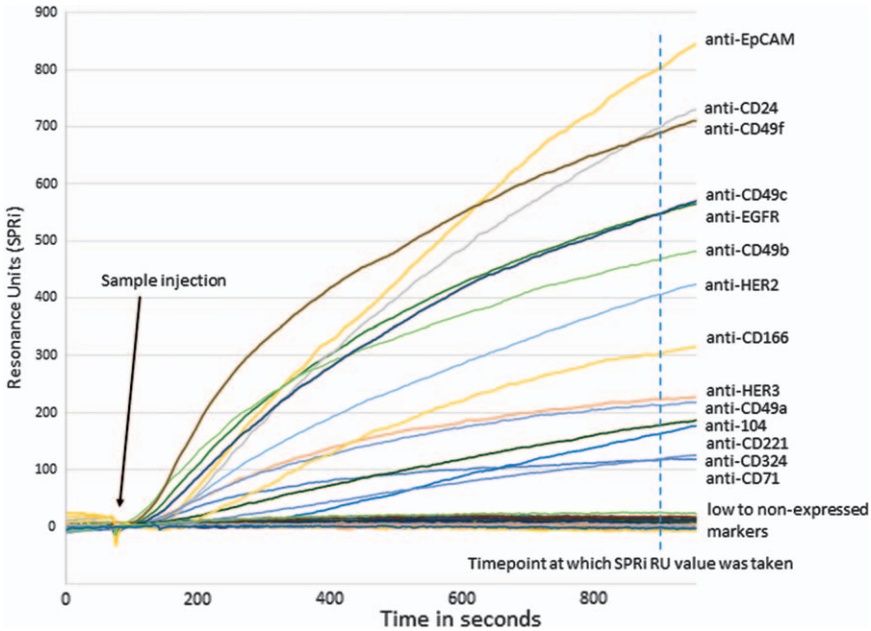


Figure 12.18 Graphical output of MCF7 cells injected 1 million cells mL^{-1} analyzed with SPRi. Shown are 44 markers which are expressed in varying levels on the cell surface of MCF7 cells but containing about the same number of cells. The higher the expression on the cells; the higher the response (in RU) will be.

spots were used as negative control surfaces and their values are also given in Figure 12.20. As a cutoff threshold, the values obtained from the anti-IgG spots were chosen which are the same as the anti-IgG PE antibody that was used for the IgG PE control stain.

12.8.2.1 Quantification of Cell Surface Markers by Flow Cytometry

The geometric mean values obtained with flow cytometry were used to determine the ABC value using the QuantiBRITE PE method. The ABC values represent the amount of antibodies that have been bound to a cell, and the higher the value the higher is the expression of the respective cell surface marker. The ABC output of flow cytometry and the RU response at 900 s of SPRi for each of the antibodies for the five cell lines were plotted against each other and are shown in Figure 12.21. For the correlation determination, only the markers with positive expression were used; markers that resulted in expression levels at or below the IgG PE control stain (for flow cytometry) or RU responses of 0 or below 0 or responses lower than or below the anti-IgG spot (for SPRi) were excluded from the correlation determination. The highest correlation was found for NCI H460 cells with $R^2 = 0.91$ and the

View Online

Published on 24 May 2017 on http://pubs.rsc.org | doi:10.1039/9781788010283-00415

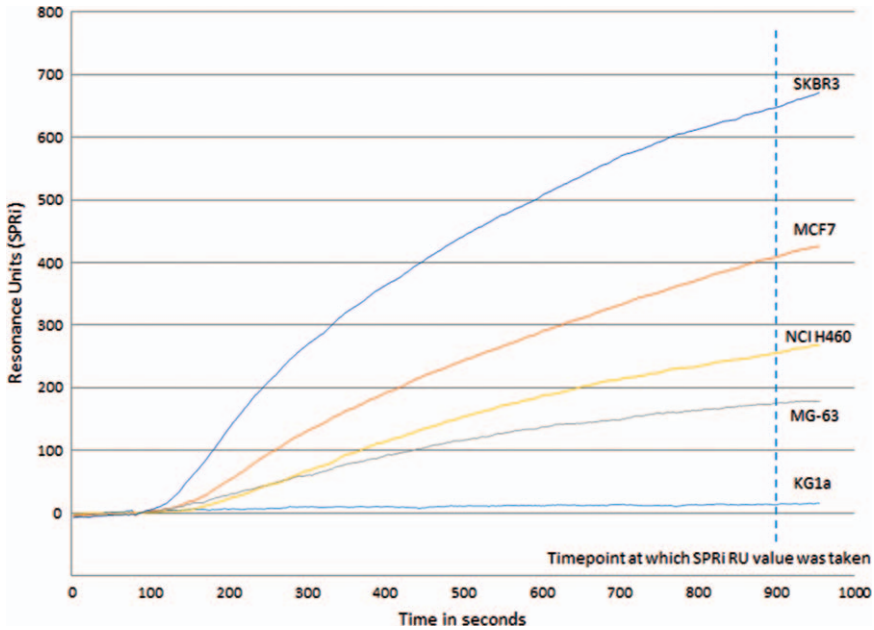


Figure 12.19 Graphical output of a single marker (HER2) analyzed with SPRi across five different cell lines all injected at 1 million cells mL^{-1}. Clearly visible is the difference in expression of the marker across the different cell lines, SKBR3 having the highest expression and KG1a the lowest.

lowest correlation for SKBR3 with $R^2 = 0.67$. The combined correlation for all cell lines and markers was $R^2 = 0.76$. The general trend of responses is largely similar on comparing flow cytometry and SPRi. ABC values for each cell line that are below the level of the unstained control are marked dark red and no expression was detected. The values between the unstained and IgG PE control sample are marked red and indicate very low or non-existent expression. All values that had recorded values higher than the IgG PE control sample were given gradually changing color shades as their expression increased (similarly to what was done with the SPR values).

In this study, it was shown that SPRi is a suitable technique for the rapid multiplex analysis of cell surface marker expression levels. KG1a, MCF7, MG63, NCI H460, and SKBR3 cells were analyzed for their expression levels of 44 cell surface markers. Data acquired using SPRi correlated well with a standard flow cytometry-based technique for cell surface marker quantification (QuantiBRITE). The determined correlations (R^2) of all positive markers in order from high to low were 0.91 (NCI H460), 0.89 (MG63), 0.82 (MCF7), 0.79 (KG1a), and 0.67 (SKBR3). The combined correlation of all positive markers across all cell lines was determined as $R^2 = 0.76$. The data show that not only is SPRi capable of analyzing cell surface marker expression on living cells in multiplex fashion, but also that the SPRi output

Published on 24 May 2017 on http://pubs.rsc.org | doi:10

KG1a			MCF7			MG-63			NCI-H460			SKBR3		
Marker	ABC	RU(SPRi)	Marker	ABC	RU(SPRi)	Marker	ABC	RU(SPRi)	Marker	ABC	RU(SPRi)	Marker	ABC	RU(SPRi)
CD44	48639	842	CD49f	110012	762	CD44	426853	2329	CD227	89832	997	CD24	191709	1555
CD45	21659	273	EpCAM	98284	887	CD49c	81333	987	CD44	60073	1194	HER2	158838	1300
CD49e	12663	429	CD49b	89604	497	CD49e	64212	654	CD49f	56021	512	EpCAM	123384	1073
CD49d	9994	308	CD24	62994	751	CD227	50185	680	CD56	55119	600	CD227	85931	853
CD166	6090	159	CD49c	55734	600	CD166	19032	438	CD24	27534	495	CD71	35500	366
CD49f	5015	167	HER2	44525	425	CD49f	16082	433	CD71	18187	266	CD49b	20942	243
CD49c	3580	218	EGFR	35005	591	CD49d	12793	496	CD49e	17089	285	CD49c	14023	181
CD71	2822	87	CD44	29102	652	CD105	11200	182	CD49b	16082	169	CD49e	11037	223
CD123	1260	40	CD71	13296	119	HER2	9684	178	EGFR	14629	269	CD166	10486	480
CD49b	1141	78	CD49a	11458	223	CD221	9135	307	CD166	12875	381	EGFR	9325	145
CD61	1039	10	CD166	9564	323	CD49b	7787	134	CD221	9766	271	HER3	6050	299
CD24	1017	28	CD104	9419	196	CD71	7531	111	HER2	8873	267	CD221	4499	159
CD105	1013	71	CD221	5994	194	CD49a	6100	138	CD49a	4731	52	CD324	4206	115
CD33	959	2	CD262	5075	-7	CD56	5928	158	CD49c	4241	82	CD105	3903	142
EGFR	957	24	CD324	4032	138	EGFR	4261	94	HER3	3858	180	CD66b	3386	8
CD261	957	7	HER3	3584	251	CD324	3980	103	CD262	1396	-14	CD49a	3046	3
CD144	924	29	CD261	1052	4	CD262	3183	-26	CD105	1371	35	CD261	3035	-9
CD227	901	18	CD103	948	7	CD113	1895	27	EpCAM	1365	-17	CD140a	2926	-10
EpCAM	860	3	CD49d	691	16	CD104	1754	6	CD113	1095	-8	CD49f	2904	-6
HER2	817	15	CD113	672	1	CD3	1732	-27	CD324	588	13	CD14	2679	-16
CD235a	802	7	CD334	657	25	CD334	1656	18	CD334	588	15	CD20	2548	0
CD56	794	13	CD61	613	16	CD106	1613	-29	CD140a	567	3	CD3	2510	-6
CD262	738	3	CD11c	379	4	CD24	1300	-27	CD123	541	8	CD44	2341	-4
CD140a	736	2	CD235a	348	0	CD103	1300	-15	CD146	478	0	CD25	2319	-5
CD334	732	14	CD227	339	-6	HER3	1251	-24	CD117	466	-1	CD262	2281	-6
CD103	725	15	CD14	268	-1	CD144	1187	-6	CD235a	435	-1	CD103	2237	3
HER3	715	25	CD49e	265	11	CD117	1095	-21	CD144	422	7	CD49d	2226	5
CD146	715	15	CD144	265	4	CD11c	1036	-24	CD66b	410	26	CD61	2210	6
CD11c	713	-4	CD20	247	11	CD261	1036	-30	CD33	408	-6	CD106	2210	-5
CD309	706	25	CD106	245	0	CD309	1015	-17	CD61	397	-5	CD104	2194	2
CD117	704	4	CD3	239	9	CD235a	972	-18	CD106	389	-1	CD8a	2188	-16
CD113	691	26	CD117	239	-2	CD14	801	-27	CD19	376	2	CD45	2134	-1
CD106	685	10	CD8a	235	-3	CD8a	790	-28	CD49d	374	5	CD113	2128	89
CD49a	679	8	CD33	229	-3	CD66b	614	-10	CD104	350	-6	CD334	2047	13
CD25	679	7	CD19	227	0	CD45	551	-21	CD261	331	9	CD56	1960	35
CD66b	634	-3	CD25	227	5	EpCAM	487	-27	CD20	308	13	CD11c	1895	-5
CD221	630	-17	CD309	227	6	CD146	487	-21	CD103	284	3	CD19	1862	-7
CD20	630	11	CD56	199	0	CD123	455	-17	CD25	280	6	CD33	1857	-14
CD104	617	27	CD45	178	-4	CD25	434	-17	CD14	272	-4	CD123	1732	5
CD324	600	18	CD140a	174	-6	CD140a	434	-35	CD45	270	0	CD144	1683	-7
CD8a	529	4	CD146	170	-5	CD20	413	-15	CD11c	261	-5	CD117	1678	-10
CD14	520	6	CD123	166	10	CD33	387	-10	CD8a	231	-12	CD309	1651	3
CD19	512	4	CD105	156	10	CD19	355	-27	CD3	223	3	CD235a	1319	-9
CD3	468	14	CD66b	137	7	CD61	334	-21	CD309	193	-6	CD146	779	-5
Correlation	0.7856		Correlation	0.8266		Correlation	0.8944		Correlation	0.9102		Correlation	0.6709	
Combined correlation	0.7578													
Unstained (flow cytometer)/anti HSA (SPRi)	153	19	Unstained	209	8	Unstained	1911	-13	Unstained	131	-20	Unstained	1373	1
IgG PE control	1280	4	IgG PE control	397	-2	IgG PE control	2453	-26	IgG PE control	424	-6	IgG PE control	2225	-6

Figure 12.20 Responses of all 44 markers obtained with flow cytometry (ABC) and SPRi cytometry (RU SPRi). The data are sorted from high expression (green colors) to low expression (red colors) (as determined by flow cytometry).

View Online

Published on 24 May 2017 on http://pubs.rsc.org | doi:10.1039/9781788010283-00415

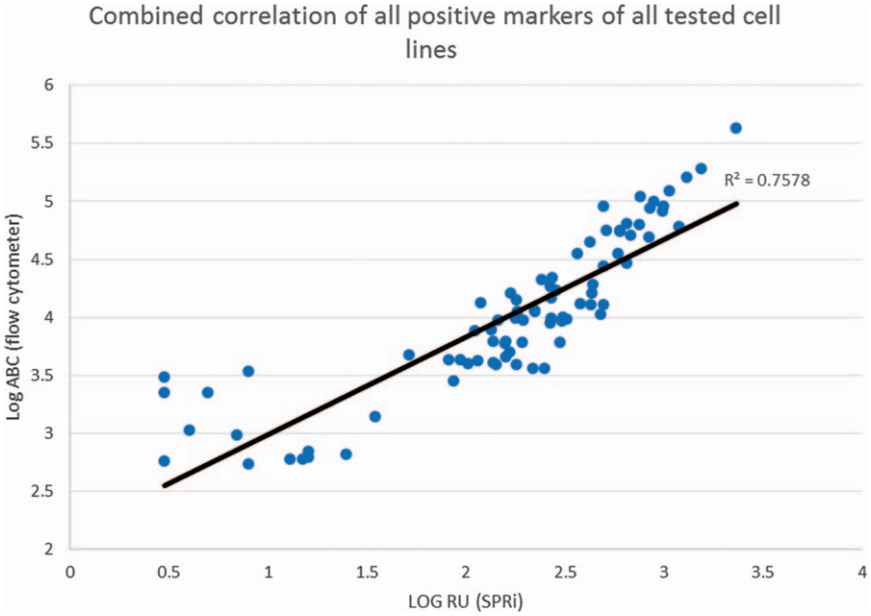


Figure 12.21 Combined correlation plot of all the positive markers of all the cell lines.

contains information about the expression levels of these cell surface markers. SPRi is able to provide the data in less than 20 min (analysis time).

12.8.3 Extracellular Vesicle Monitoring Using SPRi

Blood contains 10^8–10^{12} extracellular vesicles (EVs) per milliliter, and such EVs range in size from <100 nm to >1 μm in diameter, with most having a diameter of <200 nm (see Figures 12.22 and 12.23). Under *physiological* conditions, EVs originate from blood cells and the vessel wall. Because cells concurrently release different types of EVs, and because the molecular composition of EVs depends on the status (resting, activated, apoptotic, *etc.*) of the releasing cell, EVs are not only very abundant but also very heterogeneous in appearance and composition. In cancer, *i.e.* under *pathological* conditions, tumor-derived EVs will enter the blood. Consequently, a fraction of the EVs in blood originates from cancer cells, and reliable identification of such vesicles will provide clinically relevant information for diagnosis and development of a tumor, for example, during treatment.

The presence of tumor-derived EVs in blood from cancer patients has been determined using detection methods analyzing either total populations of vesicles[81] or on the level of single vesicles. Measurements of total populations do not identify multiple vesicle types within a mixed population, do not measure vesicle concentration, and tend to have limited sensitivity for rare vesicles. Single vesicle measurements solve these problems, yet are very

View Online

Published on 24 May 2017 on http://pubs.rsc.org | doi:10.1039/9781788010283-00415

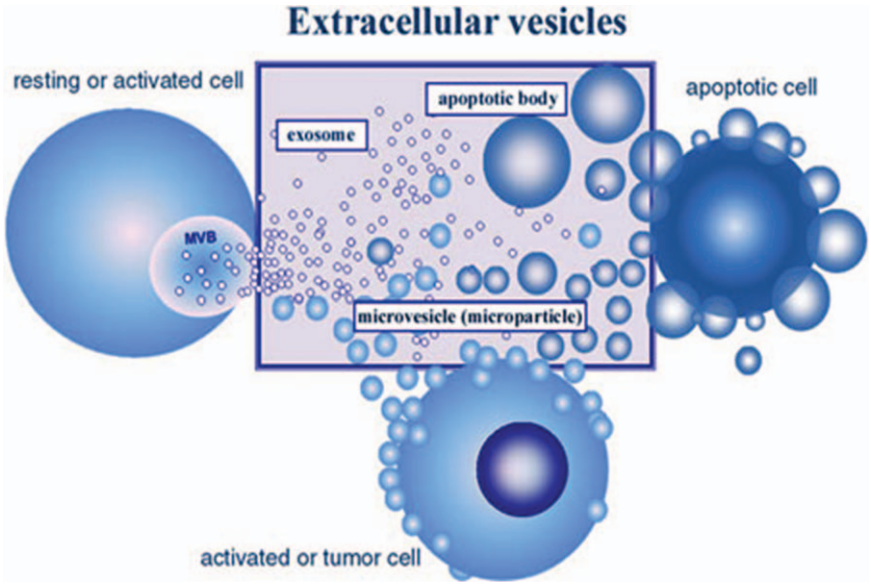


Figure 12.22 Cells release different kinds of extracellular vesicles.[81] Reprinted from B. György, T. G. Szabó, M. Pásztói, Z. Pál, P. Misják, B. Aradi, V. László, É. Pállinger, E. Pap, Á. Kittel, G. Nagy, A. Falus and E. I. Buzás, Membrane vesicles, current state-of-the-art: emerging role of extracellular vesicles, *Cell. Mol. Life Sci.*, 2011, **68**(16), 2667.

challenging because identification, labeling, and detection of single vesicles is required. Although flow cytometry has been and is still widely used, this method has several drawbacks. Primarily, up to 99% of all single vesicles are undetected because their light scatter is below the detection threshold owing to their small diameter and low RI (~1.37).[82]

The detection of tumor-derived EVs in plasma from cancer patients is performed using SPRi for multiplex label-free EV interaction monitoring. SPRi combines the advantages of single vesicle measurements with those of total population measurements. SPRi can discriminate vesicles of different cellular origin, determine the concentration of vesicles, and is more sensitive to small vesicles than flow cytometry.[83] Cells of epithelial and hematopoietic origin express antigens that allow differentiation of these cells in blood. For example, epithelial cells could be identified based on their expression of antigens typically found on carcinoma cells and the absence of antigens typically found on hematopoietic cells. This approach is applied in a US Food and Drug Administration (FDA) approved test to detect EpCAM + CK + DNA + CD45– circulating tumor cells (CTCs) in blood. In this test, however, metastatic patients typically have one CTC per milliliter of blood. One would expect to find 2–3 orders of magnitude more tumor-derived EVs, but it is not known whether these express the same antigens. For example, leukocyte-derived EVs have been found not to express CD45. The SPRi

View Online

Published on 24 May 2017 on http://pubs.rsc.org | doi:10.1039/9781788010283-00415

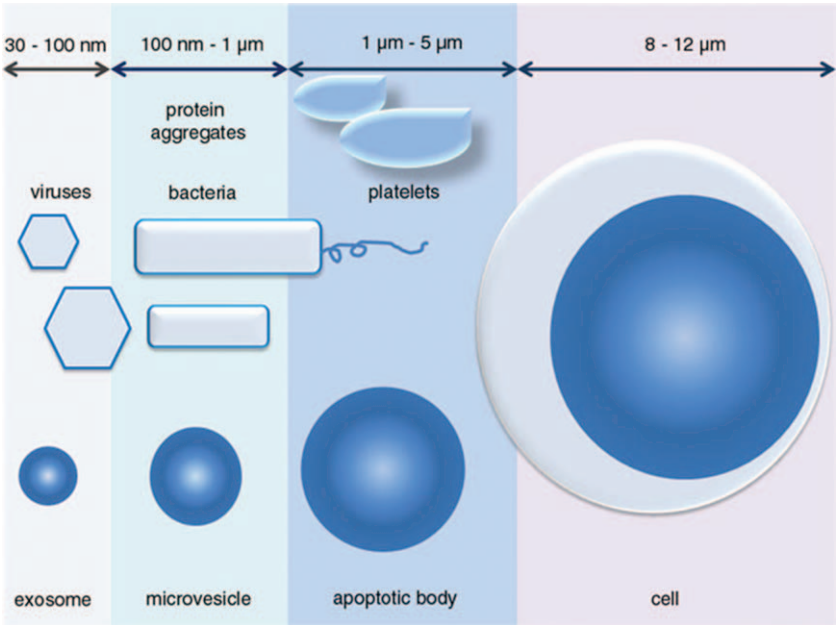


Figure 12.23 Size ranges of extracellular vesicles from less than 100 nm to >1 µm in diameter.[81]
Reprinted from B. György, T. G. Szabó, M. Pásztói, Z. Pál, P. Misják, B. Aradi, V. László, É. Pállinger, E. Pap, Á. Kittel, G. Nagy, A. Falus and E. I. Buzás, Membrane vesicles, current state-of-the-art: emerging role of extracellular vesicles, *Cell. Mol. Life Sci.*, 2011, **68**(16), 2667.

system has the capability of screening with 96 antibodies simultaneously and, moreover, this system has the sensitivity to detect single bound vesicles. This allows screening of samples containing EVs in suspension to determine their cellular origin by using an array of antibodies, including EpCAM, PSA, Her2-neu, MUC1, EGFR, VEGF, and mTOR for epithelial EVs and CD3, CD4, CD8, CD11a/b, CD14, CD16, CD20, CD34, CD41, CD45, CD104, CD148, CD61, and CD235a for hematopoietic EVs.

The IBIS MX96 will be investigated for this new purpose in cooperation with various partners in The Netherlands in academia, including AMC and Sanquin Research (Amsterdam, The Netherlands). A strong feature of the IBIS MX96 is the possibility of applying unlimited exposure times of samples for very low limits of detection. Its valveless injection of, *e.g.*, EV samples and patented tunable back-and-forth flow-based fluidics allow the injection of only 100 µL of sample for measuring simultaneously the interactions on 96 signal spots. Furthermore, it is possible to elute the vesicles from single spots. This unique feature implies that the IBIS MX96 can be used as an EV sorter, and thus offers the opportunity to sort and obtain different types of EVs from complex body fluids for further assays, including functional testing

View Online

Published on 24 May 2017 on http://pubs.rsc.org | doi:10.1039/9781788010283-00415

and PCR work. Because the shift per unit surface area is important, the smallest region of interest should be applied to measure the shift of a resonance angle. An indication of the theoretical sensitivity of an SPRi device for measuring EV is as follows.

The propagation length of a plasmon is in the order of 20 μm (see Chapter 2, Section 2.3.6.2). This means in practice that the smallest ROI that can be applied for EV detection will have a surface area of 5×20 μm (4 pixels of 5 μm in a row). If this surface area is occupied by a full coverage of particles of size 150 nm with an effective RI shift of 1.37, then a full coverage will generate a shift of 40 000 RU (1.37 RIU – 1.33 RIU = 0.04 RIU). The number of particles/EV of 0.15 μm (calculate as cubes) that can bound to a surface area of 100 $\mu m^2 = 100/0.15^2 \approx 4000$ EV. Hence a single EV will shift the resonance condition in this surface area $40\,000/4000 \approx 10$ RU. Thus SPRi is in principle sensitive enough to measure a single EV that is captured in real time in the evanescent field when these ROI dimensions are applied.

Recently, the proof of concept was shown for the specific detection of lipoparticles with a size of 150 nm. Lipoparticles incorporate high concentrations of properly folded and oriented membrane proteins on their surface. Because lipoparticles are virus-like particles (VLPs) based on the natural retroviral budding process, they are uniform in diameter (~150 nm) and maintain the orientation of incorporated membrane proteins.[84] In order to permit EV detection, a specially adapted flow cell was installed in the IBIS MX96. Figure 12.24 shows a sensorgram of injected CXCR4 lipoparticles. In addition to spots with anti-CXCR4 antibodies, the antibodies were first captured on an anti-mouse IgG spot followed by the injection of the CXCR4 particle. In order to repeat the experiment, an additional two injections of particles in serial dilution were tested.

In Figure 12.24, three tracks in three serial dilutions of the CXCR4 particles are shown in serial view. A long interaction time of 40 min was applied. A special double regeneration step was carried out in order to repeat the interaction. A huge, almost linear unsaturated signal arose as a result of the specific binding of the lipoparticles at the captured antibody spots and the directly immobilized antibody spots. Summarizing:

- It has been shown that a huge response of specific lipoparticle binding could be detected with SPRi.
- The IBIS MX96 has an open valveless microfluidics architecture that allows EV detection.
- A low consumption of 100 μL per injection over 96 spots and the ability to recover the injected EVs are attractive for reference materials and patient samples.

SPRi is an alternative detection technique for analyzing antigen exposure on submicron-sized EVs. The captured EV causes an increase in RI at the

View Online

Published on 24 May 2017 on http://pubs.rsc.org | doi:10.1039/9781788010283-00415

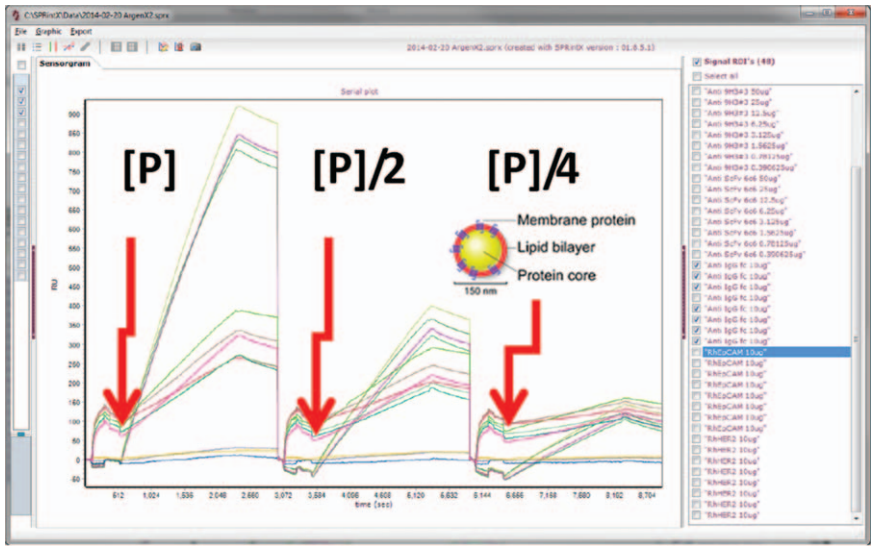


Figure 12.24 Anti-CXCR4 antibodies were captured on seven anti-IgG spots and also four spots with directly spotted anti-CXCR4 antibodies. These spots were selected to show the binding of the CXCR4 particle. First an injection of anti-CXCR4 was carried out followed by the injection of the particles at concentration [P] in serial dilutions [P], [P]/2 and [P]/4. A mass transport-limited interaction can be observed.

surface. This RI is directly proportional to the SPRi signal, which was shown to correlate with antigen exposure on EVs and cells.

12.8.4 Affinity Ranking of Cell Surface Antigens on Living Cells

Recently at Sanquin, a new approach for determining the affinity of cell receptor antibodies has been applied. This work showed for the first time that the avidity of cell interactions could be measured, which is a tool to rank different antibodies binding to various cell surface antigens of whole intact living cells. Cells will bind to the sensor surface after injecting cells in a flow chamber.[85] Companies that are developing antibodies for various cell applications need to characterize the affinity of monoclonal antibodies against *living cell* receptors! Direct detection of the antibody that binds to a sedimented cell line was not possible because of highly unstable baselines due to activity of the cells. However, we found that the release of cells from the sensor surface depends on several factors, *e.g.* the flow velocity, the number of receptors on the cell, the affinity of the cell receptor to immobilized ligand, the ligand density, *etc.*, are important parameters. When a ligand gradient is applied in combination with increasing flow rate (shear rate),

View Online

Published on 24 May 2017 on http://pubs.rsc.org | doi:10.1039/9781788010283-00415

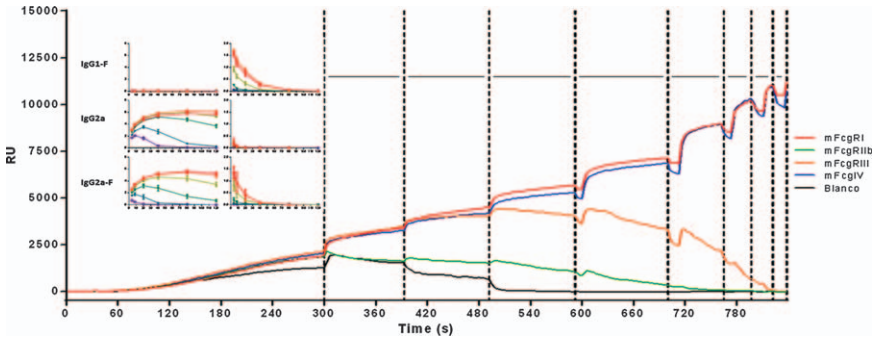


Figure 12.25 *T*/*S* sensorgram for label-free cell profiling measured in the IBIS MX96. RBCs will be bound or will dissociate depending on the affinity and number of receptors (avidity). Increasing flow rate from 1 to 120 mL s^{-1} allows how well the opsonized cells bind to the spotted FcγRs to be determined. Avidity was determined by measuring the binding strength of IgG-opsonized RBCs to C-terminally biotin tagged FcγR on a streptavidin sensor measuring binding to all FcγR simultaneously for each antibody. ($n = 6$).

then ranking the affinity could possibly be measured on multiple receptor–antibody combinations.

The shear on cells depends on the local velocity profile of the buffer stream on the immobilized cells. Figure 12.25 shows that the ligand density of the immobilized antibodies and the velocity of the buffer flow are important to cell receptor affinity ranking.

By addressing a uniform force on the cells, a ligand density series of anti-membrane antigens will tune the position where cells at a certain velocity will dissociate from the spots. In this way, affinities of receptors on cells can be compared and ranked with respect to each other when simultaneously different antibodies are immobilized in a ligand density series. The ranking can be achieved when similar conditions of functional ligand densities can be created.

Major histocompatibility complex (MHC) class I molecules [in humans, so-called human leukocyte antigen (HLA)] present peptide ligands on the cell surface for recognition by appropriate cytotoxic T cells.[86] The affinity of the T-cell receptor of T cells that bind to cancer-specific peptides present on the surface of diseased cells is too low in cancer patients and cancer cells may escape from the patient's immune system. If a cancer-specific peptide–human leukocyte antigen (pHLA) shows higher affinity to the T-cell receptor on T cells, then a remedy for the cancer could be realized.

SPR is a tool to measure the affinity of combinations of HLA and TCR interactions.[87] Recently, successful measurements of micromolar affinity interactions with soluble TCR were performed in a study using SPR array imaging.[88] If the affinity of living T cells to a multiplex peptide-loaded HLA can be determined by ranking the T cells to the 96-plex peptide–HLA sensor surface,[89] a breakthrough in specific cancer patient T-cell screening can be realized, then this SPRi application will have an enormous impact.

View Online

Published on 24 May 2017 on http://pubs.rsc.org | doi:10.1039/9781788010283-00415

12.8.5 Quantifying the Production Rate of Molecules per Individual Cell

As SPR know-how and microfluidics evolved over the last decade, various studies have reported the use of SPRi to study cellular responses and interactions.[90] From these studies, we postulated that it should be possible to measure using SPRi not only the binding of the cell itself but also the products excreted by cells on a single cellular level.

Traditionally, detection and quantification of single cell excretion are a complicated procedure.[91,92] To investigate if it is possible to measure the excreted products from a single cell, an IBIS MX96 SPR imager was modified so that cellular production could be monitored for prolonged periods at 37 °C[93] (see Figure 12.26).

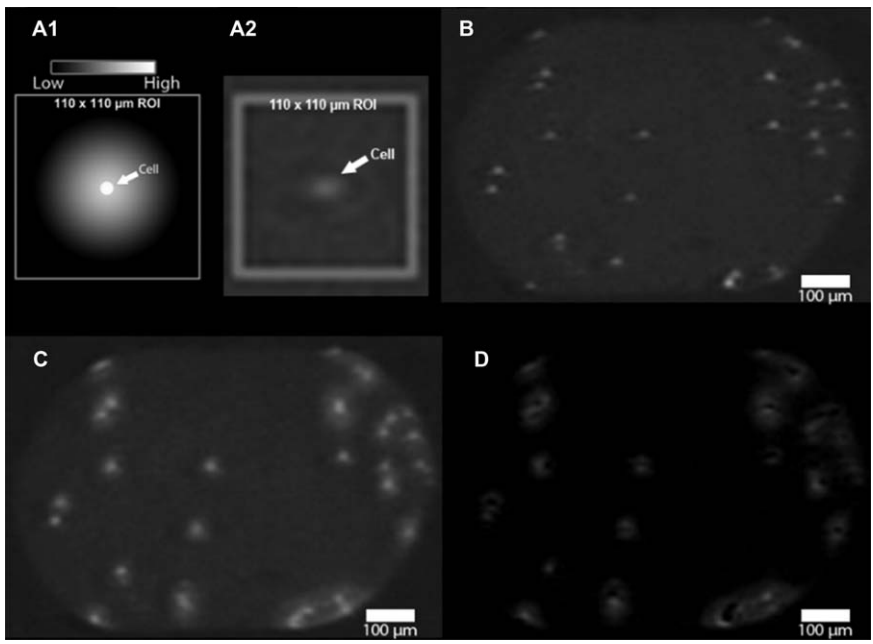


Figure 12.26 (A1) The white dot is the hybridoma cell and the gray field diminishing in intensity around the cell (halo) is the anticipated excreted product of that cell. Square ROIs are placed centered over the cell and have a size of 110×110 µm (20×20 pixels). (A2) An SPRi camera image of the actual placement of an ROI on a cell prior to the initiation of the real time following of cellular excretion. (B) Actual image of EpCAM hybridoma cells after sedimentation. (C) The same cells shown after a 60 h SPRi experiment; the halos seen around the cells are the anti EpCAM antibodies that were produced by the cell line. (D) Image showing the difference of the images in (A) and (B); only the produced antibody is shown and the remainder of the spot remains black.[93] Reprinted from I. Stojanović, T. J. G. van der Velden, H. W. Mulder, R. B. M. Schasfoort and L. W. M. M. Terstappen, Quantification of antibody production of individual hybridoma cells by surface plasmon resonance imaging, *Anal. Biochem.*, 2015, **485**, 112–118. Copyright 2015 Elsevier Inc. All rights reserved.

View Online

Published on 24 May 2017 on http://pubs.rsc.org | doi:10.1039/9781788010283-00415

As a model system, a hybridoma cell line producing VU1D9, an IgG1 monoclonal antibody (mouse) recognizing EpCAM, was used. Stojanović *et al.*[94] developed a model that showed that the antibodies of a single VU1D9 cell (production is ~100 molecules per cell per second) will bind 99.1% directly to the sensor surface and only 0.9% was lost due to diffusion into the bulk (see Figure 12.27). The capacity of the sensor surface is sufficient to capture the molecules produced by single cells. Hence SPRi can be used as an accurate quantification method for single-cell protein production.

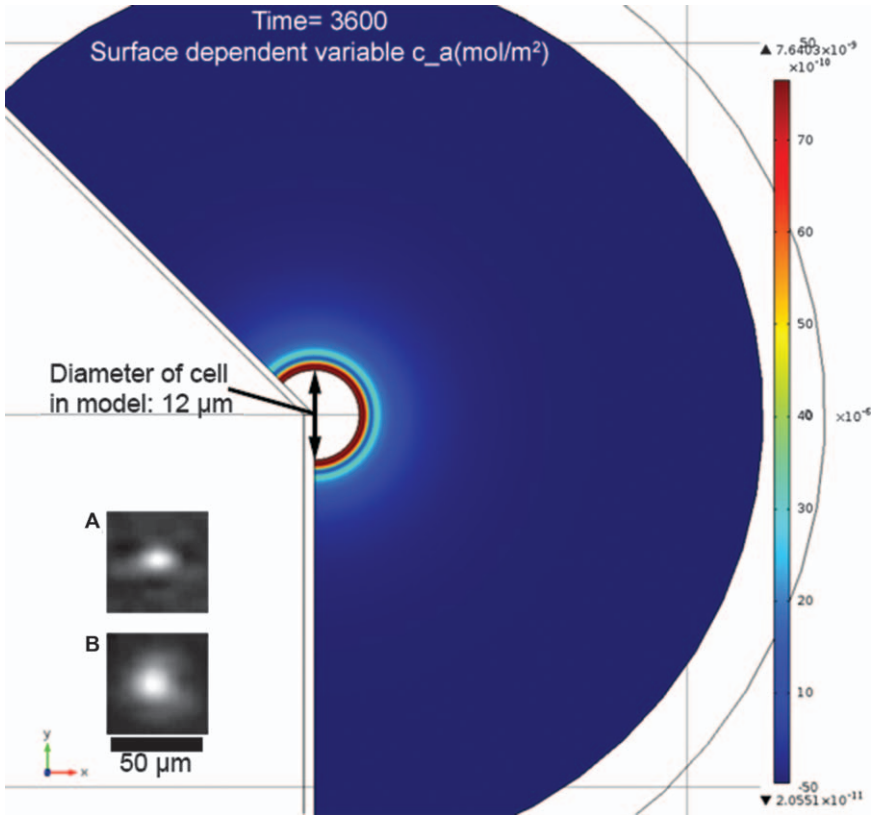


Figure 12.27 Top-down view output of the Comsol simulation. The white circle in the middle represents the cell and the colored halo around it represents the protein bound to the sensor surface. The color scale ranges from red (high amount of protein) to dark blue (low amount of protein). Inset (A) shows an actual cell on an SPR sensor upon binding and (B) shows the same cell with the excreted antibody bound on the sensor surface around the cell.[94]
Reprinted from I. Stojanović, W. Baumgartner, T. J. G. can der Velden, L. W. M. M. Terstappen and R. B. M. Schasfoort, Modeling single cell antibody excretion on a biosensor, *Anal. Biochem.*, **504**, 1–3. Copyright 2016 Elsevier Inc. All rights reserved.

View Online

Published on 24 May 2017 on http://pubs.rsc.org | doi:10.1039/9781788010283-00415

However, an identified valuable high producer cannot be picked from the sensor surface. In other words, after quantification and observing the individual cells in the SPR image, it is not a sinecure to select the cell and detach it from the sensor surface. Fortunately, we found a solution that is presented in the next section.

12.8.6 Microwell Cell Selection Using SPRi: the McSPRinter

A recent patent application[95] shows how silicon technology can be applied to isolate cells of interest.

Figure 12.28 illustrates microwell silicon technology (VyCAP, Deventer, The Netherlands) to seed single cells in individual wells. Recently, the self-seeding microwells were combined with SPRi[96] (microwell cell selection printer, McSPRinter). SPRi was used to monitor, track, and quantify the excretion of antibodies label free and in real time from each of the individual cells. It can be considered a breakthrough in single-cell screening for excreted products. Selection of cells from a pool of thousands of cells can be carried out after an overnight incubation in hours instead of weeks. Screening can be performed not only on maximum excretion of product but also on intrinsic antibody parameters such as affinity (K_D) and on- and off-rates (k_a and k_d, respectively).

The protocol for selecting single cells based on criteria as the quality and quantity of the excreted product is as follows:

- A cell suspension is transferred to a microwell chip (Figure 12.28) containing an array of microwells and, by a small vacuum, a cell suspension flow drags a single cell into a 5 μm pore in the bottom of the microwell.

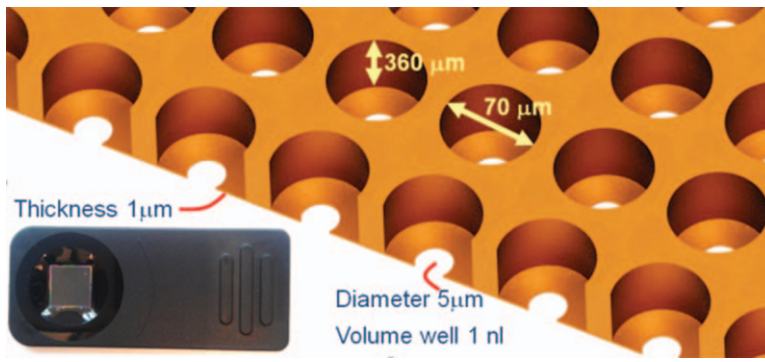


Figure 12.28 The microwell chip comprises a silicon chip containing 6400 microwells. Each of the microwells has a diameter of 70 μm and a height of 360 μm. The bottom of the well is a 1 μm thick SiN layer with a pore in the center of each well. The microwells are mounted in a plastic slide for ease of handling.
Reproduce from ref. 96 with permission from The Royal Society of Chemistry.

View Online

Published on 24 May 2017 on http://pubs.rsc.org | doi:10.1039/9781788010283-00415

- The cell blocks the pore and the remaining fluid and cells will be diverted to the next available microwell, resulting in a fast distribution of single cells in individual microwells. The principle of the self-seeding microwell chip is depicted in Figure 12.29.
- After this seeding process, the microwell device is connected to an SPRi sensor (SensEye) with a specific selection surface. The SensEye sensor and microwell filled with single cells are incubated for a certain period (*e.g.* overnight), allowing the cells to excrete specific molecules that will be captured by ligands immobilized on the sensor surface (see Figure 12.30).
- In this way, a transfer of specific molecules as individual cell product printing (*e.g.* antibodies from CHO) is captured by the sensor surface and the production of these molecules can be monitored for each cell individually.

Next, the sensor without the microwell array is inserted in an SPRi instrument (IBIS MX96) to expose the microwell arrayed sensor surface to a specific biomolecular interaction by injecting a specific analyte for the

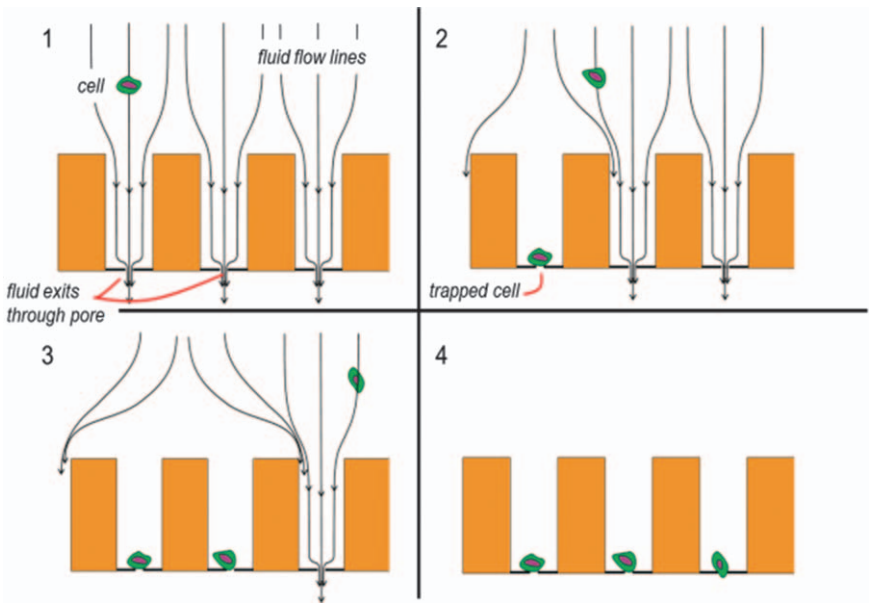


Figure 12.29 By applying a small underpressure to the bottom, the cell suspension fluid enters the well and exits through the pore in the bottom, thereby dragging the cells with it. Once a cell has landed on the pore in the bottom, the flow stops and no further cells will enter. The remaining fluid and cells will be diverted to the next available microwell, resulting in a fast distribution of single cells in individual microwells. Reproduced from ref. 96 with permission from The Royal Society of Chemistry.

View Online

Published on 24 May 2017 on http://pubs.rsc.org | doi:10.1039/9781788010283-00415

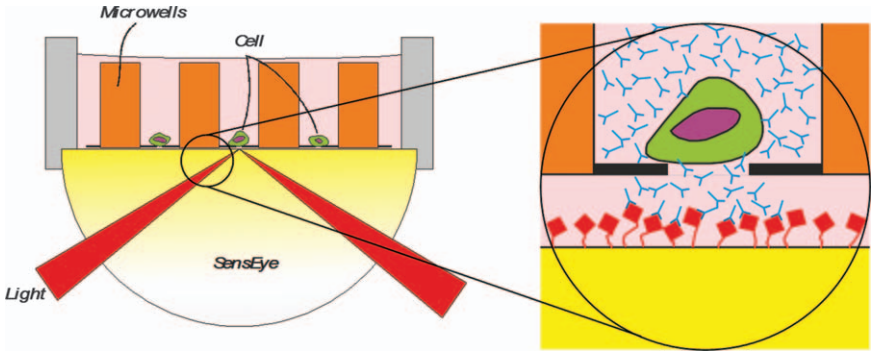


Figure 12.30 The principle of the McSPRinter. The microwells with single cells are attached to an SPR sensor surface and immersed in cultivation medium. The product of the cells diffuse *via* the 1 μm membrane to the sensor surface, which is placed at a distance of 1 μm using edge spacers.

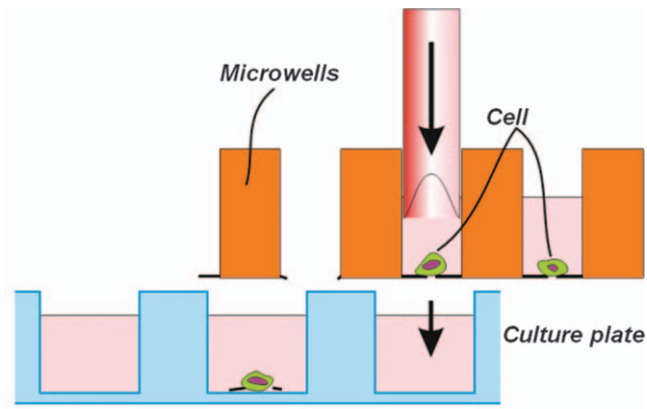


Figure 12.31 The Puncher needle will punch the selected cells out of the microwell array into a microtiter plate. The cells of interest will be cultivated further.

molecules that are produced by the cells. The amount of specific product, but also the affinity criteria such as on- and off-rates for each arrayed cell, can be determined. The criteria for selecting interesting cells are set for each position of the array with respect to corner reference points, which are set when the microwells and sensor are connected and coordinates of the cells of interest in the microwells are determined.

The single cells will be isolated based on the coordinates of SPRi measurement and set criteria thereof. Using the selection criteria as determined by SPRi analysis, the single cells will be isolated from the microwells by punching the selected cells out of the microwell array into a culture dish for clonal expansion (Figure 12.31). Microscope images of the individual microwells are used to check the monoclonality of the cells in the microwells.

View Online

The punching of the cells into a culture plate is performed under sterile conditions and optimal cultivation conditions for further expansion of isolated cells (Figure 12.32).

ClonePIX technology (Molecular Devices), in addition to limiting dilution techniques, is the current standard that is applied by many biotech and pharmaceutical companies (>90%).[97] New technologies based on microfluidic cell sorting have been developed but have the disadvantage of serial processing of single cells, which makes them slow. The features and benefits of the McSPRinter with respect to the ClonePIX system are as follows:

- In the ClonePIX instrument, relatively long incubation times (8 days) are needed in order to let the cells grow into clones for producing a significant amount of product that can be detected *via* precipitation or fluorescence techniques. McSPRinter needs just an overnight incubation to obtain sufficient product from the cells.
- In the McSPRinter, the selection criteria for the molecules can be based not only on a specific quantity but also on affinity criteria, *e.g.* on- and off-rates and equilibrium dissociation constants of the product of a cell.

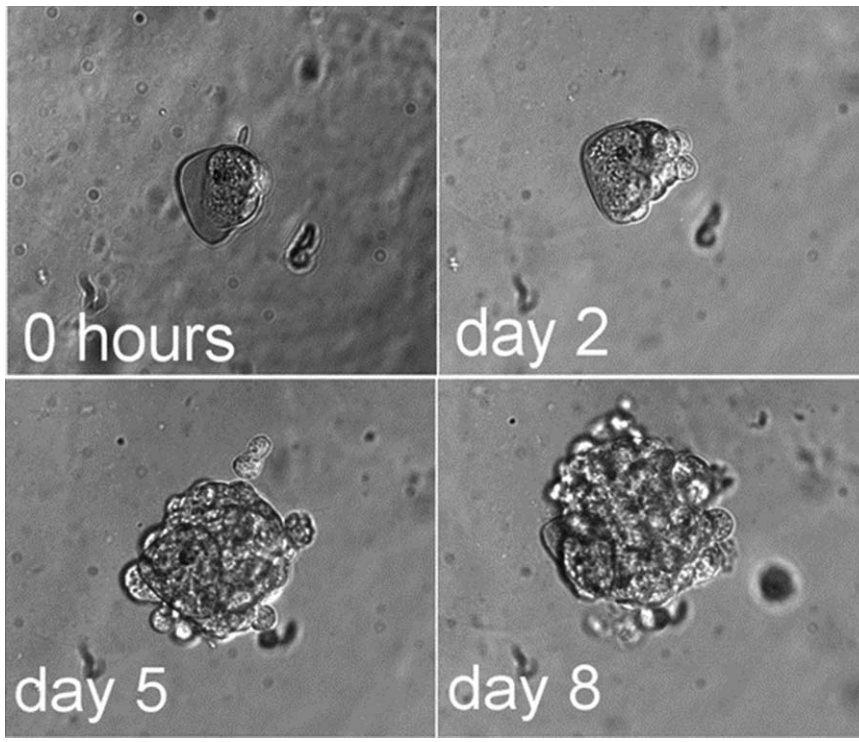


Figure 12.32 Example of an MCF-7 cell that was punched out of the microwell together with the bottom of the microwell. The single cell is dividing and expanding into a clump of cells.

Published on 24 May 2017 on http://pubs.rsc.org | doi:10.1039/9781788010283-00415

View Online

Published on 24 May 2017 on http://pubs.rsc.org | doi:10.1039/9781788010283-00415

- In the McSPRinter, the analysis of the excreted molecules is carried out without the presence of the cells whereas in the ClonePIX the cells are present during the analysis and are not separated from the product. As a result, in the McSPRinter, amplification strategies can be applied using a cascade of signal enhancers or epitope selection principles. This allows the measurement of detectable signals with only limited (overnight) cell culturing and screening of thousands of cells simultaneously.
- McSPRinter analyzes the production of single cells and can be traced back to verify monoclonality.
- The distribution of the cells in the ClonePIX is random whereas in the McSPRinter an arrayed distribution of cells is achieved for screening many more cells on a small footprint.
- The number of cells in the ClonePIX is limited to a maximum of <1000 in a single run.
- The measurement of the product in the McSPRinter is label free and signals can be enhanced, whereas the ClonePIX instrument uses non-sensitive precipitation or fluorescence for measuring the product levels.
- The production of specific molecules from the cells in the McSPRinter can be quantitated using calibrated sensor surface SPR shifts.
- The exposure of cells to harsh conditions in the McSPRinter is minimized and the process cycle period is extremely short (overnight), so screening of unstable cells can be applied.
- The overall survival rate of cells using the McSPRinter is >70%.

The procedure with the McSPRinter is shown in Figure 12.33. The potential of SPRi to measure protein production by individual cells after seeding the cells in microwells has been described.[98] Cells from a hybridoma producing monoclonal antibodies recognizing EpCAMs were used as a model system. The recombinant human EpCAM protein was immobilized on an SPRi sensor and acted as a selector for the specific interaction of antibodies produced by the hybridoma cells that were seeded in the microwells. Incubation of the microwell and SensEye sensor was performed under sterile cultivation conditions, *e.g.* growth medium, 37 °C, proper CO_2 atmosphere. After the overnight incubation, the SensEye sensor and microwell array device were detached from each other and the sensor prism was inserted in the IBIS MX96 instrument. In order to observe also tiny levels of antibody produced from the single cells, an additional amplification cascade as described in Section 12.6.2 was used, consisting of a biotinylated goat anti-mouse IgG injection (100 nM), followed by injection of neutravidin (50 nM) and finally biotinylated gold nanoparticles. ROIs were placed around small excreted product regions from individual cells. Preferably one would like to recover/isolate the highest producing cells from the measurement to obtain high-producing cell clones (see Figure 12.34).

Here we have demonstrated that the production of antibodies by individual hybridoma cells embedded in microwells is feasible using SPRi.

View Online

Published on 24 May 2017 on http://pubs.rsc.org | doi:10.1039/9781788010283-00415

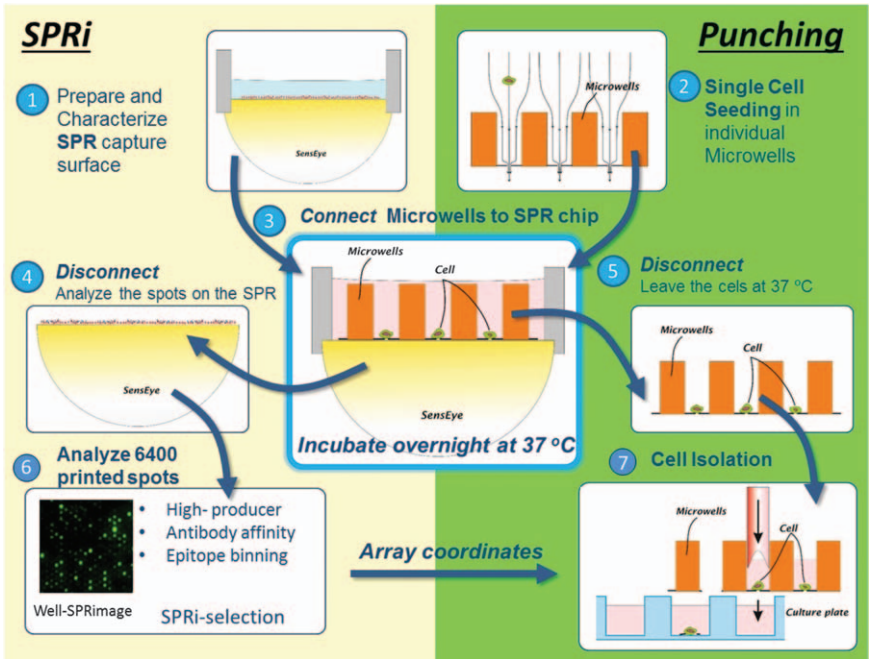


Figure 12.33 Process flow chart of the McSPRinter. The left side presents the process using the SPRi and the right side the punching part of the process. The combined SPRi sensor with the microwells attached to it is shown in the center.

The innovative McSPRinter significantly reduces the cell selection method from currently 21 days to a single overnight incubation with the ability to screen many more single cells than current technologies. Analyzing the printed spots followed by isolation of the single cells (SPRi + punching) takes ~1.5 h. During one day, 5–6 runs can be performed, leading to a total of ~30 000 cells that can be analyzed per day.

It has been shown not only that can the antibody production of individual cells be measured and quantified by SPRi but also that the coordinates of the positions of microwells can be used to select the arrayed cells of interest for further cultivation. The essence of the McSPRinter technology is a microwell chip as printing device for an SPR imaging sensor surface with three functions:

- First, single cells are self-seeded in individual microwells.
- Second, the seeded living cells still produce specific protein products and these excreted molecules diffuse from the cell to the sensor surface and will be SPR imaged in array format (McSPRinter).
- Third, the microwell printed array selection criteria and coordinates are applied for proper punching out of the cells of interest from the microwell (McPuncher).

View Online

Published on 24 May 2017 on http://pubs.rsc.org | doi:10.1039/9781788010283-00415

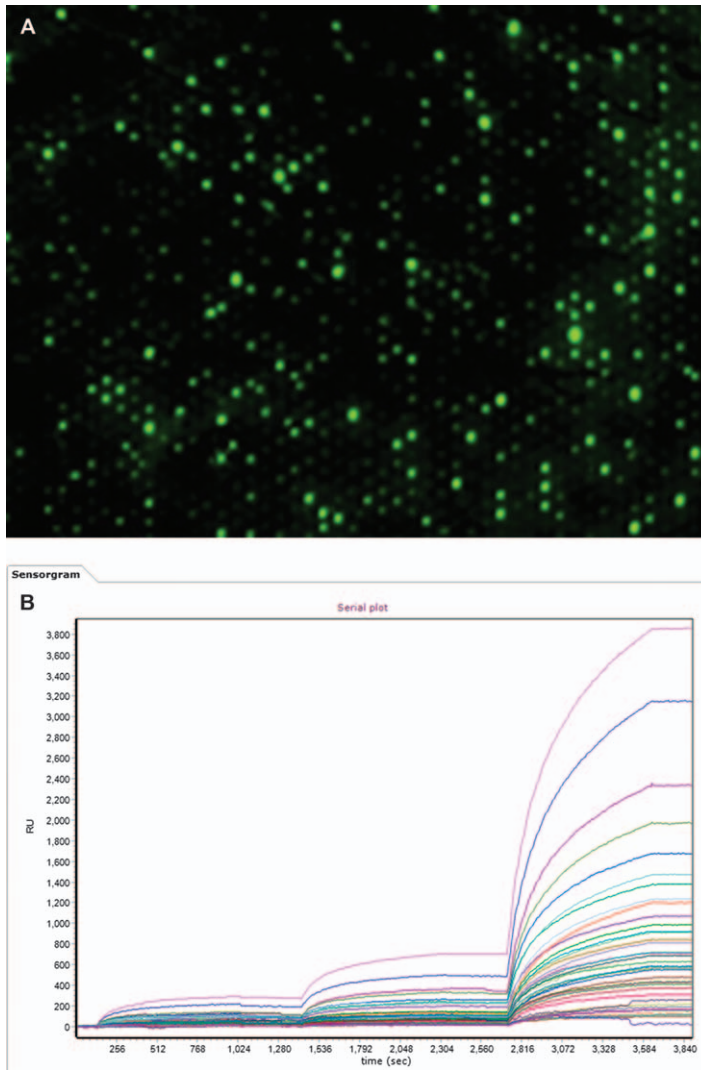


Figure 12.34 (A) Printed αEpCAM antibody dots produced by the single cells in the microwells on the SPRi imaging sensor after removing the microwell chip from the SensEye sensor. (B) Measured sensorgram of some of the printed dots. First a biotinylated goat anti-mouse IgG (100 nM) was injected, followed by neutravidin (50 nM) and finally biotinylated gold nanoparticles. The signal increase after each of the amplification steps is clearly visible.

This technology will not only have a tremendous impact in shortening the cell selection process but will also result in better quality therapeutic biologicals since many more cells can be screened. Further, it opens up a new avenue to measure products excreted by cells and harvesting the cells of interest, thereby increasing our understanding of cellular processes. One can

View Online

Published on 24 May 2017 on http://pubs.rsc.org | doi:10.1039/9781788010283-00415

envision the simultaneous measurement of a variety of products excreted by cells using SPRi such as specific proteins, hormones, neurotransmitters, cytokines, and exosomes. The McSPRinter improves the screening power of pharmaceutical and biotech companies who are in the field of discovery of new therapeutic biologicals. It is expected that the technology will become commercially available in 2017 (IBIS Technologies).

12.9 Conclusions

In this chapter, future trends are described as a personal estimate of how the SPR field will evolve. Since the first edition of this Handbook, the SPR field has continued to dominate with its presence in research on biomolecular interactions. The commercialization of BLI technology was huge but was not expected to grow to the extent of having the enormous impact that we see nowadays. In contrast, various trends (*e.g.* the impact of lab-on-a-chip and POC device technology) did not evolve as expected, but other trends can be regarded as really promising (McSPRinter). In this chapter, the trends among the instrumentation, fluidics, and surface chemistries are described. Further, a total concept, the SPR-based POC, device is envisioned. Despite the lack in the SPR field of POC devices in the past decade, it is expected that the demand for label-free technology in the market will be so great that for a certain limited set of applications a label-free (SPR) technology will become commercially available before 2020. In the research area, ranking accurate kinetic parameters is of great importance to validate the quality of biomolecules and it is expected that with the interpolation method using SPRi in combination with the distribution analysis approaches, the protocols will now be optimized for determining accurate affinity parameters.

Additionally, SPRi cytometry is a new trend and papers have been published, *e.g.* on RBC monitoring, since 2013. Not only the presence or absence of cell membrane antigens is measured but also the ratio of the number of 44-plexed cell membrane antigens. Additionally, a feasible strategy is to rank the avidity of RBCs to FcγR interactions including the potential affinity screening of peptide-HLA to TCR interactions. Further, the SPRi cytometry field includes monitoring of the cellular excretion of cellular products (*e.g.* antibodies) by living cells. The production rates of antibodies by single cells were successfully quantified, including simulation.

Finally, the microwell cell selection printer (McSPRinter) technology not only permits the simultaneous monitoring of the cellular excretion of thousands of cells but also it makes possible to isolate the individual cells of interest with microwell MEMS technology. This McSPRinter applies label-free SPRi for the detection of the excreted molecules in combination with a microwell array, where single cells are seeded in individual microwells. Only the cell product is transferred while the cell remains in the microwell and the excreted product will be captured by the underlying capture surface as an array print. The cells of interest are isolated from the microwell by punching the bottom together with the cell. The cells of interest can be cultivated

View Online

further in microtiter plates. The author's personal opinion is that this McSPRinter technology will have an enormous impact in the coming years.

12.10 Questions

1. The Biacore instruments of GE Healthcare still dominate the biomolecular interaction analysis market. Which trend changed the landscape of instruments in the last decade?
2. As shown in Figure 12.4, a 384-plex microarray with a large panel of immobilized mAbs should be ranked to each other. The interpolation strategy, as shown in Section 12.7.1, is a way to rank a panel of antibodies. Why can additionally the distribution analysis model, as described in Chapter 5 and in Section 12.7.2, be of interest for SPR analysis on microarrays?
3. The implementation of a lab-on-a-chip device with an integrated gold surface in an SPR instrument is not a sinecure. What will happen with the channel surface and the gold surface if we transport analyte directly from diluted serum to the gold surface using electroosmotic flow (EOF) as the pumping mechanism? Describe the effects.
4. POC SPR devices have not yet entered the market, although it was foreseen a decade ago. What is the possible reason?
5. What are the problems in measuring biomolecular interactions on living cells? Why did the field of SPR cytometry not develop significantly and is still in its infancy?

References

1. Future Market Insights report 'Surface Plasmon Resonance Market' for the period 2015–2025, http://www.futuremarketinsights.com/reports/surface-plasmon-resonance-spr-systems-market.
2. R. P. van Duyne, *Science*, 2004, **306**(5698), 985–986.
3. K. A. Willets and R. P. van Duyne, *Annu. Rev. Phys. Chem.*, 2007, **58**, 267–97.
4. C. L. Haynes and R. P. Van Duyne, *J. Phys. Chem. B*, 2001, **105**, 5599.
5. A. J. Haes and R. P. Van Duyne, *J. Am. Chem. Soc.*, 2002, **124**(35), 10596–604.
6. X. Hong and F. J. Kao, *Appl Opt.*, 2004, **43**(14), 2868–73.
7. A. M. C. Lokate *et al.*, *J. Am. Chem. Soc.*, 2007, **129**, 14013–14018.
8. G. MacBeath and S. L. Schreiber, *Science*, 2000, **289**, 1760–1763.
9. G. A. J. Besselink *et al.*, *J. Biosens. Bioelectron.*, 2016, **7**, 2.
10. J. LaBaer and N. Ramachandran, *Curr. Opin. Chem. Biol.*, 2005, **9**(1), 14–19.
11. Webinar Wasatch Microfluidics; Accelerated biophysical characterization and screening of biologics using array surface plasmon resonance imaging, 2016, Nature.com webcasts.

Published on 24 May 2017 on http://pubs.rsc.org | doi:10.1039/9781788010283-00415

View Online

Published on 24 May 2017 on http://pubs.rsc.org | doi:10.1039/9781788010283-00415

12. *Handbook of Surface Plasmon Resonance*, ed. R. B. M. Schasfoort and A. J. Tudos, Royal Society of Chemistry, London, March 2008.
13. C. E. H. Berger *et al.*, *Anal. Chem.*, 1998, **70**, 703–706.
14. W. Qian, D. Yao, F. Yu, B. Xu, R. Zhou, X. Bao and Z. Lu, *Clin. Chem.*, 2000, **46**, 1456–1463.
15. B. Johnsson, S. Löfas and G. Lindquist, *Anal. Biochem.*, 1991, **198**, 268–277.
16. J. R. Krone *et al.*, *Anal. Biochem.*, 1997, **244**, 124–32.
17. C. P. Sonksen, E. Nordhoff, O. Jansson, M. Malmqvist and P. Roepstorff, *Anal. Chem.*, 1998, **70**, 2731.
18. J. Grote, N. Dankbar, E. Gedig and S. Koenig, *Anal. Chem.*, 2005, **77**(4), 1157.
19. D. Nedelkov, *Methods Mol. Biol.*, 2010, **627**, 261–268.
20. E. Bouffartigues *et al.*, *Nucleic Acids Res.*, 2007, **35**(6), e39.
21. T. Natsume, H. Nakayama, O. Jansson, T. Isobe, K. Takio and K. Mikoshiba, *Anal. Chem.*, 2000, **72**, 4193.
22. J. J. Gilligan, P. Schuck and A. Yergey, *Anal. Chem.*, 2002, **74**(9), 2041.
23. M. Abrantes, M. T. Magone, L. F. Boyd and P. Schuck, *Anal. Chem.*, 2001, **73**(13), 2828.
24. N. R. Gonzales, P. Schuck, J. Schlom and S. V. Kashmiri, *J. Immunol. Methods*, 2002, **268**(2), 197–210.
25. E. Melles *et al.*, *J. Biomol. Technol.*, 2005, **16**(4), 392.
26. S. Bellon *et al.*, *Anal. Chem.*, 2009, **81**(18), 7695–7702.
27. J. W. Attridge *et al.*, *Biosens. Bioelectron.*, 1991, **6**, 201–214.
28. T. Liebermann and W. Knoll, *Colloids Surf., A*, 2000, **171**(1–3), 115–130.
29. K. M. Shakesheff *et al.*, *Langmuir*, 1995, **11**(10), 3921–3927.
30. A. Zangwill, *Physics at Surfaces*, Cambridge University Press, Cambridge, 1988, p. 186.
31. A. Manz, N. Graber and H. M. Widmer, *Sens. Actuators, B*, 1990, **1**(1–6), 244–248.
32. P. S. Dittrich, K. Tachikawa and A. Manz, *Anal. Chem.*, 2006, **78**, 3887.
33. P. S. Dittrich and A. Manz, *Nature*, 2006, **5**, 210–218.
34. Eric Ouellet *et al.*, *Lab Chip*, 2010, **10**, 581–588.
35. D. Dong Qin, Y. Xia and G. M. Whitesides, *Nat. Protoc.*, 2010, **5**(3), 491.
36. B. D. Iverson and S. V. Garimella, *Microfluid. Nanofluid.*, 2008, **5**, 145.
37. N.-T. Nguyen and Z. Wu, *J. Micromech. Microeng.*, 2005, **15**, 2.
38. D. Kohlheyer, J. C. T. Eijkel, A. van den Berg and R. B. M. Schasfoort, *Electrophoresis*, 2008, **29**(5), 977–993.
39. D. G. Myszka, *Anal. Biochem.*, 2004, **329**(2), 316–323.
40. S. Natarajan *et al.*, *Anal. Biochem.*, 2008, **373**, 141–146.
41. J. W. Jorgenson and K. D. Lukacs, *J. High Resolut. Chromatogr.*, 1981, **4**, 230.
42. R. B. M Schasfoort, S. Schlautmann, J. Hendrikse and A. van den Berg, *Science*, 1999, **286**, 942–945.
43. M. J. Jory *et al.*, *Sens. Actuators, B*, 1996, **35–36**, 197–201.
44. Lioubimov *et al.*, *Appl. Opt.*, 2004, **43**(17), 3426.

View Online

Published on 24 May 2017 on http://pubs.rsc.org | doi:10.1039/9781788010283-00415

45. A. Tadjeddine, *Electrochim. Acta*, 1989, **34**(no 1), 29–33.
46. J. Rago, Elizabeth Holmes: The Breakthrough of Instant Diagnosis, *Wall St. J.*, 2013, https://www.wsj.com/articles/SB10001424127887324123004579055003869574012. Retrieved 2013-09-16.
47. M. P. Hudson *et al.*, *Clin. Chim. Acta*, 1999, **284**, 223–237.
48. B. J. Tortella *et al.*, *Am. J. Clin. Pathol.*, 1996, **106**, 124–127.
49. J. H. Nichols, *Blood Gas News*, 1999, **8**, 4–14.
50. B. N. Feltis *et al.*, *Biosens. Bioelectron.*, 2008, **23**, 1131–1136.
51. J. Hendriks *et al.*, submitted to *Biosens. Bioelectron.*, 2017.
52. M. Abrantes, M. T. Magone, L. F. Boyd and P. Schuck, *Anal. Chem.*, 2001, **73**, 2828–2835.
53. J. J. Gilligan, P. Schuck and A. L. Yergey, *Anal. Chem.*, 2002, **74**, 2041.
54. E. J. Sundberg *et al.* in: *Protein Interactions: Biophysical Approaches for the Study of Complex Reversible Systems*, ed. P. Schuck, Springer, New York, 2007, vol. 5.
55. P. G. de Gennes, *Macromolecules*, 1980, **13**, 1069–1075.
56. A. Chakrabarti and R. Toral, *Phys. Rev. B*, 1990, **42**, 2445.
57. T. Zacher and E. Wischerhoff, *Langmuir*, 2002, **18**, 1748–1759.
58. R. B. M. Schasfoort *et al.*, *Anal. Biochem.*, 2016, **500**, 21–23.
59. R. B. M. Schasfoort, W. de Lau, A. van der Kooi, H. Clevers and G. H. M. Engbers, *Anal. Biochem.*, 2012, **421**, 794–796.
60. P. Schuck and H. Zhao, *Methods in Molecular Biology*, Springer Protocols, 2010, 627, pp. 15–54.
61. D. G. Myszka, X. He, M. Dembo, T. A. Morton and B. Goldstein, *Biophys. J.*, 1998, **75**(2), 583–94.
62. W. de Lau *et al.*, *Nature*, 2011, **476**, 293–297.
63. R. Karlsson, P. S. Katsamba, H. Nordin, E. Pol and D. G. Myszka, *Anal. Biochem.*, 2006, **349**, 136–147.
64. R. B. M. Schasfoort *et al.*, *Anal. Biochem.*, 2016, **500**, 21–23.
65. R. Karlsson and H. Roos, US Patent Application Publication US20140141529, May 22nd, 2014.
66. J. G. Quinn, R. O'Kennedy, M. Smyth, J. Moulds and T. Frame, *J. Immunol. Methods*, 1997, **206**, 87–96.
67. Y. Yanase *et al.*, *Biosens. Bioelectron.*, 2007, 23562–567.
68. V. Chabot *et al.*, *Biosens. Bioelectron.*, 2009, **24**, 1667–1673.
69. R. B. M. Schasfoort *et al.*, *Anal. Biochem.*, 2013, **439**(1), 4–6.
70. I. Stojanovic, R. B. M. Schasfoort and L. W. Terstappen, *Biosens. Bioelectron.*, 2014, **52**, 36–43.
71. S. P. Perfetto, P. K. Chattopadhyay and M. Roederer, *Nat. Rev. Immunol.*, 2004, **4**(8), 648.
72. C. Hennig, N. Adams and G. Hansen, *Cytometry, Part A*, 2009, **75**(4), 362–370.
73. K. Sukhdeo *et al.*, *PLoS One*, 2013, **8**(1), e53015.
74. I. Stojanović *et al.*, *Sens. Bio-Sens. Res.*, 2016, **7**, 48–54.
75. C. A. Buck and A. F. Horwitz, *Annu. Rev. Cell Biol.*, 1987, **3**, 179–205.
76. R. B. M. Schasfoort *et al.*, *Anal. Biochem.*, 2013, **439**(1), 4–6.

View Online

77. S. P. Perfetto, P. K. Chattopadhyay and M. Roederer, *Nat. Rev. Immunol.*, 2004, **4**(8), 648.
78. I. Stojanovic, R. B. M. Schasfoort and L. W. Terstappen, *Biosens. Bioelectron.*, 2014, **52**, 36–43.
79. S. Natarajan *et al.*, *Anal. Biochem.*, 2008, **373**, 141–146.
80. I. Stojanovic *et al.*, submitted to *Biosens. Bioelectron*.
81. B. György *et al.*, *Cell. Mol. Life Sci.*, 2011, **68**(16), 2667–2688.
82. B. György *et al.*, *Blood*, 2011, **117**(4), 39–48.
83. E. L. Gool *et al.*, submitted to *Clinical Chemistry*, 2017.
84. A. Roldão *et al.*, *Expert Rev. Vaccines*, 2010, **9**(10), 1149–1176.
85. R. B. M. Schasfoort *et al.*, *Anal. Biochem.*, 2013, **439**(1), 4–6.
86. B. Rodenko *et al.*, *Nat. Protoc.*, 2006, **1**(3), 1120–1132.
87. D. K. Cole *et al.*, *J. Immunol.*, 2007, **178**, 5727–5734.
88. R. B. M. Schasfoort, *X-scan TCR HLA-peptide Interactions Whitepaper Immunocore*, 2014.
89. N. Liddy *et al.*, *Nat. Med.*, 2012, **18**, 980.
90. I. Stojanovic, R. B. M. Schasfoort and L. W. Terstappen, *Biosens. Bioelectron.*, 2014, **52**, 36–43.
91. S. S. Ozturk and B. O. Palsson, *Biotechnol. Prog.*, 1991, **7**(6), 481–94.
92. G. M. Lee, A. Varma and B. O. Palsson, *Biotechnol. Bioengin.*, 1991, **38**(8), 821–830.
93. I Stojanović, T. J. G. van der Velden, H. W. Mulder, R. B. M. Schasfoort and L. W. M. M. Terstappen, *Anal. Biochem.*, 2015, **485**, 112–118.
94. I. Stojanović *et al.*, *Anal. Biochem.*, 2016, **504**, 1–3.
95. McSPRinter patent pending, iDepot nr. 082403, 2016, Patent Agent BV, Enschede, NL.
96. J. F. Swennenhuis *et al.*, *Lab Chip*, 2015, **15**, 3039–3046.
97. J. J. Cheng Hou *et al.*, *New Biotechnol.*, 2014, **31**(3), 214–220.
98. R. B. M. Schasfoort *et al.*, submitted to *Anal. Biochem.*, 2017.

Published on 24 May 2017 on http://pubs.rsc.org | doi:10.1039/9781788010283-00415

Published on 24 May 2017 on http://pubs.rsc.org | doi:10.1039/9781788010283-00479

APPENDIX

Questions and Answers

Chapter 1. Questions and Answers

1. How can you reduce mass transport-limited interactions?

   Answer: Mass transport-limited interactions can be reduced by increasing the flow rate, which creates a smaller stagnant layer. Diffusion from the bulk to the sensor surface is at a smaller distance. Another way is to decrease the ligand density. The analyte concentration close to the sensor surface is less depleted and the supply of analyte to the sensor surface by diffusion is less mass transport limited.

2. Eqn (1.19) expresses the R_{eq} value for various concentrations of the analyte. Calculate the values of R_{eq} in % R_{max} for $c_0 = 1/10K_D$, K_D and $10K_D$.

   Answer: The signal in RU is relative to the R_{max} and can be expressed in terms of % R_{max} and is dimensionless.
   - At $c_0 = 1/10K_D$: $R_{eq} = 9.09\%\ R_{max}$
   - At $c_0 = K_D$: $R_{eq} = 50\%\ R_{max}$
   - At $c_0 = 10K_D$: $R_{eq} = 90.9\%\ R_{max}$

3. Why is it so important for equilibrium analysis that the response of a signal spot shows exactly the same sensitivity to a common refractive index shift (*e.g.* by glycerol) as a reference spot? How do you check that these responses are similar for various glycerol concentrations?

   Answer: Common mode effects as bulk refractive index shift by changed buffer or the protein content of the sample injection will give an instant response. In order to subtract the bulk refractive index shift to observe only the specific kinetic response to the signal spot, the responses of reference and signal channel should be equal in order to obtain a clean subtracted sensorgram of the biomolecular interaction only without steps at the liquid transitions. However, in theory the signal spot contains the ligand at a certain density and the replacement

Handbook of Surface Plasmon Resonance, 2nd Edition
Edited by Richard B. M. Schasfoort
© The Royal Society of Chemistry 2017
Published by the Royal Society of Chemistry, www.rsc.org

View Online

Published on 24 May 2017 on http://pubs.rsc.org | doi:10.1039/9781788010283-00479

of water by, *e.g.*, glycerol will result in a smaller change in effective refractive index. Hence normalization or calibration of the signal to the reference spot should be carried out. In order to test the quality of referencing, one can inject glycerol at various concentrations (*e.g.* between 0.1 and 10% in system buffer) and, after referencing, the resulting response should give a perfect flat line for the baseline, association and dissociation phase.

4. The R_{max} value represents the functional ligand density. Explain this and how you can determine the R_{max} value.

   Answer: The total number of analyte molecules that can effectively be bound will give rise to a certain theoretical maximum response (R_{max}), which depends on the functional ligand density. Hence the total immobilized protein content gives rise to a certain immobilized RU level of ligand. However, only part is the effective functional ligand that is able to capture the analyte. The expected analyte signal (which compensates also for the molecular weight of the ligand and analyte) is therefore always lower than the total immobilized ligand response. When there is curvature in the sensorgram, one can determine the R_{max}. A higher quality of the R_{max} value can be obtained by a dilution series of analyte in concatenated injections. In equilibrium analysis, the RU levels show a sigmoidal curvature of the response *versus* concentration plot. The R_{max} value can be calculated from the equilibrium values *versus* concentration plot.

5. Explain why the concentration of an analyte in a direct assay should be determined in the MTL regime and in a sandwich assay by determining R_{max} of the sandwicher.

   Answer: This counts only for higher affinity specific interactions.

   (i) When the R_{max} value is very high or in other words the functional ligand density for the analyte is huge, then the diffusion of analyte molecules in the stagnant layer created by a fixed flow velocity is constant. Only the concentration of the analyte in the bulk will change the initial steepness of the response (in RU) because all analyte molecules will be captured by an almost empty surface at full MTL (only an increasing number of ligand molecules then have captured the analyte). Full mass transport limitation occurs only at the very beginning of the interaction curve and the signal should not exceed 5% of R_{max}. Because it is difficult to achieve full MTL, the CFCA method is an option to determine the concentration by applying two partly mass transport-limited flow conditions.

   (ii) In a sandwich assay, again the analyte will be exposed to the sensor surface for a certain amount of time and the analyte creates a new captured ligand on the sensor surface for the sandwicher. Then the sandwicher should be injected at a certain fixed concentration and the functional ligand concentration is determined by the R_{max} value as calculated by the curvature of the response.

View Online

Chapter 2. Questions and Answers

1. When a signal channel containing ligand molecules on the sensor surface and a reference channel without ligands is exposed to the same bulk refractive index step, will the RU shift of the reference channel be higher than, equal to, or lower than the signal channel? Please explain.

   Answer: The signal of the reference channel will be higher, when the instrument is not normalized or was not calibrated. A bulk refractive index step is caused by an exchange of liquid in the fixed volume of the evanescent field. Because ligand molecules occupy part of the volume in the evanescent field, the effective exchange of composition is relatively greater at the reference channel, resulting in a higher response. See also the answer to question 3 in Chapter 1.
2. A particular SPR application could be the detection of microorganisms in, *e.g.*, waste water, by detecting changes in *bulk* refractive index. Which SPR excitation wavelength region would be more favorable, the blue/UV or the IR region?

   Answer: The IR region is favorable because the evanescent field will still exist far from the sensor surface. While the detection of single microorganisms immobilized at the sensor surface can be monitored better in the blue region because of the lower propagation length of the plasmon, bulk refractive index changes can be detected better when a large evanescent field and a long propagation length exist.
3. SPR imaging requires lateral resolution and sensitivity. Describe what the influence is of the wavelength of the SPR excitation. Which wavelength region (blue/UV or IR) is favorable for the best lateral resolution?

   Answer: Lateral resolution can best be achieved in the blue/UV region whereas sensitivity of refractive index changes can best be measured in the IR region. Hence an all-purpose imaging instrument with sufficient sensitivity to protein binding and high image quality to detect single cells will compromise the applied wavelength. The IBIS MX96 with a selected wavelength of 840 nm shows fairly good sensitivity in combination with a good-quality SPR reflectivity image.
4. Calculate for a gold/water interface at $\lambda = 700$ nm ($\varepsilon_{gold} = -16$, $\varepsilon_{water} = 1.770$) the refractive index shift in RU of the SPR dip when ε_{water} increases to 1.775.

   Answer: The square root of the dielectric constant is the refractive index so $\sqrt{1.770} = 1.330413$ and $\sqrt{1.775} = 1.332291$. Hence the shift is 0.001877 RIU or 1877 μRIU = 1877 RU.
5. Estimate the effective refractive index for the system shown in Figure 2.18 when the gold/water interface is probed with a wavelength $\lambda = 700$ nm. The squares in the figure represent cubes of protein molecules in an aqueous environment, adsorbed on the gold surface.

Published on 24 May 2017 on http://pubs.rsc.org | doi:10.1039/9781788010283-00479

View Online

Published on 24 May 2017 on http://pubs.rsc.org | doi:10.1039/9781788010283-00479

Each protein molecule has a volume of $5\times5\times5$ nm^3 and a dielectric constant $\varepsilon_{\text{protein}} = 2.30$. The average distance between the edges of the cubes is 7 nm. (Compare the answer with the SPR-rule of thumb: 1 ng mm^{-2} protein adsorption results in a shift of ~1000 RU.)

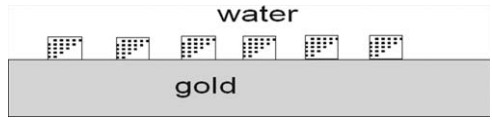


Figure 2.18 Cubes of protein molecules on gold.

Answer: At $\lambda = 700$ nm then $\omega = 2.69\times10^{-15}$ s^{-1}. We calculate for the penetration depth $1/k_{y,\text{water}}$ 238 nm from eqn (2.7). The number of cubes in the evanescent field per mm^2 $= (5+7)^2$ so $1000\times1000/0.012\times0.012 \approx 695\times10^6$ cubes with a refractive index of $\sqrt{2.3} = 1.5165$ in the submonolayer. Hence in a volume of 1 mm$^2\times$238 nm with a refractive index of 1.330413 the protein molecules will change the effective refractive index to 1.330481 or the shift will be 68 RU caused by the adsorbed protein molecules. (Compare the answer with the SPR-rule of thumb: 1 ng mm^{-2} protein adsorption results in a shift of ~1000 RU).

6. What happens with the SPR curve with respect to a reference area when a channel/region of interest contains an inhomogeneous precipitate? Please explain.

Answer: A region of interest combines the pixels of the camera and the surface is imaged to the pixel. When non-homogeneities occur then SPR curves of clean and particulate matter will be merged, resulting in a curve shifted to a higher angle and the minimum of the SPR curve also becomes higher. The effect is shown in Figure 6.18, reproduced here.

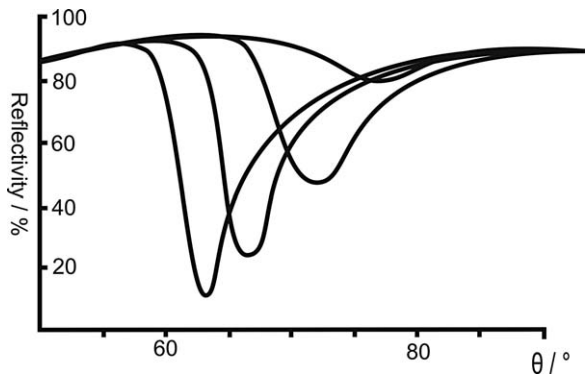


Figure 6.18 With increasing protein loading, the minimum reflectivity shifts to higher angles and flattens out until the SPR-dip completely disappears.

View Online

Chapter 3. Questions and Answers

1. An SPR instrument can be considered as a total analysis system that consists of three main technology cornerstones. Which three cornerstones are essential in an instrument for detection of biomolecular interactions?

   Answer: (1) SPR optics; (2) liquid handling system; (3) sensor chip.

2. A divergent-beam SPR instrument shows "walking of the SPR-dip over the sensor surface," as illustrated. Explain this effect.

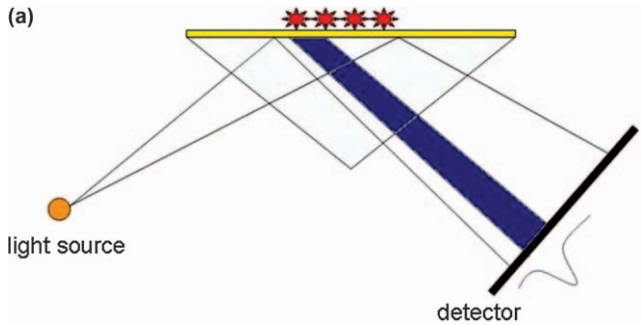


Figure 3.33a Configuration of a divergent-beam SPR instrument.

Answer: The divergent light beam hits the total sensor surface at different angles. The SPR-dip can thus be measured at once using a CCD array. When a target molecule binds, the local refractive index at the surface will raise and this will shift the resonance towards higher angles (see the arrow in the diagram). Because the different angles occur at different locations on the surface, a change in resonance angle will be measured at a different location. In this way, the dip is virtually walking over the surface while the interaction occurs.

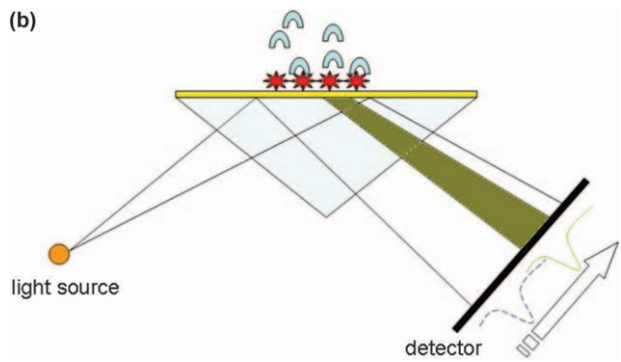


Figure 3.33b Configuration of a divergent-beam SPR instrument.

Published on 24 May 2017 on http://pubs.rsc.org | doi:10.1039/9781788010283-00479

View Online

Published on 24 May 2017 on http://pubs.rsc.org | doi:10.1039/9781788010283-00479

3. In SPR imaging instruments, a parallel beam of light will bring a homogeneous surface in full resonance. See Figure 3.23 (Plexera imager). How can we make an image of the surface and follow the SPR angle of each region of interest during the biomolecular interaction process? Also, how can we calculate the SPR angle position of each spot?

   Answer: The angle of incidence of the parallel light can be controlled by a moving-angle axis. In a fixed position of the axis, all the incident light hits the surface with an identical angle (parallel light). The reflected light is also parallel and the intensity is a measure of the refractive index. By moving the angle axis, the SPR-dip can be studied and each position on the sensor surface corresponds to a certain reflectivity (%R). Depending on the CCD resolution, more sensor patches can be applied. Theoretically, each pixel can be one sensor patch or spot.

4. Consider a scanning mirror in a Kretschmann operated instrument that vibrates periodically with a constant amplitude and frequency. The SPR curves that are generated in time before and after binding are shown here. Explain how time-resolved dip detection can be applied to monitor the SPR-dip shift in real time.

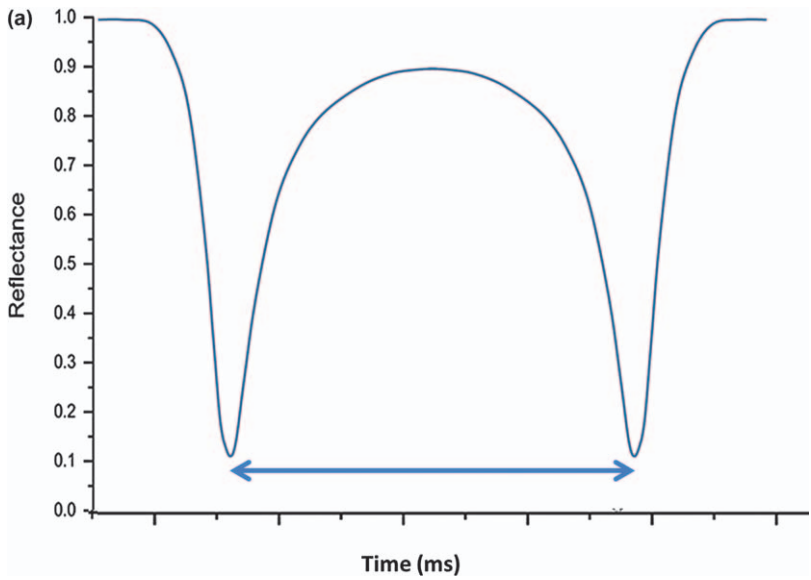


Figure 3.34a Reflectivity curve as a function of angle of incidence.

Answer: When the SPR-dip shifts, the forward and the backward dip move toward each other. A timer starts when the intensity is passing through the minimum and it stops when it detects the backward minimum. The counter that operates at high frequency is a measure of the dip position. See the illustration.

View Online

Published on 24 May 2017 on http://pubs.rsc.org | doi:10.1039/9781788010283-00479

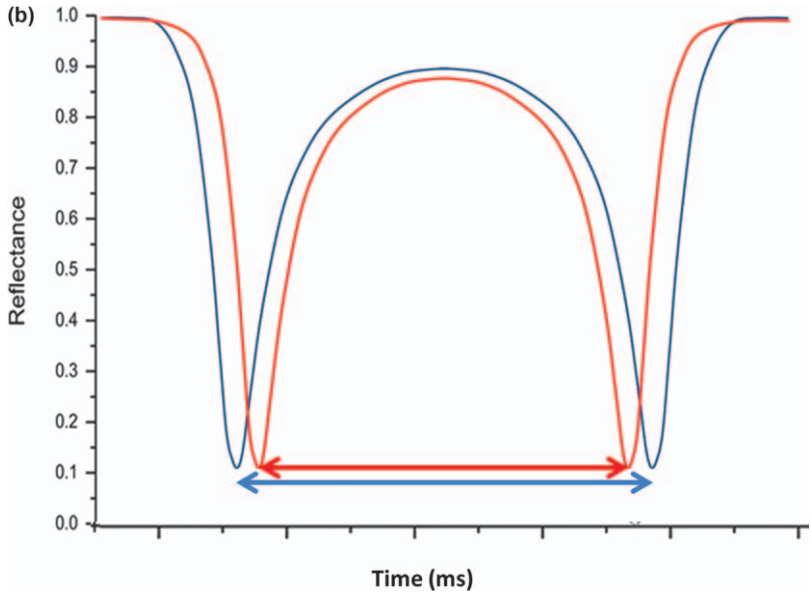


Figure 3.34b Reflectivity curve as a function of angle of incidence.

5. Each commercial instrument applies the exposure of the sample to the sensor surface. What are the major criteria of the fluidics for high-quality biomolecular interaction sensing?

   Answer: The fluidics should have the following requirements:

   - The injection of the sample should be instantaneous. The kinetic profile starts when the concentration of the analyte at the sensor surface is instantaneous at 100%.
   - The hydrodynamic condition should be fixed and equal for all channels and injections. So the flow rate that sets the stagnant layer should be fixed either statically in one direction or dynamically in back and flow control.
   - The volume of the sample should not exceed 200 μL and should fit in a microtiter plate. Rather the fluidics should allow the recovery of the sample.

Chapter 4. Questions and Answers

You can also find the answers to this quiz at www.sprpages.nl/quiz-answers, and more questions and answers at www.sprpages.nl (click on Sensorgrams – Quiz).

1. Looking at the sensorgrams in Figure 4.38, which sensorgram does not contain exponential interaction curves?

View Online

Published on 24 May 2017 on http://pubs.rsc.org | doi:10.1039/9781788010283-00479

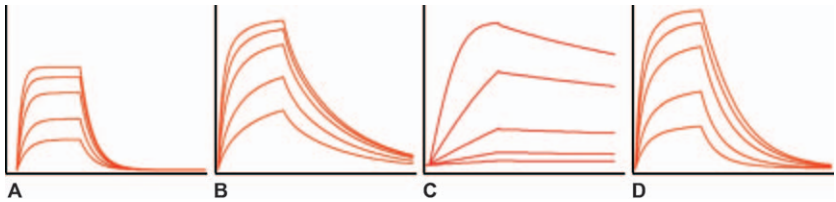


Figure 4.38 Biomolecular interaction curves.

Answer: C. Mass transport limitation. Mass transport-limited sensorgrams have an initial binding profile that is linear.

2. Which of the sensorgrams in Figure 4.39 can be used for equilibrium analysis?

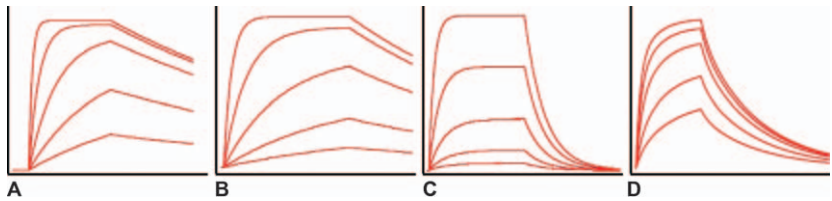


Figure 4.39 Biomolecular interaction curves.

Answer: D. Only in part (C) do all the curves come to steady state.

3. Figure 4.40 shows four curves with different kinetic rate constants but with the same affinity. Which curve has the fastest association rate constant?
   A. Curve A.
   B. Curve B.
   C. The analyte concentration should be known.
   D. R_{max} should be known.

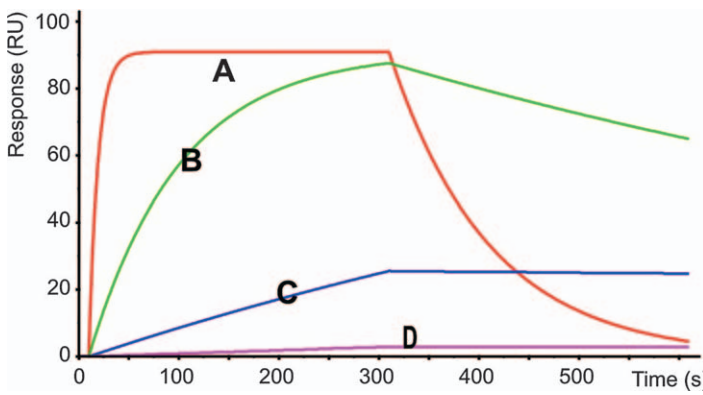


Figure 4.40 Different kinetics (same affinity).

Answer: C. The analyte concentration should be known. Because the association rate is dependent on analyte concentration, nothing can be said about the association by looking at a curve.

View Online

Published on 24 May 2017 on http://pubs.rsc.org | doi:10.1039/9781788010283-00479

4. Given the affinity plot in Figure 4.41, which curve has the highest equilibrium dissociation constant?
   A. Point A.
   B. They are all the same.
   C. The analyte concentration should be known.
   D. Point D.

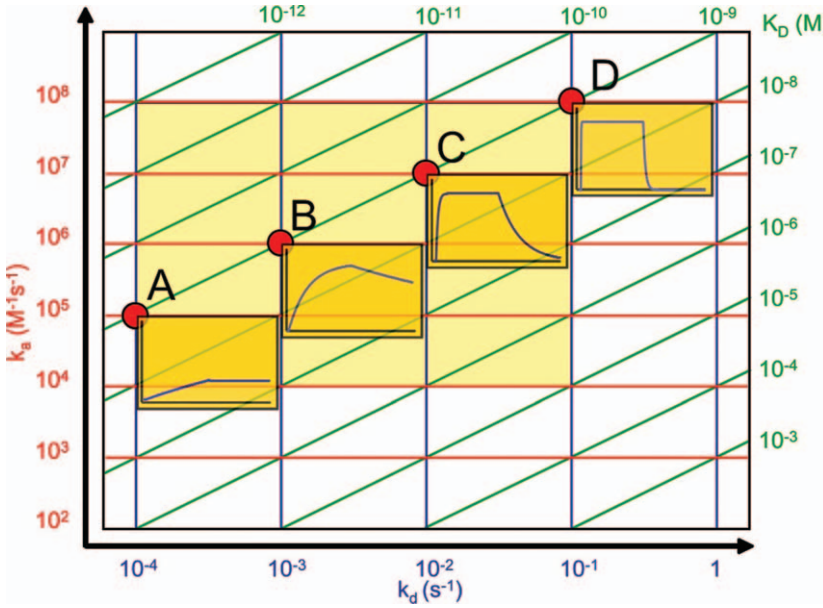


Figure 4.41 Affinity plot.

Answer: B. They are all the same. All the points are on the same green line of $K_D = 10^{-9} \times M$.

5. Which of the fitting results in Figure 4.42 should be reported?

k_a	k_d	K_D
($M^{-1}s^{-1}$)	(s^{-1})	(M)
1.1±0.1 E5	4.7±0.2 E-3	4.27 E-8

A

k_a	k_d	K_D
(1/Ms)	(1/s)	(M)
1.1±0.1 10^5	4.7±0.2 10^{-3}	4.3±0.5 10^{-8}

B

k_a	k_d	K_D
($M^{-1}s^{-1}$)	(s^{-1})	(M)
1.1±0.1 10^5	4.7±0.2 10^{-3}	4.27±0.46 10^{-8}

C

k_a	k_d	K_D
($M^{-1}s^{-1}$)	(s^{-1})	(M)
1.1±0.1 10^5	4.7±0.2 10^{-3}	4.3±0.5 10^{-8}

D

Figure 4.42 Fitting results.

Answer: D. Explanation is:
A. Wrong because this is Excel notation.

View Online

Published on 24 May 2017 on http://pubs.rsc.org | doi:10.1039/9781788010283-00479

B. Wrong because the units are not correct. It is not 1/M s but M^{-1} s^{-1} (L mol^{-1} s^{-1}).
C. Wrong because the digits in the error with the K_D are incorrect (two digits instead of one).
D. Correct.

6. With the four options below, what is the best combination to optimize the interaction in Figure 4.43?
   Option 1: lower ligand concentration.
   Option 2: match buffers better.
   Option 3: equilibrate better.
   Option 4: use higher flow rate.
   Multiple choice:
   A. Options 1 and 4.
   B. Options 1, 2 and 3.
   C. Options 1, 2 and 4.
   D. Options 2, 3 and 4.

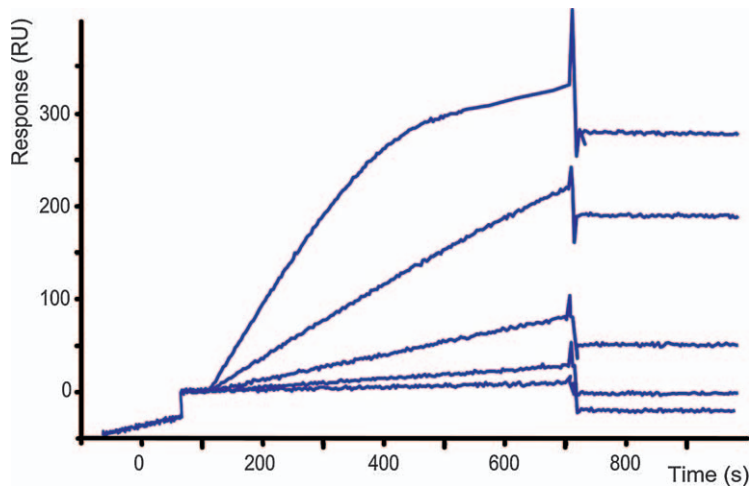


Figure 4.43 Interaction between Abc and Klm.

Answer: B.

7. When the result of the fitting is as in Figure 4.44, what is the best combination of options to improve it?
   A. Option 1: lower ligand concentration.
   B. Option 2: match buffers better.
   C. Option 3: check the ligand for purity.
   D. Option 4: use higher flow rate.
   Multiple choice:
   A. Options 1 and 3.
   B. Options 1 and 4.
   C. Options 2 and 3.
   D. Options 2 and 4.

View Online

Published on 24 May 2017 on http://pubs.rsc.org | doi:10.1039/9781788010283-00479

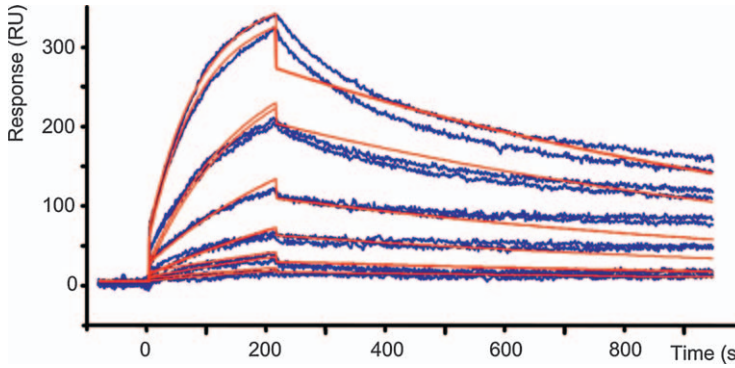


Figure 4.44 1 : 1 fit of the interaction between Gh and Sh.

Answer: A.

8. Are the values given in the inset in Figure 4.45 plausible with the sensorgram?
   A. Yes.
   B. No, dissociation looks faster.
   C. No, dissociation looks slower.
   D. No, R_{max} is to high.

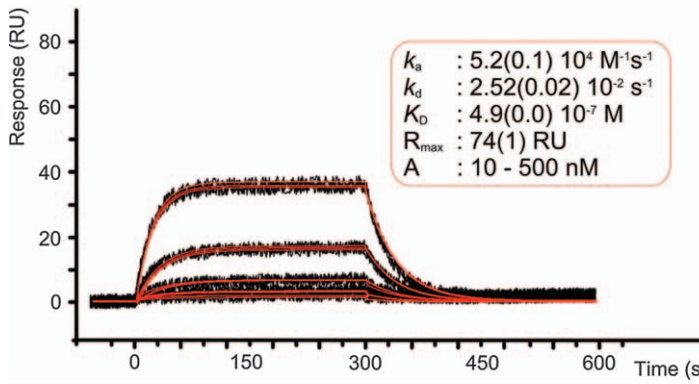


Figure 4.45 1 : 1 fitting of the interaction of A with B.

Answer: A. The analyte concentration is the same as the equilibrium dissociation constant, hence R_{eq} is half R_{max}.

9. What can be said about the sensorgram in Figure 4.46?
   A. The analyte concentration range is not wide enough.
   B. The response does not follow exponential kinetics.
   C. There is mass transport limitation.
   D. This looks an excellent sensorgram.

View Online

Published on 24 May 2017 on http://pubs.rsc.org | doi:10.1039/9781788010283-00479

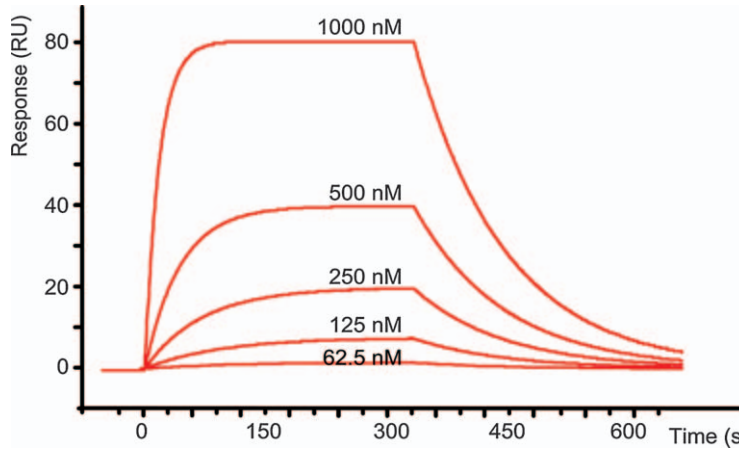


Figure 4.46 Interaction between A and L.

Answer: D. This looks an excellent sensorgram. Probably some higher analyte concentration injections would make it clearer that the ligand is saturating but evaluation of these curves will yield correct kinetic parameters.

Chapter 5. Questions and Answers

1. Which factors are potential contributors to heterogeneity of affinity of surface binding sites?
   a. Variations in the physical microenvironment of the surface, such as surface roughness.
   b. If an immobilization matrix is used composed of macromolecules such as dextran, the chain density distribution perpendicular to the surface.
   c. Variation in the amino acid residue involved in chemical crosslinking.
   d. Partial deactivation and limited unfolding of protein ligands.
   e. Mass transport limitation.

   Answer: a, b, c, d.
2. To detect mass transport-limited binding conditions, order the following experimental tests/observations according to their effectiveness, and explain why.
   a. Change of immobilization density.
   b. Change of analyte flow rate.
   c. Inspection of binding traces for convex shape in the association phase and transiently increasing signal in the dissociation phase.
   d. Application of soluble ligand in the flow during dissociation phase as competitor for rebinding.

View Online

Published on 24 May 2017 on http://pubs.rsc.org | doi:10.1039/9781788010283-00479

e. Increasing analyte concentration to compensate for mass transfer limitation.
f. Analyze data only from the approach of steady-state signals.

Answer:

1 = d: Rebinding is an aspect of mass transport limitation that is often easy to eliminate by providing soluble ligand (at concentrations $\gg K_D$) to form complexes with the analyte near the sensor surface that do not rebind and can freely diffuse away. The resulting acceleration of ''apparent dissociation rate'' is a safe indicator for mass transport limitation, and can offer an avenue to estimate k_{off}.

2 = c: No other origins of increasing slopes in the association phase and increasing signals in the dissociation phase have been reported than the combination of spatial gradients of sensor sensitivity in conjunction with moving fronts of complex saturation both laterally and vertically relative to the sensor surface. Hence these features directly reveal mass transport limitation. However, they will only appear in extreme cases, at analyte concentrations greater than K_D. Therefore, the absence of such features cannot be used as an indication for the absence of mass transport limitation.

3 = b: The variation of the analyte flow rate changes the mass transfer rate, and should therefore result in a change in the apparent binding kinetics under mass transport-limited conditions. However, the transport rate is only proportional to the cube root of the flow rate, *i.e.* a factor of 8 in flow rate will cause a factor of 2 in mass transport rate, and less of a change in apparent binding rate constants in partially mass transport-limited cases. Furthermore, the component of mass transport that originates from partitioning and diffusion within the immobilization matrix is not affected.

4 = a: Although a change in immobilization density directly alters the required mass transfer, and can therefore expose mass transfer limitation, the change in immobilization density can similarly alter the distribution of affinity and kinetic rate constants of the surface sites. Therefore, the change in immobilization density as a test for mass transport limitation can lead to false positives and false negatives.

5 = e: Higher analyte concentration certainly increases the overall diffusion flux to the sensor surface. However, the impact on the observed rate constants (*e.g.* the ratio of the measured apparent rate constant to the true rate constant) is very similar at all analyte concentrations.

6 = f: Although suggested by some in the early days of SPR analysis, this strategy is entirely without physical basis.

3. What are the units of the K_D–k_{off} distribution?

   Answer: RU×L mol^{-1}×s. Integration of the distribution leads back to RU units.

4. Explain why the regularization principle in the distribution analysis is related to the scientific principle of Occam's razor.

View Online

Published on 24 May 2017 on http://pubs.rsc.org | doi:10.1039/9781788010283-00479

Answer: Occam's razor (among competing hypotheses, the one with the fewest assumptions should be selected) prescribes the "simplest" interpretation of the data. Regularization is a method to calculate the most parsimonious distribution consistent with the data. In this way, the minimal information is drawn from the experiment, to prevent over-interpretation.

5. What is the key feature of surface binding experiments that makes it possible to study high-affinity interactions easily?

   Answer: The surface immobilization. Usually, for studying high-affinity binding, very low concentrations of both binding partners are required in order to visualize the population of both free and complex species and their concentration ratios, which enter into the law of mass action. Very low concentrations are challenging for many detection systems. In surface binding methods, one of the binding partners can be kept at a high concentration in the detection volume by attaching it at the surface. The analyte still needs to be applied at low concentrations covering the range of K_D to achieve different levels of saturation, but the signal is governed by the number of immobilized sites and can be large.

Chapter 6. Questions and Answers

1. Try to scale the dimensions roughly by drawing perpendicular to the surface (1) the gold layer thickness of an SPR device, (2) the antibody coating, (3) the evanescent field, and (4) the stagnant layer in mass transport-controlled kinetics if we use a flow cell height of (5) two white blood cells.

   Answer: The dimensions in μm are (1) 0.05, (2) 0.002, (3) 0.3, (4) 2, and (5) 25.

2. Recently, several SPR transducers have been developed that utilize localized surface plasmons. What are the differences from the standard Kretschmann configuration? Discuss the pros and cons of such setups.

   Answer:

   +: Spectral interrogation with a very simple optical setup, no coupling to prism required. Tunable sensitivity by adapting the architecture of the resonating nanostructures.

   −: More complex manufacturing process of the nanostructured transducers. Turbid or light-absorbing samples might interfere with the spectral detection. Nanostructures may not be compatible with harsh surface derivatization chemistries.

3. A protein with a p*I* of 4.8 is to be covalently immobilized on a polycarboxylate hydrogel-coated sensor chip using EDC–NHS coupling. A coupling buffer of pH 4.5 and ionic strength 10 mM after activation with 50 mM EDC–NHS is used, but unfortunately, the immobilization yield is poor.

View Online

Published on 24 May 2017 on http://pubs.rsc.org | doi:10.1039/9781788010283-00479

A. Discuss potential reasons for this observation. How would it be possible to discriminate whether the electrostatic preconcentration or the covalent coupling step cause the low immobilization level?

B. When discussing the problem in your laboratory, several proposals came up for how to improve the immobilization yield:
   i. increasing the concentration of the ligand;
   ii. increasing the EDC concentration;
   iii. lowering the pH of the immobilization buffer;
   iv. lowering the ionic strength of the immobilization buffer;
   v. using sulfo-NHS instead of NHS;
   vi. purifying (dialyzing) the ligand;

   Sort these measures by their effectiveness for the two possibilities that
   a. the electrostatic interaction, or
   b. the covalent coupling

   is the reason for the low immobilization yield.

Answer: Troubleshooting of failed EDC–NHS immobilizations usually starts with injection of ligand over a non-activated surface. If a sufficient preconcentration is observed, then the covalent coupling itself should be checked. If the preconcentration does not work, then the following of the above steps are effective, in this order: iv, iii, vi, v.

Usually, a very low ionic strength is key. Even the water quality can play a role. Lowering the pH increases the charge difference, but below pH 5 the NHS coupling reaction is less efficient plus an increasing fraction of the COOH groups becomes protonated, thus reducing the negative charge density. Using the more reactive sulfo-NHS can help, as it not only enhances the coupling yield, but also adds sulfo groups, which keep their negative charge at pH levels below 4.

Increasing the EDC concentration does not help, as it has nothing to do with the electrostatic effect – it can even decrease the preconcentration (see below for the reason). Increasing the ligand concentration above a level of a few tens of micrograms per milliliter is also not overly helpful, as the ligand concentration does not affect the preconcentration either – it just proceeds faster.

If the preconcentration level is satisfactory, then one should check the coupling reaction and try the following of the above measures: ii, vi, v.

A higher EDC concentration and sulfo-NHS increase the density and reactivity of reaction sites within the hydrogel. Purifying the ligand removes NHS reactive contaminants from the ligand preparation.

Always keep in mind that owing to the partial conversion of negative charges into neutral NHS esters, NHS-activated surfaces show a less pronounced preconcentration than the non-activated counterpart.

View Online

Published on 24 May 2017 on http://pubs.rsc.org | doi:10.1039/9781788010283-00479

4. Draw a typical sensorgram of three analysis cycles if the ligand is decoupled after each regeneration step (*e.g.* 50% loss of ligand after a regeneration step).

   Answer: If a ligand loses its activity, the R_{max} value of the sensorgram will decrease as shown in Figure 6.40 with a 50% reduction per analysis cycle. The R_{max} value is directly proportional to the functional ligand density.

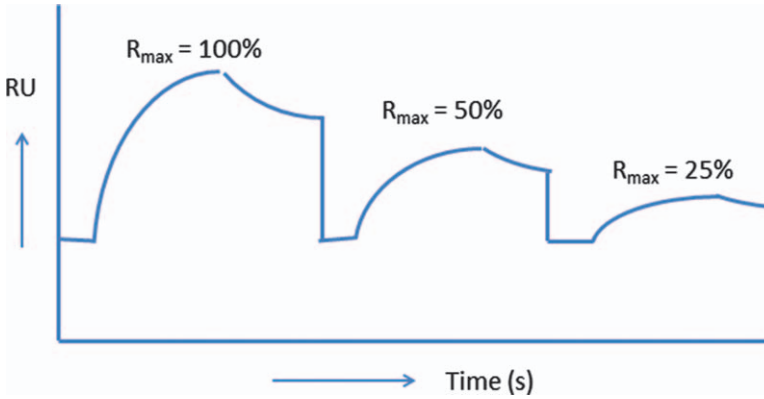


Figure 6.40 Decrease in R_{max} value.

5. The immobilization of His_6-tagged ligands on NTA-derivatized sensor chips usually results in drifting baselines. Why?
   a. How can this problem be addressed?
   b. Discuss potential pros and cons of these methods.

   Answer: Because of the relatively low (μM) affinity of the NTA–Ni–His_6 complex.

   Lowering the immobilization level of the His_6 conjugate (increased rebinding):
   - +: Easy to perform, no changes of surface and ligand required.
   - −: Moderate effectiveness, reduced signal-to-noise ratio due to lower ligand density.

   Chips with tris- or poly-NTA instead of monomeric NTA:
   - +: Very stable immobilization, no change of ligand required, high ligand densities possible.
   - −: Sometimes increased non-specific interactions, special surfaces required.

   Using longer or multiple His tags:
   - +: Increased stability on standard NTA chips.
   - −: Modification of ligand required.

   Stabilizing the immobilizate through EDC–NHS activation:
   - +: Easy to perform on standard NTA chips, does not require modification of ligand, very stable.
   - −: Alters characteristics of ligand (conversion of lysine groups), surface cannot be regenerated.

View Online

Published on 24 May 2017 on http://pubs.rsc.org | doi:10.1039/9781788010283-00479

Capturing the His_6 conjugate with anti-His_6 IgG:
+: Can increase the stability, no modification of ligand necessary.
−: Number of regeneration cycles limited (IgG less stable then NTA), ligand density relatively low, might result in higher NSB.

6. A common observation with affinity biosensors is the dependence of the electrostatic adsorption (preconcentration) and thus the immobilization capacity on the flow rate of the liquid handling system. Would you expect a higher or lower capacity with increasing flow rate? Explain the phenomenon.

   Answer: The apparent immobilization capacity typically increases with increasing flow rate or with increasing convection. Two major reasons contribute to this observation:
   - Increasing the mass transport rate towards the surface delivers fresh ligand, which rapidly occupies every free binding site. If the mass transport is slow, then already adsorbed/bound ligand spreads over the surface or – if the surface is coated with a flexible hydrogel – the hydrogel and bound ligand have more time to undergo structural changes to reach an energetically favorable state. The then occupied binding sites are thus no longer accessible for other ligand molecules.
   - The surface charge, which drives the electrostatic preconcentration, is usually neutralized by counter-ions of the buffer, which are concentrated within the slipping plane above the chip surface. If flow is applied, a fraction of these ions is removed and the apparent surface charge increases, thus enhancing the electrostatic preconcentration of the ligand.

7. Concerning immobilization:
   a. Small ligands or oligonucleotides are frequently immobilized *via* biotin–streptavidin interaction. Why?
   b. An alternative can be the direct immobilization through reactive groups. What should be obeyed in this case?
   c. Discuss the advantages and disadvantages of indirect *versus* direct immobilization.

   Answer:
   a. Because with small or negatively charged ligands the electrostatic preconcentration does not work. Furthermore, many small molecules and also oligonucleotides do not carry suitable reactive groups, often making it more straightforward to modify them right away with biotin.
   b. As there is no electrostatic preconcentration or, in the case of oligonucleotides, even repulsion, the concentration of such ligands must be very high to achieve a sufficient ligand density. Sometimes it can even be necessary to dry a solution of the ligand on the chip surface, so that the concentration reaches 100% and side reactions are minimized. Furthermore, it is often necessary to modify the ligand with reactive groups prior to covalent coupling.

View Online

Published on 24 May 2017 on http://pubs.rsc.org | doi:10.1039/9781788010283-00479

c. Indirect immobilization is often tempting, as the protocols are simple, fast, and do not require chemistry. However, one should be aware that the achievable ligand density is significantly lower – often by an order of magnitude. Furthermore, tags and especially capture molecules (streptavidin, antibodies, protein A/G) are voluminous, *i.e.* hinder the analyte diffusion, add excluded volume, which has to be accounted for, and increase the non-specific background. Limited stability of the immobilizate (leaching) and incompatibility of the linkers with the regeneration conditions may cause additional problems. Therefore, covalent coupling is usually the first choice. Only if there are striking advantages or if there is no other alternative can indirect immobilization be considered.

8. Usually, microflow spotters give higher immobilization densities and more homogeneous spots. Why? Despite these advantages, there are a few applications where droplet spotting is preferred. Which applications are these, and why?

   Answer: High convection, kinetically under control, no ligand deactivation through drying, no concentration gradient in spotted droplets while drying, continuous supply of fresh ligand until the capacity limit is reached, and more efficient reaction due to removal of reaction side products. High-volume spotting due to limited throughput of microflow spotters.

Chapter 7. Questions and Answers

1. You have determined k_a and k_d values for an LMW analyte as shown in Table 7.6. You are interested in the detection of fragments with affinities in the millimolar range. Can this surface be used for screening of a fragment library with compounds in the 150–275 Da range?

Table 7.6 k_a and k_d values determined for an LMW analyte.

Ligand molecular weight (Da)	45 000
Capture level (RU)	1500
Analyte molecular weight (Da)	516
k_a (mol L^{-1} s^{-1})	3.2×10^{6}
k_d (s^{-1})	1.3×10^{-3}
R_{max}	13.2

Answer: The maximum binding capacity for an MW of 516 RU is 13.2 RU. For a fragment with MW 150 Da, the theoretical response is

$$\frac{13.2\,\text{RU}}{\text{MW of known binder}} \times 150 = \frac{13.2}{516} \times 150 = 3.8\,\text{RU}$$

View Online

Published on 24 May 2017 on http://pubs.rsc.org | doi:10.1039/9781788010283-00479

Using a screening concentration of 1 mM, a fragment with a K_D of 1 mM will not saturate the surface but reach 50% saturation at this K_D. Thus for a 1 mM K_D fragment a response of 1.9 RU can be expected.

Conclusion: This response is very low and consequently this surface is not recommended for the screening experiments.

2. The 45 kDa ligand previously used in capture experiments (Table 7.6) was immobilized using amine coupling at pH 5.5. The activity was tested using the same analyte as in the capture experiment. Based on the saturation response the activity was now 22%. What was the activity of the ligand in capture mode? Suggest at least two ways to improve the activity of the immobilized ligand.

   Answer: The activity in the capture experiment is obtained from the ratio of response and MW of analyte and ligand:

$$\text{activity} = \frac{\text{response of analyte}}{\text{MW of analyte}} \Big/ \frac{\text{capture response}}{\text{MW of ligand}}$$

   In this case $\frac{13.2}{516} \Big/ \frac{1500}{45\,000} = 0.77$ or 77%.

   With amine coupling at pH 5.5 the activity decreased to 22%. This may be because the ligand was sensitive to low pH or the amine coupling involved the binding site. Possible approaches to increase the activity are:
   - to increase the pH of the immobilization (even a small increase can be effective), or
   - to perform the coupling in the presence of the known LMW binder, or
   - to try another immobilization chemistry.

3. Positive and negative controls in a fragment screen gave the results in Table 7.7. The molecular weight of the positive control was 235 Da. The fragment screen was performed with fragments at 1 mM concentration and with fragments in the MW range from 150 to 275 Da. What cut-off level in RU can be used for identification of a ''hit'' during screening? Can fragments with a K_D of 1 mM be detected?

Table 7.7 Results of a fragment screen of positive and negative controls.

Cycle number	5	35	65	95	125	155	185	215	245
Positive control (RU)	29.2	29.7	28.1	27.3	26.8	25.7	25.0	24.1	22.3
Cycle number	3	33	63	93	123	153	183	213	243
Negative control (RU)	1.3	1.8	2.0	1.7	1.6	2.2	1.8	1.7	1.9

   Answer: The response values from the negative control can be used to identify a cut-off level (Table 7.7.1).

View Online

Table 7.7.1

Cycles	3	33	63	93	123	153	183	213	243
Response (RU)	1.3 Whole series	1.8	2 Cycles 3–63	1.7 Cycles 33–93	1.6 Cycles 63–123	2.2 Cycles 93–153	1.8 Cycles 123–183	1.7 Cycles 153–213	1.9 Cyces 183–243
Average	1.78		1.70	1.83	1.77	1.83	1.87	1.90	1.80
Standard Deviation, SD	0.25		0.36	0.15	0.21	0.32	0.31	0.26	0.10
Cut-off average of negative control plus 3 SD	2.54		2.78	2.29	2.39	2.80	2.78	2.69	2.10

Published on 24 May 2017 on http://pubs.rsc.org | doi:10.1039/9781788010283-00479

For the whole series of cycles (3–243), the average of the negative control is 1.78 RU and the standard deviation is 0.25 RU. Using gliding averages and SD, corresponding values for intervals of 60 cycles can be calculated. Here there are only small differences over the experiment and a common cut-off level at 2.5 RU can be used.

The signal from positive control drops from 29 RU to 22 RU. Therefore, a 150 Da fragment can be expected to give a response of at least

$$\frac{22}{235} \times 150 = 14\,\text{RU}$$

At a screening concentration of 1 mM, a fragment with an affinity of 1 mM will therefore give a response of at least 7 RU.

Conclusion: This is well above the cut-off level and a 1 mM binder can therefore be detected.

4. K_D values were determined for 14 fragments using an estimated R_{max} value during the fitting procedure. The K_D values (mM) in Table 7.8 were obtained. When these fragments were allowed to compete with a known inhibitor, the binding curves shown in Figure 7.31 were obtained. The blue curve is the known inhibitor and the red curves represent injections of a mixture of the known inhibitor and the fragments. Are any of these fragments an allosteric (non-competitive) binder? In what way did the K_D values support the design of the competition experiment?

Table 7.8 K_D values determined for 14 fragments.

Fragments 1–7	1.01	1.68	2.41	2.56	3.24	3.70	4.46
Fragments 8–14	4.46	4.57	4.81	5.23	5.49	5.53	5.69

View Online

Published on 24 May 2017 on http://pubs.rsc.org | doi:10.1039/9781788010283-00479

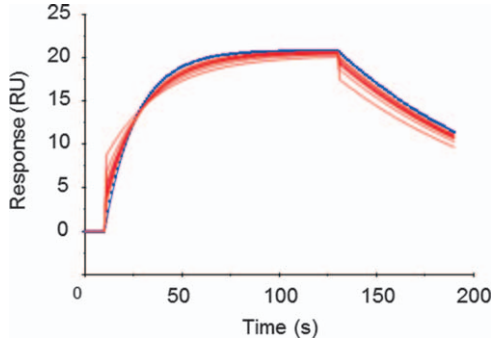


Figure 7.31 Typical binding curves for fragment interactions competing with an inhibitor.

Answer: The known binder is seen in blue and curves from the competitive experiment are shown in red in Figure 7.32. From Box A, it is clear that the low-affinity fragments bind rapidly and the signal is higher than obtained with the known binder. From Box B, it is clear that the signals drop immediately after the end of the injection and dissociation now starts from a lower level than when the known binder is injected alone. This means that binding is competitive. With an allosteric binder, the signal during injection would consistently be higher than the blue curve as signals are additive and, assuming rapid dissociation of fragments, the dissociation curve would not be shifted to a lower level. Consequently, there were no allosteric binders in this data set. The K_D values are all in the millimolar range. To be effective as binders, these fragments must therefore be injected at millimolar concentrations. K_D values were thus used to guide the experimental design and fragments were used at 1 mM concentration in the competition experiments.

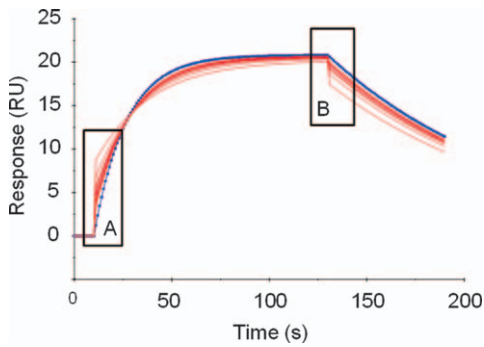


Figure 7.32 Binding curves as in Figure 7.31.

View Online

5. The ligand efficiencies for the fragments in Table 7.8 ranged from 0.20 to 0.29 kcal mol^{-1} K^{-1}. Given the uncertainties in K_D values, how would you use these values?

   Answer: Ligand efficiencies (LE) are calculated using the relation

   $$LE = -RT\ln K_D/N$$

   where N is the number of non-hydrogen atoms. K_D values may be uncertain for two reasons: first, the K_D values were extrapolated, and second, response levels were not corrected for actual refractive index increments. The best use of these ligand efficiencies may therefore be to use them as starting points and for comparison with later compounds derived from these fragments.

Chapter 8. Questions and Answers

1. In Section 8.3.1.2, we discussed the issues of epitope binning on a capture-crosslinked sensor (*i.e.* a capture sensor, on which ligands are captured, that is later crosslinked so that it may be regenerated). How would you set up your experiment to circumvent these issues? What consequences would your setup have on your data?

   Answer: On a capture-crosslinked sensor, antibodies are not immediately chemically immobilized, but first bound to a broadly reactive capture antibody that binds all or many antibodies in your binning pool (*i.e.* anti-human, anti-mouse), and then immobilized. Then, if you were to use a capture-crosslinked sensor for a binning experiment, you need to ensure that, once a second antibody is injected (in a sandwich or premix setup), the second antibody does not bind to any non-occupied binding sites on the capture antibody (that was used to bind the first antibody). Blocking the sensor with a non-reactive antibody, before cross-linking and/or during the experiment, can minimize the interaction of injected antibodies with the capture-crosslinked sensor. When analyzing binning data from such an experiment, the response of a non-reactive antibody should be subtracted from the response of any reactive antibodies, to exclude false positives.
2. Epitope mapping works best on antibodies with a linear epitope. Which experiments could you try in order to define whether your antibody has a linear epitope?

   Answer: Linear epitopes are likely to remain functional when the antigen is in a denatured state. Therefore, antibodies binding denatured antigen likely bind a linear epitope. This can be assessed experimentally by comparing binding to native and denatured antigens, for example with Western blotting or ELISA (both experiments may be performed with native or denatured antigen).
3. How can you reduce the effects of ligand (*i.e.* antibody) density variations on the outcome of your affinity ranking experiment?

   Answer: If possible, performing the immobilization/capture step with multiple ligand concentrations could minimize any non-specific

Published on 24 May 2017 on http://pubs.rsc.org | doi:10.1039/9781788010283-00479

View Online

Published on 24 May 2017 on http://pubs.rsc.org | doi:10.1039/9781788010283-00479

effects related to ligand density. Thus, on- and off-rates are simultaneously measured at high and low ligand densities, and any density-related effects would be immediately apparent. If this is not possible (*e.g.* because the amount of ligands is too large to measure each ligand at multiple densities), then all ligands should be immobilized at the same concentration, using a concentration that does not saturate the chip, as non-specific effects are more likely to occur at high ligand density.

4. Construct a node plot from Figure 8.17. Shown are injections of five secondary antibodies (A, B, C, D, and E) after antigen E2 was injected over spots with the same five antibodies.

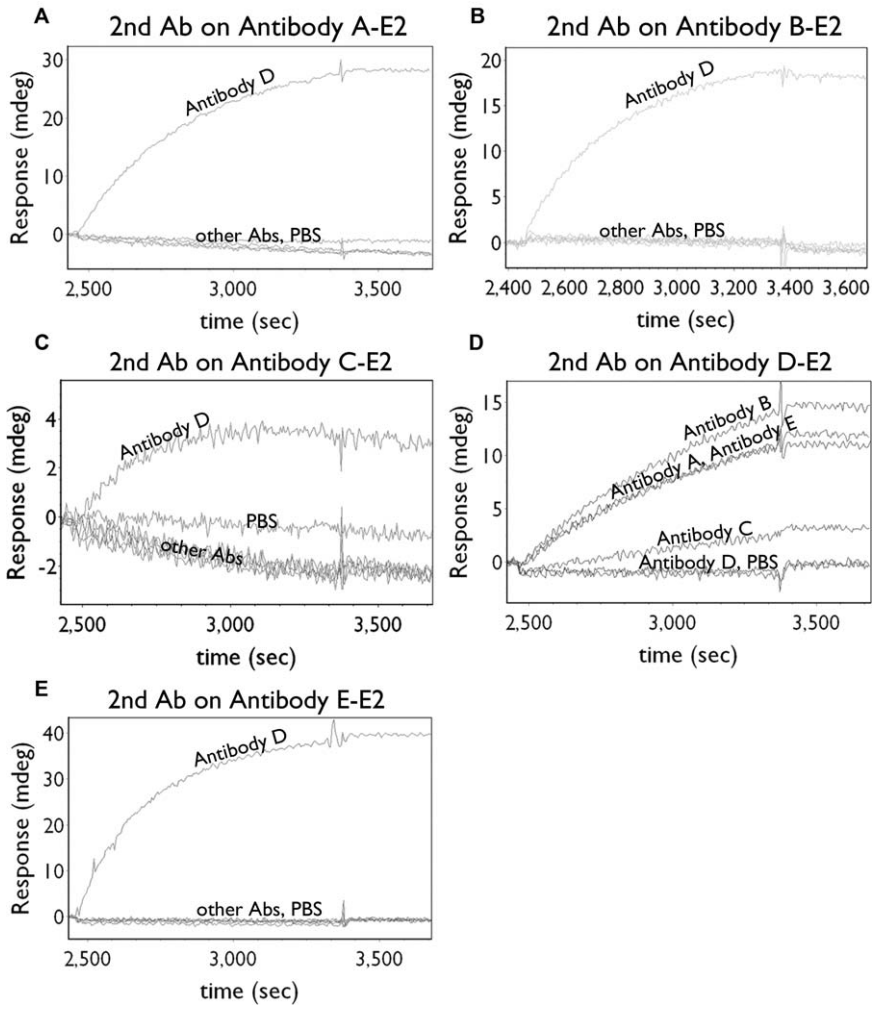


Figure 8.17 Sandwich binning of five antibodies binding HCV E2 antigen. Adapted from S. J. Merat, R. Molenkamp, K. Wagner, S. M. Koekoek, D. van de Berg, E. Yasuda *et al.*, submitted for publication, 2016).

View Online

Published on 24 May 2017 on http://pubs.rsc.org | doi:10.1039/9781788010283-00479

Answer: In Figure 8.17, it can be seen that antibody D binds when antigen E2 is bound to antibodies A, B, C, and E. On the other hand, antibodies A, B, C, and E only bind when the antigen is bound by antibody D (and not when the antigen is bound by A, B, C, or E). This suggests that antibodies A, B, C, and E have overlapping epitopes, and antibody D binds a different epitope. In a node plot, antibodies A, B, C, and E should be placed in the same bin, and antibody D in another bin. An example of a correct node plot is shown in Figure 8.18.

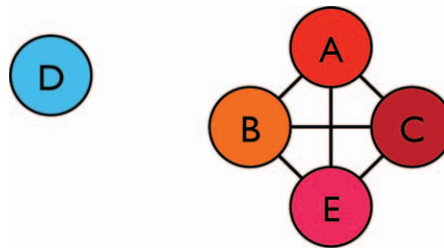


Figure 8.18 Example of a correct node plot. Antibodies A, B, C, and E bind overlapping epitopes and should be part of the same node. Antibody D does not block the other antibodies and forms a separate node.

5. Alanine scanning is discussed in Section 8.4.2. What are the key differences between alanine scanning epitope mapping and mapping by amino acid skipping? How would you address these experimentally?

Answer: Alanine scanning and amino acid skipping are complementary methods for epitope mapping. With alanine scanning, a discrete map of the antigen is made, demonstrating which residues are essential for antibody binding. From this map, antibody epitopes are then defined. In contrast with amino acid skipping, which requires a library of small peptides, alanine scanning is not restricted to peptides and can also be performed with the complete antigen; this also means that alanine scanning allows the detection of non-linear epitopes. However, performing alanine scanning on a complete antigen would require a large set of recombinant mutated antigens, which could be laborious to procure. One specific issue with alanine scanning is that replacing a single amino acid for alanine can have detrimental effects on the peptide structure, and some residues are essential for protein/peptide stability. Therefore, it should be tested experimentally if the mutated peptides/proteins are functional; this can be done by including the appropriate controls for your experiment. Also, when performing alanine scanning on peptides, you should start with native peptides that show optimal binding activity (you can find these with amino acid skipping).

With amino acid skipping, antibody binding is tested on a library of overlapping peptides, resulting in a continuous map of bound peptides, from which the antibody epitopes are then extracted. In contrast to alanine scanning, which can be performed with the complete antigen, for amino acid skipping it is necessary to use peptides rather than the complete antigen. This difference restricts amino acid skipping to

View Online

linear epitopes. On the other hand, for amino acid skipping, it is not necessary to make mutations that could affect epitope stability, and this allows the analysis of epitopes that may be difficult to assess with alanine scanning.

Published on 24 May 2017 on http://pubs.rsc.org | doi:10.1039/9781788010283-00479

Chapter 9. Questions and Answers

1. Which software package can be used for building a script to execute an experiment?
   A. BiaMethodWriter.
   B. TraceDrawer.
   C. Scrubber.
   D. CLAMP.
   Answer: A.
2. Prior to running a full experiment, what information could be derived by injection of an analyte across a newly prepared ligand surface?
   A. Ligand activity.
   B. Analyte titration range.
   C. Regeneration efficiency.
   D. Experimental dissociation times.
   E. All of the above.
   Answer: E.
3. What data processing step is specific for studies involving small molecules?
   A. Local referencing.
   B. Blank subtraction.
   C. Excluded volume correction.
   D. Cropping.
   Answer: C.
4. What is competitive epitope binning primarily used for?
   A. Determining rate constants.
   B. Clustering of mAbs based on shared antigen binding sites.
   C. Antigen concentration analysis.
   D. Biomarker screening.
   Answer: B.
5. What are the three types of competitive epitope binning formats?
   A. Classical, premix, tandem.
   B. Premix, tandem, complex.
   C. Classical, tertiary, premix.
   D. None of the above.
   Answer: A.
6. What kinetic fitting model does Scrubber use?
   A. Heterogeneous analyte.
   B. Bivalent analyte.
   C. Two-state.
   D. One-to-one.
   Answer: D.

View Online

Chapter 10. Questions and Answers

1. Why is it advisable to start with a high concentration of analyte when investigating affinity constants where the estimated K_D is unknown?

   Answer: When the estimated K_D between two binding partners is unknown, one must always assume the possibility that the binding could weak. When binding is weak, a higher concentration of the analyte is required to gain 50% binding (K_D, the inverse of K_A, is the 50% bound molecules concentration). Hence if one starts with a relatively low concentration, an assumption could be made that the molecules are inactive when no binding is observed yet they may simply be weak binders.

2. In establishing assay step times, what are the critical requirements for the association and dissociation steps?

   Answer: For the association steps, if one intends to analyze data using rate-based equations, the step must be run to allow for some curvature to be observed at the top concentrations being analyzed. If on the other hand, the goal is to use steady-state equilibrium analysis, then all concentrations must be allowed to proceed to equilibrium. For dissociation step times, slow off-rates require a longer time to allow for some decay (about 5–10%), otherwise data would not be fitted accurately.

3. Why is the biosensor-immobilized ligand stability an important consideration when running a kinetics assay?

   Answer: If the immobilized ligand is not stable on the biosensor, there is the possibility that it would still be dissociating when the biosensor is moved to the analyte for the association step. This would invariably introduce an artifact in the on-rate analysis, resulting in inaccurate data reporting.

4. Besides molecular weight, what other physical property of the ligand or analyte should be taken into consideration when predicting response signals in BLI?

   Answer: In BLI, the response signal is directly proportional to the molecular weight for a globularly folded molecule. However, if the molecule is extended, such as would happen in an unfolded protein or a linear polypeptide, the molecular weight is no longer a major factor; conformation of the molecule must therefore be considered in tandem with the molecular weight.

5. Why does sample plate shaking speed matter when running both kinetics and quantitation assays?

   Answer: Sample plate shaking is necessary to avoid or eliminate mass transport- or diffusion-limited effects when running on the Octet. Whereas in kinetics the recommended shaking speed is 1000 rpm, in quantitation assays the speed should be scouted. It is important to note that the lower the sample concentration, the faster the shaking speed

Published on 24 May 2017 on http://pubs.rsc.org | doi:10.1039/9781788010283-00479

View Online

should be, and the opposite is true for high-concentration samples. Hence if the sample concentration range is low, say 0–300 $\mu g\,mL^{-1}$, a shaking speed of 1000 rpm is recommended for quantitation assays. Concentrations above that range would require a shaking speed of $\sim$200 rpm.

Published on 24 May 2017 on http://pubs.rsc.org | doi:10.1039/9781788010283-00479

Chapter 11. Questions and Answers

1. The Biacore Flexchip instrument is very useful for identifying protein and glycosaminoglycan partners. Why do we need a combination of instruments based on different approaches (SPRi, SPR, and BLI), as also discussed in Chapter 12, Section 12.2?

   Answer: When the Biacore Flexchip reached the market, it was the first label-free SPR imaging platform to measure biomolecular interactions on 400 spots simultaneously and independently. The calculation of association and dissociation rates and of the equilibrium dissociation constants was not always reliable with this instrument when proteins were immobilized by physical adsorption on bare gold, but it gave a clear yes/no answer (binding/no binding). This is why we performed kinetic analysis using the other instruments (Biacore T200 and BLI-based Octet Red 96).

2. Why do we need to flip the BLI interaction curves (see Figure 11.6) and what is the reason why negative responses are measured as a result of biomolecular binding?

   Answer: BLI measures the changes in optical thickness by making use of the interference between waves reflected from a stable reference layer and a biolayer [hence biolayer interferometry (BLI)]. The interfering wavelength intensity pattern caused by the optical thickness creates multiple sinusoidal cycles in the measured area of the visible light. The nm shift is obtained by looking at the shift of one of these cycles. An increase in optical thickness will shift the wavelength intensity pattern, and the specific cycle for analysis, to higher wavelengths to create a positive nm shift. Negative signals can occur when the optical thickness decreases upon binding. This can be due to the release of a cofactor or when a more closely packed structure is obtained by a conformational change of the ligand. The other cause of negative signals is when large optical thickness changes occur, *e.g.* when making use of densely populated ligand surfaces or measuring the binding of nanoparticles or viruses. In this case, not only will the wavelength intensity pattern shift, but also the total number of cycles measured within the visible light will increase. The specific cycle for analysis will now appear at lower wavelengths and signals will therefore be displayed as negative. These negative responses are analyte concentration dependent and should be flipped.

View Online

Chapter 12. Questions and Answers

1. The Biacore instruments of GE Healthcare still dominate the biomolecular interaction analysis market. Which trend changed the landscape of instruments in the last decade?

   Answer: The trend of high-throughput analysis and the need for simple instrumentation changed the landscape. Now pharmaceutical companies need both high analyte throughput and multiplex power, as shown in the triangle of instruments in Figure 12.2. Additionally, low-cost L-SPR instruments entered the market in the last decade.
2. As shown in Figure 12.4, a 384-plex microarray with a large panel of immobilized mAbs can be ranked to each other. The interpolation strategy, as shown in Section 12.7.1, is a way to rank a panel of antibodies accurately. Why can additionally the distribution analysis model, as described in Chapter 5 and in Section 12.7.2, be of interest for SPR analysis on microarrays?

   Answer: The distribution analysis model can reveal similarities in contour plots for all antibodies that should be ranked to each other. For example, when the antibody binds to a dimeric epitope, it will behave differently than when binding to a monomeric epitope and the contour plot will change accordingly. Only when the contour plots and the R_{max} values are similar can the kinetic values such as K_D, k_a, and k_d be compared with each other. The additional way of characterizing the antibodies is to bin them (see Chapters 8 and 9). The antibodies which are in the same epitope bin should behave similarly in the contour plot as a function of R_{max}.
3. The implementation of a lab-on-a-chip device with an integrated gold surface in an SPR instrument is not a sinecure. What will happen with the channel surface and the gold surface if we transport analyte directly from diluted serum to the gold surface using electroosmotic flow (EOF) as the pumping mechanism? Describe the effects.

   Answer: Although attractive to apply electroosmotic flow in a network of powered channels, many issues can be addressed, as described here:
   - There will be a voltage drop along the channel.[†] Pumping is caused by the channel wall charges that drag the liquid in the direction of the free counterions migrating in the electric field. The stagnant layer that occurs in pressure-driven flow is reduced to the Debye length of the ionic strength buffer. Hence one can expect improved mass transport to the sensor surface. However, electrochemical processes will occur when the gold metal is not protected by an insulating layer. At higher voltages, electrolysis of water will occur, caused by a short-circuited gold patch, and bubble formation will destroy not only the electroosmotic flow but also proper SPR measurements.

[†]R. B. M. Schasfoort, S. Schlautmann, J. Hendrikse and A. van den Berg, *Science*, 1999, **286**, 942–945.

Published on 24 May 2017 on http://pubs.rsc.org | doi:10.1039/9781788010283-00479

View Online

4. POC SPR devices have not yet entered the market, although it was foreseen a decade ago. What is the possible reason?

   Answer: An integrated SPR device was already developed in the 1990s (SPREETA chip, Texas Instruments) and the device did not result in entry into the POC market. Still, a label is less costly than a label-free device where the instrument can be considered as the ''label.'' Both instrument and disposable are more costly than, *e.g.*, a dipstick test and the SPR-based POC instrument should have additional advantages, *e.g.* highly multiplex and very fast, hence it may have a chance in this competitive market.

5. What are the problems in measuring biomolecular interactions on living cells? Why did the field of SPR cytometry not develop significantly and is still in its infancy?

   Answer: For many researchers, Biacore is synonym for SPR. The Biacore instrument is not suitable for measuring cell interactions with the sensor surface because the vulnerable fluidics cannot inject cells without the risk of clogging channels and valves. Further, the optics is on top, so sedimentation of cells that land on the sensor surface cannot be applied. A cell can be observed ''label free'' using a simple microscope and the binding to the surface can be measured, so SPR does not have additional advantages. Additionally, flow cytometry can detect single cells and the specific cell surface antigens can be ''colored'' using fluorescent antibody conjugates. Only certain applications such as highly multiplex cell surface affinity measurements and the McSPRinter approach, which are not covered by Biacore applications, are feasible directions for the SPR cytometry field.

Published on 24 May 2017 on http://pubs.rsc.org | doi:10.1039/9781788010283-00479

Published on 24 May 2017 on http://pubs.rsc.org | doi:10.1039/9781788010283-00508

Subject Index

Note: Page numbers in *italics* refer to figures or tables.

ABA-inject 269, *269*, 287
  buffer and *286*
adhesion linking layers
  for inorganic dielectrics 186
  for noble metal surfaces 184–6
  for plastics and carbon surfaces 186–7
adsorption
  analyte molecule 6
  of biomolecules, non-specific 187–9
  electrostatic 203
  polymers 185
  of proteins 185, 188–90, *193*
  Vroman sequence 188
adsorption–desorption process *4*
adsorptive immobilization 202–3
Affinité Instruments, P4SPR of 80, *80*
affinity
  analysis, fragment screening workflow 282–5
  characterization
    of immobilized human IgG binding *368*
    Octet 382–4
  constants determination using BLI
    binding kinetics 379
    ligand surface immobilization 378–9
    protein quantitation on Octet 384–8
    setting up kinetics assays 380–84
  plot 128, *129*
affinity ranking 296–7
  of cell surface antigens on living cells 463–4
  defined 296
  human IgG binding hepatitis C virus E2 protein 297–303
  with interpolated distribution analysis method 444–6
  with interpolation method 440–44
  rabbit IgG binding MHC–peptide complexes 303–4
    binding specificity + ranking 306–7
    capture sensor preparation 304
    multiple kinetic titrations 304–6
affinity screen, fragment screening workflow 281
air-park flow cell technology, with back-and-forth flow mixing 70–71
alanine scanning, anti-human parecho virus antibody AM18 320–23, *322*
aldehydes, immobilization through hydrazide groups 217–19
amine coupling
  and biotin capture *265*
  of proteins *265*
  reductive amination 211–12
  through reductive amination 211–13
  via reactive esters 208–210, 208–11

View Online

Published on 24 May 2017 on http://pubs.rsc.org | doi:10.1039/9781788010283-00508

amine-reactive biosensors 379
amino-acid skipping 313–14
aminopropyltriethoxysilane (APTES) 186
amphipoles (APols) 238, *239*
analysis cycle
  buffer solutions for measuring 20–22
  phases of 6, *7*
analyte 5
  association rate *137*, 137
  calibration curves 9–10
  concentration *136*, 136–7
    range 121
    and R_{eq} value 112–13, *136*, 136–7
    response levels of *111*, 111
  of depletion 66
  diffusion 116–18
  diffusion, surface structure between evanescent field and 175–80
  dissociation rate 137–9, *138, 139*
  dissociation times 140–41, *141*
  injection times 140, *140*
  and mass transport limitation 109
  purity, surface site distributions 164–7
  rebinding 117
  small molecules 10, 267
angle scanning instruments 46, 83
angle shift 46, 48, *49*
antibody–antigen interaction, kinetic binding analysis *166*
antibody AT33, epitope mapping 319
antibody AT44, epitope mapping 320
antibody 131-2G
  epitope binning 310, 312
  epitope mapping 319, 320
antibody immobilization 231–2, *232*
  protein A/G surfaces for 232–3
anti-CXCR4 antibodies 462, *463*
anti-His_6 antibodies 230
anti-human capture (AHC) biosensors 362, 365, 390
  comparison of dissociation constant *369*
anti-human parecho virus antibody AM18
  alanine scanning of 321–3, *322*
  epitope mapping 320–23
anti-mouse capture (AMC) biosensors 362, 390
anti-PSA antibody–PSA antigen binding assay
  assay steps and sequence for *382*
  on Octet 382–4, *383*
anti-rabbit-coated SPR capture sensor 304
anti-RSV G antibodies
  epitope mapping 313–20, *319, 320*
  peptides used for epitope mapping *314*, 315
apparent stoichiometry 267
aptamers, ligand immobilization 234
APTES 186
arginine–glycine–aspartic acid (RGD) motif 321–3
assay 5–13
  direct binding 256, 258, 259
  direct quantitation 386–7
  inhibition 24, 258, 260
  surface competition 258
  see also immunoassays
association *4*, *6*, 9
  constants 11–12, *11–12*
  curve 109
  kinetics 125
  phase 9
  rate *114*, 137, *137*
    analyte *137*, 137
    constants 128
    exponential curve 114–16, 137, *137*
  see also dissociation
atomic force microscopy 432
ATP binding *273*

View Online

Published on 24 May 2017 on http://pubs.rsc.org | doi:10.1039/9781788010283-00508

attenuated total reflection 36
autoimmune diseases *see* immunoassays
azlactone coupling 220

baseline 8–9, 20–21, 20–21, 108
  curve 108
  drift 108
  phase 8–9
benzophenones 224
β_2-microglobulin, binding of soluble *154, 163*
Biacore AB Corporation 97
Biacore instruments 71–3, *73*
  A100/4000 68, 70, 98–101, *100–101*, 123, 420
  Flexchip 51, 56, 94, *401*
    protein-GAG interaction 400–403, 411
  history 261
  8K 69, 101–2, *102*
  S200 98–100, 276
    affinity analysis 282
  T200 *98*, 98–100, 123, 280
Biacore's CM5 sensor chips 426
BiaMethodWriter 331–2
binding curve, exponential 106–8
binding kinetics, using biolayer interferometry 367–70
binding level screen
  analysis of 280
  fragment screening workflow 276
binding site specificity *285*, 285–7, *286*
bioinert matrices
  hydrogels 192–4
  non-specific adsorption 187–9
  ultralow-fouling two-dimensional surfaces 189–91
biolayer interferometry (BLI) 52, 54, 356–8
  affinity constants
    determination using binding kinetics 379
    ligand surface immobilization 378–9
    protein quantitation on Octet 384–8
    setting up kinetics assays 380–84
  binding kinetics using 367–70
  binding of propeptide of lysyl oxidase 409, *410*
  biosensors 359–61, *361*
  "dip and read" format 358, 371
  heparin (HP)-heparan sulfate (HS) interactions 407–11
  kinetics and affinity 407–11
  platforms 358
    specifications and capabilities of *360*
  relationship between R_{eq}, R_{max}, and K_D 370
biomolecular interactions 108, *108*
  identification of 401–3
  kinetics of 13–14
    calibration-free concentration analysis 16–17
    equilibrium analysis 19–20
    interaction-controlled kinetics 17–19
    mass transport-controlled kinetics 14–16
Bio-Rad 420–21
Biosensing Instruments *76*, 76–7
biosensors
  biolayer interferometry 359–61, *361*
  chip, nanocomposite coating of 171, *172*
  classification by applications 362, *363–4*, 365
  definition 2–3
  experiment, minimal requirements for 133–5
  history of 2
    after 1990 30–31
  regeneration of 365–7
  selection 361–5
    and assay orientation 394–6

View Online

Published on 24 May 2017 on http://pubs.rsc.org | doi:10.1039/9781788010283-00508

surfaces, interaction mechanisms on 172–5
see also sensor chip
BIOSUPLAR-6 (Analytical μ-System) *78*, 78
biotin *265*, 266
biotinylated ligands, immobilization of 226–7
biotinylation 226, 381, 394
biphasic curve 112, *118*, 118–19
blank injections 122
blank subtraction 278–9, 337
bovine serum albumin (BSA) 20, 455
Brewster angle 33
buffer selection 268–9
buffer solutions, for measuring analysis cycle
baseline or system buffer 20–21
regeneration buffer 21–2

calibration curve 9–10, *10*, 15, 17
calibration-free concentration analysis (CFCA) 10, 16–17, 267, *267*, 444
capture approaches
immobilization of proteins 265–6
immobilization of small molecules 266–7
capture immobilization method, on BLI biosensor 379
carbodiimides 209
carbohydrate epitopes, conjugation of *222*
carbohydrate ligands, immobilization of 219
carbon surfaces, adhesion linking layers for 186–7
carboxymethylated dextran *see under* hydrogels
cell surface antigens, affinity ranking 463–4
cell surface markers, quantification by flow cytometry 456–9
chip *see* sensor chip
circulating tumor cells (CTCs) 460
CLAMP software 334
clean screen, fragment screening workflow 274–6
click chemistry, ligand immobilization 220–22
ClonePIX technology 470, 471
coefficient of determination (COD) 378
coherence length 38–9
collagen I 407
collagen I–heparin interaction 409
competition assay 22–4
competitive epitope binning data analysis
assay formats 338–9, *339*
characterization using epitope binning 2.0 344–9
experimental design 339–40
compound refractive index increment 268
compound solubility 268
Comsol simulation, production rates of antibodies *466*
concentration determination 9–11
concentration measurement assays, setting up on Octet 386
conformational change 188
continuous flow microspotter (CFM)
dimensions of 424
in microfluidic printing technology 422–4
Continuous Flow Microspotter™ (CFM) 71, 94–5
continuous flow microspotting (CFM)
human IgG binding hepatitis C virus E2 protein 299
convection 176
converging beam fan-shaped instrument 49
counter-ion evaporation 189
covalent coupling 263–5
covalent immobilization 203
dry immobilization 206–8
covalent stabilization 230
curve fitting 128–30, 376
deviations from 1 : 1 interaction 131–2
local and global fitting 131

View Online

Published on 24 May 2017 on http://pubs.rsc.org | doi:10.1039/9781788010283-00508

curve fitting (*continued*)
measure of goodness of 378
residual plot 130
curves *see* interaction curves
cuvette systems 66–7
CXCR4 lipoparticles 462
Cytoscape 400

data acquisition, Octet 370–71
data analysis software packages 333–5
key features for *336*
design of experiments (DOE) 269
diffusion and diffusion layer 177, 195
analyte 116–18, 175–80
mass transfer kinetics 116–18
dimethyl sulfoxide (DMSO), concentration 119–20
dip 3–4
angle 3
detection 43–4
silver *vs.* gold layer *40*
dip to real-time measurement 4–5
direct assay 22
direct binding assay (DBA) 256, 258, 259
direct detection 10, 11, 172
directed immobilization 178, 231
direct immobilization, on BLI biosensor 378–9
direct label free detection 6
direct quantitation assay 386–7
dispersion
equations 33–5
relation, for surface plasmons *35*, 35–6
dissociation
constants 11–12, *11–12*, 107, 128, 288
equilibration *126*
exponential curve 115–16, 128
curve 109
kinetics 125
and mass transfer limitation 116–18
phase 9
rate 137–9, *138, 139*
times 140–41, *141*
distribution analysis 150, 159–61, *160*, 165, 179, 444–6
disulfide exchange, thiol coupling *via* 213–16
diverging fan-shaped beam 49
DMSO 269–70
solvent correction 270
DNA
electrostatic adsorption of 203
microarray 242
protein immobilization 233
drift 108, 119–20
drug development 287
drug target
GPCRs 272–3
kinases 273
dry immobilization 206–8

Easy2Spot 427–8
Easy2Spot preactivated G-type SensEye sensors 454
EDC–NHS 135, 198, 210, 211, 246, 298, 340
chemistry
coupling procedure 211
hydrazide activation 218–19
gold 419, 439
EDC–NHS coupling procedure 209–11
EDC/(sulfo) coupling 211
electrochemical SPR (E-SPR) application 434–5
electrochemistry 76
electroosmotic flow pumping 433–4, *434*
electroosmotic microfluidic devices 433–4
electrosorption, ligand immobilization 202–3
electrostatic immobilization 202–3
electrostatic interactions 174, 175, 189

View Online

Published on 24 May 2017 on http://pubs.rsc.org | doi:10.1039/9781788010283-00508

electrostatic preconcentration 204–6
ELISA 391
  for affinity ranking 296
  conversion on Octet 385
endostatin–heparin interaction 409
entropic stabilization 192
EOF 434
epithelial cell adhesion molecule (EpCAM) 453, 471, *473*
epitope binning 307–8
  antibody 131-2G 310
  bin 1 antibodies 312
  defined 307
  Octet use in 389–91
  of respiratory syncytial virus glycoprotein 309–12, *311*
  strategies for *308*
epitope binning 2.0, characterization using 344–9
epitope mapping
  amino acid skipping 313–14
  antibody AT33 319
  antibody AT44 320
  antibody 131-2G 319, 320
  anti-RSV G antibodies 313–20, *319, 320*
    peptides used for *314*, 315
  bin 1 antibodies 319
  defined 313
epoxy-mediated immobilization 219–20, *221*
equilibrium analysis
  on curves 123–5, *124, 125*
  kinetics of biomolecular interactions 19–20
equilibrium constants 11, 14
equilibrium curve 110
equilibrium dissociation constant *443*
equilibrium signal 19
ESPRIT (KE-Instruments) 83–4, *84*
1-ethyl-3-(3-dimethylaminopropyl)-carbodiimide (EDC) 11, 211
  amine coupling 209–10
  see also EDC–NHS
evanescent field 4, 32–33, 41, 54–56, *176*
  dimensions of *177*
  and hydrogel thickness 197, 198
  intensity decay *176*
  and optical requirements 63
  surface structure between analyte diffusion and 175–80
evanescent wave 31–3
EvilFit software, affinity ranking 444–6
excitation of surface plasmons 35–7
excluded volume (EV) correction 335–6
exponential binding curve 106–8
exponential interaction curve 106–8, *108*, 114–16, *115*
extracellular matrix (ECM) 398–9
  GAG-binding proteins in 405
  heparin/heparan sulfate interactions 407
extracellular vesicles (EVs) monitoring 459–61
extrinsic defects, self-assembled monolayers *196*
EzPlex of Horiba Scientific 90, *90*

fan-shaped beam instruments 48–50, *50*, 71–7
fast association 125
fast dissociation 125
fast kinetics 125
FastStep® 77
FcRn–antibody interactions, Octet using 393–6
fiber-based SPR sensors 51–4, *53*
  development of 52
fiber Bragg gratings 53
fiber-optic SPR device (FOSPR) (FOx Diagnostics) 87–9, *88*
field enhancement 37–8
field of view, lateral resolution over 44–6
fixed angle instrument, BIOSUPLAR-6 (Analytical μ-System) *78*, 78

View Online

Published on 24 May 2017 on http://pubs.rsc.org | doi:10.1039/9781788010283-00508

fixed angle 47–8
fixed-boundary centroid algorithm 43, *43*
fixit protocol 428–30
Flexchip instrument 94, 97, 98
  gold affinity chip *401*, 402–3
"floating align point" 301, 442
flow cells 93, 99, 135
  hydrodynamic addressing (HA) 100
  planar 68–70
flow cytometry, cell surface markers quantification 456–9
flow systems 68–71
fluidics *see* microfluidics
fluorescence-activated cell sorting (FACS), for affinity ranking 295
fluoro-SPR 76
FortéBio's BLI technology 361–2
404pi (Bioptix) 84–5, *85*
fragment screening workflow
  affinity analysis 282–5
  affinity screen 281
  binding level screen 276
  clean screen 274–6
  compound solubility and concentrations in 268
  data analysis – report points and curve shapes 276–7
    report point 277–80, *278, 279*
    sensorgram 280–81
  fragment libraries 274
  site specificity – use of blocked or saturated targets *285*, 285–7
Fresnel equation 33, 35–37
FunRich tool 400, 405

gauche defects 185
GE Healthcare 71–3, 97–8
  Biacore A100/4000 100–101, *100–101*
  Biacore AB Corporation 97
  Biacore 8K 101–2, *102*
  Biacore S200 98–100
  Biacore T100 98–100
  Biacore T200 *98*, 98–100
global fitting 131
global kinetic data analysis, Scrubber 2.0 HT 340–53
glucose sensor 2
glutathione *S*-transferase (GST) capture 231
glycidylpropyltrimethoxysilane (GPTMS) 186
glycoproteins 217, 297
  oxidation 218
glycosaminoglycans (GAGs) 399, 401, *406*
gold layer 37, 39–41, 46
  adhesion linking layers 171, 185–6
  and coherence length 38–39
  and electroosmotic flow devices 433–4
  SPR sensor chips 180, *181*, 182
  3D STM images *181*
gold nanoparticles (GNP) 78, 419, 439
G protein-coupled receptors (GPCRs) 234, 272–3
  capture and reconstitution of *237*
GPTMS 186
gradient chemistries 424–6
gradient printing, for multiplex sensing 424–6
grating coupler 51, *52*, 98

HCV binding 307
heparin (HP)-heparan sulfate (HS) interactions 399, 403, 405, 407
  bio-layer interferometry 407–11
  kinetic parameters and equilibrium dissociation constant *410*
hepatitis C virus (HCV) E2 protein
  affinity ranking 297–303
  binding antibodies 299, *300*, 301, *301*
high-affinity binders 303
high-capacity capture 263–5

View Online

Published on 24 May 2017 on http://pubs.rsc.org | doi:10.1039/9781788010283-00508

higher order reaction, surface site distributions calculation 157–8
His_6 tagged ligands 227–31
HTX instrument 359, 371
human IgG binding hepatitis C virus E2 protein, affinity ranking 297–303
human leukocyte antigen (HLA) 464
human parechoviruses (HPeV) 321
human serum albumin (HSA) 20
hydrate biosensors 386
hydrazide activation/coupling 218–19
hydrodynamic addressing/isolation 70, 92–3
  flow cell 100
hydrogels 192–4
  bioinert 192–4
  protein-compatible polymers/functionalities 194, *194*
    dextran 30, *173*, 207
    epoxy activation 219–20, *221*
    film density 198–9
    film thickness 197, 198
    filter layers 199, *200*
    surface chemistry 192–4
    synthetic polycarboxylates 197
    three-dimensional nanoarchitecture 197–201
    two-dimensional surfaces 195–7
  surface stabilization 192
  three-dimensional 197–201
hydrophilic interactions 198
  protein-compatible polymers *194*
hydrophilic, protein-compatible polymers *194*
hydrophobic interactions 21, 173–5, 175, 188, 189, 202
hyphenated SPR technology
  electrochemical SPR (E-SPR) application 434–5
  lab-on-a-chip 432–4
  other techniques 431–2
  SPR and mass spectrometry 430–31

IBIS MX96 microarray imaging 56, 70–71, *94*, 94–5, 122, 304, 453, 461–2, 465
IgG titer determination, using Octet biosensors *366*
image averaging 44
imaging instruments 55–56, 89–97
  IBIS *i*SPR 94
    see also microarray imaging
immobilization
  ligand *see* ligand immobilization
  of proteins 262–3, *263*
    amine coupling *265*
    capture approaches 265–6
    covalent coupling or high-capacity capture 263–5
  of small molecules, capture approaches 266–7
immobilization matrices *see* bioinert matrices
immunoassays
  competition assay 22–4
  direct assay 22
  inhibition assay 24
  sandwich assay with secondary antibody and signal enhancers 24
Indicator-G (Sensia) 78–9, *79*
infliximab (IFX), detection of 89
influenza vaccine titer 392–3
information content, surface site distributions 158–61
inhibition assay *23*, 24, 258
inhibition in solution assay (ISA) 24, 258, 260
injection times, analytes 140, *140*
inorganic dielectrics, adhesion linking layers for 186

View Online

Published on 24 May 2017 on http://pubs.rsc.org | doi:10.1039/9781788010283-00508

instrumentation
  basics 12–13
  future trends 417–420
  general optical requirements 63–5
  imaging instruments 55–6
  interferometers 54
  liquid handling systems 65–6
    cuvette systems 66–7
    flow systems 68–71
  optical systems 46–7
    fan-shaped beam 48–50
    fiber-based SPR sensors 51–4
    fixed angle 47–8
    grating coupler 51
    imaging 55–6
    other 54–5
    scanning angle 50–51
  resonant mirror 55
  wavelength interrogation 55
instruments reviewed
  fan-shaped beam
    Biacore instruments (GE Healthcare) 71–3, *73*
    Biosensing Instruments *76*, 76–7
    Pioneer FE (SensiQ Technologies) 77, *77*
    Reichert SR7500DC and 4SPR instruments *74*, 74–5
  fixed- and scanning-angle, BIOSUPLAR-6 (Analytical μ-System) *78*, 78
  general optical requirements 63–5
  imaging instruments
    IBIS MX96 instrument *94*, 94–5
    MASS-1 (Sierra Sensors) 93, *93*
    MASS-2 (Sierra Sensors) 93, *93*
    Plasmon Imager® (Graffinity Pharmaceuticals) 92
    PlexArray® HT System (Plexera) 91–2, *92*
    ProteOn™ XPR36 (Bio-Rad Laboratories) 91, *91*
    SPRimager® II (GWC Technologies) 89–90
    Wasatch Microfluidics 94, *94*
    Xel-Plex™ OpenPlex (Horiba Scientific) 90–91
  label-free biosensing
    fiber-optic SPR device (FOSPR) (FOx Diagnostics) 87–9, *88*
    404pi (Bioptix) 84–5, *85*
    LFIRE™ (Maven Biotechnologies) 84, *85*
    MicroScale Thermophoresis (MST) (Nanotemper Technologies) 85–7
    NeoSensors 84
    Sapidyne Instruments (KinExA®) 87, *88*
  liquid handling systems 65–6
    cuvette 66–7
    flow systems 68–71
  and their manufacturers *61*
in-tandem epitope binning 389, *390*
integrated (micro)fluidics cartridge (IFC) technology 68, *69*, 420
interaction arrays 91
interaction-controlled kinetics 17–19
interaction curves
  association 109
  baseline 108
  biphasic 112, *118*, 118–19
  dissociation 109
  drift, jumps and spikes 119–20
  equilibrium and saturation 110
  exponential 106–8, *108*, 114–16, *115*
  fitting *see* curve fitting
  mass transport limitation 116–18

View Online

Published on 24 May 2017 on http://pubs.rsc.org | doi:10.1039/9781788010283-00508

maximal response (R_{max}) value 110–12
publications 132–3
evaluating results 133–4
R_{eq} value 112–13
response 112
response units 109–10
shape 114
simulation of *134*, 135–6
analyte concentration *136*, 136–7
association rate *137*, 137
dissociation rate 137–9, *138, 139*
dissociation times 140–41, *141*
injection times 140, *140*
steady state 109
time to reach equilibrium 113–14
validation 132
intermediate affinity binders 303
inter-step correction 375
intrinsic defects, self-assembled monolayers *196*
intrinsic effect 41

jumps 119–20

K_D^{R0} method, for affinity constants 441
kinases 273
binding of *273*
kinetic data analysis, software tools for SPR applications
experimental design 349
preprocessing of data using SPRint 349–50
in Scrubber 2.0 HT 340–53
kinetic parameters
accurate measurement of *8*
association and dissociation constants 11–12, *11–12*
determination of 11–12
kinetics *139*, 139–40
determination of parameters 2, 11–12
kinetics data analysis
definitions, on Octet 377–8
Octet 374–7
kinetic titration 122–3
Kretschmann configuration 12, 28, 30, 36, 46, 51, 63, 74, 78, 84, 90

label-free biosensing instruments 84–8
label-free cell membrane antigen profiling 447–52
label-free cell profiling *464*
labeling 22
lab-on-a-chip 54, 432–4
Langmuir isotherm 19
Langmuir model 13, *18*
lateral resolution 425, 432
over field of view 44–6
lead optimization 288–90
lead workflow
off-rate screening 287–8
optimization 288–90
LFIRE™ (Maven Biotechnologies) 84, *85*
ligand 5
saturation 110
surface decaying 125–6, *126*
surface immobilization 378–9
ligand–analyte (LA)
complexes 107
interaction, distribution analysis *445*
ligand density 229
ligand equilibrium 110
ligand immobilization 194, *195*, 197, 210, 296, 298, 380, 427
adsorptive methods 202–3
of aldehydes through hydrazide groups 217–19
amine coupling
through reductive amination 211–13
via reactive esters 208–11
azlactone coupling 220
biotinylated 226–7
with click chemistry 220–22

View Online

Published on 24 May 2017 on http://pubs.rsc.org | doi:10.1039/9781788010283-00508

ligand immobilization (*continued*)
coupling through epoxy groups 219–20
coupling through photocrosslinking 222–5, *224*
covalent coupling 203–4
dry immobilization 206–8
electrostatic preconcentration 204–6
electrostatic preconcentration 204–6
membrane proteins 234–8
optimization of 379, 381
overview and selection of 238–41
process, surface site distributions 161–4
spatially resolved 242–7
strategies *240–41*
surface 378–9
thiol coupling
via disulfide exchange 213–16
via maleimides 216–17
via molecular linkers
DNA-directed protein 233
of His-tagged ligands 227–30
protein A/G surfaces for antibody 232–3
streptavidin–biotin coupling 225–7
of and through aptamers 234
of and *via* antibodies 231–2
lipid bilayers, on-surface reconstitution of 236–7
lipoparticles, detection of 462
liquid handling systems *see under* instrumentation
local fitting 131
localized SPR (LSPR) sensor chips, plasmonic nanostructures 182, *183*
long-period fiber gratings (LPFGs) 53
long-range surface plasmons 182
low molecular weight (LMW) analysis
comparison of assay formats *260*
direct binding assay 256, 258, 260
selection of 258–60
solution competition or inhibition in solution assay 258, 260
surface competition assay 258
low-quality sensorgram *127*

major histocompatibility complex (MHC) class I molecules 464
major histocompatibility complex (MHC)–peptide, affinity ranking of rabbit IgG binding 303–7, *307*
maleimides, thiol coupling *via* 216–17
manufacturers *see* instruments reviewed
MASS-1 (Sierra Sensors) 68
mass spectrometry (MS) 76, 430–31
mass transport-controlled kinetics 14–16
mass transport limitation (MTL) 15, *15*, 116–18
interaction curves 116–18
surface site distributions calculation 155–7
mass transport model 376
MatrixDB, protein-GAG interaction 403–6
maximal response (R_{max}) value 110–12
MCF7 cells, expression of markers on 455, *455*
McSPRinter, in cell selection 417, 467–74
ClonePIX technology 470–71
features and benefits 470

View Online

Published on 24 May 2017 on http://pubs.rsc.org | doi:10.1039/9781788010283-00508

principle of *469*
process flow chart of 472, *472*
membrane protein immobilization 234–8
mercaptoalkyls 184
metal layer, of sensor chips 180–83
micelles, mixed 236
microarray imaging, IBIS MX96 56, 70–71, *94*, 94–5, 122, 304, 453, 461–2, 465
microarray spotting, on SPR sensor chips 421–4
microfluidic devices, electroosmotic flow 433–4, *434*
microfluidics, trends in 420–21
fixit protocol 428–30
microarray spotting on SPR sensor chips 421–4
SensEye anti-IgG 428–30
SensEye® Easy2Spot 427–8
SensEye protein A/G 428–9
sensor surfaces 426–7
microwell cell selection, using SPRi cytometry 467–74
microwell chip *467*
mixed micelles, preparation of 236
MP-SPR Navi™ (BioNavis) 81–3, *82*
multi-cycle kinetics 122
multilayered system 41
multi-parametric surface plasmon resonance (MP-SPR) Navi™ (BioNavis) 81–3, *82*

nanoarchitecture 194–5
three-dimensional hydrogels 197–201
two-dimensional surfaces *195*, 195–7
nanoparticle-based localized SPR (LSPR) 417–19
nanoparticles
gold 78, 419, 439
surface plasmons and 41–42
NanoSPR8 481 of NanoSPR LLC *80*, 80–81
nanostructures, for applications *201*
negative control 271–2
NeoSensors 84
NHS *see* EDC–NHS
(sulfo)NHS esters, aminolysis of 210
N-hydroxysuccinimide *see* EDC–NHS
Ni-NTA biosensors 362
96-channel HTX instrument 359
nitrilotriacetic acid (NTA) 225, 228, 229
surfaces, capture on 263, 266
NMR 274
noble metal surfaces, adhesion linking layers for 184–6
non-random residuals *130*
non-specific adsorption, bioinert matrices 187–9
non-specific binding (NSB) 160, 172, 187–9, 316, 336, 380
of bovine serum albumin 316, *317*
matrix components 172–5
sites 160, 161
non-SPR instruments, label-free monitoring of biomolecular interactions 72
normalization/calibration 335
NTA 225, 228, 229

O-acylisourea 210
Octet
affinity characterization 382–4
basic kinetics data analysis 374–7
data acquisition 370–71
dip and read format 391
equations used in 1 : 1 fit model for *384*
kinetics data analysis definitions 377–8
protein quantitation on 384–8
quantitation data analysis 372–4
use in epitope binning 389–91
in virus titer studies 391–3

View Online

Published on 24 May 2017 on http://pubs.rsc.org | doi:10.1039/9781788010283-00508

Octet biosensors
IgG titer determination using *366*
regeneration of 365–7
Octet 384 instrument 359, 371
Octet Red96 instrument 359
off-rate screening 287–8
oligonucleotides 202, 237
1 : 1 Langmuir interaction 129
1 : 1 model binding 441
OneStep® 77
1 : 2 bivalent analyte model 376
Open-SPR (Nicoya) 78, *79*
optical fiber biosensing, development of 52
optical systems *see under* instrumentation

Pan Assay INterference compoundS (PAINS) 274
peptide–human leukocyte antigen (pHLA) 464
Pharmacia Biosensor 30, 97
phosphatebuffered saline (PBS) 20
photocrosslinking, coupling through 222–5, *224*
photophore 224
pH regeneration 21–2
Pioneer FE (SensiQ Technologies) 77, *77*
planar flow cells 68–70
plasma deposition 187
Plasmon Imager® (Graffinity Pharmaceuticals) 92
plasmon resonance imaging (SPRi) cytometry 446–7
affinity ranking of cell surface antigens on living cells 463–4
extracellular vesicle monitoring using 459–61
with interpolation method 440–44
label-free cell membrane antigen profiling 447–52
microwell cell selection 467–74
quantifying production rate of molecules per individual cell 465–7
quantifying ratio of surface antigens per cell population 452–9
plasmons *see* surface plasmons
plastics, adhesion linking layers for 186–7
PlexArray® HT System (Plexera) 91–2, *92*
point-of-care (POC) devices 435–6
reasons for non-availability 437
signal enhancement cascade for boosting dynamic range 437–9
theranostics 436–7
polarization 36
polyhistidine (HIS) 394
poly-nitrilotriacetic acid (NTA) 229
positive control 271–2
p-polarized light 3, 12, 28, 46, 49
pre-assay studies 331
preconcentration methods 204–6
premix binning 308, *308*
premix epitope binning 389–90
prostate-specific antigen (PSA), binding with anti-human PSA mouse monoclonal antibody 382–4
protein A/G biosensor surfaces 362, 392
for antibody immobilization 232–3
protein–GAG interaction networks building and functional analysis of 403–6, *404–6*
kinetic and affinity 407–11
roadmap 400–401
protein G biosensor 392
protein microarrays
disulfide reduction 214
fabrication 242, *243, 244*
immobilization 234–8
protein–protein interaction (PPI) targets 260

View Online

Published on 24 May 2017 on http://pubs.rsc.org | doi:10.1039/9781788010283-00508

proteins
activity 267–8
adsorption models *193*
immobilization of *see* immobilization of, proteins
quantitation on Octet 384–8
ProteOn™ XPR36 (Bio-Rad Laboratories) 56, 91, *91*
P4SPR of Affinité Instruments 80, *80*

QuantiBRITE phycoerythrin (PE) method 453, 456, 457
quantitation data analysis, on Octet 372–4

rabbit anti-human serum albumin IgG (aHSA) 428, *439*
rabbit IgG binding MHC–peptide complexes, affinity ranking 303–6
random residuals *130*
rate constants 9, 12
kinetic 99, 111, 136, 160
reaction rate 11, 16
reactive esters, amine coupling *via* 208–11
rebinding 117, 381
analyte 117
red blood cell (RBC) antigens
binding of *450*, 451–2
SPR imaging detection 447–52, *451*
reductive amination, amine coupling through 211–13
reference RoI 44
referencing 336–7
reflectance 33, 39, 40
reflectivity 42, 43, 45
change 47, 49, 50, 64, 95
as function of scan angle *45*
refraction *32*
and evanescent wave 31–33
SPR principles 28
refractive index (RI) 54, 83
jumps 131, *131*
resolution 42–3
regeneration 174, *174*
buffer 9, 21–2
Octet biosensors 365–7
phase 9
solution 6–7, 9, 337
region of interest (ROI) 44, 449, 454
Reichert 4SPR instrument *74*, 74–5
Reichert SR7500DC instrument *74*, 74–5
reliable kinetic parameters, trends in measuring 439–40
affinity ranking
interpolated distribution analysis method 444–6
with interpolation method 440–44
report point analysis 277–80, *278*, *279*
R_{eq} value 112–13
residual plot 130
resolution, lateral 44–46, 425, 432
resonance 33–5
resonance unit (RU) 13
resonant mirror 55
measurements 54
respiratory syncytial virus (RSV) glycoprotein
epitope binning of 309–12, *311*
kinetic titration of *310*
response units (RU)
curve 109–10
rhodopsin 266
R_{max} value 110–12, 140

SAMs 180, 184–5, 190, *196*
sandwich assay 24
sandwich epitope binning 390
Sapidyne Instruments (KinExA®) 87, *88*
saturation curve 110
scanning angle 50–51
instruments, BIOSUPLAR-6 (Analytical μ-System) *78*, 78
Scheimpflug condition 44, 45
Schiff base, reductive amination 211–12
Screener 334

View Online

Published on 24 May 2017 on http://pubs.rsc.org | doi:10.1039/9781788010283-00508

Scrubber 334
Scrubber 2.0 HT, global kinetic data analysis in 340–53
second-generation amine reactive biosensors (AR2G) 362
self-assembled monolayers (SAMs) 180, 184–5, 190, *196*
  extrinsic defects *196*
  intrinsic defects *196*
SensEye anti-IgG 428–30
SensEye® Easy2Spot 427–8
  affinity ranking of HCV 298–9
  benefits 427
SensEye protein A/G 428–9
Sensor Chip CM7 265
sensor chips *3*
  features of 12
  metal layer 180–83
  microarray spotting on 421–4
  nanoarchitecture *172*, 194–5
    elements of 171–2
    three-dimensional hydrogels 197–201
    two-dimensional surfaces *195*, 195–7
    for various applications *201*
    see also adhesion linking layers; bioinert matrices; ligand immobilization
  trends in 426–30
sensorgram 48
  analysis 280–81
    of binding level screen *281*
  concentration determination 9–11, *10*
  of covalent immobilization cycle *173*
  dip to real-time measurement *4*, 4–5
  high-salt and buffer injection *120*
  phases of analysis cycle 6, 9, *10*
  of photoimmobilization cycle 223
  quality 127–8
SERS 41
seven transmembrane (7TM) receptors 272
shape of curve 114
signal correction software 335
signal-to-noise ratio (SNR) 42, 43
silanes 182, 186
silanization, of glass substrates with trialkoxysilanes *187*
silver layer 28–30, 38
    and coherence length 38
    SPR-dip for *40*
simulation of interaction curves 135–6
single-cell protein, quantification of 465–7
single-cycle kinetics 122–3, *123*
single radial immunodiffusion (SRID) assays 391–2
single-stranded DNA (ssDNA), hybridization of 233
single VU1D9 cell, production 466
size-exclusion chromatographic (SEC) purification 165
small molecules 10, 11, 177
Snell's law 31
software tools for SPR applications *332*
  data analysis 333–5
  fundamental data processing techniques
    blank subtraction 337
    excluded volume correction 335–6
    normalization/calibration 335
    referencing 336–7
    x-scale alignment 337
    y-scale zeroing 337
  general considerations 329–31
  kinetic data analysis
    experimental design 349
    preprocessing of data using SPRint 349–50
    in Scrubber 2.0 HT 340–53

View Online

Published on 24 May 2017 on http://pubs.rsc.org | doi:10.1039/9781788010283-00508

for pre-assay planning 331–2
pre-assay studies 331
solution competition assays 258
solvent correction 270–71, *271*
spatially resolved ligand immobilization 242–7
spectrophotometer 54
spikes 119–20
SPREETA chip 437
SPRi-Lab+™ detector 90
SPRimager® II (GWC Technologies) 89–90
SPR imaging sensor, functions 472
SPRINGLE (KE-Instruments) 83–4, *84*
SPRint, data preprocessing using
competitive epitope binning 340–43
kinetic analysis 349–50
SPRi-Plex™ model 90
SPR–mass spectrometry 76
SPRmicro and SPRi™ (K-MAC (Korea)) *61*, 82, *83*
stagnant layer 65, 177
steady-state analysis 376, 377
steady state curve 109
steady-state group K_D (SSG K_D) value 378
streptavidin (SA) biosensors 362, 389, 390
biotinylation 381
SPR image of *316*
streptavidin–biotin coupling 225–7
streptavidin–biotin linkers 24
streptavidin-modified surfaces 226–7
structure–kinetic relation (SKR) 289
surface antigens per cell population, quantifying ratio of 452–9
surface binding 440
sites, heterogeneity of 151, *152*
surface chemistry *see* sensor chips
surface competition assay (SCA) 258, 260
surface-grafted hydrogels 197–8
structural differences *198*
surface plasmon fluorescence spectroscopy (SPFS) 431
surface plasmon resonance (overview) 1–2
assay 5–13
buffer solutions for measuring the analysis cycle 20–22
calibration curve 9–10, *10*, 15, 17
dip to real-time measurement 4–5
history 1
immunoassays 22–4
instrumentation 12–13
kinetics of biomolecular interactions 13–20
surface plasmons
basic principles 28
coherence length 38–9
dispersion equations 33–5
dispersion relation *35*, 35–6
evanescent wave 31–3
excitation of 35–7
experimental parameters 39–42
field enhancement 37–8
on gold layer 39–41
imaging performance optimization
dip detection 43–4
lateral resolution over the field of view 44–6
refractive index resolution 42–3
long-range 182
and nanoparticles 41–42
properties 37–9
resonance 33–5
surface referencing 336
surface site distributions, calculating
affinity and kinetic rate *164*
analyte purity 164–7
basic principle 153–5
effect of sensor surface 161
higher order reaction 157–8
information content 158–61
ligand immobilization process 161–4
mass transport limitation 155–7

View Online

systematic evolution of ligands by exponential enrichment (SELEX) 234
system buffer 20–21

tandem blocking 308, *308*
target immobilization, defined 263
temperature stabilization 64
theranostics, point-of-care 436–7
thioethers 184, 185
thiol coupling
  via disulfide exchange 213–16, *215*
  via maleimides 216–17
thiols 185
three-dimensional hydrogels 197–201
Tikhonov regularization 155
TraceDrawer 334
tris-nitrilotriacetic acid (NTA) 229
tris-NTA–His_6 tag binding pair 230
TWINGLE (KE-Instruments) 83
two-dimensional surfaces *195*, 195–7

ultralow-fouling two-dimensional surfaces 189–91

virus-like particles (VLPs) 462
virus titer studies, Octet in 391–3
Vroman sequence 6, 188

wall-jet flow cell 68
Wasatch Microfluidics 71, 94, *94*
  CFM spotter 454
wavelength interrogation 42, 55
weak affinity binders 303

XelPlex of Horiba Scientific 90
X-ray crystallography 274
x-scale alignment 337, *343*

y-scale zeroing 337, *343*

Z' values 271–2

Published on 24 May 2017 on http://pubs.rsc.org | doi:10.1039/9781788010283-00508